**UNIVERSIDAD NACIONAL AUTÓNOMA DE MÉXICO**
PROGRAMA DE DOCTORADO EN ASTROFÍSICA
ASTROFÍSICA TEÓRICA

A POLARIZATION FOCUSED STUDY OF THE NON-THERMAL
EMISSION ON KILONOVA SCENARIO

TESIS
QUE PARA OPTAR POR EL GRADO DE:
DOCTOR EN CIENCIAS (ASTROFÍSICA)

PRESENTA:
AUGUSTO CÉSAR CALIGULA DO ESPIRITO SANTO PEDREIRA

TUTOR PRINCIPAL
DR. NISSIM ILLICH FRAIJA CABRERA
INSTITUTO DE ASTRONOMÍA

CIUDAD UNIVERSITARIA, CD. MX., FEBRERO, 2023
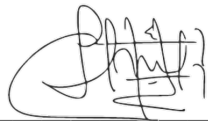
JURADO ASIGNADO:

Jurado:       Dr. Hermes León Vargas

Jurada:       Dra. Rosa Leticia Becerra Godínez

Jurado:       Dr. Simone Dichiara

Jurado:       Dr. Dany Pierre Page

Jurado:       Dr. Cristian Giovanny Bernal

La tesis se realizó en el Instituto de Astronomía, UNAM-CU.

TUTOR DE TESIS:

Dr. Nissim Illich Fraija Cabrera
Instituto de Astronomía, Ciudad Universitária

_____

# Declaración de autenticidad

Por la presente declaro que, salvo cuando se haga referencia específica al trabajo de otras personas, el contenido de esta tesis es original y no se ha presentado total o parcialmente para su consideración para cualquier otro título o grado en esta o cualquier otra Universidad. Esta tesis es resultado de mi propio trabajo y no incluye nada que sea el resultado de algún trabajo realizado en colaboración, salvo que se indique específicamente en el texto.

Augusto César Caligula do Espirito Santo Pedreira. Ciudad Universitaria, CD. MX., Febrero, 2023

# Resumen

Los destellos de rayos gamma (GRBs, por sus siglas en inglés) son destellos violentos de rayos $\gamma$ producidos de forma transitoria, con una duración que oscila entre unos pocos y cientos de segundos, que surgen debido a la muerte de estrellas masivas o coalescencia de objetos compactos. Sin embargo, a pesar de más de 50 años de trabajo, gran parte de la física subyacente de estos eventos sigue siendo un misterio.

En esta tesis, nuestro objetivo es utilizar los avances recientes en polarimetría de GRBs para explorar un análisis multifacético de los datos observacionales en torno a estos objectos. Nuestro objetivo es estudiar los escenarios de GRB cortos, que se cree que están vinculados a la coalescencia de objetos compactos y kilonovas, pero no nos limitamos a este escenario.

Nuestro trabajo se basa fundamentalmente en el análisis tradicional de la curva de luz de los GRBs con un enfoque adicional de exploración del modelado de los datos de polarización de GRBs observados. Creemos firmemente que este enfoque dual es importante para el futuro de la investigación de GRBs, ya que la exploración de las propiedades de polarización nos permite obtener información sobre la topología del campo magnético en diferentes épocas del estallido y corroborar la evidencia obtenida mediante el modelado de curvas de luz. Este último es extremadamente relevante con respecto a la degeneración típica del modelo de sincrotrón, y una aplicación que exploramos.

Presentamos en este documento el trabajo realizado durante el período del año calendario de 2019 a 2022. En el Capítulo 1 incluimos una explicación introductoria de los GRBs y algunos de sus principios subyacentes. En el Capítulo 2 presentamos un breve resumen de una técnica estadística fundamental para la mayor parte de nuestro trabajo, las simulaciones de Markov Chain Monte Carlo (MCMC). En el Capítulo 3 presentamos el texto completo de los resultados publicados en revistas de renombre, incluidos algunos que aún se encuentran en proceso de revisión, junto con un breve resumen de cada uno. Estos resultados se dividen en bloques, donde un artículo es continuación del trabajo anterior o está relacionado con él. Finalmente, en el Capítulo 4 ofrecemos nuestras conclusiones.

# Abstract

Gamma-Ray Bursts (GRBs) are violent flashes of $\gamma$-rays produced transiently, with duration ranging from a few to hundreds of seconds, arising due to the death of massive stars or coalescence of compact objects. However, despite more than 50 years of work, much of the underlying physics of these events remains clouded in mystery.

In this thesis, we aim to use the recent advances in GRB polarimetry to explore a multi-faceted analysis of GRB observational data. We aim to study the scenarios of short GRBs, believed to be linked to the coalescence of compact objects and kilonovae, but do not limit ourselves to this scenario.

Our work is fundamentally based on the traditional light curve analysis of GRBs with an added approach of exploring the modeling of observed GRB polarization data. We strongly believe such dual approach important to the future of GRB research, as the exploration of polarization properties allows us to obtain information regarding magnetic field topology across different epochs of the burst and to corroborate the evidence obtained by light curve modeling. The latter being extremely relevant regarding typical synchrotron model degeneracy, and one application that we explore.

We present in this document the work completed during the calendar year period of 2019 to 2022. In Chapter 1 we include an introductory explanation of GRBs and some its underlying principles. In Chapter 2 we present a short summary of a statistical technique fundamental to most of our work, Markov Chain Monte Carlo (MCMC) simulations. In Chapter 3 we present the full text of results published in renowned journals, including some still in the peer-review process, along with a short summary of each. These results are divided in blocks, where one paper is a continuation of the previous work or related to it. Finally, in Chapter 4 we offer our concluding remarks.

# Full List of Publications

First Author Publications:

- **Pedreira, A. C. C. d. E. S.**, Fraija, N., Galvan-Gamez, A., Betancourt Kamenetskaia, B., Veres, P., Dainotti, M. G., Dichiara, S., Becerra, R. L., 2022, Afterglow Polarization from Off-Axis GRB Jets, in press, ApJ, doi: 10.48550/ARXIV.2210.12904

- **Pedreira, A. C. C. d. E. S.**, Fraija, N., Galvan-Gamez, A., Betancourt Kamenetskaia, B., Dichiara, S., Dainotti, M.G., Becerra, R. L., Veres, P., 2022, Polarization From A Radially Stratified Off-Axis GRB Outflow, MNRAS(Submitted), doi: 10.48550/ARXIV.2211.12477

- **Pedreira, A. C. C. d. E. S.**, Fraija, N., Dichiara, S., Veres, P., Dainotti, M. G., Galvan-Gamez, A., Becerra, R. L., Betancourt Kamenetskaia, B., 2022, Exploring the Early Afterglow Polarization of GRB 190829A, ApJ (Submitted), doi: 10.48550/ARXIV.2210.12904

Collaborator:

- Fraija, N., De Colle, F., Veres, P., Dichiara, S., Barniol Duran, R., Galvan-Gamez, A., **Pedreira, A. C. Caligula do E. S.**,2019, ApJ, 871, 123, doi: [10.3847/1538-4357/aaf564](10.3847/1538-4357/aaf564)

- Fraija, N., **Pedreira, A. C. C. d. E. S.**, & Veres, P. 2019, ApJ, 871, 200, doi: [10.3847/1538-4357/aaf80e](10.3847/1538-4357/aaf80e)

- Fraija, N., Dichiara, S., **Pedreira, A. C. C. d. E. S.**, Galvan-Gamez, A., Becerra, R. L., Barniol Duran, R., Zhang, B. B., 2019a, ApJ, 879, L26, doi: [10.3847/2041-8213/ab2ae4](10.3847/2041-8213/ab2ae4)

- Fraija, N., Lopez-Camara, D., **Pedreira, A. C. C. d. E. S.**, Betancourt Kamenetskaia, B., Veres, P., Dichiara, S, 2019, ApJ, 884, 71, doi:[10.3847/1538-4357/ab40a9](10.3847/1538-4357/ab40a9)

- Fraija, N., Dichiara, S., **Pedreira, A. C. C. d. E. S.**, Galvan-Gamez, A., Becerra, R. L., Montalvo, A., Montero, J., Betancourt Kamenetskaia, B., Zhang, B. B., 2019, ApJ, 885, 29, doi: [10.3847/1538-4357/ab3e4b](10.3847/1538-4357/ab3e4b)

- Fraija, N., De Colle, F., Veres, P., Dichiara, S., Barniol Duran, R., **Caligula do E. S. Pedreira**, A. C., Galvan-Gamez, A., Betancourt Kamenetskaia, B., 2020, ApJ, 896, 25, doi: [10.3847/1538-4357/ab88b7](10.3847/1538-4357/ab88b7)

- Fraija, N., Kamenetskaia, B. Betancourt, Dainotti, M. G., Duran, R. Barniol, Gálvan Gámez, A., Dichiara, S., **Caligula do E. S. Pedreira, A. C.**, 2021, ApJ, 907, 78, doi: [10.3847/1538-4357/abcaf6](10.3847/1538-4357/abcaf6)

- Fraija, Nissim, Galvan-Gamez, Antonio, Betancourt Kamenetskaia, Boris, Dainotti, Maria G., Dichiara, Simone, Veres, P., Becerra, Rosa L., **Pedreira, A. C. Caligula do E. S.**, 2022, arXiv eprints, arXiv:2205.02459. [https://arxiv.org/abs/2205.02459](https://arxiv.org/abs/2205.02459)

- Fraija, N., Kamenetskaia, B. Betancourt, Galvan-Gamez, A., Dainotti, M. G., Becerra, R. L., Dichiara, S., Veres, P., **do E. S. Pedreira**, A. C. Caligula, 2022, ApJ, 933, 243, doi: [10.3847/1538-4357/ac714d](10.3847/1538-4357/ac714d)

# Contents

# Introduction

## 1.1 Gamma-Ray Bursts

Gamma-Ray Bursts (GRBs) are violent flashes of $\gamma$-rays produced at cosmological distances. They were first discovered in the tail end of the 1960s by the Vela satellites, a group of military satellites owned by the United States government (Klebesadel et al., 1973).

GRBs are typically located at redshifts $z > 0.2$ (Berger, 2014), are distributed isotropically and can reach isotropic energies of up to $10^{54}$ erg (Gehrels et al., 2009). They are formed by the death of massive stars (Woosley, 1993a; Paczyński, 1998; Woosley & Bloom, 2006; Cano et al., 2017) or merger of compact objects, such as neutron stars (NSs; Duncan & Thompson, 1992; Usov, 1992; Thompson, 1994; Eichler et al., 1989; Metzger et al., 2011), white dwarfs (WD; Goodman et al., 1987) and a NS - black hole (BH, Narayan et al., 1992).

GRBs spectra are non-thermal in nature, with peaks typically at 200 keV (Gehrels et al., 2009), but capable of reaching > 100 GeV (see Abdalla et al., 2019; Fraija et al., 2019e,a; Dichiara et al., 2022). Their phenomenological fit, derived by Band et al. (1993), is called the *Band function* and written as

$$N_E(E) = A \begin{cases} (\frac{E}{100\,\text{keV}})^\alpha e^{-\frac{E}{E_0}}, & \text{for } E \leq (\alpha - \beta)E_0 \\ [\frac{(\alpha-\beta)E_0}{100\,\text{keV}}]^{\alpha-\beta}(\frac{E}{100\,\text{keV}})^\beta e^{\beta-\alpha}, & \text{for } E > (\alpha - \beta)E_0 \end{cases} \tag{1.1}$$

where $A$ is the normalization factor at 100 keV, in units of photons $\text{s}^{-1}\text{cm}^{-2}\text{keV}^{-1}$, $E_0$ is the characteristic energy, $\alpha$ the low energy photon spectral index and $\beta$ the high energy photon spectral index. Despite it's strictly empirical nature, the Band function is a good fit for many observed GRBs and their underlying physics (Zhang et al., 2016).

GRBs are classified based on their $T_{90}$ duration[1], where $T_{90}$ is the time over which a GRB releases from 5% to 95% of the total measured counts: Long GRBs (lGRBs) with

---

[1] For a debate of controversial situations, see Kann et al. (2011).
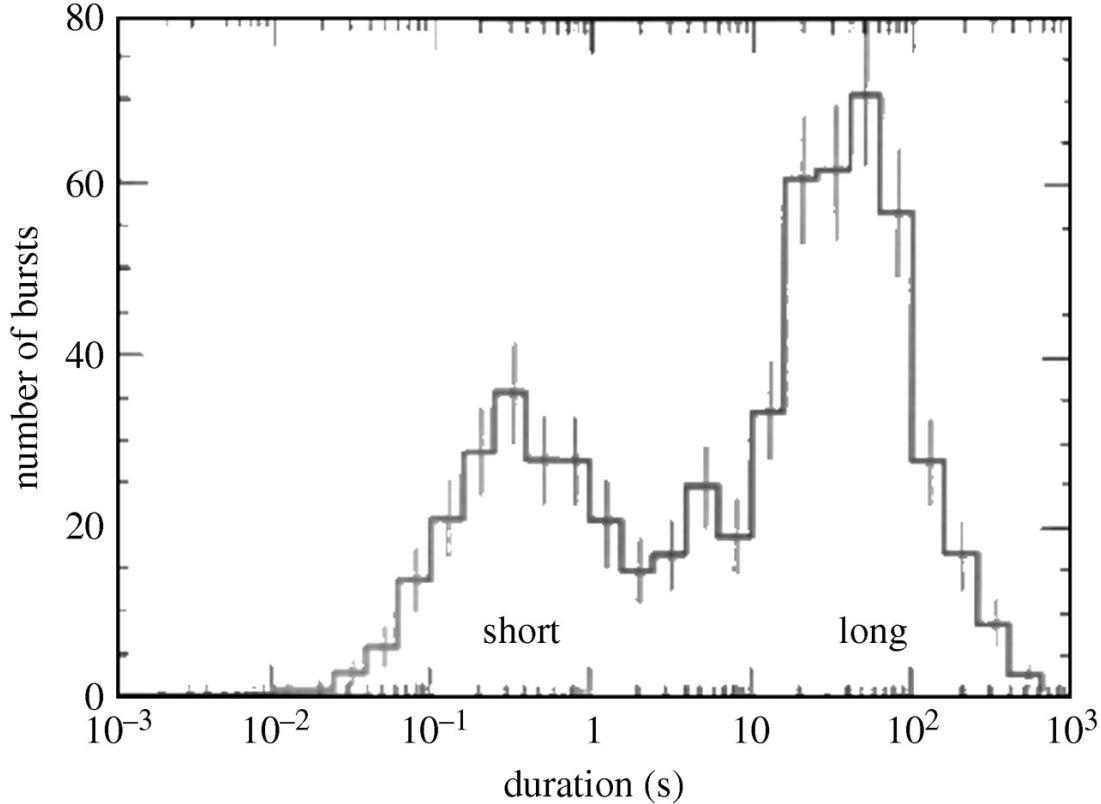
**Figure 1.1:** Histogram distribution of the $T_{90}$ observations. The bimodal distribution is generated due to the association of different progenitors for GRBs, with a division a $T_{90} = 2$s. Credits: NASA Compton Gamma-Ray Observatory.

$T_{90} \geq 2$ s, and short GRBs (sGRBs) with $T_{90} \leq 2$ s (Mazets et al., 1981; Kouveliotou et al., 1993). A histogram distribution of $T_{90}$ can be seen in Figure 1.1. The two GRB categories are typically associated with distinct sources and possess different characteristics.

### 1.1.1  Short GRBs

Substantial evidence have associated the sGRB progenitors with the merger of compact object binaries (Eichler et al., 1989; Narayan et al., 1992; Lee & Ramirez-Ruiz, 2007; Lee et al., 2004, 2005; Nakar, 2007). These progenitors are the foremost candidates to release gravitational waves (GWs) accompanied by an isotropic optical/infrared counterpart, called kilonova (KN; Li & Paczyński, 1998; Rosswog, 2005; Metzger et al., 2010; Kasen et al., 2013; Metzger, 2017). Figure 1.2 shows an artistic representation of a binary merger. Delayed radio emission, originated from the interaction of the merger ejecta with the circumburst medium, is also expected from kilonovae (KNe
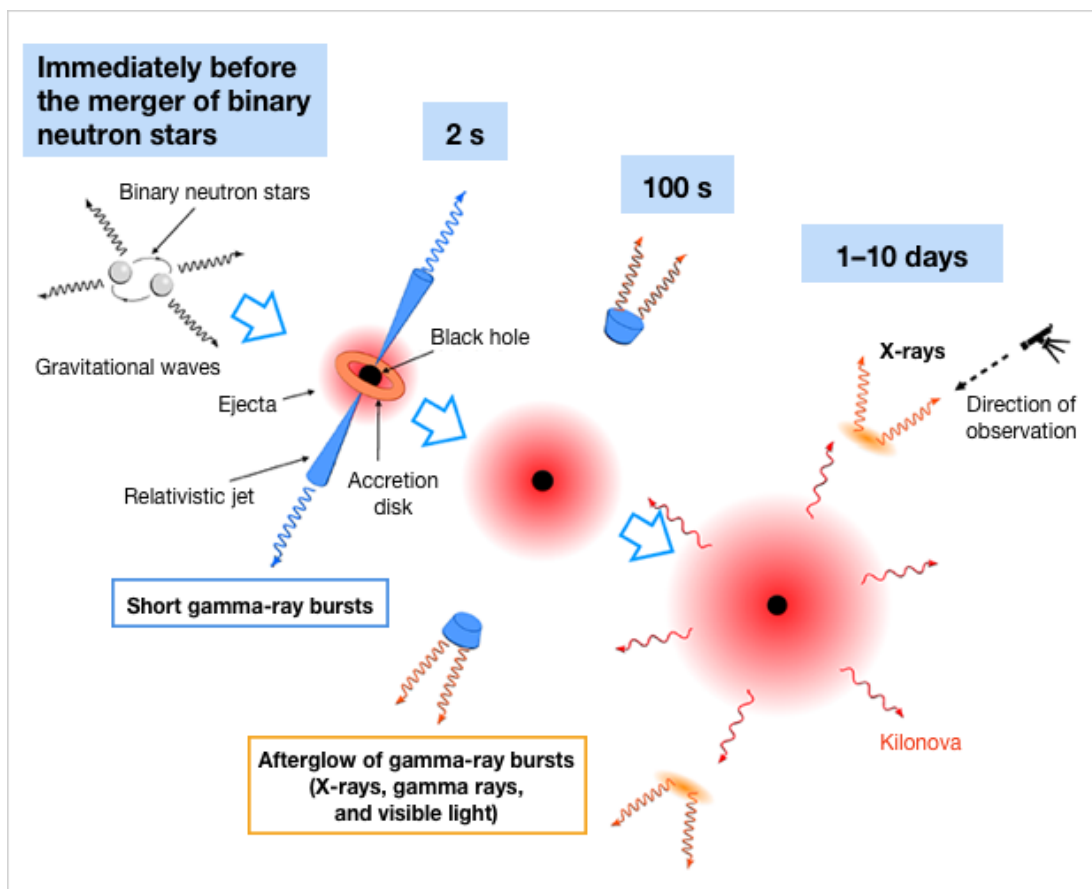
**Figure 1.2:** Artistic representation of a NS binary merger and the resulting sGRB. Credits: Kawai (2018).

Nakar & Piran, 2011; Piran et al., 2013; Hotokezaka & Piran, 2015), in addition to a harder[1] spectra (Zhang, 2014) in the $\gamma$-ray emission and a smaller value of mean redshift ($z \sim 0.5$; see Berger, 2014).

A GW transient, GW170817, associated with a binary NS system with a merger time of 12:41:04 UTC, 2017 August 17 was detected by the LIGO and Virgo experiments (Abbott et al., 2017b,a). Immediately after GRB170817A triggered the Gamma-ray Burst Monitor (GBM) onboard the Fermi Gamma-ray Space Telescope at 12:41:06 UTC (Goldstein et al., 2017) and the INTErnational Gamma-Ray Astrophysics Laboratory (INTEGRAL) detected an attenuated $\gamma$-ray flux with $\sim 3\sigma$ (Savchenko et al., 2017). GRB 170817A marked the first time a GRB could be directly associated to a GW event, and consequently, a binary merger. This observational evidence cemented the compact object merger scenario as a progenitor for sGRBs. Furthermore, GRB 170817A was the

---

[1]Spectral hardness is defined as the photon number ratio between low-energy and high-energy bands in the detector.

first GRB observed off-axis (Troja et al., 2018), allowing for a deeper study of multiple components of the jet, such as a possible cocoon (Mooley et al., 2018).

### 1.1.2 Long GRBs

Unlike sGRBs, lGRBs have a softer $\gamma$-ray spectrum (Gehrels et al., 2009) and a higher mean redshift ($z > 2$, see; Jakobsson et al., 2006). Initially, Woosley (1993b) proposed a collapsar rotating around stars whose core collapsed directly into a BH as a mechanism to emit a relativistic jet that would be seen as a GRB, if it's propagation is directly towards Earth. The author's model requires that the dying stars (initially considered to have $> 35 M_\odot$) possesses a massive core, with high angular momentum and whose hydrogen envelope has been stripped away. MacFadyen & Woosley (1999) numerical simulations of a rapidly rotating helium star returned that a highly energetic explosion, $> 10^{52}$ erg is observed, being powered by hyper-accretion into the formed BH. The jet geometry, then, would be likely due to in-fall, into the black hole, of the matter along rotational axis.

Woosley (1993b) proposed as common progenitors of collapsars the Wolf-Rayet stars (WR, see; Murdin, 2000) and these stars are also progenitors of Type Ib and Ic supernovae (SNe). Thus, certain lGRBs would be linked to SNe and emission of the supernova (SN) would appear a few days after the GRB, when the ejecta is optically thin. The detection of GRB 980425 and SN 1998bw by the *BeppoSAX* Mission was the first observational basis for this connection (Galama et al., 1998; Woosley et al., 1999). Two methods of identification for the presence of a SN-GRB association arose over the years: the first consists of the spectral lines evolution over the period of days, with the GRB spectrum turning into a typical SN spectra after a few days; the second method consists of a re-brightening in the GRB light curve in the days time-frame. Still, not all lGRBs produce a SN explosion with Woosley (1993b) suggesting either a failed SN Ib scenario or low energy deposition when the jet penetrates the star.

### 1.1.3 Fireball Model

The currently leading theory to explain the physics of GRBs is the Fireball model (Figure 1.3; Woosley, 1993a; Piran, 1999). This model assumes an explosion driven by thermal energy, with gravitational energy release during by the progenitor(s) death, which is sent to the central engine's — a black hole resulting from the binary merger (sGRBs) or collapsar (lGRBs) — base (Zhang et al., 2014). The isotropic energy of the event is denoted by
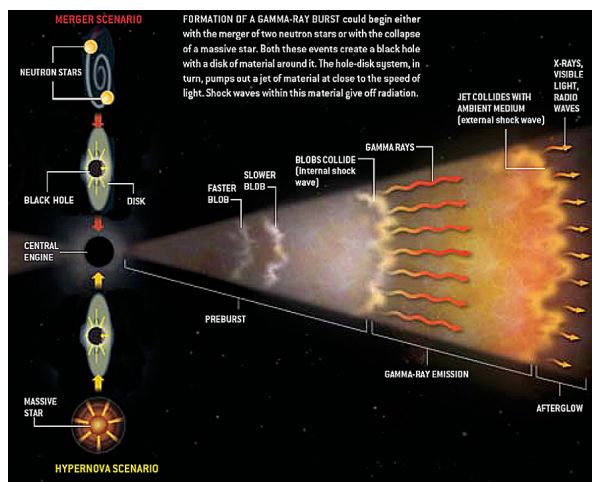
**Figure 1.3:** Artistic representation of the Fireball model, including two possible progenitors. Credits: Juan Velasco, taken from Gehrels et al. (2002).

$$E_{iso} = \frac{4\pi}{\Omega_j} E_j, \tag{1.2}$$

with $\Omega_j$ as the jet's solid angle and $E_j$ the jet's energy. Consequently, luminosity is the fraction of energy released by the burst's duration $L_{iso} \sim E_{iso}/t$. The fireball expands by thermal pressure and accelerates to relativistic speeds. The thermal energy is converted into the outflow's kinetic energy (Rees & Meszaros, 1992) which it's then dissipated by internal and external shocks (reverse and forward, respectively) as the outflow decelerates in the ambient medium.

### 1.1.3.1 The Prompt Emission

The prompt emission phase is the interval where $\gamma$-ray emission from a GRB is detected by an instrument (Rees & Meszaros, 1994; Paczynski & Xu, 1994). Prompt emission photons are commonly ascribed to the central engine activity, with $T_{90}$ duration ranges from milliseconds to thousands of seconds, and irregular light curves. The most accepted model is the *internal shocks*, where collisions between shells of the fireball with different Lorentz ($\Gamma$) factors generate shocks. The bulk kinetic energy of these shocks are then radiated via synchrotron emission (Rybicki & Lightman, 1979) and observed as $\gamma$-ray energy. The resulting Lorentz factor of the collision is

$$\Gamma_{col} \simeq \sqrt{\frac{m_a\Gamma_a + m_b\Gamma_b}{m_a/\Gamma_a + m_b/\Gamma_b}}, \tag{1.3}$$

where the indexes a and b represent each different shell and $m$ is the shell's mass. The resulting internal energy is the difference of the kinetic energy before and after collisions

$$E_{int} = m_a c^2 (\Gamma_a - \Gamma_{col}) + m_b c^2 (\Gamma_b - \Gamma_{col}), \tag{1.4}$$

with c as the speed of light. The efficiency of energy conversion is defined as

$$\epsilon_{eff} = 1 - \frac{(m_a + m_b)\Gamma_{col}}{m_a \Gamma_a + m_b \Gamma_b}. \tag{1.5}$$

To convert a significant fraction of energy, the difference between velocities of the shells must be large. Numerical simulations (Kobayashi et al., 1999; Guetta et al., 2001) have shown a value of efficiency $\epsilon_{eff} = 0.1$, while Beloborodov (2000) expects that $\Gamma_a = x\Gamma_b$, with $x > 2$, for efficient emission.

### 1.1.3.2 Afterglow

The internal shocks model proposed to explain the prompt emission cannot describe the lower energy observations — optical, infrared and radio — of GRBs. To describe these emissions, the afterglow theory was proposed by Paczynski & Rhoads (1993) and Mészáros & Rees (1997). This model takes in consideration the interaction between ejecta and circumburst medium. The relativistic shock model is fully described by Blandford & McKee (1976). The surrounding density is defined as $n(r) = A_k r^{-k}$, with $A_k = n_0(r_0) r_0^k$, where $n_0$ is the density at initial radius $r_0$. The stratification parameter, k, lies in the range $0 \leq k < 3$. In that range k = 0 corresponds to a constant-density medium (ISM), and k = 2 to a stellar wind ejected by the progenitor. For the derivations of this chapter, we consider only a constant-density medium ($k = 0$).

When the relativistic shell moves through the ISM two shocks are formed: A *forward shock* — propagating into the surrounding medium — and a *reverse shock* — propagating into the inner shell — with a contact discontinuity between them.

The accelerated particles of the forward shock can be described by a power-law distribution function and generate magnetic fields. The equations regarding the dynamics of the system are described in full detail in Blandford & McKee (1976), but of note

$$\frac{e_s}{n_s} = (\Gamma_{su} - 1)m_p c^2, \tag{1.6}$$

$$\frac{n_s}{n_u} = \frac{\hat{\Gamma}\Gamma_{su} + 1}{\hat{\Gamma} - 1}, \tag{1.7}$$

$$\Gamma_{uf}^2 = (\Gamma_{su} - 1)[\hat{\Gamma}(\Gamma_{su} - 1) + 1]^2 \hat{\Gamma}(2 - \hat{\Gamma})(\Gamma_{su} - 1) + 2 \tag{1.8}$$

where the subscripts $s, u$ represent shocked and unshocked medium, respectively, and $e$ is the internal energy, $n$ the proton density, $m_p$ the proton mass, $\hat{\Gamma}$ the adiabatic index, $\Gamma_{su}$ the relative Lorentz factor between regions, and $\Gamma_{uf}$ the relative Lorentz factor between unshocked medium and the shock front.

### 1.1.4   Forward Shock Synchrotron Emission

It's widely accepted that the physical process that explains the GRB afterglow best is Synchrotron Emission, the electromagnetic radiation emitted by relativistic particles subject to acceleration perpendicular to their velocity. This mechanism is fully explored in Rybicki & Lightman (1979), and we briefly characterize it in this section. Unless explicitly mentioned, all derivations are obtained from Rybicki & Lightman (1979).

With the electron's rest-frame electric field being

$$E = \frac{\Gamma_e v_e B}{c},\tag{1.9}$$

where the subscript $e$ will reference the electron particle unless stated otherwise, $\Gamma_e$ as the Lorentz factor, $v_e$ as the velocity, $B$ the local magnetic field (perpendicular to the particle's velocity). The radiated power, via synchrotron motion, can be recovered via Larmor's Formula

$$P = \frac{2q^4 E^2}{3c^3 m_e^2} = \frac{\sigma_T B^2 \Gamma_e^2 v_e^2}{4\pi c},\tag{1.10}$$

$$\sigma_T = \frac{8\pi q^4}{3m_e^2 c^4},\tag{1.11}$$

where $\sigma_T$ is Thomson's cross section, $q$ as the electron's charge and $m_e$ as the mass. The electron's angular frequency can be easily retrieved by a force balance between Lorent's force and the relativistic centripetal force, such as

$$\omega = \frac{q_e B}{\Gamma_e m_e c}.\tag{1.12}$$

Relativistic beaming causes the observed radiation to be constrained to when the velocity vector is within an angle of $\theta \approx 1/\Gamma_e$. The orbital time required to satisfy this angular condition is a simple correction of the factor by $1/\pi$. This implies a pulse duration by orbital time of

$$\delta t_{obs} \approx \frac{m_e c}{qB\Gamma_e^2},\tag{1.13}$$

with a cyclical frequency of

$$\nu_{syn} = \frac{\omega_{syn}}{2\pi} = \frac{1}{2\pi\delta t_{obs}} = \frac{qB\Gamma_e^2}{2\pi m_e c}.\tag{1.14}$$

The synchrotron spectrum peaks at this frequency $\nu_{syn}$ and decays with $\nu^{1/3}$ for $\nu > \nu_{syn}$ (Kumar & Zhang, 2015).
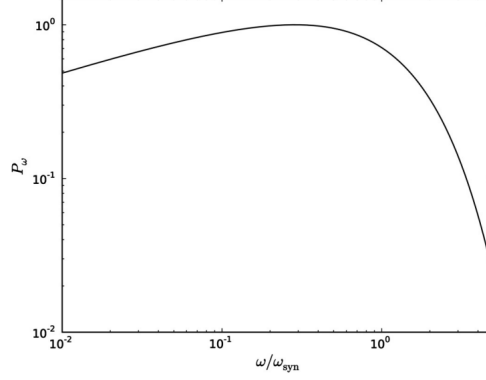
**Figure 1.4:** Synchrotron spectrum for a single particle, the y-axis is normalized by the flux peak and the x-axis is in units of $\omega_{syn}$. Credits: Kumar & Zhang (2015).

With the traditional assumption of a power-law electron distribution, i.e. $\mathrm{d}n_e \propto \Gamma_e^{-p}\,\mathrm{d}\Gamma_e$ [1] for $\Gamma_e > \Gamma_{min.}$. This corresponds to a minimum frequency $\nu_m \equiv \nu_{syn}(\Gamma_m)$. The synchroton flux can be obtained by summing over the contributions of every electron with frequency $\nu > \nu_m$ and Lorentz factor

$$\Gamma_\nu > \left(\frac{2\pi\nu m_e c}{q_e B}\right)^{1/2}. \tag{1.15}$$

The resulting flux is given by

$$F_\nu = \int_{\Gamma_\nu}^{\infty} \mathrm{d}\Gamma_e \frac{\mathrm{d}n_e}{\mathrm{d}\Gamma_e} P_{syn}(\nu) \propto \nu^{\frac{-(p-1)}{2}} \tag{1.16}$$

Another noteworthy frequency necessary to fully describe the synchrotron spectrum is the cooling frequency, $\nu_c \equiv \nu_{syn}(\Gamma_c)$. Electrons at this frequency cool down in a time $t_0$, where the fraction $\Gamma_e \gtrsim \Gamma_c$ loses most of their energy $m_e c^2 \Gamma_e$ and slow down to $< \Gamma_c$. The time $t_0$ is given by

$$t_0 \simeq \frac{m_e c^2 \Gamma_c}{\frac{\sigma_T B^2 \Gamma_c^2 c}{6\pi}} = \frac{6\pi m_e c}{\sigma_T B^2 \Gamma_c}, \tag{1.17}$$

and

$$\Gamma_c \simeq \frac{6\pi m_e c}{\sigma_T B^2 t_0}. \tag{1.18}$$

The characteristic frequency is then

---

[1] $p > 2$ is required to guarantee convergence.

$$\nu_c \simeq \frac{27\pi q m_e c}{\sigma_T^2 B^3 t_0^2}, \tag{1.19}$$

and the total flux

$$F_\nu = \int_{\Gamma_\nu}^{\infty} d\Gamma_e \frac{dn_e}{d\Gamma_e} P_{syn}(\nu) \propto \nu^{\frac{-1}{2}}, \tag{1.20}$$

for any $\nu_c < \nu_e < \nu_m$. Should $\nu_e > \nu_c > \nu_m$, the flux is

$$F_\nu = \int_{\Gamma_\nu}^{\infty} d\Gamma_e \frac{dn_e}{d\Gamma_e} P_{syn}(\nu) \propto \nu^{\frac{-p}{2}}. \tag{1.21}$$

Finally, another important quantity to take into consideration is the self-absorption frequency $\nu_a$. This becomes relevant when photons radiated are absorbed by inverse-synchrotron processes. This frequency is the one where the emergent synchrotron flux is equal to the black-body flux (Kumar & Zhang, 2015):

$$\frac{2m_e c^2 \max\left(\Gamma_a, \min\left[\Gamma_m, \Gamma_c\right]\right)\nu_a^2}{2.7c^2} \approx \frac{\sigma_T B m_e c^2 N_>}{4\pi q}, \tag{1.22}$$

where the left side of the equation is Planck's function in the Rayleigh-Jeans limit, $\Gamma_a$ is the Lorentz factor for the fraction of electrons with frequency $\nu_a$ and $N_>$ is the column density of electrons with Lorentz factor higher than $\max\left(\Gamma_a, \min\left[\Gamma_m, \Gamma_c\right]\right)$.

The synchrotron afterglow spectrum can be summarized in two scenarios:

**Fast-cooling regime** In this scenario, where $\Gamma_c < \Gamma_m$, the electrons dissipate energy quickly, the maximum flux is observed at $\nu_c$ and the flux is summarized as

$$F_\nu = \begin{cases} \left(\frac{\nu_a}{\nu_c}\right)^{1/3} \left(\frac{\nu}{\nu_a}\right)^2 F_{\nu,max} & \text{for } \nu < \nu_a, \\ \left(\frac{\nu}{\nu_c}\right)^{1/3} F_{\nu,max} & \text{for } \nu_a < \nu < \nu_c, \\ \left(\frac{\nu}{\nu_c}\right)^{-1/2} F_{\nu,max} & \text{for } \nu_c < \nu < \nu_m, \\ \left(\frac{\nu}{\nu_c}\right)^{-1/2} \left(\frac{\nu}{\nu_m}\right)^{-p/2} F_{\nu,max} & \text{for } \nu_m < \nu. \end{cases} \tag{1.23}$$

**Slow-cooling regime** In this scenario, where $\Gamma_c > \Gamma_m$, only the fraction of electrons with $\Gamma_e > \Gamma_c$ cool down. The maximum flux is observed at $\nu_m$ and the flux is surmised as
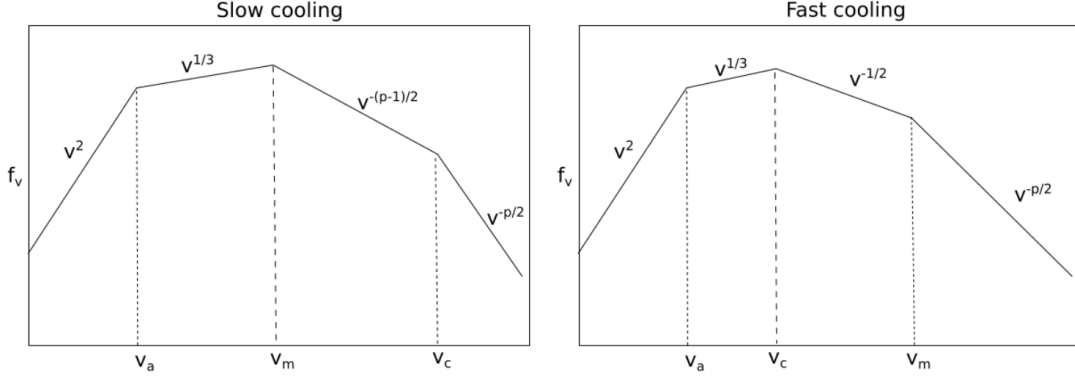
**Figure 1.5:** Summary of the synchrotron spectrum in the slow-cooling (left-side) and fast-cooling (right-side) cases. $\nu_a$ is the self-absorption frequency. Credits: Sari et al. (1998).

$$
F_\nu = \begin{cases}
\left(\frac{\nu_a}{\nu_m}\right)^{1/3} \left(\frac{\nu}{\nu_a}\right)^2 F_{\nu,max} & \text{for } \nu < \nu_a, \\[2mm]
\left(\frac{\nu}{\nu_m}\right)^{1/3} F_{\nu,max} & \text{for } \nu_a < \nu < \nu_m, \\[2mm]
\left(\frac{\nu}{\nu_m}\right)^{-(p-1)/2} F_{\nu,max} & \text{for } \nu_m < \nu < \nu_c, \\[2mm]
\left(\frac{\nu}{\nu_m}\right)^{-(p-1)/2} \left(\frac{\nu}{\nu_c}\right)^{-p/2} F_{\nu,max} & \text{for } \nu_c < \nu.
\end{cases}
\tag{1.24}
$$

A graphical representation of this broken power-law can be seen in Figure 1.5.

#### 1.1.4.1 Canonical X-Ray Light Curve

When the flux is presented in a time-evolving fashion, that plot is called a light curve. Figure 1.6 demonstrates a sample of different GRB curves modeled by Panaitescu & Kumar (2001), demonstrating the similarities.
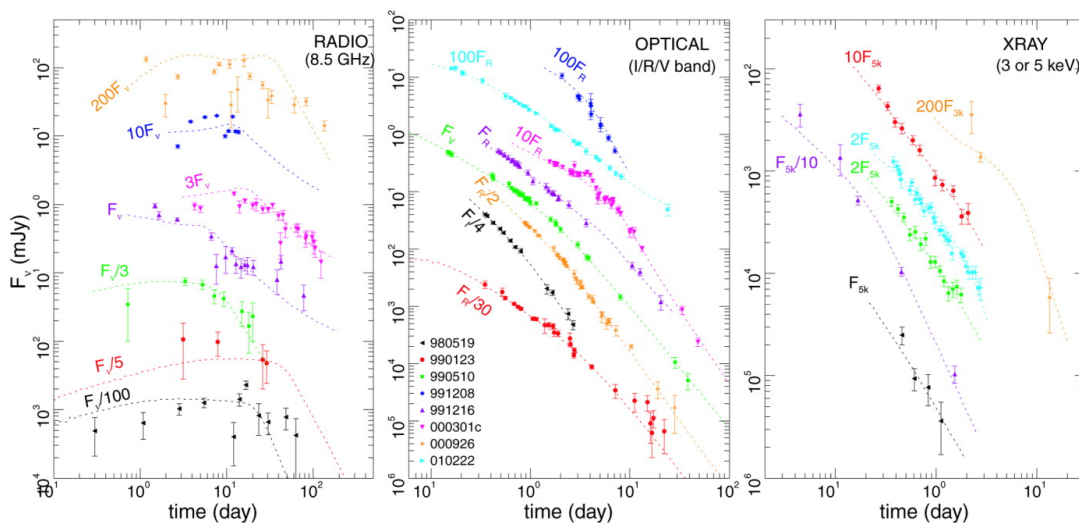
**Figure 1.6:** Radio, Optical and X-ray emission light curves for the GRBs presented in the legend. Fluxes have been multiplied by the factors in the figure, for clarity. Credits: Sari et al. (1998).

Additionally Figure 1.7 demonstrates what is considered a canonical version of the X-Ray GRB afterglow. This figure describes the observed characteristics of the canonical afterglow. Following McBreen et al. (2010), we see

I **Steep decay:** This phase is associated with the high altitude emission at end of the prompt phase, when the central engine turns off abruptly. With a temporal index of $< -2$, it reflects the time dependence of the central engine activity.

II **Plateau:** With a shallow temporal index of $\simeq -0.5$, it's presence typically indicates continuous energy injection.
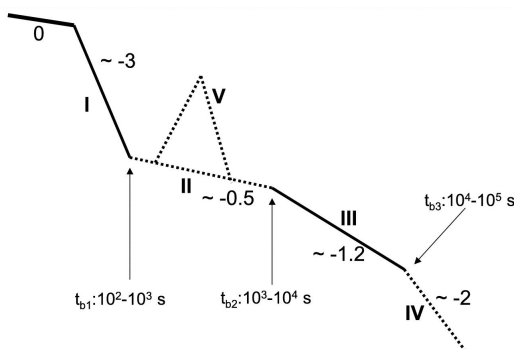


**Figure 1.7:** Afterglow canonical X-ray curve. Credits: McBreen et al. (2010); Becerra (2019).

III **Normal Decay:** With a typical temporal index of $\simeq -1$, this is the standard decay of a typical forward shock model.

IV **Late Steep Decay:** Expected to indicate the presence of a jet-break, when the jet decelerates and the photon beaming cone angle is comparable to the opening angle of the jet. It has a temporal index of $< -2$.

V **Flares:** A signal of late central engine activity, this additional peak to the X-ray light curve share similar properties to the prompt emission.

### 1.1.5 Synchrotron Polarization

Recently, with more accurate observations, polarization has become a concrete avenue to a multi-theory analysis of GRBs. In fact, polarization data are useful in corroborating synchrotron light curves modeling and to probe information that synchrotron theory cannot, such as the geometry of the magnetic fields present. While Section 1.1.4 described the properties of the synchrotron forward-shock model, this section is dedicated to describe the polarization model we use across our relevant papers.

Polarization, the restriction of the vibrations on a wave partially or wholly to a specific geometrical orientation, in Gamma Ray Bursts have been observed since 1999 (Covino et al., 2003). Since then, observations argue that while the Polarization Degree (P.D.) varies, the Polarization Angle (P.A.) is roughly the same. On Gamma Ray Bursts polarization is typically attributed to synchrotron radiation behind the shock waves, which then makes it dependent on the magnetic field configuration and the geometry of the shock as these will determine the polarization degree on each point and its integration over the unresolved image (Gill et al., 2020). The treatment is done by the Stokes Parameters, I, Q, U, V and typically only linear polarization is considered (see Nava et al., 2016, for an analysis of circular polarization in GRBs). In this case

$$V = 0, \qquad \theta_p = \frac{1}{2} \arctan \frac{U}{Q},$$
$$\frac{U}{I} = \Pi' \sin 2\theta_p, \qquad \frac{Q}{I} = \Pi' \cos 2\theta_p. \tag{1.25}$$

where $\Pi'$ is the local polarization degree and $\theta_p$ is the polarization angle. The measured stokes parameters are the sum over the flux (Granot, 2003), so

$$\frac{U}{I} = \frac{\int dF_\nu \Pi' \sin 2\theta_p}{\int dF_\nu}, \qquad \frac{Q}{I} = \frac{\int dF_\nu \Pi' \cos 2\theta_p}{\int dF_\nu}, \tag{1.26}$$

$$\Pi = \frac{\sqrt{Q^2 + U^2}}{I}. \tag{1.27}$$

While the flux element

$$\mathrm{d}F_\nu(t_{obs}, \hat{n}, r, t) = \frac{1+z}{d_L^2} \delta_D^2 j'_{\nu'} \delta(t - t_{obs} - \hat{n} \cdot r/c) \mathrm{d}t \mathrm{d}V, \qquad (1.28)$$

is the flux from a source at redshift $z$ at a luminosity distance $d_L(z)$ emitting in the direction of $\hat{n}$, towards the observer, with fluid-frame spectral emissivity $j'_{\nu'}$, lab-frame volume element $\mathrm{d}V$ and Doppler Factor

$$\delta_D(r) = \frac{1}{\Gamma(1 - \beta\tilde{\mu})}, \qquad\qquad \tilde{\mu} = \cos\tilde{\theta}. \qquad (1.29)$$

The delta function on the fluid element imposes the equal arrival time condition. This condition states that for a given observation time, $t_{obs}$, the emission comes from an equal arrival time surface or volume, depending on whether the emission is from a thin shell or finite volume scenario (Granot et al., 1999).

If the cooling timescale of the particles is much smaller than the dynamical time of the system the emission region is contained within a width of $\delta \ll R/2\Gamma^2$ in the lab frame. This is considered the thin shell scenario and for this approximation we can use, from Granot (2005),

$$\mathrm{d}F_\nu(t_{obs}, \hat{n}, r) = \frac{1+z}{16\pi^2 d_L^2} \delta_D^3 L'_{\nu'} \mathrm{d}\Omega, \qquad (1.30)$$

where $L'_{\nu'}$ is the fluid frame spectral luminosity and $\mathrm{d}\Omega$ is the element of solid angle of the fluid element with relation to the source.

Assuming a power law spectrum and dependency on the $r$, the luminosity can be described as being proportional to the frequency, magnetic field and direction unity vector (Rybicki & Lightman, 1979)

$$L'_{\nu'} \propto (\nu')^{-\alpha} (\sin\chi')^\epsilon r^m \propto (\nu')^{-\alpha} (1 - \hat{n}' \cdot \hat{B}')^{\epsilon/2} r^m. \qquad (1.31)$$

Throughout this text we assume a radially constant emissivity (i.e. $m = 0$) and that $\epsilon = 1 + \alpha$, where $\alpha$ is the spectral index. The term $\chi$ here is the angle between local magnetic field and direction of motion of the particle. Due to the fact that synchrotron emission is highly beamed that angle also represents the pitch angle between the velocity vector and magnetic field. The power law index $\epsilon$ is dependent on the electron distribution, and should it not depend on the pitch angle then $\epsilon = 1 + \alpha$. For the following calculations we will be considering $m = 0$. Maximum local polarization can be retrieved from the spectral index via

$$\Pi_{max} = \frac{1+\alpha}{5/3 + \alpha}. \qquad (1.32)$$
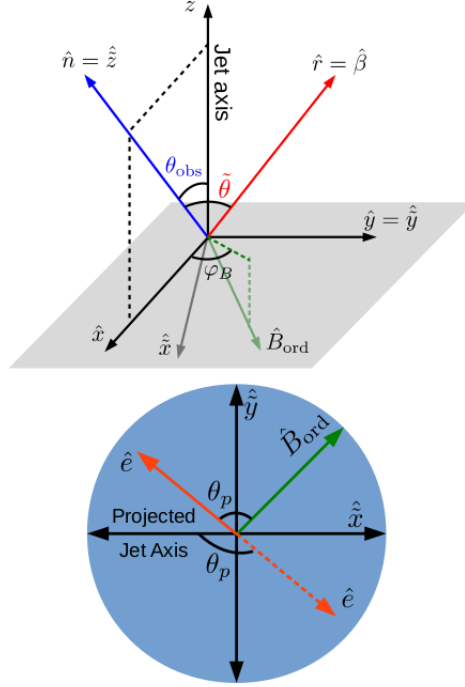
**Figure 1.8:** Visual representation of the vectors and angles necessary to obtain the geometrical considerations of synchrotron polarization. Top figure represents the coordinate system where the polarization vector is calculated, bottom figure represents it's projection on the plane of the sky. Credits: Gill et al. (2020).

In the ultra relativistic limit ($\Gamma \gg 1$) the observer receives photons from a cone of beaming angle $\tilde{\theta} = \Gamma^{-1}$ around the Line of Sight (LOS) due to relativistic beaming. Generally, the edge of the jet is not within the observer field of view (FOV) for an on-axis observer. In this case we can approximate the emission to that of an expanding thin shell, until the time of the jet break where the edge of the jet becomes visible ($\Gamma \sim \hat{\theta}_j^{-1}$). In this limit, approximations are accurate to $O(\Gamma^{-2})$, such as

$$\delta_D \approx \frac{2\Gamma}{1 + \tilde{\xi}}, \qquad\qquad \tilde{\xi} \equiv (\Gamma\tilde{\theta})^2. \qquad (1.33)$$

Using approximations $\tilde{\mu} = \cos\theta \approx 1 - \theta^2/2$ and $\beta \approx 1 - 1/2\Gamma^2$. To tackle the geometrical considerations of polarization let's define a normal vector with the direction of the emitting photon (in the lab frame) in a reference system where the Jet Axis is the z-axis, these angular considerations are demonstrated in Figure 1.8,

$$\hat{n} = \sin\theta_{obs}\hat{x} + \cos\theta_{obs}\hat{z}. \qquad (1.34)$$

Returning to the factor of the pitch angle, $\chi$, it is easy to notice that this factor carries all the geometric information of the problem, from the structure of the magnetic field ($\hat{B}'$) to the direction of emission ($\hat{n}'$) in the fluid frame,

$$\Lambda = \left\langle (1 - \hat{n}' \cdot \hat{B}')^{\epsilon/2} \right\rangle, \tag{1.35}$$

where the average is done over the local probability distribution of the magnetic field. We can do a Lorentz transformation on the unit vectors such as $\hat{n}$ in Equation (1.34), or a prescription of $\hat{B}$, by using [see, Lyutikov et al. (2003)]

$$\hat{X}' = \frac{(1 + \Gamma)\hat{X} + \Gamma^2(\hat{X} \cdot \mathbf{v})\mathbf{v}}{(1 + \Gamma)\sqrt{1 + \Gamma^2(\hat{X} \cdot \mathbf{v})}}, \tag{1.36}$$

so that we can express $\Lambda$ in terms of different magnetic field configurations (Gill et al., 2020; Granot & Taylor, 2005; Lyutikov et al., 2003; Granot, 2003):

$$\Lambda_{ord} \approx \left[ \left( \frac{1 - \tilde{\xi}}{1 + \tilde{\xi}} \right) \cos^2 \varphi_B + \sin^2 \varphi_B \right]^{\epsilon/2}, \tag{1.37}$$

$$\Lambda_{\perp} \approx \left\langle \Lambda_{ord}(\tilde{\xi}, \varphi_B) \right\rangle_{\varphi_B}, \tag{1.38}$$

$$\Lambda_{\parallel} \approx \left[ \frac{\sqrt{4\tilde{\xi}}}{1 + \tilde{\xi}} \right]^{\epsilon}, \tag{1.39}$$

$$\Lambda_{tor} \approx \left[ \left( \frac{1 - \tilde{\xi}}{1 + \tilde{\xi}} \right) + \frac{4\tilde{\xi}}{(1 + \tilde{\xi})^2} \frac{(a + \cos \tilde{\varphi})^2}{1 + a^2 + 2a \cos \tilde{\varphi}} \right]^{\epsilon/2}, \tag{1.40}$$

where for $\Lambda_{ord}$ we have an ordered magnetic field on the plane of the ejecta. For $\Lambda_{\perp}$ we average over the uniform distribution of possible values for $\varphi_B$ within the plane. For $\Lambda_{\parallel}$ we have a magnetic field parallel to the plane of the ejecta. And for $\Lambda_{tor}$ a toroidal field for which $a = \tilde{\theta}/\theta_{obs}$ is a ratio between the polar angle and the angle of observation. In the equations above $\varphi_B$ is measured from an arbitrary reference direction and $\tilde{\varphi}$ from the projection of the Jet Axis in the sky.

In this ultra-relativistic limit the Polarization Angle becomes (Granot, 2003; Granot

& Taylor, 2005; Gill et al., 2020)

$$\theta_p = \varphi_B + \arctan\left(\frac{1-\tilde{\xi}}{1+\tilde{\xi}}\cot\varphi_b\right), \tag{1.41}$$

$$\theta_p = \tilde{\varphi}, \tag{1.42}$$

$$\theta_p = \begin{cases} 0, & \Pi' > 0 \\ \pi/2, & \Pi' < 0 \end{cases}, \tag{1.43}$$

$$\theta_p = \tilde{\varphi} - \arctan\left(\frac{1-\tilde{\xi}}{1+\tilde{\xi}}\frac{\sin\tilde{\varphi}}{a+\cos\tilde{\varphi}}\right). \tag{1.44}$$

For the ordered case, Equation (1.41), the angle is measured from the direction of the local magnetic field. For all other cases it is measured from the projection of the jet axis on the sky. Figure 1.8 shows a representation of the measurement and directions of the angles.

For an observer with $\theta_{obs} = 0$, if the magnetic field configuration is either random or toroidal, the polarization vanishes over the averaged image. This arises due to the axisymmetry of the outflow around the LOS. To break this symmetry the jet must be seen at $\theta_{obs} > 0$, with the observed polarization becoming more significant when the observer is near the edge of the jet (see Pedreira et al., 2022c, in section 3.1 for a further explanation of polarization behavior with $q$ in time evolving scenarios). In the case of the toroidal magnetic field the axisymmetry is broken naturally due to its geometry, however for a random field symmetric to the LOS a condition that the outflow has to be sufficiently inhomogeneous in $\theta$ must be imposed.

**Random Magnetic Field - Perpendicular Configuration**  In the perpendicular case the symmetry of the random magnetic field configuration causes the polarization to vanish over the image, if viewed at $\theta_{obs} = 0$. To break the symmetry, the jet must be viewed close to its edge ($q \gtrsim 1 \pm \xi_j^{-1/2}$) where missing emission (from $\theta > \theta_j$) results only on partial cancellation (Waxman, 2003). The equation necessary to calculate this polarization can be obtained from Equation (1.48) by using Equation (1.38). This leads to Eq. 5 in (Granot, 2003),

$$\begin{aligned}
\frac{\Pi_\perp}{\Pi_{max}} &= \left[\frac{1}{2\pi}\int_{\xi_-}^{\xi_+}\frac{\mathrm{d}\tilde{\xi}\sin 2\psi(\tilde{\xi})}{(1+\tilde{\xi})^{2+\alpha}}\int_0^\pi \mathrm{d}\varphi_B\left(\frac{(1-\tilde{\xi})^2}{(1+\tilde{\xi})^2}\cos^2\varphi_B - \sin^2\varphi_B\right)\times \right. \\
&\quad \left(1-\frac{4\tilde{\xi}\cos^2\varphi_B}{(1+\tilde{\xi})^2}\right)^{(\epsilon-2)/2}\left[H(1-q)\int_0^{\xi_-}\frac{\mathrm{d}\tilde{\xi}}{(1+\tilde{\xi})^{2+\alpha}}\times \right. \\
&\quad \left.\left.\int_0^\pi \mathrm{d}\varphi_B\left(1-\frac{4\tilde{\xi}\cos^2\varphi_B}{(1+\tilde{\xi})^2}\right)^{\epsilon/2}\int_{\xi_-}^{\xi_+}\frac{\mathrm{d}\tilde{\xi}(\pi+\psi(\tilde{\xi}))}{\pi(1+\tilde{\xi})^{2+\alpha}}\int_0^\pi \mathrm{d}\varphi_B\left(1-\frac{4\tilde{\xi}\cos^2\varphi_B}{(1+\tilde{\xi})^2}\right)^{\epsilon/2}\right]^{-1},\right.
\end{aligned} \tag{1.45}$$

where $H(1-q)$ is the Heaviside step function and

$$q = \frac{\theta_{obs}}{\theta_j}, \qquad \xi_j = (\Gamma\theta_j)^2, \qquad \xi_{\pm} = (1 \pm q)^2 \xi_j, \tag{1.46}$$

$$\cos\psi(\tilde{\xi}) = \frac{(1-q)^2\xi_j - \tilde{\xi}}{2q\sqrt{\xi_j\tilde{\xi}}}. \tag{1.47}$$



**Figure 1.9:** Polarization behavior as dependent on the observation angle. Perpendicular Magnetic Field case. Reproduction of Gill et al. (2020).

Figure 1.9, a reproduction of Gill et al. (2020), demonstrates the polarization degree by $q$.

**Ordered Magnetic Field - Parallel Configuration** For the parallel configuration the calculation follows Granot (2003), with $\Lambda(\tilde{\xi}) = \Lambda_{\|}$ from Equation (1.39). This yields

$$\frac{\Pi_{\|}}{\Pi_{max}} = \frac{\int_{\xi_-}^{\xi_+} \frac{d\tilde{\xi}}{(1+\tilde{\xi})^{2+\alpha}} \int_{\xi_-}^{\xi_+} \Lambda(\tilde{\xi}) \sin 2\psi(\tilde{\xi})}{H(1-q)\int_0^{\xi_-} \frac{d\tilde{\xi}\Lambda(\tilde{\xi})}{(1+\tilde{\xi})^{2+\alpha}} + \int_{\xi_-}^{\xi_+} \frac{d\tilde{\xi}[\pi - \psi(\tilde{\xi})]\Lambda(\tilde{\xi})}{\pi(1+\tilde{\xi})^{2+\alpha}}}. \tag{1.48}$$

Figure 1.10, a reproduction of Gill et al. (2020), demonstrates the polarization degree by $q$.
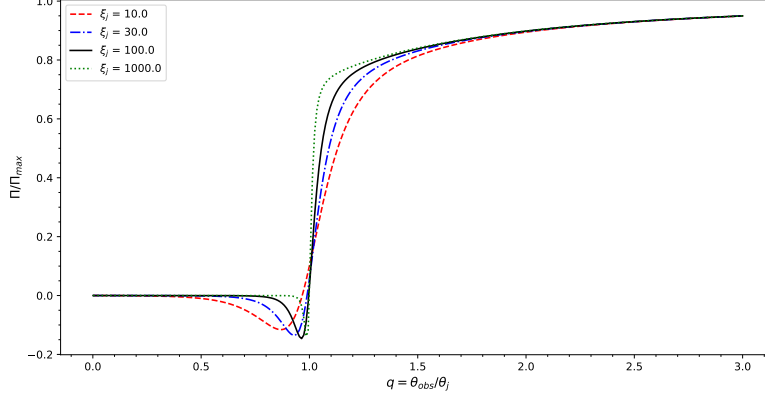
**Figure 1.10:** Same as Figure 1.9, for a Parallel Magnetic Field Case. Reproduction of Gill et al. (2020).

**Ordered Magnetic Field - Toroidal Configuration** Similar to the perpendicular case, if the outflow is viewed on-axis, the polarization vanishes when averaged over the image. Therefore the observer must be at $\theta_{obs} > 0$. The local polarization for any point in the projection in the plane of the sky is the same as the one from an ordered field in the plane of the ejecta. More complexity, however, is added due to the global configuration of the field. Following the calculations of (Granot & Taylor, 2005), we have the time-integrated polarization

$$
\begin{aligned}
\frac{\Pi_{tor}}{\Pi_{max}} &= \left[ H(1-q) \int_0^{\xi_-} \frac{\mathrm{d}\tilde{\xi}}{(1+\tilde{\xi})^{2+\alpha}} \int_0^{2\pi} \mathrm{d}\tilde{\varphi}\Lambda_{tor}(\tilde{\xi},\tilde{\varphi},a)\cos 2\theta_p + \int_{\xi_-}^{\xi_+} \frac{\mathrm{d}\tilde{\xi}}{(1+\tilde{\xi})^{2+\alpha}} \times \right. \\
&\quad \left. \int_\psi^{2\pi-\psi} \mathrm{d}\tilde{\varphi}\Lambda_{tor}(\tilde{\xi},\tilde{\varphi},a)\cos 2\theta_p \right] \left[ H(1-q) \int_0^{\xi_-} \frac{\mathrm{d}\tilde{\xi}}{(1+\tilde{\xi})^{2+\alpha}} \times \right. \\
&\quad \left. \int_0^{2\pi} \mathrm{d}\tilde{\varphi}\Lambda_{tor}(\tilde{\xi},\tilde{\varphi},a) + \int_{\xi_-}^{\xi_+} \frac{\mathrm{d}\tilde{\xi}}{(1+\tilde{\xi})^{2+\alpha}} \int_\psi^{2\pi-\psi} \mathrm{d}\tilde{\varphi}\Lambda_{tor}(\tilde{\xi},\tilde{\varphi},a) \right]^{-1}. \quad (1.49)
\end{aligned}
$$

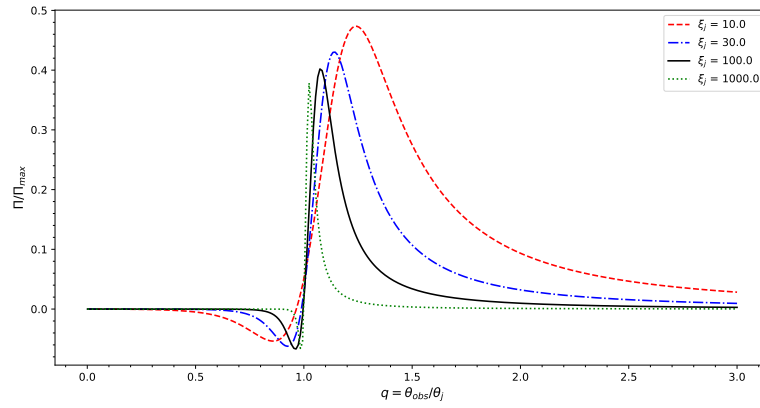Figure 1.11, a reproduction of Gill et al. (2020), demonstrates the polarization degree by $q$.

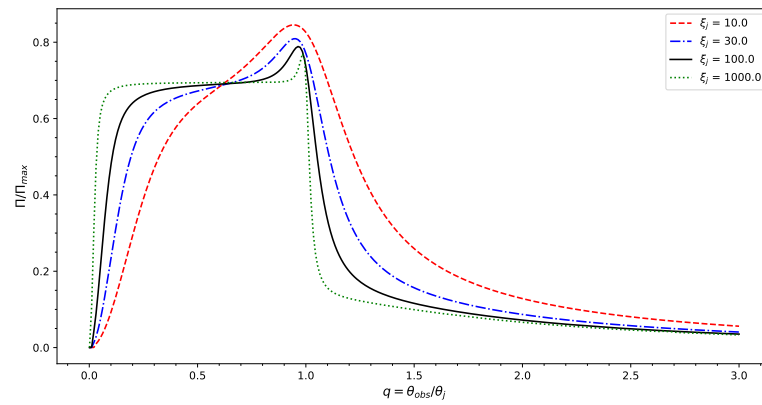**Figure 1.11:** Polarization behavior as dependent on the observation angle. Toroidal Magnetic Field case. Reproduction of Gill et al. (2020).

# Bayesian Statistics

There are two approaches to mainstream statistical analysis in theoretical astrophysics, Frequentist and Bayesian statistics (for a review, see; Wakefield, 2013). Frequentism defines probability as the relative frequency of an event over time and it is an intrinsic property of the observed object,

$$P(x) = \lim_{N \to \infty} \frac{N_x}{N}, \tag{2.1}$$

where $P(x)$ is the probability of an event $x$, $N_x$ the number of $x$ events observed and $N$ the total number of events. Frequentism requires infinite repetition of trials, with the probability being different for each measurement should trials be finite. This is an issue as in theory the probability should be equal regardless of trial numbers. Another issue is that the frequentist definition is circular by nature, it necessitates the assumption of *equally likely outcomes*, where equally likely means `having the same probability`.

On theoretical astrophysics, the most used and accepted frequentist statistical analysis tool is the $\chi^2$ (chi squared, see; F.R.S., 1900) method. It is used to determine if there is a statistically significant difference between the expected and observed frequencies in one or more categories of a frequency distribution. Pearson's $\chi^2$ method is written as

$$\chi^2 = \sum_{i=1}^{k} \frac{(\mathbb{O}_i - \mathbb{E}_i)^2}{\mathbb{E}_i}, \tag{2.2}$$

where $\mathbb{O}_i$ is the observed value and $\mathbb{E}_i$ the expected value.

On the other hand, Bayesian statistics approach probability in a different manner. Per definition, probability becomes the degree of belief of the observer, and it is a subjective status imposed upon the object. The requirements are different than the ones for Frequentist statistics, here an *a priori* assumption, dependent on the observer's judgment, is required (Bayes & Price, 1763). The issue then arises from all the possible a priori choices employed by each observer, transforming probability into a *reference class* problem. In the following section we present the methodology of Bayesian Statistics we

have used in parts of our work. The notation $P(x|y)$ indicates a probability distribution of type $P$[1] (special distributions will be displayed with special letters, e.g. $\mathcal{N}$ for a Normal distribution), observed data $x$ and parameter/parameter space $y$.

## 2.1 Introduction

Bayes equation gives the conditional probability of an event

$$P(\theta|x) = \frac{P(x|\theta)P(\theta)}{P(x)}, \tag{2.3}$$

where $P(\theta)$ is a probability distribution containing our a priori assumptions, called Prior Distribution (shortened to Prior, from here on out); $P(x|\theta)$ is the Likelihood, a probability distribution chosen to describe the observed data; $P(x)$ is the Evidence that this data was generated by the chosen model; and $P(\theta|x)$ is the updated beliefs regarding the system, after taking into consideration the Likelihood, Prior, and Evidence, this is called Posterior Distribution (shortened to Posterior, from here on out).

The major complexity in solving this equation comes from the denominator. The evidence is described via an integration over all possible parameter values (Wakefield, 2013)

$$P(x) = \int_\Theta P(x, \theta), \tag{2.4}$$

and even the simplest non-trivial scenario is incredibly hard to solve. It is, however, possible to obtain an approximate solution.

## 2.2 Markov Chain Monte Carlo

To start solving the integral of $P(x)$, we can take randomly drawn samples of the parameter space, $\Theta$, average the samples over the probability of occurrence and scale by the amount drawn. This, new random variable, is mathematically expressed as

$$F_n = \frac{1}{n} \sum_{i=1}^{n} \frac{f(X_i)}{p(X_i)}, \tag{2.5}$$

and it's expected value should approximate to Eq. 2.4

$$E[F_n] = \frac{1}{n} \sum_{i=1}^{n} \int_{-\infty}^{\infty} \frac{f(x, \theta)}{p(x, \theta)} p(x, \theta) \mathrm{d}\theta = \frac{1}{n} \sum_{i=1}^{n} \int_\Theta f(x, \theta) \mathrm{d}\theta. \tag{2.6}$$

---

[1]We will use P for probability when the shape is irrelevant, undisclosed, or unknown

**Figure 2.1:** Visualization of a simple Markov Chain with the memorylessness condition. Generated with *setosa.io*. This figure's animation can be seen in the digital version of this document, requires *Adobe Reader*[1].

The issue that surges from this approach is that, now, to obtain the samples from the distribution $P(x)$ and solve it through the Monte Carlo method it would be necessary to not only solve Bayes Equation (Eq. 2.3), but also invert it. To help compute the Monte Carlo integration a Markov Chain can be utilized.

### 2.2.1 Markov Chain

A Markov Chain is an stochastic model that describes a sequence of events where the probability of each event only depends on the previous event's state (Gelman et al., 2004).

The formal definition for a discrete system is the memorylessness condition (Gelman et al., 2004)

$$P(X_{n+1} = x | X_1 = x_1, ..., X_n = x_n) = P(X_{n+1} = x | X_n = x_n). \tag{2.7}$$

While in the continuous context, it is the solution of Kolmogorov's Equations (Kolmogoroff, 1931)

$$\frac{\delta P_{ij}}{\delta t}(s;t) = \quad \sum_k P_{ik}(s;t) A_{kj}(t),$$
$$\frac{\delta P_{ij}}{\delta s}(s;t) = \ -\sum_k A_{ik}(s) P_{kj}(s;t). \tag{2.8}$$

By creating a Markov Chain, whose stationary solution is an approximation of the Posterior, the parameter space can be sampled. These samples can be used in the Monte Carlo integration and solve Bayes' Equation. With every new iteration, the approximate Posterior improves and get closer to the target Posterior. Its shape and

range is determined by the Likelihood and Prior, while the sampling method describes how each sample is taken and the Markov Chain is created . This method, or class of algorithms, is called Markov Chain Monte Carlo (MCMC).

### 2.2.2 Samplers

Two major samplers are considered when applying MCMC, the Metropolis-Hastings (Hastings, 1970) and the No U-Turn Sampler (NUTS; Hoffman et al., 2014).

**Metropolis-Hastings** This algorithm is a variation of the Random Walk, with an acceptance rule that allows convergence to a target distribution.

By drawing a starting point $\theta^0$ from a starting distribution $P(\theta^0)$, such that $P(\theta^0|x) > 0$, a sample $\theta^*$ can be taken from a proposal distribution (or jumping distribution) $J_t(\theta^*|\theta^{t-1})$ at a time $t$. A density ratio

$$r = \frac{P(\theta^*|x)}{J_t(\theta^*|\theta^{t-1})} \left[\frac{P(\theta^{t-1}|x)}{J_t(\theta^{t-1}|\theta^*)}\right]^{-1}, \tag{2.9}$$

is calculated to determine the acceptance of the sample. The following then is implemented

$$\theta^t = \begin{cases} \theta^* & \text{with probability } \min(r,1), \\ \theta^{t-1} & \text{otherwise}, \end{cases} \tag{2.10}$$

and a iteration is considered done, even if the jump is not accepted ($\theta^* = \theta^{t-1}$). Given these conditions, the transition distribution $T(\theta^t|\theta^{t-1})$ of the Markov Chain is a mixture of a point mass at $\theta^t = \theta^{t-1}$ and a weighted version of $J_t(\theta^*|\theta^{t-1})$ adjusted for the density ratio.

**No U-Turn Sampler** NUTS is a variation of the Hamiltonian Monte Carlo sampling method (HMC; Betancourt, 2017) that requires no manual fine-tuning. HMC uses a momentum variable, $r$, for each model variable, $\theta$, and apply a Störmer–Verlet method (Hairer et al., 2003, also known as Leapfrog, see;) algorithm with L number of leaps and $\varepsilon$ step-size . These momentum variables are drawn from $\mathcal{N}(0,1)$ and yield an unnormalized distribution

$$p(\theta, r) \propto e^{\mathcal{L}(\theta) - \frac{1}{2}r \cdot r}, \tag{2.11}$$

where $\mathcal{L}$ is the logarithm of the joint distribution of the variables $\theta$. The Leapfrog integrator proceeds with the following rules

$$\begin{aligned} r^{t+\varepsilon/2} &= r^t + (\varepsilon/2)\boldsymbol{\nabla} \cdot_\theta \mathcal{L}(\theta^t), \\ \theta^{t+\varepsilon} &= \theta^t + \varepsilon r^{t+\epsilon/2}, \\ r^{t+\varepsilon} &= r^{t+\varepsilon/2} + (\varepsilon/2)\boldsymbol{\nabla} \cdot_\theta \mathcal{L}(\theta^{t+\varepsilon}), \end{aligned} \tag{2.12}$$

for L times.

To automate the number of leaps, L, NUTS applies a condition on the dot product of $(\theta^* - \theta^0) \cdot r^*$,

$$\frac{\mathrm{d}}{\mathrm{d}t} \frac{(\theta^* - \theta^0) \cdot (\theta^* - \theta^0)}{2} = (\theta^* - \theta^0) \cdot r^*, \tag{2.13}$$

where $\theta^*$ is the current position vector, $\theta^0$ the initial position vector, and $r^*$ the current momentum vector. This condition is applied after generating a balanced tree using leapfrog. When this derivative is $< 0$ (which describes an "U-turn") the leapfrog halts and samples are drawn from this finalized tree. $\varepsilon$ is adaptively tuned using Robbins and Monro stochastic approximation (see Robbins & Monro, 1951).

## 2.3 Examples

### 2.3.1 Linear Regression

This example is a reproduction adapted from Wiecki (2013).

Linear Regression is a linear approach to modeling the relationship between a scalar response and one or more explanatory variables (for a review, see; Freedman, 2009). In the frequentist approach, a linear regression is defined as

$$Y = x\beta + \varepsilon. \tag{2.14}$$

In the Bayesian approach we can define it as a normal distribution of mean $x\beta$ and standard deviation $\sigma^2$

$$Y \sim \mathcal{N}(Y, \sigma^2) = \sqrt{\frac{1}{2\pi\sigma^2}} e^{-\frac{1}{2}(\frac{x-Y}{\sigma})^2}. \tag{2.15}$$

To calculate the MCMC of this model we use the `PyMC3` library (Salvatier et al., 2016) of the `Python` (for manual, see; Van Rossum & Drake, 2009) programming language. Code snippets will be presented in figure formatting, obtained by using the code in `Jupyter` notebook (Kluyver et al., 2016).

In Figure 2.2 we present the code used to call the necessary packages for `PyMC3` and generate dummy data. This dummy data has 200 points, generated by Eq. 2.14 over the range $x = [0, 1]$, assuming $\beta = 2$ and $\varepsilon = 1$. This data is then modified additively by noise sampled randomly from $\mathcal{N}(Y, 0.5)$. The dummy data (noise added) and the theoretical regression line (the data without the noise) are shown in Figure 2.3.

```
In [ ]:  #Preamble
         import pymc3
         from pymc3 import *
         import numpy
         import matplotlib.pyplot
         import os
         from theano import as_op
         import theano.tensor
         from scipy import stats


         root_path = os.path.dirname(os.path.abspath(__file__))
         folders_dict = {"plot_folders":["Plots/Normal/", "Plots/Robust/",
                         "Plots/Prior_Update/"]}
         for folder in folders_dict["plot_folders"]:
             os.makedirs(os.path.join(root_path,folder),exist_ok=True)

In [4]:  #Data generation
         size = 200
         th_intercept = 1
         th_slope = 2

         x = numpy.linspace(0,1,size)
         th_regression_line = th_intercept + th_slope * x
         y = th_regression_line + numpy.random.normal(scale=.5, size=size)

         data = dict(x=x, y=y)
```

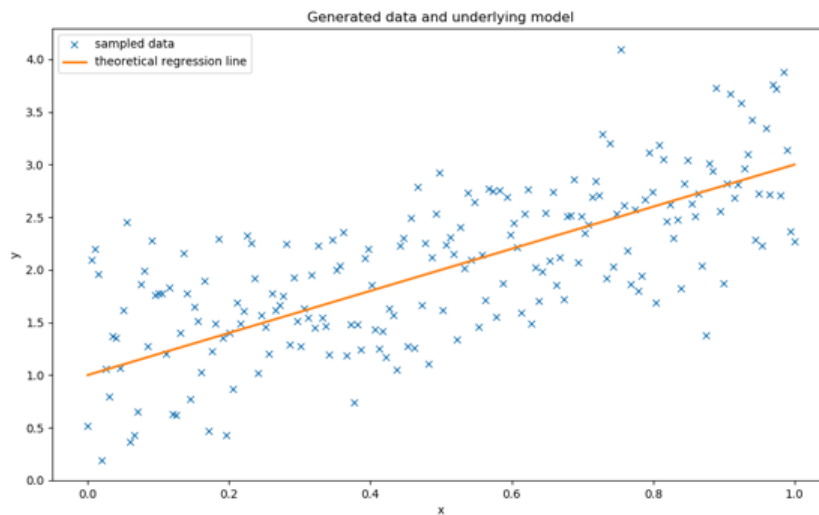**Figure 2.2:** Preamble and data generation.



**Figure 2.3:** Linear Regression Line and Noise Modified Data.

Figure 2.4 shows the MCMC code used. The following distributions are assumed as priors

$$\begin{aligned}
\beta &\sim \quad \mathcal{N}(0, 20), \\
\varepsilon &\sim \quad \mathcal{N}(0, 20), \\
\sigma &\sim \quad \mathcal{HC}(0, 20),
\end{aligned} \tag{2.16}$$

where $\mathcal{HC}(x, \beta)$ is the Half-Cauchy distribution

$$\mathcal{HC}(x, \beta) = \frac{2}{\pi\beta[1 + (\frac{x}{\beta})^2]}, \tag{2.17}$$

and a normal distribution is passed as the likelihood, with $Y$ as it's mean

$$\mathcal{L} \sim \mathcal{N}(\beta x + \varepsilon, \sigma). \tag{2.18}$$

Finally, the NUTS sampler is called to obtain the posterior distributions.

Figure 2.5 and Figure 2.6 show the results of the MCMC. The former presents a Trace plot of the sampling process. This plot is composed of the Posterior (left side) for each chain (instance) of the MCMC and the drawn samples (right side). The right-side x-axis is the parameter values, while the y-axis is the probability associated to this value. For the left side, the x-axis is the sample number, while the y-axis the sample value. The latter Figure shows the merged Posterior (a merger of all chains) and the associated highest density interval (HDI) for each.

```
In [ ]: #MCMC
        with Model() as Normal_GLM:
            # Priors
            sigma = HalfCauchy('sigma', beta=10, testval=1.)
            intercept = Normal('Intercept', 0, sd=20)
            x_coeff = Normal('x', 0, sd=20)

            #Likelihood
            likelihood = Normal('y', mu=intercept + x_coeff * x,
                                sd=sigma, observed=y)

            # Inference
            trace = sample(progressbar=False) #NUTS
```

**Figure 2.4:** MCMC model.
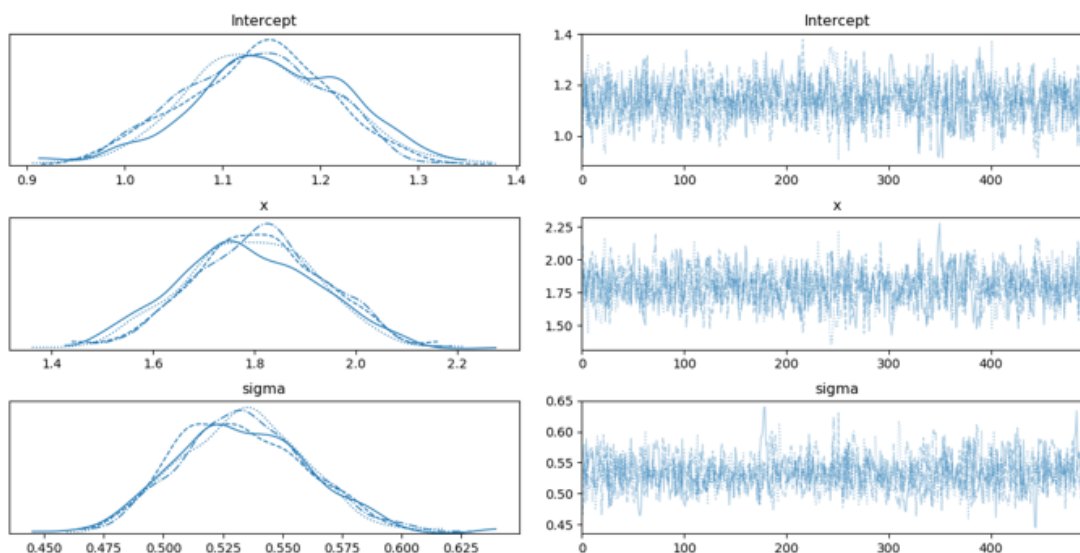
**Figure 2.5:** Trace plot of the posterior distribution. On the left side the marginal Posterior, on the right side the samples drawn.
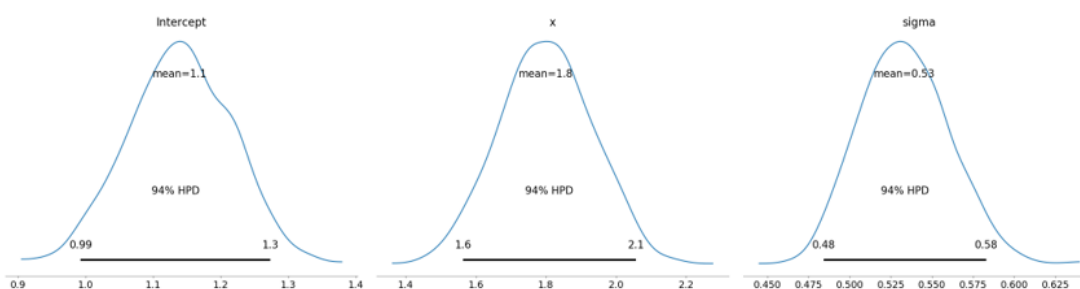


**Figure 2.6:** Posterior distributions. Black lines indicate the 94% highest density interval.
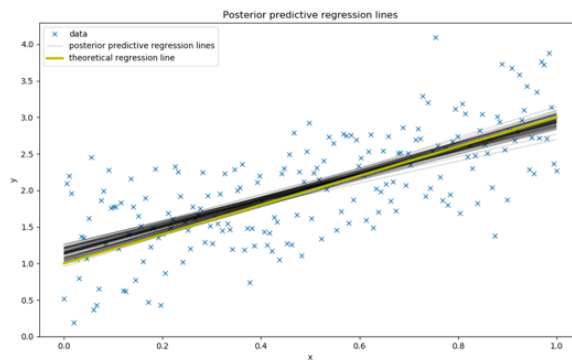
**Figure 2.7:** Bayesian linear regression model. Each line is a combination of values passed by the Posteriors.

Figure 2.7 shows the resulting linear regression lines obtained with the posterior distribution. Each line represents a combination of parameter values. It is clear to see that the the results are very close to the theoretical linear regression line used to generate the data. However, due to the limited data and choice of wide Priors ($\sigma = 20$), a certain degree of uncertainty is present. This uncertainty is visible on variability of the lines.

### 2.3.2  Application: Synchrotron Forward Shock Scenarios

We have used MCMC across our publications to obtain the most likely values of the parameter space describing our models (Fraija, Nissim et al., 2019; Fraija et al., 2019d,a,c,e, 2020, 2022). On here we present the results of one such implementation, in the form of MCMC corner plots — a combination of 2D and 1D Kernel Density Estimation (KDE) plots — and flux light curves, sans the code snippets.

**GRB 170817A**  Figures 2.8 and 2.9 shows the corner plot of the MCMC, for the X-ray and Optical bands. The shaded areas in the light curve are obtained using the uncertainty in the Posteriors.

**Table 2.1:** Table of parameters reported for GRB 170817A

| Parameters | Values |
|---|---|
| $\tilde{E}\,(10^{49}\,\mathrm{erg})$ | $6.263^{+0.494}_{-0.483}$ |
| $\mathrm{n}\,(\mathrm{cm}^{-4})$ | $2.848^{+0.412}_{-0.395}$ |
| $p$ | $2.248^{+0.010}_{-0.010}$ |
| $\varepsilon_{\mathrm{b}}\,(10^{-4})$ | $6.927^{+0.500}_{-0.508}$ |
| $\varepsilon_{\mathrm{e}}\,(10^{-1})$ | $0.935^{+0.100}_{-0.102}$ |
| $\theta_{\mathrm{j}}\,(\mathrm{deg})$ | $7.545^{+0.296}_{-0.296}$ |
| $\Delta\theta\,(\mathrm{deg})$ | $18.793^{+0.254}_{-0.261}$ |
| $\alpha_{\mathrm{s}}$ | $3.000^{+0.098}_{-0.099}$ |

Table 2.1 demonstrates a way of typesetting the results of a posterior distribution in the notation of $\Theta = A^{+b}_{-c}$. A slightly modified version of the corner plot and light curve was published in Fraija et al. (2019c).
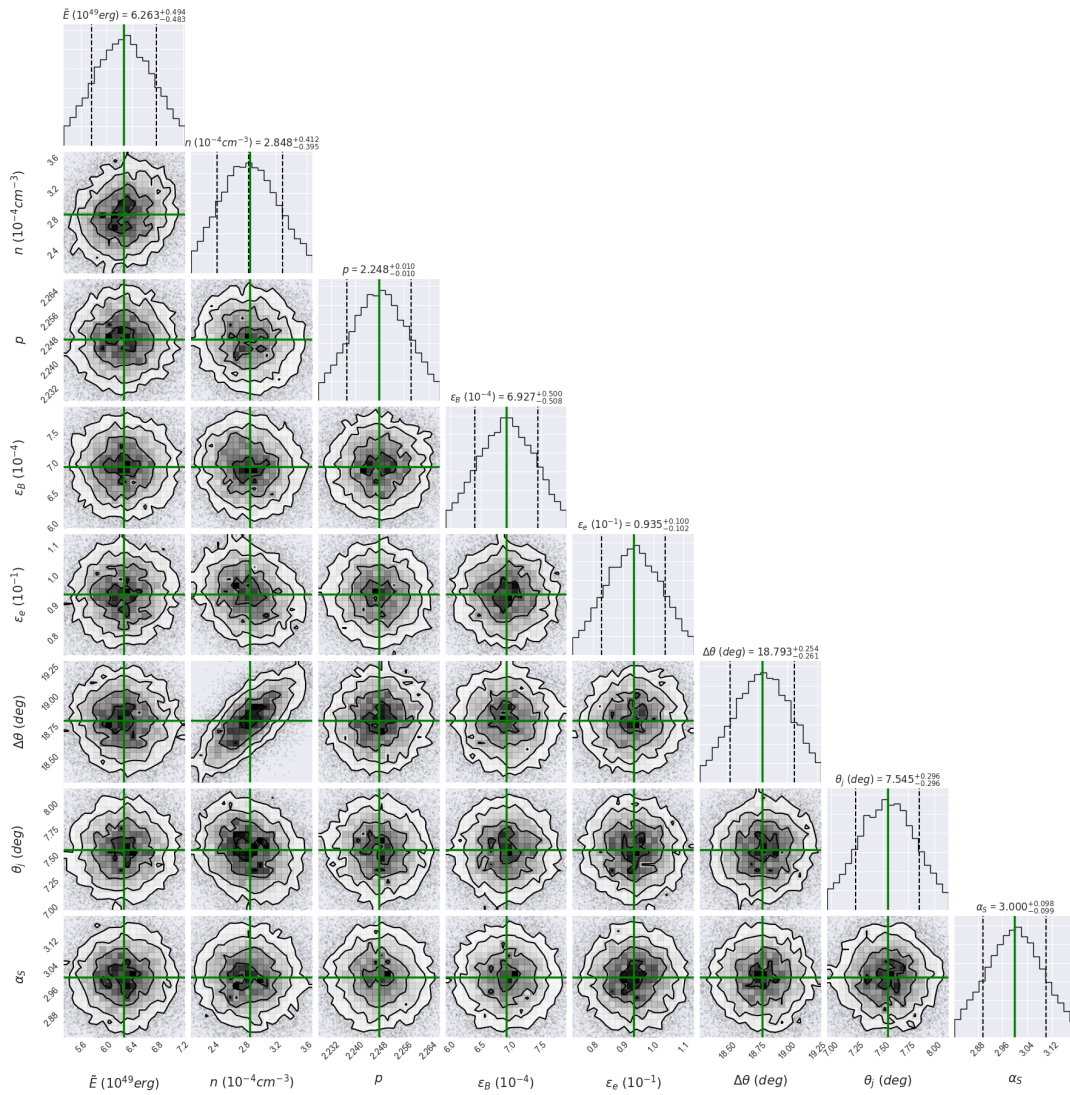
**Figure 2.8:** MCMC results. A similar version was published in Fraija et al. (2019c).
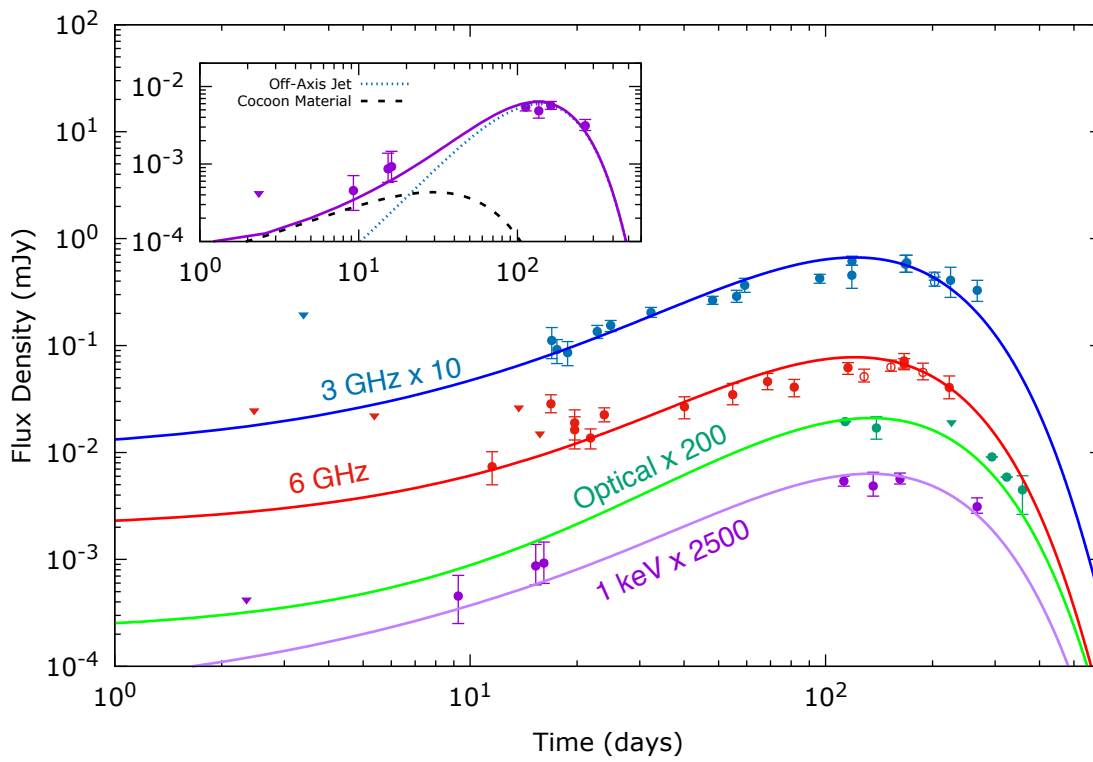
**Figure 2.9:** Light curves for GRB 170817A. A similar version was published in Fraija et al. (2019c).

**GRB 160921B** Section 2.3.2 and figs. 2.10 and 2.11 shows the corner plot of the MCMC, for the X-ray and Optical bands. The shaded areas in the light curve are obtained using the uncertainty in the Posteriors. A slightly modified version of the corner plot and light curve was published in Fraija et al. (2020).
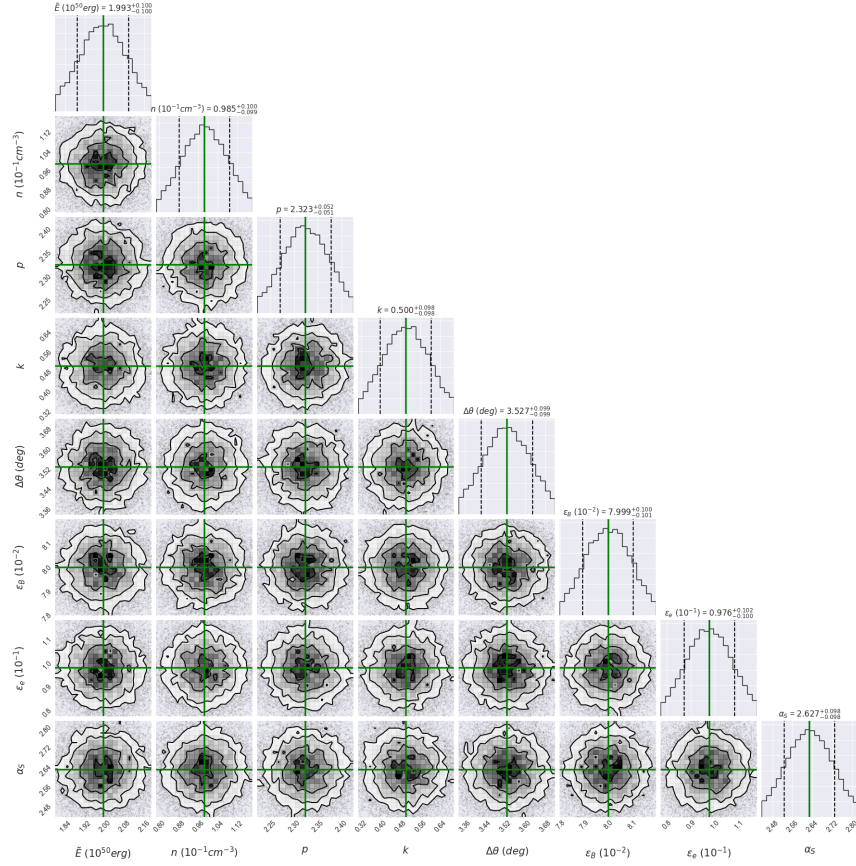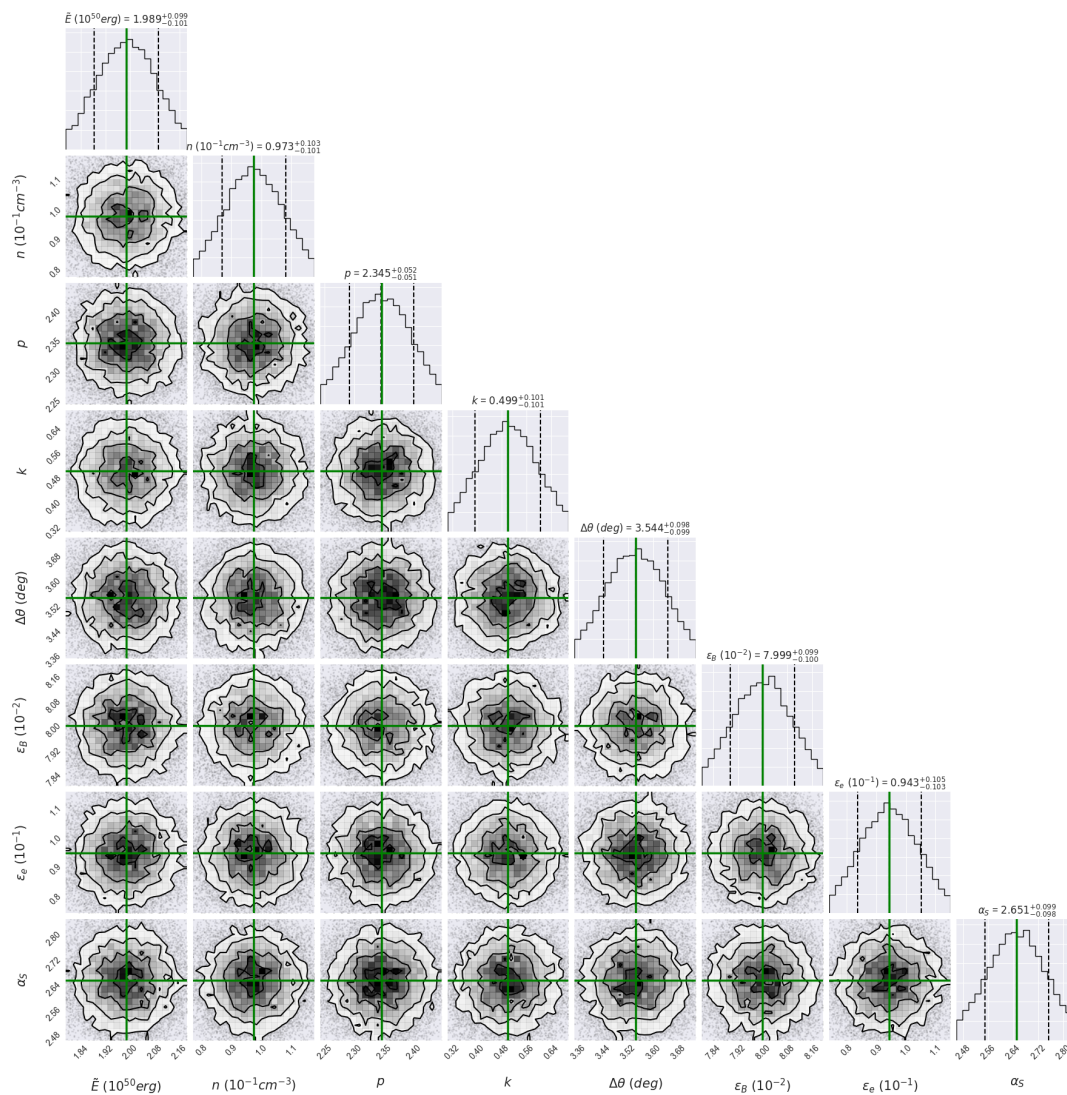
**Figure 2.10:** MCMC results for the Optical band. A similar version was published in Fraija et al. (2020).
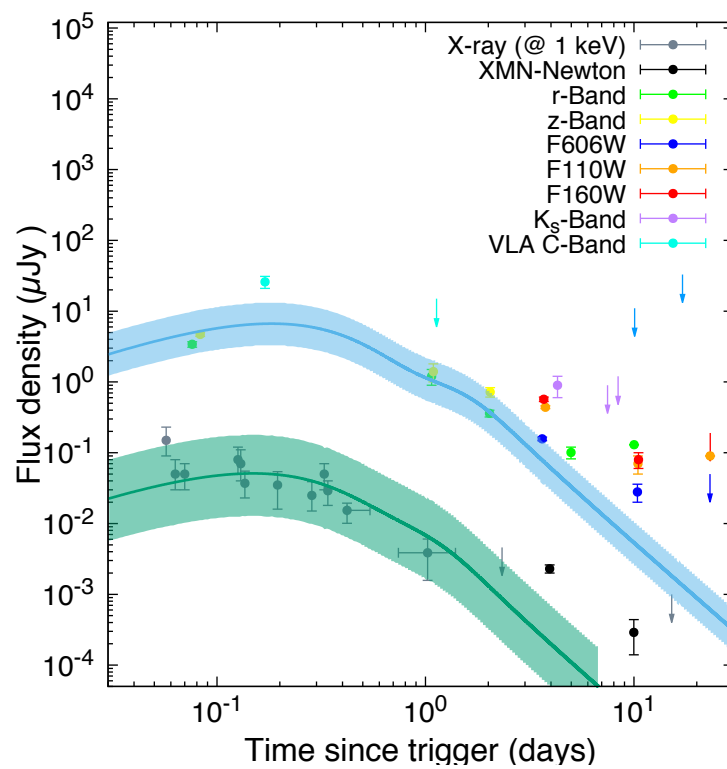
**Figure 2.11:** Light curves for GRB 160821B. The shaded are indicate uncertainty on the results. A similar version was published in Fraija et al. (2020).

**GRB 080503** Figures 2.12 to 2.14 show the corner plot of the MCMC, a plot of the auto-correlation between samples (for select parameters) and the light curve generated by the parameters. A slightly modified version of the corner plot and light curve was published in Fraija et al. (2020). We use the auto-correlation plot as a visual diagnostic tool. A high correlation between samples indicate that the sampler is not fully exploring the Posterior and it is carrying bias towards certain values within the parameter space. Low correlation indicates that the Posterior is being fully explored.
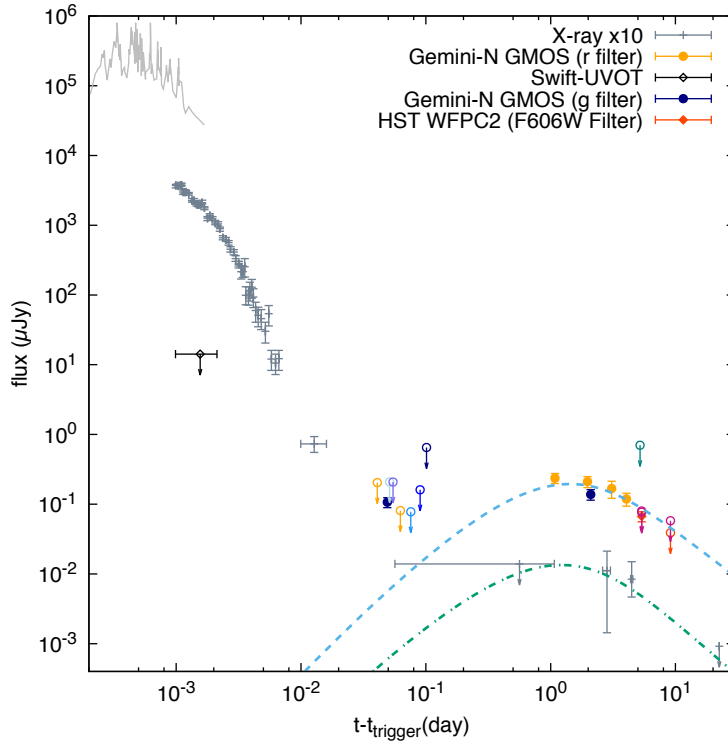


**Figure 2.12:** Light curves for GRB 080503. A version in a different style was published in Fraija et al. (2020).
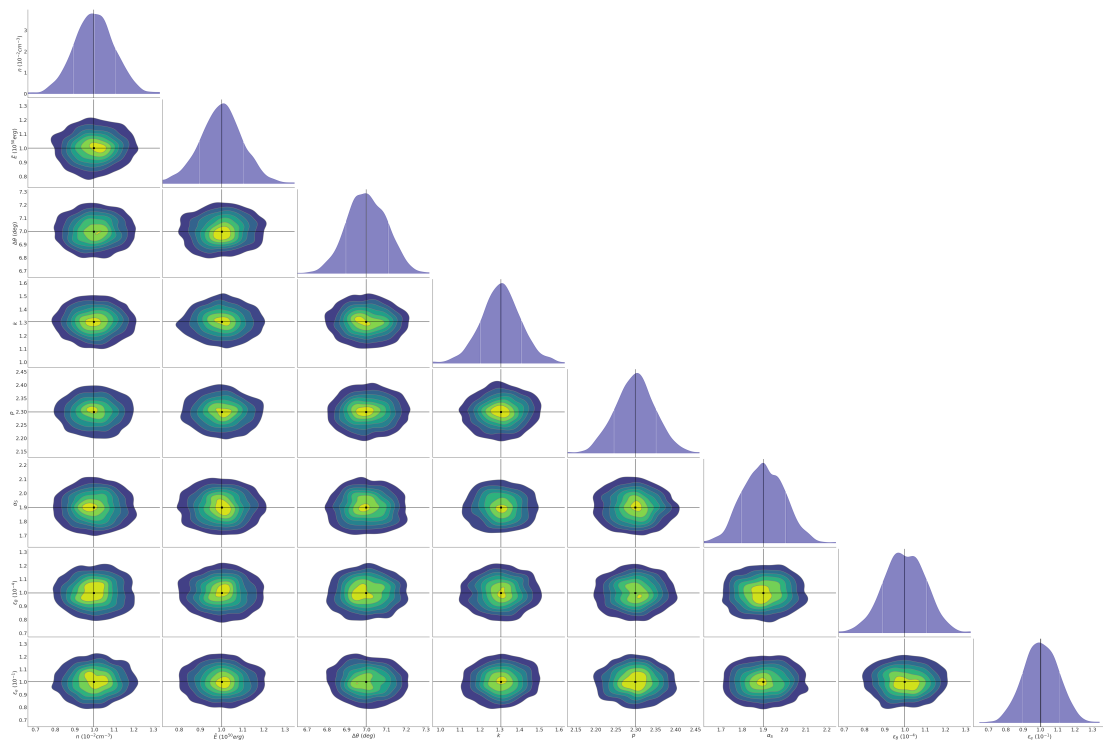
**Figure 2.13:** MCMC results for the X-ray band. A version in a different style was published in Fraija et al. (2020).
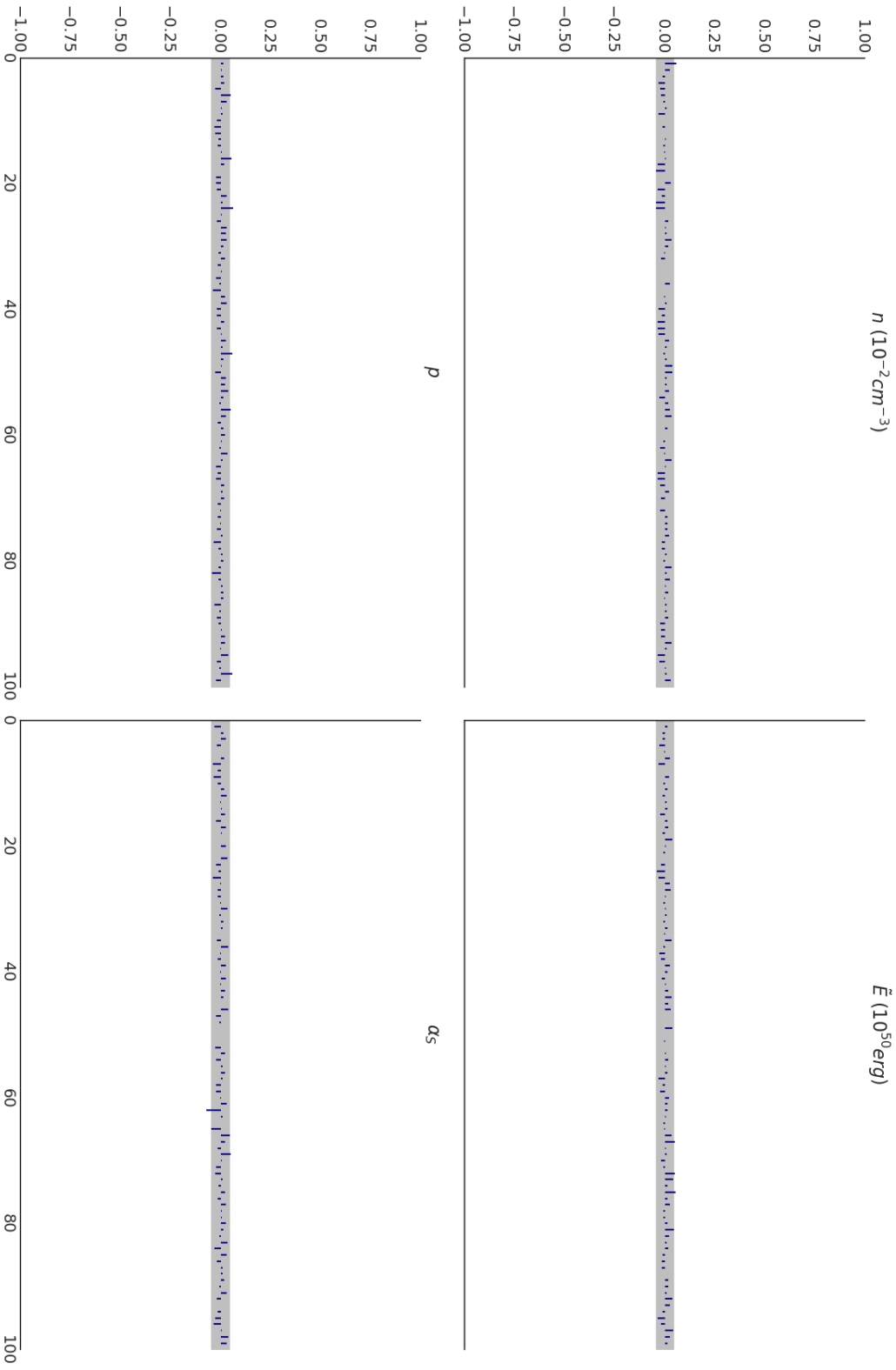
**Figure 2.14:** MCMC sample auto-correlation. High auto-correlation between samples indicate bad exploration of the parameter space.

# Results and Publications

In this following chapter we present the works developed over the course of the PhD program. We group these papers based on their connection (sorted in chronological order), as some are directly connected to a previous work, and present a summary of the conclusions for each grouping and paper. In Section 3.1 we present three papers in which we explore the typical Synchrotron Forward-Shock Off-Axis model. The goal in these works was to model a variety of GRBs with the traditional model in a range of media stratification, with this calculations we could finally attain the fiducial polarization that allows us to explore GRBs in a dual avenue of synchrotron and polarization fitting. In Section 3.2 we apply the same principles to a different Synchrotron Forward-Shock Off-Axis, one where the outflow is radially stratified and parameterized over a velocity power-law distribution and obtain its fiducial polarization. Finally, in Section 3.3 we present a set of works with lGRBs possessing VHE photons, we explore these bursts in a more disjointed nature, as the works were not planned with each one in mind, but their connection as such unique bursts merit exploration and the chosen grouping.

## 3.1 Polarization in Off-Axis Top-Hat Jet Scenario

In this section we group the following works based on their continuity:

- **Pedreira, A. C. C. d. E. S.**, Fraija, N., Galvan-Gamez, A., Betancourt Kamenetskaia, B., Veres, P., Dainotti, M. G., Dichiara, S., Becerra, R. L., 2022, Afterglow Polarization from Off-Axis GRB Jets, in press, ApJ, doi: `10.48550/ARXIV.2210.12904`

- Fraija, Nissim, Galvan-Gamez, Antonio, Betancourt Kamenetskaia, Boris, Dainotti, Maria G., Dichiara, Simone, Veres, P., Becerra, Rosa L., **Pedreira, A. C. Caligula do E. S.**, 2022, arXiv eprints, arXiv:2205.02459. `https://arxiv.org/abs/2205.02459`

- Fraija, N., Lopez-Camara, D., **Pedreira, A. C. C. d. E. S.**, Betancourt

In Fraija et al. (2019c) we present a scenario where the outflow is modeled by an off-axis homogeneous jet and a quasi-spherical component. For this work we assume that each component is calculated separately and the individual contributions summed to obtain the total flux. We take the following relations for the outflow's kinetic energy

$$
E_{\rm k} = \begin{cases} \tilde{E}\Gamma^{-\alpha_{\rm s}} & \text{for a quasi-spherical outflow,} \\ \frac{2\tilde{E}}{\theta_{\rm j}^2} & \text{for an off-axis jet.} \end{cases} \tag{3.1}
$$

Where $\tilde{E}$ is the fiducial energy and $\alpha_{\rm s}$ is a power-law parameterization factor. Through Blandford-McKee's self similar solution (Blandford & McKee, 1976) we find the bulk Lorentz factor for a homogeneous

$$
\Gamma = \begin{cases} 3.8 \left(\frac{1+z}{1.022}\right)^{\frac{3}{\alpha_s+8}} n_{-1}^{-\frac{1}{\alpha_s+8}} \tilde{E}_{50}^{\frac{1}{\alpha_s+8}} t_{\rm 1d}^{-\frac{3}{\alpha_s+8}} & \text{for a quasi-spherical outflow,} \\ 321.1 \left(\frac{1+z}{1.022}\right)^{\frac{3}{2}} n_{-1}^{-\frac{1}{2}} \theta_{\rm j,5^\circ}^{-1} \Delta\theta_{15^\circ}^3 \tilde{E}_{50}^{\frac{1}{2}} t_{\rm 1d}^{-\frac{3}{2}} & \text{for an off-axis jet.} \end{cases} \tag{3.2}
$$

And wind-like medium

$$
\Gamma = \begin{cases} 16.7 \left(\frac{1+z}{1.022}\right)^{\frac{1}{\alpha_s+4}} \xi^{-\frac{2}{\alpha_s+4}} A_{\star,-4}^{-\frac{1}{\alpha_s+4}} \tilde{E}_{50}^{\frac{1}{\alpha_s+4}} t_{\rm 10s}^{-\frac{1}{\alpha_s+4}} & \text{for a quasi-spherical outflow,} \\ 2.4 \times 10^3 \left(\frac{1+z}{1.022}\right)^{\frac{1}{2}} \xi^{-1} A_{\star,-1}^{-\frac{1}{2}} \theta_{\rm j,5^\circ}^{-1} \Delta\theta_{15^\circ} \tilde{E}_{50}^{\frac{1}{2}} t_{\rm 1d}^{-\frac{1}{2}} & \text{for an off-axis jet.} \end{cases} \tag{3.3}
$$

For these equations, $A_\star$ is the wind-like medium density and $\xi$ is a parameter associated with the EATS condition. The lateral expansion phase can be found in the full text. In this paper we presented the fiducial calculations for homogeneous and wind-like media, with both Synchrotron and Synchrotron Self-Compton (SSC) emission mechanisms. We show that the synchrotron emission of the quasi-spherical component dominates the light curve in early times (< 20 days), but weaker than the off-axis emission afterwards. In addition, we present the particular case of GRB 170817A, which we model by applying a MCMC algorithm to the synchrotron emission model. With this successful modeling, we show that our model is in agreement with observed data.

In Fraija et al. (2022) we present the full extent of the synchrotron afterglow model for an off-axis homogeneous jet, generalized for any degree of ambient media stratification. By using Blandford-McKee's solution the bulk Lorentz factor can be summarized as

$$
\Gamma = \begin{cases} \Gamma_0 & \text{coasting phase,} \\ \left(\frac{3}{4\pi\, m_p c^{5-k}}\right)^{\frac{1}{2}} (1+z)^{-\frac{k-3}{2}} (1-\beta\cos\Delta\theta)^{-\frac{(k-3)}{2}} A_{\rm k}^{-\frac{1}{2}} E^{\frac{1}{2}} t^{\frac{k-3}{2}} & \text{off-axis phase,} \\ \left(\frac{3}{(2c)^{5-k}\pi\, m_p}\right)^{\frac{1}{8-2k}} (1+z)^{-\frac{k-3}{8-2k}} A_{\rm k}^{-\frac{1}{8-2k}} E^{\frac{1}{8-2k}} t^{\frac{k-3}{8-2k}} & \text{on-axis phase,} \\ \left(\frac{3}{(2c)^{5-k}\pi\, m_p}\right)^{\frac{1}{6-2k}} (1+z)^{-\frac{k-3}{6-2k}} A_{\rm k}^{-\frac{1}{6-2k}} E^{\frac{1}{6-2k}} \theta_j^{\frac{3-k}{6-2k}} t^{\frac{k-3}{6-2k}} & \text{lateral expansion.} \end{cases} \tag{3.4}
$$

We present the light curves of several bursts with similar afterglow characteristics: GRB 080503, GRB 140903A, GRB 150101B, GRB 160821B, and SN 2020bvc. To obtain the parameters required to calculate the light curves, we once again apply a MCMC algorithm. With this successful modeling, we show that our model is in agreement with observed data.

In Pedreira et al. (2022c) we present the temporal evolution of polarization for the fiducial model of Fraija et al. (2022), using the model presented in Section 1.1.5. In addition, we model the theoretical polarization for the set of bursts modeled in the aforementioned paper (no observed data) and successfully model the polarization upper limits of GRB 170817A. We show that the most commonly assumed scenarios for magnetic field anisotropy do not respect the imposed upper limits, when taking in consideration the off-axis synchrotron forward shock model as the underlying physics of the afterglow. The obtained results are in accordance with the literature. The version presented has currently been accepted for publication and is on editing and printing process by the *Astrophysical Journal*. The in-journal version, unfortunately, could not be ready in time for the submission of this document.

# Signatures from a Quasi-spherical Outflow and an Off-axis Top-hat Jet Launched in a Merger of Compact Objects: An Analytical Approach

N. Fraija[1] , D. Lopez-Camara[2] , A. C. Caligula do E. S. Pedreira[1], B. Betancourt Kamenetskaia[1], P. Veres[3], and S. Dichiara[4,5]

[1] Instituto de Astronomía, Universidad Nacional Autónoma de México, Apdo. Postal 70-264, Cd. Universitaria, Ciudad de México 04510, México
[2] CONACyT—Instituto de Astronomía, Universidad Nacional Autónoma de México, Apdo. Postal 70-264, Cd. Universitaria, Ciudad de México 04510, México
[3] Center for Space Plasma and Aeronomic Research (CSPAR), University of Alabama in Huntsville, Huntsville, AL 35899, USA
[4] Department of Astronomy, University of Maryland, College Park, MD 20742-4111, USA
[5] Astrophysics Science Division, NASA Goddard Space Flight Center, 8800 Greenbelt Rd, Greenbelt, MD 20771, USA

## Abstract

The production of both gravitational waves and short gamma-ray bursts (sGRBs) is widely associated with the merger of compact objects. Several studies have modeled the evolution of the electromagnetic emission using the synchrotron emission produced by the deceleration of both a relativistic top-hat jet seen off-axis, and a wide-angle quasi-spherical outflow (both using numerical studies). In this study, we present an analytical model of the synchrotron and synchrotron self-Compton (SSC) emission for an off-axis top-hat jet and a quasi-spherical outflow. We calculate the light curves obtained from an analytic model in which the synchrotron and SSC emission (in the fast- or slow-cooling regime) of an off-axis top-hat jet and a quasi-spherical outflow are decelerated in either a homogeneous or a wind-like circumburst medium. We show that the synchrotron emission of the quasi-spherical outflow is stronger than that of the off-axis jet during the first ∼10–20 days, and weaker during the next $\gtrsim$80 days. Moreover, we show that if the off-axis jet is decelerated in a wind-like medium, then the SSC emission is very likely to be detected. Applying an MCMC code to our model (for synchrotron emission only), we find the best-fit values for the radio, optical and X-ray emission of GRB 170817A that are in accordance with observations. For GRB 170817A, we find, using our model, that the synchrotron emission generated by the quasi-spherical outflow and off-axis top-hat jet increase as $F_\nu \propto t^\alpha$ with $\alpha \lesssim 0.8$ and $\alpha > 3$, respectively. Finally, we obtain the corresponding SSC light curves that are in accordance with the very-high-energy gamma-ray upper limits derived with the GeV–TeV observatories.

*Key words:* acceleration of particles – gamma-ray burst: individual (GRB 170817A) – gravitational waves – ISM: general – radiation mechanisms: non-thermal – stars: neutron

## 1. Introduction

The merger of two neutron stars (NSs) is believed to be a potential candidate for the production of both gravitational waves (GWs) and short gamma-ray bursts (sGRBs, $T_{90} \lesssim 2$ s) with an extended non-thermal emission (for reviews, see Nakar 2007; Berger 2014). Since the first detection of an sGRB, GWs had been exhaustively searched without success.

On 2017 August 17, for the first time, a GW source (GW 170817; Abbott et al. 2017a, 2017b) was associated with a faint electromagnetic γ-ray counterpart which is most probably the prompt emission of an sGRB (GRB 170817A; Goldstein et al. 2017; Savchenko et al. 2017), although today an off-axis emission from the top-hat jet is not the common knowledge (e.g., see Matsumoto et al. 2019).

GRB 170817A was followed up by an enormous observational campaign covering a large fraction of the electromagnetic spectrum. The X-ray counterpart was detected by the *Chandra* and *XMM-Newton* satellites (Margutti et al. 2017b, 2018; Troja et al. 2017; Alexander et al. 2018; D'Avanzo et al. 2018; Haggard et al. 2018). In optical bands, the non-thermal optical afterglow emission was revealed by the *Hubble Space Telescope* (Lyman et al. 2018; Margutti et al. 2018).[6] The radio emission at 3 and 6 GHz was identified by the Very Large Array (Abbott et al. 2017b; Mooley et al. 2018b; Troja et al. 2017; Dobie et al. 2018). The GW170917/

GRB 170817A event was also within the field of view of the Large Area Telescope (LAT) on-board the Fermi satellite and the field of view of two of the TeV γ-ray observatories: the High Energy Stereoscopic System (H.E.S.S.) Telescope and the High Altitude Water Cerenkov (HAWC). *Fermi*-LAT began observing around the position of GW170817 at ∼1000 s after the GBM trigger (Abbott et al. 2017b). No counts were registered and upper limits were derived. Observations with the HAWC observatory began on 2017 August 17 at 20:53 UTC and finished 2.03 hr later (Martinez-Castellanos et al. 2017). Although no significant excess was detected, upper limits for energies larger than 40 TeV were placed. The H.E.S.S. telescope searched for very-high-energy γ-ray emission at two opportunities (Abdalla et al. 2017): first, 5.3 hr after the GBM trigger, and second, from 0.22 to 5.2 days after the trigger. No statistically significant excess of counts was found by this TeV observatory and upper limits were derived.

The temporal behavior of the electromagnetic (EM) counterpart of GW170817 was atypical. The extended X-ray and radio afterglow were initially described by a simple power law, which gradually increased as ∼$t^{0.8}$ (Mooley et al. 2018b; Margutti et al. 2018), reached its peak at ∼140 days after the NS merger, and was followed by relatively fast decline. A miscellaneous set of models based on external shocks such as off-axis top-hat jets (Alexander et al. 2017; Ioka & Nakamura 2017; Margutti et al. 2017a; Troja et al. 2017; Fraija et al. 2019b, 2019c), radially stratified ejecta (Mooley et al. 2018b; Hotokezaka et al. 2018; Fraija et al. 2019f) and structured jets

---
[6] By "optical" we refer to the optical afterglow emission rather than the kilonova emission.

(Kasliwal et al. 2017; Lamb & Kobayashi 2017; Lazzati et al. 2018) were developed to interpret the behavior of this atypical afterglow. Mooley et al. (2018a) reported the detection of superluminal apparent motion in the radio band using Very Long Baseline Interferometry (VLBI), thus favoring models with successful jets and their respective quasi-spherical outflows. The successful jet models were also favored by VLBI radio observations performed by Ghirlanda et al. (2019) at 207.4 days. In the latter, the authors constrained the size of the source, indicating that GRB 170817A was produced by a structured relativistic jet. The structured jet models (Kasliwal et al. 2017; Lamb & Kobayashi 2017; Lazzati et al. 2018) suggest that the early-time radio flux during the two weeks after the merger is mostly produced by the radiation of an optically thin quasi-spherical outflow, while the late radio flux is dominated by the emission of a relativistic and collimated jet (immersed in the quasi-spherical outflow, which is now optically thin) with an opening angle less than $\lesssim 5°$ and observed from a viewing angle of $20° \pm 5°$.

*Fermi*-LAT has detected more than 50 GRBs with photons above 100 MeV and $\sim$12 bursts with photons above 10 GeV (see Ackermann et al. 2013, 2014, and references therein). Several authors have suggested that, although photons with energies larger than $\geqslant$100 MeV can be explained in the framework of the synchrotron forward-shock (FS) model (Kumar & Barniol Duran 2009; Wang et al. 2013; Fraija et al. 2016a, 2017a, 2019a, 2019d, 2019e), the maximum photon energy in this process is $\sim$10 GeV $\left(\frac{\Gamma}{100}\right)(1 + z)^{-1}$, where $\Gamma$ is the bulk Lorentz factor and $z$ is the redshift. Furthermore, taking into account that the bulk Lorentz factor during the afterglow phase evolves as $\propto t^{-\frac{3}{8}}$ and $\propto t^{-\frac{1}{4}}$ for a homogeneous and a wind-like medium, respectively, GeV photons from synchrotron radiation are not expected at timescales of $\sim$100 s. Recently, the MAGIC collaboration reported the detection of 300 GeV photons for almost 20 minutes in the direction of GRB 190114C (Mirzoyan 2019). Therefore, a different leptonic radiation mechanism of synchrotron radiation such as synchrotron self-Compton (SSC) in the forward-shock scenario has to be considered (e.g., see, Zhang & Mészáros 2004; Kumar & Zhang 2015; Fraija et al. 2017b; Fraija 2014).

In this study, we present a general analytic model (based on external forward shocks) where the synchrotron and SSC emission from material that is being decelerated in an arbitrary direction with respect to the observer, are obtained. Specifically, we calculate the flux from material that is in the relativistic phase and also material that is in the laterally expanding phase, and that are decelerating in either a homogeneous or a wind-like circumburst medium. As a particular case, we focus on the emission from a quasi-spherical outflow that is viewed on-axis and a relativistic top-hat jet viewed off-axis. As an application of our model, we describe the extended X-ray, optical, and radio emission exhibited in GRB 170817A. Hereafter, when we mention a jet, we refer to a top-hat jet. This paper is arranged as follows: In Section 2, we construct our model and show the synchrotron and SSC light curves from material that is being decelerated in an arbitrary direction with respect to the observer. In Section 3, we show the particular cases of a quasi-spherical outflow viewed on-axis and a relativistic jet viewed off-axis. In Section 4, we compare our model to the EM counterpart of GW170817. In Section 5, we present our conclusions.

## 2. Electromagnetic FS Emission Radiated in an Arbitrary Direction

During the fusion of a binary NS (BNS) system, a wind may be ejected in practically all directions and, once the BNS merges, a relativistic jet and its correspondent quasi-spherical outflow may be powered (e.g., see Gill & Granot 2018). Once the jet/quasi-spherical outflow sweeps enough circumburst medium (which may have been affected by the BNS wind), the relativistic electrons accelerated through the forward shocks (FSs) are mainly cooled down by synchrotron and SSC radiation. Consequently, we derive the synchrotron and SSC fluxes in the fully adiabatic regime from material that is moving relativistically and material that is being decelerated in an arbitrary direction (with respect to the observer) by either a homogeneous or a wind-like medium. We must note that we only consider the electrons accelerated by FSs because they produce extended emissions, and not by reverse shocks as they produce short-lived emissions.

### 2.1. Homogeneous Medium

The FS dynamics in the fully adiabatic regime for material spreading through a homogeneous medium has been explored for the case when the radiation is pointing directly in the observer's direction (see, e.g., Sari et al. 1998), not for the case when it points in an arbitrary direction. Therefore, we derive and present in the following section the synchrotron and SSC fluxes during the relativistic and lateral expansion phases for radiation pointing in any arbitrary direction.

#### 2.1.1 Relativistic Phase of the Deceleration Material

*Synchrotron radiation*—Accelerated electrons in FS models are distributed in accordance with their Lorentz factors ($\gamma_e$) and described by the electron power index $p$ as $N(\gamma_e)d\gamma_e \propto \gamma_e^{-p} d\gamma_e$ for $\gamma_m \leqslant \gamma_e \leqslant \gamma_c$, where $\gamma_m$ and $\gamma_c$ are the minimum and cooling electron Lorentz factors. These are given by:

$$\gamma_m = 3.1 \times 10^2 \, g(p)\varepsilon_{e,-1}\Gamma_1$$
$$\gamma_c = 5.8 \times 10^4 \left(\frac{1 + z}{1.022}\right)(1 + Y)^{-1}\varepsilon_{B,-3}^{-1} \, n_{-1}^{-1}\Gamma_1^{-2}\delta_{D,1}^{-1}t_{1d}^{-1},$$

(1)

where $g(p) = \frac{p - 2}{p - 1} \simeq 0.17$ for $p = 2.2$, $n$ is the density of the circumburst medium, $Y$ is the Compton parameter, $\varepsilon_B$ and $\varepsilon_e$ are the microphysical parameters associated with the magnetic field and the energy density given to accelerate electrons, $t_{1d}$ is the timescale of the order of one day, and $\delta_D$ is the Doppler factor. The Doppler factor is $\delta_D = \frac{1}{\Gamma(1 - \mu\beta)}$ where $\mu = \cos\Delta\theta$, $\beta$ is the velocity of the material, and $\Delta\theta = \theta_{obs} - \theta_j$ is given by the viewing angle ($\theta_{obs}$) and the aperture angle of the jet ($\theta_j$). We adopt the convention $Q_x = Q/10^x$ in cgs units.

Given the fact that $\epsilon_i^{syn} \propto \gamma_i^2$ (for $i = m, c$ with $m$ the characteristic and $c$ the cooling break) with Equation (1), the synchrotron spectral breaks ($\epsilon_m^{syn}$ and $\epsilon_c^{syn}$) and the maximum

flux ($F_{\mathrm{max}}^{\mathrm{syn}}$) become:

$$\epsilon_{\mathrm{m}}^{\mathrm{syn}} \simeq 15.9 \text{ GHz} \left(\frac{1+z}{1.022}\right)^{-1} g(p)^2 \varepsilon_{e,-1}^2 \varepsilon_{B,-3}^{\frac{1}{2}} n_{-1}^{\frac{1}{2}} \delta_{D,1} \Gamma_1^3$$

$$\epsilon_{\mathrm{c}}^{\mathrm{syn}} \simeq 6.2 \text{ eV} \left(\frac{1+z}{1.022}\right) (1+Y)^{-2} \varepsilon_{B,-3}^{-\frac{3}{2}} n_{-1}^{-\frac{3}{2}} \delta_{D,1}^{-1} \Gamma_1^{-3} t_{1\mathrm{d}}^{-2}$$

$$F_{\mathrm{max}}^{\mathrm{syn}} \simeq 5.8 \times 10^4 \text{ mJy} \left(\frac{1+z}{1.022}\right)^{-1} \varepsilon_{B,-3}^{\frac{1}{2}} n_{-1}^{\frac{3}{2}} D_{26.5}^{-2} \delta_{D,1}^6 \Gamma_1^4 t_{1\mathrm{d}}^3.$$

(2)

Given the spectral breaks and the maximum flux from Equation (2), the synchrotron light curve for the fast-cooling regime ($\epsilon_{\mathrm{c}}^{\mathrm{syn}} < \epsilon_{\mathrm{m}}^{\mathrm{syn}}$) is:

$$F_{\nu}^{\mathrm{syn}} \propto \begin{cases} \delta_D^{\frac{19}{3}} \Gamma^5 t^{\frac{11}{3}} \epsilon_{\gamma}^{\frac{1}{3}}, & \epsilon_{\gamma} < \epsilon_{\mathrm{c}}^{\mathrm{syn}}, \\ \delta_D^{\frac{11}{2}} \Gamma^{\frac{5}{2}} t^2 \epsilon_{\gamma}^{-\frac{1}{2}}, & \epsilon_{\mathrm{c}}^{\mathrm{syn}} < \epsilon_{\gamma} < \epsilon_{\mathrm{m}}^{\mathrm{syn}}, \\ \delta_D^{\frac{p+10}{2}} \Gamma^{\frac{3p+2}{2}} t^2 \epsilon_{\gamma}^{-\frac{p}{2}}, & \epsilon_{\mathrm{m}}^{\mathrm{syn}} < \epsilon_{\gamma} \end{cases}$$

(3)

Meanwhile, the light curve for the slow-cooling regime ($\epsilon_{\mathrm{m}}^{\mathrm{syn}} < \epsilon_{\mathrm{c}}^{\mathrm{syn}}$) is:

$$F_{\nu}^{\mathrm{syn}} \propto \begin{cases} \delta_D^{\frac{17}{3}} \Gamma^3 t^3 \epsilon_{\gamma}^{\frac{1}{3}}, & \epsilon_{\gamma} < \epsilon_{\mathrm{m}}^{\mathrm{syn}}, \\ \delta_D^{\frac{p+11}{2}} \Gamma^{\frac{3p+5}{2}} t^3 \epsilon_{\gamma}^{-\frac{p-1}{2}}, & \epsilon_{\mathrm{m}}^{\mathrm{syn}} < \epsilon_{\gamma} < \epsilon_{\mathrm{c}}^{\mathrm{syn}}, \\ \delta_D^{\frac{p+10}{2}} \Gamma^{\frac{3p+2}{2}} t^2 \epsilon_{\gamma}^{-\frac{p}{2}}, & \epsilon_{\mathrm{c}}^{\mathrm{syn}} < \epsilon_{\gamma}, \end{cases}$$

(4)

with $\epsilon_{\gamma}$, in general, the energy at which the flux is observed.

### 2.1.1.2 SSC emission

—Accelerated electrons in the FSs can up-scatter synchrotron photons from low to high energies as $\epsilon_{\mathrm{i}}^{\mathrm{ssc}} \sim \gamma_{\mathrm{i}}^2 \epsilon_{\mathrm{i}}^{\mathrm{syn}}$ with an SSC flux $F_{\mathrm{max}}^{\mathrm{ssc}} \sim 4g(p)^{-1}\tau F_{\mathrm{max}}^{\mathrm{syn}}$, where $\tau$ is the optical depth ($\tau = \frac{1}{3}\sigma_T nR$ with $R$ being the deceleration radius and $\sigma_T$ the Thompson cross section). Using Equations (1) and (2), the spectral breaks and the maximum flux of SSC emission are, respectively:

$$\epsilon_{\mathrm{m}}^{\mathrm{ssc}} \simeq 6.2 \text{ eV} \left(\frac{1+z}{1.022}\right)^{-1} g(p)^4 \varepsilon_{e,-1}^4 \varepsilon_{B,-3}^{\frac{1}{2}} n_{-1}^{\frac{1}{2}} \delta_{D,1} \Gamma_1^5$$

$$\epsilon_{\mathrm{c}}^{\mathrm{ssc}} \simeq 20.6 \text{ GeV} \left(\frac{1+z}{1.022}\right)^3 (1+Y)^{-4} \varepsilon_{B,-3}^{-\frac{7}{2}} n_{-1}^{-\frac{7}{2}} \delta_{D,1}^{-3} \Gamma_1^{-7}$$
$$\times t_{1\mathrm{d}}^{-4}$$

$$F_{\mathrm{max}}^{\mathrm{ssc}} \simeq 7.8 \times 10^{-3} \text{ mJy} \left(\frac{1+z}{1.022}\right)^{-2} g(p)^{-1} \varepsilon_{B,-3}^{\frac{1}{2}} n_{-1}^{\frac{5}{2}} D_{26.5}^{-2}$$
$$\times \delta_{D,1}^7 \Gamma_1^5 t_{1\mathrm{d}}^4.$$

(5)

The Klein–Nishina (KN) suppression effect must be considered in SSC emission. The break energy in the KN regime is:

$$\epsilon_{\mathrm{KN}}^{\mathrm{ssc}} \simeq 288.2 \text{ GeV} (1+Y)^{-1} \varepsilon_{B,-1}^{-1} n_{-1}^{-1} \Gamma_1^{-2} t_{1\mathrm{d}}^{-1}.$$

(6)

Using the synchrotron fluxes found in Equations (3) and (4), the SSC light curves for the fast- and slow-cooling regimes are, respectively:

$$F_{\nu}^{\mathrm{ssc}} \propto \begin{cases} \delta_D^8 \Gamma^{\frac{22}{3}} t^{\frac{16}{3}} \epsilon_{\gamma}^{\frac{1}{3}}, & \epsilon_{\gamma} < \epsilon_{\mathrm{c}}^{\mathrm{ssc}}, \\ \delta_D^{\frac{11}{2}} \Gamma^{\frac{3}{2}} t^2 \epsilon_{\gamma}^{-\frac{1}{2}}, & \epsilon_{\mathrm{c}}^{\mathrm{ssc}} < \epsilon_{\gamma} < \epsilon_{\mathrm{m}}^{\mathrm{ssc}}, \\ \delta_D^{\frac{p+10}{2}} \Gamma^{\frac{5p-2}{2}} t^2 \epsilon_{\gamma}^{-\frac{p}{2}}, & \epsilon_{\mathrm{m}}^{\mathrm{ssc}} < \epsilon_{\gamma}, \end{cases}$$

(7)

$$F_{\nu}^{\mathrm{ssc}} \propto \begin{cases} \delta_D^{\frac{20}{3}} \Gamma^{\frac{10}{3}} t^4 \epsilon_{\gamma}^{\frac{1}{3}}, & \epsilon_{\gamma} < \epsilon_{\mathrm{m}}^{\mathrm{ssc}}, \\ \delta_D^{\frac{p+13}{2}} \Gamma^{\frac{5(p+1)}{2}} t^4 \epsilon_{\gamma}^{-\frac{p-1}{2}}, & \epsilon_{\mathrm{m}}^{\mathrm{ssc}} < \epsilon_{\gamma} < \epsilon_{\mathrm{c}}^{\mathrm{ssc}}, \\ \delta_D^{\frac{p+10}{2}} \Gamma^{\frac{5p-2}{2}} t^2 \epsilon_{\gamma}^{-\frac{p}{2}}, & \epsilon_{\mathrm{c}}^{\mathrm{ssc}} < \epsilon_{\gamma}. \end{cases}$$

(8)

### 2.1.2. Lateral Expansion Phase of the Deceleration Material

As the relativistic material sweeps through the medium and decelerates, its beaming cone broadens until it reaches the field of view of the observer ($\Gamma \sim \Delta\theta^{-1}$; Granot et al. 2002, 2018). We will refer to this phase as the lateral expansion phase. In this phase, the Doppler factor becomes $\delta_D \approx 2\Gamma$ and the maximum flux must be corrected by dividing by $\Omega = 4\pi\delta_D^2$ (Rybicki & Lightman 1986; Lamb et al. 2018; Fraija et al. 2019f). Taking into account that the lateral expansion phase is expected in a timescale that goes from several hours to days (e.g., see Kumar & Zhang 2015), the fast-cooling regime for the synchrotron and SSC emission would be negligible and the slow-cooling regime will dominate. For this reason, we only derive the synchrotron and SSC light curves in the slow-cooling regime during this phase.

*Synchrotron radiation*—The synchrotron spectral breaks can be calculated through Equation (2) with $\delta_D \approx 2\Gamma$, and the correction of $\Omega = 4\pi\delta_D^2$ for the maximum flux. In this case, the synchrotron flux for the slow-cooling regime becomes:

$$F_{\nu}^{\mathrm{syn}} \propto \begin{cases} \Gamma^{\frac{20}{3}} t^3 \epsilon_{\gamma}^{\frac{1}{3}}, & \epsilon_{\gamma} < \epsilon_{\mathrm{m}}^{\mathrm{syn}}, \\ \Gamma^{2(p+3)} t^3 \epsilon_{\gamma}^{-\frac{p-1}{2}}, & \epsilon_{\mathrm{m}}^{\mathrm{syn}} < \epsilon_{\gamma} < \epsilon_{\mathrm{c}}^{\mathrm{syn}}, \\ \Gamma^{2(p+2)} t^2 \epsilon_{\gamma}^{-\frac{p}{2}}, & \epsilon_{\mathrm{c}}^{\mathrm{syn}} < \epsilon_{\gamma} \end{cases}$$

(9)

### 2.1.2.1. SSC emission

—The SSC spectral breaks can be calculated through Equation (5) with the same corrections of $\delta_D$ and $\Omega$ as for the synchrotron radiation. In this case, the SSC flux for the slow-cooling regime becomes:

$$F_{\nu}^{\mathrm{ssc}} \propto \begin{cases} \Gamma^8 t^4 \epsilon_{\gamma}^{\frac{1}{3}}, & \epsilon_{\gamma} < \epsilon_{\mathrm{m}}^{\mathrm{ssc}}, \\ \Gamma^{3p+7} t^4 \epsilon_{\gamma}^{-\frac{p-1}{2}}, & \epsilon_{\mathrm{m}}^{\mathrm{ssc}} < \epsilon_{\gamma} < \epsilon_{\mathrm{c}}^{\mathrm{ssc}}, \\ \Gamma^{3p+2} t^2 \epsilon_{\gamma}^{-\frac{p}{2}}, & \epsilon_{\mathrm{c}}^{\mathrm{ssc}} < \epsilon_{\gamma} \end{cases}$$

(10)

## 2.2. Wind-like Medium

A non-homogeneous density produced by the ejected mass near the vicinity of the NS binary system has been studied numerically (Bauswein et al. 2013; Hotokezaka et al. 2013; Nagakura et al. 2014). Nagakura et al. (2014) studied the

propagation of a relativistic jet through the ejected mass using a density profile of $\rho(r) \propto \frac{M_{ej}}{r_0^3} r^{-k}$ with $r_0$ the initial radius and $M_{ej}$ the ejecta mass. Since the density profile around the merger can be approximated as a medium with $k = 2$, we derive the dynamics for material either in the relativistic or the lateral expanding phase in a density profile that scales as $\rho(r) \propto r^{-2}$. Specifically, we assume that the wind-like medium is $\rho(r) = A \, r^{-2}$, with $A = \frac{\dot{M}}{4\pi \, v} = A_\star \, 5 \times 10^{11} \, \text{g cm}^{-1}$, $\dot{M}$ the mass-loss rate, $v$ the velocity of the outflow, and $A_\star$ a dimensional parameter ($A_\star \sim 10^{-1}$–$10^{-6}$). Given that the lateral expansion phase is expected in a timescale that goes from several hours to hundreds of days (e.g., see Kumar & Zhang 2015), thus the lateral expansion phase in a wind-like medium is negligible (compared to the relativistic phase). Hence, we only derive the synchrotron and SSC fluxes of the relativistic phase.

### 2.2.1. Relativistic Phase of the Deceleration Material

#### 2.2.1.1 Synchrotron emission

—The minimum and cooling Lorentz factors in a wind-like medium are given by:

$$
\begin{aligned}
\gamma_m &= 3.1 \times 10^2 \, g(p)\varepsilon_{e,-1}\Gamma_1 \\
\gamma_c &= 1.4 \times 10^3 \left(\frac{1+z}{1.022}\right)^{-1} \xi^2 (1+Y)^{-1}\varepsilon_{B,-3}^{-1} A_{\star,-4}^{-1} \, \delta_{D,1} \\
&\quad \times t_{10s},
\end{aligned}
\tag{11}
$$

where $\xi$ is a constant parameter ($\xi \approx 1$) (Panaitescu & Mészáros 1998).

Using Equation (11) in the synchrotron emission, the spectral breaks and the maximum flux are:

$$
\begin{aligned}
\epsilon_m^{\text{syn}} &\simeq 9.4 \times 10^4 \, \text{GHz} \, g(p)^2 \, \xi^{-2} \varepsilon_{e,-1}^2 \, \varepsilon_{B,-3}^{\frac{1}{2}} \, A_{\star,-4}^{\frac{1}{2}} \, \Gamma_1^2 \, t_{10s}^{-1} \\
\epsilon_c^{\text{syn}} &\simeq 1.1 \, \text{eV} \left(\frac{1+z}{1.022}\right)^{-2} \xi^2 (1+Y)^{-2} \, \varepsilon_{B,-3}^{-\frac{3}{2}} A_{\star,-4}^{-\frac{3}{2}} \, \delta_{D,1}^2 \, t_{10s} \\
F_{\max}^{\text{syn}} &\simeq 18.4 \, \text{mJy} \left(\frac{1+z}{1.022}\right)^2 \varepsilon_{B,-3}^{\frac{1}{2}} \, A_{\star,-4}^{\frac{3}{2}} \, D_{26.5}^{-2} \, \delta_{D,1}^3 \Gamma_1.
\end{aligned}
\tag{12}
$$

Using Equation (12) in the synchrotron emission, the flux for the fast- and slow-cooling regimes are, respectively:

$$
F_\nu^{\text{syn}} \propto 
\begin{cases}
\delta_D^{\frac{7}{3}} \, \Gamma \, t^{-\frac{1}{3}} \, \epsilon_\gamma^{\frac{1}{3}}, & \epsilon_\gamma < \epsilon_c, \\
\delta_D^4 \, \Gamma \, t^{\frac{1}{2}} \, \epsilon_\gamma^{-\frac{1}{2}}, & \epsilon_c < \epsilon_\gamma < \epsilon_m, \\
\delta_D^4 \, \Gamma^p \, t^{-\frac{p}{2}+1} \, \epsilon_\gamma^{-\frac{p}{2}}, & \epsilon_m < \epsilon_\gamma,
\end{cases}
\tag{13}
$$

$$
F_\nu^{\text{syn}} \propto 
\begin{cases}
\delta_D^3 \, \Gamma^{\frac{1}{3}} \, t^{\frac{1}{3}} \, \epsilon_\gamma^{\frac{1}{3}}, & \epsilon_\gamma < \epsilon_m, \\
\delta_D^3 \, \Gamma^p \, t^{-\frac{p-1}{2}} \, \epsilon_\gamma^{-\frac{p-1}{2}}, & \epsilon_m < \epsilon_\gamma < \epsilon_c, \\
\delta_D^4 \, \Gamma^p \, t^{-\frac{p}{2}+1} \, \epsilon_\gamma^{-\frac{p}{2}}, & \epsilon_c < \epsilon_\gamma.
\end{cases}
\tag{14}
$$

#### 2.2.1.2 SSC emission

—Given the electron Lorentz factors (Equation (11)) and the synchrotron spectral breaks (Equation (12)), the SSC spectral breaks and the maximum flux are:

$$
\begin{aligned}
\epsilon_m^{\text{ssc}} &\simeq 3.6 \, \text{keV} \, g(p)^4 \xi^{-2} \varepsilon_{e,-1}^4 \, \epsilon_{B,-3}^{\frac{1}{2}} \, A_{\star,-4}^{\frac{1}{2}} \, \Gamma_1^4 \, t_{10s}^{-1} \\
\epsilon_c^{\text{ssc}} &\simeq 2.3 \, \text{MeV} \left(\frac{1+z}{1.022}\right)^{-4} \xi^6 (1+Y)^{-4} \, \epsilon_{B,-3}^{-\frac{7}{2}} \, A_{\star,-4}^{-\frac{7}{2}} \, \delta_{D,1}^4 \, t_{10s}^3 \\
F_{\max}^{\text{ssc}} &\simeq 1.1 \times 10^{-4} \, \text{mJy} \left(\frac{1+z}{1.022}\right)^3 g(p)^{-1}\xi^{-2}\varepsilon_{B,-3}^{\frac{1}{2}} A_{\star,-4}^{\frac{5}{2}} \\
&\quad \times D_{26.5}^{-2} \delta_{D,1}^2 t_{10s}^{-1}.
\end{aligned}
\tag{15}
$$

The break energy in the SSC emission due to the KN effect is:

$$
\epsilon_{\text{KN}}^{\text{ssc}} \simeq 7.2 \, \text{GeV} \left(\frac{1+z}{1.022}\right)^{-2} (1+Y)^{-1} \xi^2 \, \varepsilon_{B,-3}^{-1} \, A_{\star,-4}^{-1} \, \delta_{D,1}^2.
\tag{16}
$$

Using the SSC spectrum, the spectral breaks and the maximum flux (Equation (15)), the SSC light curves for fast- and slow-cooling regimes are, respectively:

$$
F_\nu^{\text{ssc}} \propto 
\begin{cases}
\delta_D^{\frac{2}{3}} \, t^{-2} \, \epsilon_\gamma^{\frac{1}{3}}, & \epsilon_\gamma < \epsilon_c, \\
\delta_D^4 \, t^{\frac{1}{2}} \, \epsilon_\gamma^{-\frac{1}{2}}, & \epsilon_c < \epsilon_\gamma < \epsilon_m, \\
\delta_D^4 \, \Gamma^{2p-2} \, t^{-\frac{p}{2}+1} \, \epsilon_\gamma^{-\frac{p}{2}}, & \epsilon_m < \epsilon_\gamma,
\end{cases}
\tag{17}
$$

$$
F_\nu^{\text{ssc}} \propto 
\begin{cases}
\delta_D^2 \, \Gamma^{-\frac{4}{3}} \, t^{-\frac{2}{3}} \, \epsilon_\gamma^{\frac{1}{3}}, & \epsilon_\gamma < \epsilon_m, \\
\delta_D^2 \, \Gamma^{2(p-1)} \, t^{-\frac{p+1}{2}} \, \epsilon_\gamma^{-\frac{p-1}{2}}, & \epsilon_m < \epsilon_\gamma < \epsilon_c, \\
\delta_D^4 \, \Gamma^{2p-2} \, t^{-\frac{p}{2}+1} \, \epsilon_\gamma^{-\frac{p}{2}}, & \epsilon_c < \epsilon_\gamma.
\end{cases}
\tag{18}
$$

## 3. Quasi-spherical Outflow and Off-axis Jet

We now calculate the electromagnetic radiation for the specific case of an off-axis jet plus a wide-angle quasi-spherical outflow in a homogeneous and wind-like medium. Figure 1 shows the schematic representation of the electromagnetic emission produced by an off-axis jet and its corresponding quasi-spherical outflow. On one hand, the decelerated material from the quasi-spherical outflow releases photons at nearly all the viewing angles. On the other hand, only a small fraction of the emission from the material in the relativistic jet is observable (due to relativistic beaming $\theta_j \propto 1/\Gamma$). Once the outflow and the off-axis jet sweep up enough circumburst medium, the electron population inside either case cool down, emitting synchrotron and SSC radiation. In the case of the quasi-spherical outflow, the Doppler factor can be approximated to $\delta_D \approx 2\Gamma$ and, in the case of the off-axis jet, this factor can be approximated to $\delta_D \simeq \frac{2}{\Gamma \Delta \theta^2}$ for $\Gamma^2 \Delta \theta^2 \gg 1$. With these approximations in the obtained fluxes from Section 2 we derive the dynamics for each case.

### 3.1. Quasi-spherical Outflow

The synchrotron and SSC emission of a quasi-spherical outflow in the relativistic phase and in the lateral expansion phase, moving through either a homogeneous medium or a wind-like medium, are next calculated.
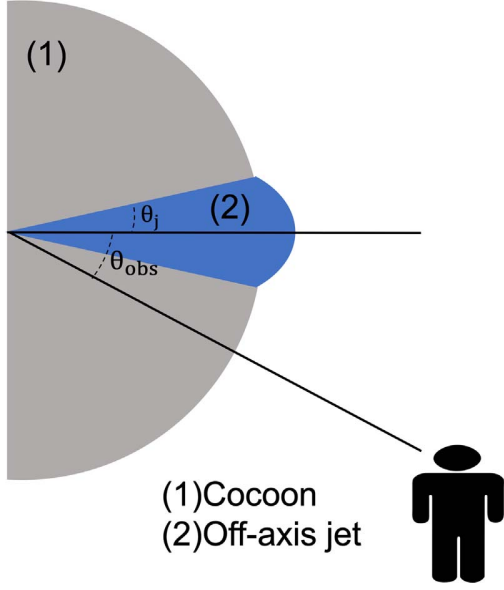
**Figure 1.** Schematic representation of the quasi-spherical outflow, the off-axis jet, and the observer. The quasi-spherical outflow emits photons at nearly all the viewing angles while the off-axis jet emits mainly toward the propagation direction.

### 3.1.1. Homogeneous Medium: Relativistic Phase

Assuming that the equivalent kinetic energy ($E_k$) associated with the material that is accelerated in the quasi-spherical outflow can be written as $E_k = \tilde{E}\,\Gamma^{-\alpha_s}$, and considering the Blandford–McKee solution (Blandford & McKee 1976), where $E_k = \frac{4\pi}{3}\,m_p\,n\,R^3\Gamma^2$, then the bulk Lorentz factor ($\Gamma$) can be written as:

$$\Gamma = 3.8\left(\frac{1+z}{1.022}\right)^{\frac{3}{\alpha_s+8}} n_{-1}^{-\frac{1}{\alpha_s+8}}\,\tilde{E}_{50}^{\frac{1}{\alpha_s+8}}\,t_{1d}^{-\frac{3}{\alpha_s+8}}, \qquad (19)$$

where $z$ is the redshift, $\tilde{E}$ is the fiducial energy given by $\tilde{E} = \frac{32\pi}{3}\,m_p(1+z)^{-3}\,n\Gamma^{\alpha_s+8}\,t^3$, $m_p$ is the proton mass, and $\alpha_s$ is the power index of the velocity distribution. Using Equation (19) in Equations (3), (4), (7) and (8), we next obtain the synchrotron and SSC emission of a quasi-spherical outflow in the relativistic phase moving through a homogeneous medium.

#### 3.1.1.1 Synchrotron light curves

—Given the evolution of the bulk Lorentz factor (Equation (19)) and the synchrotron spectra (Equations (13) and (14)), the fluxes for the fast-cooling and slow-cooling regimes can be written, respectively, as:

$$F_\nu^{\rm syn} \propto \begin{cases} t^{\frac{11\alpha_s+4}{3(\alpha_s+8)}}\,\epsilon_\gamma^{\frac{1}{3}}, & \epsilon_\gamma < \epsilon_{\rm c}, \\ t^{\frac{2(\alpha_s-1)}{\alpha_s+8}}\,\epsilon_\gamma^{-\frac{1}{2}}, & \epsilon_{\rm c} < \epsilon_\gamma < \epsilon_{\rm m}, \\ t^{\frac{2(\alpha_s-3p+2)}{\alpha_s+8}}\,\epsilon_\gamma^{-\frac{p}{2}}, & \epsilon_{\rm m} < \epsilon_\gamma, \end{cases} \qquad (20)$$

$$F_\nu^{\rm syn} \propto \begin{cases} t^{\frac{3\alpha_s+4}{\alpha_s+8}}\,\epsilon_\gamma^{\frac{1}{3}}, & \epsilon_\gamma < \epsilon_{\rm m}^{\rm syn}, \\ t^{\frac{3(\alpha_s-2p+2)}{\alpha_s+8}}\,\epsilon_\gamma^{-\frac{p-1}{2}}, & \epsilon_{\rm m}^{\rm syn} < \epsilon_\gamma < \epsilon_{\rm c}^{\rm syn}, \\ t^{\frac{2(\alpha_s-3p+2)}{\alpha_s+8}}\,\epsilon_\gamma^{-\frac{p}{2}}, & \epsilon_{\rm c}^{\rm syn} < \epsilon_\gamma \end{cases} \qquad (21)$$

The synchrotron spectral breaks $\epsilon_{\rm m}^{\rm syn}$ and $\epsilon_{\rm c}^{\rm syn}$ and the maximum flux are given in Equation (48).

*SSC light curves*—Given the evolution of the bulk Lorentz factor (Equation (19)) and the SSC spectra (Equations (17) and (18)), the fluxes for the fast-cooling and slow-cooling regimes, respectively, can be written as:

$$F_\nu^{\rm ssc} \propto \begin{cases} t^{\frac{8(2\alpha_s+1)}{3(\alpha_s+8)}}\,\epsilon_\gamma^{\frac{1}{3}}, & \epsilon_\gamma < \epsilon_{\rm c}^{\rm ssc}, \\ t^{\frac{2\alpha_s+1}{\alpha_s+8}}\,\epsilon_\gamma^{-\frac{1}{2}}, & \epsilon_{\rm c}^{\rm ssc} < \epsilon_\gamma < \epsilon_{\rm m}^{\rm ssc}, \\ t^{\frac{2\alpha_s-9p+10}{\alpha_s+8}}\,\epsilon_\gamma^{-\frac{p}{2}}, & \epsilon_{\rm m}^{\rm ssc} < \epsilon_\gamma, \end{cases} \qquad (22)$$

$$F_\nu^{\rm ssc} \propto \begin{cases} t^{\frac{4(\alpha_s+2)}{\alpha_s+8}}\,\epsilon_\gamma^{\frac{1}{3}}, & \epsilon_\gamma < \epsilon_{\rm m}^{\rm ssc}, \\ t^{\frac{4\alpha_s-9p+11}{\alpha_s+8}}\,\epsilon_\gamma^{-\frac{p-1}{2}}, & \epsilon_{\rm m}^{\rm ssc} < \epsilon_\gamma < \epsilon_{\rm c}^{\rm ssc}, \\ t^{\frac{2\alpha_s-9p+10}{\alpha_s+8}}\,\epsilon_\gamma^{-\frac{p}{2}}, & \epsilon_{\rm c}^{\rm ssc} < \epsilon_\gamma \end{cases} \qquad (23)$$

The SSC spectral breaks $\epsilon_{\rm m}^{\rm ssc}$ and $\epsilon_{\rm c}^{\rm ssc}$ and the maximum flux are given in Equation (49).

### 3.1.2. Homogeneous Medium: Lateral Expansion Phase

The relativistic beaming effect of the emitting shock causes the afterglow emission to be beamed into a beaming angle ($\theta_b \sim 1/\Gamma$), which, for fast flows ($v \sim c$), is narrower than the angle with which the jet is launched ($\theta_l$) and narrower than the observers viewing angle. Eventually, when the outflow decelerates, the beaming effect weakens and the emission inside the beaming cone expands sideways and broadens. When $\theta_b \geqslant \theta_l$, a break in the light curve is expected (e.g., see Salmonson 2003; Granot et al. 2017).

Considering the Blandford–McKee solution and the fact that $E_k = \tilde{E}\,\Gamma^{-\alpha_s}$ during the lateral expansion phase, the bulk Lorentz factor can be written as

$$\Gamma = 2.1\left(\frac{1+z}{1.022}\right)^{\frac{3}{\alpha_s+6}} n_{-1}^{-\frac{1}{\alpha_s+6}}\,\beta^{-\frac{\alpha_s}{\alpha_s+6}}\,\tilde{E}_{50}^{\frac{1}{\alpha_s+6}}\,t_{30d}^{-\frac{3}{\alpha_s+6}}. \qquad (24)$$

Using Equation (24) in Equations (3), (4), (7), and (8), we next obtain the synchrotron and SSC of a quasi-spherical outflow in the lateral expansion phase moving through a homogeneous medium.

*Synchrotron light curves*—The synchrotron light curve for the slow-cooling regime is:

$$F_\nu^{\rm syn} \propto \begin{cases} t^{\frac{3\alpha_s-2}{\alpha_s+6}}\,\epsilon_\gamma^{\frac{1}{3}}, & \epsilon_\gamma < \epsilon_{\rm m}, \\ t^{\frac{3(\alpha_s-2p)}{\alpha_s+6}}\,\epsilon_\gamma^{-\frac{p-1}{2}}, & \epsilon_{\rm m} < \epsilon_\gamma < \epsilon_{\rm c}, \\ t^{\frac{2(\alpha_s-3p)}{\alpha_s+6}}\,\epsilon_\gamma^{-\frac{p}{2}}, & \epsilon_{\rm c} < \epsilon_\gamma. \end{cases} \qquad (25)$$

Once the bulk Lorentz factor becomes less than $\sim 2$, the quasi-spherical outflow goes into a non-relativistic phase. In this case, the spectral breaks and the maximum flux evolve as: $\epsilon_{\rm m} \propto t^{-\frac{15}{\alpha_s+5}}$, $\epsilon_{\rm c} \propto t^{-\frac{2\alpha_s+1}{\alpha_s+5}}$ and $F_{\rm max} \propto t^{\frac{3(\alpha_s+1)}{\alpha_s+5}}$. The synchrotron

light curve in the non-relativistic phase is

$$
F_\nu^{\rm syn} \propto \begin{cases} t^{\frac{3\alpha_s+8}{\alpha_s+5}} \, \epsilon_\gamma^{\frac{1}{3}}, & \epsilon_\gamma < \epsilon_{\rm m}, \\ t^{\frac{6\alpha_s-15p+21}{2(\alpha_s+5)}} \, \epsilon_\gamma^{-\frac{p-1}{2}}, & \epsilon_{\rm m} < \epsilon_\gamma < \epsilon_{\rm c}, \\ t^{\frac{4\alpha_s-15p+20}{2(\alpha_s+5)}} \, \epsilon_\gamma^{-\frac{p}{2}}, & \epsilon_{\rm c} < \epsilon_\gamma. \end{cases} \tag{26}
$$

*SSC light curves*—The SSC light curve for the slow-cooling regime is:

$$
F_\nu^{\rm ssc} \propto \begin{cases} t^{\frac{4\alpha_s}{\alpha_s+6}} \, \epsilon_\gamma^{\frac{1}{3}}, & \epsilon_\gamma < \epsilon_{\rm m}^{\rm ssc}, \\ t^{\frac{4\alpha_s-9p+3}{\alpha_s+6}} \, \epsilon_\gamma^{-\frac{p-1}{2}}, & \epsilon_{\rm m}^{\rm ssc} < \epsilon_\gamma < \epsilon_{\rm c}^{\rm ssc}, \\ t^{\frac{2\alpha_s-9p+6}{\alpha_s+6}} \, \epsilon_\gamma^{-\frac{p}{2}}, & \epsilon_{\rm c}^{\rm ssc} < \epsilon_\gamma. \end{cases} \tag{27}
$$

In the case when the quasi-spherical outflow is in the non-relativistic phase, the spectral breaks and the maximum flux evolve as: $\epsilon_{\rm m}^{\rm ssc} \propto t^{-\frac{27}{\alpha_s+5}}$, $\epsilon_{\rm c}^{\rm ssc} \propto t^{-\frac{4\alpha_s}{\alpha_s+5}}$ and $F_{\rm max}^{\rm ssc} \propto t^{\frac{4(\alpha_s+5)}{\alpha_s+5}}$. The SSC light curve in the non-relativistic phase is

$$
F_\nu^{\rm ssc} \propto \begin{cases} t^{\frac{4\alpha_s+14}{\alpha_s+5}} \, \epsilon_\gamma^{\frac{1}{3}}, & \epsilon_\gamma < \epsilon_{\rm m}^{\rm ssc}, \\ t^{\frac{8\alpha_s+37-27p}{2(\alpha_s+5)}} \, \epsilon_\gamma^{-\frac{p-1}{2}}, & \epsilon_{\rm m}^{\rm ssc} < \epsilon_\gamma < \epsilon_{\rm c}^{\rm ssc}, \\ t^{\frac{4\alpha_s+38-27p}{2(\alpha_s+5)}} \, \epsilon_\gamma^{-\frac{p}{2}}, & \epsilon_{\rm c}^{\rm ssc} < \epsilon_\gamma. \end{cases} \tag{28}
$$

### 3.1.3. Wind-like Medium

As already stated in Section 2.2, for the wind-like medium, the lateral expansion phase is negligible compared to the relativistic phase. Thus, we only calculate the synchrotron and SSC fluxes of the relativistic phase in this regime.

Considering the Blandford–McKee solution for a wind-like medium, the bulk Lorentz factor can be written as:

$$
\Gamma = 16.7 \left( \frac{1+z}{1.022} \right)^{\frac{1}{\alpha_s+4}} \xi^{-\frac{2}{\alpha_s+4}} A_{\star,-4}^{-\frac{1}{\alpha_s+4}} \tilde{E}_{50}^{\frac{1}{\alpha_s+4}} t_{10s}^{-\frac{1}{\alpha_s+4}}, \tag{29}
$$

where $\tilde{E} = \frac{32\pi}{3}(1+z)^{-1} \xi^2 A_\star \Gamma^{\alpha_s+4} t$. Using Equation (29) in (13), (14), (17), and (18), we next obtain the synchrotron and SSC light curves of a quasi-spherical outflow in the relativistic phase moving through a wind-like medium.

*Synchrotron light curves*—Given the synchrotron spectrum, the light curves for the fast- and the slow-cooling regimes are, respectively:

$$
F_\nu^{\rm syn} \propto \begin{cases} t^{-\frac{\alpha_s+8}{3(\alpha_s+4)}} \, \epsilon_\gamma^{\frac{1}{3}}, & \epsilon_\gamma < \epsilon_{\rm c}^{\rm syn}, \\ t^{\frac{\alpha_s-2}{2(\alpha_s+4)}} \, \epsilon_\gamma^{-\frac{1}{2}}, & \epsilon_{\rm c}^{\rm syn} < \epsilon_\gamma < \epsilon_{\rm m}^{\rm syn}, \\ t^{\frac{2\alpha_s-6p+4-\alpha_s p}{2(\alpha_s+4)}} \, \epsilon_\gamma^{-\frac{p}{2}}, & \epsilon_{\rm m}^{\rm syn} < \epsilon_\gamma, \end{cases} \tag{30}
$$

$$
F_\nu^{\rm syn} \propto \begin{cases} t^{\frac{\alpha_s}{3(\alpha_s+4)}} \, \epsilon_\gamma^{\frac{1}{3}}, & \epsilon_\gamma < \epsilon_{\rm m}^{\rm syn}, \\ t^{\frac{\alpha_s-6p+2-\alpha_s p}{2(\alpha_s+4)}} \, \epsilon_\gamma^{-\frac{p-1}{2}}, & \epsilon_{\rm m}^{\rm syn} < \epsilon_\gamma < \epsilon_{\rm c}^{\rm syn}, \\ t^{\frac{2\alpha_s-6p+4-\alpha_s p}{2(\alpha_s+4)}} \, \epsilon_\gamma^{-\frac{p}{2}}, & \epsilon_{\rm c}^{\rm syn} < \epsilon_\gamma. \end{cases} \tag{31}
$$

The synchrotron spectral breaks $\epsilon_{\rm m}^{\rm syn}$ and $\epsilon_{\rm c}^{\rm syn}$, and the maximum flux are given in Equation (55).

*SSC light curves*—Given the synchrotron spectrum, the light curves for the fast- and the slow-cooling regimes are,

respectively:

$$
F_\nu^{\rm ssc} \propto \begin{cases} t^{-\frac{2(3\alpha_s+10)}{3(\alpha_s+4)}} \, \epsilon_\gamma^{\frac{1}{3}}, & \epsilon_\gamma < \epsilon_{\rm c}^{\rm ssc}, \\ t^{\frac{\alpha_s}{2(\alpha_s+4)}} \, \epsilon_\gamma^{-\frac{1}{2}}, & \epsilon_{\rm c}^{\rm ssc} < \epsilon_\gamma < \epsilon_{\rm m}^{\rm ssc}, \\ t^{\frac{2\alpha_s-8p+8-\alpha_s p}{2(\alpha_s+4)}} \, \epsilon_\gamma^{-\frac{p}{2}}, & \epsilon_{\rm m}^{\rm ssc} < \epsilon_\gamma, \end{cases} \tag{32}
$$

$$
F_\nu^{\rm ssc} \propto \begin{cases} t^{-\frac{2(\alpha_s+2)}{3(\alpha_s+4)}} \, \epsilon_\gamma^{\frac{1}{3}}, & \epsilon_\gamma < \epsilon_{\rm m}^{\rm ssc}, \\ t^{-\frac{\alpha_s+8p+\alpha_s p}{2(\alpha_s+4)}} \, \epsilon_\gamma^{-\frac{p-1}{2}}, & \epsilon_{\rm m}^{\rm ssc} < \epsilon_\gamma < \epsilon_{\rm c}^{\rm ssc}, \\ t^{\frac{2\alpha_s-8p+8-\alpha_s p}{2(\alpha_s+4)}} \, \epsilon_\gamma^{-\frac{p}{2}}, & \epsilon_{\rm c}^{\rm ssc} < \epsilon_\gamma. \end{cases} \tag{33}
$$

The SSC spectral breaks $\epsilon_{\rm m}^{\rm ssc}$ and $\epsilon_{\rm c}^{\rm ssc}$, and the maximum flux are given in Equation (56).

### 3.2. Off-axis Jet

The synchrotron and SSC emission of an off-axis jet in the relativistic and the lateral expansion phase, moving through either a homogeneous medium or a wind-like medium, are next calculated.

#### 3.2.1. Homogeneous Medium: Relativistic Phase

The equivalent kinetic energy is $E_{\rm k} = \frac{\tilde{E}}{1-\cos\theta_j} \approx \frac{2\tilde{E}}{\theta_j^2}$ with the fiducial energy $\tilde{E} = \frac{16\pi}{3} m_p (1+z)^{-3} n \, \theta_j^2 \, \Delta\theta^{-6} \, \Gamma^2 \, t^3$. In this case, the bulk Lorentz factor evolves as:

$$
\Gamma = 321.1 \left( \frac{1+z}{1.022} \right)^{\frac{3}{2}} n_{-1}^{-\frac{1}{2}} \tilde{E}_{50}^{\frac{1}{2}} \theta_{j,5^\circ}^{-1} \Delta\theta_{15^\circ}^3 \, t_{1\rm d}^{-\frac{3}{2}}. \tag{34}
$$

Using Equation (34) in (3), (4), (7), and (8), we next obtain the synchrotron and SSC light curves of an off-axis jet in the relativistic phase moving through a homogeneous medium.

*Synchrotron light curves*—The synchrotron light curves for the fast- and slow-cooling regimes are, respectively:

$$
F_\nu^{\rm syn} \propto \begin{cases} t^{\frac{17}{3}} \, \epsilon_\gamma^{\frac{1}{3}}, & \epsilon_\gamma < \epsilon_{\rm m}^{\rm syn}, \\ t^{\frac{13}{2}} \, \epsilon_\gamma^{-\frac{p-1}{2}}, & \epsilon_{\rm m}^{\rm syn} < \epsilon_\gamma < \epsilon_{\rm c}^{\rm syn}, \\ t^{\frac{-3p+16}{2}} \, \epsilon_\gamma^{-\frac{p}{2}}, & \epsilon_{\rm c}^{\rm syn} < \epsilon_\gamma, \end{cases} \tag{35}
$$

$$
F_\nu^{\rm syn} \propto \begin{cases} t^7 \, \epsilon_\gamma^{\frac{1}{3}}, & \epsilon_\gamma < \epsilon_{\rm m}^{\rm syn}, \\ t^{\frac{-3p+15}{2}} \, \epsilon_\gamma^{-\frac{p-1}{2}}, & \epsilon_{\rm m}^{\rm syn} < \epsilon_\gamma < \epsilon_{\rm c}^{\rm syn}, \\ t^{\frac{-3p+16}{2}} \, \epsilon_\gamma^{-\frac{p}{2}}, & \epsilon_{\rm c}^{\rm syn} < \epsilon_\gamma. \end{cases} \tag{36}
$$

The synchrotron spectral breaks $\epsilon_{\rm m}^{\rm syn}$ and $\epsilon_{\rm c}^{\rm syn}$, and the maximum flux are given in Equation (59).

*SSC light curves*—The SSC light curves for the fast- and slow-cooling regimes are, respectively:

$$
F_\nu^{\rm ssc} \propto \begin{cases} t^{\frac{19}{3}} \, \epsilon_\gamma^{\frac{1}{3}}, & \epsilon_\gamma < \epsilon_{\rm c}^{\rm ssc}, \\ t^8 \, \epsilon_\gamma^{-\frac{p-1}{2}}, & \epsilon_{\rm c}^{\rm ssc} < \epsilon_\gamma < \epsilon_{\rm m}^{\rm ssc}, \\ t^{-3p+11} \, \epsilon_\gamma^{-\frac{p}{2}}, & \epsilon_{\rm m}^{\rm ssc} < \epsilon_\gamma, \end{cases} \tag{37}
$$

$$F_\nu^{\rm ssc} \propto \begin{cases} t^9 \, \epsilon_\gamma^{\frac{1}{3}}, & \epsilon_\gamma^{\rm ssc} < \epsilon_{\rm m}^{\rm ssc}, \\ t^{-3p+10} \, \epsilon_\gamma^{-\frac{p-1}{2}}, & \epsilon_{\rm m}^{\rm ssc} < \epsilon_\gamma < \epsilon_{\rm c}^{\rm ssc}, \\ t^{-3p+11} \, \epsilon_\gamma^{-\frac{p}{2}}, & \epsilon_{\rm c}^{\rm ssc} < \epsilon_\gamma. \end{cases} \quad (38)$$

The SSC spectral breaks $\epsilon_{\rm m}^{\rm ssc}$ and $\epsilon_{\rm c}^{\rm ssc}$, and the maximum flux are given in Equation (60).

### 3.2.2. Homogeneous Medium: Lateral Expansion Phase

In the lateral expansion phase ($\Delta\theta \sim 1/\Gamma$), the fiducial energy becomes $\tilde{E} = \frac{16\pi}{3} m_p (1+z)^{-3} n \, \Gamma^6 \, t^3$ and then the bulk Lorentz factor can be written as:

$$\Gamma = 3.2 \left( \frac{1+z}{1.022} \right)^{\frac{1}{2}} n_{-1}^{-\frac{1}{6}} \tilde{E}_{50}^{\frac{1}{6}} t_{100{\rm d}}^{-\frac{1}{2}}. \quad (39)$$

Using Equation (39) in (3), (4), (7), and (8), we next obtain the synchrotron and SSC light curves of a quasi-spherical outflow in the lateral expansion regime moving through a homogeneous medium.

*Synchrotron light curves*—The synchrotron light curve for the slow-cooling regime is:

$$F_\nu^{\rm syn} \propto \begin{cases} t^{-\frac{1}{3}} \, \epsilon_\gamma^{\frac{1}{3}}, & \epsilon_\gamma < \epsilon_{\rm m}^{\rm syn}, \\ t^{-p} \, \epsilon_\gamma^{-\frac{p-1}{2}}, & \epsilon_{\rm m}^{\rm syn} < \epsilon_\gamma < \epsilon_{\rm c}^{\rm syn}, \\ t^{-p} \, \epsilon_\gamma^{-\frac{p}{2}}, & \epsilon_{\rm c}^{\rm syn} < \epsilon_\gamma. \end{cases} \quad (40)$$

The synchrotron spectral breaks $\epsilon_{\rm m}^{\rm syn}$ and $\epsilon_{\rm c}^{\rm syn}$, and the maximum flux are given in Equation (63).

*SSC light curves*—The SSC light curve for the slow-cooling regime is:

$$F_\nu^{\rm ssc} \propto \begin{cases} t^0 \, \epsilon_\gamma^{\frac{1}{3}}, & \epsilon_\gamma < \epsilon_{\rm m}^{\rm ssc}, \\ t^{\frac{1-3p}{2}} \, \epsilon_\gamma^{-\frac{p-1}{2}}, & \epsilon_{\rm m}^{\rm ssc} < \epsilon_\gamma < \epsilon_{\rm c}^{\rm ssc}, \\ t^{\frac{2-3p}{2}} \, \epsilon_\gamma^{-\frac{p}{2}}, & \epsilon_{\rm c}^{\rm ssc} < \epsilon_\gamma. \end{cases} \quad (41)$$

The SSC spectral breaks $\epsilon_{\rm m}^{\rm ssc}$ and $\epsilon_{\rm c}^{\rm ssc}$, and the maximum flux are given in Equation (64).

### 3.2.3. Wind-like Medium

Considering the Blandford–McKee solution for a wind-like medium, the bulk Lorentz factor can be written as:

$$\Gamma = 2.4 \times 10^3 \left( \frac{1+z}{1.022} \right)^{\frac{1}{2}} \xi^{-1} A_{\star,-1}^{-\frac{1}{2}} \tilde{E}_{50}^{\frac{1}{2}} \theta_{j,5^\circ}^{-1} \Delta\theta_{15^\circ} t_{1{\rm d}}^{-\frac{1}{2}}, \quad (42)$$

where $\tilde{E}$ is the same as that for the quasi-spherical outflow in a wind-like medium.

*Synchrotron light curves*—The synchrotron light curves for the fast- and the slow-cooling regimes are, respectively:

$$F_\nu^{\rm syn} \propto \begin{cases} t^{\frac{1}{3}} \, \epsilon_\gamma^{\frac{1}{3}}, & \epsilon_\gamma < \epsilon_{\rm c}^{\rm syn}, \\ t^2 \, \epsilon_\gamma^{-\frac{p-1}{2}}, & \epsilon_{\rm m}^{\rm syn} < \epsilon_\gamma < \epsilon_{\rm c}^{\rm syn}, \\ t^{3-p} \, \epsilon_\gamma^{-\frac{p}{2}}, & \epsilon_{\rm c}^{\rm syn} < \epsilon_\gamma, \end{cases} \quad (43)$$

$$F_\nu^{\rm syn} \propto \begin{cases} t^{\frac{5}{3}} \, \epsilon_\gamma^{\frac{1}{3}}, & \epsilon_\gamma < \epsilon_{\rm m}^{\rm syn}, \\ t^{-p+2} \, \epsilon_\gamma^{-\frac{p-1}{2}}, & \epsilon_{\rm m}^{\rm syn} < \epsilon_\gamma < \epsilon_{\rm c}^{\rm syn}, \\ t^{3-p} \, \epsilon_\gamma^{-\frac{p}{2}}, & \epsilon_{\rm c}^{\rm syn} < \epsilon_\gamma. \end{cases} \quad (44)$$

The synchrotron spectral breaks $\epsilon_{\rm m}^{\rm syn}$ and $\epsilon_{\rm c}^{\rm syn}$, and the maximum flux are given in Equation (66).

*SSC light curves*—The SSC light curves for the fast- and the slow-cooling regimes are, respectively:

$$F_{\nu, off}^{\rm ssc} \propto \begin{cases} t^{-\frac{5}{3}} \, \epsilon_\gamma^{\frac{1}{3}}, & \epsilon_\gamma < \epsilon_{\rm c}^{\rm ssc}, \\ t^{\frac{5}{2}} \, \epsilon_\gamma^{-\frac{p-1}{2}}, & \epsilon_{\rm c}^{\rm ssc} < \epsilon_\gamma < \epsilon_{\rm m}^{\rm ssc}, \\ t^{-\frac{3p}{2}+4} \, \epsilon_\gamma^{-\frac{p}{2}}, & \epsilon_{\rm m}^{\rm ssc} < \epsilon_\gamma, \end{cases} \quad (45)$$

$$F_\nu^{\rm ssc} \propto \begin{cases} t \, \epsilon_\gamma^{\frac{1}{3}}, & \epsilon_\gamma < \epsilon_{\rm m}^{\rm ssc}, \\ t^{-\frac{3}{2}(p-1)} \, \epsilon_\gamma^{-\frac{p-1}{2}}, & \epsilon_{\rm m}^{\rm ssc} < \epsilon_\gamma < \epsilon_{\rm c}^{\rm ssc}, \\ t^{-\frac{3p}{2}+4} \, \epsilon_\gamma^{-\frac{p}{2}}, & \epsilon_{\rm c}^{\rm ssc} < \epsilon_\gamma. \end{cases} \quad (46)$$

The synchrotron spectral breaks $\epsilon_{\rm m}^{\rm ssc}$ and $\epsilon_{\rm c}^{\rm ssc}$, and the maximum flux are given in Equation (67).

### 3.3. Multiwavelength Light Curves

Figures 2 and 3 show the resulting $\gamma$-ray, X-ray, optical, and radio light curves of the synchrotron and SSC FS radiation produced by a quasi-spherical outflow, or an off-axis jet, and decelerating either in a homogeneous or a wind-like medium. The purple, green, and blue lines correspond to 6 GHz, 1 eV, and 1 keV in the left-hand panels and 100 keV, 100 MeV, and 100 GeV in the right-hand panels, respectively, and the standard values of GRB afterglows were used.[7] The figures show the light curves from 1 to 1000 days for six electromagnetic bands: $\gamma$-ray at 100 GeV, 100 MeV, and 100 keV, X-ray at 1 keV, optical at 1 eV, and radio at 6 GHz. It is worth noting that the synchrotron and SSC light curves shown in the previous figures lie in the slow-cooling regime.

For density values ($n = 10^{-4}\,{\rm cm}^{-3}$ for the homogeneous medium, and $A_\star = 10^{-4}$ for the wind-like medium), the synchrotron and SSC fluxes produced by the quasi-spherical outflow are noticeably larger in a wind-like medium than in a homogeneous medium. The synchrotron light curves in a wind-like medium are 2–7 orders of magnitude larger than in a homogeneous medium (see the upper-left panel in Figure 2). Meanwhile, the SSC light curves in a wind-like medium are 6–10 orders of magnitude larger than in a homogeneous medium (see the upper-right panel in Figure 2). The disparity between the synchrotron and SSC emission depends on the energy band, the timescale considered, and the chosen $A_\star$ parameter (as $A_\star$ increases, so do the fluxes in the wind-like medium). We also find that the synchrotron and SSC light curves of a quasi-spherical outflow expanding through a homogeneous or a wind-like medium behave differently. The synchrotron and SSC fluxes of a quasi-spherical outflow in a homogeneous medium increase gradually during the first $\sim$20–50 days, then reach a maximum value and decrease afterward. In a wind-like medium, on the other hand, the quasi-spherical outflow emission decreases monotonically in

---

[7] $E = 5 \times 10^{49}$ erg, $n = 5 \times 10^{-4}\,{\rm cm}^{-3}$, $A_\star = 10^{-4}$, $\varepsilon_B = 5 \times 10^{-4}$, $\varepsilon_e = 0.1$, $\Delta\theta = 18^\circ$, $\theta_j = 7^\circ$, $\alpha_s = 3.0$, $p = 2.25$ and $D = 100$ Mpc.
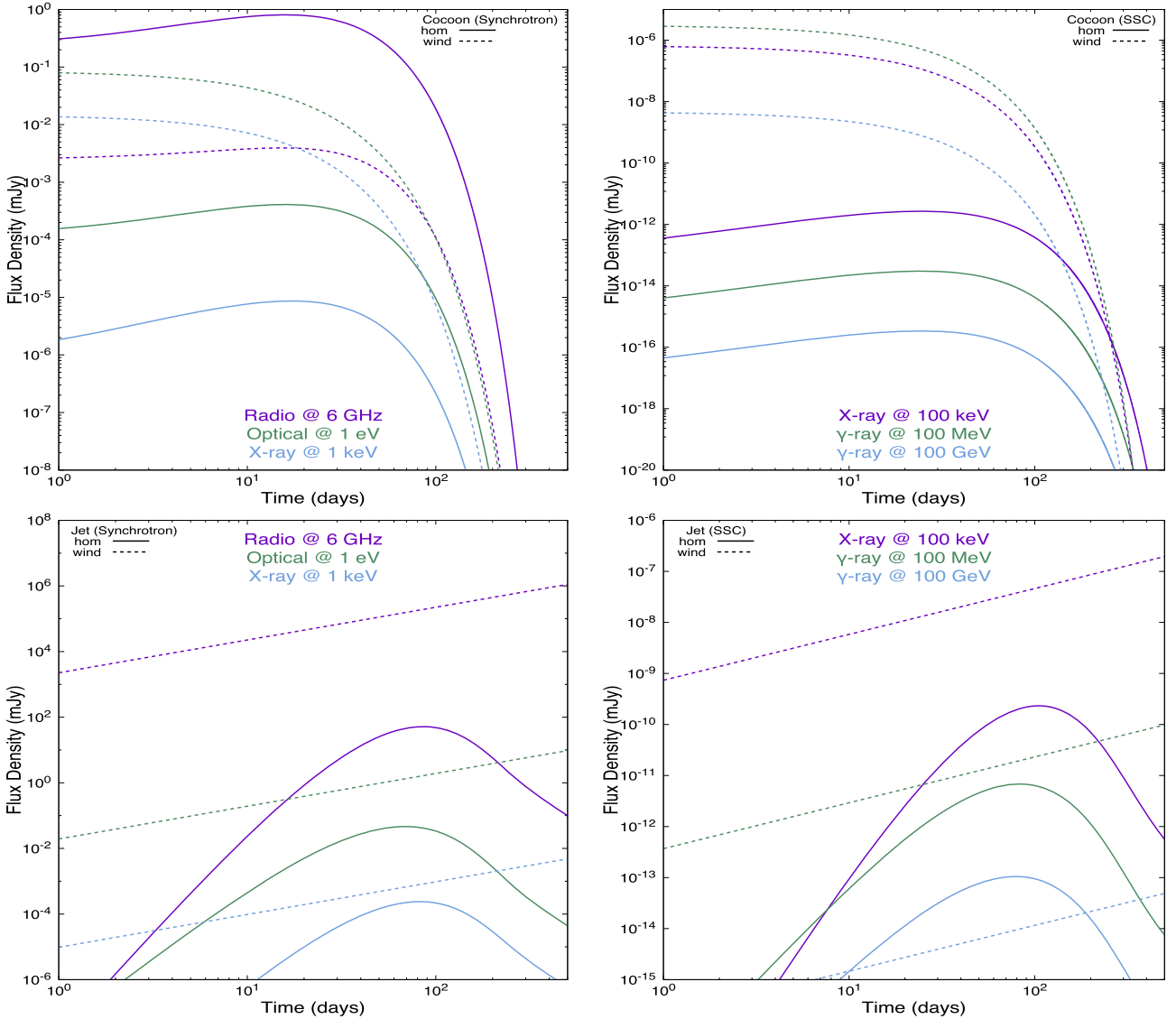
**Figure 2.** Synchrotron (left-hand panels) and SSC (right-hand panels) light curves produced by a quasi-spherical outflow (upper panels) or an off-axis jet (lower panels). The purple, green, and blue lines correspond to 6 GHz, 1 eV, and 1 keV in the left-hand panels and 100 keV, 100 MeV, and 100 GeV in right-hand panels. The continuous lines correspond to a homogeneous medium, and the dashed lines to a wind-like medium. The values used are $E = 5 \times 10^{49}$ erg, $n = 5 \times 10^{-4}$ cm$^{-3}$, $A_\star = 10^{-4}$, $\varepsilon_B = 5 \times 10^{-4}$, $\varepsilon_e = 0.1$, $\Delta\theta = 18°$, $\theta_j = 7°$, $\alpha = 3.0$, $p = 2.25$ and $D = 100$ Mpc.

all electromagnetic bands (except in the radio band where it increases). For the off-axis jet, we find that the synchrotron and SSC fluxes produced have similar values (see the bottom panels of Figure 2). The synchrotron and SSC fluxes of an off-axis jet in a homogeneous medium increase during the first ∼100 days, then reach a maximum value and decrease rapidly afterward. In a wind-like medium, the jet's emission increases monotonically in all electromagnetic bands. Comparing the synchrotron emission of the quasi-spherical outflow with that of the off-axis jet (in the same ambient medium regime), it is clear that the emission of the quasi-spherical outflow is stronger than that of the off-axis jet during the first ∼10–20 days, and then weaker during the next ∼80 days. A similar behavior occurs for the SSC. In the stellar-wind medium, except for the radio band, the flux generated by the quasi-spherical outflow governs during the timescale considered. In the case of the radio band, during the

first ∼80 days, the radio flux emitted by the quasi-spherical outflow prevails, afterward the radio flux from the off-axis jet dominates.

Figure 3 shows the total light curves (built by the sum of the emission from the quasi-spherical outflow and the jet) for the synchrotron and SSC cases produced in a homogeneous or a wind-like medium. The light curves produced in a homogeneous medium increase during the first ∼100 days, then reach their respective maximum, and decrease afterward. The synchrotron light curves for the wind-like medium have different behaviors; whereas the radio flux is an increasing function, the optical and X-ray fluxes are decreasing functions. Meanwhile, regardless of the energy band, the SSC light curves from the wind-like medium, are decreasing functions. It is worth noting that the SSC emission produced in wind-like medium is at least four orders of magnitude larger than that produced in a homogeneous medium.
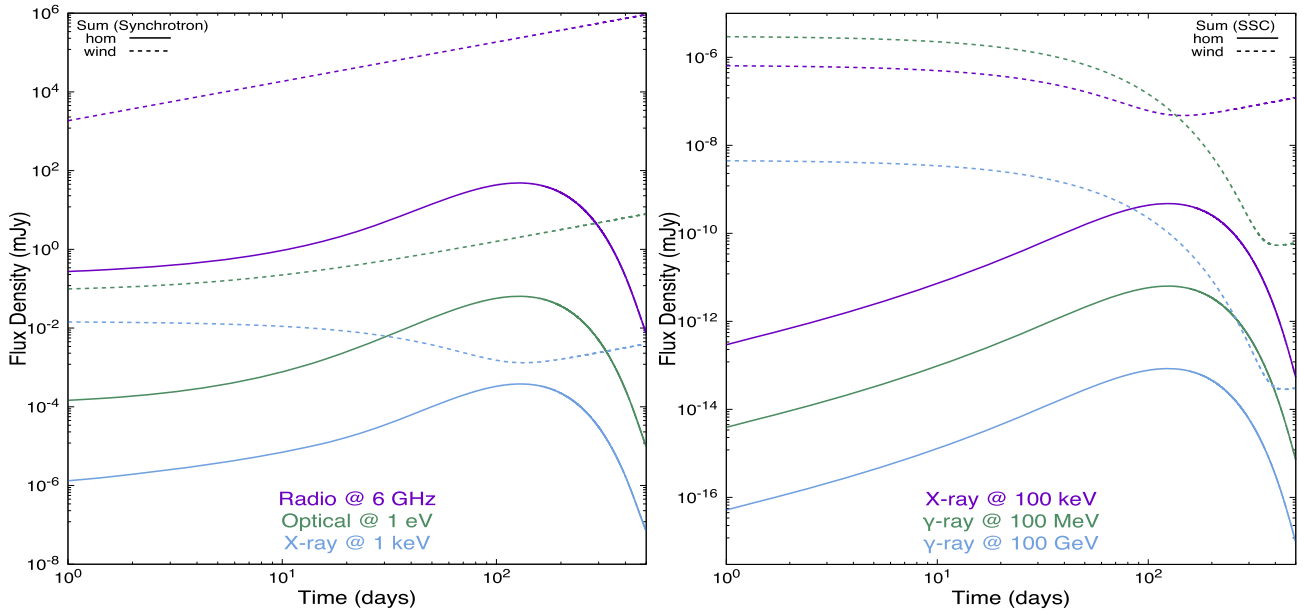
**Figure 3.** Synchrotron (left-hand panels) and SSC (right-hand panels) light curves produced by a quasi-spherical outflow and an off-axis jet. The colors, continuous or dashed lines and values used, are the same as those in Figure 2.

The standard synchrotron FS model predicts that the spectral evolution of frequencies evolves as $\epsilon_{\rm m} \propto t^{-\frac{3}{2}}$ and $\epsilon_{\rm m} \propto t^{\frac{1}{2}}$ in wind-like medium and $\epsilon_{\rm m} \propto t^{-\frac{3}{2}}$ and $\epsilon_{\rm m} \propto t^{-\frac{1}{2}}$ in a homogeneous medium. Giblin et al. (1999) found a new component during the prompt phase, different from the Band function, for GRB 980923. The analysis revealed that the spectral evolution of this component was similar to that described by the evolution of the cooling frequency in the synchrotron FS model $\epsilon_{\rm c} \propto t^{-0.5}$, thus arguing that external shocks can be created during the prompt phase. Subsequently, several papers (Barthelmy et al. 2005; Yamazaki et al. 2006; Veres et al. 2018; Fraija 2015; Fraija et al. 2019f) were written in this direction in order to identify the early afterglow phase during the gamma-ray prompt emission. In this manuscript, we provide useful tools to identify this early afterglow in a homogeneous or wind-like medium (see Appendix A). For instance, the evolution of the spectral component generated by the deceleration of the quasi-spherical outflow in a wind-like medium is $\epsilon_{\rm m} \propto t^{-\frac{3}{\alpha_s+8}}$ and $\epsilon_{\rm c} \propto t^{-\frac{1-\alpha_s}{\alpha_s+8}}$ and, in a homogeneous medium, it is $\epsilon_{\rm m} \propto t^{-\frac{3}{\alpha_s+8}}$ and $\epsilon_{\rm c} \propto t^{-\frac{1-\alpha_s}{\alpha_s+8}}$. In the particular case of $\alpha_{\rm s} = 0$, the temporal evolution of the synchrotron spectral breaks derived in Sari et al. (1998), Fraija et al. (2016b), Dai & Lu (1999), Huang & Cheng (2003), Dermer et al. (2000), Granot et al. (2002), and Rees (1999) are recovered. The evolution of the synchrotron spectral breaks generated by the deceleration of the off-axis jet in a wind-like medium is $\epsilon_{\rm m} \propto t^{\frac{3}{\alpha_s+8}}$ and $\epsilon_{\rm c} \propto t^{\frac{\alpha_s+3}{\alpha_s+4}}$, and in a homogeneous medium it is $\epsilon_{\rm m} \propto t^{-2}$ and $\epsilon_{\rm c} \propto t^2$. We emphasize that we ignore the scattering from the jet when we calculate the SSC from the quasi-spherical outflow.

## 4. Application: GRB 170817A

To find the best-fit values that describe the non-thermal emission of GRB 170817A, we use a Markov chain Monte Carlo (MCMC) code (see Fraija et al. 2019f). The MCMC code calculates the synchrotron emission of a quasi-spherical outflow and an off-axis jet and is described by a set of eight

parameters, $\{\tilde{E}, {\rm n}, {\rm p}, \theta_j, \Delta\theta, \varepsilon_B, \varepsilon_e, \alpha_s\}$. A total of 17,600 samples with 5150 tuning steps were run. The best-fit parameters of $\Delta\theta$, $p$, n, $\varepsilon_{\rm B}$, $\varepsilon_e$, $\alpha_s$, and $\tilde{E}$ are displayed in Figure 4 (radio: 3 GHz, 6 GHz; optical: 1 eV; and X-ray: 1 keV). The best-fit values for GRB 170817A are reported in Table 1. The obtained values are consistent with those reported by other authors (Kasliwal et al. 2017; Lamb & Kobayashi 2017; Lazzati et al. 2018; Mooley et al. 2018b; Hotokezaka et al. 2018; Fraija et al. 2019f). We note that the synchrotron flux equations are degenerate in these parameters such that, for a completely different set of parameters, the same results can be obtained. Therefore, our result is not unique, but is only one possible solution to GRB 170817A.

Figure 5 shows the obtained light curves (left panel) and the spectral energy distributions (SEDs, right panel) of the X-ray, optical, and radio bands of GRB 170817A, the data points were taken from Troja et al. (2017), Margutti et al. (2017a), Margutti et al. (2017b), Haggard et al. (2018), Troja et al. (2018), Margutti et al. (2018), Hallinan et al. (2017), Mooley et al. (2018b), and Alexander et al. (2017). The light curves are shown in radio wavelengths at 3 and 6 GHz, optical band at 1 eV and X-rays at 1 keV. The SEDs are exhibited at $15 \pm 2$, $110 \pm 5$, and $145 \pm 20$ days.

The multiwavelength data (radio wavelengths at 3 and 6 GHz, optical band at 1 eV, and X-rays at 1 keV) were described through the best-fit curves of synchrotron radiation emitted from the deceleration of the quasi-spherical outflow and the off-axis jet. The maximum value of the flux density in each band is interpreted by the broadening of the beaming cone of the radiation. It occurs when the off-axis jet has slowed down and expanded laterally. A zoom of the X-ray light curve, with the correspondent emission produced by the quasi-spherical outflow and the off-axis jet, is also shown in the left-hand panel. The dashed-black line shows the contribution of the quasi-spherical outflow and the dotted-blue line shows the contribution of the off-axis jet. This figure shows that emission from the quasi-spherical outflow dominates during the
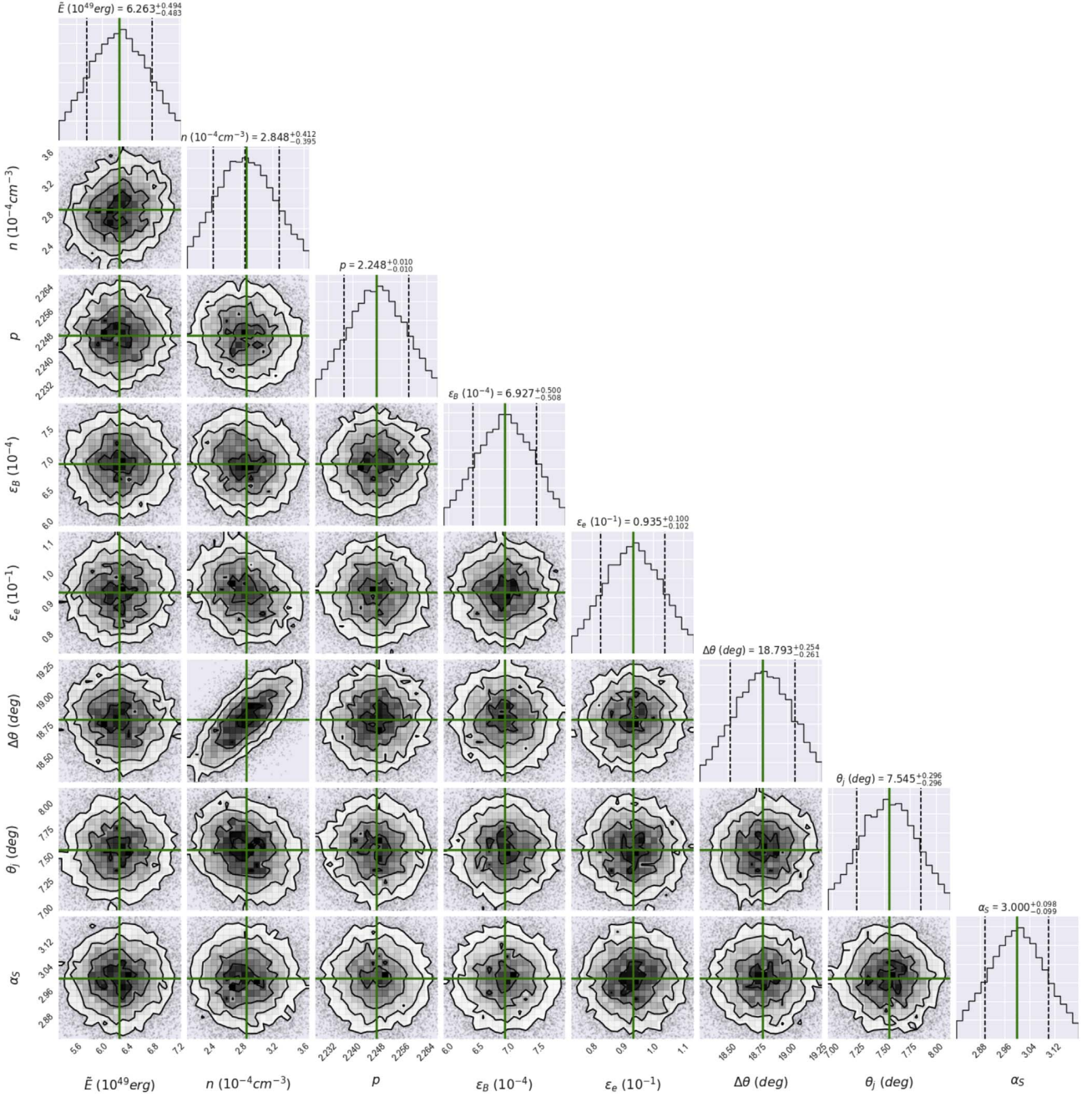
**Figure 4.** Best-fit results for the light curves at 3 GHz using the proposed model and the MCMC calculations for GRB 170817A. The "corner plots" exhibit the results obtained from the MCMC simulation. Labels above the 1D KDE plot illustrate the 15%, 50%, and 85% quantiles for all parameters. The best-fit values are shown in green and reported in Table 1.

**Table 1**
Best-fit Values for GRB 170817A

| Parameters | Median |
|---|---|
| $\tilde{E}$ ($10^{49}$ erg) | $6.263^{+0.494}_{-0.485}$ |
| n ($10^{-4}$ cm$^{-3}$ ) | $2.848^{+0.412}_{-0.395}$ |
| p | $2.248^{+0.010}_{-0.010}$ |
| $\theta_j$ (deg) | $7.545^{+0.296}_{-0.296}$ |
| $\Delta\theta$ (deg) | $18.793^{+0.254}_{-0.261}$ |
| $\varepsilon_B$ ($10^{-4}$) | $6.927^{+0.500}_{-0.508}$ |
| $\varepsilon_e$ ($10^{-1}$) | $0.935^{+0.100}_{-0.102}$ |
| $\alpha_s$ | $3.000^{+0.098}_{-0.099}$ |

~20 days and the emission from the off-axis jet dominates after the ~60 days.

Using the values of the best-fit parameters reported in Table 1 and Equation (19), we find that the bulk Lorentz factor is $\Gamma_c \simeq 3.1(t/15\,\mathrm{day})^{-0.24}$ and the equivalent kinetic energy is $E_{\mathrm{obs,k}} \simeq 3.31 \times 10^{47}$ erg. Using the previous values, we obtain that the efficiency to convert the kinetic energy to gamma-ray energy is ~16%. This value is consistent with the range of values reported in afterglows (e.g., see Zhang & Mészáros 2004; Fraija et al. 2012; Kumar & Zhang 2015). The cooling and characteristic spectral breaks are $\epsilon_c \sim 22.3$ eV and $\epsilon_m \sim 1.1 \times 10^{-2}$ GHz, respectively, at 15 days. This result is
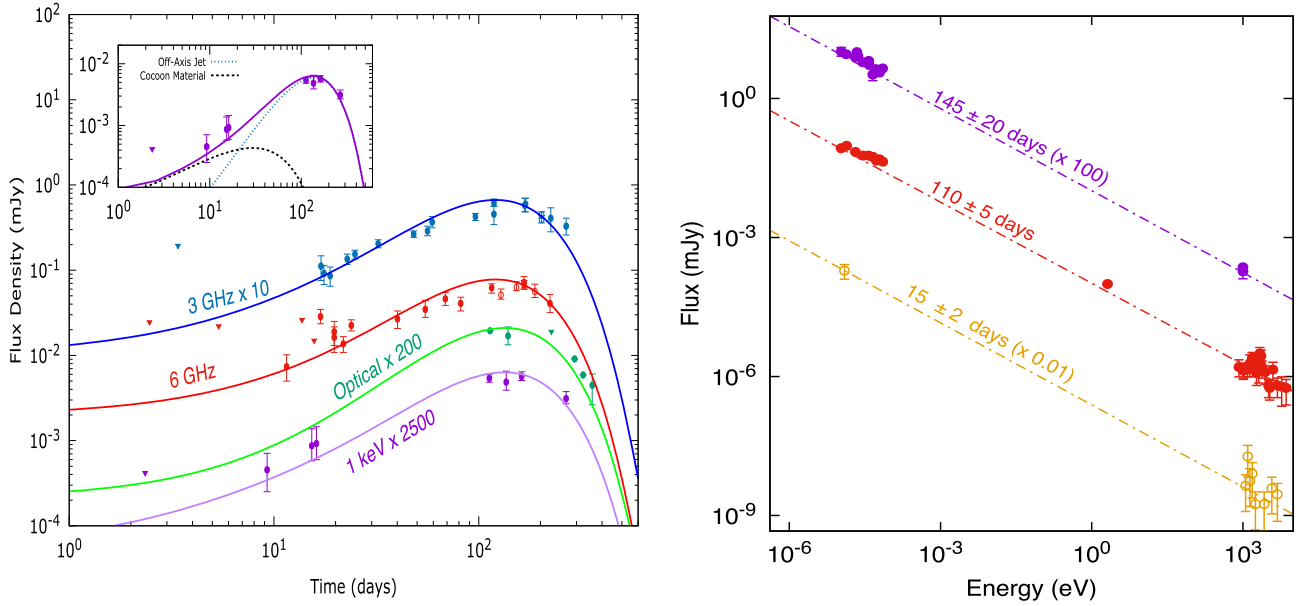
**Figure 5.** Left: the best-fit light curves obtained using the synchrotron emission from a quasi-spherical outflow and an off-axis jet decelerated in a homogeneous medium. These light curves are exhibited at different energy bands with their respective observations (points). The radio energy band at 3 GHz is shown in cyan, the radio energy band at 6 GHz is shown in red, the optical band at 1 eV is shown in green, and the X-ray at 1 keV in purple. A zoom of the X-ray light curve and the emission produced by the quasi-spherical outflow and off-axis jet is also shown (upper-left). The data points are the observations, see the text for their references. Right: the best-fit SEDs of the X-ray (red), optical (green), and radio (blue) afterglow observations at $15 \pm 2$, $110 \pm 5$, and $145 \pm 20$ days, respectively. The values that best describe the light curves and the SED are reported in Table 1.

consistent with the evolution of synchrotron radiation in the slow-cooling regime of the quasi-spherical outflow in a homogeneous medium, where the X-ray, optical, and radio fluxes are described by the third and second power-law segment in Equation (21). The X-ray, optical, and radio fluxes increase as $F_\nu \propto t^{0.15}$, peak at $\sim 20$ days, and then evolve as $F_\nu \propto t^{-0.76}$ and $\propto t^{-1.03}$. On the other hand, the optical and radio fluxes continue evolving as $F_\nu \propto t^{-0.76}$. Given the values of the best-fit parameters reported in Table 5 and Equation (34), we find that the bulk Lorentz factor of the relativistic jet reaches $\Gamma_j \simeq 5.3(t/100 \, \text{day})^{-\frac{3}{2}}$. The cooling spectral break $\epsilon_c \sim 2.6 \, \text{keV}$ is above the X-ray band, and its characteristic break $\epsilon_m = 0.04 \, \text{GHz}$ is below the radio band at 100 days. As for the quasi-spherical outflow, this result is consistent with the evolution of synchrotron radiation in the slow-cooling regime of an off-axis jet expanding in a homogeneous medium (where the X-ray, optical, and radio fluxes are described by the second power-law segment in Equation (44)). During this period, the observed flux increases as $F_\nu \propto t^{4.2}$ as predicted in Nakar & Piran (2018). The X-ray, optical, and radio fluxes peak at $\sim 140$ days, and then evolve as $F_\nu \propto t^{-2.2}$. It is worth noting that for a timescale of seconds, an equivalent kinetic energy above $\sim 5 \times 10^{52}$ erg, a circumburst density higher than $1 \, \text{cm}^{-3}$, and equipartition parameters $\varepsilon_B \sim 0.1$, $\varepsilon_e \sim 0.1$, the synchrotron and SSC light curves would lie in the fast-cooling regime.

The results reported in the radio energy band by Mooley et al. (2018a) reported superluminal motion, with an apparent speed of $\sim 4$ at almost 150 days (between 75 and 230 days after the GBM trigger), which implies that a relativistic jet is present. This result was confirmed by the radio observations performed 207.4 days after the NS fusion (Ghirlanda et al. 2019). These observations provide compelling evidence that the progenitor of the GW170817 event ejected a structured relativistic jet with a bulk Lorentz factor of $\sim 4$ (at the time of measurement), observed from a viewing angle of $20° \pm 5°$. The model

proposed in this manuscript is consistent with the results obtained in the radio wavelengths, which, at earlier times, show that the non-thermal emission is dominated by the slower quasi-spherical outflow material and, at later times, the non-thermal emission ($\gtrsim 80$ days post-merger) is dominated by a relativistic off-axis jet. Considering the values of $\Delta\theta \simeq 18°$ and $\theta_j \simeq 7°$ reported in Table 1, the value of the viewing angle $\theta_{\text{obs}} \sim 25°$ is found, which agrees with that reported in Mooley et al. (2018a).

Using values obtained with the MCMC simulation for GRB 170817A, we calculate the correspondent fluxes of the SSC model to compare them with *Fermi*-LAT, HAWC, and H.E.S.S. upper limits. The left-hand panel from Figure 6 shows the obtained SSC light curves (solid lines) as well as the upper limits obtained by *Fermi*-LAT, HAWC, and H.E.S.S.. The light curves at 100 MeV (purple), 1 TeV (blue), and 45 TeV (green) were obtained using the values reported in Table 1. The effect of the extragalactic background light absorption model of Franceschini & Rodighiero (2017) was used. The obtained SSC flux at different energy bands agrees with the LAT, H.E.S.S., and HAWC observatories. The right-hand panel of Figure 6 shows the SSC light curves in a wind-like medium. If the SSC flux would have been emitted in a wind-like medium, it could have been observed by LAT, H.E.S.S., or HAWC Observatories. For instance, with $A_\star = 10^{-4}$ the SSC electromagnetic signal would have been detected in these observatories, but not with $A_\star = 10^{-6}$. This result is very interesting since the material that surrounds the progenitor of the short GRB may be affected by the wind and launched material produced during the merger of the NSs (e.g., see, Burns et al. 2018).

## 5. Conclusions

We have derived an analytic model of the FS, produced by the ejection of material (after the merger of two NSs), and
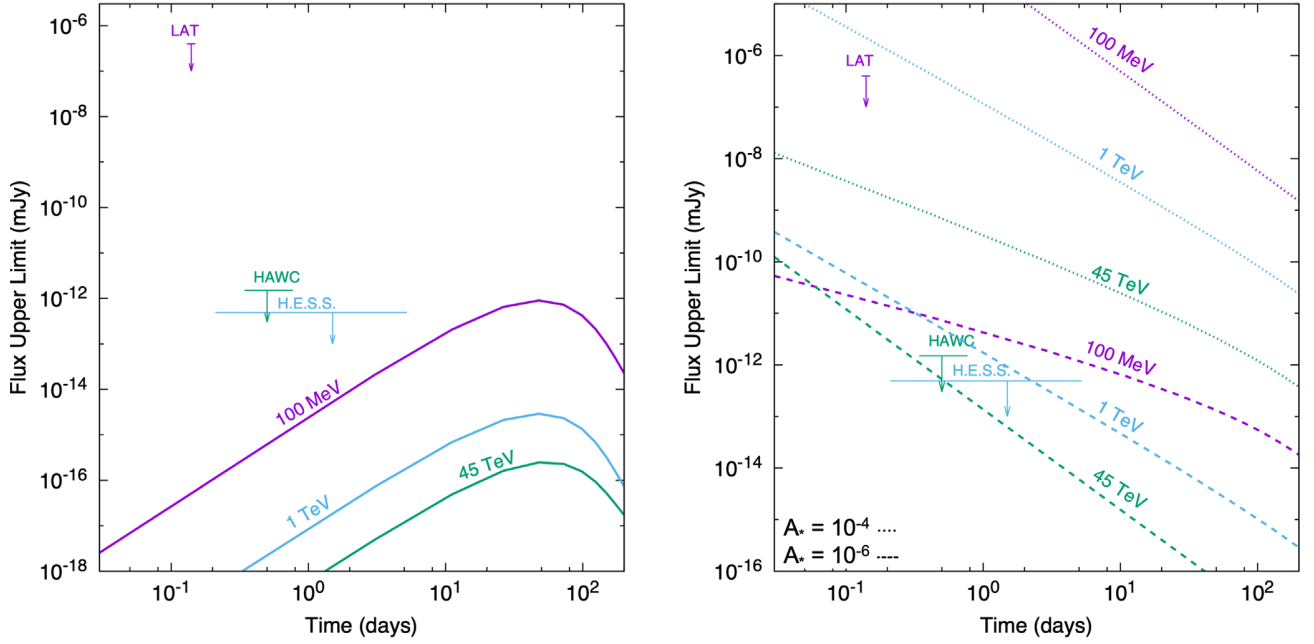
**Figure 6.** Upper limits derived with the *Fermi*-LAT, HAWC, and H.E.S.S. observatories with the SSC model from an off-axis jet and quasi-spherical outflow. In the left-hand panel, we have used the values found to describe the X-ray, optical, and radio light curves of GRB 170817A moving in a homogeneous medium (see Table 5 in Fraija et al. 2019b). In the right-hand panel, we have assumed that the off-axis jet and quasi-spherical outflow evolve in a wind-like medium.

which is moving either in a homogeneous or a wind-like medium. Explicitly, we have obtained the SSC and synchrotron light curves in the fast- and slow-cooling regimes during the relativistic and lateral expansion phases in the fully adiabatic regime with arbitrary line of sights for an observer. We focus our model in the emission from a quasi-spherical outflow that is viewed on-axis and an off-axis relativistic (top-hat) jet, and we describe the extended X-ray, optical, and radio emission exhibited in GRB 170817A. We find that the SSC and synchrotron light curves produced by a quasi-spherical outflow can be expressed when the equivalent kinetic energy is $\tilde{E}\,\Gamma^{-\alpha_s}$, and the light curves produced by an off-axis jet when the equivalent kinetic energy is $2\tilde{E}/\theta_j^2$. In the particular case of $\alpha_s = 0$, the SSC and synchrotron light curves derived in Sari et al. (1998), Fraija et al. (2016b), Dai & Lu (1999), Huang & Cheng (2003), Dermer et al. (2000), Granot et al. (2002), and Rees (1999) are recovered. The flux of a quasi-spherical outflow, which is expanding in a wind-like medium, is several orders of magnitude larger than that generated in a homogeneous medium. The latter is also the case for the off-axis jet at early times ($t \lesssim 15$ days). The flux produced by the quasi-spherical outflow peaks before the flux of the off-axis jet and dominates during the first 10–20 days (compared to that from the off-axis jet). At later times ($\gtrsim 100$ days), the emission of the off-axis jet peaks and dominates. We show that the evolution of the spectral component generated by the deceleration of the quasi-spherical outflow in a wind-like medium is $\epsilon_m \propto t^{-\frac{3}{\alpha_s+8}}$ and $\epsilon_c \propto t^{-\frac{1-\alpha_s}{\alpha_s+8}}$, and in a homogeneous medium is $\epsilon_m \propto t^{-\frac{3}{\alpha_s+8}}$ and $\epsilon_c \propto t^{-\frac{1-\alpha_s}{\alpha_s+8}}$. The evolution of the synchrotron spectral breaks generated by the deceleration of the off-axis jet in a wind-like medium is $\epsilon_m \propto t^{\frac{3}{\alpha_s+8}}$ and $\epsilon_c \propto t^{\frac{\alpha_s+3}{\alpha_s+4}}$ and, in a homogeneous medium, is $\epsilon_m \propto t^{-2}$ and $\epsilon_c \propto t^2$.

In order to interpret the non-thermal emission detected from GRB 170817A, we calculated the synchrotron and SSC contributions from both the off-axis jet and the quasi-spherical

outflow moving through a homogeneous medium using an MCMC code. We ran a large set of samples to find the best-fit values of $\tilde{E}$, n, p, $\theta_j$, $\Delta\theta$, $\varepsilon_B$, $\varepsilon_e$, and $\alpha_s$ that describe the non-thermal emission. Our model is consistent with the results obtained in the radio wavelengths. We find that, at earlier times, the non-thermal emission is dominated by the slower quasi-spherical outflow and, at later times, the non-thermal emission ($\gtrsim 80$ days post-merger) is mainly produced by a relativistic off-axis jet. For the quasi-spherical outflow, we found that the bulk Lorentz factor is mildly relativistic, which corresponds to an equivalent kinetic efficiency of $\sim 16\%$. The cooling spectral breaks found for the cocoon and off-axis jet are consistent with synchrotron radiation in the slow-cooling regime. During the first $\sim 120$ days, we find that the observed flux generated by the deceleration of the off-axis jet increases as $F_\nu \propto t^\alpha$ with $\alpha > 3$. Using the values obtained with the MCMC simulation for GRB 170817A, we found that the SSC light curves are consistent with the upper limits placed by *Fermi*-LAT, HAWC, and H.E.S.S.. For a wind-like medium we found that an electromagnetic signature would have been detected by these high-energy observatories.

## Appendix A
## Quasi-spherical Outflow

### A.1. Homogeneous Medium

Using the bulk Lorentz factor (Equation (19)), we derive and show the observable quantities when the quasi-spherical outflow is decelerated in a homogeneous medium.

Synchrotron radiation—in this case, the minimum and cooling Lorentz factors are given by

$$\gamma_m \simeq 1.1 \times 10^3 \left(\frac{1+z}{1.022}\right)^{\frac{3}{\alpha_s+8}}$$
$$\times \, g(p)\varepsilon_{e,-1}\, n_{-1}^{-\frac{1}{\alpha_s+8}}\, \tilde{E}_{50}^{\frac{1}{\alpha_s+8}}\, t_{1d}^{-\frac{3}{\alpha_s+8}}$$
$$\gamma_c \simeq 6.3 \times 10^5\, \text{GHz} \left(\frac{1+z}{1.022}\right)^{\frac{\alpha_s-1}{\alpha_s+8}}$$
$$\times \, (1+Y)^{-1}\varepsilon_{B,-1}^{-1}\, n_{-1}^{-\frac{\alpha_s+5}{\alpha_s+8}}\, \tilde{E}_{50}^{-\frac{3}{\alpha_s+8}}\, t_{1d}^{\frac{1-\alpha_s}{\alpha_s+8}}. \quad (47)$$

Given the synchrotron radiation ($\epsilon_k^{\text{syn}} \propto \gamma_k^2$ for $k = $ m, c) and the electron Lorentz factors (Equation (47)), the synchrotron spectral breaks and the maximum flux is

$$\epsilon_m^{\text{syn}} \simeq 0.5\, \text{GHz} \left(\frac{1+z}{1.022}\right)^{\frac{4-\alpha_s}{\alpha_s+8}}$$
$$\times \, g(p)^2 \varepsilon_{e,-1}^2\, \varepsilon_{B,-3}^{\frac{1}{2}}\, n_{-1}^{\frac{\alpha_s}{2(\alpha_s+8)}}\, \tilde{E}_{50}^{\frac{4}{\alpha_s+8}}\, t_{1d}^{-\frac{12}{\alpha_s+8}}$$
$$\epsilon_c^{\text{syn}} \simeq 5.9 \times 10^{-3}\, \text{eV} \left(\frac{1+z}{1.022}\right)^{\frac{\alpha_s-4}{\alpha_s+8}}$$
$$\times \, (1+Y)^{-2}\, \varepsilon_{B,-3}^{-\frac{3}{2}}\, n_{-1}^{-\frac{3\alpha_s+16}{2(\alpha_s+8)}}\, \tilde{E}_{50}^{-\frac{4}{\alpha_s+8}}\, t_{1d}^{-\frac{2(\alpha_s+2)}{\alpha_s+8}},$$
$$F_{\text{max}}^{\text{syn}} \simeq 1.9 \times 10^{-1}\, \text{mJy} \left(\frac{1+z}{1.022}\right)^{-\frac{4(\alpha_s+2)}{\alpha_s+8}}$$
$$\times \, \varepsilon_{B,-3}^{\frac{1}{2}}\, n_{-1}^{\frac{3\alpha_s+8}{2(\alpha_s+8)}}\, D_{26.5}^{-2}\, \tilde{E}_{50}^{\frac{8}{\alpha_s+8}}\, t_{1d}^{\frac{3\alpha_s}{\alpha_s+8}}. \quad (48)$$

SSC emission—from the electrons Lorentz factors (Equations (47)) and synchrotron spectral breaks (Equations (48)), the SSC spectral break and the maximum flux is

$$\epsilon_m^{\text{ssc}} \simeq 2.5 \times 10^{-2}\, \text{eV} \left(\frac{1+z}{1.022}\right)^{\frac{10-\alpha_s}{\alpha_s+8}}$$
$$\times \, g(p)^4\, \varepsilon_{e,-1}^4\, \varepsilon_{B,-3}^{\frac{1}{2}}\, n_{-1}^{\frac{\alpha_s-4}{2(\alpha_s+8)}}\, \tilde{E}_{50}^{\frac{6}{\alpha_s+8}}\, t_{1d}^{-\frac{18}{\alpha_s+8}}$$
$$\varepsilon_c^{\text{ssc}} \simeq 2.4\, \text{GeV} \left(\frac{1+z}{1.022}\right)^{\frac{3(\alpha_s-2)}{\alpha_s+8}}$$
$$\times \, (1+Y)^{-4}\, \varepsilon_{B,-3}^{-\frac{7}{2}}\, n_{-1}^{-\frac{7\alpha_s+36}{2(\alpha_s+8)}}\, \tilde{E}_{50}^{-\frac{10}{\alpha_s+8}}\, t_{1d}^{-\frac{2(2\alpha_s+1)}{\alpha_s+8}},$$
$$F_{\text{max}}^{\text{ssc}} \simeq 6.8 \times 10^{-9}\, \text{mJy} \left(\frac{1+z}{1.022}\right)^{-\frac{5(\alpha_s+2)}{\alpha_s+8}}$$
$$\times \, g(p)^{-1}\varepsilon_{B,-3}^{\frac{1}{2}}\, n_{-1}^{\frac{5(\alpha_s+4)}{2(\alpha_s+8)}}\, D_{26.5}^{-2}\, \tilde{E}_{50}^{\frac{10}{\alpha_s+8}}\, t_{1d}^{\frac{2(\alpha_s+2)}{\alpha_s+8}}. \quad (49)$$

The break energy due to KN effect is

$$\varepsilon_{\text{KN}}^{\text{ssc}} \simeq 1.1\, \text{TeV} \left(\frac{1+z}{1.022}\right)^{\frac{2\alpha_s-6}{\alpha_s+8}} (1+Y)^{-1}$$
$$\times \, \varepsilon_{B,-3}^{-1}\, n_{-1}^{-\frac{\alpha_s+6}{\alpha_s+8}}\, \tilde{E}_{50}^{-\frac{2}{\alpha_s+8}}\, t_{1d}^{-\frac{\alpha_s+2}{\alpha_s+8}}. \quad (50)$$

### A.2. Lateral Expansion

Using the bulk Lorentz factor (Equation (24)), we derive and show the observable quantities when the quasi-spherical outflow lies in the lateral expansion phase.

Synchrotron radiation—in this case, the minimum and cooling Lorentz factors are given by

$$\gamma_m \simeq 63.5 \left(\frac{1+z}{1.022}\right)^{\frac{3}{\alpha_s+6}} g(p)\varepsilon_{e,-1}$$
$$\times \, n_{-1}^{-\frac{1}{\alpha_s+6}}\, \beta^{-\frac{\alpha_s}{\alpha_s+6}}\tilde{E}_{50}^{\frac{1}{\alpha_s+6}}\, t_{30d}^{-\frac{3}{\alpha_s+6}}$$
$$\gamma_c \simeq 1.1 \times 10^5 \left(\frac{1+z}{1.022}\right)^{\frac{\alpha_s-3}{\alpha_s+6}} (1+Y)^{-1}$$
$$\times \, \varepsilon_{B,-1}^{-1}\, n_{-1}^{-\frac{\alpha_s+3}{\alpha_s+6}}\, \beta^{\frac{3\alpha_s}{\alpha_s+6}}\tilde{E}_{50}^{-\frac{3}{\alpha_s+6}}\, t_{30d}^{\frac{3-\alpha_s}{\alpha_s+6}}. \quad (51)$$

Given the synchrotron radiation ($\epsilon_k^{\text{syn}} \propto \gamma_k^2$ for $k = $ m,c) and Equation (51), the spectral break and the maximum flux of synchrotron radiation is

$$\epsilon_m^{\text{syn}} \simeq 0.3 \times 10^{-2}\, \text{GHz} \left(\frac{1+z}{1.022}\right)^{\frac{6-\alpha_s}{\alpha_s+6}}$$
$$\times \, g(p)^2\varepsilon_{e,-1}^2\, \varepsilon_{B,-3}^{\frac{1}{2}}\, n_{-1}^{\frac{\alpha_s-2}{2(\alpha_s+6)}}\, \beta^{-\frac{4\alpha_s}{\alpha_s+6}}\tilde{E}_{50}^{\frac{4}{\alpha_s+6}}\, t_{30d}^{-\frac{12}{\alpha_s+6}}$$
$$\epsilon_c^{\text{syn}} \simeq 5.5 \times 10^{-3}\, \text{keV} \left(\frac{1+z}{1.022}\right)^{\frac{\alpha_s-6}{\alpha_s+6}}$$
$$\times \, (1+Y)^{-2}\, \varepsilon_{B,-3}^{-\frac{3}{2}}\, n_{-1}^{-\frac{3\alpha_s+10}{2(\alpha_s+6)}}\, \beta^{\frac{4\alpha_s}{\alpha_s+6}}\tilde{E}_{50}^{-\frac{4}{\alpha_s+6}}\, t_{30d}^{-\frac{2\alpha_s}{\alpha_s+6}},$$
$$F_{\text{max}}^{\text{syn}} \simeq 4.3\, \text{mJy} \left(\frac{1+z}{1.022}\right)^{-\frac{4\alpha_s}{\alpha_s+6}}$$
$$\times \, \varepsilon_{B,-3}^{\frac{1}{2}}\, n_{-1}^{\frac{3\alpha_s+2}{2(\alpha_s+6)}}\, \beta^{-\frac{8\alpha_s}{\alpha_s+6}}D_{26.5}^{-2}\, \tilde{E}_{50}^{\frac{8}{\alpha_s+6}}\, t_{30d}^{\frac{3(\alpha_s-2)}{\alpha_s+6}}. \quad (52)$$

SSC emission—From the electrons Lorentz factors (Equations (51)) and synchrotron spectral breaks (Equations (52)), the SSC spectral break and the maximum flux is

$$\epsilon_m^{\text{ssc}} \simeq 4.9 \times 10^{-4}\, \text{eV} \left(\frac{1+z}{1.022}\right)^{\frac{12-\alpha_s}{\alpha_s+6}}$$
$$\times \, g(p)^4\varepsilon_{e,-1}^4\, \varepsilon_{B,-3}^{\frac{1}{2}}\, n_{-1}^{\frac{\alpha_s-6}{2(\alpha_s+6)}}\, \beta^{-\frac{6\alpha_s}{\alpha_s+6}}\tilde{E}_{50}^{\frac{6}{\alpha_s+6}}\, t_{30d}^{-\frac{18}{\alpha_s+6}}$$
$$\epsilon_c^{\text{ssc}} \simeq 62.9\, \text{GeV} \left(\frac{1+z}{1.022}\right)^{\frac{3(\alpha_s-4)}{\alpha_s+6}}$$
$$\times \, (1+Y)^{-4}\, \varepsilon_{B,-3}^{-\frac{7}{2}}\, n_{-1}^{-\frac{7\alpha_s+22}{2(\alpha_s+6)}}\, \beta^{\frac{10\alpha_s}{\alpha_s+6}}\tilde{E}_{50}^{-\frac{10}{\alpha_s+6}}\, t_{30d}^{-\frac{2(2\alpha_s-3)}{\alpha_s+6}},$$
$$F_{\text{max}}^{\text{ssc}} \simeq 1.5 \times 10^{-6}\, \text{mJy} \left(\frac{1+z}{1.022}\right)^{-\frac{5\alpha_s}{\alpha_s+6}}$$
$$\times \, g(p)^{-1}\varepsilon_{B,-3}^{\frac{1}{2}}\, n_{-1}^{\frac{5(\alpha_s+2)}{2(\alpha_s+6)}}\, D_{26.5}^{-2}\, \beta^{-\frac{10\alpha_s}{\alpha_s+6}}\tilde{E}_{50}^{\frac{10}{\alpha_s+6}}\, t_{30d}^{\frac{2(2\alpha_s-3)}{\alpha_s+6}}. \quad (53)$$

### A.3. Wind-like Medium

Using the bulk Lorentz factor (Equation (29)), we derive and show the observable quantities when the quasi-spherical outflow is decelerated in a wind-like medium.

*Synchrotron radiation*—In this case, the minimum and cooling Lorentz factors are given by

$$\gamma_m = 5.1 \times 10^2 \left(\frac{1+z}{1.022}\right)^{\frac{1}{\alpha_s+4}} \xi^{-\frac{2}{\alpha_s+4}} g(p)\varepsilon_{e,-1}$$
$$\times A_{\star,-4}^{-\frac{1}{\alpha_s+4}} \tilde{E}_{50}^{\frac{1}{\alpha_s+4}} t_{10s}^{-\frac{1}{\alpha_s+4}}$$
$$\gamma_c = 3.7 \times 10^4 \left(\frac{1+z}{1.022}\right)^{-\frac{\alpha_s+3}{\alpha_s+4}} (1+Y)^{-1}$$
$$\times \xi^{\frac{2(2\alpha_s+7)}{\alpha_s+4}} \varepsilon_{B,-3}^{-1} A_{\star,-4}^{-\frac{\alpha_s+5}{\alpha_s+4}} \tilde{E}_{50}^{\frac{1}{\alpha_s+4}} t_{10s}^{\frac{\alpha_s+3}{\alpha_s+4}}. \quad (54)$$

Given the synchrotron radiation ($\epsilon_k^{\text{syn}} \propto \gamma_k^2$ for k = m, c) and the electron Lorentz factors (Equation (54)), the synchrotron spectral breaks and the maximum flux is

$$\epsilon_m^{\text{syn}} \simeq 0.2 \text{ eV} \left(\frac{1+z}{1.022}\right)^{\frac{2}{\alpha_s+4}} g(p)^2 \xi^{-\frac{2(\alpha_s+6)}{\alpha_s+4}}$$
$$\times \varepsilon_{e,-1}^2 \varepsilon_{B,-3}^{\frac{1}{2}} A_{\star,-4}^{\frac{\alpha_s}{2(\alpha_s+4)}} \tilde{E}_{50}^{\frac{2}{\alpha_s+4}} t_{10s}^{-\frac{(\alpha_s+6)}{\alpha_s+4}}$$
$$\epsilon_c^{\text{syn}} \simeq 3.7 \text{ keV} \left(\frac{1+z}{1.022}\right)^{-\frac{2(\alpha_s+3)}{\alpha_s+4}} \xi^{\frac{2(3\alpha_s+10)}{\alpha_s+4}} (1+Y)^{-2}$$
$$\times \varepsilon_{B,-3}^{-\frac{3}{2}} A_{\star,-4}^{-\frac{16+3\alpha_s}{2(\alpha_s+4)}} \tilde{E}_{50}^{\frac{2}{\alpha_s+4}} t_{10s}^{\frac{\alpha_s+2}{\alpha_s+4}},$$
$$F_{\max}^{\text{syn}} \simeq 0.2 \text{ mJy} \left(\frac{1+z}{1.022}\right)^{-\frac{\alpha_s+2}{\alpha_s+4}}$$
$$\times \xi^{-\frac{4}{\alpha_s+4}} \varepsilon_{B,-3}^{\frac{1}{2}} A_{\star,-4}^{\frac{3\alpha_s+8}{2(\alpha_s+4)}} D_{26.5}^{-2} \tilde{E}_{50}^{\frac{2}{\alpha_s+4}} t_{10s}^{-\frac{2}{\alpha_s+4}}. \quad (55)$$

*SSC emission*—from the electron Lorentz factors (Equations (54)) and synchrotron spectral breaks (Equations (55)), the SSC spectral break and the maximum flux is

$$\epsilon_m^{\text{ssc}} \simeq 42.7 \text{ keV} \left(\frac{1+z}{1.022}\right)^{\frac{4}{\alpha_s+4}} g(p)^4 \xi^{-\frac{2(\alpha_s+8)}{\alpha_s+4}}$$
$$\times \varepsilon_{e,-1}^4 \varepsilon_{B,-3}^{\frac{1}{2}} A_{\star,-4}^{\frac{\alpha_s-4}{2(\alpha_s+4)}} \tilde{E}_{50}^{\frac{4}{\alpha_s+4}} t_{10s}^{-\frac{(\alpha_s+8)}{\alpha_s+4}}$$
$$\epsilon_c^{\text{ssc}} \simeq 5.4 \text{ TeV} \left(\frac{1+z}{1.022}\right)^{-\frac{4(\alpha_s+3)}{\alpha_s+4}} \xi^{\frac{2(7\alpha_s+24)}{\alpha_s+4}}$$
$$\times (1+Y)^{-4} \varepsilon_{B,-3}^{-\frac{7}{2}} A_{\star,-4}^{-\frac{7\alpha_s+36}{2(\alpha_s+4)}} \tilde{E}_{50}^{\frac{4}{\alpha_s+4}} t_{10s}^{\frac{3\alpha_s+8}{\alpha_s+4}},$$
$$F_{\max}^{\text{ssc}} \simeq 2.2 \times 10^{-7} \text{ mJy } g(p)^{-1} \xi^{-2} \varepsilon_{B,-3}^{\frac{1}{2}} A_{\star,-4}^{\frac{5}{2}} D_{26.5}^{-2} t_{10s}^{-1}. \quad (56)$$

The break energy due to KN effect is

$$\epsilon_{\text{KN}}^{\text{ssc}} \simeq 313.9 \text{ GeV} \left(\frac{1+z}{1.022}\right)^{-\frac{2\alpha_s+6}{\alpha_s+4}} \xi^{\frac{2(2\alpha_s+6)}{\alpha_s+4}}$$
$$\times (1+Y)^{-1} \varepsilon_{B,-3}^{-1} A_{\star,-4}^{-\frac{\alpha_s+6}{\alpha_s+4}} \tilde{E}_{50}^{\frac{2}{\alpha_s+4}} t_{10s}^{\frac{\alpha_s+2}{\alpha_s+4}}. \quad (57)$$

# Appendix B
# Off-axis Jet

## B.1. Homogeneous Medium

Using the bulk Lorentz factor (Equation (34)), we derive and show the observable quantities when the off-axis jet is decelerated in a homogeneous medium.

*Synchrotron radiation*—in this case, the minimum and cooling electron Lorentz factors are given by

$$\gamma_m = 6.9 \times 10^3 \, \varepsilon_{e,-1} \left(\frac{1+z}{1.022}\right)^{\frac{3}{2}}$$
$$\times g(p) \, n_{-4}^{-\frac{1}{2}} \tilde{E}_{50}^{\frac{1}{2}} \Delta\theta_{15°}^3 \theta_{j,5°}^{-1} t_{1d}^{-\frac{3}{2}},$$
$$\gamma_c = 8.7 \times 10^3 \left(\frac{1+z}{1.022}\right)^{-\frac{1}{2}} (1+Y)^{-1}$$
$$\times \varepsilon_{B,-4}^{-1} n_{-1}^{-\frac{1}{2}} E_{50}^{-\frac{1}{2}} \Delta\theta_{15°}^{-1} \theta_{j,5°} t_{1d}^{\frac{1}{2}}. \quad (58)$$

Given the synchrotron radiation ($\epsilon_k^{\text{syn}} \propto \gamma_k^2$ for k = m, c) and the electron Lorentz factors (Equation (58)), the synchrotron spectral breaks and the maximum flux is

$$\epsilon_m^{\text{syn}} \simeq 4.7 \times 10^3 \text{ GHz} \left(\frac{1+z}{1.022}\right)^2$$
$$\times g(p)^2 \varepsilon_{e,-1}^2 \varepsilon_{B,-3}^{\frac{1}{2}} n_{-1}^{-\frac{1}{2}} E_{50} \Delta\theta_{15°}^4 \theta_{j,5°}^{-2} t_{1d}^{-3}$$
$$\epsilon_c^{\text{syn}} \simeq 8.1 \times 10^{-3} \text{ keV} \left(\frac{1+z}{1.022}\right)^{-2}$$
$$\times (1+Y)^{-2} \varepsilon_{B,-3}^{-\frac{3}{2}} n_{-1}^{-\frac{1}{2}} E_{50}^{-1} \Delta\theta_{15°}^{-4} \theta_{j,5°}^2 t_{1d},$$
$$F_{\max}^{\text{syn}} \simeq 3.5 \times 10^{-2} \text{ mJy} \left(\frac{1+z}{1.022}\right)^{-4}$$
$$\times \varepsilon_{B,-3}^{\frac{1}{2}} n_{-1}^{\frac{5}{2}} D_{26.5}^{-2} E_{50}^{-1} \Delta\theta_{15°}^{-18} \theta_{j,5°}^2 t_{1d}^6. \quad (59)$$

*SSC emission*—from the electron Lorentz factors (Equations (51)) and synchrotron spectral breaks (Equations (59)), the SSC spectral break and the maximum flux is

$$\epsilon_m^{\text{ssc}} \simeq 0.9 \text{ MeV} \left(\frac{1+z}{1.022}\right)^5$$
$$\times g(p)^4 \varepsilon_{e,-1}^4 \varepsilon_{B,-3}^{\frac{1}{2}} n_{-4}^{-\frac{3}{2}} E_{50}^2 \Delta\theta_{15°}^{10} \theta_{j,5°}^{-4} t_{100 \, d}^{-6}$$
$$\epsilon_c^{\text{ssc}} \simeq 0.6 \text{ MeV} \left(\frac{1+z}{1.022}\right)^{-3} (1+Y)^{-4}$$
$$\times \varepsilon_{B,-3}^{-\frac{7}{2}} n_{-4}^{-\frac{3}{2}} E_{50}^{-2} \Delta\theta_{15°}^{-6} \theta_{j,5°}^4 t_{100 \, d}^2,$$
$$F_{\max}^{\text{ssc}} \simeq 2.7 \times 10^{-9} \text{ mJy} \left(\frac{1+z}{1.022}\right)^{-5}$$
$$\times g(p)^{-1} \varepsilon_{B,-3}^{\frac{1}{2}} n_{-4}^{\frac{7}{2}} D_{26.5}^{-2} E_{50}^{-1} \Delta\theta_{15°}^{-20} \theta_{j,5°}^2 t_{100 \, d}^7. \quad (60)$$

The break energy due to KN effect is

$$\epsilon_{\text{KN}}^{\text{ssc}} \simeq 1.4 \text{ TeV} (1+Y)^{-1} \varepsilon_{B,-3}^{-1} n_{-4}^{-1} \Delta\theta_{15°}^2 t_{100 \, d}^{-1}. \quad (61)$$

## B.2. Lateral Expansion

Using the bulk Lorentz factor (Equation (39)), we derive and show the observable quantities when the off-axis jet lies in the lateral expansion phase.

*Synchrotron radiation*—in this case, the minimum and cooling Lorentz factors are given by

$$\gamma_{\rm m} \simeq 50.2 \left(\frac{1+z}{1.022}\right)^{\frac{1}{2}} g(p) \varepsilon_{e,-1} n_{-1}^{-\frac{1}{6}} \tilde{E}_{50}^{\frac{1}{6}} t_{\rm 1d}^{-\frac{1}{2}}$$

$$\gamma_{\rm c} \simeq 1.3 \times 10^5 \,{\rm GHz} \left(\frac{1+z}{1.022}\right)^{-\frac{1}{2}}$$

$$\times (1+Y)^{-1} \varepsilon_{B,-1}^{-1} n_{-1}^{-\frac{1}{2}} \tilde{E}_{50}^{-\frac{1}{2}} t_{\rm 1d}^{\frac{1}{2}}. \tag{62}$$

Given the synchrotron radiation ($\epsilon_k^{\rm syn} \propto \gamma_k^2$ for $k =$ m, c) and Equation (62), the spectral break and the maximum flux of synchrotron radiation is

$$\epsilon_{\rm m}^{\rm syn} \simeq 1.2 \times 10^{-2} \,{\rm GHz} \left(\frac{1+z}{1.022}\right)$$

$$\times g(p)^2 \varepsilon_{e,-1}^2 \varepsilon_{B,-3}^{\frac{1}{2}} n_{-1}^{-\frac{1}{6}} E_{50}^{\frac{2}{3}} t_{\rm 1d}^{-2}$$

$$\epsilon_{\rm c}^{\rm syn} \simeq 1.4 \,{\rm eV} \left(\frac{1+z}{1.022}\right)^{-1}$$

$$\times (1+Y)^{-2} \varepsilon_{B,-3}^{-\frac{3}{2}} n_{-1}^{-\frac{5}{6}} E_{50}^{-\frac{2}{3}}$$

$$F_{\rm max}^{\rm syn} \simeq 24.2 \,{\rm mJy} \left(\frac{1+z}{1.022}\right)^3$$

$$\times \varepsilon_{B,-3}^{\frac{1}{2}} n_{-1}^{\frac{1}{6}} D_{26.5}^{-2} E_{50}^{\frac{4}{3}} t_{\rm 1d}^{-1}. \tag{63}$$

SSC radiation—from the electron Lorentz factors (Equations (62)) and synchrotron spectral breaks (Equations (63)), the SSC spectral break and the maximum flux is

$$\epsilon_{\rm m}^{\rm ssc} \simeq 1.4 \times 10^{-4} \,{\rm eV} \left(\frac{1+z}{1.022}\right)^2$$

$$\times g(p)^4 \epsilon_{e,-1}^4 \varepsilon_{B,-3}^{\frac{1}{2}} n_{-1}^{-\frac{1}{2}} E_{50} t_{\rm 1d}^{-3}$$

$$\epsilon_{\rm c}^{\rm ssc} \simeq 23.4 \,{\rm GeV} \left(\frac{1+z}{1.022}\right)^{-2}$$

$$\times (1+Y)^{-4} \varepsilon_{B,-3}^{-\frac{7}{2}} n_{-1}^{-\frac{11}{6}} E_{50}^{-\frac{5}{3}} t_{\rm 1d},$$

$$F_{\rm max}^{\rm ssc} \simeq 1.7 \times 10^{-5} \,{\rm mJy} \left(\frac{1+z}{1.022}\right)^3$$

$$\times g(p)^{-1} \varepsilon_{B,-3}^{\frac{1}{2}} n_{-1}^{\frac{5}{6}} D_{26.5}^{-2} E_{50}^{\frac{5}{3}} t_{\rm 1d}^{-1}. \tag{64}$$

### B.3. Wind-like Medium

Using the bulk Lorentz factor (Equation (42)), we derive and show the observable quantities when the off-axis jet is decelerated in a wind-like medium.

Synchrotron radiation—in this case, the minimum and cooling Lorentz factors are given by

$$\gamma_m = 8.7 \times 10^4 \left(\frac{1+z}{1.022}\right)^{\frac{1}{2}}$$

$$\times \xi^{-1} g(p) \varepsilon_{e,-1} A_{\star,-4}^{-\frac{1}{2}} \theta_{j,5^\circ}^{-1} \Delta\theta_{15^\circ}^{\frac{1}{2}} \tilde{E}_{50}^{\frac{1}{2}} t_{\rm 10s}^{-\frac{1}{2}}$$

$$\gamma_c = 1.5 \times 10^{-3} \left(\frac{1+z}{1.022}\right)^{-\frac{3}{2}} (1+Y)^{-1}$$

$$\times \xi^3 \varepsilon_{B,-3}^{-1} A_{\star,-4}^{-\frac{1}{2}} \theta_{j,5^\circ} \Delta\theta_{15^\circ}^{-3} \tilde{E}_{50}^{-\frac{1}{2}} t_{\rm 10s}^{\frac{3}{2}}. \tag{65}$$

Given the synchrotron radiation ($\epsilon_k^{\rm syn} \propto \gamma_k^2$ for $k =$ m, c) and the electron Lorentz factors (Equation (65)), the synchrotron

spectral breaks and the maximum flux is

$$\epsilon_{\rm m}^{\rm syn} \simeq 95.5 \,{\rm keV} \left(\frac{1+z}{1.022}\right) g(p)^2 \xi^{-4}$$

$$\times \varepsilon_{e,-1}^2 \varepsilon_{B,-3}^{\frac{1}{2}} A_{\star,-4}^{-\frac{1}{2}} E_{50} \Delta\theta_{15^\circ}^2 \theta_{j,5^\circ}^{-2} t_{\rm 10s}^{-2}$$

$$\epsilon_{\rm c}^{\rm syn} \simeq 8.4 \times 10^{-13} \,{\rm eV} \left(\frac{1+z}{1.022}\right)^{-3} \xi^4 (1+Y)^{-2}$$

$$\times \varepsilon_{B,-3}^{-\frac{3}{2}} A_{\star,-4}^{-\frac{1}{2}} E_{50}^{-1} \Delta\theta_{15^\circ}^{-6} \theta_{j,5^\circ}^2 t_{\rm 10s}^2,$$

$$F_{\rm max}^{\rm syn} \simeq 0.2 \,{\rm mJy} \left(\frac{1+z}{1.022}\right) \xi^2 \varepsilon_{B,-3}^{\frac{1}{2}}$$

$$\times A_{\star,-4}^{\frac{5}{2}} D_{26.5}^{-2} E_{50}^{-1} \Delta\theta_{15^\circ}^{-8} \theta_{j,5^\circ}^2 t_{\rm 10s}. \tag{66}$$

SSC emission—from the electron Lorentz factors (Equations (65)) and synchrotron spectral breaks (Equations (66)), the SSC spectral break and the maximum flux is

$$\epsilon_{\rm m}^{\rm ssc} \simeq 3.1 \,{\rm GeV} \left(\frac{1+z}{1.022}\right)^2 g(p)^4 \xi^{-6}$$

$$\times \varepsilon_{e,-1}^4 \varepsilon_{B,-3}^{\frac{1}{2}} A_{\star,-4}^{-\frac{3}{2}} E_{50}^2 \Delta\theta_{15^\circ}^4 \theta_{j,5^\circ}^{-4} t_{\rm 10s}^{-3}$$

$$\epsilon_{\rm c}^{\rm ssc} \simeq 1.8 \times 10^{-18} \,{\rm eV} \left(\frac{1+z}{1.022}\right)^{-6} \xi^{10} (1+Y)^{-4}$$

$$\times \varepsilon_{B,-3}^{-\frac{7}{2}} A_{\star,-4}^{-\frac{3}{2}} E_{50}^{-2} \Delta\theta_{15^\circ}^{-12} \theta_{j,5^\circ}^4 t_{\rm 10s}^5,$$

$$F_{\rm max}^{\rm ssc} \simeq 3.1 \,{\rm mJy} \left(\frac{1+z}{1.022}\right)^2$$

$$\times g(p)^{-1} \varepsilon_{B,-3}^{\frac{1}{2}} A_{\star,-4}^{\frac{7}{2}} D_{26.5}^{-2} E_{50}^{-1} \Delta\theta_{15^\circ}^{-6} \theta_{j,5^\circ}^2. \tag{67}$$

The break energy due to KN effect is

$$\epsilon_{\rm KN}^{\rm ssc} \simeq 2.4 \times 10^{-3} \,{\rm GeV} \left(\frac{1+z}{1.022}\right)^{-2}$$

$$\times \xi^2 (1+Y)^{-1} \varepsilon_{B,-3}^{-1} A_{\star,-4}^{-1} \Delta\theta_{15^\circ}^{-2} t_{\rm 10s}. \tag{68}$$

## ORCID iDs

N. Fraija ⬤ https://orcid.org/0000-0002-0173-6453
D. Lopez-Camara ⬤ https://orcid.org/0000-0001-9512-4177

## References

Abbott, B. P., Abbott, R., Abbott, T. D., et al. (LIGO Scientific Collaboration and Virgo Collaboration) 2017a, PhRvL, 119, 161101
Abbott, B. P., Abbott, R., Abbott, T. D., et al. 2017b, ApJL, 848, L12
Abdalla, H., Abramowski, A., Aharonian, F., et al. 2017, ApJ, 850, L22
Ackermann, M., Ajello, M., Asano, K., et al. 2013, ApJS, 209, 11
Ackermann, M., Ajello, M., Asano, K., et al. 2014, Sci, 343, 42
Alexander, K. D., Berger, E., Fong, W., et al. 2017, ApJ, 848, L21
Alexander, K. D., Margutti, R., Blanchard, P. K., et al. 2018, ApJL, 863, 18
Barthelmy, S. D., Cannizzo, J. K., Gehrels, N., et al. 2005, ApJ, 635, L133
Bauswein, A., Goriely, S., & Janka, H.-T. 2013, ApJ, 773, 78
Berger, E. 2014, ARA&A, 52, 43
Blandford, R. D., & McKee, C. F. 1976, PhFl, 19, 1130
Burns, E., Veres, P., Connaughton, V., et al. 2018, ApJ, 863, L34
Dai, Z. G., & Lu, T. 1999, ApJ, 519, L155
D'Avanzo, P., Campana, S., Salafia, O. S., et al. 2018, A&A, 613, 1
Dermer, C. D., Chiang, J., & Mitman, K. E. 2000, ApJ, 537, 785
Dobie, D., Kaplan, D. L., Murphy, T., et al. 2018, ApJ, 858, L15
Fraija, N. 2014, MNRAS, 437, 2187
Fraija, N. 2015, ApJ, 804, 105
Fraija, N., Barniol Duran, R., Dichiara, S., & Beniamini, P. 2019a, ApJ, 883, 162
Fraija, N., De Colle, F., Veres, P., et al. 2019b, ApJ, 871, 123

Fraija, N., De Colle, F., Veres, P., et al. 2019c, arXiv:1906.00502
Fraija, N., Dichiara, S., Pedreira, A. C. C. d. E. S., et al. 2019d, arXiv:1905.13572
Fraija, N., Dichiara, S., Pedreira, A. C. C. d. E. S., et al. 2019e, ApJ, 879, L26
Fraija, N., González, M. M., & Lee, W. H. 2012, ApJ, 751, 33
Fraija, N., Lee, W. H., Araya, M., et al. 2017a, ApJ, 848, 94
Fraija, N., Lee, W., & Veres, P. 2016a, ApJ, 818, 190
Fraija, N., Lee, W. H., Veres, P., & Duran, R. B. 2016b, ApJ, 831, 22
Fraija, N., Pedreira, A. C. C. d. E. S., & Veres, P. 2019f, ApJ, 871, 200
Fraija, N., Veres, P., Zhang, B. B., et al. 2017b, ApJ, 848, 15
Franceschini, A., & Rodighiero, G. 2017, A&A, 603, A34
Ghirlanda, G., Salafia, O. S., Paragi, Z., et al. 2019, Sci, 363, 968
Giblin, T. W., van Paradijs, J., Kouveliotou, C., et al. 1999, ApJ, 524, L47
Gill, R., & Granot, J. 2018, MNRAS, 478, 4128
Goldstein, A., Veres, P., Burns, E., et al. 2017, ApJ, 848, L14
Granot, J., Gill, R., Guetta, D., & Colle, F. De. 2018, MNRAS, 481, 1597
Granot, J., Guetta, D., & Gill, R. 2017, ApJ, 850, L24
Granot, J., Panaitescu, A., Kumar, P., & Woosley, S. E. 2002, ApJ, 570, L61
Haggard, D., Nynka, M., Ruan, J. J., Evans, P., & Kalogera, V. 2018, ATel, 11242, 1
Hallinan, G., Corsi, A., Mooley, K. P., et al. 2017, Sci, 358, 1579
Hotokezaka, K., Kiuchi, K., Shibata, M., Nakar, E., & Piran, T. 2018, ApJ, 867, 95
Hotokezaka, K., Kyutoku, K., Tanaka, M., et al. 2013, ApJ, 778, L16
Huang, Y. F., & Cheng, K. S. 2003, MNRAS, 341, 263
Ioka, K., & Nakamura, T. 2017, arXiv:1710.05905
Kasliwal, M. M., Nakar, E., Singer, L. P., et al. 2017, Sci, 358, 1559
Kumar, P., & Barniol Duran, R. 2009, MNRAS, 400, L75
Kumar, P., & Zhang, B. 2015, Phys. Rep., 561, 1
Lamb, G. P., & Kobayashi, S. 2017, MNRAS, 472, 4953
Lamb, G. P., Mandel, I., & Resmi, L. 2018, MNRAS, 481, 2581
Lazzati, D., Perna, R., Morsony, B. J., et al. 2018, PhRvL, 120, 241103
Lyman, J. D., Lamb, G. P., Levan, A. J., et al. 2018, arXiv:1801.02669
Margutti, R., Alexander, K. D., Xie, X., et al. 2018, ApJL, 856, 18
Margutti, R., Berger, E., Fong, W., et al. 2017a, ApJ, 848, L20
Margutti, R., Fong, W., Eftekhari, T., et al. 2017b, ATel, 11037, 1
Martinez-Castellanos, I., Smith, A. & HAWC Collaboration 2017, GCN, 21683
Matsumoto, T., Nakar, E., & Piran, T. 2019, MNRAS, 486, 1563
Mirzoyan, R. 2019, ATel, 12390, 1
Mooley, K. P., Deller, A. T., Gottlieb, O., et al. 2018a, Natur, 561, 355
Mooley, K. P., Nakar, E., Hotokezaka, K., et al. 2018b, Natur, 554, 207
Nagakura, H., Hotokezaka, K., Sekiguchi, Y., Shibata, M., & Ioka, K. 2014, ApJ, 784, L28
Nakar, E. 2007, PhR, 442, 166
Nakar, E., & Piran, T. 2018, MNRAS, 478, 407
Panaitescu, A., & Mészáros, P. 1998, ApJ, 493, L31
Rees, M. J. 1999, A&AS, 138, 491
Rybicki, G. B., & Lightman, A. P. 1986, Radiative Processes in Astrophysics (New York: Wiley)
Salmonson, J. D. 2003, ApJ, 592, 1002
Sari, R., Piran, T., & Narayan, R. 1998, ApJ, 497, L17
Savchenko, V., Ferrigno, C., Kuulkers, E., et al. 2017, ApJ, 848, L15
Troja, E., Lipunov, V. M., Mundell, C. G., et al. 2017, Nature, 547, 425
Troja, E., Piro, L., Ryan, G., et al. 2018, MNRAS, 478, 18
Troja, E., Piro, L., van Eerten, H., et al. 2017, Natur, 000, 1
Veres, P., Mészáros, P., Goldstein, A., et al. 2018, arXiv:1802.07328
Wang, X.-Y., Liu, R.-Y., & Lemoine, M. 2013, ApJ, 771, L33
Yamazaki, R., Toma, K., Ioka, K., & Nakamura, T. 2006, MNRAS, 369, 311
Zhang, B., & Mészáros, P. 2004, IJMPA, 19, 2385

# MODELING GAMMA-RAY BURST AFTERGLOW OBSERVATIONS WITH AN OFF-AXIS JET EMISSION

N. Fraija[1†], A. Galvan-Gamez[1], B. Betancourt Kamenetskaia[2,3], M.G. Dainotti[4,5], S. Dichiara[6,7], P. Veres[8], R. L. Becerra[9] and A. C. Caligula do E. S. Pedreira[1]

[1] Instituto de Astronomía, Universidad Nacional Autónoma de México, Circuito Exterior, C.U., A. Postal 70-264, 04510 Cd. de México, México.
[2] LMU Physics Department, Ludwig Maxmillians University,Theresienstr. 37, 80333 Munich, Germany
[3] TUM Physics Department, Technical University of Munich, James-Franck-Str, 85748 Garching, Germany
[4] National Astronomical Observatory of Japan, Division of Science, Mitaka, 2-chome
[5] Space Science Institute, Boulder, Colorado
[6] Department of Astronomy, University of Maryland, College Park, MD 20742-4111, USA
[7] Astrophysics Science Division, NASA Goddard Space Flight Center, 8800 Greenbelt Rd, Greenbelt, MD 20771, USA
[8] Center for Space Plasma and Aeronomic Research (CSPAR), University of Alabama in Huntsville, Huntsville, AL 35899, USA and
[9] Instituto de Ciencias Nucleares, Universidad Nacional Autónoma de México, Apartado Postal 70-264, 04510 México, CDMX, Mexico

(Dated: May 6, 2022)
*Draft version May 6, 2022*

## ABSTRACT

Gamma-ray bursts (GRBs) are fascinating extragalactic objects. They represent a fantastic opportunity to investigate unique properties not exhibited in other sources. Multi-wavelength afterglow observations from some short- and long-duration GRBs reveal an atypical long-lasting emission that evolves differently from the canonical afterglow light curves favoring the off-axis emission. We present an analytical synchrotron afterglow scenario, and the hydrodynamical evolution of an off-axis top-hat jet decelerated in a stratified surrounding environment. The analytical synchrotron afterglow model is shown during the coasting, deceleration (off- and on-axis emission), and the post-jet-break decay phases, and the hydrodynamical evolution is computed by numerical simulations showing the time evolution of the Doppler factor, the half-opening angle, the bulk Lorentz factor, and the deceleration radius. We show that numerical simulations are in good agreement with those derived with our analytical approach. We apply the current synchrotron model and describe successfully the delayed non-thermal emission observed in a sample of long and short GRBs with evidence of off-axis emission. Furthermore, we provide constraints on the possible afterglow emission by requiring the multi-wavelength upper limits derived for the closest Swift-detected GRBs and promising gravitational-wave events.

*Subject headings:* Gamma-ray bursts: individual — Stars: neutron — Physical data and processes: acceleration of particles — Physical data and processes: radiation mechanism: nonthermal — ISM: general - magnetic fields

## 1. INTRODUCTION

Gamma-ray bursts (GRBs) are among the most powerful transient events in the Universe. These events are detected as brief, non-repeating flashes in the gamma-rays bands. Depending on the burst duration (from milliseconds to thousands of seconds), GRBs are commonly classified as short (sGRBs) and long GRBs (lGRBs) (Kouveliotou et al. 1993). A lGRB is associated with the core collapse (CC) of dying massive star (Woosley 1993; Galama et al. 1998) that lead to supernova (SNe; Bloom et al. 1999; Woosley & Bloom 2006). At the same time, a sGRB is linked with the merger of a neutron star (NS) with a black hole (BH, Narayan et al. 1992) or two NSs (Duncan & Thompson 1992; Usov 1992; Thompson 1994; Metzger et al. 2011) as demonstrated by the historical gravitational-wave (GW) and electromagnetic detections of the GW170817 event (Abbott et al. 2017a).

On August 17, 2017, the joint detection of two messengers of the fusion of two NSs was achieved for the first time: the GW event (GW170817) by the Laser Interferometer Gravitational-Wave Observatory (LIGO) and VIRGO (Abbott et al. 2017a; von Kienlin et al. 2017) and the associated low-luminosity burst, GRB 170817A by the Fermi Gamma-ray Space Telescope (von Kienlin et al. 2017) and The INTErnational Gamma-Ray Astrophysics Laboratory (INTEGRAL; Savchenko et al. 2017). The results of this joint observation confirmed that NS fusion is a progenitor of sGRBs (Abbott et al. 2017). The association of GW170817A with the near host galaxy NGC 4993, located at a redshift of $z \simeq 0.01$ (Coulter et al. 2017; Margutti et al. 2017b) suggested the presence of a local population of low-luminosity bursts following the merger of two NSs (Abbott et al. 2017). Immediately, GRB 170817A was followed up by large observational campaigns covering the X-ray (Troja et al. 2017; Margutti et al. 2018; Alexander et al. 2018; D'Avanzo et al. 2018; Margutti et al. 2017a; Haggard et al. 2018), optical (Lyman et al. 2018; Margutti et al. 2018) and radio (Abbott et al. 2017b; Mooley et al. 2017; Dobie et al. 2018; Troja et al. 2017) bands, among others. In order to describe the delayed multi-wavelength observations in timescales of days, synchrotron external-shock models radiated from off-axis top-hat jets (Troja et al. 2017; Margutti et al. 2017b; Ioka & Nakamura 2017; Alexander et al. 2017; Fraija et al. 2019a,b), radially stratified ejecta (Mooley et al. 2017; Fraija et al. 2019c; Hotokezaka et al. 2018) and structured jets (Kasliwal et al. 2017; Lazzati et al. 2017) were proposed. Later, analyses performed by Burns *et al.* (Burns et al. 2018) and other authors (Troja et al. 2018; Burns et al. 2018; Fong et al. 2016) showed that GRB 150101B exhibits characteristics similar to GRB 170817A, in terms of its two-component structure and an undetected afterglow in a timescale of days followed by bright X-ray emission. Similar features in the multi-wavelength afterglow have been found in GRB 080503 (Perley et al. 2009),

GRB 140903A (Troja et al. 2016) and GRB 160821B (Lü et al. 2017; Stanbro & Meegan 2016). On the other hand, several searches for afterglow emission around the closest bursts ($\lesssim 200\,\mathrm{Mpc}$) reported by the Burst Alert Telescope (BAT) instrument onboard the Neil Gehrels Swift Observatory (Dichiara et al. 2020) and the GW events by Advanced LIGO and Advanced VIRGO detectors (Abbott et al. 2021; The LIGO Scientific Collaboration et al. 2021) have been performed without successful, but setting multi-wavelength upper limits.

The density profile of the medium surrounding a burst has been addressed previously in different contexts. For instance, for the case of SNe, Chevalier (1982) studied the interaction of an adiabatic flow in a circumstellar density profile for Type II SNe of the form $\propto r^{-2}$. Ever since, subsequent authors have adopted this proposal for modeling the circumstellar medium, and it has even been applied in the research of different SN types. Examples of such studies are those by Blondin et al. (1996), Soderberg et al. (2006), Kotak et al. (2004), and Chevalier (1984), among others. Nevertheless, a generalization of this power law has also been considered. A later study, Moriya & Tominaga (2012) showed that the diversity might explain the spectral diversity of Type II luminous SNe in the density slope of the surrounding dense wind. To this effect, they proposed a wind density structure in the form $\propto r^{-k}$. They noticed that the ratio of the diffusion timescale in the optically thick region of the wind and the shock propagation timescale after the shock breakout strongly depends on the stratification parameter $k$, which led to differences in the spectral SN evolution. On the other hand, the requirement of a stratified environment condition has been proposed in some cases for modeling the multi-wavelength afterglows, such as in work by Yi et al. (2013). The authors analyzed more than one dozen GRBs and concluded that the circumburst environment could be neither a homogeneous nor a stellar-wind medium but something in between, with a general density distribution with a stratification parameter in the range $0.4 \leq k \leq 1.4$. A more recent example of an analysis that links SN and GRB emission with a stratified environment is the one by Izzo et al. (2020), in which the authors studied SN 2020bvc. They found an excellent agreement with the GRB-associated, broad-lined Ic SN 1998bw; thus, it was categorized as a young broad-lined Ic SN. They also noted that its X-ray light curve was consistent with simulations of an off-axis GRB afterglow in a stratified medium with $k = 1.5$; thus, this event represented the first case of an off-axis GRB discovered via its associated SN. It was later argued by Ho et al. (2020b), however, that such a model would predict an 8.5 GHz radio light curve several orders of magnitude more luminous than their measurements. Nevertheless, they stated that an off-axis jet could not be ruled out, and future radio observations would be needed.

In this work, we extend the analytical synchrotron afterglow scenario of the off-axis top-hat jet used to describe the multi-wavelength afterglow observations in GRB 170817A (see Fraija et al. 2019b) adding several ingredients. Here we consider i) the circumburst external medium as stratified with a profile density $\propto r^{-k}$ with k in the range of $0 \leq k < 3$, ii) the synchrotron radiation in self-absorption regime, iii) the afterglow emission during the transition from off-axis to on-axis before the lateral expansion phase (relativistic phase), iv) the hydrodynamical evolution computed by numerical simulations and v) a fraction of electrons accelerated by the shock front. We apply the current model to describe the delayed non-thermal emission observed in GRB 080503, GRB 140903A, GRB 150101B, GRB 160821B, and SN 2020bvc, and to provide constraints on the possible afterglow emission using multi-wavelength upper limits associated with the closest Swift-detected sGRBs and the promising GW events. This paper is arranged as follows: Section 2 presents the analytical synchrotron scenario and an hydrodynamical evolution of an off-axis top-hat jet decelerated in a stratified surrounding environment. In Section 3, we apply the proposed analytical model to describe the multi-wavelength observations of a sample of bursts and provide constraints to other ones. In Section 4, we present our conclusions.

## 2. OFF-AXIS TOP HAT MODEL

### 2.1. *Radiative model*

Accelerated electrons in forward-shock models are distributed in accordance with their Lorentz factors ($\gamma_e$) and are described by the electron power index $p$ as $N(\gamma_e)\, d\gamma_e \propto \gamma_e^{-p}\, d\gamma_e$ for $\gamma_m \leq \gamma_e$, where $\gamma_m = m_\mathrm{p}/m_\mathrm{e}\, g(p)\varepsilon_\mathrm{e}(\Gamma - 1)\zeta_e^{-1}$ is the minimum electron Lorentz factor with $\Gamma$ the bulk Lorentz factor, $m_\mathrm{p}$ and $m_\mathrm{e}$ the proton and electron mass, $\varepsilon_\mathrm{e}$ is the fraction of energy given to accelerate electrons, $\zeta_e$ denotes the fraction of electrons that were accelerated by the shock front (Fan & Piran 2006) and $g(p) = \frac{p-2}{p-1}$. The comoving of the magnetic field strength in the blastwave $B'^2/(8\pi) = \varepsilon_B e$ is derived from the energy density $e = [(\hat{\gamma}\Gamma + 1)/(\hat{\gamma} - 1)](\Gamma - 1)n(r)m_p c^2$ with $\hat{\gamma}$ the adiabatic index (Huang et al. 1999) and its respective fraction given to magnetic field ($\varepsilon_B$). Hereafter, we adopt the unprimed and prime terms to refer them in the observer and comoving frames, respectively. The term $\hat{\gamma}$ is the adiabatic index and $n(r) = A_\mathrm{k}\, r^{-\mathrm{k}} = \frac{\dot{M}_\mathrm{W}}{4\pi v_\mathrm{W}}\, r^{-\mathrm{k}}$, where $v_\mathrm{W}$ is the wind velocity and $\dot{M}_\mathrm{W}$ is the mass-loss rate. The sub-index k lies in the range $0 \leq k \leq 3$, with k $= 0$ the constant-density medium ($A_0 = n$), and k $= 2$ the stellar wind ejected by its progenitor ($A_2 \simeq A_\mathrm{W}\, 3 \times 10^{35}\mathrm{cm}^{-1}$) where $A_\mathrm{W}$ is the density parameter. The cooling electron Lorentz factor is $\gamma_\mathrm{c} = (6\pi m_e c/\sigma_T)(1 + Y)^{-1}\Gamma^{-1}B'^{-2}t^{-1}$, where $\sigma_T$ is the cross-section in the Thomson regime and $Y$ is the Compton parameter (Sari & Esin 2001; Wang et al. 2010). The synchrotron spectral breaks and the synchrotron radiation power per electron in the comoving frame are given by $\nu_\mathrm{i}' = q_e/(2\pi m_e c)\gamma_\mathrm{i}^2 B'$ and $P_{\nu_m'}' \simeq \sqrt{3}q_e^3/(m_e c^2)B'$, respectively, with hereafter the subindex i $=$ m and c for the characteristic and cooling break, and the constants $q_e$ and $c$ the elementary charge and the speed of light, respectively (e.g., see Sari et al. 1998; Fraija 2015). The synchrotron spectral breaks in the self-absorption regime are derived from $\nu_{\mathrm{a},1}' = \nu_\mathrm{c}'\tau_{0,m}^{\frac{3}{5}}$, $\nu_{\mathrm{a},2}' = \nu_\mathrm{m}'\tau_{0,m}^{\frac{2}{p+4}}$ and $\nu_{\mathrm{a},3}' = \nu_\mathrm{m}'\tau_{0,c}^{\frac{3}{5}}$ with the optical depth given by $\tau_{0,i} \simeq \frac{5}{3-k}\frac{q_e n(r)r}{B'\gamma_\mathrm{i}^5}$ with $r$ the shock radius (Panaitescu & Mészáros 1998). Considering the total number of emitting electrons $N_e = (\Omega/4\pi)\, n(r)\frac{4\pi}{3-k}r^3$ and also taking into account the transformation laws for the solid angle ($\Omega = \Omega'/\delta_D^2$), the radiation power ($P_{\nu_m} = \delta_D/(1 + z)P_{\nu_m'}'$) and the spectral breaks ($\nu_\mathrm{i} = \delta_D/(1 + z)\nu_\mathrm{i}'$), the maximum flux given by synchrotron radiation is

$$F_{\nu,\max} = \frac{(1+z)^2 \delta_D^3}{4\pi d_z^2} N_e P'_{\nu'_m} , \tag{1}$$

where $d_z = (1+z)\frac{c}{H_0}\int_0^z \frac{d\tilde{z}}{\sqrt{\Omega_M(1+\tilde{z})^3+\Omega_\Lambda}}$ (Weinberg 1972) is the luminosiy distance, $r = \delta_D/(1+z)\Gamma\beta ct$ is the shock radius, and $\delta_D = \frac{1}{\Gamma(1-\mu\beta)}$ is the Doppler factor with $\mu = \cos\Delta\theta$, $\beta = v/c$ with $v$ the velocity of the material, and $\Delta\theta = \theta_{\rm obs} - \theta_{\rm j}$ is given by the viewing angle ($\theta_{\rm obs}$) and the half-opening angle of the jet ($\theta_{\rm j}$). We assume for the cosmological constants a spatially flat universe $\Lambda$CDM model with $H_0 = 69.6\,{\rm km\,s^{-1}\,Mpc^{-1}}$, $\Omega_M = 0.286$ and $\Omega_\Lambda = 0.714$ (Planck Collaboration et al. 2016).

## 2.2. *Hydrodynamical evolution vs analytical approach*

### 2.2.1. *Hydrodynamical evolution*

We consider the dynamical equations proposed by Huang et al. (1999, 2000). The dynamical evolution of the relativistic outflow into the circumburst medium can be described by

$$\begin{aligned}
\frac{dr}{dt} &= \beta c\Gamma\left(\Gamma + \sqrt{\Gamma^2-1}\right), & \frac{dm}{dr} &= 2\pi(1-\cos\theta_{\rm j})r^2 n m_p \\
\frac{d\theta_{\rm j}}{dt} &= \frac{c_s}{r}(\Gamma + \sqrt{\Gamma^2-1}), & \frac{d\Gamma}{dm} &= -\frac{\Gamma^2-1}{M_{\rm ej}+\epsilon m + 2(1-\epsilon)\Gamma m},
\end{aligned} \tag{2}$$

where $c_s = \sqrt{\hat{\gamma}(\gamma-1)(\Gamma-1)c^2/(1+\hat{\gamma}(\Gamma-1))}$ with $\hat{\gamma} \approx (4\Gamma+1)/3\Gamma$, $M_{\rm ej}$ is the initial value of the ejected mass and $\epsilon$ is the radiative efficiency with $\epsilon = 0$ in the adiabatic regime and $\epsilon = 1$ in the fully radiative regime. The previous equations are consistent with the self-similar solution during the ultra-relativistic (Blandford-McKee solution; Blandford & McKee 1976) and the Newtonian phase (Sedov-Taylor solution), respectively, and consider the beaming effect (Rhoads 1999).

The observed quantities are integrated over the equal arrival time surface (EATS) determined by (Waxman 1997)

$$t = (1+z)\int \frac{dr}{\beta\Gamma c\delta_D} \equiv {\rm const.} \tag{3}$$

### 2.2.2. *Analytical approach*

During the coasting phase (before the deceleration phase), the relativistic outflow is not affected by the circumburst medium, so the bulk Lorentz factor is constant $\Gamma_{\rm cp} = \Gamma_0$ and the radius evolves as $r = c\beta_0 t/[(1+z)(1-\beta_0\mu)]$ with $\beta_0 = \sqrt{\Gamma_0^2-1}/\Gamma_0$. During the deceleration phase, the relativistic outflow transfers a large amount of its energy to the circumstellar medium driving a forward shock. Considering the adiabatic evolution of the forward shock with an isotropic equivalent-kinetic energy $E = \frac{4\pi}{3}m_p c^2 A_{\rm k} r^3 \Gamma^2$(Blandford-McKee solution; Blandford & McKee 1976) and a radial distance $r = c\beta_{\rm of} t/[(1+z)(1-\beta_{\rm of}\mu)]$, the bulk Lorentz factor evolves as

$$\Gamma_{\rm of} = \left(\frac{3}{4\pi\,m_p c^{5-k}}\right)^{\frac{1}{2}} (1+z)^{-\frac{k-3}{2}}(1-\beta\cos\Delta\theta)^{-(k-3)} A_{\rm k}^{-\frac{1}{2}} E^{\frac{1}{2}} t^{\frac{k-3}{2}} , \tag{4}$$

with $\beta_{\rm of} = \sqrt{\Gamma_{\rm of}^2-1}/\Gamma_{\rm of}$. The deceleration time scale $t_{\rm dec}$ can be defined using eq. 4. As the bulk Lorentz factor becomes $\Gamma \simeq 1/\Delta\theta$, the observed flux becomes in our field of view. During the on-axis emission, the bulk Lorentz factor in the adiabatic regime evolves as

$$\Gamma_{\rm on} = \left(\frac{3}{(2c)^{5-k}\pi\,m_p}\right)^{\frac{1}{8-2k}} (1+z)^{-\frac{k-3}{8-2k}} A_{\rm k}^{-\frac{1}{8-2k}} E^{\frac{1}{8-2k}} t^{\frac{k-3}{8-2k}} , \tag{5}$$

with the radius $r \simeq 2\beta_{\rm on}\Gamma_{\rm on}^2 ct/(1+z)$ and $\beta_{\rm on} = \sqrt{\Gamma_{\rm on}^2-1}/\Gamma_{\rm on}$, before the outflow enters to the post-jet-break decay phase ($\Gamma \simeq 1/\theta_j$). During the post-jet-break decay phase, the bulk Lorentz factor evolves as

$$\Gamma_{\rm le} = \left(\frac{3}{(2c)^{5-k}\pi\,m_p}\right)^{\frac{1}{6-2k}} (1+z)^{-\frac{k-3}{6-2k}} A_{\rm k}^{-\frac{1}{6-2k}} E^{\frac{1}{6-2k}} \theta_j^{\frac{1}{3-k}} t^{\frac{k-3}{6-2k}} , \tag{6}$$

with the shock's radius and velocity given by $r \simeq 2\beta_{\rm le}\Gamma_{\rm le}^2 ct/(1+z)$ and $\beta_{\rm le} = \sqrt{\Gamma_{\rm le}^2-1}/\Gamma_{\rm le}$, respectively. We summarize the evolution of the bulk Lorentz factor as

$$\Gamma \propto \begin{cases} t^0, & t < t_{\rm dec}, \\ t^{\frac{k-3}{2}}, & t_{\rm dec} \leq t \leq t_{\rm pk}, \\ t^{\frac{k-3}{8-2k}}, & t_{\rm pk} \leq t \leq t_{\rm br}, \\ t^{\frac{k-3}{6-2k}} & t_{\rm br} \leq t, \end{cases} \tag{7}$$

where the respective timescales are

$$t_{\rm dec} = t_{\rm dec,0}(1+z)(1 - \beta \cos \Delta\theta)^2 A_{\rm k}^{-\frac{1}{k-3}} E^{\frac{1}{k-3}} \Gamma^{-\frac{2}{3-k}}$$
$$t_{\rm pk} = t_{\rm pk,0}(1+z)A_{\rm k}^{\frac{1}{k-3}} E^{-\frac{1}{k-3}} \Delta\theta^{-\frac{8-2k}{k-3}}$$
$$t_{\rm br} = t_{\rm br,0}(1+z)A_{\rm k}^{-\frac{1}{3-k}} E^{\frac{1}{3-k}} \theta_{\rm j}^2 \,, \tag{8}$$

with $t_{\rm dec,0} = (3/4\pi\, m_p c^{5-k})^{\frac{1}{3-k}}$ and $t_{\rm pk,0} = t_{\rm br,0} = (3/(2c)^{5-k} \pi\, m_p)^{\frac{1}{3-k}}$. It is worth noting that the afterglow emission enters in the observer's field of view at $t_{\rm pk}$. For instance, the bulk Lorentz factor in a constant-density medium evolves as first $\propto t^0$ (Sari & Piran 1999), then $t^{-\frac{3}{2}}$ (Nakar & Piran 2018; Fraija et al. 2019b), moreover $t^{-\frac{3}{8}}$ (Sari et al. 1998), and finally $t^{-\frac{1}{2}}$ (Sari et al. 1999), as expected.

The minimum and cooling electron Lorentz factors, the spectral breaks, the maximum flux and the synchrotron light curves during the coasting, deceleration (off- and on-axis) and post-jet-break decay phases are shown in Appendix A and Tables 1, 2 and 3.

## 2.3. *Comparison of our model with previous simulations*

Figure 1 presents examples of the time evolution of the Doppler factor, the half-opening angle, the bulk Lorentz factor, and the deceleration radius, all in a constant circumburst medium ($k = 0$). The solid lines characterize the numerical simulations, while the dashed lines stand-in for the theoretical approximations, which are detailed in Appendix A. Lines in black color corresponds to quantities observed off-axis and in gray color the ones observed on-axis.

For the case of $\delta_D$, the upper left panel shows an excellent agreement between the simulations and the model at early times up to $t_{\rm obs} \approx 10^2$ s. After this point, there are very slight variations between both solutions, specifically in the steepness of the rise and fall of this quantity. The numerical simulation predicts a sharper peak, while the theoretical approximation anticipates a wider profile. Despite this slight difference, both curves drop in parallel, showing that their delinquent behavior follows the same power law. In the case of the half-opening angle $\theta_{\rm j}$ (lower left panel), as in the case of $\delta_D$, the early time evolution is the same between both curves. The difference in their behavior is first made apparent at $t_{\rm obs} \approx 10^2$ s. At this time, the theoretical solution presents a faster rise than the simulation. The initial variation between both curves keeps increasing and becomes substantial at times $\geq 10^6$ s.

The upper right panel compares the bulk Lorentz factors when the emission is off- and on-axis. For the off-axis case, the same features mentioned in the last two panels are repeated, namely perfect agreement at early times and variations at late times. However, the on-axis emission is different as there are slight differences initially, but both solutions tend to be the same as time progresses. Finally, the right panel on the bottom presents the shock's radius for the on- and off-axis cases. For the on-axis curves, the simulation and the theoretical approximation differ early, but they unite late. There is also a difference in their shapes at the beginning, as the theoretical curve is a straight line, which corresponds to a single power law. At the same time, the simulation shows that there is a transition from a flatter curve to a steeper one. The case of the off-axis emission presents similar differences. In general, the simulation and the theoretical variables exhibited in Figure 1 are in good agreement.

## 2.4. *Analysis and description of the synchrotron light curves*

The analytical synchrotron afterglow model during the coasting, deceleration (off- and on-axis emission), and the post-jet-break decay phases are shown in Appendix A. Table 1 shows the evolution of the synchrotron light curves, and Table 2 shows closure relations of synchrotron radiation as a function of $k$ during the coasting, deceleration (off- and on-axis emission), and the post-jet-break decay phases in the stratified environment. We can note in both tables that a break is expected around the transition time between fast- and slow-cooling regimes during the deceleration phase when the afterglow emission is seemed off-axis, but not during another phase.

Figures 2 and 3 show the predicted synchrotron light curves produced by the deceleration of the off-axis top-hat jet in the circumburst medium described by a density profile with k = 0, 1.0, 1.5 and 2.0, respectively. Panels from top to bottom correspond to radio wavelength at 6 GHz, optical at R-band and X-rays at 1 keV for typical values of GRB afterglow.[1] These figures display that regardless of the viewing angle, the X-ray, optical, and radio fluxes increase gradually, reach the maximum value, and finally, they begin to decrease. It can be observed that as the viewing angle increases, the maximum value moves to later times. For the chosen parameters, in most cases the maximum value lies in the range $(10^{-1} - 10^2)$ days for $0 \leq \theta_{\rm obs} \leq 60$ deg. This is different, however, when the medium is like a stellar wind, as the right column of Figure 3 shows that the maximum happens later, namely in the range $(10^{-1} - 10^4)$ days. Figures 2 and 3 show that the bump is less evident in the light curves with $1.0 \leq k \leq 2.0$. Then, a clear rebrightening in a timescale from days to weeks with GW detection could be associated with the deceleration of the off-axis jet launched by a BNS or BH-NS merger. The synchrotron fluxes in all these panels lie in the slow-cooling regime, although for a different set of parameters with values (for instance, the equivalent kinetic energy $E = 10^{54}$ erg, the uniform-density medium $n \approx 1$ cm$^{-3}$, the equipartition parameters $\varepsilon_{\rm e} = 0.1$ and $\varepsilon_{\rm B} = 10^{-4}$), these would

---

[1] $E = 10^{54}$ erg, $\varepsilon_{\rm B} = 10^{-4}$, $\varepsilon_{\rm e} = 10^{-1}$, $\zeta_e = 1.0$ and $d_z = 1$ Gpc. Henceforth, we adopt the convention $Q_{\rm x} = Q/10^{\rm x}$ in cgs units for all variables except angles. For angles, we adopt the convention $Q_{\rm x} = Q/{\rm x}$ in degrees.

lie in the fast-cooling regime.

Table 4 shows the evolution of the density parameter in each cooling condition of the synchrotron afterglow model. For instance, the synchrotron light curve as a function of the density parameter in the cooling condition $\nu_{a,1} < \nu_m < \nu < \nu_c$ is given by $F_\nu : \propto A_k^{\alpha_k}$, with $\alpha_k = \frac{p+5}{4}, \frac{11-p}{4}, \frac{2}{4-k}$ and $\frac{3-p}{4(3-k)}$, for the coasting, deceleration (off- and on-axis) and post-jet-break decay phases, respectively. Any transition between a stratified environment and density-constant medium could be detected during the post jet-break phase and the deceleration phase when the afterglow emission (for this cooling condition) is seemed on-axis but not off-axis. Table 4 shows that in general during the coasting phase and the deceleration phase when the afterglow emission is seemed off-axis cannot be detected a transition between different environments. Table 4 displays that synchrotron fluxes do not depend on the density parameter when these are observed at the lowest-energy ($\nu < \min\{\nu_{a,1}, \nu_{a,2}, \nu_{a,3}\}$) and the highest-energy ($\max\{\nu_m, \nu_c\} < \nu$) frequencies when the afterglow emission is seemed off- and on-axis, respectively. During the post jet-break phase, any transition between a stratified environment and density-constant medium will be better observed in low-energy frequencies, such as radio wavelengths.

The uniform medium with constant density is expected for sGRBs associated with binary compact objects, and the stratified medium with non-constant density is expected for lGRBs related to massive stars with different evolution at the end of their lives (Ramirez-Ruiz et al. 2005; van Marle et al. 2006). For instance, an external stratified medium with $0.4 \leq k \leq 1.4$ was found by Yi et al. (2013) after modeling the afterglow emission in a GRB example, and a density profile with $k > 2$ was reported by Kumar et al. (2008) after studying the accretion of the stellar envelope by a BH as the possible origin of the plateau phase in X-ray light curves.

Giblin et al. (1999) analyzed the prompt gamma-ray emission in the BATSE[2] detected burst GRB 980923. The light curve exhibited a main prompt episode lasting $\sim 32\,\mathrm{s}$ followed by a smooth emission tail that lasted $\sim 390\,\mathrm{s}$. The authors found that the spectrum in the smooth tail evolved as the synchrotron cooling break $t^{-0.52\pm0.12}$, concluding that the gamma-ray emission was associated with the afterglow evolution and also it had begun during the prompt gamma-ray episode. Afterward, spectra analyses of GRB tails were done to identify early afterglows (Barthelmy et al. 2005; Yamazaki et al. 2006). We could identify the off-axis synchrotron emission from an off-axis outflow analyzing the spectral break evolution. In this case, the spectral breaks of the synchrotron radiation generated from the deceleration of the off-axis jet in the relativistic phase evolve as a $\nu_m \propto t^{-\frac{6-k}{3}}$ and $\nu_c \propto t^{\frac{2+k}{2}}$, respectively. For instance, with $k = 1$ the characteristic and cooling breaks evolve as $\nu_m \propto t^{-\frac{5}{3}}$ and $\nu_c \propto t^{\frac{3}{2}}$, respectively, which fully different to those breaks that evolve when the afterglow emission is on-axis (e.g., $\nu_m \propto t^{-\frac{3}{2}}$ and $\nu_c \propto t^{-\frac{1}{6}}$).

## 3. A SAMPLE OF SOME BURSTS WITH EVIDENCE OF OFF-AXIS AFTERGLOW EMISSION

### 3.1. *Multi-wavelength Observations*

*GRB 080503* — On 2008 May 3 at 12:26:13 UTC the *Swift*-BAT instrument detected and triggered on the short burst GRB 080503 (Mao et al. 2008; Ukwatta et al. 2008). The prompt episode was evaluated in the $(15 - 150)$ keV energy range and reported with a duration of $(0.32 \pm 0.07)\,\mathrm{s}$, while its observed flux was measured to be $(1.2 \pm 0.2) \times 10^{-7}\,\mathrm{erg\,cm^{-2}\,s^{-1}}$. The *Swift* X-ray Telescope (XRT) instrument and Chandra ACIS-S satellite also performed subsequent observations in the X-ray band (Guidorzi & Mao 2008; Perley et al. 2009). For the case of *Swift*-XRT, it took data on the burst in the timeframe from $\sim 82$ s to 1 day after the initial *Swift*-BAT trigger. On the other hand, Chandra measured the burst throughout two observational campaigns, the first from 2008 May 07 (19:18:23 UTC) to 08 (04:09:59 UTC), during which an X-ray flux was detected, which coincided with the location of the optical afterglow. The second campaign took place from 2008 May 25 (18:11:36) to 26 (03:04:28), during which the X-ray source was monitored. There was a lack of detection, but constraining limits were provided. Several efforts were also taken to monitor this burst in the optical energy range. Observations and upper limits were obtained with the *Swift* Ultra-Violet Optical Telescope (UVOT) instrument (UVOT; Brown & Mao 2008), the Hubble Space Telescope (HST) using the Wide-Field Planetary Camera (WFPC2) in the F606W, F450W and F814W bands (Bloom et al. 2008; Perley et al. 2008f,b,c), and with the Keck-I telescope equipped with LRIS (Perley et al. 2008e). The Gemini-N observatory also observed the burst using the Multi-Object Spectrograph (GMNOS) through the g, r, i and z optical bands and NIRI through the Ks band (Perley et al. 2008a; Bloom & Perley 2008). Regarding the radio energy band, the Karl G. Jansky Very Large Array (VLA) was used to observe GRB 080503 at a frequency of 8.46 GHz without any detection but providing a 3-sigma upper limit (Frail & Chandra 2008).

*GRB 140903A* — The *Swift*-BAT detected GRB 140903A at 15:00:30 UT on 2014 September 14 (Cummings et al. 2014). This burst was located with coordinates R.A.= $238.036°$ and Dec = $+27.578°$ (J2000). The BAT light curve exhibited a peak with a duration of 0.45 s (Cummings 2014). The XRT instrument began observing the position of this burst 59 s after the BAT trigger and monitored the X-ray afterglow until this emission faded below the detector sensitivity threshold. The MAXI-GSC observed the position reported by BAT 12 s after the trigger. Although no object was detected, upper limits were derived at the $(4-10)$ keV energy range. The Chandra satellite began observing the X-ray afterglow $\sim 2.7$ s after the BAT trigger (Sakamoto et al. 2014). This burst was observed in the optical r-band $(20.4 \pm 0.5)$ mag by the 2-m telescope Faulkes Telescope North $\sim 15.6$ hours after the BAT trigger (Dichiara et al. 2014). The Nordic Optical Telescope (NOT) observed the field of this burst, reporting an optical emission of $(20.1 \pm 0.5)$ and $(16.1 \pm 0.3)$ mag in the $R$- and $H$-bands. Cucchiara et al. (2014) identified a strong absorption doublet feature of the wavelengths in the range of 795.4 and 796.5 nm (Cucchiara et al. 2014). These lines were associated to

---

[2] Burst and Transient Source Experiment

NaID in absorption and H-beta in emission at the usual redshift of $z = 0.351$. Later, the detection of optical variability, together with a coincident radio detection (Fong 2014), confirmed the host association of this redshift (Cenko et al. 2014).

*GRB 150101B* — The *Swift*-BAT and *Fermi*-GBM detected GRB 150101B at 15:23:35 and 15:24:34.468 UT on 2015 January 01, respectively (Cummings 2015; Stanbro 2015; Burns et al. 2018). Data analysis of *Swift*-BAT revealed a bright source, constraining the location at R.A.=188.044° and Dec: -10.956° (J2000). The $\gamma$-ray pulse in the $(15 - 150)$ keV band consisted of a single pulse with duration and fluence of $(0.012 \pm 0.001)$ s and $F_\gamma = (6.1 \pm 2.2) \times 10^{-8} \,\mathrm{erg\,cm^{-2}}$, respectively (Lien et al. 2016). Recently, Burns et al. (2018) presented a new analysis of fine timescales revealing a two-component structure; a short hard spike followed by a longer soft tail. The total duration of the prompt episode shown as a two-component structure was $0.08 \pm 0.93$ s and the fluence was $(1.2 \pm 0.1) \times 10^{-7} \,\mathrm{erg\,cm^{-2}}$ for the main peak and $(2.0 \pm 0.2) \times 10^{-8} \,\mathrm{erg\,cm^{-2}}$ for the soft tail. The Chandra X-ray Observatory ACIS-S reported two observations, 7.94 and 39.68 days after the BAT trigger, with durations of $\sim$ 4.1 hours each one (Fong et al. 2016). Optical/near IR observations and upper limits were collected with Magellan/Baade using IMACS with r, g, i and z optical bands, Very Large Telescope (VLT) equipped with the High Acuity Wide field K-band Imager I (HAWK-I) with the J, H, K and Y optical bands (Fong 2015; Levan et al. 2015), TNG using NICS with the J optical band (D'Avanzo et al. 2015), Gemini-S instrumented with GMOS (r band) (Fong et al. 2015), UKIRT with the instrument WFCAM (J and K bands) and HST using the WFC3 with the F160W and F606 W bands (Fong et al. 2016). Spectroscopic observations in the wavelength range $530 - 850\,\mathrm{nm}$ of 2MASX J12320498-1056010, revealed several prominent absorption features that could associate GRB 150101B to an early-type host galaxy located at $z = 0.1343 \pm 0.0030$ (Levan et al. 2015; Fong et al. 2016).

*GRB 160821B* — The *Swift*-BAT and *Fermi* Gamma-Ray Monitor (GBM) Instrument triggered and located GRB 160821B at 22:29:13 and 22:29:13.33 UT on 2016 August 21, respectively (Siegel et al. 2016; Stanbro & Meegan 2016). The *Swift*-BAT light curve in the energy range of $(15 - 150)$ keV exhibited a single peak with duration and total fluence of $(0.48 \pm 0.07)$ s and $(1.1 \pm 0.1) \times 10^{-7} \,\mathrm{erg\,cm^{-2}}$, respectively (Palmer et al. 2016). The *Fermi*-GBM light curve in the energy range of $(8 - 1000)$ keV showed a single peak (similar to the *Swift*-BAT profile) with duration and total fluence of $\sim$ 1.2 s and $(2.52 \pm 0.19) \times 10^{-6} \,\mathrm{erg\,cm^{-2}}$, respectively (Lü et al. 2017). They estimated that the isotropic energy released in gamma-rays was $E_{\mathrm{iso}} = (2.1 \pm 0.2) \times 10^{50}$ erg. *Swift*-XRT started detecting photons 57 s after the trigger time (Siegel et al. 2016). *Swift*-UVOT began observing the field of GRB 160821B 76 s after the *Swift*-BAT trigger. Although no photons in the optical band were detected during the first hours, constraining upper limits were placed (Evans et al. 2016). The William Herschel Telescope on La Palma, detected diverse emission lines in visible (including H-beta, [OIII] (4959/5007) and H-alpha), locating this burst with a redshift of $z = 0.16$ (Levan et al. 2016).

*SN 2020bvc* — On 2020 February 04 14:52:48 UTC SN 2020bvc was first detected by the ASAS-SN Brutus instrument using the g-Sloan filter with a reported location of R.A.=$14^{\mathrm{h}} : 33^{\mathrm{m}} : 57.024^{\mathrm{s}}$ and Dec=$+40° : 14' : 36.85''$ (J2000). It was associated to the host galaxy UGC 09379, with a redshift of $z = 0.025235$ (Stanek 2020). A later report confirmed this association and redshift and based on the blue featureless continuum and the absolute magnitude at the discovery of -18.1 classified this event as a young core-collapse supernova (Hiramatsu et al. 2020). A later analysis (Perley et al. 2020) of the spectrum obtained with the SPRAT spectrograph on the 2 m robotic Liverpool Telescope showed excellent agreement with the GRB-associated, broad-lined SN Ic 1998bw, thus it was categorized as a young broad-lined Ic SN. It was noticed to have an extremely fast rise by a steep decay in the two days following the first detection. It was later shown to rise towards a second peak. The decay temporal index reported by Izzo et al. (2020) was $\alpha_{\mathrm{dec}} = 1.35 \pm 0.9$. Twelve days later, on February 16, the Very Large Array (VLA) observed the position of SN 2020bvc and detected a point source with a flux density of 66 $\mu$Jy in the X-band and a luminosity of $1.3 \times 10^{27} \,\mathrm{erg\,s^{-1}\,Hz^{-1}}$ (Ho 2020). On the same day, a 10ks Chandra observation was obtained. The data was reduced, and the spectrum fitted with a power-law source model with a flux of approximately $10^{-14} \,\mathrm{erg\,cm^{-2}\,s^{-1}}$ (Ho et al. 2020a).

### 3.2. *Analysis and Discussion*

*GRB 080503* — We apply the Bayesian statistical approach of Markov-Chain Monte Carlo (MCMC) simulations to determine the best-fit values of the parameters that characterize the multi-wavelength afterglow observations with their upper limits (e.g., see Fraija et al. 2019c). A set of eight parameters, $\{E, n, p, \varepsilon_B, \Gamma, \varepsilon_e, \theta_{\mathrm{j}}$ and $\theta_{\mathrm{obs}}\}$, is required by our synchrotron afterglow model evolving in a constant-density medium to describe the multi-wavelength observations. A total of 17300 samples and 4100 tuning steps is used to describe the entire dataset. Normal distributions are used to characterize all the parameters. Corner plots illustrate the best-fit values and the median of the posterior distributions of the parameters, as shown in Figure 5, respectively. In this figure, the best-fit values are highlighted in green, and the median of the posterior distributions are presented in Table 5.

The multi-wavelength afterglow observations, together with the fits computed using the synchrotron off-axis model evolving in a constant-density medium are shown in Figure 4. The synchrotron light curves obtained with the same electron population and displayed in the optical (R and g) and X-ray bands support the scenario of one-emitting zone inside an off-axis outflow. The fact that the beaming cone of synchrotron radiation reaches our line of sight is compatible with the best-fit value of the viewing angle $\theta_{\mathrm{obs}} = 15.412^{+0.268}_{-0.269}$ deg and the re-brightening in all bands at $\sim$ one day. The best-fit value of the electron spectral index $p = 2.319^{+0.049}_{-0.049}$ matches the typical value observed when forward-shocked electrons radiate by synchrotron emission (see, e.g. Kumar & Zhang 2015). It confirms that these multi-wavelength observations originate during the afterglow.

The best-fit value of the constant-density medium $n = 4.221^{+0.102}_{-0.103} \times 10^{-2} \,\mathrm{cm^{-3}}$ indicates that GRB 080503 took place in a medium with very low density comparable to an intergalactic density environment with $\sim 10^{-3} \,\mathrm{cm^{-3}}$. The best-fit values

of bulk Lorentz factor ($\Gamma = 2.939^{+0.101}_{-0.078} \times 10^2$) and the equivalent-kinetic energy ($E = 2.156^{+0.294}_{-0.295} \times 10^{52}$ erg) indicate that synchrotron radiation is emitted from a narrowly collimated outflow.

Perley et al. (2009) analyzed the multi-wavelength observations at ∼ one day. The authors dismissed the kilonova-like emission proposed by Li & Paczyński (1998) and gave an afterglow explanation, pointing out that the X-ray and optical data had similar evolutions. They hypothesized that the late optical and X-ray bumps might be explained in a slightly off-axis jet or a refreshed shock. The faint afterglow compared to the intense prompt emission could be described in the very low circumburst medium. Gao et al. (2015) claimed that under certain requirements on the bulk Lorentz factor and the beaming angle of the relativistic jet, refreshed shocks in the synchrotron forward- and reverse-shock scenario could adequately describe the late re-brightening in GRB 080503. Finally, Gao et al. (2015) proposed that the late optical peak was due to the emission from a magnetar-powered "merger-nova", and the X-ray hump from magnetic dissipation of the magnetar dipole spin-down luminosity. According to our analysis, these observations at ∼ one day are consistent with the afterglow emission found off-axis. It is worth noting that measurements of the linear polarization of the optical emission could discriminate between an on- and off-axis scenario and gravitational waves would provide information about the progenitor (a merger of NS - NS, BH - NS or a stable NS).

*GRB 140903A* — We once again conducted MCMC simulations with a set of eight parameters, {$E$, $n$, $p$, $\varepsilon_B$, $\Gamma$, $\varepsilon_e$, $\theta_j$ and $\theta_{obs}$}, to find the best-fit values that describe the multi-wavelength afterglow observations with their upper limits. A set of eight parameters, {$E$, $n$, $p$, $\varepsilon_B$, $\Gamma$, $\varepsilon_e$, $\theta_j$ and $\theta_{obs}$}, is required. To represent the entire observations in this scenario, a total of 16200 samples and 4150 tuning steps were used. Figure 7 displays the best-fit values and the median of the posterior distributions of the parameters. In Table 5, the best-fit values are shown in green, and the median of the posterior distributions is presented.
The multi-wavelength observations of GRB 140903A are shown in Figure 6, together with the fits derived using the synchrotron off-axis model evolving in a homogenous density. The best-fit values of the viewing angle $\theta_{obs} = 5.162^{+0.271}_{-0.267}$ deg and the half-opening angle $\theta_j = 3.210^{+0.080}_{-0.081}$ deg indicate that the relativistic outflow was slightly off-axis. The best-fit value of the constant density medium $n = 4.219^{+0.102}_{-0.101} \times 10^{-2}$ cm$^{-3}$ indicates that GRB 140903A took place in a medium with very low density comparable to an intergalactic density environment. The best-fit values of bulk Lorentz factor ($\Gamma = 3.627^{+0.100}_{-0.100} \times 10^2$) and the equivalent-kinetic energies ($E = 3.163^{+0.290}_{-0.296} \times 10^{52}$ erg) indicate that synchrotron emission is radiated from a narrowly collimated jet. The best-fit values of the microphysical parameters $\varepsilon_e = 5.104^{+0.298}_{-0.302} \times 10^{-2}$ and $\varepsilon_B = 4.050^{+0.909}_{-0.921} \times 10^{-3}$, and the best-fit value of the spectral index of the shocked electrons $2.073^{+0.048}_{-0.050}$, are similar to those reported in Troja et al. (2016). This spectral index is in the typical range to those accelerated in forward shocks (see, e.g. Kumar & Zhang 2015), thus reaffirming the afterglow as its origin.

Troja et al. (2016) reported and analyzed the afterglow observations of GRB 140903A for the first two weeks. Applying the fireball scenario, the authors demonstrated that this burst was caused by a collimated jet seen off-axis and was also connected with a compact binary object. The X-ray "plateau" seen in GRB 140903A was attributed to the energy injection into the decelerating blast wave by Zhang et al. (2017). The authors then modelled the late afterglow emission, which required a half-opening angle of ≈ 3 deg, similar to the value found with our model. GRB 140903A was formed in a collimated outflow observed off-axis that decelerates in a uniform density, according to our findings.

*GRB 150101B* — We use MCMC simulations with the eight parameters used for GRB 080503 and GRB 140903A to find the best-fit values that model the X-ray afterglow observations with the optical upper limits. To represent the entire data in this case, a total of 15900 samples and 4400 tuning steps are used. Figure 9 displays the best-fit values and the median of the posterior distributions of the parameters. In Table 5, the best-fit values are shown in green, and the median of the posterior distributions is presented.

The X-ray, optical and radio observations and upper limits, as well as the fit obtained using the synchrotron off-axis model evolving in homogeneous density are shown in Figure 8. The left-hand panel shows the light curves at 1 keV (gray), R-band (blue), F606W filter (orange) and F160W filter (dark green), and the right-hand panel displays the broadband SEDs at 2 (red) and 9 (green) days. The red area corresponds to the spectrum of AT2017gfo, which is adapted by Troja et al. (2018). The best-fit values of the viewing angle $\theta_{obs} = 14.114^{+2.327}_{-2.179}$ deg and the half-opening angle $\theta_j = 6.887^{+0.662}_{-0.682}$ deg can explain the lack of X-ray emission during the first day. The best-fit value of the constant density medium $n = 0.164^{+0.021}_{-0.021} \times 10^{-2}$ cm$^{-3}$ indicates that GRB 150101B, like other short bursts, happened in an environment with very low density. The best-fit values of bulk Lorentz factor ($\Gamma = 4.251^{+0.468}_{-0.453} \times 10^2$) and the equivalent-kinetic energy ($E = 1.046^{+0.120}_{-0.124} \times 10^{52}$ erg) suggest that synchrotron afterglow emission is emitted from a narrowly collimated jet. The values of the spectral index of the electron population, the circumburst density, the microphysical parameters, and the viewing angle disfavor the isotropic cocoon model reported in Troja et al. (2018) and are consistent with the values of an outflow when homogeneous density is taken into account. The best-fit values of the spectral index of the shocked electrons $2.150^{+0.217}_{-0.215}$ is similar to those reported in synchrotron afterglow models (see, e.g. Kumar & Zhang 2015).

*GRB 160821B* — We require MCMC simulations with eight parameters used in the previous bursts to find the best-fit values that describe the multi-wavelength afterglow observations with their upper limits. To characterize the complete data in this scenario, a total of 17300 samples and 7400 tuning steps are used. Figure 11 exhibits the best-fit values and the median of the

posterior distributions of the parameters. In Table 5, the best-fit values and the medians of the posterior distributions are presented.

The multi-wavelength observations since 0.2 days after the GBM trigger are shown in Figure 10, together with the fits found requiring the synchrotron off-axis model evolving in a homogeneous density. The left-hand panel exhibits the light curves at 1 keV (gray), z-band (purple), F606W filter (dark red), R-band (salmon), F110W filter (cyan), F160W filter (blue sky), $K_s$-band (blue), X-channel (olive) and C-channel (emerald green), and the right-hand panel shows the broadband SEDs of the X-ray, optical and radio afterglow observations at 2 h (red), 2 days (blue) and 4 days (green). The shaded areas in blue and green correspond to blackbody spectra with decreasing temperatures firstly suggested in Jin et al. (2018) and then confirmed by Lamb et al. (2019) and Troja et al. (2019a). The kilonova emission is the most natural explanation for the "new" radiation component. The *Swift*-XRT-UVOT data were received from the public database from the official Swift website.[3] The C-band displays radio data, the white, v, b, u, UVW1, UVW2, and UVM2 bands display *Swift*-UVOT data, and the 1 keV band displays XRT data. Using the conversion factor proposed in Evans et al. (2010), the flux density of XRT data is extrapolated from 10 keV to 1 keV. The best-fit values of circumburst density $n = 0.869^{+0.093}_{-0.090} \times 10^{-2} \, \mathrm{cm}^{-3}$, spectral index of shocked electrons $p = 2.220^{+0.021}_{-0.021}$, viewing angle $\theta_{\mathrm{obs}} = 10.299^{+1.125}_{-1.135} \deg$ and the half-opening angle $\theta_{\mathrm{j}} = 8.002^{+0.817}_{-0.809} \deg$ are similar to those previously reported in Troja et al. (2019b). The best-fit values of the viewing angle $\theta_{\mathrm{obs}} = 10.299^{+1.125}_{-1.135} \deg$ and the half-opening angle $\theta_{\mathrm{j}} = 8.002^{+0.817}_{-0.809} \deg$ suggest that the relativistic outflow was slightly off-axis. The best-fit values of bulk Lorentz factor ($\Gamma = 4.559^{+0.361}_{-0.358} \times 10^2$) and the equivalent-kinetic energy ($E = 0.118^{+0.021}_{-0.021} \times 10^{52} \, \mathrm{erg}$) indicate that synchrotron afterglow emission is emitted from a narrowly collimated jet.

*SN 2020bvc* — We use MCMC simulations to find the best-fit values of the parameters that describe the X-ray afterglow observations. A set of eight parameters, $\{E, A_w, p, \varepsilon_B, \Gamma, \varepsilon_e, \theta_{\mathrm{j}} \text{ and } \theta_{\mathrm{obs}}\}$, is used to describe the X-ray observations. To characterize the complete data in this scenario, a total of 17100 samples and 7200 tuning steps are used. Figure 13 exhibits the best-fit values and the median of the posterior distributions of the parameters. In Table 5, the best-fit values are shown in green, and the medians of the posterior distributions are presented. We assumed a stratified medium with a parameter $k = 1.5$, consistent with the proposal by Izzo et al. (2020). Our best fit values, however, are slightly different. We propose that the emission is due to an off-axis jet that is $\approx 5$ times more energetic and with half of the off-axis angle compared to the values of Izzo et al. (2020). This discrepancy is due to a different choice of the electron velocity distribution index $p$, as our MCMC simulation suggested $p = 2.313^{+0.037}_{-0.035}$, in contrast with the value of $p = 2$ used by the cited authors. Figure 12 shows the X-ray observations of SN 2020bvc with the best-fit synchrotron light curve generated by the deceleration of an off-axis jet in a medium with stratification parameter $k = 1.5$.

Our results are consistent with the X-ray observations before and after $\sim 4 \, \mathrm{days}$ since the trigger time; when the observed flux increases and decreases, respectively. Initially, the flux increases with a minimum rise index of $\alpha_{\mathrm{m,ris}} > 1.65$ and later the observed flux decreases with $\alpha_{\mathrm{dec}} = -1.35 \pm 0.09$ (Izzo et al. 2020). The allowed value of the minimum rise index is estimated considering a simple power-law function, the X-ray upper limit and the maximum flux. For instance, given the best-fit value of $p = 2.313^{+0.037}_{-0.035}$ and for $0 < k < 1.5$, the temporal rise and decay indexes are $1.65 \pm 0.03 \le \alpha_{\mathrm{ris}} \le 4.53 \pm 0.03$ and $\alpha_{\mathrm{dec}} = -1.24 \pm 0.03$, respectively, for $\nu_c < \nu$ (see Table 1). For $k > 1.5$, the expected rise index would be $\alpha_{\mathrm{ris}} < 1.65$, which cannot reproduce the X-ray observations.

The synchrotron scenario from on-axis outflow in a very-low density environment is disfavored for $p \sim 2$. The closure relations of synchrotron on-axis model from an outflow decelerating in a stratified environment for $k$ in general can be estimated. During the coasting and the deceleration phases the bulk Lorentz factor evolves as $\Gamma \propto t^0$ and $\Gamma \propto t^{\frac{k-3}{8-2k}}$, respectively. Therefore, the synchrotron flux during the slow-cooling regime evolves as $F_\nu \propto t^{\frac{12-k(p+5)}{4}} \nu^{-\frac{p-1}{2}}$ for $\nu_m < \nu < \nu_c$ and $\propto t^{\frac{8-k(p+2)}{4}} \nu^{-\frac{p}{2}}$ for $\nu_c < \nu$ during the coasting phase, and $F_\nu \propto t^{-\frac{12(p-1)+k(5-3p)}{4(4-k)}} \nu^{-\frac{p-1}{2}}$ for $\nu_m < \nu < \nu_c$ and $\propto t^{-\frac{3p-2}{4}} \nu^{-\frac{p}{2}}$ for $\nu_c < \nu$, during the deceleration phase. It is worth noting that for the cooling condition $\nu_c < \nu$ and with a value of $p = 2.5$, the temporal evolution is only consistent for $k \lesssim 0.3$

The best-fit values of bulk Lorentz factor ($\Gamma = 2.291^{+0.100}_{-0.100} \times 10^2$), the equivalent-kinetic energy ($E = 2.38^{+0.01}_{-0.01} \times 10^{51} \, \mathrm{erg}$) and the half-opening angle $\theta_{\mathrm{j}} = 2.121^{+0.078}_{-0.079} \deg$ indicate that synchrotron emission is produced from a narrowly collimated outflow decelerating in an external medium. The best-fit values of the viewing angle $\theta_{\mathrm{obs}} = 12.498^{+0.268}_{-0.281} \deg$ and the half-opening angle $\theta_{\mathrm{j}} = 2.121^{+0.078}_{-0.079} \deg$ are consistent with the lack of early multi-wavelength observations.

Lü et al. (2012) discovered a correlation between the bulk Lorentz factors and the isotropic gamma-ray luminosities in a sample of GRBs. Fan et al. (2012) showed that the correlation of these parameters were consistent with the parameters predicted in the photospheric emission model. Figure 14 shows the diagram of the bulk Lorentz factors and the isotropic gamma-ray luminosities of sGRBs described in this work (red) with those (gray) reported in Lü et al. (2012). For off-axis sGRBs, we found an empirical correlation $\Gamma = a(L/10^{52} \, \mathrm{erg})^b$ with a $= (3.27 \pm 0.39) \times 10^2$ and b $= -(4.9 \pm 2.0) \times 10^{-2}$.

---

[3] https://swift.gsfc.nasa.gov/cgi-bin/sdc/ql?

## 4. CONSTRAINS ON POSSIBLE AFTERGLOW EMISSION

### 4.1. *The closest sGRBs detected by Swift ($100 \leq d_z \leq 200$ Mpc)*

*GRB 050906* — *Swift*-BAT was triggered by GRB 050906 at 10:32:18 UTC on September 5, 2005, with a reported location of R.A.=$03^h31^m13^s$ and Dec=$-14°37'30''$ (J2000) with a positional accuracy of $3'$(Krimm et al. 2005). The light curve revealed an excess in the $(25-100)$ keV energy range. The duration and measured fluence in the energy range of 15 - 150 keV were $128 \pm 16$ ms and $(5.9 \pm 3.2) \times 10^{-8}$ erg cm$^{-2}$, respectively (Parsons et al. 2005). Levan et al. (2008) provided the specifics of Swift's deep optical and infrared observations. According to the authors, no X-ray nor optical/IR afterglow was detected to deep limits, and no residual optical or IR emission was observed.

*GRB 070810B* — *Swift*-BAT was triggered by GRB 070810B at 15:19:17 UTC on August 10, 2007, with a reported location of R.A. = $00^h35^m46^s$ and Dec = $+08°50'07''$ (J2000) with a positional accuracy of $3'$(Marshall et al. 2007). The KANATA 1.5-m telescope, the Xinlong TNT 80 cm telescope, the 2-m Faulkes Telescope South, the Shajn 2.6 m telescope, and the Keck I telescope (HST) conducted follow-up observations after the initial detection, which are summarized in Bartos et al. (2019). From the whole observational campaign, only the Shajn telescope detected a source inside the error box of GRB 070810B (Rumyantsev et al. 2007).

*GRB 080121* — *Swift*-BAT was triggered by GRB 080121 at 21:29:55 UTC on January 21, 2008, with a reported location of R.A. = $09^h08^m56^s$, Dec = $+41°50'29''$ (J2000) and a positional accuracy of $3'$. In the $(15-150)$ keV energy range, the duration and measured fluence were $(0.7 \pm 0.2)$ s and $(3 \pm 2) \times 10^{-8}$ erg cm$^{-2}$ s$^{-1}$, respectively, according to Cummings & Palmer (2008). Follow-up observations were carried out 2.3 days following the burst using the *Swift*/UVOT and the *Swift*/XRT. Within the *Swift*-BAT error circle, however, no X-ray afterglow candidate or sources were discovered (Cucchiara & Schady 2008; Troja & Burrows 2008). Within the *Swift*-BAT error circle, two galaxies were found, indicating a redshift of $z \sim 0.046$ for GRB 080121, however the isotropic energy released would be several orders of magnitude lower than usual short-hard bursts (Perley et al. 2008d).

*GRB 100216A* — *Swift*-BAT and *Fermi*-GBM were triggered by GRB 100216A at 10:07:00 UTC on February 16, 2010 with a reported location of R.A. = $10^h17^m03.2^s$, Dec = $+35°31'27.5''$ (J2000) with a positional accuracy of $3'$. In the energy range of $(15-350)$ keV, the duration and measured fluence of the single peak were 0.3 s and $(4.7 \pm 3) \times 10^{-8}$ erg cm$^{-2}$, respectively (Cummings et al. 2010). The burst was followed up by *Swift*-XRT and *Swift*-UVOT from 214.4 to 249.2 ks after the BAT trigger. Within the observation, no fading sources were found, but a source presumed to be 1RXS J101702.9+353404 was discovered within the error circle (Rowlinson et al. 2010; Siegel & Rowlinson 2010).

Figure 15 shows the UV and optical upper limits of the closest sGRBs detected by Swift between 100 and 200 Mpc with the synchrotron light curves from an off-axis outflow decelerating in a constant-density medium. The synchrotron light curves are exhibited at the R-band (black) and the UVW1-band (gray). The parameter values used to generate the synchrotron light curves are reported in Table 6. We report two values for each parameter; the upper values correspond to synchrotron light curves on the left-hand panels and lower ones on the right panels. For typical values of GRB afterglow reported in Table 6, the synchrotron emission is ruled out for a density of $n = 1$ cm$^{-3}$, but not for $n = 10^{-2}$ cm$^{-3}$. The value of the uniform-density medium ruled out in our model is consistent with the mean value reported for sGRBs (e.g., see Berger 2014). It is worth noting that for values of $\varepsilon_B < 10^{-4.3}$ and $\varepsilon_e < 10^{-1.2}$, the value of the density $n = 1$ cm$^{-3}$ would be allowed.

### 4.2. *Promising GW events in the third observing run (O3) that could generate electromagnetic emission*

The Advanced LIGO and Advanced Virgo produced 56 non-retracted alerts of gravitational waves candidates during the O3 run, covering almost one year of operations (from 2019 April 01 to 2020 March 27). Nevertheless, three of them have a probability of being terrestrial larger than 50%. The O3 observing run was divided into two epochs associated to "O3a" (from April 01 to September 30) and "O3b" (from November 01 to March 27, 2020). The GW events in the O3a and O3b runs are listed in the Gravitational Wave Transient (GWTC-2) Catalog 2 (Abbott et al. 2021) and (GWTC-3) Catalog 3 (The LIGO Scientific Collaboration et al. 2021), respectively, where from GCNs there were 31 and 22 candidate events discovered during O3a and O3b respectively. The promising candidates that are consistent with a source with $m_2 < 3M_\odot$ and that could generate electromagnetic emission are GW190425, GW190426_152155, GW190814 in GWTC-2 (Abbott et al. 2021) and GW191219_163120, GW200105_162426, GW200115_042309, GW200210_092254 in GWTC-3 (The LIGO Scientific Collaboration et al. 2021). Table 7 enumerates the main characteristics of these candidates.

Figure 16 shows the multi-wavelength upper limits of GW events in GWTC-2 and GWTC-3 consistent with a source with $m_2 < 3M_\odot$ and that could generate electromagnetic emission and the synchrotron light curves from an off-axis outflow decelerating in a constant-density medium with $n = 1$ cm$^{-3}$ (left panels) and $10^{-2}$ cm$^{-3}$ (right panels). The synchrotron light curves are presented at 1 keV (green), R-band (brown) (from Becerra et al. (2021a)) and 3 GHz (red). The parameter values used are $E = 5 \times 10^{50}$ erg, $\theta_j = 3$ deg, $\theta_{obs} = 6$ deg, $\Gamma = 100$, $\varepsilon_e = 0.1$, $p = 2.5$, $\zeta_e = 1.0$ and $\varepsilon_B = 10^{-2}$. The left-hand panels associated to the S190425z, S190426c, S190814bv and S200115j events show that a uniform-density is ruled out for $n = 1$ cm$^{-3}$, but not for $n = 10^{-2}$ cm$^{-3}$. For instance, we can note that in the panel related to S190426c the synchrotron emission at 1 keV, at the R-band and at 3 GHz is above the upper limits around $\sim$ one day for $n = 1$ cm$^{-3}$, and in the panel associated to S190814bv the synchrotron flux at the R-band and 3 GHz is above the upper limits, but not at 1 keV. The value of the constant-density

medium ruled out in our model is consistent with the densities derived by Dobie et al. (2019); Ackley et al. (2020); Gomez et al. (2019) using distinct off-axis jet models. We need further observations on different timescales and energy bands to derive tighter constraints.

## 5. CONCLUSIONS

We have extended the synchrotron off-axis model presented in Fraija et al. (2019b) initially proposed to describe the multi-wavelength afterglow observations in GRB 170817A. In the current model, we have considered i) the circumburst external medium as stratified with a profile density $\propto r^{-k}$ with k in the range of $0 \leq k \leq 3$, ii) the synchrotron radiation in self-absorption regime, iii) the afterglow emission during the transition from off-axis to on-axis before the lateral expansion phase (relativistic phase), iv) the hydrodynamical evolution computed by numerical simulations and v) a fraction of electrons accelerated by the shock front. The time evolution of the Doppler factor, the half-opening angle, the bulk Lorentz factor, and the deceleration radius computed by numerical simulations are in good agreement with those derived with an analytical approach. The advantage of this general approach (with a density profile $A_k \propto r^{-k}$) is that this model allows us to take into account not only both a homogeneous medium ($k = 0$) and a wind-like medium ($k = 2$) but regions with non-standard stratification parameters, such as $k = 1.0, 1.5$ or $2.5$.

We have calculated the synchrotron light curves and presented the closure relations in a stratified environment, including the self-absorption regime for all cooling conditions during the coasting, deceleration (off- and on-axis emission), and the post-jet-break decay phases. We have noted that a break is expected around the transition between fast- and slow-cooling regimes during the deceleration phase when the afterglow emission seems off-axis, but not during other stages. We have analyzed the behavior of the flux for different parameters of the density distribution. We have noticed that the behavior during the relativistic phase approaches flatness as the stratification parameter is raised. On the other hand, we have shown that the time evolution of the light curves after the jet break is independent of $k$, so this model gives freedom to explain the early-time evolution of the radiation while keeping the long-time results invariant. Furthermore, we have derived the change of the density parameter in the entire phase. We have shown that: In general, during the coasting and the deceleration phases, when the afterglow emission seems off-axis, a transition between different environments cannot be detected, contrary to the post-jet-break phase and the deceleration phase with on-axis emission. The synchrotron fluxes do not depend on the density parameter when these are observed at the lowest and the highest frequencies when the afterglow emission seems off- and on-axis, respectively. During the post-jet-break phase, any transition between a stratified environment and density-constant medium will be better observed in low frequencies, such as radio wavelengths.

In particular, we have applied our model to describe the delayed non-thermal emission observed in a sample of bursts with evidence of off-axis emission. In accordance with the best-fit values for sGRBs, we found that i) the constant-density medium required to model the multi-wavelength observations is low ($10^{-2} \leq n \leq 0.4 \, \mathrm{cm}^{-3}$), indicating that the central engine are located in a low density circumstellar medium, ii) the spectral indexes of the shocked electrons ($2.1 \leq p \leq 2.3$) are in the range of those reported after the description of the afterglow observations (see, e.g. Kumar & Zhang 2015; Fraija et al. 2017; Becerra et al. 2019a,b,c, 2021b), and iii) the half-opening angles ($1.5 \leq \theta_\mathrm{j} \leq 6.6 \deg$), the bulk Lorentz factors ($130 \leq \Gamma \leq 450$) and the equivalent-kinetic energies ($0.2 \leq E \leq 5.7 \times 10^{52} \, \mathrm{erg}$) provide evidence of narrowly collimated outflow expanding into a constant-density environment. The previous results confirm that the multi-wavelength observations are emitted from the GRB afterglow and indicate a merger of compact objects (two NSs or NS-BH) as possible progenitors of these bursts. The low-density medium agrees with the larger offsets of sGRBs compared with lGRBs. Regarding SN 2020bvc, we found that an atypical stratification parameter of $k = 1.5$ is required, supporting the CC-SN scenario. The best-fit values of the half-opening angle $2.121^{+0.078}_{-0.079} \deg$, the viewing angle $12.498^{+0.268}_{-0.281} \deg$, the equivalent-kinetic energy $2.38^{+0.11}_{-0.10} \times 10^{51} \, \mathrm{erg}$ and the bulk-Lorentz factor $2.291^{+0.100}_{-0.100} \times 10^2$ provide evidence of the scenario of off-axis GRB afterglow.

We have applied the current model to provide constraints on the possible afterglow emission using multi-wavelength upper limits associated with the closest Swift-detected sGRBs ($< 200 \, \mathrm{Mpc}$) and the promising GW events. We have shown that the value of the constant-density medium is ruled out, which is consistent with the mean value of densities reported in for sGRBs (e.g., see Berger 2014) and those derived by S190814bv event (e.g., see Dobie et al. 2019; Ackley et al. 2020; Gomez et al. 2019) using different models. To derive tighter constraints, further observations on timescales from months to years post-merger phase are required.

## REFERENCES

Abbott, B. P., Abbott, R., Abbott, T. D., & et al. 2017a, Phys. Rev. Lett., 119, 161101

—. 2017b, The Astrophysical Journal Letters, 848, L12

Abbott, B. P., Abbott, R., Abbott, T. D., et al. 2017, ApJ, 848, L13

Abbott, R., Abbott, T. D., Abraham, S., et al. 2021, Physical Review X, 11, 021053

Ackley, K., Amati, L., Barbieri, C., et al. 2020, arXiv e-prints, arXiv:2002.01950

Alexander, K. D., Berger, E., Fong, W., et al. 2017, ApJ, 848, L21

Alexander, K. D., Margutti, R., Blanchard, P. K., et al. 2018, ArXiv e-prints, arXiv:1805.02870

Andreoni, I., Goldstein, D. A., Kasliwal, M. M., et al. 2020, ApJ, 890, 131

Barthelmy, S. D., Cannizzo, J. K., Gehrels, N., et al. 2005, ApJ, 635, L133

Bartos, I., Lee, K. H., Corsi, A., Márka, Z., & Márka, S. 2019, MNRAS, 485, 4150

Becerra, R. L., De Colle, F., Watson, A. M., et al. 2019a, ApJ, 887, 254

Becerra, R. L., Watson, A. M., Fraija, N., et al. 2019b, ApJ, 872, 118

Becerra, R. L., Dichiara, S., Watson, A. M., et al. 2019c, ApJ, 881, 12

—. 2021a, MNRAS, 507, 1401

Becerra, R. L., De Colle, F., Cantó, J., et al. 2021b, ApJ, 908, 39

Berger, E. 2014, ARA&A, 52, 43

Blandford, R. D., & McKee, C. F. 1976, Physics of Fluids, 19, 1130

Blondin, J. M., Lundqvist, P., & Chevalier, R. A. 1996, ApJ, 472, 257

Bloom, J. S., & Perley, D. A. 2008, GRB Coordinates Network, 7667

Bloom, J. S., Kulkarni, S. R., Djorgovski, S. G., et al. 1999, Nature, 401, 453

Bloom, J. S., Li, W., Levan, A. J., et al. 2008, GRB Coordinates Network, 7703

Bochenek, C. 2019a, LIGO/Virgo S190425z: STARE2 simultaneous L-band radio observations, The Gamma-ray Coordinates Network

—. 2019b, LIGO/Virgo S190426c: STARE2 simultaneous L-band radio observations, The Gamma-ray Coordinates Network

Brown, P. J., & Mao, J. 2008, GRB Coordinates Network, 7675

Burns, E., Veres, P., Connaughton, V., et al. 2018, ApJ, 863, L34

Cenko, S. B., Capone, J., Toy, V., et al. 2014, GRB Coordinates Network, Circular Service, No. 16785, #1 (2014), 16785

Chevalier, R. A. 1982, ApJ, 258, 790

—. 1984, ApJ, 285, L63

Corsi, A. 2019, LIGO/Virgo S190426c: VLA Follow-Up Observations of ZTF19aassfws, The Gamma-ray Coordinates Network

Coulter, D. A., Foley, R. J., Kilpatrick, C. D., et al. 2017, Science, 358, 1556

Cucchiara, A., Cenko, S. B., Perley, D. A., Capone, J., & Toy, V. 2014, GRB Coordinates Network, Circular Service, No. 16774, #1 (2014), 16774

Cucchiara, A., & Schady, P. 2008, GRB Coordinates Network, 7217

Cummings, J. R. 2014, GRB Coordinates Network, Circular Service, No. 16765, #1 (2014), 16765

—. 2015, GRB Coordinates Network, Circular Service, No. 17267, #1 (2015), 17267

Cummings, J. R., Barthelmy, S. D., Fox, D. B., et al. 2010, GRB Coordinates Network, 10428

Cummings, J. R., Burrows, D. N., Evans, P. A., et al. 2014, GRB Coordinates Network, Circular Service, No. 16763, #1 (2014), 16763

Cummings, J. R., & Palmer, M. 2008, GRB Coordinates Network, 7209

D'Avanzo, P., D'Elia, V., Lorenzi, V., et al. 2015, GRB Coordinates Network, Circular Service, No. 17326, #1 (2015), 17326

D'Avanzo, P., Campana, S., Salafia, O. S., et al. 2018, ArXiv e-prints, arXiv:1801.06164

Dichiara, S., Guidorzi, C., & Japelj, J. 2014, GRB Coordinates Network, Circular Service, No. 16781, #1 (2014), 16781

Dichiara, S., Troja, E., O'Connor, B., et al. 2020, MNRAS, 492, 5011

Dobie, D., Stewart, A., Murphy, T., et al. 2019, ApJ, 887, L13

Dobie, D., Kaplan, D. L., Murphy, T., et al. 2018, ApJ, 858, L15

Duncan, R. C., & Thompson, C. 1992, ApJ, 392, L9

Evans, P. A., Goad, M. R., Osborne, J. P., & Beardmore, A. P. 2016, GRB Coordinates Network, 19837, 1

Evans, P. A., Willingale, R., Osborne, J. P., et al. 2010, A&A, 519, A102

Fan, Y., & Piran, T. 2006, MNRAS, 369, 197

Fan, Y.-Z., Wei, D.-M., Zhang, F.-W., & Zhang, B.-B. 2012, The Astrophysical Journal, 755, L6

Fong, W. 2014, GRB Coordinates Network, Circular Service, No. 16777, #1 (2014), 16777

—. 2015, GRB Coordinates Network, Circular Service, No. 17288, #1 (2015), 17288

Fong, W., Berger, E., Fox, D., & Shappee, B. J. 2015, GRB Coordinates Network, Circular Service, No. 17333, #1 (2015), 17333

Fong, W., Margutti, R., Chornock, R., et al. 2016, ApJ, 833, 151

Fraija, N. 2015, ApJ, 804, 105

Fraija, N., De Colle, F., Veres, P., et al. 2019a, ApJ, 871, 123

Fraija, N., Lee, W. H., Araya, M., et al. 2017, ApJ, 848, 94

Fraija, N., Lopez-Camara, D., Pedreira, A. C. C. d. E. S., et al. 2019b, ApJ, 884, 71

Fraija, N., Pedreira, A. C. C. d. E. S., & Veres, P. 2019c, ApJ, 871, 200

Frail, D. A., & Chandra, P. 2008, GRB Coordinates Network, 7684

Galama, T. J., Vreeswijk, P. M., van Paradijs, J., et al. 1998, Nature, 395, 670

Gao, H., Ding, X., Wu, X.-F., Dai, Z.-G., & Zhang, B. 2015, ApJ, 807, 163

Giblin, T. W., van Paradijs, J., Kouveliotou, C., et al. 1999, ApJ, 524, L47

Gomez, S., Hosseinzadeh, G., Cowperthwaite, P. S., et al. 2019, ApJ, 884, L55

Granot, J., Gill, R., Guetta, D., & De Colle, F. 2017, ArXiv e-prints, arXiv:1710.06421

Granot, J., Panaitescu, A., Kumar, P., & Woosley, S. E. 2002, ApJ, 570, L61

Guidorzi, C., & Mao, J. 2008, GRB Coordinates Network, 7674

Haggard, D., Nynka, M., Ruan, J. J., Evans, P., & Kalogera, V. 2018, The Astronomer's Telegram, 11242

Hiramatsu, D., Arcavi, I., Burke, J., et al. 2020, Transient Name Server Classification Report, No. 2020-403, 1

Ho, A. Y. Q. 2020, Transient Name Server AstroNote 2020-42, 1

Ho, A. Y. Q., Cenko, B., Perley, D., Corsi, A., & Brightman, M. 2020a, Transient Name Server AstroNote 2020-45, 1

Ho, A. Y. Q., Kulkarni, S. R., Perley, D. A., et al. 2020b, ApJ, 902, 86

Hotokezaka, K., Kiuchi, K., Shibata, M., Nakar, E., & Piran, T. 2018, ApJ, 867, 95

Huang, Y. F., Dai, Z. G., & Lu, T. 1999, MNRAS, 309, 513

—. 2000, MNRAS, 316, 943

Ioka, K., & Nakamura, T. 2017, ArXiv e-prints, arXiv:1710.05905

Izzo, L., Auchettl, K., Hjorth, J., et al. 2020, A&A, 639, L11

Jin, Z.-P., Li, X., Wang, H., et al. 2018, ApJ, 857, 128

Kasliwal, M. M., Nakar, E., Singer, L. P., et al. 2017, Science, 358, 1559

Kotak, R., Meikle, W. P. S., Adamson, A., & Leggett, S. K. 2004, MNRAS, 354, L13

Kouveliotou, C., Meegan, C. A., Fishman, G. J., et al. 1993, The Astrophysical Journal, 413, L101

Krimm, H., La Parola, V., de Pasquale, M., et al. 2005, GRB Coordinates Network, 3926, 1

Kumar, P., Narayan, R., & Johnson, J. L. 2008, Science, 321, 376

Kumar, P., & Zhang, B. 2015, Phys. Rep., 561, 1

Lamb, G. P., Tanvir, N. R., Levan, A. J., et al. 2019, ApJ, 883, 48

Lazzati, D., Perna, R., Morsony, B. J., et al. 2017, ArXiv e-prints, arXiv:1712.03237

Levan, A. J., Hjorth, J., Wiersema, K., & Tanvir, N. R. 2015, GRB Coordinates Network, Circular Service, No. 17281, #1 (2015), 17281

Levan, A. J., Wiersema, K., Tanvir, N. R., et al. 2016, GRB Coordinates Network, 19846, 1

Levan, A. J., Tanvir, N. R., Jakobsson, P., et al. 2008, MNRAS, 384, 541

Li, L.-X., & Paczyński, B. 1998, ApJ, 507, L59

Lien, A. 2020, LIGO/Virgo S200115j: no counterpart candidates in the Swift/BAT observations, The Gamma-ray Coordinates Network

Lien, A., Sakamoto, T., Barthelmy, S. D., et al. 2016, ApJ, 829, 7

LIGO Scientific Collaboration, & Virgo Collaboration. 2019, GRB Coordinates Network, 25324, 1

Lü, H.-J., Zhang, H.-M., Zhong, S.-Q., et al. 2017, ApJ, 835, 181

Lü, J., Zou, Y.-C., Lei, W.-H., et al. 2012, The Astrophysical Journal, 751, 49

Lyman, J. D., Lamb, G. P., Levan, A. J., et al. 2018, ArXiv e-prints, arXiv:1801.02669

Mao, J., Guidorzi, C., Ukwatta, T., et al. 2008, GCN Report, 138, 1

Margutti, R., Fong, W., Eftekhari, T., et al. 2017a, The Astronomer's Telegram, 11037

Margutti, R., Berger, E., Fong, W., et al. 2017b, ApJ, 848, L20

Margutti, R., Alexander, K. D., Xie, X., et al. 2018, ArXiv e-prints, arXiv:1801.03531

Marshall, F. E., Brown, P. J., Cummings, J. R., et al. 2007, GRB Coordinates Network, 6743, 1

Metzger, B. D., Giannios, D., Thompson, T. A., Bucciantini, N., & Quataert, E. 2011, MNRAS, 413, 2031

Mooley, K. P., Nakar, E., Hotokezaka, K., et al. 2017, ArXiv e-prints, arXiv:1711.11573

Moriya, T. J., & Tominaga, N. 2012, ApJ, 747, 118

Nakar, E., & Piran, T. 2018, ArXiv e-prints, arXiv:1801.09712

Narayan, R., Paczynski, B., & Piran, T. 1992, ApJ, 395, L83

Palmer, D. M., Barthelmy, S. D., Cummings, J. R., et al. 2016, GRB Coordinates Network, 19844, 1

Panaitescu, A., & Mészáros, P. 1998, ApJ, 501, 772

Parsons, A., Sarazin, C., Barbier, L., et al. 2005, GRB Coordinates Network, 3935, 1

Perley, D., Schulze, S., & Bruch, R. 2020, Transient Name Server AstroNote 2020-37, 1

Perley, D. A., Bloom, J. S., & Li, W. 2008a, GRB Coordinates Network, 7695

Perley, D. A., Bloom, J. S., & Prochaska, J. X. 2008b, GRB Coordinates Network, 7678

—. 2008c, GRB Coordinates Network, 7679

Perley, D. A., Foley, R. J., & Bloom, J. S. 2008d, GRB Coordinates Network, 7210

Perley, D. A., Lai, D., Rockosi, C., & Bloom, J. S. 2008e, GRB Coordinates Network, 7666

Perley, D. A., Bloom, J. S., Levan, A. J., et al. 2008f, GRB Coordinates Network, 7749

Perley, D. A., Metzger, B. D., Granot, J., et al. 2009, ApJ, 696, 1871

Planck Collaboration, Ade, P. A. R., Aghanim, N., et al. 2016, A&A, 594, A13

Ramirez-Ruiz, E., Garcia-Segura, G., Salmonson, J. D., & Perez-Rendon, B. 2005, ApJ, 631, 435

Rhoads, J. E. 1999, ApJ, 525, 737

Rhodes, L. 2019, LIGO/Virgo S190426c: AMI-LA radio observations of ZTF19aassfws, The Gamma-ray Coordinates Network

Ridnaia, A. 2020a, LIGO/Virgo S200105ae: Upper limits from Konus-Wind observations, The Gamma-ray Coordinates Network

—. 2020b, LIGO/Virgo S200115j: Upper limits from Konus-Wind observations, The Gamma-ray Coordinates Network

Rowlinson, A., Page, K., & Lyons, N. 2010, GRB Coordinates Network, 10435

Rumyantsev, V., Biryukov, V., & Pozanenko, A. 2007, GRB Coordinates Network, 6762, 1

Sakamoto, T., Troja, E., Gehrels, N., et al. 2014, GRB Coordinates Network, Circular Service, No. 16813, #1 (2014), 16813

Sari, R., & Esin, A. A. 2001, ApJ, 548, 787

Sari, R., & Piran, T. 1999, A&AS, 138, 537

Sari, R., Piran, T., & Halpern, J. P. 1999, ApJ, 519, L17

Sari, R., Piran, T., & Narayan, R. 1998, ApJ, 497, L17

Savchenko, V., Ferrigno, C., Kuulkers, E., et al. 2017, ApJ, 848, L15

Siegel, M. 2019, LIGO/Virgo S190425z: Transient found in Swift/UVOT counterpart search, The Gamma-ray Coordinates Network

Siegel, M. H., Barthelmy, S. D., Burrows, D. N., et al. 2016, GRB Coordinates Network, 19833, 1

Siegel, M. H., & Rowlinson, A. 2010, GRB Coordinates Network, 10442

Soderberg, A. M., Chevalier, R. A., Kulkarni, S. R., & Frail, D. A. 2006, ApJ, 651, 1005

Stanbro, M. 2015, GRB Coordinates Network, Circular Service, No. 17295, #1 (2015), 17295

Stanbro, M., & Meegan, C. 2016, GRB Coordinates Network, 19843, 1

Stanek, K. 2020, Transient Name Server Discovery Report, No. 2020-381, 1

The LIGO Scientific Collaboration, the Virgo Collaboration, the KAGRA Collaboration, et al. 2021, arXiv e-prints, arXiv:2111.03606

Thompson, C. 1994, MNRAS, 270, 480

Tohuvavohu, A. 2019a, LIGO/Virgo S190425z: Swift/UVOT and XRT pre-images at the position of the potential Swift/UVOT counterpart, The Gamma-ray Coordinates Network

—. 2019b, LIGO/Virgo S190426c: Swift rapid follow-up observations of S190425z and S190426c and URL for observation log for all future events, The Gamma-ray Coordinates Network

Troja, E., & Burrows, D. N. 2008, GRB Coordinates Network, 7224

Troja, E., Lipunov, V. M., Mundell, C. G., & et al. 2017, Nature, 547, 425

Troja, E., Piro, L., van Eerten, H., & et al. 2017, Nature, 000, 1

Troja, E., Sakamoto, T., Cenko, S. B., et al. 2016, ApJ, 827, 102

Troja, E., Ryan, G., Piro, L., et al. 2018, Nature Communications, 9, 4089

Troja, E., Castro-Tirado, A. J., Becerra González, J., et al. 2019a, MNRAS, 489, 2104

Troja, E., Castro-Tirado, A. J., Gonzalez, J. B., et al. 2019b, arXiv e-prints, arXiv:1905.01290

Ukwatta, T., Stamatikos, M., Sakamoto, T., Norris, J., & Barthelmy, S. D. 2008, GRB Coordinates Network, 7677

Usov, V. V. 1992, Nature, 357, 472

van Marle, A. J., Langer, N., Achterberg, A., & Garcia-Segura, G. 2006, A&AS, 460, 105

Vieira, N., Ruan, J. J., Haggard, D., et al. 2020, arXiv e-prints, arXiv:2003.09437

von Kienlin, A., Meegan, C., & Goldstein, A. 2017, GRB Coordinates Network, Circular Service, No. 21520, #1 (2017), 21520

Wang, X.-Y., He, H.-N., Li, Z., Wu, X.-F., & Dai, Z.-G. 2010, ApJ, 712, 1232

Watson, A. M., Butler, N. R., Lee, W. H., et al. 2020, MNRAS, 492, 5916

Waxman, E. 1997, ApJ, 491, L19

Weinberg, S. 1972, Gravitation and Cosmology

Woosley, S. E. 1993, ApJ, 405, 273

Woosley, S. E., & Bloom, J. S. 2006, ARA&A, 44, 507

Yamazaki, R., Toma, K., Ioka, K., & Nakamura, T. 2006, MNRAS, 369, 311

Yi, S. X., Wu, X. F., & Dai, Z. G. 2013, ApJ, 776, 120

Zhang, S., Jin, Z.-P., Wang, Y.-Z., & Wei, D.-M. 2017, ApJ, 835, 73

TABLE 1
EVOLUTION OF THE SYNCHROTRON LIGHT CURVES ($F_\nu \propto t^{-\alpha}\nu^{-\beta}$) FROM AN OFF-AXIS OUTFLOW DECELERATED IN A STRATIFIED ENVIRONMENT

| | | Coasting phase | Deceleration phase (off-axis afterglow) | Deceleration phase (on-axis afterglow) | Post jet-break phase |
|---|---|---|---|---|---|
| | $\beta$ | $\alpha$ | $\alpha$ | $\alpha$ | $\alpha$ |
| $\nu_{a,3} < \nu_c < \nu_m$ | | | | | |
| $\nu < \nu_{a,3}$ | $-2$ | $-(1+k)$ | $-4$ | $-\frac{4}{4-k}$ | $-1$ |
| $\nu_{a,3} < \nu < \nu_c$ | $-\frac{1}{3}$ | $\frac{6k-11}{3}$ | $\frac{8k-17}{3}$ | $\frac{3k-2}{3(4-k)}$ | $1$ |
| $\nu_c < \nu < \nu_m$ | $\frac{1}{2}$ | $\frac{3k-8}{4}$ | $\frac{9k-26}{4}$ | $\frac{1}{4}$ | $1$ |
| $\nu_m < \nu$ | $\frac{p}{2}$ | $\frac{k(p+2)-8}{4}$ | $\frac{6(p-5)-(p-11)k}{4}$ | $\frac{3p-2}{4}$ | $p$ |
| $\nu_{a,1} < \nu_m < \nu_c$ | | | | | |
| $\nu < \nu_{a,1}$ | $-2$ | $-2$ | $-2$ | $-\frac{2}{4-k}$ | $0$ |
| $\nu_{a,1} < \nu < \nu_m$ | $-\frac{1}{3}$ | $\frac{4k-9}{3}$ | $\frac{8k-21}{3}$ | $\frac{k-2}{4-k}$ | $\frac{1}{3}$ |
| $\nu_m < \nu < \nu_c$ | $\frac{p-1}{2}$ | $\frac{k(p+5)-12}{4}$ | $\frac{6(p-5)-(p-11)k}{4}$ | $-\frac{12(1-p)+k(3p-5)}{4(4-k)}$ | $p$ |
| $\nu_c < \nu$ | $\frac{p}{2}$ | $\frac{k(p+2)-8}{4}$ | $\frac{2(3p-16)-(p-10)k}{4}$ | $\frac{3p-2}{4}$ | $p$ |
| $\nu_m < \nu_{a,2} < \nu_c$ | | | | | |
| $\nu < \nu_m$ | $-2$ | $-2$ | $-2$ | $-\frac{2}{4-k}$ | $0$ |
| $\nu_m < \nu < \nu_{a,2}$ | $-\frac{5}{2}$ | $-\frac{8+k}{4}$ | $\frac{k-14}{4}$ | $\frac{3k-20}{4(4-k)}$ | $-1$ |
| $\nu_{a,2} < \nu < \nu_c$ | $\frac{p-1}{2}$ | $\frac{k(p+5)-12}{4}$ | $\frac{6(p-5)-(p-11)k}{4}$ | $-\frac{12(1-p)+k(3p-5)}{4(4-k)}$ | $p$ |
| $\nu_c < \nu$ | $\frac{p}{2}$ | $\frac{k(p+2)-8}{4}$ | $\frac{2(3p-16)-(p-10)k}{4}$ | $\frac{3p-2}{4}$ | $p$ |

TABLE 2
CLOSURE RELATIONS OF SYNCHROTRON RADIATION FROM OFF-AXIS AFTERGLOW MODEL IN A STRATIFIED ENVIRONMENT

| | | Coasting phase | Deceleration phase (off-axis afterglow) | Deceleration phase (on-axis afterglow) | Post jet-break phase |
|---|---|---|---|---|---|
| $\nu_{a,3} < \nu_c < \nu_m$ | | | | | |
| $\nu < \nu_{a,3}$ | $-2$ | $\frac{(k+1)\beta}{2}$ | $2\beta$ | $\frac{2\beta}{4-k}$ | $\frac{\beta}{2}$ |
| $\nu_{a,3} < \nu < \nu_c$ | $-\frac{1}{3}$ | $(11-6k)\beta$ | $(17-8k)\beta$ | $\frac{(2-3k)\beta}{4-k}$ | $-3\beta$ |
| $\nu_c < \nu < \nu_m$ | $\frac{1}{2}$ | $\frac{(3k-8)\beta}{2}$ | $\frac{(9k-26)\beta}{2}$ | $-\frac{\beta}{2}$ | $2\beta$ |
| $\nu_m < \nu$ | $\frac{p}{2}$ | $\frac{(\beta+1)k-4}{2}$ | $\frac{2(6-k)\beta+11k-30}{4}$ | $\frac{3\beta-1}{2}$ | $2\beta$ |
| $\nu_{a,1} < \nu_m < \nu_c$ | | | | | |
| $\nu < \nu_{a,1}$ | $-2$ | $\beta$ | $\beta$ | $\frac{\beta}{4-k}$ | $0$ |
| $\nu_{a,1} < \nu < \nu_m$ | $-\frac{1}{3}$ | $(9-4k)\beta$ | $(21-8k)\beta$ | $\frac{3(2-k)\beta}{4-k}$ | $-1$ |
| $\nu_m < \nu < \nu_c$ | $\frac{p-1}{2}$ | $\frac{k(\beta+3)-6}{2}$ | $\frac{(6-k)\beta+5k-12}{2}$ | $\frac{3(4-k)\beta+k}{2(4-k)}$ | $2\beta+1$ |
| $\nu_c < \nu$ | $\frac{p}{2}$ | $\frac{(\beta+1)k-8}{2}$ | $\frac{(6-k)\beta+5k-16}{2}$ | $\frac{3\beta-1}{2}$ | $2\beta$ |
| $\nu_m < \nu_{a,2} < \nu_c$ | | | | | |
| $\nu < \nu_m$ | $-2$ | $\beta$ | $\beta$ | $\frac{\beta}{4-k}$ | $0$ |
| $\nu_m < \nu < \nu_{a,2}$ | $-\frac{5}{2}$ | $\frac{(k+8)\beta}{10}$ | $\frac{(14-k)\beta}{10}$ | $\frac{(20-3k)\beta}{10(4-k)}$ | $\frac{2\beta}{5}$ |
| $\nu_{a,2} < \nu < \nu_c$ | $\frac{p-1}{2}$ | $\frac{k(\beta+3)-6}{2}$ | $\frac{(6-k)\beta+5k-12}{2}$ | $\frac{3(4-k)\beta+k}{2(4-k)}$ | $2\beta+1$ |
| $\nu_c < \nu$ | $\frac{p}{2}$ | $\frac{(\beta+1)k-8}{2}$ | $\frac{(6-k)\beta+5k-16}{2}$ | $\frac{3\beta-1}{2}$ | $2\beta$ |

TABLE 3
THE PROPORTIONALITY CONSTANTS OF THE RELEVANT QUANTITIES IN SYNCHROTRON MODEL

| | k = 0 | k = 1.0 | k = 1.5 | k = 2.0 | k = 2.5 |
|---|---|---|---|---|---|
| $A_k$ | $1\,\mathrm{cm^{-3}}$ | $1.4 \times 10^{28}\,\mathrm{cm^{-2}}$ | $2.8 \times 10^{36}\,\mathrm{cm^{-\frac{3}{2}}}$ | $2.8 \times 10^{44}\,\mathrm{cm^{-1}}$ | $1.4 \times 10^{51}\,\mathrm{cm^{-\frac{1}{2}}}$ |
| **Coasting phase** | | | | | |
| $\gamma_m^0\ (\times 10^3)$ | 9.15 | 9.15 | 9.15 | 9.15 | 9.15 |
| $\gamma_c^0$ | $1.60 \times 10^5$ | $1.03 \times 10$ | 1.85 | $6.65 \times 10^{-1}$ | 4.77 |
| $\nu_{a,1}^0\ (\mathrm{Hz})$ | $4.47 \times 10^{-8}$ | 1.23 | $2.72 \times 10$ | $1.72 \times 10^2$ | 4.96 |
| $\nu_{a,2}^0\ (\mathrm{Hz})$ | $5.46 \times 10^{-3}$ | 2.66 | 8.30 | $1.64 \times 10$ | 4.44 |
| $\nu_{a,3}^0\ (\times 10^{-3}\,\mathrm{Hz})$ | $7.80 \times 10^{-4}$ | 1.39 | 5.51 | $1.25 \times 10$ | 2.59 |
| $\nu_m^0\ (\times 10^4\,\mathrm{Hz})$ | $1.62 \times 10^{-2}$ | 1.74 | 4.12 | 6.87 | 2.57 |
| $\nu_c^0\ (\times 10^{-3}\,\mathrm{Hz})$ | $4.93 \times 10^7$ | $2.22 \times 10$ | 1.69 | $3.63 \times 10^{-1}$ | 6.97 |
| $F_{\max}^0\ (\times 10^3\,\mathrm{mJy})$ | $6.57 \times 10^{-8}$ | $8.22 \times 10^{-2}$ | 1.08 | 5.04 | $2.62 \times 10^{-1}$ |
| **Deceleration phase (Off-axis)** | | | | | |
| $\gamma_m^0\ (\times 10)$ | 7.56 | 3.48 | 6.59 | $2.06 \times 10$ | $1.96 \times 10^2$ |
| $\gamma_c^0\ (\times 10^4)$ | 2.80 | $4.08 \times 10^{-1}$ | 1.98 | $8.44 \times 10$ | $9.33 \times 10^6$ |
| $\nu_{a,1}^0\ (\times 10^{-6}\,\mathrm{Hz})$ | $7.55 \times 10^{-2}$ | 1.80 | $1.35 \times 10^{-1}$ | $2.45 \times 10^{-4}$ | $6.72 \times 10^{-13}$ |
| $\nu_{a,2}^0\ (\times 10^{-5}\,\mathrm{Hz})$ | 1.00 | 1.93 | 1.13 | $2.47 \times 10^{-1}$ | $1.05 \times 10^{-3}$ |
| $\nu_{a,3}^0\ (\times 10^{-5}\,\mathrm{Hz})$ | 2.80 | $2.11 \times 10$ | 4.04 | $1.00 \times 10^{-1}$ | $3.20 \times 10^{-6}$ |
| $\nu_m^0\ (\times 10^{-6}\,\mathrm{Hz})$ | 3.03 | 1.20 | 2.58 | 7.04 | 8.87 |
| $\nu_c^0\ (\times 10^{-1}\,\mathrm{Hz})$ | 4.17 | $1.65 \times 10^{-1}$ | 2.32 | $1.18 \times 10^3$ | $2.01 \times 10^{11}$ |
| $F_{\max}^0\ (\times 10\,\mathrm{mJy})$ | 4.10 | 7.66 | 4.59 | $7.02 \times 10^{-1}$ | $1.39 \times 10^{-4}$ |
| **Deceleration phase (On-axis)** | | | | | |
| $\gamma_m^0\ (\times 10^3)$ | 2.83 | 1.43 | 1.51 | 1.96 | 8.19 |
| $\gamma_c^0\ (\times 10^2)$ | $3.95 \times 10$ | 1.36 | 1.78 | 6.32 | $1.28 \times 10^4$ |
| $\nu_{a,1}^0\ (\times 10^{-3}\,\mathrm{Hz})$ | $1.80 \times 10^{-2}$ | 6.77 | 4.23 | $4.54 \times 10^{-1}$ | $1.02 \times 10^{-6}$ |
| $\nu_{a,2}^0\ (\times 10^{-2}\,\mathrm{Hz})$ | $5.74 \times 10^{-1}$ | 3.25 | 2.83 | 1.47 | $3.78 \times 10^{-2}$ |
| $\nu_{a,3}^0\ (\times 10^{-4}\,\mathrm{Hz})$ | $2.51 \times 10^{-1}$ | 6.44 | 4.98 | 1.47 | $1.58 \times 10^{-3}$ |
| $\nu_m^0\ (\mathrm{Hz})$ | 3.17 | 3.10 | 3.11 | 3.14 | 3.21 |
| $\nu_c^0\ (\times 10^{-2}\,\mathrm{Hz})$ | $6.15 \times 10^2$ | 2.81 | 4.31 | $3.28 \times 10$ | $7.79 \times 10^6$ |
| $F_{\max}^0\ (\times 10^3\,\mathrm{mJy})$ | $1.14 \times 10^{-1}$ | 1.69 | 1.36 | $4.95 \times 10^{-1}$ | $1.68 \times 10^{-3}$ |
| **Post-jet-break decay phase** | | | | | |
| $\gamma_m^0\ (\times 10)$ | 4.68 | 1.95 | 4.03 | $1.69 \times 10$ | $1.74 \times 10^2$ |
| $\gamma_c^0\ (\times 10^4)$ | 3.92 | $4.89 \times 10^{-1}$ | 2.71 | $1.52 \times 10^2$ | $2.32 \times 10^7$ |
| $\nu_{a,1}^0\ (\times 10^{-8}\,\mathrm{Hz})$ | 3.40 | $9.82 \times 10$ | 6.22 | $7.57 \times 10^{-03}$ | $1.20 \times 10^{-11}$ |
| $\nu_{a,2}^0\ (\times 10^{-6}\,\mathrm{Hz})$ | 4.80 | 9.38 | 5.43 | 1.21 | $4.48 \times 10^{-3}$ |
| $\nu_{a,3}^0\ (\times 10^{-5}\,\mathrm{Hz})$ | 2.85 | $2.47 \times 10$ | 4.19 | $6.83 \times 10^{-2}$ | $1.60 \times 10^{-6}$ |
| $\nu_m^0\ (\times 10^{-7}\,\mathrm{Hz})$ | 6.06 | 2.10 | 5.05 | $2.37 \times 10$ | $3.13 \times 10$ |
| $\nu_c^0\ (\times 10^{-1}\,\mathrm{Hz})$ | 4.25 | $1.32 \times 10^{-1}$ | 2.29 | $1.93 \times 10^3$ | $5.55 \times 10^{11}$ |
| $F_{\max}^0\ (\mathrm{mJy})$ | $2.14 \times 10$ | $4.28 \times 10$ | $2.41 \times 10$ | 4.97 | $7.81 \times 10^{-4}$ |

TABLE 4
EVOLUTION OF THE DENSITY PARAMETER $F_\nu \propto A_{\mathrm{k}}^{\alpha_{\mathrm{k}}}$ IN EACH COOLING CONDITION OF THE SYNCHROTRON AFTERGLOW MODEL

| | | Coasting phase | Deceleration phase (off-axis afterglow) | Deceleration phase (on-axis afterglow) | Post jet-break phase |
|---|---|---|---|---|---|
| | $\beta$ | $\alpha_{\mathrm{k}}$ | $\alpha_{\mathrm{k}}$ | $\alpha_{\mathrm{k}}$ | $\alpha_{\mathrm{k}}$ |
| $\nu_{\mathrm{a,3}} < \nu_{\mathrm{c}} < \nu_{\mathrm{m}}$ | | | | | |
| $\nu < \nu_{\mathrm{a,3}}$ | $-2$ | $-1$ | $0$ | $-\frac{4}{4-k}$ | $-\frac{3}{3-k}$ |
| $\nu_{\mathrm{a,3}} < \nu < \nu_{\mathrm{c}}$ | $-\frac{1}{3}$ | $2$ | $\frac{8}{3}$ | $\frac{10}{3(4-k)}$ | $-\frac{4}{3(3-k)}$ |
| $\nu_{\mathrm{c}} < \nu < \nu_{\mathrm{m}}$ | $\frac{1}{2}$ | $\frac{3}{4}$ | $\frac{9}{4}$ | $0$ | $-\frac{3}{4(3-k)}$ |
| $\nu_{\mathrm{m}} < \nu$ | $\frac{p}{2}$ | $\frac{p+2}{4}$ | $\frac{10-p}{4}$ | $0$ | $-\frac{p+2}{4(3-k)}$ |
| $\nu_{\mathrm{a,1}} < \nu_{\mathrm{m}} < \nu_{\mathrm{c}}$ | | | | | |
| $\nu < \nu_{\mathrm{a,1}}$ | $-2$ | $-2$ | $0$ | $-\frac{2}{4-k}$ | $-\frac{2}{3-k}$ |
| $\nu_{\mathrm{a,1}} < \nu < \nu_{\mathrm{m}}$ | $-\frac{1}{3}$ | $\frac{4}{3}$ | $\frac{8}{3}$ | $\frac{2}{4-k}$ | $-\frac{2}{3(3-k)}$ |
| $\nu_{\mathrm{m}} < \nu < \nu_{\mathrm{c}}$ | $\frac{p-1}{2}$ | $\frac{p+5}{4}$ | $\frac{11-p}{4}$ | $\frac{2}{4-k}$ | $\frac{3-p}{4(3-k)}$ |
| $\nu_{\mathrm{c}} < \nu$ | $\frac{p}{2}$ | $\frac{p+2}{4}$ | $\frac{10-p}{4}$ | $0$ | $-\frac{p+2}{4(3-k)}$ |
| $\nu_{\mathrm{m}} < \nu_{\mathrm{a,2}} < \nu_{\mathrm{c}}$ | | | | | |
| $\nu < \nu_{\mathrm{m}}$ | $-2$ | $0$ | $0$ | $-\frac{2}{4-k}$ | $-\frac{2}{3-k}$ |
| $\nu_{\mathrm{m}} < \nu < \nu_{\mathrm{a,2}}$ | $-\frac{5}{2}$ | $-\frac{1}{4}$ | $\frac{1}{4}$ | $-\frac{2}{4-k}$ | $-\frac{7}{4(3-k)}$ |
| $\nu_{\mathrm{a,2}} < \nu < \nu_{\mathrm{c}}$ | $\frac{p-1}{2}$ | $\frac{p+5}{4}$ | $\frac{11-p}{4}$ | $\frac{2}{4-k}$ | $\frac{3-p}{4(3-k)}$ |
| $\nu_{\mathrm{c}} < \nu$ | $\frac{p}{2}$ | $\frac{p+2}{4}$ | $\frac{10-p}{4}$ | $0$ | $-\frac{p+2}{4(3-k)}$ |

TABLE 5
MEDIAN VALUES OF PARAMETERS USED TO DESCRIBE THE MULTI-WAVELENGTH AFTERGLOW OBSERVATIONS OF A SAMPLE OF SHORT AND LONG GRBS

| Parameters | GRB 080503 | GRB 140903A | GRB 150101B | GRB 160821B | SN 2020bvc |
|---|---|---|---|---|---|
| $E\,(10^{52}\,\mathrm{erg})$ | $2.156^{+0.294}_{-0.295}$ | $3.163^{+0.290}_{-0.296}$ | $1.046^{+0.120}_{-0.124}$ | $0.118^{+0.021}_{-0.021}$ | $0.238^{+0.011}_{-0.010}$ |
| n $(10^{-2}\,\mathrm{cm}^{-3})$ | $4.221^{+0.102}_{-0.103}$ | $4.219^{+0.102}_{-0.101}$ | $0.164^{+0.021}_{-0.021}$ | $0.869^{+0.093}_{-0.090}$ | – |
| [a]$A_{\mathrm{w}}\,(10^{-13}\,\mathrm{cm}^{1/2})$ | – | – | – | – | $3.340^{+0.195}_{-0.193}$ |
| p | $2.319^{+0.049}_{-0.049}$ | $2.073^{+0.048}_{-0.050}$ | $2.150^{+0.217}_{-0.215}$ | $2.220^{+0.021}_{-0.021}$ | $2.313^{+0.037}_{-0.035}$ |
| $\varepsilon_{\mathrm{B}}\,(10^{-3})$ | $3.168^{+0.911}_{-0.897}$ | $4.050^{+0.909}_{-0.921}$ | $0.147^{+0.124}_{-0.094}$ | $0.559^{+0.437}_{-0.365}$ | $5.623^{+0.020}_{-0.020}$ |
| $\varepsilon_{\mathrm{e}}\,(10^{-2})$ | $3.745^{+0.298}_{-0.288}$ | $5.104^{+0.298}_{-0.302}$ | $1.001^{+0.176}_{-0.164}$ | $0.155^{+0.021}_{-0.021}$ | $38.951^{+0.295}_{-0.288}$ |
| $\Gamma\,(10^{2})$ | $2.939^{+0.101}_{-0.097}$ | $3.627^{+0.100}_{-0.100}$ | $4.251^{+0.468}_{-0.453}$ | $4.559^{+0.361}_{-0.358}$ | $2.291^{+0.100}_{-0.100}$ |
| $\theta_{\mathrm{j}}$ (deg) | $6.589^{+0.081}_{-0.078}$ | $3.210^{+0.080}_{-0.081}$ | $6.887^{+0.662}_{-0.682}$ | $8.002^{+0.817}_{-0.809}$ | $2.121^{+0.078}_{-0.079}$ |
| $\theta_{\mathrm{obs}}$ (deg) | $15.412^{+0.268}_{-0.269}$ | $5.162^{+0.271}_{-0.267}$ | $14.114^{+2.327}_{-2.179}$ | $10.299^{+1.125}_{-1.135}$ | $12.498^{+0.268}_{-0.281}$ |

[a]This value is used when k = 1.5

TABLE 6
VALUES USED IN THE SYNCHROTRON LIGHT CURVES OF THE CLOSEST SGRBS DETECTED BY THE SWIFT SATELLITE

| Parameters | GRB 050906 | GRB 070810B | GRB 080121 | GRB 100216A |
|---|---|---|---|---|
| $E\,(10^{50}\,\mathrm{erg})$ | 5.00 | 5.00 | 5.00 | 5.00 |
| | 5.00 | 5.00 | 5.00 | 5.00 |
| $n\,(10^{-2}\,\mathrm{cm}^{-3})$ | 1.00 | 1.00 | 1.00 | 1.00 |
| | 100.00 | 100.00 | 100.00 | 100.00 |
| $p$ | 2.50 | 2.50 | 2.50 | 2.50 |
| | 2.50 | 2.50 | 2.50 | 2.50 |
| $\varepsilon_B\,(10^{-4})$ | 1.00 | 1.00 | 1.00 | 1.00 |
| | 1.00 | 1.00 | 1.00 | 1.00 |
| $\varepsilon_e\,(10^{-1})$ | 3.00 | 3.00 | 3.00 | 3.00 |
| | 3.00 | 3.00 | 3.00 | 3.00 |
| $\Gamma$ | 100.0 | 100.0 | 150.0 | 80.0 |
| | 100.0 | 100.0 | 100.0 | 100.0 |
| $\theta_{\mathrm{j}}$ (deg) | 3.00 | 3.00 | 3.00 | 3.00 |
| | 3.00 | 3.00 | 3.00 | 3.00 |
| $\theta_{obs}$ (deg) | 15.00 | 15.00 | 15.00 | 15.00 |
| | 15.00 | 15.00 | 15.0 | 15.00 |

TABLE 7
QUANTITIES DERIVED OF THE PROMISING GW EVENTS FROM GWTC-2 AND GWTC-3

|  | Event | SID | Mass 1 $(M_\odot)$ | Mass 2 $(M_\odot)$ | z | References |
|---|---|---|---|---|---|---|
| GWTC-2 | GW190425 | S190425z | $3.4^{+0.3}_{-0.1}$ | $1.44^{+0.02}_{-0.02}$ | $0.03^{+0.01}_{-0.02}$ | [a], [b], [c] |
| | GW190426_152155 | S190426c | $5.7^{+3.9}_{-2.3}$ | $1.5^{+0.8}_{-0.5}$ | $0.08^{+0.04}_{-0.03}$ | [d], [e], [f], [g] |
| | GW190814 | S190814bv | $23.2^{+1.1}_{-1.0}$ | $2.59^{+0.08}_{-0.09}$ | $0.05^{+0.009}_{-0.010}$ | [h], [i], [l], [m], [n], [o] |
| GWTC-3 | GW191219_163120 | | $31.1^{+2.2}_{-2.8}$ | $1.17^{+0.07}_{-0.06}$ | $0.11^{+0.05}_{-0.03}$ | [p] |
| | GW200105_162426 | S200105ae | $9.0^{+1.7}_{-1.7}$ | $1.91^{+0.33}_{-0.24}$ | $0.06^{+0.02}_{-0.02}$ | [q] |
| | GW200115_042309 | S200115j | $5.9^{+2.0}_{-2.5}$ | $1.44^{+0.85}_{-0.29}$ | $0.05^{+0.009}_{-0.010}$ | [r], [s] |
| | GW200210_092254 | | $24.1^{+7.5}_{-4.6}$ | $2.83^{+0.47}_{-0.42}$ | $0.19^{+0.08}_{-0.06}$ | [p] |

References: [a] Siegel (2019), [b] Tohuvavohu (2019a), [c] Bochenek (2019a), [d] Rhodes (2019), [e] Corsi (2019), [f] Bochenek (2019b), [g] Tohuvavohu (2019b), [h] LIGO Scientific Collaboration & Virgo Collaboration (2019), [i] Andreoni et al. (2020), [l] Dobie et al. (2019), [m] Watson et al. (2020), 12] Ackley et al. (2020), [o] Vieira et al. (2020), [p] The LIGO Scientific Collaboration et al. (2021), [q] Ridnaia (2020a), [r] Lien (2020) and [s] Ridnaia (2020b)
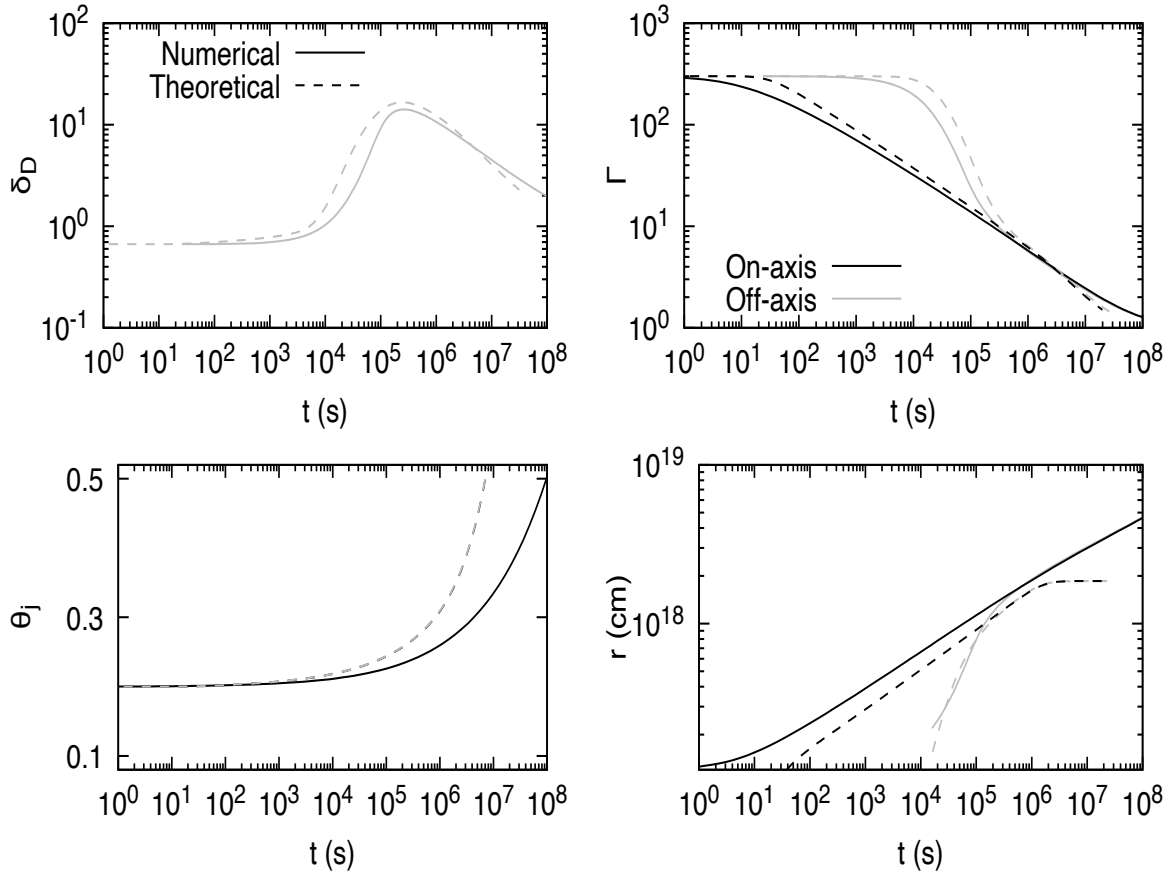
FIG. 1.— Comparison of numerical simulations (solid lines) and a theoretical approach (dashed lines) of Doppler factor ($\delta_D$), the jet's opening angle $\theta_j$, the bulk Lorentz factor ($\Gamma_j$) and the deceleration radius ($r$), all of them evolving in a constant circumburst medium. Variables observed for a observed off- and on-axis are in black and gray color, respectively. The following parameters $E = 10^{54}$ erg, $n = 1.0\,\mathrm{cm}^{-3}$, $\Delta\theta = 5.72\,\mathrm{deg}$ and $\Gamma_0 = 300$ are used.
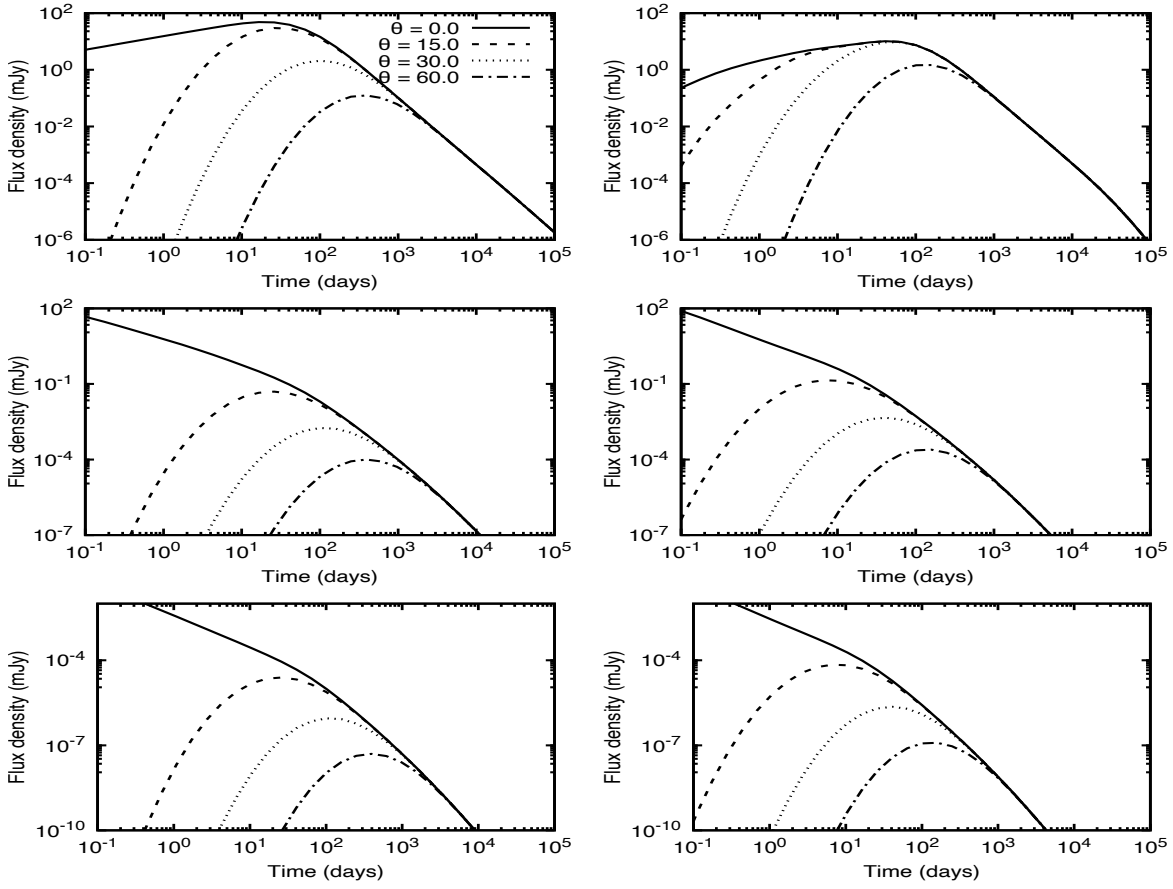
FIG. 2.— Synchrotron light curves generated by the deceleration of the off-axis jet for $k = 0$ (left) and $k = 1$ (right). Panels from top to bottom correspond to radio (1.6 GHz), optical (R) and X-ray (1 keV) bands, respectively. The following parameters $E = 10^{51}$ erg, $\varepsilon_B = 10^{-4}$, $\varepsilon_e = 10^{-1}$, $\Gamma = 300$, $p = 2.2$, $\zeta_e = 1.0$ and $d_z = 6.6$ Gpc are used.
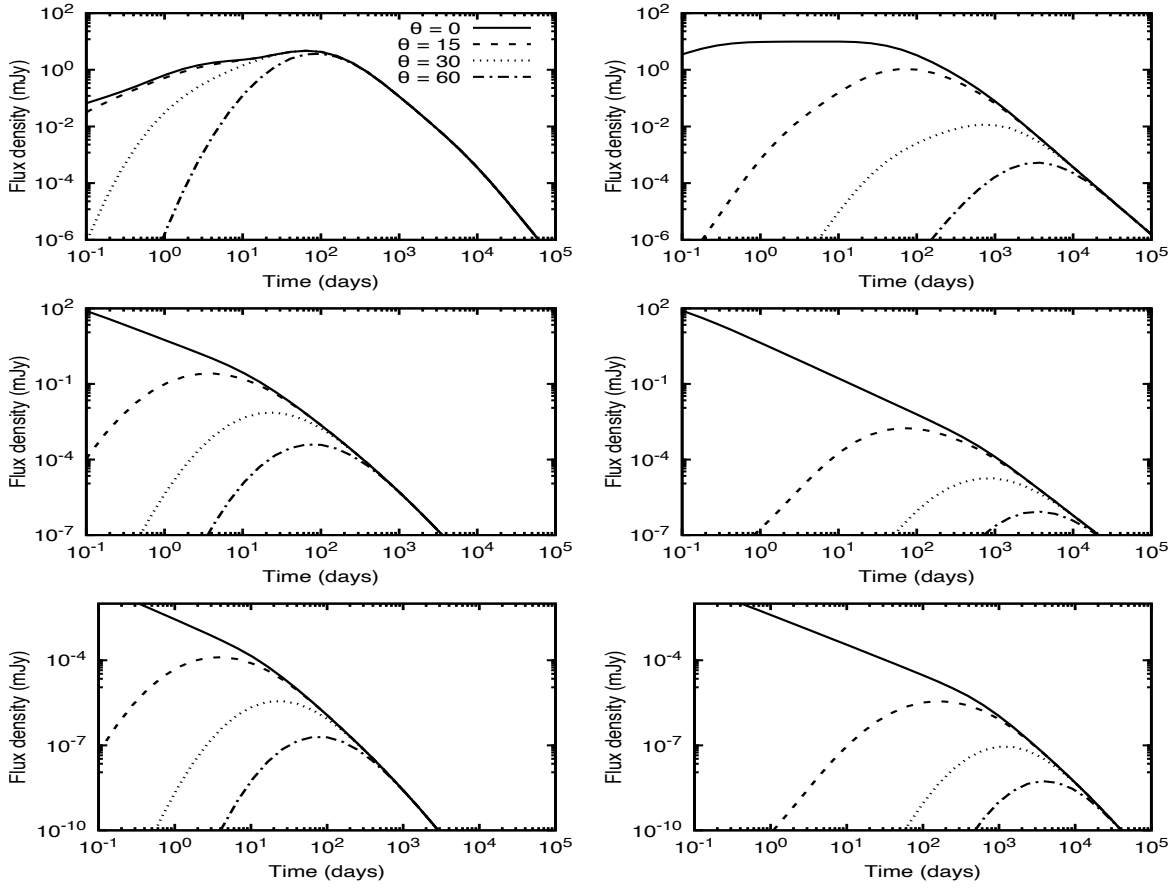
FIG. 3.— Synchrotron light curves generated by the deceleration of the off-axis jet for $k = 1.5$ (left) and $k = 2$ (right). Panels from top to bottom correspond to radio (1.6 GHz), optical (R) and X-ray (1 keV) bands, respectively. The following parameters $E = 10^{51}$ erg, $\varepsilon_{\rm B} = 10^{-4}$, $\varepsilon_{\rm e} = 10^{-1}$, $\Gamma = 300$, $p = 2.2$, $\zeta_e = 1.0$ and $d_z = 6.6$ Gpc are used.
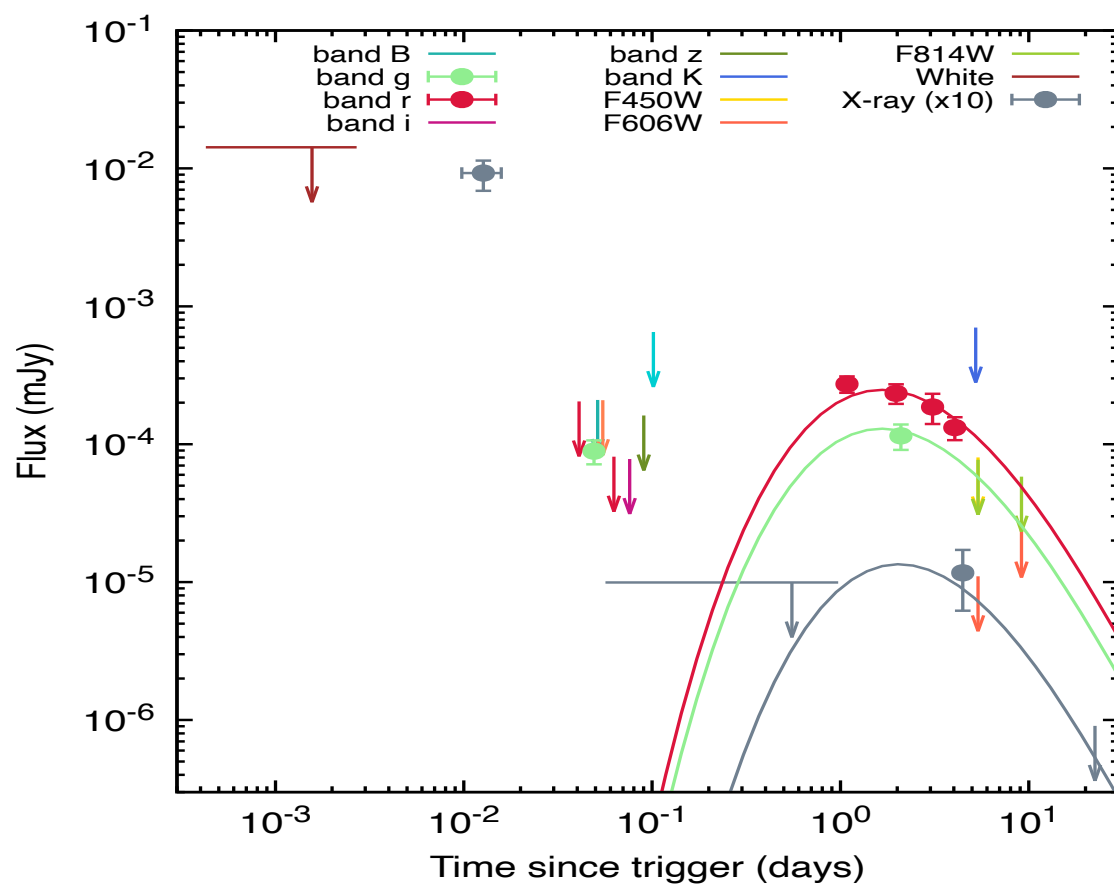
FIG. 4.— X-ray and optical light curves of GRB 080503 with the best-fit curve of synchrotron afterglow model. The synchrotron light curves are shown at 1 keV (gray), R-band (red) and g-band (green).Data points are taken from Perley et al. (2009).
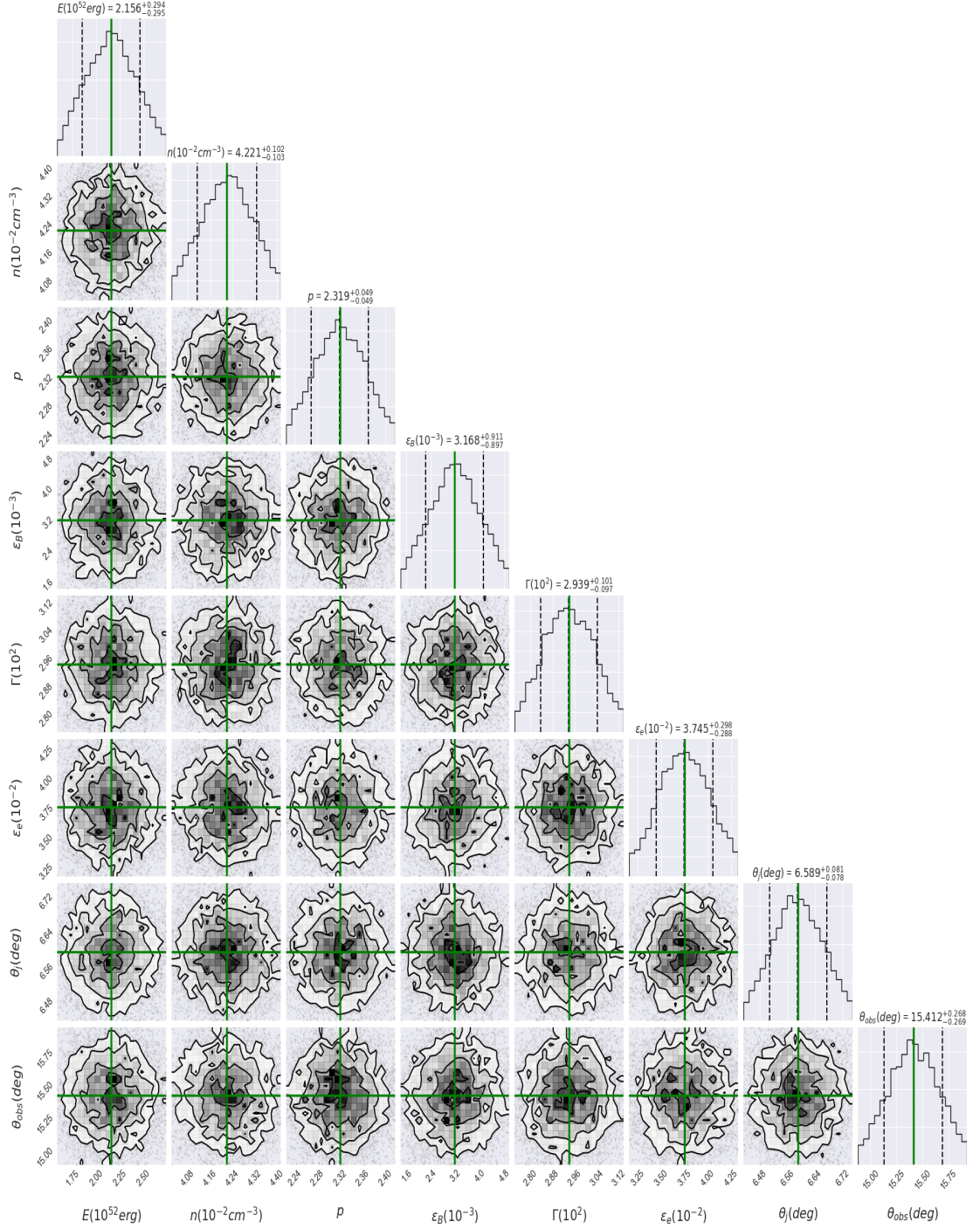
Fig. 5.— Corner plot of the parameters derived from fitting the multi-wavelength light curves of GRB 080503 with a synchrotron off-axis model, together with median values (green lines) and $1\sigma$ credible intervals (dashed lines). MCMC summary statistics for all parameters are listed in Table 5. A set of normal distributions are made for the priors.
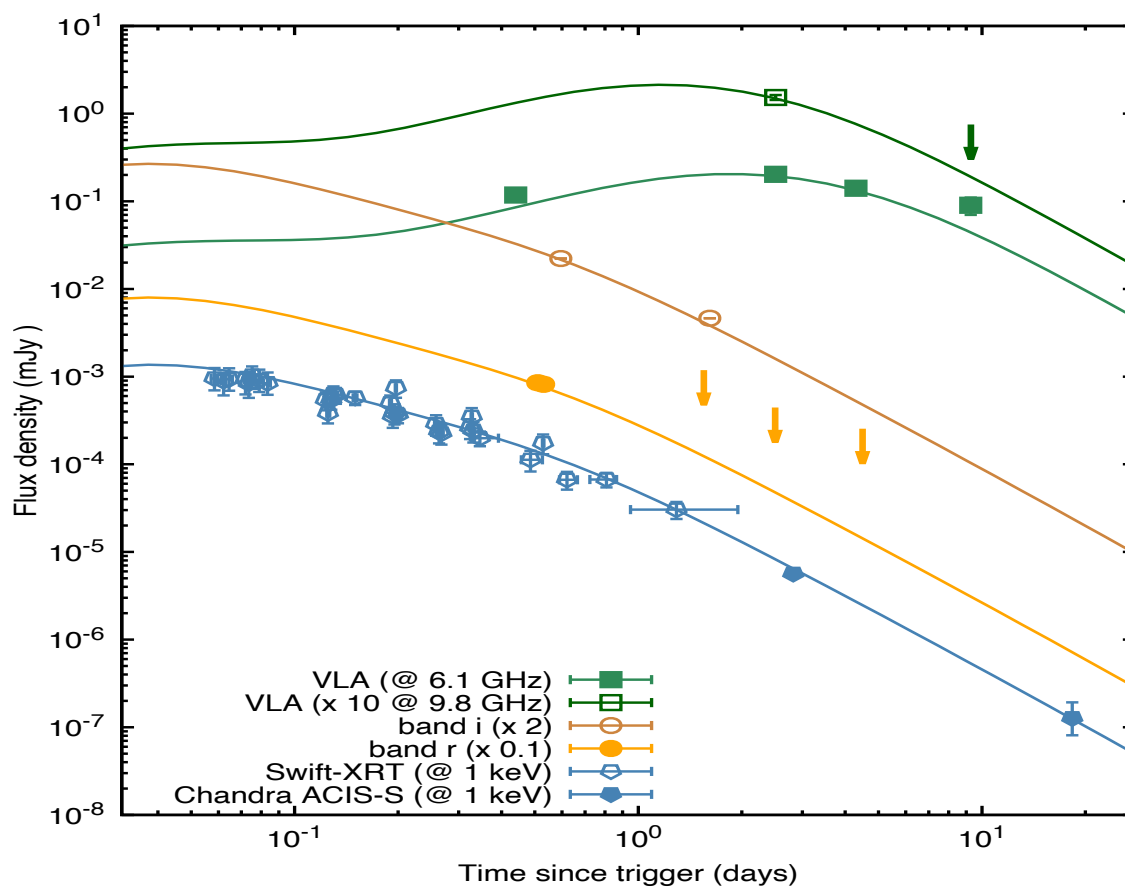
Fig. 6.— X-ray, optical and radio light curves of GRB 140903A with the best-fit curve of synchrotron afterglow model. The synchrotron light curves are shown at 1 keV (blue), R-band (gold), i-band (brown) s, 9.8 GHz (dark green) and 6.1 GHz (light green). Data points are taken from Troja et al. (2016).

Fraija N.
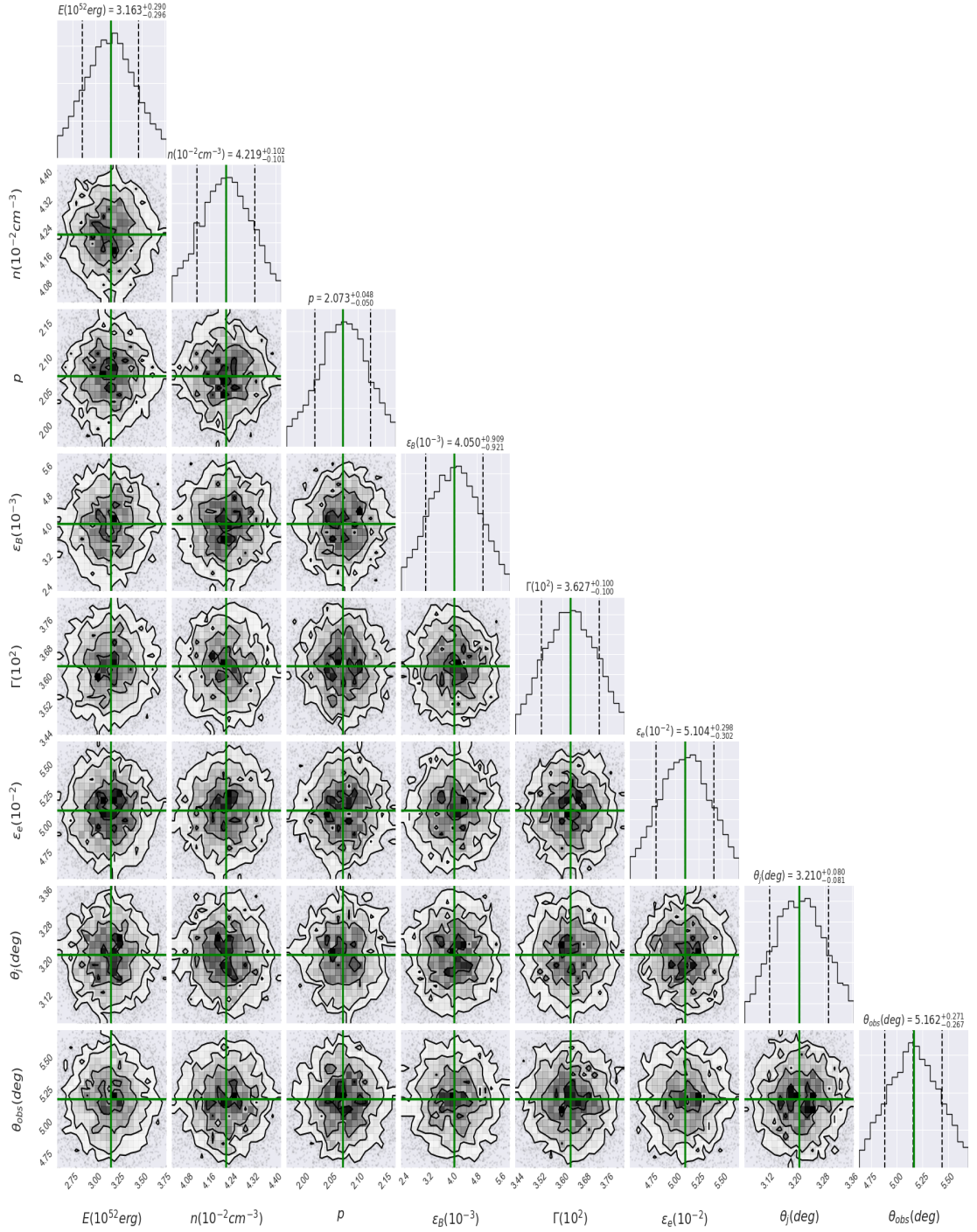


Fɪɢ. 7.— The same as Figure GRB 080503, but for GRB 140903A.
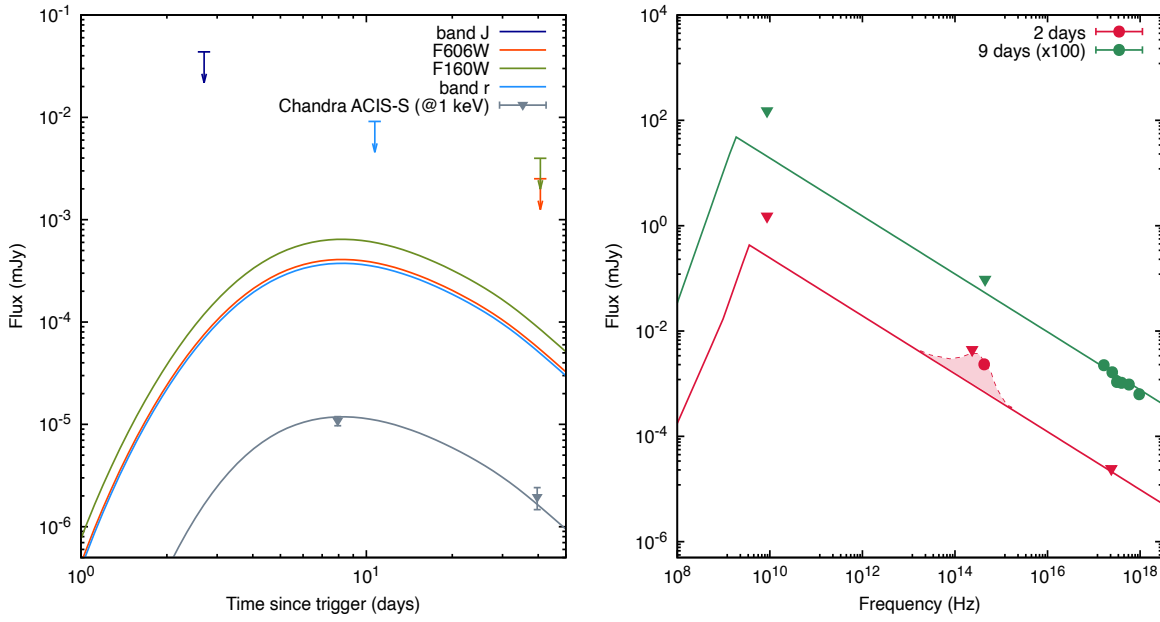
FIG. 8.— Left: X-ray light curves with the optical upper limits of GRB 150101B with the best-fit curve of synchrotron afterglow model. The synchrotron light curves are shown at 1 keV (gray), R-band (blue), F606W filter (orange) and F160W filter (dark green). Data points are taken from Fong et al. (2016) and Troja et al. (2018). Right: The broadband SEDs of the X-ray, optical and radio afterglow observations and upper limits with the best-fit synchrotron curves (lines) at 2 days (red) and 9 (green) days, respectively. The red area corresponds to the spectrum of AT2017gfo, which is adapted by Troja et al. (2018).

Fraija N.
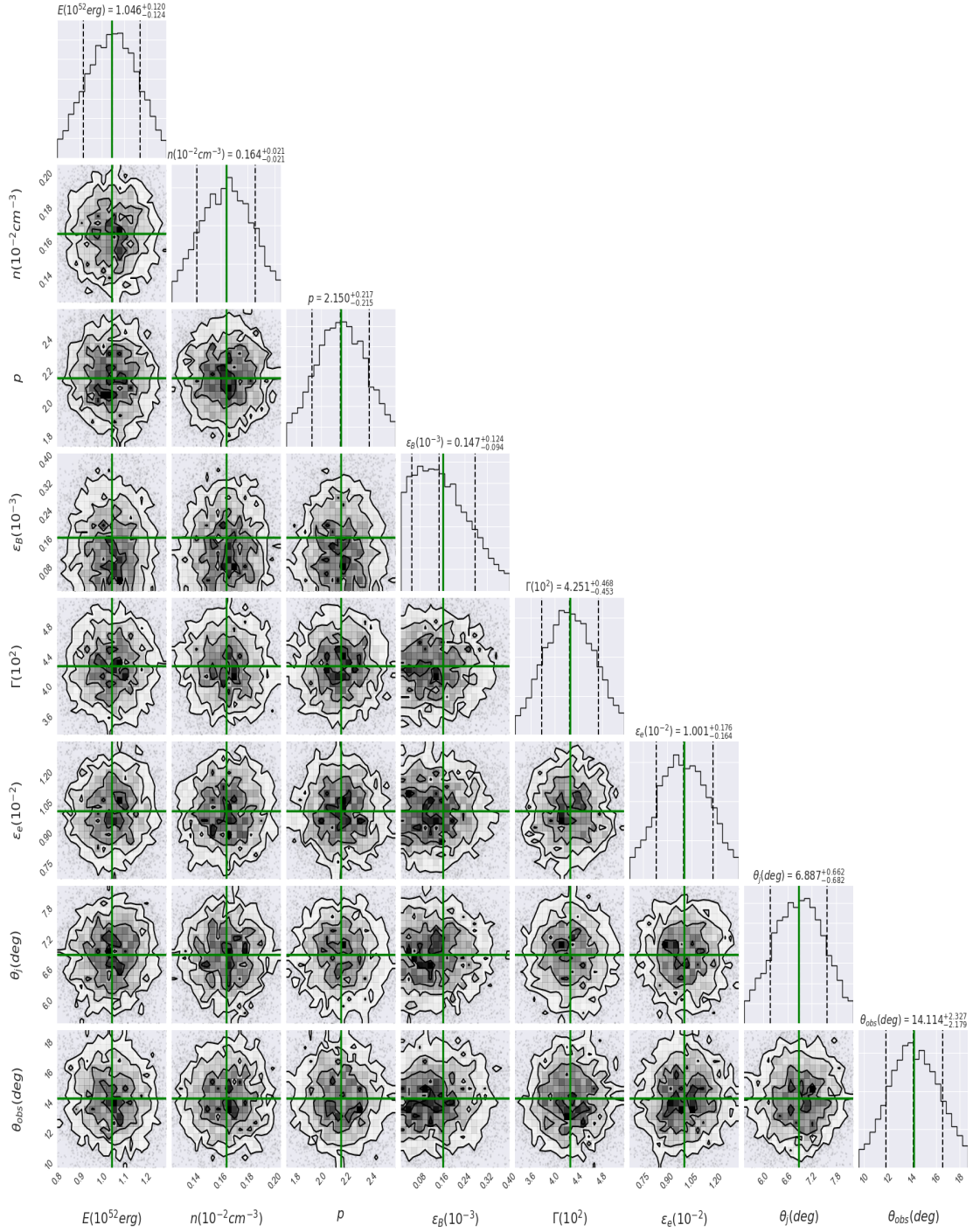


FIG. 9.— The same as Figure GRB 080503, but for GRB 150101B.
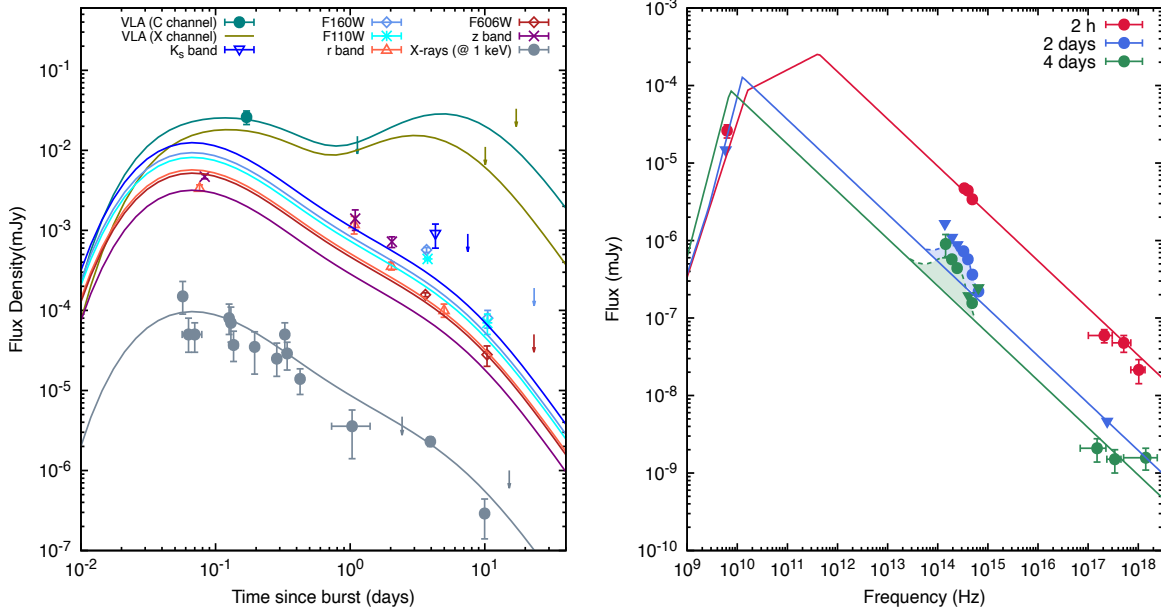
FIG. 10.— Left: X-ray, optical and radio light curves of GRB 160821B with the best-fit curve of synchrotron afterglow model. The synchrotron light curves are shown at 1 keV (gray), z-band (purple), F606W filter (dark red), R-band (salmon), F110W filter (cyan), F160W filter (blue sky), $K_s$-band (blue), X-channel (olive) and C-channel (emerald green). Data points are taken from Troja et al. (2019a). Right: The broadband SEDs of the X-ray, optical and radio afterglow observations with the best-fit synchrotron curves (lines) at 2 h (red), 2 days (blue) and 4 (green) days, respectively. The shaded areas correspond to blackbody spectra with decreasing temperatures from Troja et al. (2019a).
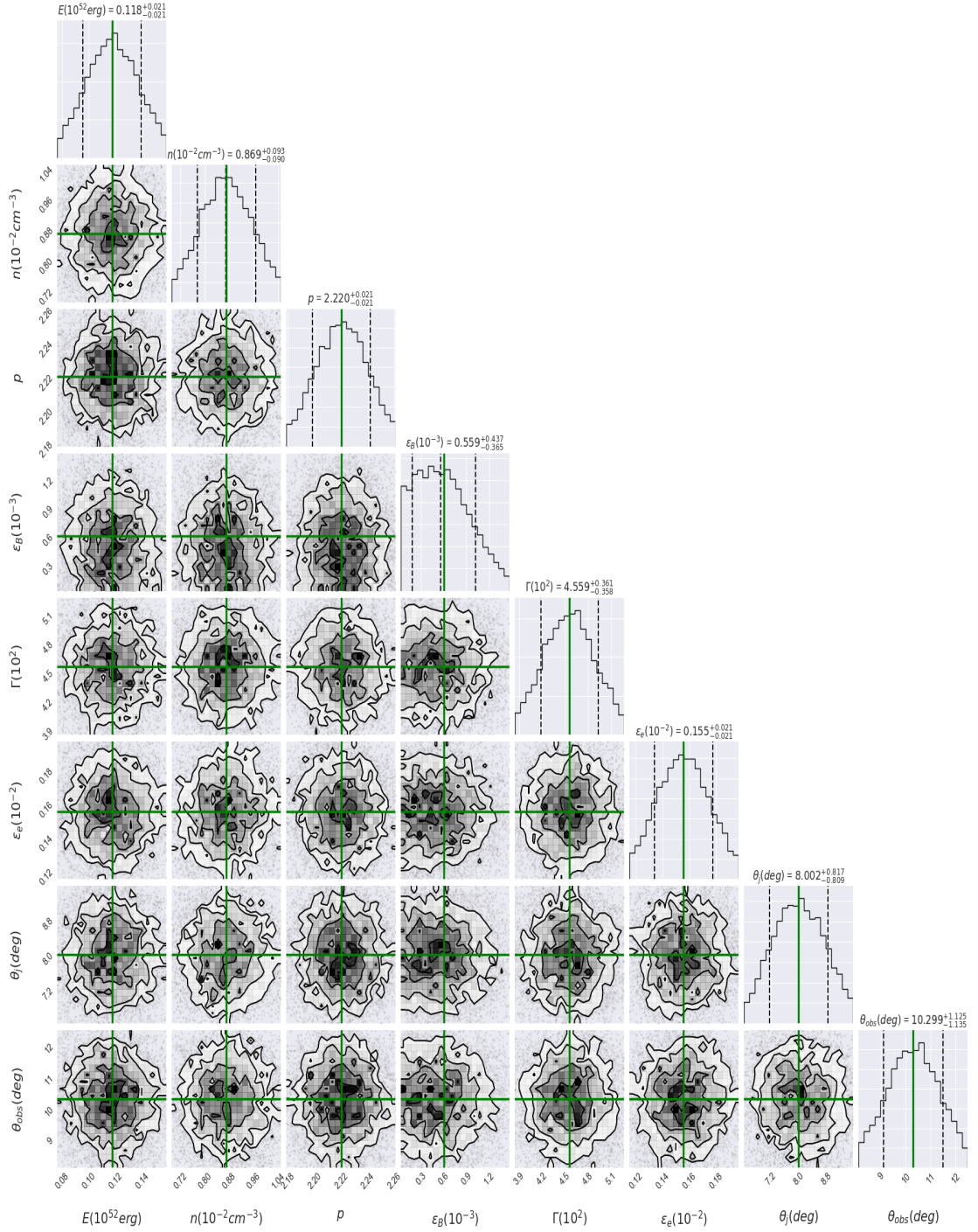
FIG. 11.— The same as Figure GRB 080503, but for GRB 160821B.
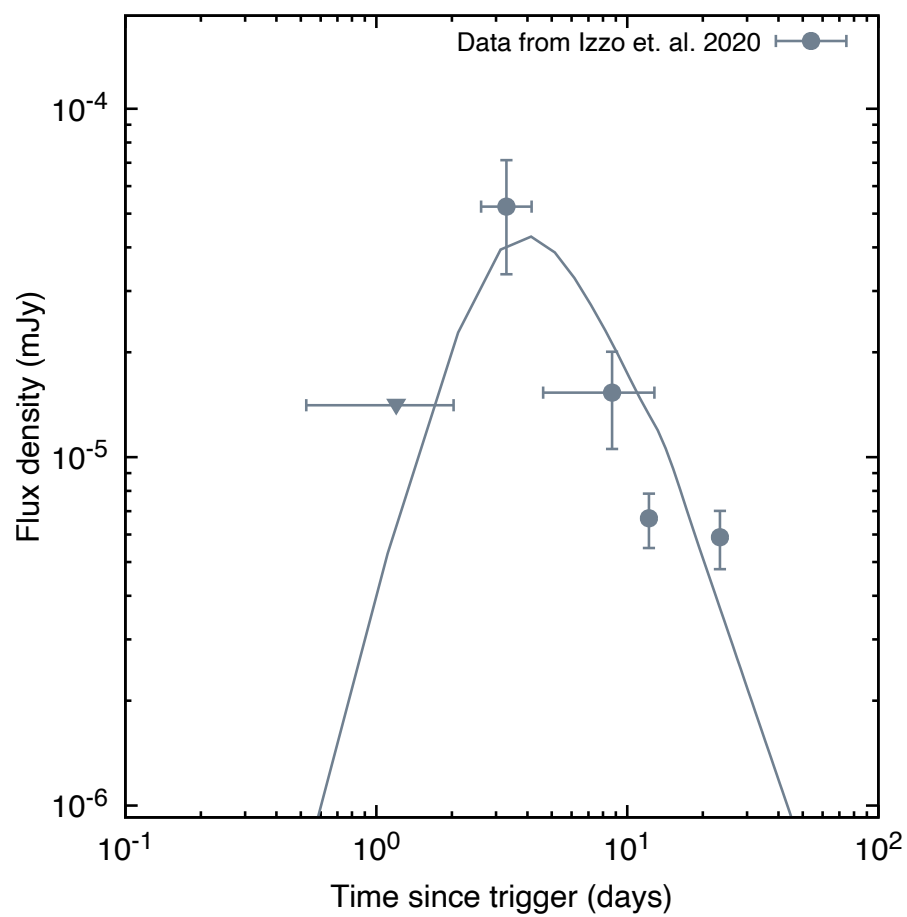
FIG. 12.— The X-ray data points of SN 2020bvc with the best-fit curve obtained with the model presented in this article for a stratification parameter of $k = 1.5$. The synchrotron light curve are shown at 1 keV. Data points are taken from Izzo et al. (2020).
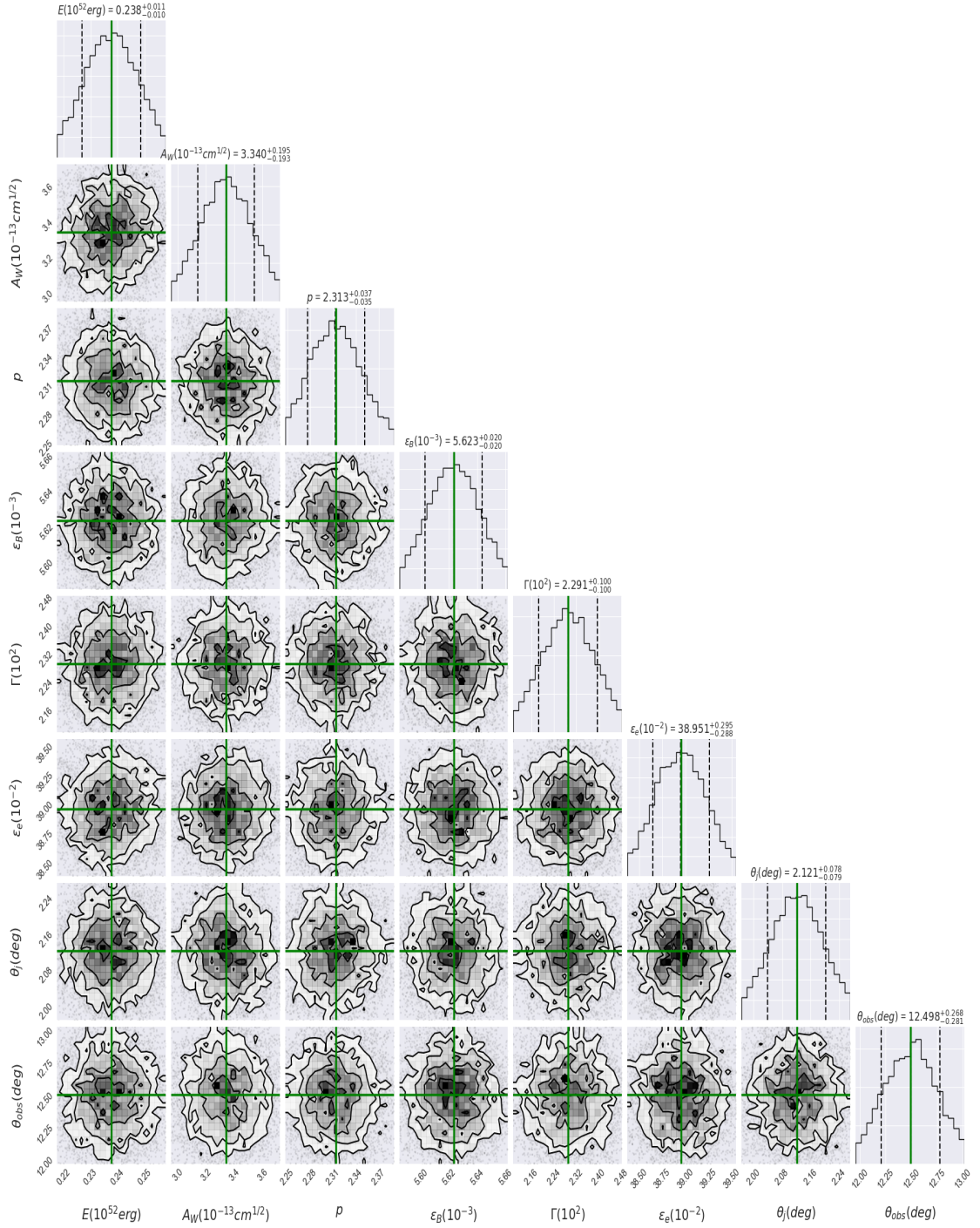
FIG. 13.— The same as Figure GRB 080503, but for SN 2020bvc.
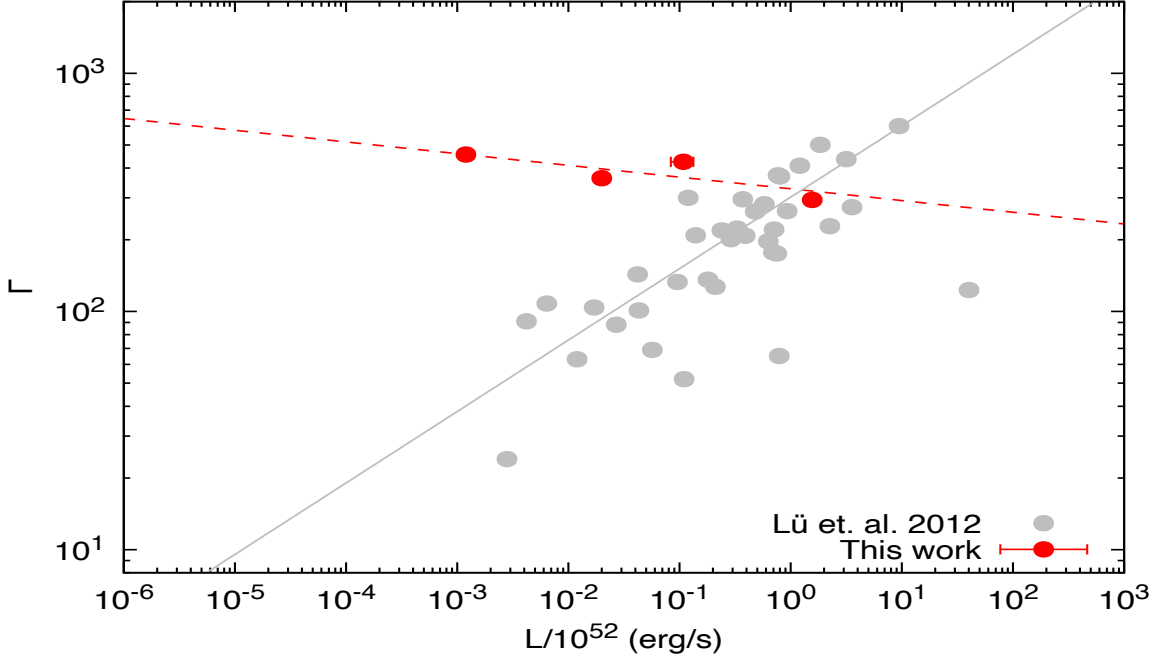
FIG. 14.— Diagram of bulk Lorentz factors and Luminosities for the GRBs discussed in Fan et al. (2012) and Lü et al. (2012), and for sGRBs described in this work. The red dashed line corresponds to the best-fit $\Gamma = a(L/10^{52} \text{ erg})^b$ with a = $(3.27 \pm 0.39) \times 10^2$ and b = $-(4.9 \pm 0.20) \times 10^{-2}$.
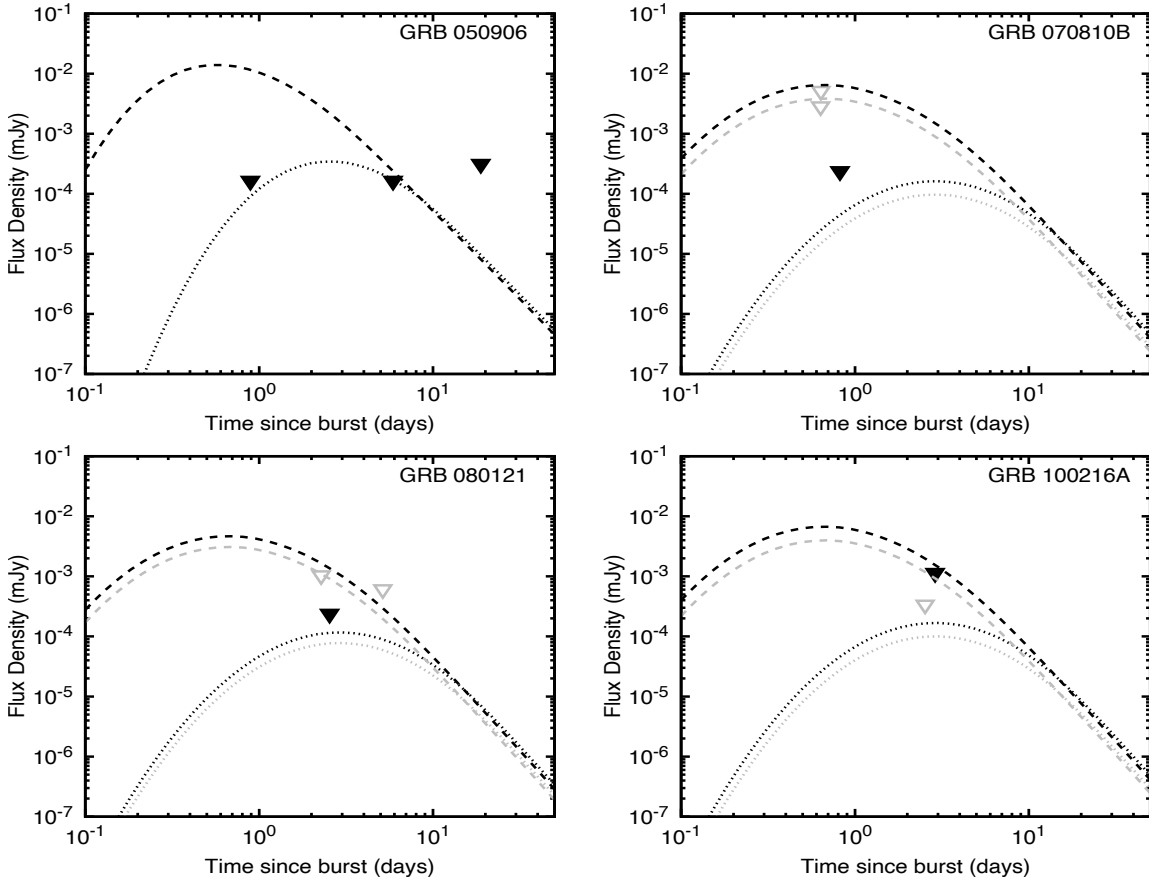
FIG. 15.— Optical (u- and r-band) upper limits for GRB 050906, GRB 070810B, GRB 080121 and GRB 100216A with a set of synchrotron light curves evolving in a constant-density medium. The dashed and dotted lines are shown with $n = 1\,\mathrm{cm^{-3}}$ and $n = 10^{-2}\,\mathrm{cm^{-3}}$, respectively. The parameter values used are $E = 5 \times 10^{50}\,\mathrm{erg}$, $\theta_\mathrm{j} = 3\,\mathrm{deg}$, $\theta_\mathrm{obs} = 15\,\mathrm{deg}$, $\Gamma = 100$, $\varepsilon_\mathrm{e} = 0.3$, $p = 2.5$, $\zeta_e = 1.0$ and $\varepsilon_\mathrm{B} = 10^{-4}$. Upper limits are taken from Dichiara et al. (2020).
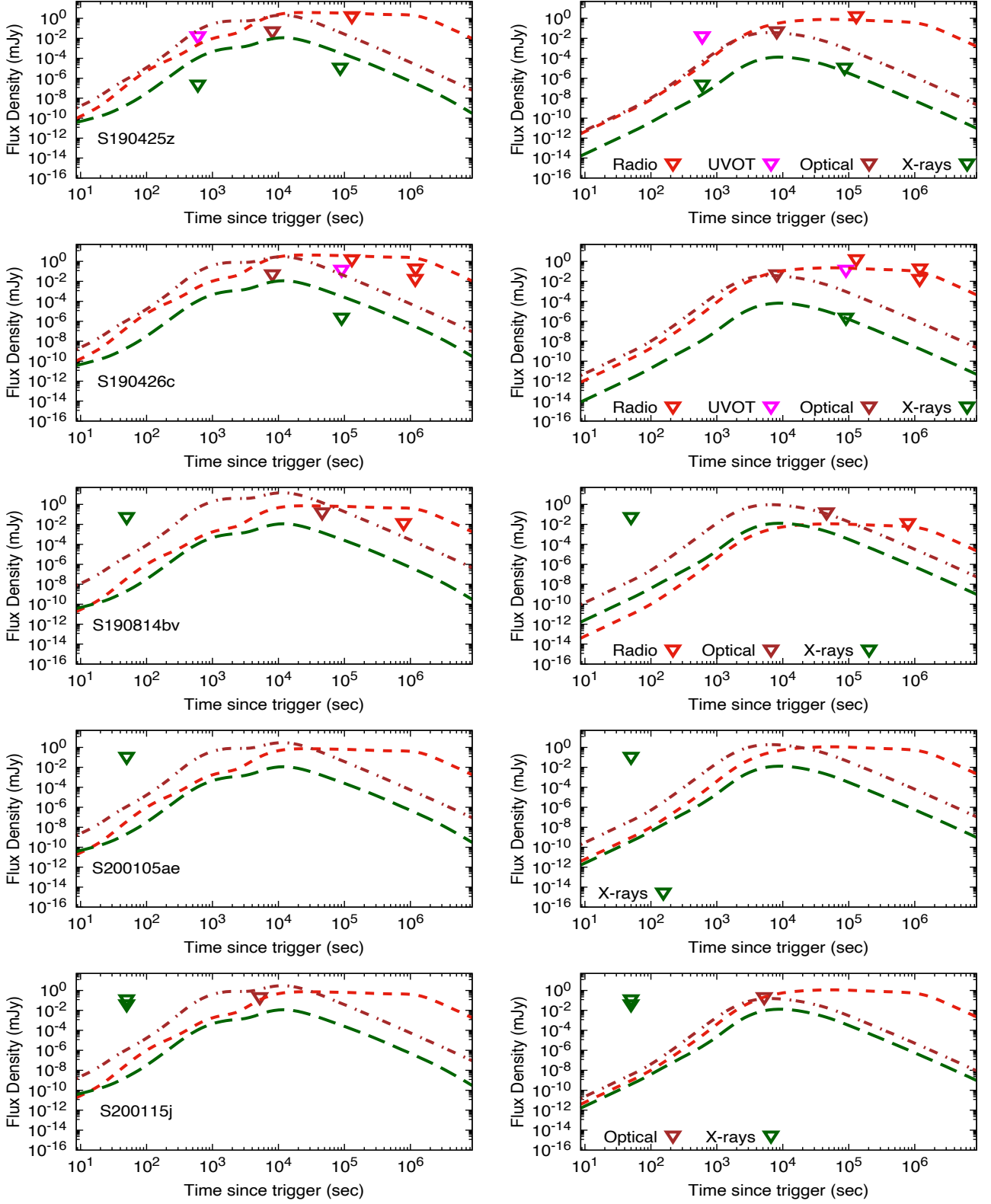
FIG. 16.— Promising GW events in the third observing run (O3) that could generate electromagnetic emission with the synchrotron light curves evolving in a constant-density medium with $n = 1\,\mathrm{cm}^{-3}$ (left panels) and $n = 10^{-2}\,\mathrm{cm}^{-3}$ (right panels), which are decelerating in a constant-density medium. The synchrotron light curves are shown in X-ray (1 keV; green), optical (R-band; brown) and radio (3 GHz; red) bands. The parameter values used are $E = 5 \times 10^{50}\,\mathrm{erg}$, $\theta_{\mathrm{j}} = 3\,\mathrm{deg}$, $\theta_{\mathrm{obs}} = 6\,\mathrm{deg}$, $\Gamma = 100$, $\varepsilon_{\mathrm{e}} = 0.1$, $p = 2.5$, $\zeta_e = 1.0$ and $\varepsilon_{\mathrm{B}} = 10^{-2}$. Upper limits are taken from .

ANALYTICAL SYNCHROTRON AFTERGLOW MODEL FROM AN OFF-AXIS OUTFLOW

*2.1 Coasting phase*

During the coasting phase, the bulk Lorentz factor is constant. The minimum and the cooling electron Lorentz factor are given by

$$\gamma_m = \gamma_m^0 \, g(p)\, \varepsilon_{e,-1}\zeta_e^{-1}\Gamma_{2.5},$$
$$\gamma_c = \gamma_c^0 \left(\frac{1+z}{1.022}\right)^{1-k} (1+Y)^{-1}\varepsilon_{B,-4}^{-1}A_k^{-1}\,\Gamma_{2.5}^{-1}\,f(\Delta\theta)^{k-1}t^{k-1},$$

where $f(\Delta\theta) \equiv \frac{1}{1-\mu\beta}$. The synchrotron spectral breaks and maximum flux are

$$\nu_m \simeq \nu_m^0 \left(\frac{1+z}{1.022}\right)^{\frac{k-2}{2}} g(p)^2\,\zeta_e^{-2}\varepsilon_{e,-1}^2\,\varepsilon_{B,-4}^{\frac{1}{2}}\,A_k^{\frac{1}{2}}\,f(\Delta\theta)^{\frac{2-k}{2}}\Gamma_{2.5}^2\,t^{-\frac{k}{2}}$$

$$\nu_c \simeq \nu_c^0 \left(\frac{1+z}{1.022}\right)^{\frac{2-3k}{2}} (1+Y)^{-2}\,\varepsilon_{B,-4}^{-\frac{3}{2}}A_k^{-\frac{3}{2}}\,f(\Delta\theta)^{\frac{3k-2}{2}}\Gamma_{2.5}^{-2}\,t^{\frac{3k-4}{2}}$$

$$F_{\max} \simeq F_{\max}^0 \left(\frac{1+z}{1.022}\right)^{\frac{3k-2}{2}} \zeta_e\,\varepsilon_{B,-4}^{\frac{1}{2}}A_k^{\frac{3}{2}}\,f(\Delta\theta)^{\frac{12-3k}{2}}d_{z,28.3}^{-2}\Gamma_{2.5}^{-2}\,t^{\frac{6-3k}{2}}\,. \tag{A1}$$

In the self-absorption regime, the spectral breaks are

$$\nu_{a,1} \simeq \nu_{a,1}^0\,g(p)^{-1}\left(\frac{1+z}{1.022}\right)^{\frac{4(k-2)}{5}} \zeta_e^{\frac{8}{5}}A_k^{\frac{4}{5}}\varepsilon_{e,-1}^{-1}\varepsilon_{B,-4}^{\frac{1}{5}}\,f(\Delta\theta)^{\frac{4(2-k)}{5}}\Gamma_{2.5}^{-\frac{8}{5}}t^{\frac{3-4k}{5}}$$

$$\nu_{a,2} \simeq \nu_{a,2}^0\,g(p)^{\frac{2(p-1)}{p+4}}\left(\frac{1+z}{1.022}\right)^{\frac{(k-2)(p+6)}{2(p+4)}} \zeta_e^{\frac{2(2-p)}{p+4}}A_k^{\frac{p+6}{2(p+4)}}\varepsilon_{B,-4}^{\frac{p+2}{2(p+4)}}\varepsilon_{e,-1}^{\frac{2(p-1)}{p+4}}\,f(\Delta\theta)^{\frac{(2-k)(p+6)}{2(p+4)}}\Gamma_{2.5}^{\frac{2(p-2)}{p+4}}t^{\frac{4-k(p+6)}{2(p+4)}}$$

$$\nu_{a,3} \simeq \nu_{a,3}^0\left(\frac{1+z}{1.022}\right)^{\frac{9k-13}{5}} \zeta_e^{\frac{3}{5}}(1+Y)A_k^{\frac{9}{5}}\varepsilon_{B,-4}^{\frac{6}{5}}f(\Delta\theta)^{\frac{13-9k}{5}}\Gamma_{2.5}^{\frac{2}{5}}t^{\frac{8-9k}{5}}\,. \tag{A2}$$

Given the spectral breaks and the maximum flux from eqs. A1 and A2, the evolution of synchrotron light curves through the spectral and temporal indexes are listed in Table 1. Similarly, the closure relations for each cooling condition during the coasting phase are reported in Table 2.

*2.2 Deceleration phase (Off-axis afterglow emission)*

During the deceleration phase before afterglow emission enters in the observer's field of view, the bulk Lorentz factor is given by Eq. 4. The minimum and cooling electron Lorentz factors are given by

$$\gamma_m = \gamma_m^0\left(\frac{1+z}{1.022}\right)^{\frac{3-k}{2}} \zeta_e^{-1}A_k^{-\frac{1}{2}}\varepsilon_{e,-1}\theta_{j,10}^{-1}\Delta\theta_{15}^{3-k}E_{54}^{\frac{1}{2}}t_{6.7}^{\frac{k-3}{2}}$$

$$\gamma_c = \gamma_c^0\left(\frac{1+z}{1.022}\right)^{-\frac{k+1}{2}} A_k^{-\frac{1}{2}}(1+Y)^{-1}\varepsilon_{B,-4}^{-1}\theta_{j,5}\Delta\theta_{15}^{-(k+1)}E_{54}^{-\frac{1}{2}}t_{6.7}^{\frac{k+1}{2}}\,,$$

which correspond to a comoving magnetic field given by $B' \propto \left(\frac{1+z}{1.022}\right)^{\frac{3}{2}}\varepsilon_{B,-4}^{\frac{1}{2}}\theta_{j,10}^{-1}\Delta\theta_{15}^3 E_{54}^{\frac{1}{2}}t_{6.7}^{-\frac{3}{2}}$. The synchrotron spectral breaks and the maximum flux can be written as

$$\nu_m = \nu_m^0\left(\frac{1+z}{1.022}\right)^{\frac{4-k}{2}} \zeta_e^{-2}A_k^{-\frac{1}{2}}\varepsilon_{e,-1}^2\varepsilon_{B,-4}^{\frac{1}{2}}\theta_{j,10}^{-2}\Delta\theta_{15}^{4-k}E_{54}t_{6.7}^{\frac{k-6}{2}}$$

$$\nu_c = \nu_c^0\left(\frac{1+z}{1.022}\right)^{-\frac{k+4}{2}} A_k^{-\frac{1}{2}}(1+Y)^{-2}\varepsilon_{B,-4}^{-\frac{3}{2}}\theta_{j,10}^2\Delta\theta_{15}^{-(k+4)}E_{54}^{-1}t_{6.7}^{\frac{k+2}{2}}$$

$$F_{\max} = F_{\max}^0\left(\frac{1+z}{1.022}\right)^{\frac{5k-8}{2}} \zeta_e A_k^{\frac{5}{2}}\varepsilon_{B,-4}^{\frac{1}{2}}d_{z,28.3}^{-2}\theta_{j,10}^2\Delta\theta_{15}^{5k-18}E_{54}^{-1}t_{6.7}^{\frac{12-5k}{2}}\,. \tag{A3}$$

In the self-absorption regime, the spectral breaks are given by

$$\nu_{a,1} \simeq \nu_{a,1}^0\left(\frac{1+z}{1.022}\right)^{\frac{4(2k-5)}{5}} \zeta_e^{\frac{8}{5}}A_k^{\frac{8}{5}}\varepsilon_{e,-1}^{-1}\varepsilon_{B,-4}^{\frac{1}{5}}\theta_{j,10}^{\frac{8}{5}}\Delta\theta_{15}^{\frac{8(2k-5)}{5}}E_{54}^{-\frac{4}{5}}t_{6.7}^{\frac{15-8k}{5}}$$

$$\nu_{a,2} \simeq \nu_{a,2}^0 \left(\frac{1+z}{1.022}\right)^{-\frac{24-10k-4p+kp}{2(p+4)}} \zeta_e^{\frac{2(2-p)}{p+4}} A_k^{\frac{10-p}{2(p+4)}} \varepsilon_{B,-4}^{\frac{p+2}{2(p+4)}} \varepsilon_{e,-1}^{\frac{2(p-1)}{p+4}} \theta_{j,10}^{\frac{2(2-p)}{p+4}} \Delta\theta_{15}^{\frac{4(p-6)-k(p-10)}{p+4}} E_{54}^{\frac{p-2}{p+4}} t_4^{\frac{16-10k-6p+kp}{2(p+4)}}$$

$$\nu_{a,3} \simeq \nu_{a,3}^0 \left(\frac{1+z}{1.022}\right)^{\frac{2(4k-5)}{5}} \zeta_e^{\frac{3}{5}} (1+Y) A_k^{\frac{8}{5}} \varepsilon_{B,-4}^{\frac{6}{5}} \theta_{j,10}^{-\frac{2}{5}} \Delta\theta_{15}^{\frac{4(4k-5)}{5}} E_{54}^{\frac{1}{5}} t_{6.7}^{\frac{5-8k}{5}} . \tag{A4}$$

Given the spectral breaks and the maximum flux from eqs. A3 and A4, the evolution of synchrotron light curves through the spectral and temporal indexes are listed in Table 1. Similarly, the closure relations for each cooling condition during the deceleration phase before the afterglow emission is seemed off-axis are reported in Table 2.

### 2.3 Deceleration phase (On-axis afterglow emission)

As the bulk Lorentz factor becomes $\Gamma \sim \Delta\theta^{-1}$, the afterglow emission becomes on-axis, being in our field of view. For the adiabatic regime, the bulk Lorentz factor is given by Eq. 5. As $\Delta\theta$ becomes close to zero ($\Delta\theta \approx 0$), the bulk Lorentz factor during the relativistic phase $\Gamma \approx 1/2(1-\beta)$, and therefore, the Doppler factor can be approximated to $\delta_D \approx 2\Gamma$. The minimum and cooling electron Lorentz factors are given by

$$\gamma_m = \gamma_m^0 \left(\frac{1+z}{1.022}\right)^{\frac{3-k}{2(4-k)}} \zeta_e^{-1} A_k^{-\frac{1}{2(4-k)}} \varepsilon_{e,-1} E_{54}^{\frac{1}{2(4-k)}} t_3^{\frac{k-3}{2(4-k)}}$$

$$\gamma_c = \gamma_c^0 \left(\frac{1+z}{1.022}\right)^{-\frac{k+1}{2(4-k)}} A_k^{-\frac{5}{2(4-k)}} (1+Y)^{-1} \varepsilon_{B,-4}^{-1} E_{54}^{\frac{2k-3}{2(4-k)}} t_3^{\frac{k+1}{2(4-k)}} ,$$

which correspond to a comoving magnetic field given by $B' \propto \left(\frac{1+z}{1.022}\right)^{\frac{3}{2(4-k)}} A_k^{\frac{3}{2(4-k)}} \varepsilon_{B,-4}^{\frac{1}{2}} E_{54}^{\frac{1-k}{2(4-k)}} t_3^{-\frac{3}{2(4-k)}}$. The synchrotron spectral breaks and the maximum flux can be written as

$$\nu_m = \nu_m^0 \left(\frac{1+z}{1.022}\right)^{\frac{1}{2}} \zeta_e^{-2} \varepsilon_{e,-1}^2 \varepsilon_{B,-4}^{\frac{1}{2}} E_{54}^{\frac{1}{2}} t_3^{-\frac{3}{2}}$$

$$\nu_c = \nu_c^0 \left(\frac{1+z}{1.022}\right)^{-\frac{k+4}{2(4-k)}} A_k^{-\frac{4}{4-k}} (1+Y)^{-2} \varepsilon_{B,-4}^{-\frac{3}{2}} E_{54}^{\frac{3k-4}{2(4-k)}} t_3^{\frac{3k-4}{2(4-k)}}$$

$$F_{max} = F_{max}^0 \left(\frac{1+z}{1.022}\right)^{\frac{16-3k}{2(4-k)}} \zeta_e A_k^{\frac{2}{4-k}} \varepsilon_{B,-4}^{\frac{1}{2}} d_{z,28.3}^{-2} E_{54}^{\frac{8-3k}{2(4-k)}} t_3^{-\frac{k}{2(4-k)}} . \tag{A5}$$

In the self-absorption regime, the spectral breaks are given by

$$\nu_{a,1} \simeq \nu_{a,1}^0 \left(\frac{1+z}{1.022}\right)^{\frac{4(2k-5)}{5(4-k)}} \zeta_e^{\frac{8}{5}} A_k^{\frac{12}{5(4-k)}} \varepsilon_{e,-1}^{-1} \varepsilon_{B,-4}^{\frac{1}{5}} E_{54}^{-\frac{4(1-k)}{5(4-k)}} t_3^{-\frac{3k}{5(4-k)}}$$

$$\nu_{a,2} \simeq \nu_{a,2}^0 \left(\frac{1+z}{1.022}\right)^{\frac{4(p-6)-k(p-10)}{2(4-k)(p+4)}} \zeta_e^{\frac{2(2-p)}{p+4}} A_k^{\frac{8}{(4-k)(p+4)}} \varepsilon_{B,-4}^{\frac{p+2}{2(p+4)}} \varepsilon_{e,-1}^{\frac{2(p-1)}{p+4}} E_{54}^{\frac{4(p+2)-k(p+6)}{2(4-k)(p+4)}} t_3^{-\frac{4(3p+2)+k(2-3p)}{2(4-k)(p+4)}}$$

$$\nu_{a,3} \simeq \nu_{a,3}^0 \left(\frac{1+z}{1.022}\right)^{\frac{2(4k-5)}{5(4-k)}} \zeta_e^{\frac{3}{5}} (1+Y) A_k^{\frac{22}{5(4-k)}} \varepsilon_{B,-4}^{\frac{6}{5}} E_{54}^{\frac{14-9k}{5(4-k)}} t_3^{-\frac{10+3k}{5(4-k)}} . \tag{A6}$$

Given the spectral breaks and the maximum flux from eqs. A5 and A6, the evolution of synchrotron light curves through the spectral and temporal indexes are listed in Table 1. Similarly, the closure relations for each cooling condition during the deceleration phase once the afterglow emission is observer's field of view are reported in Table 2.

### 2.4 Post-jet-break decay phase

The bulk Lorentz factor decelerating in the stratified environment far away from the progenitor becomes $\Gamma \sim \theta_j^{-1}$ (Sari et al. 1999; Granot et al. 2002, 2017). During the post-jet-break decay phase, the bulk Lorentz factor evolves following Eq. 6. The minimum and cooling electron Lorentz factors are given by

$$\gamma_m = \gamma_m^0 \left(\frac{1+z}{1.022}\right)^{\frac{1}{2}} \zeta_e^{-1} \varepsilon_{e,-1} A_k^{\frac{1}{2(k-3)}} E_{54}^{-\frac{1}{2(k-3)}} t_7^{-\frac{1}{2}}$$

$$\gamma_c = \gamma_c^0 \left(\frac{1+z}{1.022}\right)^{-\frac{1}{2}} (1+Y)^{-1} \varepsilon_{B,-4}^{-1} A_k^{\frac{3}{2(k-3)}} E_{54}^{\frac{3-2k}{2(k-3)}} t_7^{\frac{1}{2}} .$$

In this case, the synchrotron spectral breaks and the maximum flux become

$$\nu_m \simeq \nu_m^0 \left(\frac{1+z}{1.022}\right) \zeta_e^{-2} A_k^{\frac{1}{2(k-3)}} \varepsilon_{e,-1}^2 \varepsilon_{B,-4}^{\frac{1}{2}} E_{54}^{\frac{k-4}{2(k-3)}} t_7^{-2}$$

$$\nu_c \simeq \nu_c^0 \left(\frac{1+z}{1.022}\right)^{-1} A_k^{\frac{5}{2(k-3)}} \varepsilon_{B,-4}^{-\frac{3}{2}} (1+Y)^{-2} E_{54}^{\frac{4-3k}{2(k-3)}} t_7$$

$$F_{\max} \simeq F_{\max}^0 \left( \frac{1+z}{1.022} \right)^3 \zeta_e A_k^{\frac{1}{2(3-k)}} \varepsilon_{B,-4}^{\frac{1}{2}} d_{z,28.3}^{-2} E_{54}^{\frac{8-3k}{2(3-k)}} t_7^{-1} \,. \tag{A7}$$

Taking into account the self-absorption regime, the spectral breaks are given by

$$\nu_{a,1} = \nu_{a,1}^0 \left( \frac{1+z}{1.022} \right)^{-\frac{4}{5}} \zeta_e^{\frac{8}{5}} A_k^{\frac{8}{5(3-k)}} \varepsilon_{e,-1}^{-1} \varepsilon_{B,-4}^{\frac{1}{5}} E_{54}^{\frac{4(k-1)}{5(k-3)}} t_7^{-\frac{1}{5}}$$

$$\nu_{a,2} = \nu_{a,2}^0 \left( \frac{1+z}{1.022} \right)^{\frac{p-2}{p+4}} \zeta_e^{\frac{2(2-p)}{p+4}} A_k^{\frac{p-10}{2(p+4)(k-3)}} \varepsilon_{B,-4}^{\frac{p+2}{2(p+4)}} \varepsilon_{e,-1}^{\frac{2(p-1)}{p+4}} E_{54}^{\frac{k(p+6)-4(p+2)}{2(p+4)(k-3)}} t_7^{-\frac{2(p+1)}{p+4}} \,. \tag{A8}$$

Given the spectral breaks and the maximum flux from eqs. A7 and A8, the evolution of synchrotron light curves through the spectral and temporal indexes are listed in Table 1. Similarly, the closure relations for each cooling condition during the post-jet-break decay phase are reported in Table 2.

The terms $\gamma_m^0$, $\gamma_c^0$, $\nu_m^0$, $\nu_c^0$, $F_{\max}^0$, $\nu_{a,1}^0$, $\nu_{a,2}^0$ and $\nu_{a,3}^0$ during the coasting, deceleration (off- and on-axis emission) and the post-jet-break decay phases are shown in Table 3 for k = 0, 1, 1.5 and 2.

# Afterglow Polarization from Off-Axis GRB Jets

A. C. Caligula Do E. S. Pedreira,[1] N. Fraija,[1] A. Galvan-Gamez,[1] B. Betancourt Kamenetskaia,[2] P. Veres,[3] M.G. Dainotti,[4, 5, 6, 7] S. Dichiara,[8, 9] and R. L. Becerra[10]

[1]*Instituto de Astronomía, Universidad Nacional Autónoma de México, Circuito Exterior, C.U., A. Postal 70-264, 04510, CDMX, Mexico*
[2]*TUM Physics Department, Technical University of Munich, James-Franck-Str, 85748 Garching, Germany*
[3]*Center for Space Plasma and Aeronomic Research (CSPAR), University of Alabama in Huntsville, Huntsville, AL 35899, USA*
[4]*Division of Science, National Astronomical Observatory of Japan, 2-21-1 Osawa, Mitaka, Tokyo 181-8588, Japan*
[5]*The Graduate University for Advanced Studies (SOKENDAI), 2-21-1 Osawa, Mitaka, Tokyo 181-8588, Japan*
[6]*Space Science Institute, 4750 Walnut Street, Boulder, CO 80301, USA*
[7]*SLAC National Accelerator Laboratory, 2575 Sand Hill Road, Menlo Park, CA 94025, USA*
[8]*Department of Astronomy, University of Maryland, College Park, MD 20742-4111, USA*
[9]*Astrophysics Science Division, NASA Goddard Space Flight Center, 8800 Greenbelt Rd, Greenbelt, MD 20771, USA*
[10]*Instituto de Ciencias Nucleares, Universidad Nacional Autónoma de México, Apartado Postal 70-264, 04510 México, CDMX, Mexico*

## ABSTRACT

As we further our studies on Gamma-ray bursts (GRBs), both on theoretical models and observational tools, more and more options begin to open for exploration of its physical properties. As transient events primarily dominated by synchrotron radiation, it is expected that the synchrotron photons emitted by GRBs should present some degree of polarization throughout the evolution of the burst. Whereas observing this polarization can still be challenging due to the constraints on observational tools, especially for short GRBs, it is paramount that the groundwork is laid for the day we have abundant data. In this work, we present a polarization model linked with an off-axis spreading top-hat jet synchrotron scenario in a stratified environment with a density profile $n(r) \propto r^{-k}$. We present this model's expected temporal polarization evolution for a realistic set of afterglow parameters constrained within the values observed in the GRB literature for four degrees of stratification $k = 0, 1, 1.5$ and $2$ and two magnetic field configurations with high extreme anisotropy. We apply this model and predict polarization from a set of GRBs exhibiting off-axis afterglow emission. In particular, for GRB 170817A, we use the available polarimetric upper limits to rule out the possibility of a extremely anisotropic configuration for the magnetic field.

*Keywords:* polarization; grbs; synchrotron; particle acceleration; magnetic fields;

## 1. INTRODUCTION

Gamma-ray bursts (GRBs) are the most luminous phenomena in the Universe. They originate from the deaths of massive stars (Woosley 1993; Paczyński 1998; Woosley & Bloom 2006; Cano et al. 2017) or the merging of two compact objects, like neutron stars (NSs; Eichler et al. 1989; Duncan & Thompson 1992; Usov 1992; Thompson 1994; Metzger et al. 2011) or a NS with a black hole (BH, Narayan et al. 1992). GRBs are analyzed according to their phenomenology observed during the early and late phases and generally described through the fireball model (Sari et al. 1998) to differentiate the distinct origins. The early and main emission, called the "prompt emission". is observed from hard X-rays to $\gamma$-rays and explained through interactions of internal shells of material thrown violently from the central engine at different ve-

locities. The late emission, called "afterglow" (e.g., Costa et al. 1997; Sari et al. 1998; Granot & Sari 2002; van Paradijs et al. 1997; Piro et al. 1998; Gehrels et al. 2009; Wang et al. 2015), corresponds to the long-lasting multiwavelength emission observed in gamma-rays, X-rays, optical, and radio. The afterglow is usually modelled with synchrotron emission generated when the relativistic outflow transfers a significant fraction of its energy to the external medium. GRBs are usually classified as long GRBs (lGRBs) and short (sGRBs), depending on their duration: $T_{90} \leq 2\,\mathrm{s}$ or $T_{90} \geq 2\,\mathrm{s}$,[1] respectively (Mazets et al. 1981; Kouveliotou et al. 1993).

---

[1] $T_{90}$ is the time over which a GRB releases from 5% to 95% of the total measured counts.

It is thought that the primary emission mechanism in GRB afterglows is synchrotron emission (Kumar & Zhang 2015; Mészáros & Rees 1997). This synchrotron emission, arising from radiating electrons at the forward shock, is dependent on the local magnetic field. The magnetic field behind the shock can originate from the compression of an existing magnetic field within the interstellar medium (Laing 1980; Teboul & Shaviv 2021) and from shock-generated two-stream instabilities (Weibel 1959; Medvedev & Loeb 1999). The interstellar medium magnetic field can be composed of multiple components: a large scale coherent component, a small scale random component, and a striated component that changes directions randomly on small scales but remains aligned over large scales (Boulanger et al. 2018); while the magnetic field generated by plasma instabilities is random in orientation but mostly confined to the plane of the shock (Gill & Granot 2020). There is a tremendous challenge in pinning down the source and configuration of those fields and other physical parameters of GRBs through modeling. This has led to the necessity of other avenues of exploration of these complex systems. One such means is linear polarization.

Synchrotron radiation is naturally polarized. The flux of synchrotron photons emitted throughout the shock peaks on gamma-rays in seconds, on lower frequencies in minutes to hours (e.g., optical bands), eventually reaching radio after a day. Linear polarization has been measured, up to a few percent, from the afterglow of several GRBs. Some examples are GRB 191221B ($\Pi = 1.2\%$, Buckley et al. (2021)) for the late afterglow, GRB 190114C ($\Pi = 0.8 \pm 0.13\%$, Laskar et al. (2019)) on the radio band, and the upper limits determinations of GRB 991216 (yielding $\Pi < 7\%$, Granot & Taylor 2005) and GRB 170817A (yielding $\Pi < 12\%$, on the 2.8 GHz radio band Corsi et al. 2018). Since the degree of polarization is intrinsically dependent upon the configuration of the magnetic field and jet structure, analysis of the polarization degree across all epochs of the GRB allows us to look further into these configurations and, consequently, their sources. Many researchers, such as Granot & Königl (2003); Gill et al. (2020); Rossi et al. (2004); Lyutikov et al. (2003); Nakar et al. (2003); Teboul & Shaviv (2021); Stringer & Lazzati (2020), have already addressed their investigation on the viability of using polarization models to obtain information related to the source. One of the most significant obstacles has been the scarcity of polarization data for GRBs due to the unfortunate small number of orbital polarimeters and the typical difficulties in observing these luminous events. Despite that, advances have been made in the area, and thanks to efforts like the POLAR project (Orsi & Polar Collaboration 2011), it is expected that in future years we should have an abundance of data for the test of different models.

This work extends the analytical synchrotron afterglow scenario, of the off-axis jet in a stratified environment used to describe the multi-wavelength observations in GRB 170817A, and a sample of some GRBs showing off-axis emission with similar characteristics. We present, in general, the temporal evolution of polarization from the synchrotron afterglow stratified model and compute the expected polarization for bursts previously modeled by an off-axis emission: GRB 080503 (Perley et al. 2009; Gao et al. 2015), GRB 140903A (Troja et al. 2016; Zhang et al. 2017), GRB 150101B (Troja et al. 2018), GRB 160821B (Troja et al. 2019), GRB 170817A (Kasliwal et al. 2017; Lamb & Kobayashi 2017; Mooley et al. 2018; Hotokezaka et al. 2018; Fraija et al. 2019b) and SN2020bvc (also, see Fraija et al. 2022, for a more detailed discussion on the modeling of these events) – which is thought to be linked to an off-axis GRB (Izzo et al. 2020). In particular, for GRB 170817A, we use the available polarimetric upper limits. With this in mind, the structure of the paper is as follows. In Section 2, we briefly show the off-axis jet synchrotron model derived in Fraija et al. (2022). In Section 3, we introduce the polarization model to be utilized throughout this paper. In Section 4, we compute the expected polarization and present the results for a sample of bursts showing off-axis afterglow emission. Finally, in Section 5, we summarize our work and offer our concluding remarks.

## 2. SYNCHROTRON POLARIZATION FROM AN OFF-AXIS TOP-HAT JET

In the following section, we present the off-axis equations of the synchrotron scenario presented in Fraija et al. (2022), which is applied to the polarization model for time-evolving calculations.

### 2.1. Synchrotron scenario

In forward-shock models, accelerated electrons are described by taking into account their Lorentz factors ($\gamma_e$) and the electron power index $p$. This leads to a distribution of the form $N(\gamma_e)\, d\gamma_e \propto \gamma_e^{-p}\, d\gamma_e$ for $\gamma_m \leq \gamma_e$, where $\gamma_m = m_{\rm p}/m_{\rm e} g(p)\varepsilon_{\rm e}(\Gamma - 1)\zeta_e^{-1}$ is the minimum electron Lorentz factor with $\Gamma$ the bulk Lorentz factor, $m_{\rm p}$ and $m_{\rm e}$ the proton and electron mass, respectively, $\varepsilon_{\rm e}$ the fraction of energy given to accelerate electrons, $\zeta_e$ the fraction of electrons that were accelerated by the shock front (Fan & Piran 2006) and $g(p) = \frac{p-2}{p-1}$. The comoving magnetic field strength in the blast wave can be expressed as $B'^2/(8\pi) = \varepsilon_B e$, where knowledge of the energy density $e = [(\hat{\gamma}\Gamma + 1)/(\hat{\gamma} - 1)](\Gamma - 1)n(r)m_p c^2$, adiabatic index $\hat{\gamma}$ (Huang et al. 1999) and fraction of energy

provided to the magnetic field ($\varepsilon_B$) is necessary. In what follows, we adopt the unprimed and prime terms to refer them in the observer and comoving frames, respectively.

In this work, we will consider the evolution of the forward shock in a stratified medium. To this end, we model the surrounding number density as $n(r) = A_k r^{-k}$ with $A_k = n_0(r_0) r_0^k$, where $n_0$ is the density at initial radius $r_0$. The stratification parameter, k, lies in the range $0 \leq k < 3$, with k = 0 corresponding to a constant-density medium, and k = 2 to a stellar wind ejected by its progenitor. The cooling electron Lorentz factor is written as $\gamma_c = (6\pi m_e c/\sigma_T)(1+Y)^{-1}\Gamma^{-1}B'^{-2}t^{-1}$, where $\sigma_T$ is the Thomson cross-section and $Y$ is the Compton parameter (Sari & Esin 2001; Wang et al. 2010). The synchrotron spectral breaks can now be expressed in terms of previously defined quantities as $\nu'_i = q_e/(2\pi m_e c)\gamma_i^2 B'$, where the sub-index i = m and c will stand for the characteristic or cooling break, respectively. The constants $q_e$ and $c$ are the elementary charge and the speed of light, respectively. The synchrotron radiation power per electron in the comoving frame is given by $P'_{\nu'_m} \simeq \sqrt{3}q_e^3/(m_e c^2)B'$ (e.g., see Sari et al. 1998; Fraija 2015). Considering the total number of emitting electrons $N_e = (\Omega/4\pi)\,n(r)\frac{4\pi}{3-k}r^3$ and also taking into account the transformation laws for the solid angle ($\Omega = \Omega'/\delta_D^2$), the radiation power ($P_{\nu_m} = \delta_D/(1+z)P'_{\nu'_m}$) and the spectral breaks ($\nu_i = \delta_D/(1+z)\nu'_i$), the maximum flux given by synchrotron radiation is

$$F_{\nu,\max} = \frac{(1+z)^2\delta_D^3}{4\pi d_z^2}N_e P'_{\nu'_m}\,, \qquad (1)$$

where $d_z = (1+z)\frac{c}{H_0}\int_0^z \frac{d\tilde{z}}{\sqrt{\Omega_M(1+\tilde{z})^3+\Omega_\Lambda}}$ (Weinberg 1972) is the luminosity distance, $r = \delta_D/(1+z)\Gamma\beta ct$ is the shock radius, and $\delta_D = \frac{1}{\Gamma(1-\mu\beta)}$ is the Doppler factor with $\mu = \cos\Delta\theta$, $\beta = v/c$, where $v$ is the velocity of the material, and $\Delta\theta = \theta_{obs} - \theta_j$ is given by the viewing angle ($\theta_{obs}$) and the half-opening angle of the jet ($\theta_j$). For the cosmological constants, we assume a spatially flat universe $\Lambda$CDM model with $H_0 = 69.6\,\mathrm{km\,s^{-1}\,Mpc^{-1}}$, $\Omega_M = 0.286$ and $\Omega_\Lambda = 0.714$ (Planck Collaboration et al. 2016).

We assume an adiabatic evolution of the forward shock with an isotropic equivalent-kinetic energy $E = \frac{4\pi}{3-k}r^{3-k}m_p c^2 A_k \Gamma^2$ (Blandford-McKee solution; Blandford & McKee 1976) and a radial distance $r = c\beta t/[(1+z)(1-\beta\mu)]$. Then, the evolution of the bulk Lorentz factor is given by

$$\Gamma = \left(\frac{3}{4\pi\,m_p c^{5-k}}\right)^{\frac{1}{2}}(1+z)^{-\frac{k-3}{2}}(1-\beta\cos\Delta\theta)^{-\frac{k-3}{2}}A_k^{-\frac{1}{2}}$$
$$\times E^{\frac{1}{2}}t^{\frac{k-3}{2}}\,, \quad (2)$$

with $\beta = \sqrt{\Gamma^2-1}/\Gamma$. The deceleration time scale $t_{dec}$ can be defined using Eq. 2.

During the deceleration phase before afterglow emission enters in the observer's field of view, the bulk Lorentz factor is given by Eq. 2. The minimum and cooling electron Lorentz factors are given by

$$\gamma_m = \gamma_m^0\left(\frac{1+z}{1.025}\right)^{\frac{3-k}{2}}\zeta_e^{-1}A_k^{-\frac{1}{2}}\varepsilon_{e,-1}\theta_{j,5}^{-1}\Delta\theta_{15}^{3-k}E_{51}^{\frac{1}{2}}t_{7.0}^{\frac{k-3}{2}}$$

$$\gamma_c = \gamma_c^0\left(\frac{1+z}{1.025}\right)^{-\frac{k+1}{2}}A_k^{-\frac{1}{2}}(1+Y)^{-1}\varepsilon_{B,-3}^{-1}\theta_{j,5}\Delta\theta_{15}^{-(k+1)}E_{51}^{-\frac{1}{2}}$$
$$\times t_{7.0}^{\frac{k+1}{2}}\,,$$

respectively, which correspond to a comoving magnetic field given by $B' \propto \left(\frac{1+z}{1.025}\right)^{\frac{3}{2}}\varepsilon_{B,-3}^{\frac{1}{2}}\theta_{j,5}^{-1}\Delta\theta_{15}^{3}E_{51}^{\frac{1}{2}}t_{7.0}^{-\frac{3}{2}}$. The synchrotron spectral breaks and the maximum flux can be written as

$$\nu_m = \nu_m^0\left(\frac{1+z}{1.025}\right)^{\frac{4-k}{2}}\zeta_e^{-2}A_k^{-\frac{1}{2}}\varepsilon_{e,-1}^2\varepsilon_{B,-3}^{\frac{1}{2}}\theta_{j,5}^{-2}\Delta\theta_{15}^{4-k}E_{51}^{\frac{k-6}{2}}t_{7.0}^{\frac{k-6}{2}}$$

$$\nu_c = \nu_c^0\left(\frac{1+z}{1.025}\right)^{-\frac{k+4}{2}}A_k^{-\frac{1}{2}}(1+Y)^{-2}\varepsilon_{B,-3}^{-\frac{3}{2}}\theta_{j,5}^2\Delta\theta_{15}^{-(k+4)}$$
$$\times E_{51}^{-1}t_{7.0}^{\frac{k+2}{2}}$$

$$F_{\max} = F_{\max}^0\left(\frac{1+z}{1.025}\right)^{\frac{5k-8}{2}}\zeta_e A_k^{\frac{5}{2}}\varepsilon_{B,-3}^{\frac{1}{2}}d_{z,26.5}^{-2}\theta_{j,5}^2\Delta\theta_{15}^{5k-18}$$
$$\times E_{51}^{-1}t_{7.0}^{\frac{12-5k}{2}}\,, \quad (3)$$

respectively. The synchrotron spectral breaks in the self-absorption regime are derived from $\nu'_{a,1} = \nu'_c\tau_{0,m}^{\frac{3}{5}}$, $\nu'_{a,2} = \nu'_m\tau_{0,m}^{\frac{2}{p+4}}$ and $\nu'_{a,3} = \nu'_m\tau_{0,c}^{\frac{3}{5}}$ with the optical depth given by $\tau_{0,i} \simeq \frac{5}{3-k}\frac{q_e n(r)r}{B'\gamma_i^5}$, with $r$ the shock radius (Panaitescu & Mészáros 1998). Therefore, the spectral breaks in the self-absorption regime are given by

$$\nu_{a,1} \simeq \nu_{a,1}^0\left(\frac{1+z}{1.025}\right)^{\frac{4(2k-5)}{5}}\zeta_e^{\frac{8}{5}}A_k^{\frac{8}{5}}\varepsilon_{e,-1}^{-1}\varepsilon_{B,-3}^{\frac{1}{5}}\theta_{j,5}^{\frac{8}{5}}\Delta\theta_{15}^{\frac{8(2k-5)}{5}}$$
$$\times E_{51}^{-\frac{4}{5}}t_{7.0}^{\frac{15-8k}{5}}$$

$$\nu_{a,2} \simeq \nu_{a,2}^0\left(\frac{1+z}{1.025}\right)^{-\frac{24-10k-4p+kp}{2(p+4)}}\zeta_e^{\frac{2(2-p)}{p+4}}A_k^{\frac{10-p}{2(p+4)}}\varepsilon_{B,-3}^{\frac{p+2}{2(p+4)}}\varepsilon_{e,-1}^{\frac{2(p-1)}{p+4}}$$
$$\theta_{j,5}^{\frac{2(2-p)}{p+4}}\Delta\theta_{15}^{\frac{4(p-6)-k(p-10)}{p+4}}E_{51}^{\frac{p-2}{p+4}}t_{7.0}^{\frac{16-10k-6p+kp}{2(p+4)}}$$

$$\nu_{a,3} \simeq \nu_{a,3}^0\left(\frac{1+z}{1.025}\right)^{\frac{2(4k-5)}{5}}\zeta_e^{\frac{3}{5}}(1+Y)A_k^{\frac{8}{5}}\varepsilon_{B,-3}^{\frac{6}{5}}\theta_{j,5}^{-\frac{2}{5}}\Delta\theta_{15}^{\frac{4(4k-5)}{5}}$$
$$\times E_{51}^{\frac{1}{5}}t_{7.0}^{\frac{5-8k}{5}}\,. \quad (4)$$

The dynamics of the model post the off-axis phase are explored in further detail in Fraija et al. (2022).

## 3. POLARIZATION MODEL

The phenomenon of polarization, the restriction of the vibrations on a wave partially or wholly to a specific geometrical orientation, in GRBs has been observed since

1999 (Covino et al. 2003). Polarization is typically attributed to synchrotron radiation behind the shock waves, which then makes it dependent on the magnetic field configuration and the geometry of the shock, as these will determine the polarization degree (Π) on each point and its integration over the unresolved image (Gill et al. 2020). The treatment is done by the Stokes parameters, I, Q, U, and V, and typically only linear polarization is considered. From here on forward, we will use the terms unprimed and prime to refer to them in the observer and comoving frames, respectively. In this case,

$$V = 0, \tag{5}$$

$$\frac{U}{I} = \Pi' \sin 2\theta_p, \tag{6}$$

$$\frac{Q}{I} = \Pi' \cos 2\theta_p, \tag{7}$$

$$\theta_p = \frac{1}{2} \arctan \frac{U}{Q}, \tag{8}$$

where $\theta_p$ is the polarization degree. The measured stokes parameters are the sum over the flux (Granot 2003), so

$$\frac{U}{I} = \frac{\int \mathrm{d}F_\nu \Pi' \sin 2\theta_p}{\int \mathrm{d}F_\nu}, \tag{9}$$

$$\frac{Q}{I} = \frac{\int \mathrm{d}F_\nu \Pi' \cos 2\theta_p}{\int \mathrm{d}F_\nu}, \tag{10}$$

and the polarization is given by

$$\Pi = \frac{\sqrt{Q^2 + U^2}}{I}. \tag{11}$$

In a thin shell scenario, $\mathrm{d}F_\nu \propto \delta_D^3 L'_{\nu'} \mathrm{d}\Omega$ where $L'_{\nu'}$ is the spectral luminosity and $\mathrm{d}\Omega$ is the element of solid angle of the fluid element in relation to the source. Using the approximations $\tilde{\mu} = \cos \tilde{\theta} \approx 1 - \tilde{\theta}^2/2$ and $\beta \approx 1 - 1/2\Gamma^2$, $\delta_D$ can be rewritten as $\delta_D \approx \frac{2\Gamma}{1+\tilde{\xi}}$, where $\beta$ is the velocity of the material in terms of the speed of light, $\tilde{\theta}$ the polar angle measured from the Line of Sight (LOS) and $\tilde{\xi} \equiv (\Gamma\tilde{\theta})^2$.

Assuming a power-law spectrum and dependency on the $r$, the luminosity can be described as being proportional to the frequency, magnetic field, and direction unity vector (Rybicki & Lightman 1979)

$$L'_{\nu'} \propto (\nu')^{-\alpha} (\sin \chi')^\epsilon r^m \propto (\nu')^{-\alpha} (1 - \hat{n}' \cdot \hat{B}')^{\epsilon/2} r^m. \tag{12}$$

We assume, throughout the text, a power-law spectrum and power-law dependency on emissitivy, furthermore we take that the emissivity is radially constant (i.e. $m = 0$; Gill et al. 2020). The index $\epsilon$ is dependent on the electron

distribution, and we take that $\epsilon = 1 + \alpha$, where $\alpha$ is the spectral index. The term $\chi$ here is the angle between the local magnetic field and the particle's direction of motion. Since synchrotron emission is highly beamed, the pitch angle is also between the velocity vector and magnetic field. The pitch angle, $\chi$, carries the geometric information of the problem, from the structure of the magnetic field ($\hat{B}'$) to the direction of emission ($\hat{n}'$). The geometrical idiosyncrasies of polarization can then be taken in consideration by averaging this factor over the local probability distribution of the magnetic field (see Eq. 15 of Gill et al. 2020),

$$\Lambda = \left\langle (1 - \hat{n}' \cdot \hat{B}')^{\epsilon/2} \right\rangle. \tag{13}$$

A Lorentz transformation can be done on either of the unit vectors such as $\hat{n} = \sin\theta_{\mathrm{obs}}\hat{x} + \cos\theta_{\mathrm{obs}}\hat{z}$, a normal vector with the direction of the emitting photon in a reference system where the jet axis is in the z-axis, or a prescription of $\hat{B}$, by using [see, Lyutikov et al. (2003)]

$$\hat{X}' = \frac{(1+\Gamma)\hat{X} + \Gamma^2(\hat{X} \cdot \mathbf{v})\mathbf{v}}{(1+\Gamma)\sqrt{1 + \Gamma^2(\hat{X} \cdot \mathbf{v})}}, \tag{14}$$

so that $\Lambda$ can be expressed in terms of different magnetic field configurations (Gill et al. 2020; Granot & Taylor 2005; Lyutikov et al. 2003; Granot 2003), as required.

The following equations (see Eqs. 28 and 29 of Gill et al. (2020))

$$\cos\psi(\tilde{\xi}) = \frac{(1-q)^2\xi_j - \tilde{\xi}}{2q\sqrt{\xi_j\tilde{\xi}}} \qquad q = \frac{\theta_{\mathrm{obs}}}{\theta_j}$$

$$\xi_j = (\Gamma\theta_j)^2, \qquad \xi_\pm = (1\pm q)^2\xi_j, \tag{15}$$

regarding the limits of integration of the polarization, can be used to link our synchrotron model to polarization by introducing the bulk Lorentz Factor and the dynamical evolution of the jet's half-opening angle, and thus the physical parameters of the system, obtained in Fraija et al. (2022). We want to emphasize that the $q$ parameter evolves with time $q = q(t) = \theta_{\mathrm{obs}}/\theta_j(t)$ for a spreading jet.

One of the still-unsolved mysteries of GRBs is the configuration of the magnetic field. As such, various possible configurations must be explored in a topic where magnetic field geometry is of paramount relevance, like polarization. The more used arguments for the symmetry of the magnetic field are varied based on the GRB epoch of relevance for each model. For a scenario where the afterglow is being modeled by a forward shock, two of the

most suitable configurations are a random perpendicular configuration, confined to the shock plane (i.e. a field with anisotropy factor $b \equiv \frac{2\langle B_\parallel^2 \rangle}{\langle B_\perp^2 \rangle} = 0$ ) and a parallel configuration along the velocity vector (i.e. a field with anisotropy factor $b \to \infty$). Here we limit ourselves to these cases — an ordered magnetic field parallel to the velocity vector and a random magnetic field generated on the forward shock. However, we would like to add that exploring more complex configurations, such as anisotropic magnetic fields (Gill & Granot 2020; Teboul & Shaviv 2021; Stringer & Lazzati 2020; Corsi et al. 2018) or evolving configurations, is warranted and needed.

*Ordered magnetic field (parallel configuration)* —The symmetry of the magnetic field configuration causes the polarization to vanish over the image if viewed on-axis ($\theta_{\rm obs} = 0$) or if the beaming cone is wholly contained within the jet aperture. To break the symmetry, the jet must be viewed close to its edge ($q \gtrsim 1 + \xi_j^{-1/2}$) where missing emission (from $\theta > \theta_j$) results only in partial cancellation (Waxman 2003). For the parallel configuration, the calculation follows Eq. 4 of Granot (2003), or using $\Lambda(\tilde\xi) = \Lambda_\parallel$ from equation 16 of Gill et al. (2020) on Eq. 30 of the same paper.

*Random magnetic field (perpendicular configuration)* —The same symmetry concerns regarding the parallel configuration carry over to the random magnetic field. The equation necessary to calculate this polarization follows equation 5 in (Granot 2003), or Equation 34 on Gill et al. (2020) when using $\Lambda(\tilde\xi) = \Lambda_\perp$.

### 3.1. *Polarization evolution in a stratified medium*

Figures 1 and 2 show the temporal evolution of the polarization degree for the parallel and perpendicular magnetic field configurations and four different possible scenarios to the bulk Lorentz factor defined with each density profile for $k = 0, 1, 1.5$, and 2. Table 2 shows the values utilized to generate these Figures. These generic values are chosen based on the typical ones found for each parameter in the GRB synchrotron literature. The values of observation angle are varied over a range between 1.2 and 5 times the initial opening angle of the jet. This range of values is shown in these figures with different colored lines, each standing for a value of $q_0 = \frac{\theta_{\rm obs}}{\theta_{j,0}}$, the ratio between the observation angle and the initial opening angle of the jet. Figure 3 shows the evolution of $q(t)$ for each value of $k$ mentioned above, where $\theta_j(t)$ is associated with the dynamical evolution of the jet (see

equations 1 to 4 of Huang et al. 2000).[2] It can be seen that the values of $q$ decline over time and evolves toward $q \to 0$. This is dictated by jet dynamics, as the opening angle of the jet expands as the jet evolves. By looking at higher values of $q_0$, such as $q_0 = 4$, we can see from the evolution of this parameter that $q \approx 1.9$ and 0.8 at $t = 0.9$ and 10 days, respectively, for $k = 0$. The angular evolution of the outflow is essential, as one of the significant issues in polarization is that the fluence drops rapidly for $q > 1$, for a top-hat jet where the emission drops sharply past the edges of the jet, which causes difficulties in observing the polarization. This can be easily observed in rows 3 of Figures 1 and 2, where we present the flux light curves[3] at the radio frequency for our chosen parameters. An increase of $q_0$ leads to a decrease of the flux magnitude at earlier times, with the previously mentioned value of $q_0 = 4$ returning an initial flux eight orders of magnitude smaller than the value of $q_0 = 1.2$, for $k = 0$.

Figure 1 shows the polarization behavior for the cases with a constant medium – $k = 0$ and $\Gamma \propto \cos \Delta\theta^{\frac{3}{2}} t^{-\frac{3}{2}}$ – and a stratified medium, with $k = 1$ and $\Gamma \propto \cos \Delta\theta t^{-1}$. In the perpendicular case, the evolution observed for the $k = 0$ scenario presents a distinct polarization peak whose magnitude depends on the geometric parameter $q_0$, a measure of how off-axis the observer is. We can see that the initial polarization for all configurations is at zero. This initial polarization quickly evolves towards a peak once the deceleration timescale ($t_{dec}$) is achieved; the jet expands faster and eventually breaks, which causes the polarization to evolve towards zero after the second peak. Two peaks are present for each value of $q_0$, with the magnitude of the peak increasing with $q_0$ and the peaks merging towards a single peak as $q_0$ increases. This characteristic has been observed before (see Granot et al. 2002; Rossi et al. 2004, for examples of this dual peak behavior on an off-axis jet polarization case) and we find our curves to behave similarly.[4] It is believed that each peak is associated with the contribution of the nearest and furthest edges of the jet. The parallel configuration demonstrates a higher duration on the variability of the

---

[2] We use a theoretical approach instead of hydrodynamical simulations. See Sec. 2.3 of Fraija et al. (2022) for the comparison with the hydrodynamical model.

[3] The slope variation, circa dozens of days, in the light curve is due to the passage of the synchrotron cooling break through the R-band (15.5 GHz).

[4] The polarization achieved by our model decays faster than for those of the cited works, we believe this is due the chosen evolution of the bulk Lorentz factor and the fact our approach to the evolution of $\theta_j$ has faster increase than the hydrodynamical approach on a timescale of days.

polarization – with a total decreasing behavior across the observation time, but a short interval where a local minimum is generated, with this variance dependent on $q_0$ – alongside initially high polarization yields.

For the $k > 0$ cases, the polarization has been pushed to an earlier time. As such, the evolution starts earlier and peaks earlier. For the sake of clarity, the lower boundary of the x-axis was lowered further. This time behavior happens due to the fact that the afterglow timescale is $\propto (E/A_k)^{1/(3-k)}$ (Kumar & Zhang 2015; Lazzati et al. 2003; Fraija et al. 2022). As such, for the parameters we have chosen for our calculations, the afterglow polarization is shown at earlier times. For more typical parameters, the lower densities of a wind-like medium cause the polarization to evolve slower (Lazzati et al. 2004). The same behavior can be observed in Figure 2, where the polarization is presented for the $k = 1.5$ – $\Gamma \propto \cos \Delta \theta^{\frac{3}{4}} t^{-\frac{3}{4}}$ – and $k = 2.0$ – $\Gamma \propto \cos \Delta \theta^{\frac{1}{2}} t^{-\frac{1}{2}}$ – cases.

## 4. POLARIZATION FROM GRBS SHOWING OFF-AXIS AFTERGLOW EMISSION

In this following section, we describe the polarization obtained for a group of GRBs that show similar characteristics on their afterglow: GRB 080503, GRB 140903A, GRB 150101B, GRB 160821B, GRB 170817A (see Fraija et al. 2019a, for an analysis of the similarities) and SN2020bvc. For a more thorough analysis of the light curves modeling, the Markov Chain Monte Carlo (MCMC) simulations utilized to obtain the parameters used for these calculations, and observation data regarding these bursts, see Fraija et al. (2022) and the references therein. For this section, we will adopt the notation $f(q_0 = x_{\pm z}^{\pm y}) = a_{\pm c}^{\pm b}$.

GRB 080503—The first column in Figure 5 shows the theoretical polarization evolution calculated for GRB 080503 for the magnetic field configurations — perpendicular and parallel, from top to bottom, respectively. The parameters for calculating this polarization are presented on the first row of Table 3. A negligible influence of the value of $q_0$ is observed on the peak polarization for both configurations, with peak polarization $|\Pi|(B_\perp) \approx 41\%$ and initial polarization $\Pi(B_\parallel) \approx 65\%$. For the perpendicular field, the somewhat small effect of $q_0$ can be observed on the peak time, with $t_{peak}(q_0 = 2.37_{-0.05}^{+0.05}) \approx 2.15_{-0.21}^{+0.28}$ days and null polarization is reached at $\sim 15$ days — the second peak is observed at $t \approx 3.8_{-0.4}^{+0.5}$ with $|\Pi| \approx 30\%$. The local minimum polarization of the parallel magnetic field configuration is observed at $t \approx 2.71_{-0.31}^{+0.34}$ days, with a magnitude of $\Pi(q_0 = 2.37_{-0.05}^{+0.05}) \approx 52_{-0.4}^{+0.2}\%$ and a $\sim 2\%$ increase is observed after $\sim 1.6_{-0.1}^{+0.2}$ days. Af-

ter that event, the polarization decreases steadily to $\Pi(t = 100) \approx 13.5_{-0.5}^{+0.5}\%$.

GRB 140903A—The second column in Figure 5 shows the theoretical polarization evolution estimated for GRB 140903A, similarly to the previous case. The parameters are presented on the second row of Table 3. The chosen value of $q_0$ shows a higher degree of influence for this burst, even if changed just slightly. The perpendicular case shows a peak polarization of $|\Pi|(q_0 = 1.61^{+0.08} - 0.08) \approx 33_{-1.0}^{+1.2}\%$ at the times $t_{peak}(q_0 = 1.61^{+0.08} - 0.08) \approx 4.1_{-1.2}^{+1.7} \times 10^{-2}$ days. The second peak manifests at $t = 6.5_{-1.9}^{+1.7} \times 10^{-2}$ days, with magnitudes of $|\Pi| \approx 24.9_{-1.0}^{+0.7}\%$, and zero polarization is reached at $\approx 0.4$ days. For the parallel configuration the initial polarization is $\Pi \approx 58.2_{-1.2}^{+1.0}\%$. The local minimum is $\Pi \approx 41.7_{-2.0}^{+1.4}\%$ at the times $t = 5.8_{-1.7}^{+2.4} \times 10^{-2}$ days and an increase of $\approx 8_{-1}^{+1}\%$ is observed after $7_{-1}^{+3} \times 10^{-2}$ days before steady decline. A polarization of $\Pi \approx 1\%$ is observed at the 100 day mark.

GRB 150101B—The third column in Figure 5 shows the theoretical polarization calculated for GRB 150101B. The parameters for calculating this polarization are presented on the third row of Table 3. In a similar manner to GRB 080503, the different values of $q_0$ offer at best a differential change on the polarization. For the perpendicular case we observe the following: peak polarization of $|\Pi| \approx 38\%$ at $t_{peak}(q_0 = 2.08_{-0.04}^{+0.04}) \approx 4.8_{-0.5}^{+0.2}$ days, with zero reached at 13 days — the second peak is observed at $t \approx 3.8_{-0.4}^{+0.5}$ with $|\Pi| \approx 28\%$. For the parallel case we see that the initial polarization is $|\Pi| \approx 63\%$, the local minimum is observed at $t = 2.15_{-0.20}^{+0.25}$ days, with a magnitude of $\Pi(q_0 = 2.08_{-0.04}^{+0.04}) \approx 48.8_{-0.5}^{+0.2}\%$, and a $\sim 4\%$ increase is observed after $\sim 2.2_{-0.5}^{+0.2}$ days. After that event, the polarization decreases steadily to $\Pi(t = 100) \approx 16_{-1}^{+1}\%$ .

GRB 160821B—The fourth column in Figure 5 shows the theoretical evolution of polarization calculated for GRB 160821B. The parameters for calculating this polarization are presented on the fourth row of Table 3. These polarization curves behave more similarly to the ones observed in GRB 140903A, with some peculiarities. The perpendicular case shows a peak polarization of $|\Pi|(q_0 = 1.27^{+0.13} - 0.13) \approx 28.4_{-2.9}^{+1.6}\%$ at the times $t_{peak}(q_0 = 1.27_{-0.08}^{+0.08}) \approx 2.9_{-2.4}^{+5.1} \times 10^{-2}$ days. The second peak is fairly prominent, showing at $t = 5.2_{-4.2}^{+5.4} \times 10^{-2}$ days, with magnitude of $|\Pi| \approx 21_{-6}^{+2}\%$. The polarization eventually reaches zero at $t = 1.6_{-1.2}^{+3.7} \times 10^{-1}$ days. For the parallel case, a pulsation of small magnitude ($\lesssim 1\%$) is observed at the initial period of time, where the polarization is expected to decrease softly with our fiducial model, for $q_0 = (1.27, 1.40)$. This pulsation is not observed for $q_0 = 1.14$ likely due to the fact

that a smaller value of $q_0$ pushes the polarization faster in time, causing it to happen before our lower time boundary. Overall, the polarization at initial times is $\Pi \approx 54.8^{+2.0}_{-2.2}\% \pm 1\%$. The local minimum polarization is $\Pi \approx 30^{+6}_{-8}\%$ at $t_{peak} = 4.6^{+8.6}_{-3.7} \times 10^{-2}$ days, a $\sim 17^{-5}_{+7}\%$ increase is observed after $\sim 8.6^{+11.7}_{-6.6} \times 10^{-2}$ days. After which, the polarization steadily decreases to $\Pi(t = 100) \approx 3^{+1}_{-1}\%$.

*GRB 170817A*—Figure 4 shows the expected polarization, calculated with our model, for the different configurations of magnetic fields. An extensive analysis of the synchrotron light curves was done by Fraija et al. (2019b), where the authors have fitted the synchrotron light curves with a dual component model, and we aim to expand this analysis to the polarization. The off-axis component dominates the late afterglow period after two weeks (see Kasliwal et al. 2017; Lamb & Kobayashi 2017; Mooley et al. 2018; Hotokezaka et al. 2018; Fraija et al. 2019b); thus we only use the off-axis component, an expanding top-hat jet, to calculate the polarization. A similar approach was done by Teboul & Shaviv (2021), whom also used a dual component outflow — albeit with a structured jet. We have used the values reported in Table 1 of Fraija et al. (2019b) to generate the polarization curves. The synchrotron analysis done for GRB 170817A was calculated for the scenario where $k = 0$, and the same condition is applied to our model. As such, the polarization presents a similar behavior as the left side of Figure 1.

First, we see across the different configurations that the chosen array of observation angles, chosen based on MCMC simulations, leads to a granular increment of $q_0$ that has little to no effect on the overall polarization evolution. As such, we will limit ourselves to the analysis of a single value of $q_0 = 3.28$. For the perpendicular case, we see that the polarization is initially null and shows a rapid increase to a peak of $|\Pi| \approx 46\%$ at $t \approx 141$ days and declines to zero again when $t \approx 432$ days, where it remains. The parallel case has an initially high polarization of $\Pi \approx 68\%$ that decreases softly until a sharper decrease happens at $t \approx 180$ days and the polarization becomes $\Pi \approx 54\%$. A small increase of $\sim 1\%$ happens again at $t \approx 240$ days from where the polarization starts to decrease sharply, reaching $\sim 33\%$ at $t \approx 10^3$ days. Corsi et al. (2018) report an upper limit of $\Pi < 12\%$, with 99% confidence at 2.8 GHz and $t_{\rm obs} \approx 244$ days. Our results for both configurations of magnetic fields return values that infringe on the upper limits. As such, based on our model of jet dynamics, presented in further detail in Fraija et al. (2022) and Fraija et al. (2019b), we can rule out the fully anisotropic scenario.

We want to highlight that some authors (e.g., see Gill & Granot 2018; Stringer & Lazzati 2020; Gill & Granot 2020; Teboul & Shaviv 2021) have already tried to constrain the magnetic field configuration using the polarization upper limit, from radio observations, for this particular burst. Gill & Granot (2018) have calculated the polarization for a gaussian jet, power-law jet, and quasi-spherical outflow with energy injections for three anisotropy values, $b = (0.0, 0.5, 1.5)$. They have found that the structured jets produce a high polarization degree ($\Pi \approx 60\%$, for $b = 0$) peaking at $\sim 300$ days, with the wide-angle quasi-spherical outflow with energy injection returning a lower polarization degree ($\Pi \approx 10\%$) at all times, with all values of $b$. Teboul & Shaviv (2021) and Gill & Granot (2020) have obtained the polarization for different anisotropy factors and found, for the dynamical evolution dictated by their jet models, that a random magnetic field should be close to isotropic (b=1) to satisfy the polarization upper limits. Teboul & Shaviv (2021) also expanded that a magnetic field with two components, an ordered and a random, could satisfy the upper limits should $0.85 < b < 1.16$ and the ordered component be as high as half the random one. Stringer & Lazzati (2020) have analyzed the measured and theoretical polarization ratio for a non-spreading top-hat off-axis jet that constrains the geometry of the magnetic fields to a dominant perpendicular component, but with a sub-dominant parallel component ($b > 0$). Of these authors, Teboul & Shaviv (2021); Gill & Granot (2020) and Gill & Granot (2018) have explored the $b = 0$ scenario for GRB 170817A. They reported $\Pi \approx 60\%$ at $\sim 300$ days, with the polarization still decreasing softly for times upwards of $10^3$ days. While our polarization values and evolution are somewhat different, likely due to different synchrotron models and parameters, it remains that our explored cases have also broken the available upper limits, ruling out the $b = 0(b \to \infty)$ possibilities.

More observations on a shorter post-burst period would be needed to constrain the magnetic field configuration further. Unfortunately, there were no polarization observations at any other frequency and time (Corsi et al. 2018).

*SN 2020bvc*—Figure 6 shows the expected polarization for SN 2020bvc calculated for a stratified medium where $k = 1.5$. The parameters used to calculate the values of polarization are presented on the fifth row of Table 3. The perpendicular case shows a peak polarization of $|\Pi|(q_0 = 5.85^{+0.09}_{-0.10}) \approx 42^{-1}_{+1}\%$ at the times $t_{peak}(q_0 = 1.61^{+0.08}_{-0.08}) \approx 16.1^{+2.0}_{-0.1}$ days, with a null polarization state at 44 days. The parallel case, on the other hand, has a initial maximum polarization of $\Pi \approx 70\%$, a local minimum of $\Pi \approx 47\%$ at $t_{peak} = 26$ days, a $\sim 1\%$

increase is observed after $\sim 8$ days. After which, the polarization steadily decreases to $\Pi(t = 100) \approx 10\%$.

## 5. CONCLUSIONS

We have introduced a polarization model as an extension of the analytical synchrotron afterglow off-axis scenario presented in Fraija et al. (2019b, 2022). We have shown this model's expected temporal polarization evolution, dependent on the physical parameters associated with afterglow GRB emission. This synchrotron model describes the multiwavelength afterglow for homogeneous and stratified ambient media based on the parameter $k$ ($k = 0$ for homogeneous and $k > 0$ for stratified). The polarization allows us to speculate on the nature of the magnetic field, which originates the synchrotron flux on the afterglow. We have calculated the polarization for a broad set of parameters, constrained within the typical values observed for off-axis GRBs, for four different stratification states ($k = [0, 1, 1.5, \text{and } 2]$) and the two magnetic field configurations. We assumed a wholly perpendicular configuration contained to the shock plane (i.e., the anisotropy factor $b = 0$) or a wholly ordered configuration parallel to the shock normal (i.e., the anisotropy factor $b \to \infty$).

For these simulations, we were able to distinctly see the difference in possible polarization caused by the stratification of the ambient medium for both field configurations. The perpendicular magnetic field configuration shows prominent peaks whose magnitude becomes increasingly higher as the observer is further away from the edge of the jet. The parallel configuration, on the other hand, showed initially high polarization yields with a local minimum observed, before a regrowth and eventual decrease towards zero as the jet laterally expands. The influence of the $q_0$ ratio is evident, as the initial polarization is higher with an increasing $q_0$, but the magnitude of the local minimum decreases inversely with $q_0$. This influence of the observation angle on the peak of the polarization is a result that agrees with the polarization literature (Ghisellini & Lazzati 1999; Granot 2003; Rossi et al. 2004; Gill et al. 2020). The effect of stratification on the polarization seems to be two-fold, one result coming from typical GRB behavior, where the afterglow timescale is proportional to the inverse of the density $- t \propto A_k^{-1/(3-k)}$, as such higher or lower densities push the polarization to different timescales; the second result comes at the magnitude of a discontinuity observed at the time of the jet-break, with this "polarization break" becoming increasingly higher with the stratification parameter.

We have also obtained the expected polarization curves for a sample of bursts showing off-axis afterglow emission - GRB 080503, GRB 140903A, GRB 150101B, GRB 160821B, GRB 170817A, and SN2020bvc. In particular, we have used the available polarimetric upper limits of GRB 170817A, $|\Pi| < 12\%$ at 2.8 GHz and $t \approx 244$ days (Corsi et al. 2018), in a attempt to constrain the magnetic field geometry. The polarization obtained with our jet dynamics and the chosen anisotropy returns a value that breaks the established upper limits on both of the configurations, which in turn allow us to rule out the $b = 0 (b \to \infty)$ cases.

Although the remaining bursts have neither detected polarization nor constrained upper limits to compare with, analysis of these bursts that appear to show similar nature can be of use in the occasion more similar bursts are found in the future. From our calculations we have observed the following similarities:

For the perpendicular field configuration, GRB 080503 and GRB 150101B show somewhat similar magnitudes of polarization at similar times. GRB 140903A and GRB 160821B also present some similarities on their polarization magnitudes, but here a higher difference on the time at which the peaks are displayed is present, with the lowest value of $q_0$ used for GRB 160821B having a polarization peak one order of magnitude earlier in time. In all likelihood this differentiation between the two groups of bursts comes from the angular properties of the jet, as for the latter group the initial value of $q_0$ is closer to unity. Furthermore, the differences between GRB 140903A and GRB 160821B likely also come from angular properties, as they become more amplified for even small changes in $q_0$, as $q_0$ is close to unity. The polarization obtained, with our model, for GRB 170817A is closer to that presented for the former group than the latter. With the peaks showing as $|\Pi| \approx 41\%$ at $\sim 2.15$ days (GRB 080503), $|\Pi| \approx 38\%$ at $\sim 4.8$ days (GRB 150101B) and $|\Pi| \approx 46\%$ at $\sim 141$ days (GRB 170817A). SN2020bvc is modeled in a stratified medium, $k = 1.5$, unlike the bursts mentioned above. As such, the expected polarization should be similar to the left side of Figure 2 and that holds true. However, a particularity of our modelling of SN2020bvc is that the initial value of $q_0$ is incredibly high, which in turn leaves the polarization in a similar state to the $k = 0$ scenario for similarly high values of $q_0$. For all these bursts the peak of polarization has roughly coincided with the peak of the flux for an off-axis observer (see Fraija et al. 2022, for the flux fitting), which is a result that agrees with the literature (Ghisellini & Lazzati 1999; Granot & Königl 2003; Rossi et al. 2004; Teboul & Shaviv 2021). Overall, we can see that certain similarities can be observed between the bursts' polarizations. However, the peculiarities of each burst make so none are the same. More observations on durations from seconds to months after the trigger

are needed to infer tighter constraints on polarization and proper fitting of the flux data needed to dissolve the degeneracy between models.

## REFERENCES

Blandford, R. D., & McKee, C. F. 1976, Physics of Fluids, 19, 1130, doi: 10.1063/1.861619

Boulanger, F., Enßlin, T., Fletcher, A., et al. 2018, J. Cosmology Astropart. Phys., 2018, 049, doi: 10.1088/1475-7516/2018/08/049

Buckley, D. A. H., Bagnulo, S., Britto, R. J., et al. 2021, MNRAS, 506, 4621, doi: 10.1093/mnras/stab1791

Cano, Z., Wang, S.-Q., Dai, Z.-G., & Wu, X.-F. 2017, Advances in Astronomy, 2017, 8929054, doi: 10.1155/2017/8929054

Corsi, A., Hallinan, G. W., Lazzati, D., et al. 2018, ApJ, 861, L10, doi: 10.3847/2041-8213/aacdfd

Costa, E., Frontera, F., Heise, J., et al. 1997, Nature, 387, 783, doi: 10.1038/42885

Covino, S., Ghisellini, G., Lazzati, D., & Malesani, D. 2003, Polarization of Gamma–Ray Burst Optical and Near-Infrared Afterglows. https://arxiv.org/abs/astro-ph/0301608

Duncan, R. C., & Thompson, C. 1992, ApJ, 392, L9, doi: 10.1086/186413

Eichler, D., Livio, M., Piran, T., & Schramm, D. N. 1989, Nature, 340, 126, doi: 10.1038/340126a0

Fan, Y., & Piran, T. 2006, MNRAS, 369, 197

Fraija, N. 2015, ApJ, 804, 105, doi: 10.1088/0004-637X/804/2/105

Fraija, N., De Colle, F., Veres, P., et al. 2019a, arXiv e-prints, arXiv:1906.00502. https://arxiv.org/abs/1906.00502

Fraija, N., Galvan-Gamez, A., Betancourt Kamenetskaia, B., et al. 2022, arXiv e-prints, arXiv:2205.02459. https://arxiv.org/abs/2205.02459

Fraija, N., Lopez-Camara, D., Pedreira, A. C. C. d. E. S., et al. 2019b, ApJ, 884, 71, doi: 10.3847/1538-4357/ab40a9

Gao, H., Ding, X., Wu, X.-F., Dai, Z.-G., & Zhang, B. 2015, ApJ, 807, 163, doi: 10.1088/0004-637X/807/2/163

Gehrels, N., Ramirez-Ruiz, E., & Fox, D. B. 2009, ARA&A, 47, 567, doi: 10.1146/annurev.astro.46.060407.145147

Ghisellini, G., & Lazzati, D. 1999, MNRAS, 309, L7, doi: 10.1046/j.1365-8711.1999.03025.x

Gill, R., & Granot, J. 2018, MNRAS, 478, 4128, doi: 10.1093/mnras/sty1214

—. 2020, MNRAS, 491, 5815, doi: 10.1093/mnras/stz3340

Gill, R., Granot, J., & Kumar, P. 2020, MNRAS, 491, 3343, doi: 10.1093/mnras/stz2976

Granot, J. 2003, ApJ, 596, L17, doi: 10.1086/379110

Granot, J., & Königl, A. 2003, ApJ, 594, L83, doi: 10.1086/378733

Granot, J., Panaitescu, A., Kumar, P., & Woosley, S. E. 2002, ApJ, 570, L61, doi: 10.1086/340991

Granot, J., & Sari, R. 2002, ApJ, 568, 820, doi: 10.1086/338966

Granot, J., & Taylor, G. B. 2005, ApJ, 625, 263, doi: 10.1086/429536

Hotokezaka, K., Kiuchi, K., Shibata, M., Nakar, E., & Piran, T. 2018, ApJ, 867, 95, doi: 10.3847/1538-4357/aadf92

Huang, Y. F., Dai, Z. G., & Lu, T. 1999, MNRAS, 309, 513, doi: 10.1046/j.1365-8711.1999.02887.x

—. 2000, MNRAS, 316, 943, doi: 10.1046/j.1365-8711.2000.03683.x

Izzo, L., Auchettl, K., Hjorth, J., et al. 2020, A&A, 639, L11, doi: 10.1051/0004-6361/202038152

Kasliwal, M. M., Nakar, E., Singer, L. P., et al. 2017, Science, 358, 1559, doi: 10.1126/science.aap9455

Kouveliotou, C., Meegan, C. A., Fishman, G. J., et al. 1993, The Astrophysical Journal, 413, L101

Kumar, P., & Zhang, B. 2015, Phys. Rep., 561, 1, doi: 10.1016/j.physrep.2014.09.008

Laing, R. A. 1980, MNRAS, 193, 439, doi: 10.1093/mnras/193.3.439

Lamb, G. P., & Kobayashi, S. 2017, MNRAS, 472, 4953, doi: 10.1093/mnras/stx2345

Laskar, T., Alexander, K. D., Gill, R., et al. 2019, ApJ, 878, L26, doi: 10.3847/2041-8213/ab2247

Lazzati, D., Covino, S., di Serego Alighieri, S., et al. 2003, A&A, 410, 823, doi: 10.1051/0004-6361:20031321

Lazzati, D., Covino, S., Gorosabel, J., et al. 2004, A&A, 422, 121, doi: 10.1051/0004-6361:20035951

Lyutikov, M., Pariev, V. I., & Blandford, R. D. 2003, ApJ, 597, 998, doi: 10.1086/378497

Mazets, E., Golenetskii, S., Il'Inskii, V., et al. 1981, Astrophysics and Space Science, 80, 3

Medvedev, M. V., & Loeb, A. 1999, ApJ, 526, 697, doi: 10.1086/308038

Mészáros, P., & Rees, M. J. 1997, ApJ, 476, 232

Metzger, B. D., Giannios, D., Thompson, T. A., Bucciantini, N., & Quataert, E. 2011, MNRAS, 413, 2031, doi: 10.1111/j.1365-2966.2011.18280.x

Mooley, K. P., Deller, A. T., Gottlieb, O., et al. 2018, Nature, 561, 355, doi: 10.1038/s41586-018-0486-3

Nakar, E., Piran, T., & Waxman, E. 2003, J. Cosmology Astropart. Phys., 2003, 005, doi: 10.1088/1475-7516/2003/10/005

Narayan, R., Paczynski, B., & Piran, T. 1992, ApJ, 395, L83, doi: 10.1086/186493

Orsi, S., & Polar Collaboration. 2011, Astrophysics and Space Sciences Transactions, 7, 43, doi: 10.5194/astra-7-43-2011

Paczyński, B. 1998, ApJ, 494, L45, doi: 10.1086/311148

Panaitescu, A., & Mészáros, P. 1998, ApJ, 501, 772, doi: 10.1086/305856

Perley, D. A., Metzger, B. D., Granot, J., et al. 2009, ApJ, 696, 1871, doi: 10.1088/0004-637X/696/2/1871

Piro, L., Amati, L., Antonelli, L. A., et al. 1998, A&A, 331, L41. https://arxiv.org/abs/astro-ph/9710355

Planck Collaboration, Ade, P. A. R., Aghanim, N., et al. 2016, A&A, 594, A13, doi: 10.1051/0004-6361/201525830

Rossi, E. M., Lazzati, D., Salmonson, J. D., & Ghisellini, G. 2004, MNRAS, 354, 86, doi: 10.1111/j.1365-2966.2004.08165.x

Rybicki, G. B., & Lightman, A. P. 1979, Radiative processes in astrophysics

Sari, R., & Esin, A. A. 2001, ApJ, 548, 787, doi: 10.1086/319003

Sari, R., Piran, T., & Narayan, R. 1998, ApJ, 497, L17, doi: 10.1086/311269

Stringer, E., & Lazzati, D. 2020, ApJ, 892, 131, doi: 10.3847/1538-4357/ab76d2

Teboul, O., & Shaviv, N. J. 2021, MNRAS, 507, 5340, doi: 10.1093/mnras/stab2491

Thompson, C. 1994, MNRAS, 270, 480, doi: 10.1093/mnras/270.3.480

Troja, E., Sakamoto, T., Cenko, S. B., et al. 2016, ApJ, 827, 102, doi: 10.3847/0004-637X/827/2/102

Troja, E., Ryan, G., Piro, L., et al. 2018, Nature Communications, 9, 4089, doi: 10.1038/s41467-018-06558-7

Troja, E., Castro-Tirado, A. J., Becerra González, J., et al. 2019, MNRAS, 489, 2104, doi: 10.1093/mnras/stz2255

Usov, V. V. 1992, Nature, 357, 472, doi: 10.1038/357472a0

van Paradijs, J., Groot, P. J., Galama, T., et al. 1997, Nature, 386, 686, doi: 10.1038/386686a0

Wang, X.-G., Zhang, B., Liang, E.-W., et al. 2015, ApJS, 219, 9, doi: 10.1088/0067-0049/219/1/9

Wang, X.-Y., He, H.-N., Li, Z., Wu, X.-F., & Dai, Z.-G. 2010, ApJ, 712, 1232, doi: 10.1088/0004-637X/712/2/1232

Waxman, E. 2003, Nature, 423, 388, doi: 10.1038/423388a

Weibel, E. S. 1959, Phys. Rev. Lett., 2, 83, doi: 10.1103/PhysRevLett.2.83

Weinberg, S. 1972, Gravitation and Cosmology

Woosley, S. E. 1993, ApJ, 405, 273, doi: 10.1086/172359

Woosley, S. E., & Bloom, J. S. 2006, ARA&A, 44, 507, doi: 10.1146/annurev.astro.43.072103.150558

Zhang, S., Jin, Z.-P., Wang, Y.-Z., & Wei, D.-M. 2017, ApJ, 835, 73, doi: 10.3847/1538-4357/835/1/73

**Table 1.** Constants of the relevant quantities in the synchrotron scenario from Section 2.1

| | $k = 0$ | $k = 1.0$ | $k = 1.5$ | $k = 2.0$ |
|---|---|---|---|---|
| $A_\mathrm{k}$ | $1\,\mathrm{cm}^{-3}$ | $10^{17}\,\mathrm{cm}^{-2}$ | $3.1 \times 10^{25}\,\mathrm{cm}^{-\frac{3}{2}}$ | $10^{34}\,\mathrm{cm}^{-1}$ |
| $\gamma_\mathrm{m}^0\,(\times 10)$ | $1.15 \times 10^{-1}$ | $1.36 \times 10^{-3}$ | $5.16 \times 10^{-4}$ | $2.85 \times 10^{-4}$ |
| $\gamma_\mathrm{c}^0\,(\times 10^4)$ | $1.53 \times 10^1$ | $7.46 \times 10^{-3}$ | $1.59 \times 10^{-3}$ | $6.20 \times 10^{-4}$ |
| $\nu_{\mathrm{a},1}^0\,(\times 10^{-6}\,\mathrm{Hz})$ | $9.73 \times 10^{-4}$ | $1.32 \times 10^{+2}$ | $1.50 \times 10^{+3}$ | $6.58 \times 10^{+3}$ |
| $\nu_{\mathrm{a},2}^0\,(\times 10^{-5}\,\mathrm{Hz})$ | $2.96 \times 10^{-2}$ | $2.46 \times 10^{-1}$ | $3.82 \times 10^{-1}$ | $4.98 \times 10^{-1}$ |
| $\nu_{\mathrm{a},3}^0\,(\times 10^{-5}\,\mathrm{Hz})$ | $1.29 \times 10^1$ | $7.21 \times 10^4$ | $4.61 \times 10^5$ | $1.43 \times 10^6$ |
| $\nu_\mathrm{m}^0\,(\times 10^{-6}\,\mathrm{Hz})$ | $2.52 \times 10^{-4}$ | $1.08 \times 10^{-6}$ | $3.24 \times 10^{-7}$ | $1.54 \times 10^{-7}$ |
| $\nu_\mathrm{c}^0\,(\times 10^{-1}\,\mathrm{Hz})$ | $4.42 \times 10^1$ | $3.25 \times 10^{-4}$ | $3.06 \times 10^{-5}$ | $7.31 \times 10^{-6}$ |
| $F_\mathrm{max}^0\,(\times 10\,\mathrm{mJy})$ | $1.27$ | $3.90 \times 10^1$ | $8.12 \times 10^1$ | $1.27 \times 10^2$ |

**Table 2.** Table of values used to obtain the Polarization curves for the general case

| | $k = 0$ | $k = 1.0$ | $k = 1.5$ | $k = 2.0$ |
|---|---|---|---|---|
| $A_k$ | $1\,\mathrm{cm}^{-3}$ | $10^{19}\,\mathrm{cm}^{-2}$ | $2.6 \times 10^{27}\,\mathrm{cm}^{-3/2}$ | $10^{36}\,\mathrm{cm}^{-1}$ |
| $E(10^{52}\,\mathrm{erg})$ | $5$ | $5$ | $5$ | $5$ |
| $\theta_j(\mathrm{deg})$ | $4$ | $4$ | $4$ | $4$ |
| $\theta_\mathrm{obs}(\mathrm{deg})$ | $[1.2, 5]\theta_j$ | $[1.2, 5]\theta_j$ | $[1.2, 5]\theta_j$ | $[1.2, 5]\theta_j$ |

The range $[1.2, 5]$ for $\theta_\mathrm{obs}$ represents the interval $[1.2, 1.7, 2.0, 3.0, 4.0, 5.0]$

A. Pedreira et al.

**Table 3.** Median Values of Parameters used to calculate the polarization curves for a sample of short and long GRBs.

| Parameters | $E\,(10^{52}\,\mathrm{erg})$ | $A_0\,(10^{-2}\,\mathrm{cm}^{-3})$ | $A_{1.5}\,(10^{22}\,\mathrm{cm}^{-3/2})$ | $\theta_{\mathrm{j}}\,(\mathrm{deg})$ | $\theta_{\mathrm{obs}}\,(\mathrm{deg})$ | p[a] |
|---|---|---|---|---|---|---|
| GRB 080503 | $2.156^{+0.294}_{-0.295}$ | $4.221^{+0.102}_{-0.103}$ | – | $6.589^{+0.081}_{-0.078}$ | $15.412^{+0.268}_{-0.269}$ | $2.319^{+0.049}_{-0.049}$ |
| GRB 140903A | $3.163^{+0.290}_{-0.296}$ | $4.219^{+0.102}_{-0.101}$ | – | $3.210^{+0.080}_{-0.081}$ | $5.162^{+0.271}_{-0.267}$ | $2.073^{+0.048}_{-0.050}$ |
| GRB 150101B | $1.046^{+0.120}_{-0.124}$ | $0.164^{+0.021}_{-0.021}$ | – | $6.887^{+0.662}_{-0.682}$ | $14.114^{+2.327}_{-2.179}$ | $2.150^{+0.217}_{-0.215}$ |
| GRB 160821B | $0.118^{+0.021}_{-0.021}$ | $0.869^{+0.093}_{-0.090}$ | – | $8.002^{+0.817}_{-0.809}$ | $10.299^{+1.125}_{-1.135}$ | $2.220^{+0.021}_{-0.021}$ |
| SN 2020bvc | $0.238^{+0.011}_{-0.010}$ | – | $9.984^{+0.195}_{-0.193}$ | $2.121^{+0.078}_{-0.079}$ | $12.498^{+0.268}_{-0.281}$ | $2.313^{+0.037}_{-0.035}$ |

[a]  The electron power-law index, p, returns the spectral index by taking $\alpha = \frac{p-1}{2}$
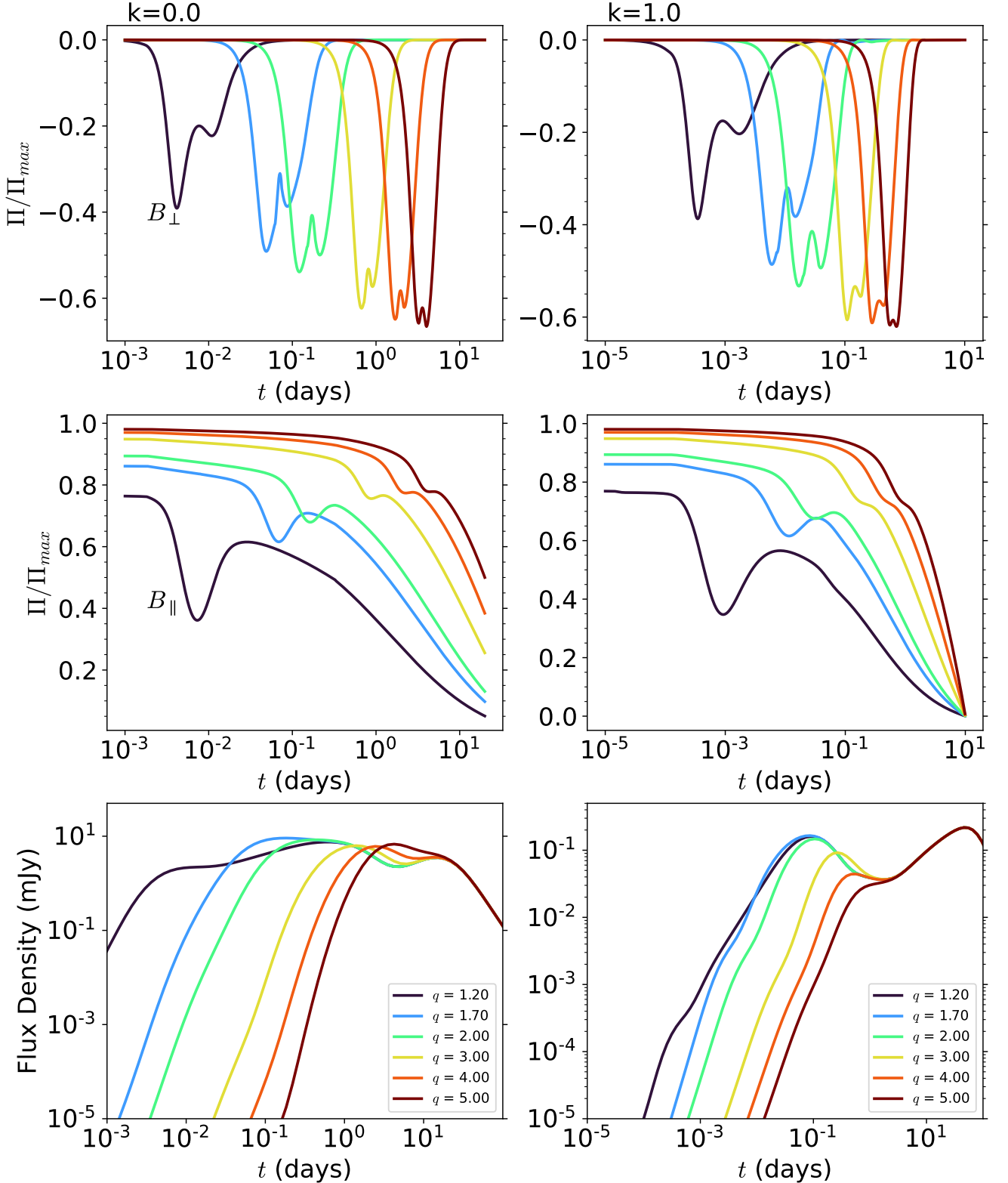
**Figure 1.** Temporal evolution of the polarization presented for two configurations of magnetic fields - Perpendicular ($B_\perp$) and Parallel ($B_\parallel$), for values of $k = 0, 1$ (from left to right). These polarization curves were calculated for a set of general parameters of GRBs observed in the literature (see Table 2). Here, $q_0$ represents the fraction between the observation and the initial opening angle of the jet. The values of $A_k$ are dependent on which values of $k$ are used. These curves may need to be re-scaled by a factor of $<1$, as $\Pi_{max} = 70\%$ **(corresponding to** $\alpha = 0.60$) was chosen arbitrarily. To obtain the flux light curves, at the radio frequency of $15.5\,\mathrm{GHz}$, the additional parameters of $\varepsilon_B = 10^{-4}$, $\varepsilon_e = 10^{-1}$, $p = 2.2$, $\zeta_e = 1$, initial Lorentz factor $\Gamma_0 = 100$, and $d_z = 6.6\,\mathrm{Gpc}$ were used.

**Figure 2.** Temporal evolution of the polarization presented for two configurations of magnetic fields - Perpendicular ($B_\perp$) and Parallel ($B_\parallel$), for values of $k = 1.5, 2$ (from left to right). These polarization curves were calculated for a set of general parameters of GRBs observed in the literature (see Table 2). Here, $q_0$ represents the fraction between the observation and the initial opening angle of the jet. The values of $A_k$ are dependent on which values of $k$ are used. These curves may need to be re-scaled by a factor of $<1$, as $\Pi_{max} = 70\%$ (corresponding to $\alpha = 0.60$) was chosen arbitrarily. To obtain the flux light curves, at the radio frequency of $15.5\,\mathrm{GHz}$, the additional parameters of $\varepsilon_B = 10^{-4}$, $\varepsilon_e = 10^{-1}$, $p = 2.2$, $\zeta_e = 1$, initial Lorentz factor $\Gamma_0 = 100$, and $d_z = 6.6\,\mathrm{Gpc}$ were used.

**Figure 3.** Temporal evolution of the $q$ parameter, for the four stratification scenarios presented on Figures 1 and 2.
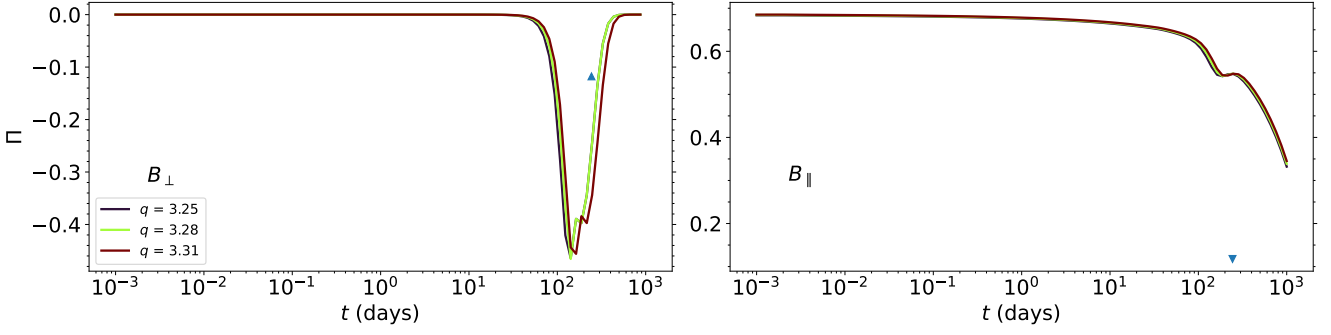
**Figure 4.** Expected Temporal evolution of the polarization for GRB 170817A for two configurations of magnetic fields - Perpendicular ($B_\perp$), Parallel ($B_\parallel$). These polarization curves were calculated using the best fit values presented in Table 1 of Fraija et al. (2019b): $\tilde{E} \approx 6.3 \times 10^{49}$erg, $n \approx 2.8 \times 10^{-4}$cm$^{-3}$, $\theta_{\rm obs} \approx [24.5, 24.7, 25.0]$ and $\theta_j = 7.6$ deg, $p \approx 2.24$. The blue triangles represent the Radio upper limit of $|\Pi| = 12\%$. Radio upper limit at 2.8 GHz was taken from Corsi et al. (2018).
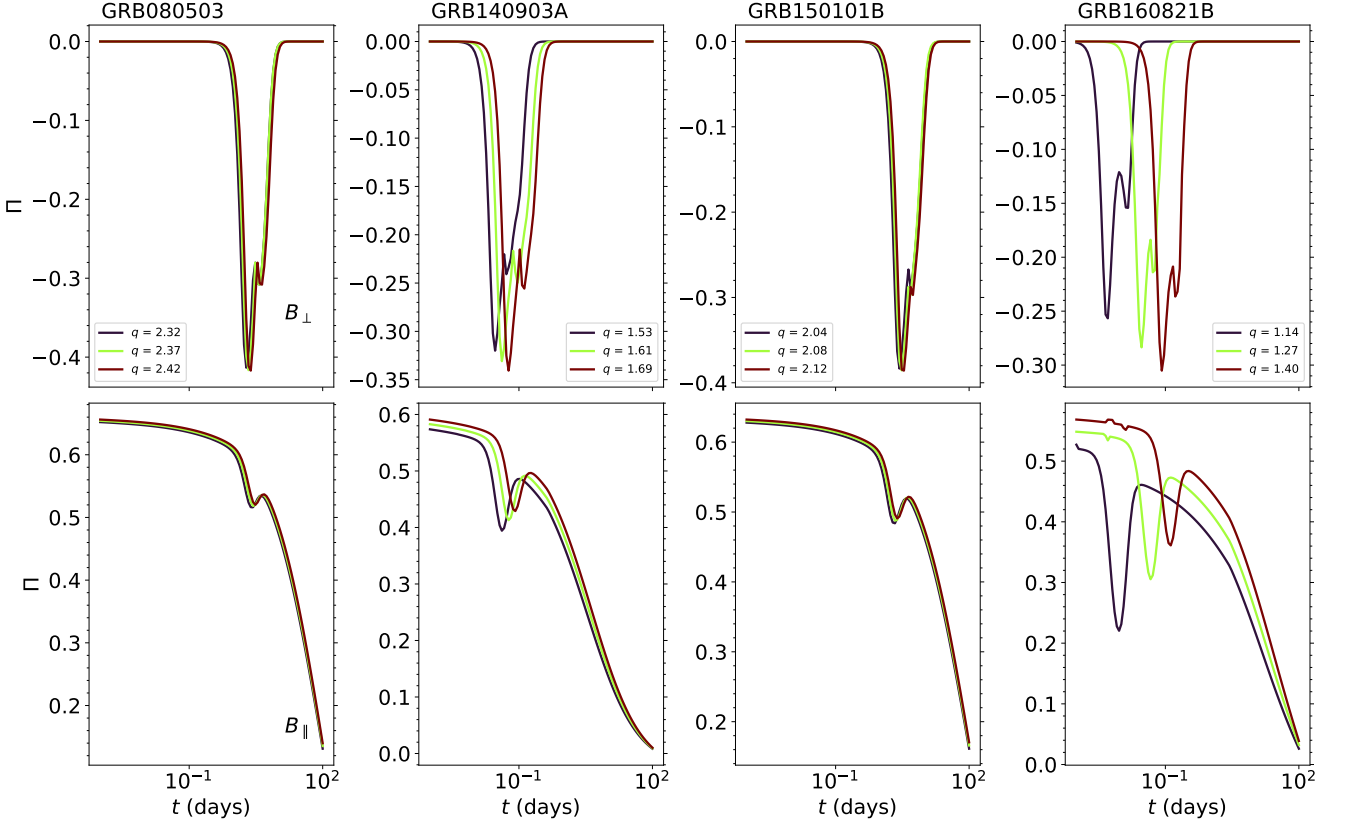
**Figure 5.** Expected temporal evolution of the polarization for the bursts GRB 080503, GRB140903, GRB150101B, GRB160821B - respectively, from left to right. Each burst has its polarization calculated for 3 possible magnetic field configurations - Perpendicular ($B_\perp$), Parallel ($B_\parallel$) and Toroidal ($B_{tor}$), respectively from top to bottom - for the set of parameters presented on Table 3. The uncertainty of the observation angle, $\theta_{\rm obs}$, was used to return a range of values for the fraction $q_0$, represented by the colormap legend on the figure. All polarizations are calculated for the case $k = 0$.
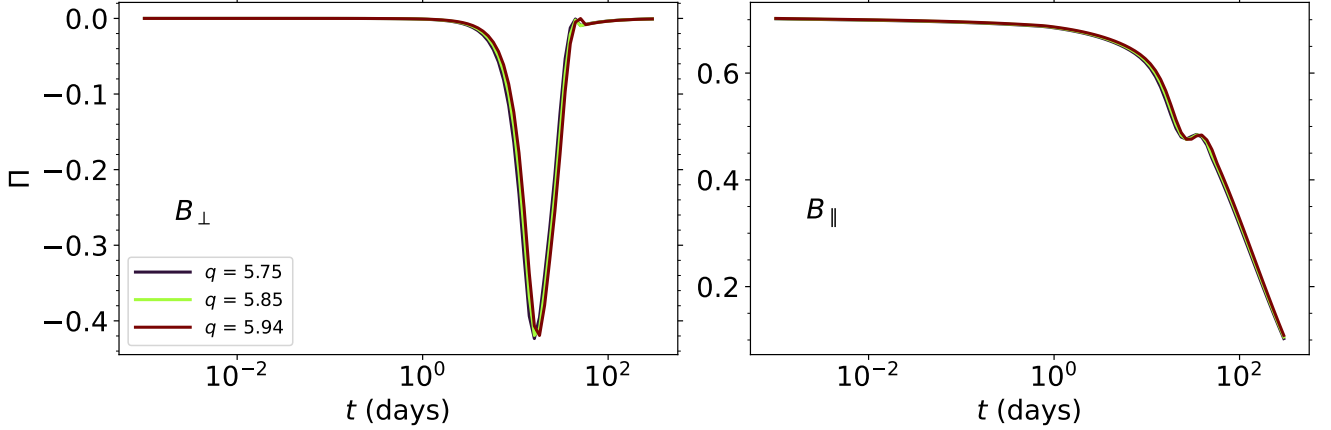


**Figure 6.** Expected temporal evolution of the polarization for the supernova SN2020bvc, calculated for 3 possible magnetic field configurations - Perpendicular ($B_\perp$), Parallel ($B_\parallel$) and Toroidal ($B_{tor}$), respectively, from left to right. The set of parameters presented on Table 3 were used, with the uncertainty of the observation angle, $\theta_{\rm obs}$, used to return a range of values for the fraction $q_0$, represented by the colormap legend. For this case, $k = 1.5$.

## 3.2  Polarization for a Radially Stratified Outflow

In this section we group the following works based on their continuity:

- **Pedreira, A. C. C. d. E. S.**, Fraija, N., Galvan-Gamez, A., Betancourt Kamenetskaia, B., Dichiara, S., Dainotti, M.G., Becerra, R. L., Veres, P., 2022, Polarization From A Radially Stratified Off-Axis GRB Outflow, MNRAS(Submitted), doi: `10.48550/ARXIV.2211.12477`

- Fraija, N., De Colle, F., Veres, P., Dichiara, S., Barniol Duran, R., **Caligula do E. S. Pedreira**, A. C., Galvan-Gamez, A., Betancourt Kamenetskaia, B., 2020, ApJ, 896, 25, doi: `10.3847/1538-4357/ab88b7`

In Fraija et al. (2020) we present a radially stratified outflow, parameterized with a power-law velocity distribution, to model GRB afterglows with Synchrotron and SSC emission mechanisms in a forward shock scenario. This model is presented for both a homogeneous and wind-like media. The outflow's kinetic energy is written as

$$E_k = \frac{\tilde{E}}{\Gamma^{\alpha_s}\left(1 + \Delta\theta^2\Gamma^2\right)^3},\tag{3.5}$$

and Blandford-McKee's solution returns

$$\Gamma = \begin{cases} 10.1\left(\frac{1+z}{1.022}\right)^{\frac{3}{\delta+8}} n_{-4}^{-\frac{1}{\delta+8}} \Delta\theta_{15°}^{-\frac{6}{\delta+8}} \tilde{E}_{52}^{\frac{1}{\delta+8}} t_{1d}^{-\frac{3}{\delta+8}} & \text{homogeneous medium,} \\ 16.4\left(\frac{1+z}{1.022}\right)^{\frac{1}{\delta+4}} \xi^{-\frac{2}{\delta+4}} A_{\star,-1}^{-\frac{1}{\delta+4}} \Delta\theta_{15°}^{-\frac{6}{\delta+4}} \tilde{E}_{52}^{\frac{1}{\delta+4}} t_{1s}^{-\frac{1}{\delta+4}} & \text{wind-like medium,} \end{cases}\tag{3.6}$$

where $\delta = \alpha_s + 6$. The lateral expansion phase can be found in the full text.

As particular case, we show in this work that the delayed, long-lasting afterglow emission in GRB 080503, GRB 140903A, GRB 150101B, and GRB 160821B can be interpreted in a similar scenario to GRB 170817A.

In Pedreira et al. (2022b) we present the temporal evolution of polarization for the fiducial model of Fraija et al. (2020). We further expand the model to include the parameters $\Gamma_0$, the initial Lorentz factor, $\xi$, the parameter associated with the EATS condition, and $\epsilon$ to specify whether the scenario is adiabatic or radiative. The Lorentz factor becomes

$$\Gamma_{hom} = 9.8\left(\frac{1+z}{1.022}\right)^{\frac{3}{\delta+8-\epsilon}} \xi^{-\frac{6}{\delta+8-\epsilon}} n_{-4}^{-\frac{1}{\delta+8-\epsilon}} \Delta\theta_{15°}^{-\frac{6}{\delta+8-\epsilon}} \Gamma_0^{-\frac{\epsilon}{\delta+8-\epsilon}} \tilde{E}_{52}^{\frac{1}{\delta+8-\epsilon}} t_5^{-\frac{3}{\delta+8-\epsilon}},\tag{3.7}$$

$$\Gamma_{wind} = 16.2\left(\frac{1+z}{1.022}\right)^{\frac{1}{\delta+4-\epsilon}} \xi^{-\frac{2}{\delta+4-\epsilon}} A_{W,-1}^{-\frac{1}{\delta+4-\epsilon}} \Delta\theta_{15°}^{-\frac{6}{\delta+4-\epsilon}} \Gamma_0^{-\frac{\epsilon}{\delta+4-\epsilon}} \tilde{E}_{52}^{\frac{1}{\delta+4-\epsilon}} t_5^{-\frac{1}{\delta+4-\epsilon}}.$$

In addition, we model the theoretical polarization for the set of bursts modeled in the aforementioned paper (no observed polarization data). We use these curves to further strengthen the observed similarities between these bursts. This work is currently under peer-review process. Unfortunately, an accepted version cannot be presented in time for the submission of this document.

CrossMark

# Description of Atypical Bursts Seen Slightly Off-axis

N. Fraija[1] , F. De Colle[2], P. Veres[3] , S. Dichiara[4,5], R. Barniol Duran[6], A. C. Caligula do E. S. Pedreira[1], A. Galvan-Gamez[1], and B. Betancourt Kamenetskaia[1]

[1] Instituto de Astronomía, Universidad Nacional Autónoma de México, Circuito Exterior, C.U., A. Postal 70-264, 04510 Cd. de México, México; nifraija@astro.unam.mx
[2] Instituto de Ciencias Nucleares, Universidad Nacional Autónoma de México, Circuito Exterior, C.U., A. Postal 70-264, 04510 Cd. de México, México
[3] Center for Space Plasma and Aeronomic Research (CSPAR), University of Alabama in Huntsville, Huntsville, AL 35899, USA
[4] Department of Astronomy, University of Maryland, College Park, MD 20742-4111, USA
[5] Astrophysics Science Division, NASA Goddard Space Flight Center, 8800 Greenbelt Rd, Greenbelt, MD 20771, USA
[6] Department of Physics and Astronomy, California State University, Sacramento, 6000 J Street, Sacramento, CA 95819-6041, USA
*Received 2019 June 5; revised 2020 February 1; accepted 2020 April 10; published 2020 June 9*

## Abstract

The detection of gravitational waves together with their electromagnetic counterpart, in the gamma-ray burst GRB 170817A, marked a new era of multi-messenger astronomy. Several theoretical models have been proposed to explain the atypical behavior of this event. Recently, it was shown th0at the multiwavelength afterglow of GRB 170817A was consistent with a synchrotron forward-shock model when the outflow was viewed off-axis, decelerated in a uniform medium and parameterized through a power-law velocity distribution. Motivated by the upper limits on the very high-energy emission, and the stratified medium in the close vicinity of a binary neutron star merger proposed to explain the gamma-ray flux in the short GRB 150101B, we extend the mechanism proposed to explain GRB 170817A to a more general scenario deriving the synchrotron self-Compton and synchrotron forward-shock model when the off-axis outflow is decelerated in a uniform and stratified circumburst density. As particular cases, we show that the delayed and long-lasting afterglow emission observed in GRB 080503, GRB 140903A, GRB 150101B, and GRB 160821B could be interpreted by a scenario similar to the one used to describe GRB 170817A. In addition, we show that the proposed scenario agrees with the Major Atmospheric Gamma-ray Imaging Cherenkov telescope, Fermi-Large Area Telescope, and High Energy Stereoscopic System upper limits on gamma-ray emission from GRB 160821B and GRB 170817A.

*Unified Astronomy Thesaurus concepts:* Gamma-ray bursts (629)

## 1. Introduction

Gravitational-wave (GW) detection with its electromagnetic counterpart marked a new era of multi-messenger astronomy. The second run (02) of the Advanced Laser Interferometer Gravitational-Wave Observatory and Advanced Virgo (Abbott et al. 2017a, 2017b) led to the important discovery of the first GWs associated with the short gamma-ray burst GRB 170817A, which was detected by the Gamma-ray Burst Monitor (GBM) on board Fermi Gamma-ray Space Telescope (Goldstein et al. 2017) and The INTErnational Gamma-Ray Astrophysics Laboratory (Savchenko et al. 2017). The progenitor of this transient event was promptly associated with the merger of two neutron stars (NSs) located in the host galaxy NGC 4993, at a redshift of $z \simeq 0.01$. (Coulter et al. 2017; Margutti et al. 2017a). Due to its low luminosity and the detection of a delayed and long-lasting non-thermal emission (afterglow) observed in the radio, optical, and X-ray bands, this short gamma-ray burst (sGRB) was classified as atypical (Margutti et al. 2017a, 2017b, 2018; Troja et al. 2017a; Haggard et al. 2018; Lamb et al. 2019a). These long-lasting observations were described by synchrotron emission generated by the deceleration of off-axis top-hat jets (Alexander et al. 2017; Ioka & Nakamura 2017; Margutti et al. 2017a; Troja et al. 2017b; Fraija et al. 2019a; Gill et al. 2019), radially stratified ejecta (Mooley et al. 2018; Hotokezaka et al. 2018; Fraija et al. 2019c), and structured jets (Kasliwal et al. 2017; Lamb & Kobayashi 2017; Lazzati et al. 2018; Kathirgamaraju et al. 2019) in a homogeneous medium. In particular, it was shown in Fraija et al. (2019a) that the delayed non-thermal multiwavelength emission observed in GRB 170817A was consistent with the synchrotron forward-shock

model when the outflow was viewed off-axis, decelerated in a homogeneous medium and parameterized through a power-law velocity distribution.

Similar observational features of GRB 170817A such as a short gamma-ray spike and an undetected afterglow on a timescale of days followed by very bright emission in X-rays, optical, and/or radio bands can support the idea that sGRBs generally launch collimated outflows out of the observer's line of sight. This is the case for the short GRB 080503 (Perley et al. 2009), GRB 140903A (Troja et al. 2016), GRB 150101B (Fong et al. 2016; Burns et al. 2018; Troja et al. 2018b) and GRB 160821B (Stanbro & Meegan 2016; Lü et al. 2017; Jin et al. 2018; Lamb et al. 2019b; Troja et al. 2019) that exhibited a short gamma-ray spike together with a rebrightening on a timescale of hours to days detected in several energy bands. The GBM Collaboration studied GRB 150101B and found that the gamma-ray light curve composed of a short hard spike and a long soft tail exhibited features similar to those of GRB 170817A (Burns et al. 2018). This collaboration derived the condition for the long tail occurring at the external shocks in a stratified stellar wind-like medium.

Since the Fermi satellite began scientific operations, the Large Area Telescope (LAT) has reported the detection of very high-energy photons (VHE; $\gtrsim 10$ GeV) in more than a dozen GRBs (see Abdo et al. 2009; Ackermann et al. 2013, 2014; Liu et al. 2014; Longo et al. 2016; Fraija et al. 2017b, 2019b, 2019d, 2019e, 2020 and references therein). Although the search for VHE photons by means of Imaging Atmospheric Cerenkov Telescopes has been a challenge because the time required to repoint to the burst position may take minutes, the

Major Atmospheric Gamma-ray Imaging Cherenkov (MAGIC) telescope recently detected photons in the direction of GRB 190114C with energies above 300 GeV for almost 20 minutes (Mirzoyan 2019). In the framework of the fireball model, the standard synchrotron radiation originated during the deceleration phase has been successful at explaining the long-lasting emission. However, this is not the case when the photons detected are greater than the maximum synchrotron photon energy $\sim 10\,\mathrm{GeV}\left(\frac{\Gamma}{200}\right)\left(\frac{1+z}{2}\right)^{-1}$ (Piran & Nakar 2010; Barniol Duran & Kumar 2011, and references therein), where $\Gamma$ is the bulk Lorentz factor of the decelerated outflow. In order to interpret the VHE photons, the standard synchrotron self-Compton (SSC) model in the forward shocks has been used (e.g., see, Sari & Esin 2001).

In this paper, the mechanism proposed to describe GRB 170817A and introduced in Fraija et al. (2019a) is extended to a more general scenario deriving the synchrotron and SSC emission from forward shocks when the outflow, parameterized with a power-law velocity distribution, is decelerated in a homogeneous interstellar medium (ISM)-like medium and in a stellar wind-like medium. We show that the delayed non-thermal emission observed in GRB 080503, GRB 140903A, GRB 150101B, and GRB 160821B could be interpreted by a jet with a velocity distribution seen slightly off-axis. In addition, we show that the proposed scenario agrees with the VHE gamma-ray upper limits derived by the GeV–TeV observatories. The paper is organized as follows. In Section 2 we present the SSC and synchrotron forward-shock model when the outflow is decelerated in a homogeneous and a wind-like medium. In Section 3 we apply this model to describe the delayed multiwavelength afterglow observed in GRB 080503, GRB 140903A, GRB GRB 150101B, and GRB 160821B, and also to obtain the SSC emission that should have been emitted during GRB 160821B and GRB 170817A. In Section 4, we present our conclusions.

## 2. Theoretical Model

Once the outflow launched by the NS merger sweeps up enough circumburst material (stratified wind-like and/or uniform ISM-like medium), electrons originally accelerated during the forward shocks are cooled down by synchrotron and SSC radiation. We use the corresponding equivalent kinetic energy defined in Fraija et al. (2019a)

$$E_{\mathrm{k}} = \tilde{E}\,\Gamma^{-\alpha_s}(1 + \Delta\theta^2\Gamma^2)^{-3}, \qquad (1)$$

with $\tilde{E}$ being the fiducial energy, and $\Delta\theta = \theta_{\mathrm{obs}} - \theta_j$ being defined by the viewing angle ($\theta_{\mathrm{obs}}$) and the opening angle ($\theta_j$). The kinetic energy can be interpreted as the contribution of two parts: (i) an off-axis jet concentrated within an opening angle ("top-hat jet") with equivalent kinetic energy $\propto (1 + \Delta\theta^2\Gamma^2)^{-3}$ and (ii) an isotropic material with equivalent kinetic energy $\propto \Gamma^{-\alpha_s}$ with $\alpha_s = 1.1$ for $\beta\Gamma \gg 1$ and $\alpha_s = 5.2$ for $\beta\Gamma \ll 1$ for the adiabatic case (Sari & Mészáros 2000; Tan et al. 2001; Hotokezaka et al. 2013; Kyutoku et al. 2014; Barniol Duran et al. 2015; Hotokezaka & Piran 2015; Fraija et al. 2019c).

### 2.1. Uniform ISM-like Medium

#### 2.1.1. Relativistic Stage

In the relativistic regime ($\Gamma^2\Delta\theta^2 \gg 1$), the equivalent kinetic energy becomes $E_{\mathrm{k}} = \tilde{E}\,\Delta\theta^{-6}\Gamma^{-\delta}$ with $\delta = \alpha_s + 6$. Given the

adiabatic evolution of the forward shock (Blandford & McKee 1976; Sari 1997), the bulk Lorentz factor evolves as

$$\Gamma = 10.1\left(\frac{1+z}{1.022}\right)^{\frac{3}{\delta+8}} n_{-4}^{-\frac{1}{\delta+8}}\,\Delta\theta_{15^\circ}^{-\frac{6}{\delta+8}}\,\tilde{E}_{52}^{\frac{1}{\delta+8}}\,t_{1\,\mathrm{day}}^{-\frac{3}{\delta+8}}, \qquad (2)$$

where the fiducial energy is given by $\tilde{E} = \frac{32\pi}{3}\,m_p(1+z)^{-3}\,n\,\Gamma^{\delta+8}\,\Delta\theta^6\,t^3$, $m_p$ is the proton mass, $z$ is the redshift, $n$ is the number density of the uniform ISM-like medium, and $t$ is the timescale of the outflow during the deceleration phase. A hypothetical event located at 100 Mpc ($z \approx 0.022$) is considered. The convention $\hbar = c = 1$ in natural units, $Q_x = Q/10^x$ in c.g.s. units, and the values of cosmological parameters reported in Planck Collaboration et al. (2018) are adopted.

*Synchrotron Light Curves.* Using the bulk Lorentz factor (Equation (2)) and the synchrotron afterglow theory introduced in Sari et al. (1998) for the fully adiabatic regime, in this formalism we derive the relevant quantities of synchrotron emission originated from the forward shocks. The minimum and cooling electron Lorentz factors are given by

$$\gamma_m = 33.6\left(\frac{1+z}{1.022}\right)^{\frac{3}{\delta+8}} g(p)\,\epsilon_{e,-2}\,n_{-4}^{-\frac{1}{\delta+8}}\,\Delta\theta_{15^\circ}^{-\frac{6}{\delta+8}}\,\tilde{E}_{52}^{\frac{1}{\delta+8}}$$
$$\times\,t_{1\,\mathrm{day}}^{-\frac{3}{\delta+8}}$$

$$\gamma_c = 4.3\times10^8\left(\frac{1+z}{1.022}\right)^{\frac{\delta-1}{\delta+8}}(1+Y)^{-1}\,\epsilon_{B,-4}^{-1}\,n_{-4}^{-\frac{\delta+5}{\delta+8}}\,\Delta\theta_{15^\circ}^{\frac{18}{\delta+8}}$$
$$\times\,\tilde{E}_{52}^{-\frac{3}{\delta+8}}\,t_{1\,\mathrm{day}}^{\frac{1-\delta}{\delta+8}}, \qquad (3)$$

respectively, which correspond to a comoving magnetic field given by

$$B' \simeq 0.4\,\mathrm{mG}\left(\frac{1+z}{1.022}\right)^{\frac{3}{\delta+8}}\,\epsilon_{B,-4}^{\frac{1}{2}}\,n_{-4}^{\frac{\delta+6}{2(\delta+8)}}\,\Delta\theta_{15^\circ}^{-\frac{6}{\delta+8}}$$
$$\times\,E_{52}^{\frac{1}{\delta+8}}\,t_{1\,\mathrm{day}}^{-\frac{3}{\delta+8}}. \qquad (4)$$

Here, $Y$ is the Compton parameter, $g(p) = (p-2)/(p-1)$, $p$ is the spectral index of the electron population, and $\epsilon_e$ and $\epsilon_B$ are the microphysical parameters related to the energy density given to accelerate electrons and amplify the magnetic field, respectively (e.g., see Fraija & Veres 2018). Using the electron Lorentz factors (Equation (3)), the characteristic and cooling spectral breaks for synchrotron radiation are

$$\epsilon_{\mathrm{m}}^{\mathrm{syn}} \simeq 2.3\times10^{-3}\,\mathrm{GHz}\left(\frac{1+z}{1.022}\right)^{-\frac{\delta-4}{\delta+8}}\,\epsilon_{e,-2}^2\,\epsilon_{B,-4}^{\frac{1}{2}}\,n_{-4}^{-\frac{\delta}{2(\delta+8)}}$$
$$\times\,\Delta\theta_{15^\circ}^{-\frac{24}{\delta+8}}\,E_{52}^{\frac{4}{\delta+8}}\,t_{1\,\mathrm{day}}^{-\frac{18}{\delta+8}}$$

$$\epsilon_{\mathrm{c}}^{\mathrm{syn}} \simeq 8.7\times10^4\,\mathrm{keV}\left(\frac{1+z}{1.022}\right)^{\frac{\delta-4}{\delta+8}}(1+Y)^{-2}\,\epsilon_{B,-4}^{-\frac{3}{2}}\,n_{-4}^{-\frac{3\delta+16}{2(\delta+8)}}$$
$$\times\,\Delta\theta_{15^\circ}^{\frac{24}{\delta+8}}\,E_{52}^{-\frac{4}{\delta+8}}\,t_{1\,\mathrm{day}}^{-\frac{2(\delta+2)}{\delta+8}}, \qquad (5)$$

respectively. Considering the maximum emissivity, the total number of radiating electrons and the luminosity distance $D$ from this hypothetical event, the maximum flux emitted by

synchrotron radiation is given by

$$
\begin{aligned}
F_{\max}^{\mathrm{syn}} \simeq & \; 1.6 \times 10^{-1}\,\mathrm{mJy} \left(\frac{1+z}{1.022}\right)^{\frac{16-\delta}{\delta+8}} \epsilon_{B,-4}^{\frac{1}{2}} \, n_{-4}^{\frac{3\delta+8}{2(\delta+8)}} \, \Delta\theta_{15^{\circ}}^{-\frac{48}{\delta+8}} \\
& \times D_{26.3}^{-2}\, E_{52}^{\frac{8}{\delta+8}}\, t_{1\,\mathrm{day}}^{\frac{3\delta}{\delta+8}}.
\end{aligned}
$$
(6)

Using the spectral breaks (Equation (5)) and the maximum flux (Equation (6)), the light curves of the synchrotron emission evolving in the fast- and slow-cooling regime can be written as

$$
F_{\nu}^{\mathrm{syn}} \propto
\begin{cases}
t^{\frac{11\delta+4}{3(\delta+8)}} \, \epsilon_{\gamma}^{\frac{1}{3}}, & \epsilon_{\gamma} < \epsilon_{\mathrm{c}}^{\mathrm{syn}} \\[6pt]
t^{\frac{2(\delta-1)}{\delta+8}} \, \epsilon_{\gamma}^{-\frac{1}{2}}, & \epsilon_{\mathrm{c}}^{\mathrm{syn}} < \epsilon_{\gamma} < \epsilon_{\mathrm{m}}^{\mathrm{syn}} \\[6pt]
t^{\frac{2\delta-6p+4}{\delta+8}} \, \epsilon_{\gamma}^{-\frac{p}{2}}, & \epsilon_{\mathrm{m}}^{\mathrm{syn}} < \epsilon_{\gamma},
\end{cases}
$$
(7)

and

$$
F_{\nu}^{\mathrm{syn}} \propto
\begin{cases}
t^{\frac{3\delta+4}{\delta+8}} \, \epsilon_{\gamma}^{\frac{1}{3}}, & \epsilon_{\gamma} < \epsilon_{\mathrm{m}}^{\mathrm{syn}} \\[6pt]
t^{\frac{3\delta-6p+6}{\delta+8}} \, \epsilon_{\gamma}^{-\frac{p-1}{2}}, & \epsilon_{\mathrm{m}}^{\mathrm{syn}} < \epsilon_{\gamma} < \epsilon_{\mathrm{c}}^{\mathrm{syn}} \\[6pt]
t^{\frac{2\delta-6p+4}{\delta+8}} \, \epsilon_{\gamma}^{-\frac{p}{2}}, & \epsilon_{\mathrm{c}}^{\mathrm{syn}} < \epsilon_{\gamma},
\end{cases}
$$
(8)

respectively. Considering the particular scenario of $\delta = 0$, the observable quantities derived in Sari et al. (1998) and the light curves of the synchrotron forward-shock emission are recovered (e.g., see Fraija et al. 2016b).

*SSC Light Curves.* Synchrotron photons generated at the forward shock can be up-scattered by the same electron population as $\epsilon_{\mathrm{m}}^{\mathrm{ssc}} \sim \gamma_{\mathrm{m}}^{2}\,\epsilon_{\mathrm{m}}^{\mathrm{syn}}$ and $\epsilon_{\mathrm{c}}^{\mathrm{ssc}} \sim \gamma_{\mathrm{c}}^{2}\,\epsilon_{\mathrm{c}}^{\mathrm{syn}}$ (e.g., see Fraija 2014). Therefore, given Equations (3) and (5), the characteristic and cooling spectral breaks for the SSC process in the fully adiabatic regime are

$$
\begin{aligned}
\epsilon_{\mathrm{m}}^{\mathrm{ssc}} \simeq & \; 1.1 \times 10^{-5}\,\mathrm{eV} \left(\frac{1+z}{1.022}\right)^{\frac{10-\delta}{\delta+8}} g(p)^2 \, \epsilon_{e,-2}^{4} \, \epsilon_{B,-4}^{\frac{1}{2}} \, n_{-4}^{\frac{\delta-4}{2(\delta+8)}} \\
& \times \Delta\theta_{15^{\circ}}^{-\frac{36}{\delta+8}} \, E_{52}^{\frac{6}{\delta+8}} \, t_{1\,\mathrm{day}}^{-\frac{18}{\delta+8}} \\[6pt]
\epsilon_{\mathrm{c}}^{\mathrm{ssc}} \simeq & \; 1.6 \times 10^{13}\,\mathrm{TeV} \left(\frac{1+z}{1.022}\right)^{\frac{3(\delta-2)}{\delta+8}} (1+Y)^{-4} \, \epsilon_{B,-4}^{-\frac{7}{2}} \, n_{-4}^{-\frac{7\delta+36}{\delta+8}} \\
& \times \Delta\theta_{15^{\circ}}^{\frac{60}{\delta+8}} \, E_{52}^{-\frac{10}{\delta+8}} \, t_{1\,\mathrm{day}}^{-\frac{2(2\delta+1)}{\delta+8}},
\end{aligned}
$$
(9)

respectively. The break energy, due to the Klein–Nishina (KN) effect, is given by

$$
\begin{aligned}
\epsilon_{\mathrm{KN}}^{\mathrm{ssc}} \simeq & \; 2.4 \times 10^{3}\,\mathrm{GeV} \left(\frac{1+z}{1.022}\right)^{-\frac{6}{\delta+8}} (1+Y)^{-1} \, \epsilon_{B,-4}^{-1} \, n_{-4}^{-\frac{\delta+6}{\delta+8}} \\
& \times \Delta\theta_{15^{\circ}}^{\frac{12}{\delta+8}} \, E_{52}^{-\frac{2}{\delta+8}} \, t_{1\,\mathrm{day}}^{\frac{\delta+2}{\delta+8}}.
\end{aligned}
$$
(10)

Considering the maximum flux of the synchrotron radiation and the optical depth (see Sari & Esin 2001), the maximum flux emitted by the SSC process is given by

$$
\begin{aligned}
F_{\max}^{\mathrm{ssc}} \simeq & \; 5.1 \times 10^{-11}\,\mathrm{mJy} \left(\frac{1+z}{1.022}\right)^{-\frac{5(\delta+2)}{\delta+8}} \epsilon_{B,-4}^{\frac{1}{2}} \, n_{-4}^{\frac{5(\delta+4)}{2(\delta+8)}} \\
& \times \Delta\theta_{15^{\circ}}^{-\frac{60}{\delta+8}} D_{26.3}^{-2} \, E_{52}^{\frac{10}{\delta+8}} \, t_{1\,\mathrm{day}}^{\frac{2(2\delta+1)}{\delta+8}}.
\end{aligned}
$$
(11)

Using the spectral breaks (Equation (9)) and the maximum flux (Equation (11)), the light curves of the SSC process evolving in the fast- and slow-cooling regime can be written as

$$
F_{\nu}^{\mathrm{ssc}} \propto
\begin{cases}
t^{\frac{8(2\delta+1)}{3(\delta+8)}} \, \epsilon_{\gamma}^{\frac{1}{3}}, & \epsilon_{\gamma} < \epsilon_{\mathrm{c}}^{\mathrm{ssc}}, \\[6pt]
t^{\frac{2\delta+1}{\delta+8}} \, \epsilon_{\gamma}^{-\frac{1}{2}}, & \epsilon_{\mathrm{c}}^{\mathrm{ssc}} < \epsilon_{\gamma} < \epsilon_{\mathrm{m}}^{\mathrm{ssc}}, \\[6pt]
t^{\frac{10+2\delta-9p}{\delta+8}} \, \epsilon_{\gamma}^{-\frac{p}{2}}, & \epsilon_{\mathrm{m}}^{\mathrm{ssc}} < \epsilon_{\gamma},
\end{cases}
$$
(12)

and

$$
F_{\nu}^{\mathrm{ssc}} \propto
\begin{cases}
t^{\frac{4(\delta+2)}{\delta+8}} \, \epsilon_{\gamma}^{\frac{1}{3}}, & \epsilon_{\gamma} < \epsilon_{\mathrm{m}}^{\mathrm{ssc}}, \\[6pt]
t^{\frac{4\delta-9p+11}{\delta+8}} \, \epsilon_{\gamma}^{-\frac{p-1}{2}}, & \epsilon_{\mathrm{m}}^{\mathrm{ssc}} < \epsilon_{\gamma} < \epsilon_{\mathrm{c}}^{\mathrm{ssc}}, \\[6pt]
t^{\frac{2\delta-9p+10}{\delta+8}} \, \epsilon_{\gamma}^{-\frac{p}{2}}, & \epsilon_{\mathrm{c}}^{\mathrm{ssc}} < \epsilon_{\gamma},
\end{cases}
$$
(13)

respectively. Considering the particular scenario of $\delta = 0$, the observable quantities derived in Sari & Esin (2001) are recovered.

### 2.1.2. Lateral Expansion Stage

During the lateral expansion stage, the beaming cone of the radiation emitted off-axis broadens increasingly until this cone reaches the observer's field of view ($\Gamma \sim \Delta\theta^{-1}$; Granot et al. 2002, 2017). Recently, based on relativistic numerical jet calculations during this stage, Duffell & Laskar (2018) presented a semi-analytical model to calculate the corresponding Lorentz factor and opening angle as the jet spreads; however, here we treat this stage approximately (e.g., Granot et al. 2002). Given that the timescale for the lateral expansion phase to occur is much longer than the timescale of the transition from the fast- to the slow-cooling regime, only the synchrotron and SSC light curves in the slow-cooling regime are derived in this stage. Given the Blanford–McKee solution and the equivalent kinetic energy (Equation (1)), during the lateral expansion stage the kinetic energy can be approximated as $E_{\mathrm{k}} \approx \frac{1}{8}\tilde{E}\,\Gamma^{-\alpha_s}$. In this approximation, the bulk Lorentz factor evolves as

$$
\Gamma = 4.1 \left(\frac{1+z}{1.022}\right)^{\frac{3}{\delta+8}} n_{-4}^{-\frac{1}{\delta+8}} \, \Delta\theta_{15^{\circ}}^{-\frac{6}{\delta+8}} \, \tilde{E}_{52}^{\frac{1}{\delta+8}} \, t_{10\,\mathrm{day}}^{-\frac{3}{\delta+8}}.
$$
(14)

Similarly, the timescale for the cone to reach the observer's field of view can be written as (Granot et al. 2017)

$$
t_{\mathrm{br}} = 23.3\,\mathrm{days}\; k \left(\frac{1+z}{1.022}\right) n_{-4}^{-\frac{1}{3}} \, \tilde{E}_{52}^{\frac{1}{3}} \, \Delta\theta_{15^{\circ}}^{2},
$$
(15)

where the value of the parameter $k$ varies from one model to another (Granot et al. 2002; Nakar et al. 2002). In this case, the fiducial energy can be obtained from Equation (14).

*Synchrotron Light Curves.* Using the bulk Lorentz factor (Equation (14)) and the evolution of a jet after it slows down and spreads laterally introduced in Sari et al. (1999), we derive the electron Lorentz factors, the spectral breaks, the maximum flux, and the light curves when the synchrotron emission is evolving in the fully adiabatic slow-cooling regime. The

minimum and cooling electron Lorentz factors are given by

$$
\gamma_{\rm m} = 14.4 \left(\frac{1+z}{1.022}\right)^{\frac{3}{\delta+6}} g(p)\, \epsilon_{\rm e,-2}\, n_{-4}^{-\frac{1}{\delta+6}}\, \tilde{E}_{52}^{\frac{1}{\delta+6}}\, t_{10\,{\rm days}}^{-\frac{3}{\delta+6}}
$$

$$
\gamma_{\rm c} = 2.7 \quad \times \quad 10^8 \left(\frac{1+z}{1.022}\right)^{\frac{\delta-3}{\delta+6}} (1+Y)^{-1}\, \epsilon_{B,-4}^{-1}\, n_{-4}^{-\frac{\delta+3}{\delta+6}}
$$
$$
\times \tilde{E}_{52}^{-\frac{3}{\delta+6}}\, t_{10\,{\rm days}}^{\frac{3-\delta}{\delta+6}}, \tag{16}
$$

respectively. Their corresponding characteristic and cooling spectral breaks become

$$
\epsilon_{\rm m}^{\rm syn} \simeq 7.8 \quad \times \quad 10^{-5}\,{\rm GHz} \left(\frac{1+z}{1.022}\right)^{\frac{6-\delta}{\delta+6}} g(p)\, \epsilon_{e,-2}^2\, \epsilon_{B,-4}^{\frac{1}{2}}\, n_{-4}^{\frac{\delta-2}{2(\delta+6)}}
$$
$$
\times\, E_{52}^{\frac{4}{\delta+6}}\, t_{10\,{\rm days}}^{-\frac{12}{\delta+6}}
$$

$$
\epsilon_{\rm c}^{\rm syn} \simeq 8.7 \quad \times \quad 10^3\,{\rm keV} \left(\frac{1+z}{1.022}\right)^{\frac{\delta-6}{\delta+6}} (1+Y)^{-2}\, \epsilon_{B,-4}^{-\frac{3}{2}}\, n_{-4}^{-\frac{3\delta+10}{2(\delta+6)}}
$$
$$
\times\, E_{52}^{-\frac{4}{\delta+6}}\, t_{10\,{\rm days}}^{-\frac{2\delta}{\delta+6}}. \tag{17}
$$

Taking into account the maximum emissivity, the total number of radiating electrons, and the distance from this source, the maximum flux radiated by synchrotron emission during this phase is given by

$$
F_{\rm max}^{\rm syn} \simeq 7.2 \quad \times \quad 10^{-13}\,{\rm mJy} \left(\frac{1+z}{1.022}\right)^{\frac{18-\delta}{\delta+6}} \epsilon_{B,-4}^{\frac{1}{2}}\, n_{-4}^{\frac{3\delta+2}{2(\delta+6)}}\, E_{52}^{\frac{8}{\delta+6}}
$$
$$
\times\, D_{26.3}^{-2}\, t_{10\,{\rm days}}^{-\frac{3(2-\delta)}{\delta+6}}. \tag{18}
$$

Using the spectral breaks (Equation (17)) and the maximum flux (Equation (18)), then the light curves of the synchrotron emission evolving in the slow-cooling regime become

$$
F_\nu^{\rm syn} \propto \begin{cases} t^{\frac{3\delta-2}{\delta+6}}\, \epsilon_\gamma^{\frac{1}{3}}, & \epsilon_\gamma < \epsilon_{\rm m}, \\ t^{\frac{3(\delta-2p)}{\delta+6}}\, \epsilon_\gamma^{-\frac{p-1}{2}}, & \epsilon_{\rm m} < \epsilon_\gamma < \epsilon_{\rm c}, \\ t^{\frac{2(\delta-3p)}{\delta+6}}\, \epsilon_\gamma^{-\frac{p}{2}}, & \epsilon_{\rm c} < \epsilon_\gamma. \end{cases} \tag{19}
$$

Considering the particular value of $\delta = 0$, the observable quantities derived in Sari et al. (1999) are recovered.

*SSC Light curves.* Using the electron Lorentz factors (Equation (16)) and the characteristic and cooling spectral breaks of the synchrotron emission (Equation (17)), the characteristic and cooling spectral breaks for SSC in the fully adiabatic regime are

$$
\epsilon_{\rm m}^{\rm ssc} \simeq 6.8 \quad \times \quad 10^{-8}\,{\rm eV} \left(\frac{1+z}{1.022}\right)^{\frac{12-\delta}{\delta+6}} g(p)^2\, \epsilon_{e,-2}^4\, \epsilon_{B,-4}^{\frac{1}{2}}
$$
$$
n_{-4}^{\frac{\delta-6}{2(\delta+6)}} \quad \times \quad E_{52}^{\frac{6}{\delta+6}}\, t_{10\,{\rm days}}^{-\frac{18}{\delta+6}}
$$

$$
\epsilon_{\rm c}^{\rm ssc} \simeq 6.6 \quad \times \quad 10^8\,{\rm TeV} \left(\frac{1+z}{1.022}\right)^{\frac{3(\delta-4)}{\delta+6}} (1+Y)^{-4}\, \epsilon_{B,-4}^{-\frac{7}{2}}
$$
$$
\times\, n_{-4}^{-\frac{7\delta+22}{2(\delta+6)}}\, E_{52}^{-\frac{10}{\delta+6}}\, t_{10\,{\rm days}}^{\frac{2(3-2\delta)}{\delta+6}}, \tag{20}
$$

respectively. Taking into account the maximum flux of the synchrotron radiation (Equation (18)) and the optical depth (see, Sari & Esin 2001), the maximum flux emitted by the SSC

process can be written as

$$
F_{\rm max}^{\rm ssc} \simeq 2.1 \quad \times \quad 10^{-22}\,{\rm mJy} \left(\frac{1+z}{1.022}\right)^{\frac{18-2\delta}{\delta+6}} \epsilon_{B,-4}^{\frac{1}{2}}\, n_{-4}^{\frac{5(\delta+2)}{2(\delta+6)}}
$$
$$
\times\, D_{26.3}^{-2}\, E_{52}^{\frac{10}{\delta+6}}\, t_{10\,{\rm days}}^{\frac{2(2(\delta-3))}{\delta+6}}. \tag{21}
$$

Using the spectral breaks (Equation (20)) and the maximum flux (Equation (21)), then the light curves of the SSC process evolving in the slow-cooling regime become

$$
F_\nu^{\rm ssc} \propto \begin{cases} t^{\frac{4\delta}{\delta+6}}\, \epsilon_\gamma^{\frac{1}{3}}, & \epsilon_\gamma < \epsilon_{\rm m}^{\rm ssc}, \\ t^{\frac{3+4\delta-9p}{\delta+6}}\, \epsilon_\gamma^{-\frac{p-1}{2}}, & \epsilon_{\rm m}^{\rm ssc} < \epsilon_\gamma < \epsilon_{\rm c}^{\rm ssc}, \\ t^{\frac{6+2\delta-9p}{\delta+6}}\, \epsilon_\gamma^{-\frac{p}{2}}, & \epsilon_{\rm c}^{\rm ssc} < \epsilon_\gamma, \end{cases} \tag{22}
$$

respectively.

Figure 1 shows the synchrotron and SSC light curves generated by the deceleration of the outflow in a uniform ISM-like medium. The solid lines in the left panel show the synchrotron fluxes in the radio at 1.4 GHz (magenta), optical at 1 eV (green), and X-rays at 1 keV (gray) and the right panels present the SSC fluxes in gamma-rays at 10 GeV (blue), and $\gamma$-rays at 100 GeV (gold) for the typical values of GRB afterglow parameters reported in the literature.[7] Dashed lines correspond to the sensitivities of the Expanded Very Large Array[8] (EVLA) at 1.4 GHz (magenta), the Large Synoptic Survey Telescope[9] (LSST) at 1 eV(green), the X-ray Telescope on board Swift [10] (XRT) at 1 keV (gray), the Large Area Telescope on board Fermi [11] (LAT), and MAGIC[12] at 100 GeV (gold). The effect of the extragalactic background light (EBL) absorption proposed by Franceschini & Rodighiero (2017) is used to obtain the SSC light curves. With the parameter values used in these panels, the synchrotron and SSC light curves evolve in the slow-cooling regime. For another set of parameter values such as: a timescale of seconds, a higher uniform ISM-like medium ($\geqslant 1\,{\rm cm}^{-3}$), and equipartition parameters $\varepsilon_B \sim 0.1$, the synchrotron and SSC light curves would evolve in the fast-cooling regime. These panels show that depending on the parameters used, the intensity of the fluxes will vary, but they will have similar behaviors in all electromagnetic bands; they increase during the first $\sim 10$–$50$ days, then reach their respective maxima, and afterward decrease. It is worth mentioning that with the parameter values used in Fraija et al. (2019a) to model the electromagnetic counterpart of GW170817, the observed fluxes in the X-ray, optical, and radio bands increase during $\sim 120$ days. The left panels show that the evolution of synchrotron light curves at the radio, optical, and X-ray bands could or could not be detected by EVLA, LSST, and Swift XRT, depending on the values of GRB afterglow parameters. For instance, the upper panel shows that these fluxes can be detected, whereas the lower panel displays the opposite case. On the other hand, the right panels show that the

[7] The upper panels display the light curves for the values of $\tilde{E} = 5 \times 10^{52}$ erg, $n = 10^{-4}$ cm$^{-3}$, $\epsilon_B = 10^{-2}$, $\Delta\theta = 20°$, and $\alpha_s = 2.1$ and the lower panels present the values of $\tilde{E} = 10^{51}$ erg, $n = 10^{-3}$ cm$^{-3}$, $\epsilon_B = 10^{-4}$, $\Delta\theta = 30°$, and $\alpha_s = 1.1$. In all panels the values of $\epsilon_e = 0.1$, $p = 2.2$ and $D = 100$ Mpc were used.
[8] https://public.nrao.edu/telescopes/vla/
[9] https://www.lsst.org/
[10] https://swift.gsfc.nasa.gov/about_swift/xrt_desc.html
[11] Data taken from Piron (2016).
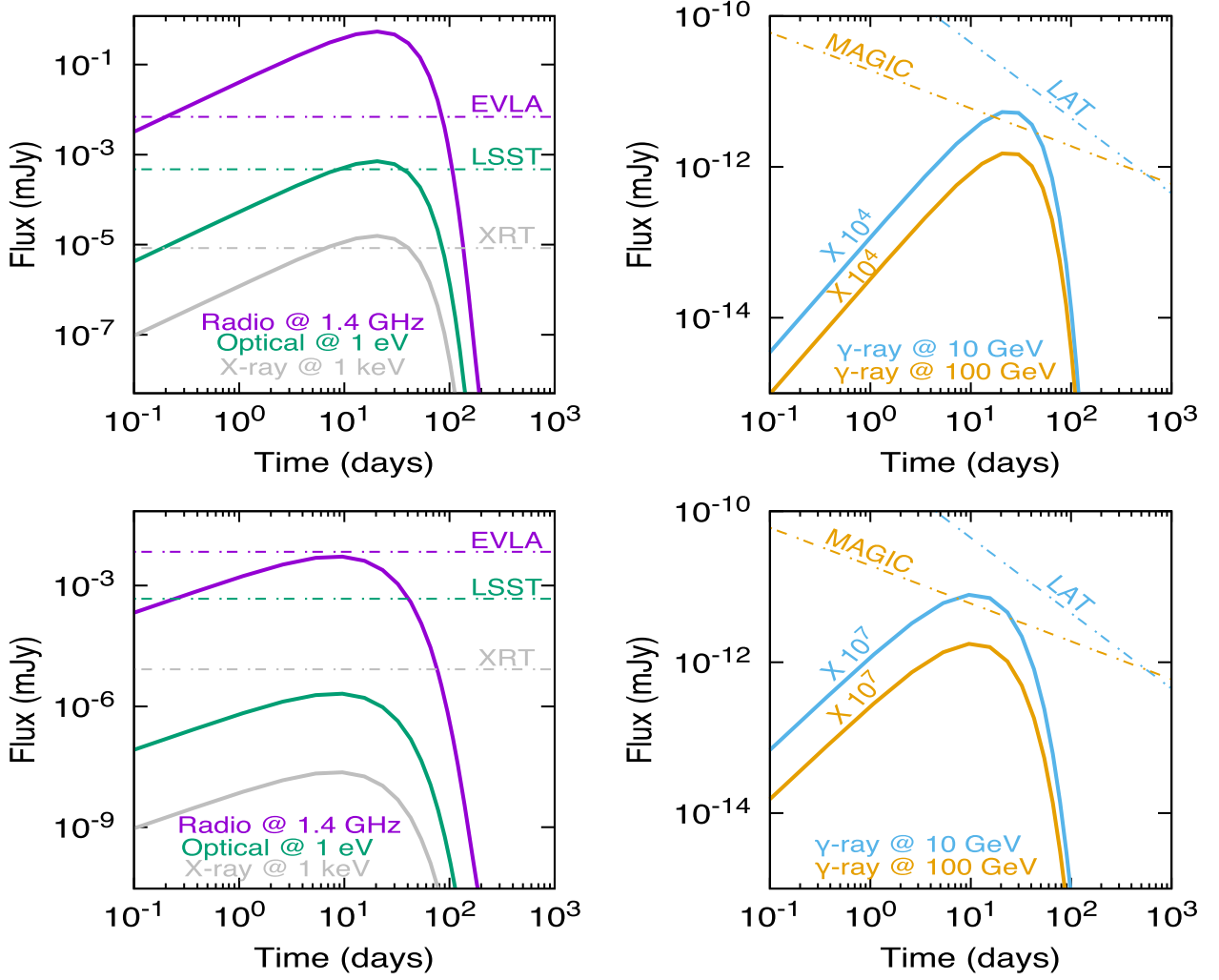[12] Data taken from Takahashi et al. (2008).

**Figure 1.** Light curves of the synchrotron (left panels) and SSC (right panels) fluxes radiated from the decelerated outflow in a homogeneous density for the values of $\tilde{E} = 5 \times 10^{52}$ erg, $n = 10^{-4}$ cm$^{-3}$, $\epsilon_B = 10^{-2}$, $\Delta\theta = 20°$, and $\alpha_s = 2.1$ (upper panels); and $\tilde{E} = 10^{51}$ erg, $n = 10^{-3}$ cm$^{-3}$, $\epsilon_B = 10^{-4}$, $\Delta\theta = 30°$, and $\alpha_s = 1.1$ (lower panels). The values of $\epsilon_e = 0.1$, $p = 2.2$ and $D = 100$ Mpc were assumed in all the panels.

evolution of SSC light curves at 10 and 100 GeV is too small to be detected by the LAT and MAGIC observatories; $\sim 10^4$ (upper) and $\sim 10^7$ (lower) times smaller.

### 2.2. Stratified Stellar Wind-like Medium

Nagakura et al. (2014) numerically studied the jet propagation in the material ejected by the neutrino-driven wind produced in the coalescence of an NS binary system. They used a density profile of the ejection along the pole given by $\rho(r) \propto r^{-\lambda}$. Considering the ejecta mass in the range of $10^{-3} \leqslant \frac{M_{ej}}{M_\odot} \leqslant 10^{-1}$ and onset times of jet injection up to $\sim 1$ s, the authors found the dynamics of the jet in the expanding ejecta with the power-law index of the density distribution $\lambda = 3.5$. Hotokezaka et al. (2013) investigated the numerical results on the ejected material (its mass and total energy) for $\lambda = 2$ and $\lambda = 3$. They found that the quantities depend weakly on the values of $\lambda$ and that if the ejected mass increased by $\sim 10\%$ the value of $\lambda$ varies from $2 \leqslant \lambda < 3$. Bauswein et al. (2013) also investigated the dynamics of the ejected mass of a merger of two NSs. They argued that the circumburst medium in the close vicinity of a merger could be

approximated as a wind medium with a density given by the power-law $\rho \propto r^{-2}$. Burns et al. (2018) analyzed the GBM data of the short GRB 150101B and used $\lambda = 2$ to explain the observed gamma-ray flux.

In this work the value of $\lambda = 2$ will be chosen for our analysis. Taking into account that the lateral expansion phase is expected to occur pretty far from the close vicinity of the merger, then the lateral expansion phase in a wind-like medium is not considered. Therefore, we only derive the synchrotron and SSC light curves in the relativistic phase. In the case of a stratified stellar wind-like medium, the number density is given by $n(r) = \frac{\rho(r)}{m_p} = \frac{A}{m_p} r^{-2}$, where $A = \frac{\dot{M}}{4\pi v} = 5 \times 10^{11} A_\star$ g cm$^{-1}$, $\dot{M}$ is the mass-loss rate, $v$ is the velocity of the outflow, and $A_\star$ is a density parameter (e.g., see Fraija et al. 2016a; Becerra et al. 2017).

Taking into account the Blandford–McKee solution for a stratified stellar wind-like medium, the bulk Lorentz factor derived through the adiabatic evolution (Blandford & McKee 1976; Sari 1997) is given by,

$$\Gamma = 16.4 \left(\frac{1+z}{1.022}\right)^{\frac{1}{\delta+4}} \xi^{-\frac{2}{\delta+4}} A_{\star,-1}^{-\frac{1}{\delta+4}} \Delta\theta_{15°}^{-\frac{6}{\delta+4}} \tilde{E}_{52}^{\frac{1}{\delta+4}} t_{1\,s}^{-\frac{1}{\delta+4}}, \quad (23)$$

with the fiducial energy given by $\tilde{E} = \frac{16\pi}{3}(1+z)^{-1}$ $\xi^2 A_\star \Delta\theta^6 \Gamma^{\delta+4} t$ .

*Synchrotron Light curves.* Using the bulk Lorentz factor (Equation (23)) and the synchrotron afterglow theory for a wind-like medium (Chevalier & Li 2000; Panaitescu & Kumar 2000), we derive the relevant quantities of synchrotron emission for our model in the fully adiabatic regime. The minimum and cooling electron Lorentz factors are given by

$$\gamma_m = 42.1\left(\frac{1+z}{1.022}\right)^{\frac{1}{\delta+4}} \xi^{-\frac{2}{\delta+4}} g(p)\,\epsilon_{e,-2}\,\Delta\theta_{15°}^{\frac{-6}{\delta+4}} A_{\star,-1}^{-\frac{1}{\delta+4}} \tilde{E}_{52}^{\frac{1}{\delta+4}}$$
$$\times\, t_{1s}^{-\frac{1}{\delta+4}}$$

$$\gamma_c = 45.6\left(\frac{1+z}{1.022}\right)^{-\frac{\delta+3}{\delta+4}}(1+Y)^{-1}\xi^{\frac{2(\delta+3)}{\delta+4}} \epsilon_{B,-4}^{-1} A_{\star,-1}^{-\frac{\delta+5}{\delta+4}}$$
$$\times\, \Delta\theta_{15°}^{-\frac{6}{\delta+4}} \tilde{E}_{52}^{\frac{1}{\delta+4}} t_{1s}^{\frac{\delta+3}{\delta+4}},$$

(24)

which correspond to a comoving magnetic field given by

$$B' \simeq 9.5 \;\times\; 10^2 \text{ mG}\left(\frac{1+z}{1.022}\right)^{-\frac{\delta+5}{\delta+4}}\xi^{-\frac{2(\delta+3)}{\delta+4}}\epsilon_{B,-4}^{\frac{1}{\delta+4}} A_{\star,-1}^{\frac{\delta+6}{2(\delta+4)}} \Delta\theta_{15°}^{\frac{6}{\delta+4}}$$
$$\times\, E_{52}^{-\frac{1}{\delta+4}} t_{1\text{ day}}^{-\frac{\delta+3}{\delta+4}}.$$

(25)

The characteristic and cooling spectral breaks for synchrotron emission are

$$\epsilon_m^{\text{syn}} \simeq 0.2 \text{ eV}\left(\frac{1+z}{1.022}\right)^{\frac{2}{\delta+4}}\xi^{-\frac{2(\delta+6)}{\delta+4}}\epsilon_{e,-2}^2 \epsilon_{B,-4}^{\frac{1}{\delta+4}}$$
$$\times\, A_{\star,-1}^{\frac{\delta}{2(\delta+4)}}\Delta\theta_{15°}^{-\frac{12}{\delta+4}} E_{52}^{\frac{2}{\delta+4}} t_{1s}^{-\frac{\delta+6}{\delta+4}}$$

$$\epsilon_c^{\text{syn}} \simeq 0.1 \text{ eV}\left(\frac{1+z}{1.022}\right)^{-\frac{2(\delta+3)}{\delta+4}}\xi^{\frac{2(\delta+2)}{\delta+4}}(1+Y)^{-2}$$
$$\times\, \epsilon_{B,-4}^{-\frac{3}{2}} A_{\star,-1}^{-\frac{3\delta+16}{2(\delta+8)}} \Delta\theta_{15°}^{-\frac{12}{\delta+4}} E_{52}^{\frac{2}{\delta+4}} t_{1s}^{\frac{\delta+2}{\delta+4}},$$

(26)

respectively. Given the maximum emissivity in a stratified stellar wind-like medium, the maximum flux radiated by synchrotron emission is given by

$$F_{\text{max}}^{\text{syn}} \simeq 1.9 \;\times\; 10^3 \text{ mJy}\left(\frac{1+z}{1.022}\right)^{\frac{2(\delta+5)}{\delta+4}}\xi^{-\frac{4}{\delta+4}} \epsilon_{B,-4}^{\frac{1}{2}} A_{\star,-1}^{\frac{3\delta+8}{2(\delta+4)}}$$
$$\times\, D_{26.3}^2 \Delta\theta_{15°}^{-\frac{12}{\delta+4}} E_{52}^{\frac{2}{\delta+4}} t_{1s}^{-\frac{2}{\delta+4}}.$$

(27)

Using the synchrotron spectral breaks (Equation (26)) and the maximum flux (Equation (27)), the synchrotron light curves in the fast- and slow-cooling regime can be written as

$$F_\nu^{\text{syn}} \propto \begin{cases} t^{-\frac{\delta+8}{3(\delta+4)}} \epsilon_\gamma^{\frac{1}{3}}, & \epsilon_\gamma < \epsilon_c^{\text{syn}}, \\ t^{\frac{\delta-2}{2(\delta+4)}} \epsilon_\gamma^{-\frac{p-1}{2}}, & \epsilon_c^{\text{syn}} < \epsilon_\gamma < \epsilon_m^{\text{syn}}, \\ t^{\frac{4+2\delta-p\delta-6p}{2(\delta+4)}} \epsilon_\gamma^{-\frac{p}{2}}, & \epsilon_m^{\text{syn}} < \epsilon_\gamma, \end{cases}$$

(28)

and

$$F_\nu^{\text{syn}} \propto \begin{cases} t^{\frac{\delta}{3(\delta+4)}} \epsilon_\gamma^{\frac{1}{3}}, & \epsilon_\gamma < \epsilon_m^{\text{syn}}, \\ t^{\frac{2+\delta-6p-p\delta}{2(\delta+4)}} \epsilon_\gamma^{-\frac{p-1}{2}}, & \epsilon_m^{\text{syn}} < \epsilon_\gamma < \epsilon_c^{\text{syn}}, \\ t^{\frac{4+2\delta-p\delta-6p}{2(\delta+4)}} \epsilon_\gamma^{-\frac{p}{2}}, & \epsilon_c^{\text{syn}} < \epsilon_\gamma, \end{cases}$$

(29)

respectively. Considering the particular scenario of $\delta = 0$, the observable quantities derived in (Chevalier & Li 2000; Panaitescu & Kumar 2000) and the light curves explicitly shown in Fraija (2015) are recovered.

*SSC Light curves.* Using Equations (24) and (26), the characteristic and cooling spectral breaks of SSC emission are

$$\epsilon_m^{\text{ssc}} \simeq 0.1 \;\times\; 10^{-3} \text{ eV}\left(\frac{1+z}{1.022}\right)^{\frac{4}{\delta+4}}\xi^{-\frac{2(\delta+8)}{\delta+4}}\epsilon_{e,-2}^4 \epsilon_{B,-4}^{\frac{1}{2}}$$
$$\times\, A_{\star,-1}^{\frac{\delta-4}{2(\delta+4)}}\Delta\theta_{15°}^{-\frac{24}{\delta+4}} E_{52}^{\frac{4}{\delta+4}} t_{1\text{ s}}^{-\frac{\delta+8}{\delta+4}}$$

$$\epsilon_c^{\text{ssc}} \simeq 0.2 \text{ keV}\left(\frac{1+z}{1.022}\right)^{-\frac{4(\delta+3)}{\delta+4}}\xi^{\frac{2(3\delta+8)}{\delta+4}}(1+Y)^{-4}$$
$$\times\, \epsilon_{B,-4}^{-\frac{7}{2}} A_{\star,-1}^{-\frac{7\delta+36}{2(\delta+4)}} \Delta\theta_{15°}^{-\frac{24}{\delta+4}} E_{52}^{\frac{4}{\delta+4}} t_{1\text{ s}}^{\frac{3\delta+8}{\delta+4}},$$

(30)

respectively. The break energy due to the KN effect is given by

$$\epsilon_{\text{KN}}^{\text{ssc}} \simeq 0.3 \text{ GeV}\left(\frac{1+z}{1.022}\right)^{-\frac{2(\delta+3)}{\delta+4}}(1+Y)^{-1}\xi^{\frac{2(\delta+2)}{\delta+4}} \epsilon_{B,-4}^{-1}$$
$$\times\, A_{\star,-1}^{-\frac{\delta+6}{\delta+4}} \Delta\theta_{15°}^{-\frac{12}{\delta+4}} E_{52}^{\frac{2}{\delta+4}} t_{1\text{ s}}^{\frac{\delta+2}{\delta+4}}.$$

(31)

Considering the maximum flux of synchrotron emission (Equation (27)), the maximum flux emitted by the SSC process can be written as

$$F_{\text{max}}^{\text{ssc}} \simeq 19.2 \text{ mJy}\left(\frac{1+z}{1.022}\right)^3 \xi^{-2} \epsilon_{B,-4}^{\frac{1}{2}} A_{\star,-1}^{\frac{5}{2}} D_{26.3}^{-2} t_{1\text{ s}}^{-1}. \quad (32)$$

Using the characteristic and cooling spectral breaks (Equation (30)) and the maximum flux (Equation (32)), the light curves in the fast- and slow-cooling regimes are

$$F_\nu^{\text{ssc}} \propto \begin{cases} t^{-\frac{2(3\delta+10)}{3(\delta+4)}} \epsilon_\gamma^{\frac{1}{3}}, & \epsilon_\gamma < \epsilon_c^{\text{ssc}}, \\ t^{\frac{\delta}{2(\delta+4)}} \epsilon_\gamma^{-\frac{1}{2}}, & \epsilon_c^{\text{ssc}} < \epsilon_\gamma < \epsilon_m^{\text{ssc}}, \\ t^{\frac{8+2\delta-8p-p\delta}{2(\delta+4)}} \epsilon_\gamma^{-\frac{p}{2}}, & \epsilon_m^{\text{ssc}} < \epsilon_\gamma, \end{cases}$$

(33)

and

$$F_\nu^{\text{ssc}} \propto \begin{cases} t^{-\frac{2(\delta+2)}{3(\delta+4)}} \epsilon_\gamma^{\frac{1}{3}}, & \epsilon_\gamma < \epsilon_m^{\text{ssc}}, \\ t^{\frac{\delta+8p+p\delta}{2(\delta+4)}} \epsilon_\gamma^{-\frac{p-1}{2}}, & \epsilon_m^{\text{ssc}} < \epsilon_\gamma < \epsilon_c^{\text{ssc}}, \\ t^{\frac{8+2\delta-8p-p\delta}{2(\delta+4)}} \epsilon_\gamma^{-\frac{p}{2}}, & \epsilon_c^{\text{ssc}} < \epsilon_\gamma, \end{cases}$$

(34)

respectively.

Figure 2 shows the light curves of the synchrotron (left panels) and SSC (right panels) fluxes radiated from the decelerated off-axis jet for typical parameter values of a GRB evolving in a stratified stellar wind-like medium.[13] The

---

[13] The upper panels show the light curves for values of $\tilde{E} = 10^{51}$ erg, $A_\star = 10^4$, $\epsilon_B = 10^{-1}$, $\Delta\theta = 15°$, and $\alpha_s = 1.1$, and the lower panels for the values of $\tilde{E} = 10^{50}$ erg, $A_\star = 10^2$, $\epsilon_B = 10^{-2}$, $\Delta\theta = 15°$, and $\alpha_s = 2.1$. In all panels the values of $\epsilon_e = 0.1$, $p = 2.2$, and $D = 100$ Mpc were used.
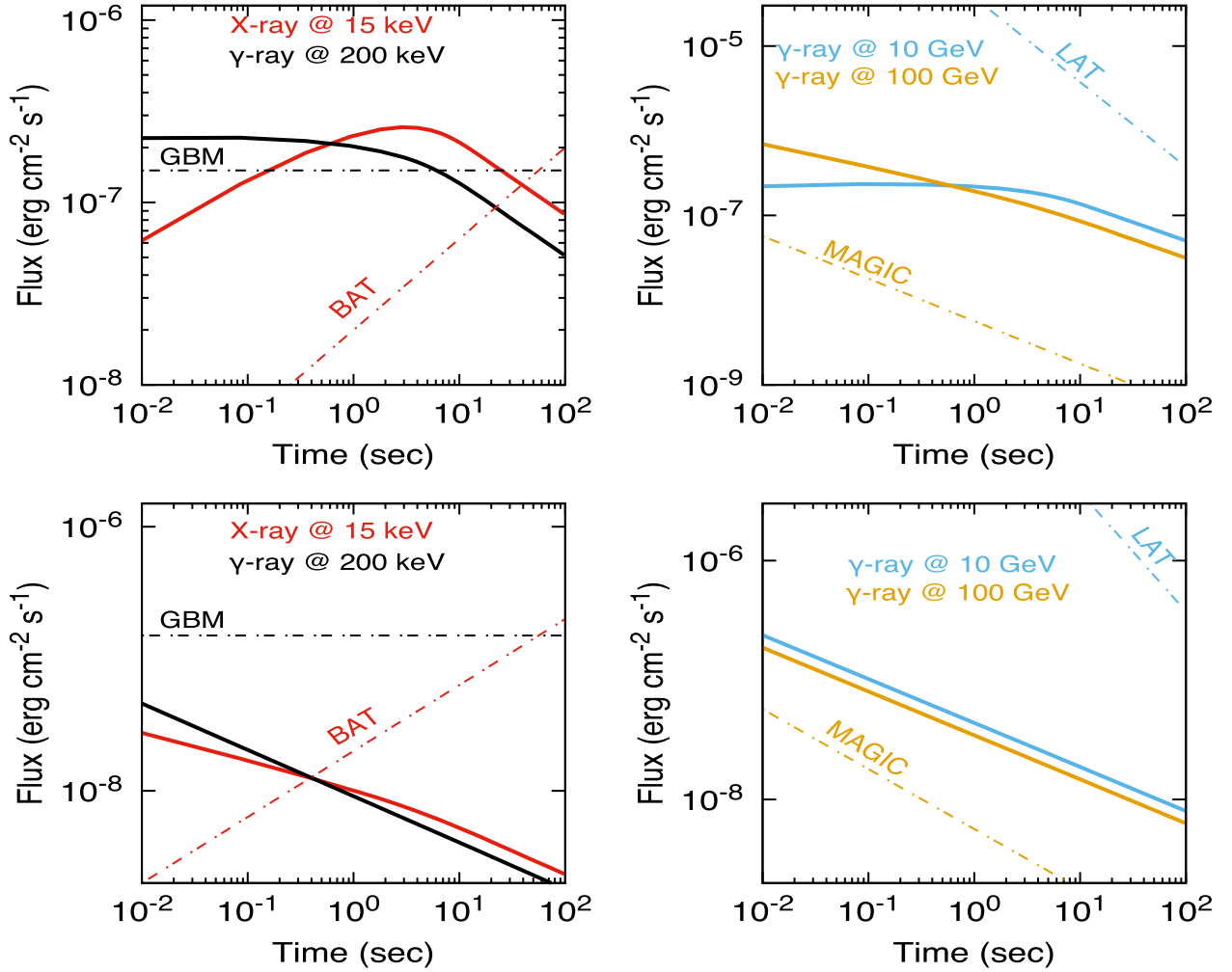
**Figure 2.** Light curves of the synchrotron (left panels) and SSC (right) fluxes radiated from the decelerated outflow in a wind-like density for the values of $E = 10^{51}$ erg, $A_\star = 10^4$, $\epsilon_B = 10^{-1}$, $\Delta\theta = 15°$, and $\alpha_s = 1.1$ (upper panels); and $\tilde{E} = 10^{50}$ erg, $A_\star = 10^2$, $\epsilon_B = 10^{-2}$, $\Delta\theta = 15°$, and $\alpha_s = 2.1$ (lower panels). The values of $\epsilon_e = 0.1$, $p = 2.2$, and $D = 100$ Mpc were assumed in all the panels.

synchrotron and SSC light curves are displayed for two electromagnetic bands and for the chosen parameters these correspond to earlier times than Figure 1. The parameters are as follows: for synchrotron emission X-rays are at 15 keV and $\gamma$-rays are at 200 keV; and for SSC emission $\gamma$-rays are at 10 and 100 GeV. Dashed lines correspond to the sensitivities of the GBM on board Fermi at 200 keV (black) and the Burst Alert Telescope (BAT) on board Swift at 15 keV (red),[14] Fermi-LAT (see footnote 11) and MAGIC (see footnote 12) at 100 GeV (gold). The effect of the EBL absorption introduced in Franceschini & Rodighiero (2017) is used to obtain the SSC light curves. With the parameter values used in these panels, the synchrotron and SSC light curves evolve in the fast-cooling regime. For another set of parameter values such as a timescale of hours and equipartition parameters $\varepsilon_B \sim 0.4$, the synchrotron and SSC light curves would evolve in the slow-cooling regime. These panels shows that depending on the instrument used to detect the electromagnetic emission and the parameters introduced in the model, the observed fluxes will have distinct behaviors. For instance, the synchrotron flux observed at

15 keV increases during the first $\sim$5 s, then reaches its respective maximum, and decreases afterward, and the synchrotron flux observed at 200 keV is almost constant during the first second and then starts to decrease. The SSC flux observed at 10 GeV remains constant during the first 3 s and then decreases, and at 100 GeV, it decreases monotonically. The upper panel shows that the evolution of synchrotron light curves at X-ray and $\gamma$-ray bands could be detected during the first $\sim$5–10 s and the lower panel shows that Swift BAT could detect the synchrotron emission up to 0.2 s and Fermi BAT could not have detected the $\gamma$-ray emission. The right panels show that SSC emission cannot be observed by Fermi-LAT, whereas it can be detected by the MAGIC telescope irrespective of the parameter values used.

## 3. Applications

### 3.1. GRB 080503

GRB 080503 triggered Swift BAT at 2008 May 3 12:26:13 UTC. The duration and the observed flux of the initial main spike in the energy range of 15–150 keV were $0.32 \pm 0.07$ s and $(1.2 \pm 0.2) \times 10^{-7}$ erg cm$^{-2}$ s$^{-1}$, respectively. The details of the X-ray and optical afterglow observations collected with

---

[14] https://swift.gsfc.nasa.gov/proposals/tech_appd/swiftta_v12/node25.html

Swift, Chandra, Keck I, Gemini-N, and Hubble Space Telescope are reported in Perley et al. (2009).

To obtain the best-fit values of the parameters that describe the optical and X-ray data with their upper limits of GRB 080503, we use the Bayesian statistical method of Markov-Chain Monte Carlo (MCMC) simulations (e.g., see, Fraija et al. 2019b). The model can be explained by a set of eight parameters, $\{\tilde{E}, n, p, \Delta\theta, \varepsilon_e, \varepsilon_B, k, \text{and } \alpha_s\}$. To describe the full data, a total of 16,500 samples and 4200 tuning steps were run. All parameters are described by normal distributions. The best-fit values and the median of the posterior distributions of the parameters are exhibited in the corner plots, as shown in Figures 3 and 4 for optical and X-ray data, respectively. The best-fit values in these figures are shown in green and the median of the posterior distributions are reported in Table 1.

Figure 5 shows the optical and X-ray light curves with the fits and uncertainties obtained with the synchrotron forward-shock model evolving in a homogeneous density. The non-thermal optical and X-ray observations are consistent with the outflow described by Equation (1). This suggests that multi-wavelength observations were generated at the same emitting region and by the same radiative process. The peak time in the observed flux at ~one day and after the fast decay is consistent with the fact that the beaming cone of the synchrotron radiation reaches our line of sight. The best-fit values of the parameters for optical (column 2) and X-ray (column 3) are reported in Table 1.

The value of the homogeneous medium required to describe the non-thermal long-lasting emission indicates that the progenitor of GRB 080503, like other sGRBs, exploded in a very low-density environment. The very low density is in agreement with the larger offsets of sGRBs compared with long GRBs.

The value of the spectral index of the electron population is consistent with the typical value reported when relativistic electrons accelerated in the forward shocks are cooled down by synchrotron radiation (see, e.g., Kumar & Zhang 2015). It reaffirms that this emission originated in the GRB afterglow.

Although significant efforts to find the jet breaks in sGRBs have been made, only a few detections have been successful. Given these detections, Berger (2014) showed that the mean of the jet breaks lies around $\theta_j \approx 3° - 6°$. Assuming a value of 4° for GRB 080503, the viewing angle becomes $\theta_{\rm obs} \approx 3°$. Given the observed fluxes of the main spike reported by Swift BAT (Perley et al. 2009) during the first second and the long-lasting emission with a timescale of days, it can be seen that the main spike is fainter than the long-lasting afterglow emission. We argue that the main spike component was viewed nearly off-axis, whereas the component associated with the long-lasting afterglow emission was viewed more widely beamed.

Perley et al. (2009) analyzed the optical and the X-ray observations at ~1 day. Pointing out that the X-ray and optical observations exhibited similar evolutions, the authors discarded the kilonova-like emission proposed by Li & Paczyński (1998) and provided an afterglow interpretation. They proposed that the faint afterglow relative to the bright prompt emission could be explained in terms of the very low circumburst medium and also argued that the late optical and X-ray bumps could be interpreted in the framework of a slightly off-axis jet or a refreshed shock. Hascoët et al. (2012) showed that the origin of the late rebrightening in GRB 080503 could be due to refreshed shocks. Gao et al. (2015) argued that the late optical and X-ray

bump was consistent with the emission from a magnetar-powered "merger-nova." Our analysis indicates that the X-ray and optical observations at ~1 day are consistent with the afterglow emission seen slightly off-axis.

### 3.2. GRB 140903A

GRB 140903A was detected by the Swift BAT at 15:00:30 UT on 2014 September 14. The details of the X-ray, optical, and radio afterglow observations collected with Swift, Chandra, different optical telescopes, and the Very Large Array are reported in Troja et al. (2016).

To obtain the best-fit values of the parameters that adjust the radio, optical, and X-ray observations of GRB 140903A, once again we used the MCMC simulations. In this case, a total of 16,600 samples and 4300 tuning steps were performed to describe the full data. The best-fit values and the median of the posterior distributions of the parameters are exhibited in Figures 6–8. The best-fit values are shown in green and the medians of the posterior distributions are reported in Table 1. The best-fit values of radio, optical, and X-ray data are shown in columns 4, 5, and 6, respectively.

Figure 9 shows the radio, optical and X-ray light curves of GRB 140903A with the fits obtained with the synchrotron forward-shock model evolving in a homogeneous density. Taking into account a typical value of 2°–4° (Berger 2014), the viewing angle becomes $\theta_{\rm obs} \approx 3°$. These values suggest that the jet is seen slightly off-axis. The viewing angle and the best-fit values of the spectral index of the electron population $p = 2.4$, and the microphysical parameters $\epsilon_{\rm e} \simeq 9 \times 10^{-2}$ and $\epsilon_{\rm B} \simeq 8 \times 10^{-2}$ are similar to those reported in Troja et al. (2016). The value of the power-law index of the electron population indicates that the long-lasting emission originated in the GRB afterglow. The derived value of the kinetic energy $\sim 10^{51}$ erg suggests that pair annihilation of $\nu$s and $\bar{\nu}$s is a possible mechanism to provide the energy budget $L_{\nu\bar{\nu}} \lesssim 10^{51}$ erg s$^{-1}$. This result agrees with numerical simulations of merging NS–NS or NS–BH systems (Setiawan et al. 2004; Birkl et al. 2007; Giacomazzo et al. 2013; Giacomazzo & Perna 2013).

Troja et al. (2016) reported and gave a complete analysis of the afterglow observations up to ~15 days of GRB 140903A. Requiring the fireball scenario, authors showed that this burst originated from a collimated jet seen off-axis and also associated with a compact binary object. Zhang et al. (2017) attributed the X-ray "plateau" exhibited in GRB 140903A to the energy injection into the decelerating blast wave and then they modeled the late afterglow emission requiring a jet opening angle of ≈3°. Our analysis finds that GRB 140903A was generated in a collimated jet seen off-axis that decelerated in a homogeneous density.

### 3.3. GRB 150101B

The Swift BAT and Fermi GBM detected GRB 150101B at 15:23:35 and 15:24:34.468 UT on 2015 January 1, respectively (Burns et al. 2018). Data analysis of Swift BAT revealed a bright $\gamma$-ray pulse with a duration and fluence of $T_{90} = 0.012 \pm 0.001$ s and $F_\gamma = (6.1 \pm 2.2) \times 10^{-8}$ erg cm$^{-2}$, respectively. The details of the X-ray and optical afterglow observations with their upper limits are reported in Fong et al. (2016) and Troja et al. (2018b).

To obtain the best-fit values of the parameters that adjust the X-ray and optical observations of GRB 150101B, once again
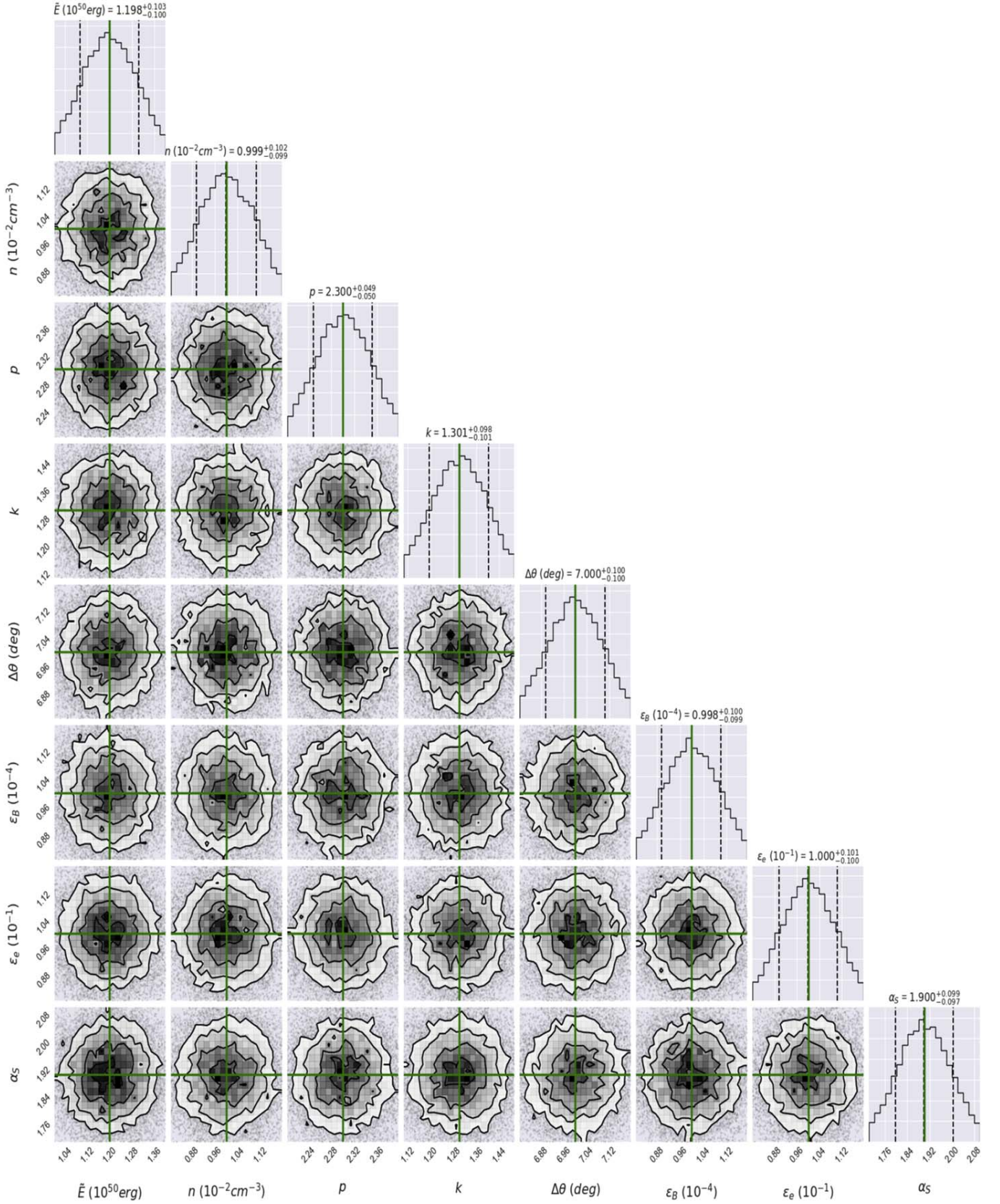
**Figure 3.** Corner plot demonstrating the results obtained from the MCMC simulation for our parameter set (Fraija et al. 2019d). The fit results for the optical light curve of GRB 080503 were found using the synchrotron forward-shock model produced by a decelerated jet in a homogeneous medium viewed off-axis. The labels above the 1-D KDE plot indicate the quantiles chosen for each parameter. The best-fit value is shown in green. Values are reported in Table 1 (Column 2).
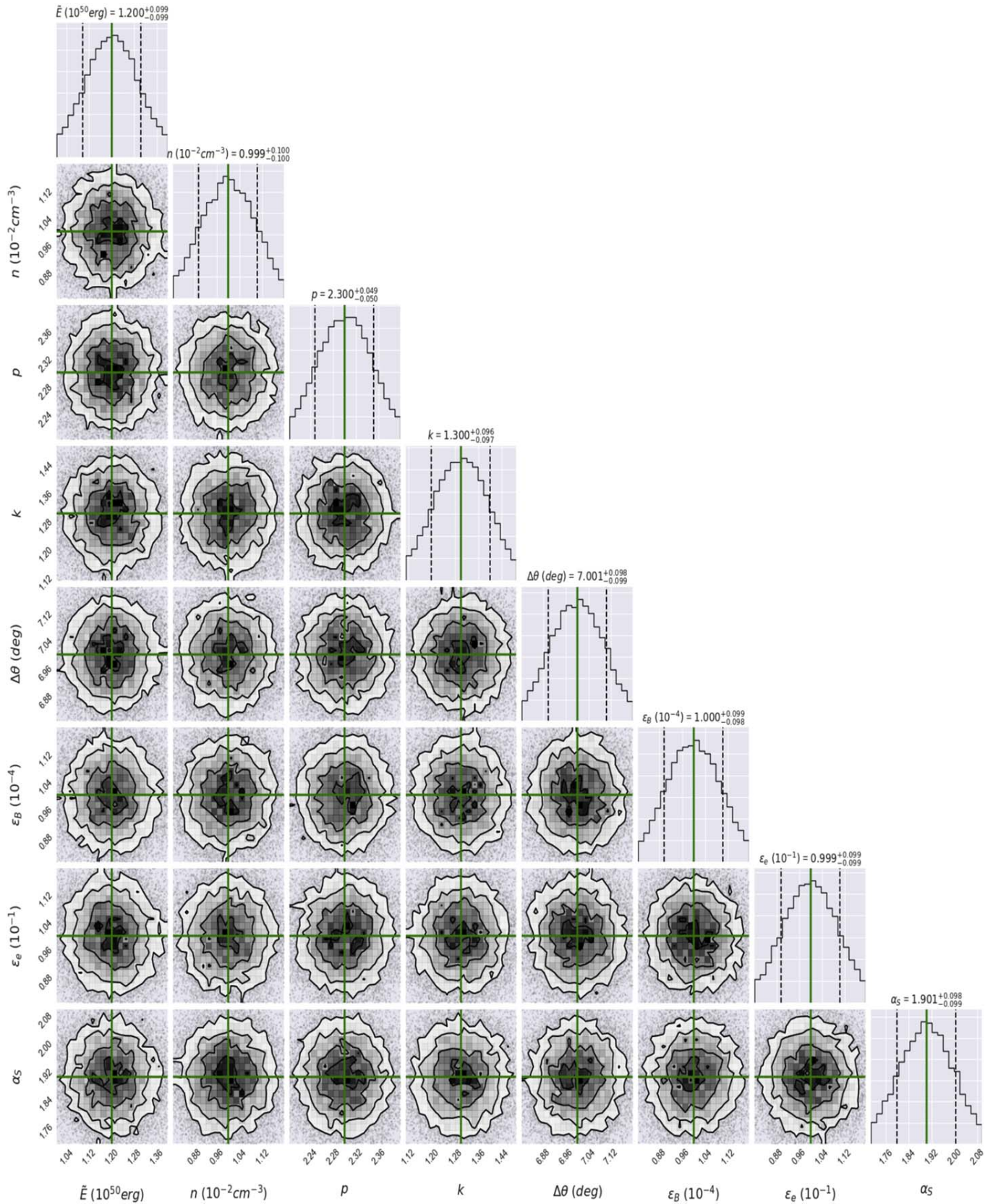
**Figure 4.** Same as Figure 3, but for the fit results for the X-ray light curve of GRB 080503. Values are reported in Table 1 (Column 3).
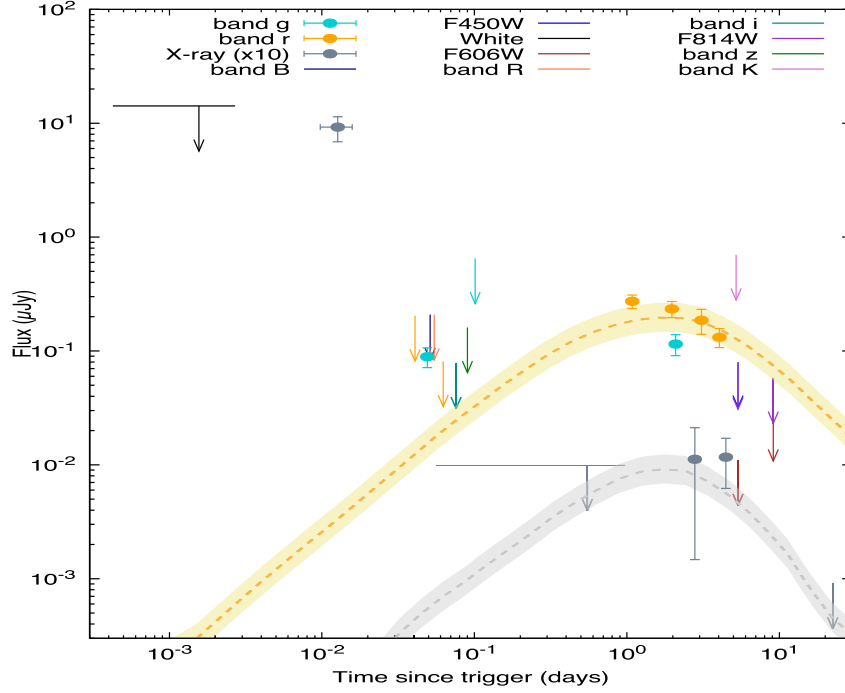
**Figure 5.** Best-fit synchrotron light curves generated when the outflow is decelerated in a uniform ISM-like medium. These synchrotron light curves are displayed at the optical (yellow) and X-ray (gray) energy bands with the data points and upper limits of GRB 080503. Data are taken from Perley et al. (2009). The best-fit values of the parameters used in our model for the optical (column 2) and X-ray (column 3) bands are reported in Table 1.

**Table 1**
The Median and Symmetrical Quantiles (0.15, 0.5, 0.85) Reported after the Description of the X-ray, Optical, and Radio Observations for GRB 080503, GRB 140903A, GRB 150101B, and GRB 160821B

| Parameters | GRB 080503 | | GRB 140903A | | | GRB 150101B | | GRB 160821B |
|---|---|---|---|---|---|---|---|---|
| | Optical | X-Ray | Radio (Wind) | Optical (ISM) | X-Ray | X-Ray | | X-Ray |
| $\tilde{E}$ ($10^{50}$ erg) | $1.19^{+0.10}_{-0.10}$ | $1.20^{+0.09}_{-0.09}$ | $(1.20^{+0.48}_{-0.48}$ | $1.50^{+0.49}_{-0.48}$ | $1.50^{+0.47}_{-0.48}) \times 10^1$ | $2.85^{+1.12}_{-1.15} \times 10^1$ | $1.10^{+0.29}_{-0.30} \times 10^1$ | $1.99^{+0.10}_{-0.10}$ |
| $n$ ($10^{-1}$ cm$^{-3}$) | $(0.99^{+0.10}_{-0.09}$ | $0.99^{+0.10}_{-0.10}) \times 10^{-1}$ | $(1.11^{+0.48}_{-0.49}$ | $1.307^{+0.49}_{-0.48}$ | $1.30^{+0.49}_{-0.49}) \times 10$ | ... | $1.00^{+0.29}_{-0.29} \times 10^{-1}$ | $0.98^{+0.10}_{-0.09}$ |
| $A_\star$ ($10^{-1}$) | | | | | | $0.91^{+0.31}_{-0.33} \times 10^{-1}$ | ... | |
| $p$ | $2.30^{+0.04}_{-0.05}$ | $2.30^{+0.04}_{-0.05}$ | $2.39^{+0.05}_{-0.04}$ | $2.39^{+0.10}_{-0.09}$ | $2.40^{+0.04}_{-0.05}$ | $2.23^{+0.05}_{-0.05}$ | $2.30^{+0.05}_{-0.05}$ | $2.32^{+0.05}_{-0.05}$ |
| $k$ | $1.30^{+0.09}_{-0.10}$ | $1.30^{+0.09}_{-0.09}$ | $0.40^{+0.09}_{-0.10}$ | $0.39^{+0.10}_{-0.09}$ | $0.40^{+0.10}_{-0.09}$ | ... | $0.50^{+0.29}_{-0.29}$ | $0.50^{+0.09}_{-0.09}$ |
| $\Delta\theta$ (deg) | $7.00^{+0.10}_{-0.10}$ | $7.00^{+0.09}_{-0.09}$ | $8.00^{+0.48}_{-0.50}$ | $5.99^{+0.49}_{-0.49}$ | $5.99^{+0.50}_{-0.48}$ | $17.04^{+0.46}_{-0.49}$ | $15.99^{+0.30}_{-0.29}$ | $3.52^{+0.09}_{-0.09}$ |
| $\varepsilon_B$ ($10^{-3}$) | $(0.99^{+0.09}_{-0.09}$ | $1.00^{+0.09}_{-0.09}) \times 10^{-1}$ | $(7.49^{+0.48}_{-0.48}$ | $8.00^{+0.50}_{-0.51}$ | $7.99^{+0.49}_{-0.50}) \times 10$ | $5.99^{+0.58}_{-0.59} \times 10$ | $1.00^{+0.30}_{-0.29} \times 10$ | $0.79^{+0.10}_{-0.10}$ |
| $\varepsilon_e$ ($10^{-1}$) | $1.00^{+0.10}_{-0.10}$ | $0.99^{+0.09}_{-0.09}$ | $(8.48^{+0.50}_{-0.49}$ | $8.99^{+0.49}_{-0.48}$ | $8.99^{+0.50}_{-0.48}) \times 10^{-1}$ | $0.87^{+0.32}_{-0.34}$ | $0.99^{+0.29}_{-0.29}$ | $0.97^{+0.10}_{-0.10}$ |
| $\alpha_s$ | $1.90^{+0.09}_{-0.09}$ | $1.90^{+0.09}_{-0.09}$ | $1.39^{+0.19}_{-0.20}$ | $1.59^{+0.19}_{-0.20}$ | $1.59^{+0.19}_{-0.19}$ | $2.10^{+0.10}_{-0.09}$ | $1.50^{+0.29}_{-0.29}$ | $2.62^{+0.09}_{-0.09}$ |

**Note.** These values are obtained using the theoretical model and the MCMC simulations.

we use the MCMC simulations. In this case, a total of 16,400 samples and 4300 tuning steps were performed to describe the full data. The best-fit values and the median of the posterior distributions of the parameters are shown in Figures 10 and 11. The best-fit values are shown in green and the medians of the posterior distributions are reported in Table 1 (columns 7 and 8).

Figure 12 shows the X-ray light curve of GRB 150101B with the fit and uncertainties obtained with the synchrotron forward-shock model evolving in a wind (left) and homogeneous (right) density. As the homogeneous density is considered, the values of the spectral index of the electron population, the circumburst density, the microphysical parameters, and the viewing angle disfavor the isotropic cocoon

model reported in Troja et al. (2018b) and are consistent with the values of a structured jet. Fong et al. (2016) modeled the evolution of the afterglow observations in GRB 150101B and estimated the isotropic-equivalent kinetic energy of $\approx(6-14) \times 10^{51}$ erg and a jet opening angle of $\gtrsim 9°$. Our analysis leads to similar values of kinetic energy and a jet opening angle. Given the observed flux of the short and hard spike reported by Fermi GBM (Burns et al. 2018) and the X-ray afterglow emission detected on a timescale of days, it can be observed that the short and hard spike is fainter than the X-ray emission. We conclude that the bright spike component was viewed nearly off-axis, whereas the long-lasting emission was viewed more widely beamed. The best-fit value of the circumburst medium obtained suggests that the progenitor of
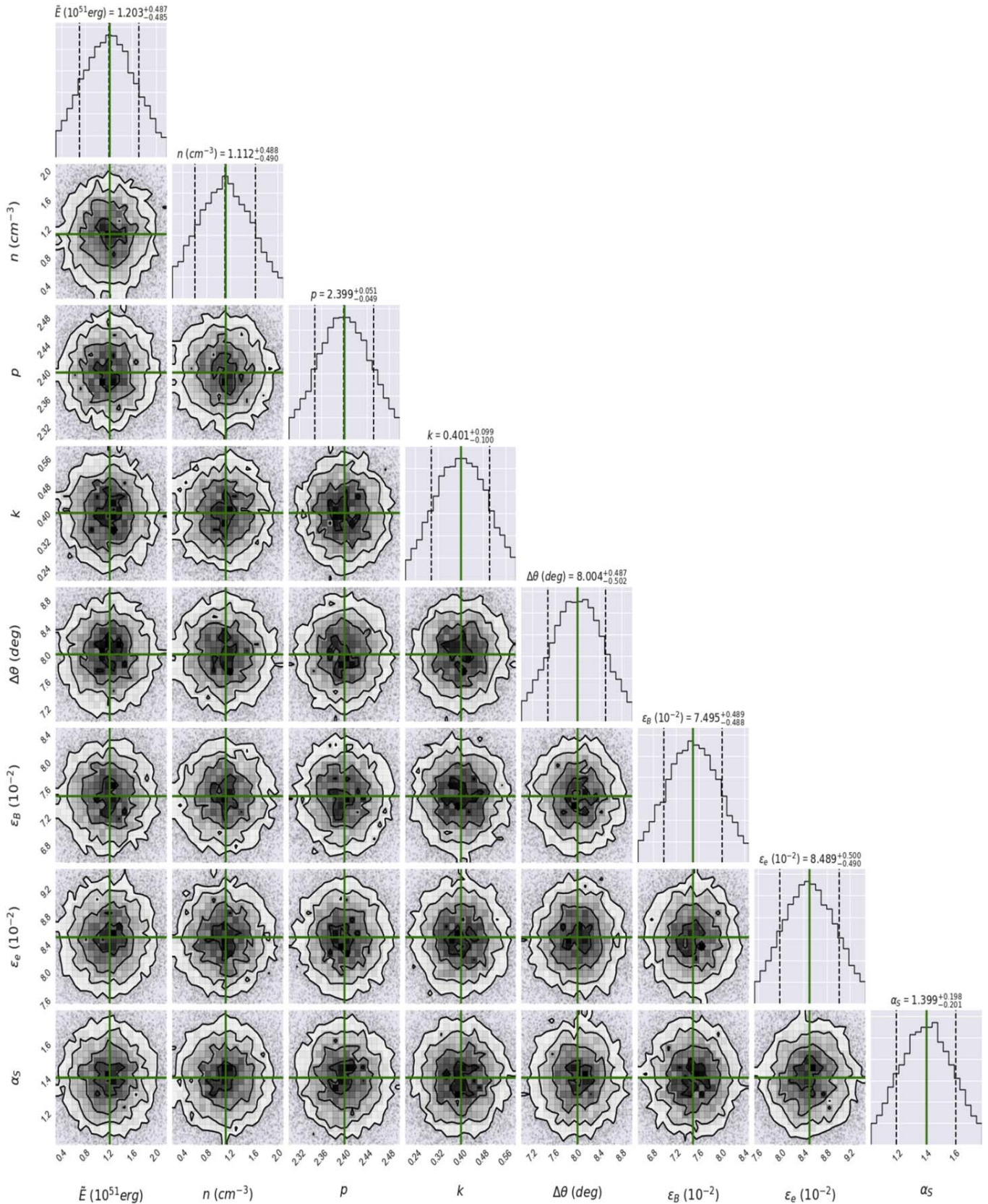
**Figure 6.** Same as Figure 3, but for the fit results for the radio light curve of GRB 140903A. Values are reported in Table 1 (Column 4).
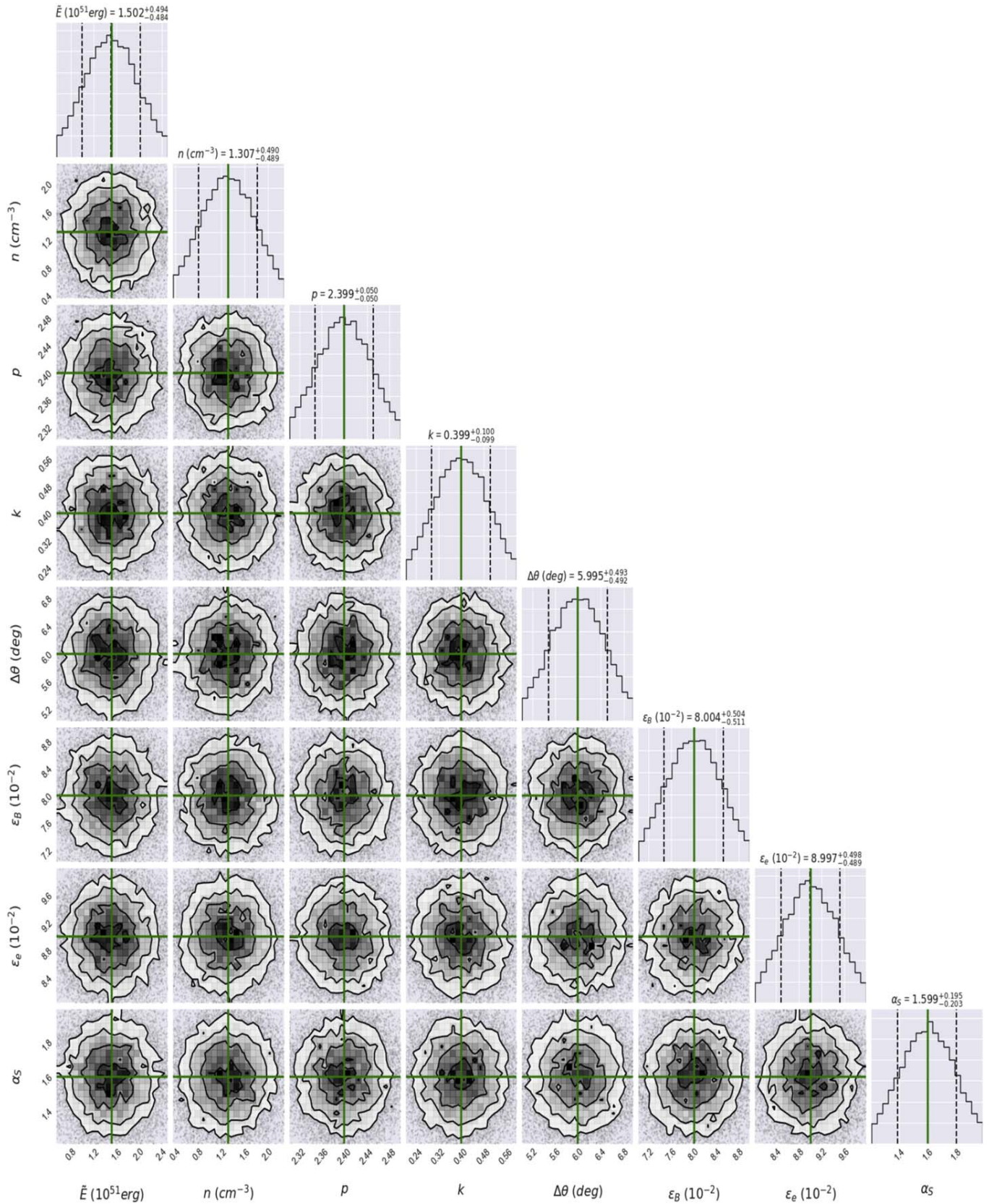
**Figure 7.** Same as Figure 3, but for the fit results for the optical light curve of GRB 140903A. Values are reported in Table 1 (Column 5).
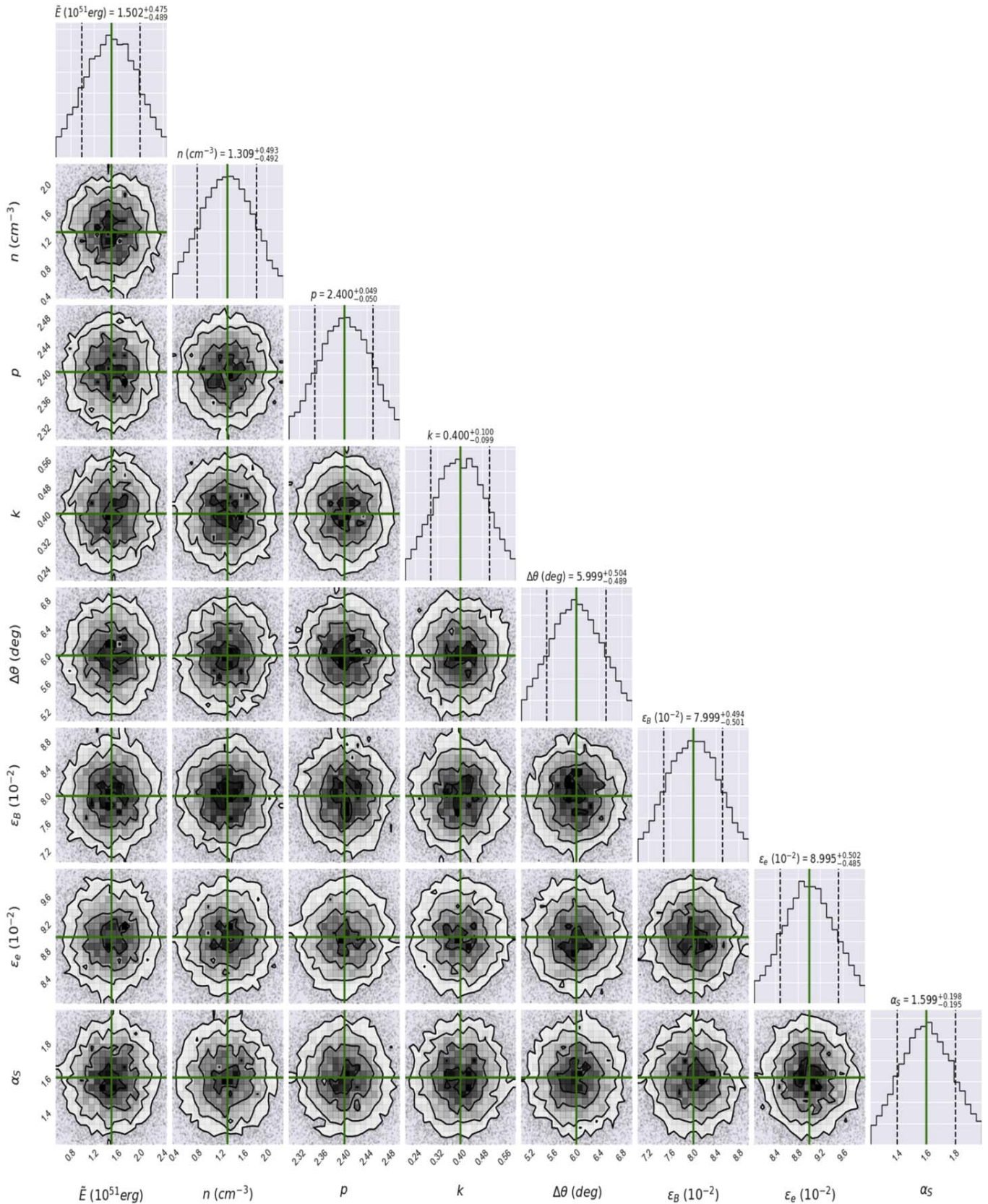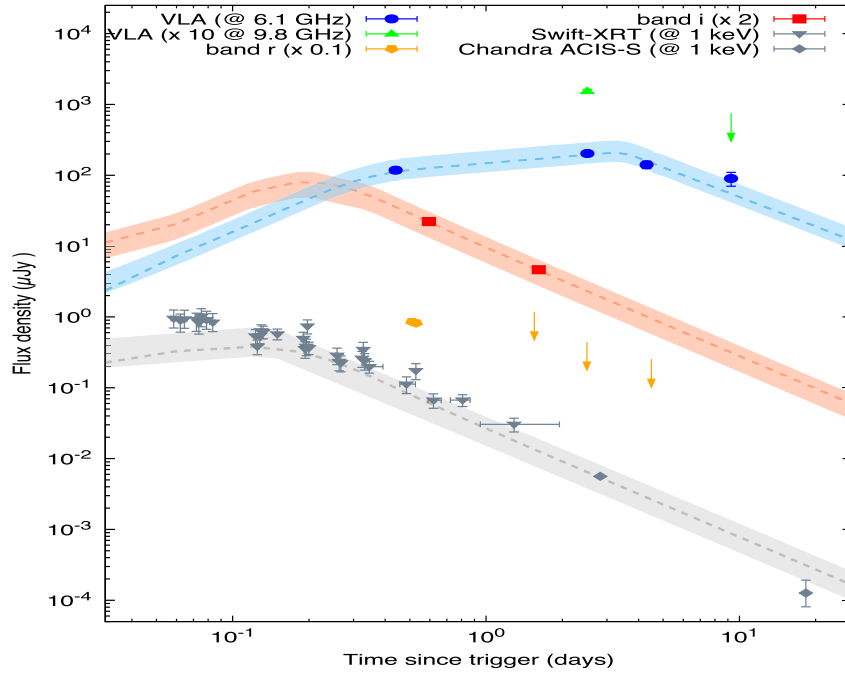
**Figure 8.** Same as Figure 3, but for the fit results for the X-ray light curve of GRB 140903A. Values are reported in Table 1 (Column 6).

**Figure 9.** Best-fit synchrotron light curves generated when the outflow is decelerated in a uniform ISM-like medium. These synchrotron light curves are displayed at the radio (blue), optical (red), and X-ray (gray) energy bands with the data points and upper limits of GRB 140903A. Data are taken from Troja et al. (2016). The best-fit values of the parameters used in our model for radio (column 4), optical (column 5), and X-ray (column 6) bands are reported in Table 1.

GRB 150101B, like other short bursts, exploded in a low-density environment. When the wind-like medium is considered, our model can consistently describe the X-ray data and optical upper limits. In this case, the value of the equivalent kinetic energy is lower and the magnetic microphysical parameter is larger than those derived assuming a homogeneous medium. The result of the density parameter derived with our model is consistent with the allowed range of values reported by the GBM collaboration (Burns et al. 2018) after describing the short and hard gamma-ray peaks.

### 3.4. GRB 160821B

The Swift BAT and Fermi GBM triggered and located GRB 160821B at 22:29:13 and 22:29:13.33 UT on 2016 August 21, respectively. The Swift XRT data were obtained using the publicly available database at the official Swift website.[15] The flux density is extrapolated from 10 to 1 keV using the conversion factor introduced in Evans et al. (2010). The details of the optical and radio afterglow observations with their upper limits are reported in Troja et al. (2019). Fermi-LAT searched for high-energy $\gamma$-ray emission in the 0.1–300 GeV range and MAGIC searched for VHE photons above >500 GeV from GRB 160821B. In both cases, no photons were detected at the position of this burst and upper limits were derived (Palatiello et al. 2017).

To obtain the best-fit values of the parameters that fit the X-ray light curve of GRB 160821B, once again we use the MCMC simulations. In this case, a total of 18,200 samples and 8100 tuning steps were performed to describe all the data. The best-fit values and the median of the posterior distributions of the parameters are exhibited in Figure 13. The best-fit values of

the X-ray band are shown in green and the medians of the posterior distributions are reported in Table 1 (column 9).

Figure 14 shows the multiwavelength observations of GRB 160821B from 0.2 to 5 days, after the GBM trigger. The upper limit collected with Fermi-LAT was obtained from the online data repository[16] and the upper limit derived with the MAGIC observatory is available in Palatiello et al. (2017). The left panel shows the best-fit light curves obtained using the synchrotron forward-shock model that evolves in a homogeneous density. These light curves are shown at the radio, optical, and X-ray bands. The radio, optical, and X-ray light curves are displayed at 8 GHz, 3 eV and 1 keV, respectively. It is worth noting that although our off-axis model can describe the X-ray and radio observations, it cannot explain all the optical data. Therefore, the kilonova-like emission as proposed by Troja et al. (2019) and Lamb et al. (2019b) has to be required. In our analysis we did not consider the 5 GHz radio afterglow observations that were described with a contribution from a reverse shock (Lamb et al. 2019b). The best-fit values of the circumburst density, the spectral index of the electron population, the microphysical parameters, and the viewing angle are similar to those recently reported in Troja et al. (2019) and Lamb et al. (2019b). Given the observed flux of the short peak detected by Fermi GBM (Stanbro & Meegan 2016) and the long-lasting multiwavelength emission, it can be observed that the short peak is weaker than the long-lasting multiwavelength emission. We conclude that the bright peak and the long-lasting afterglow emission were viewed nearly off-axis. The best-fit value of the circumburst medium obtained suggests that the progenitor of GRB 160821B, like other short bursts, exploded in a low-density environment. On the other hand, Lü et al. (2017) assumed that the central engine of GRB 160821 was a new born supramassive magnetar and then could

---

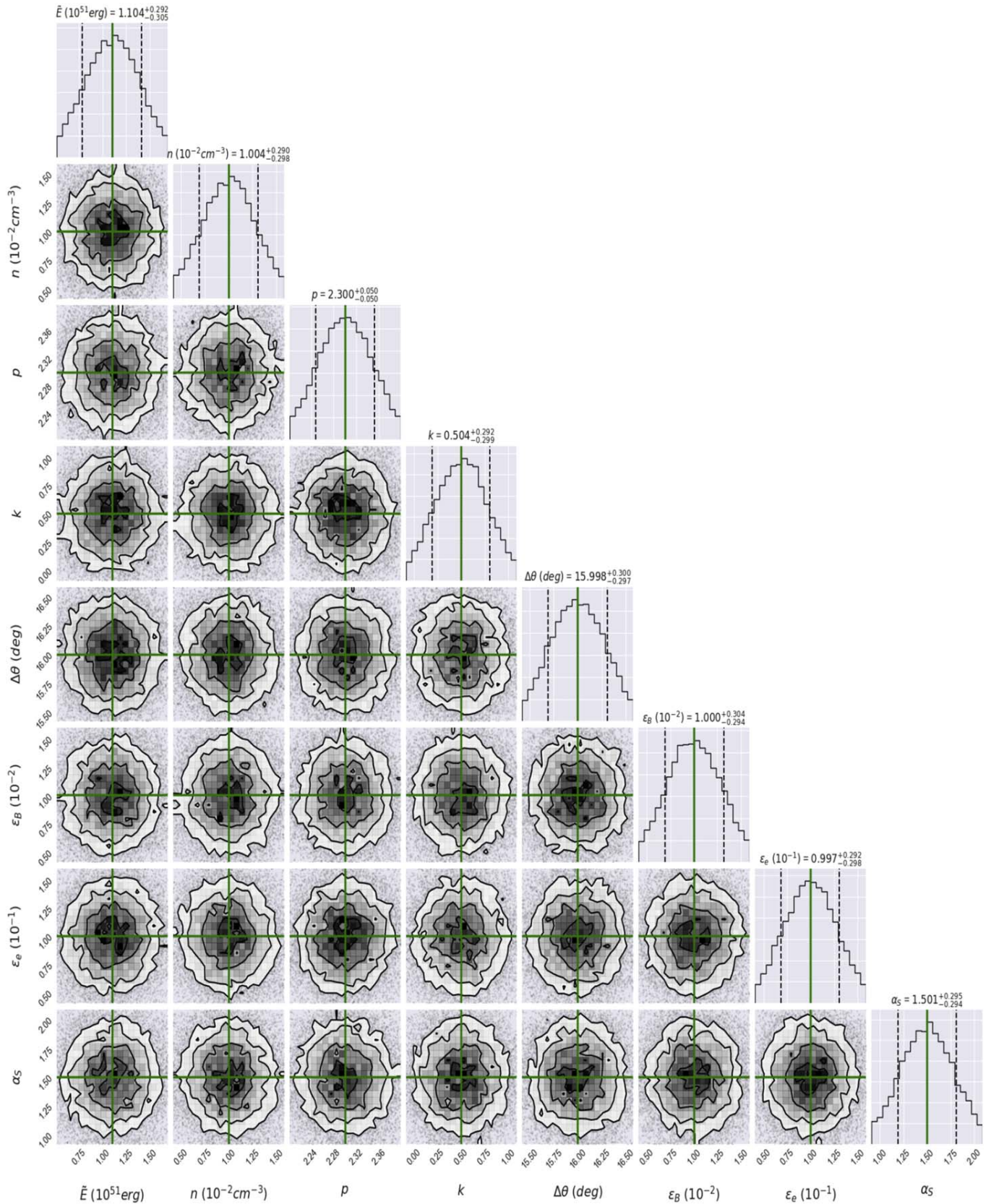**Figure 10.** Same as Figure 3, but for the fit results for the X-ray light curve of GRB 150101B. Values are reported in Table 1 (Column 7).
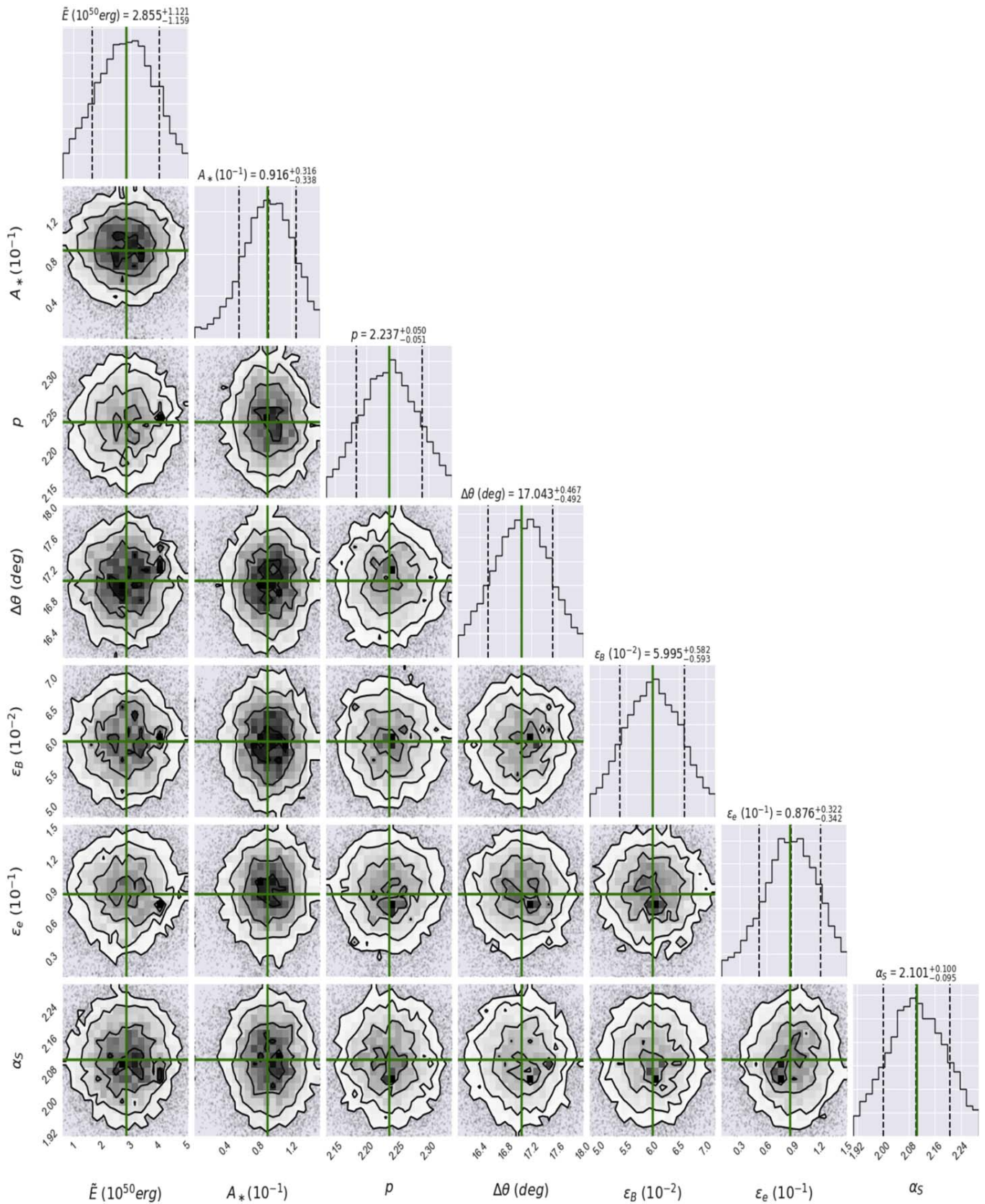
**Figure 11.** Same as Figure 10, but for the fit results for the X-ray light curve of GRB 150101B using the synchrotron forward-shock model produced by a decelerated jet viewed off-axis in a wind-like medium. Values are reported in Table 1 (Column 8).
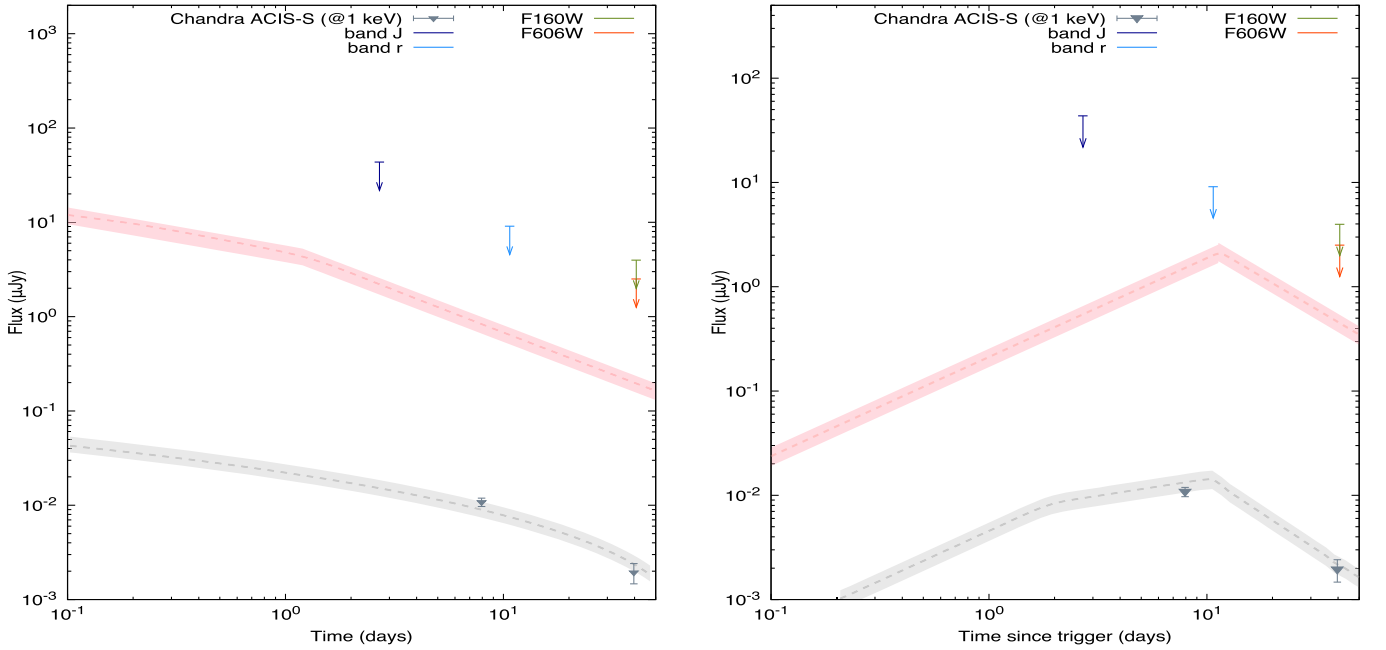
**Figure 12.** Best-fit synchrotron light curves generated when the outflow is decelerated in a wind-like (right) and a uniform ISM-like (left) medium. These synchrotron light curves are displayed at the optical (red) and X-ray (gray) energy bands, with the data points and upper limits of GRB 150101B. X-ray data are taken from Fong et al. (2016) and optical upper limits are taken from Troja et al. (2018b). The best-fit values of the parameters used in our model for X-rays (columns 7 and 8) are reported in Table 1.

interpret this burst in the framework of the jet radiation and the spin-down of the pulsar wind.

The right panel shows the upper limits derived with the Fermi-LAT and MAGIC observatories with the SSC light curves derived in this work. We obtain the VHE $\gamma$-ray light curves at 1 GeV (purple) and 200 GeV (blue) using the values found after describing the X-ray and optical light curves of GRB 160821B. The effect of the EBL absorption described in Franceschini & Rodighiero (2017) is used. With the best-fit values found for this burst, the break energy derived in the KN regime is 486 GeV, which is above the VHE upper limits set by Fermi-LAT and MAGIC. This panel shows that the SSC flux is consistent with LAT and MAGIC upper limits. Therefore, the SSC model, as well as the values used to fit the delayed non-thermal emission, are in accordance with the observations.

### 3.5. GRB 170817A

Fraija et al. (2019a) described in detail the multiwavelength data collected for this event. Here we use the SSC model with the parameters they found and the VHE $\gamma$-ray upper limits. The Large Area Telescope (Fermi-LAT) and The High Energy Stereoscopic System (H.E.S.S.) Imaging Air Cerenkov Telescope searched for VHE $\gamma$-ray emission from the GW170817 event (Abbott et al. 2017b; Abdalla et al. 2017). GW170817A was in the field of view of Fermi-LAT ∼1000 s after the merger trigger. No significant excess was detected at the position of GW170817 and upper limits were derived (Abdalla et al. 2017). Observations with the H.E.S.S. $\gamma$-ray telescope were obtained on two occasions. The first observation was obtained 5.3 hr after the GW trigger. During the second epoch the HESS observatory covered timescales from 0.22 to 5.2 days and an energy range from 270 GeV to 8.55 TeV. Although no statistically significant excess of counts was found by this TeV observatory, constraining upper limits were derived.

Figure 15 shows the upper limits placed with the Fermi-LAT and H.E.S.S. observatories and the corresponding SSC light curves derived in this work. We derive the VHE $\gamma$-ray light curves at 100 MeV (purple) and 1 TeV (blue) using the values found by Fraija et al. (2019a) after describing the X-ray, optical, and radio light curves of GRB 170817A. The effect of the EBL absorption described in Franceschini & Rodighiero (2017) is used. With the best-fit values found for GRB 170817A, the break energy derived in the KN regime is 2.6 TeV, which is above the VHE upper limits set by the Fermi-LAT and H.E.S.S. observatories. As shown in this figure, the SSC flux is too low to be detected by LAT and H.E.S.S. observatories. Therefore, the SSC model, as well as the values used to fit the delayed non-thermal emission, are in accordance with the observations reported by the GeV–TeV $\gamma$-ray observatories.

### 4. Conclusions

Several studies have modeled the evolution of the afterglow requiring the synchrotron emission generated by the deceleration of a relativistic jet seen off-axis. In particular, some of them have discussed the afterglow, opening angle, jet geometry, and orientation (e.g.,see Lazzati et al. 2017, 2018; Jin et al. 2018; Lamb et al. 2018). In this paper, we have extended the analytical scenario shown in Fraija et al. (2019a) by deriving, for a more general case, the SSC and synchrotron forward-shock light curves when this outflow is decelerated in a homogeneous and wind-like circumburst medium in the fully adiabatic regime. In the particular case of $\delta = 0$, the SSC and synchrotron light curves derived in a homogeneous and wind-like medium are recovered (Sari et al. 1998, 1999; Chevalier & Li 2000; Sari & Esin 2001). We have computed the light curves considering the values of observables and parameters in the typical ranges: $\tilde{E} = 10^{50} - 10^{52}$ erg, $n = 10^{-4} - 10^{-3}$ cm$^{-3}$,
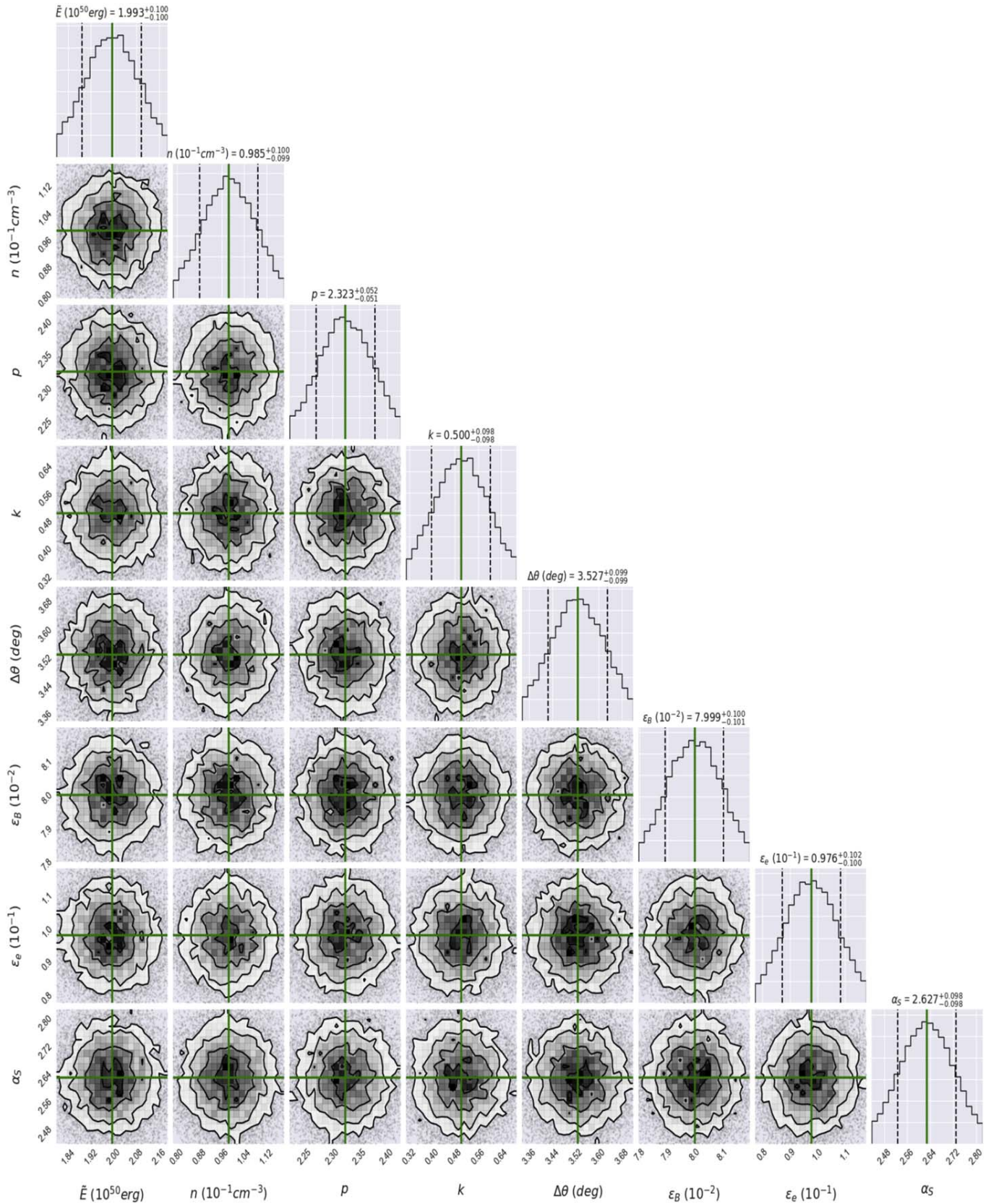
**Figure 13.** Same as Figure 3, but for the fit results for the X-ray light curve of GRB 160821B. Values are reported in Table 1 (Column 11).
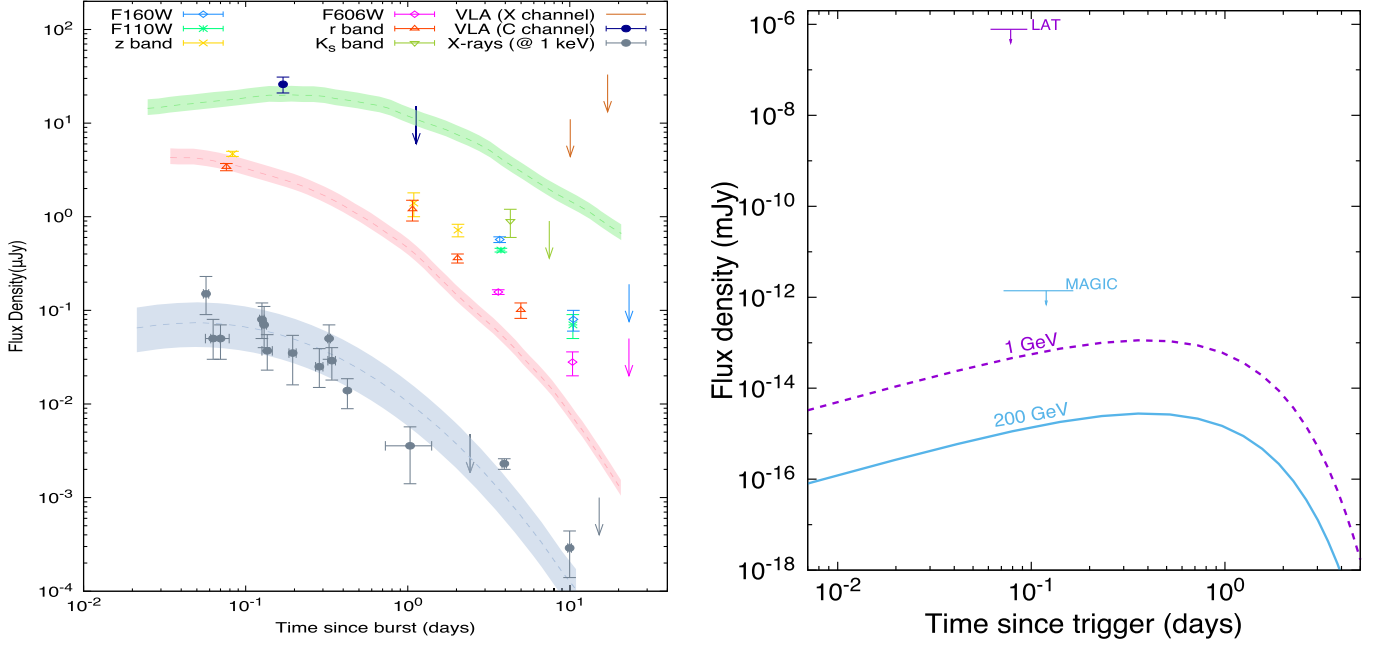
**Figure 14.** Left: best-fit synchrotron light curves generated when the outflow is decelerated in a uniform ISM-like medium. These synchrotron light curves are displayed at the radio (green), optical (red), and X-ray (gray) energy bands with the data points and upper limits of GRB 160821B. The best-fit values of the parameters used in our model for X-rays (column 9) are reported in Table 1. Right: upper limits placed by the Fermi-LAT and the MAGIC with the SSC light curves obtained in our model at 1 GeV (purple) and 200 TeV (blue), generated in a uniform ISM-like medium. The effect of the EBL absorption described in Franceschini & Rodighiero (2017) is considered.
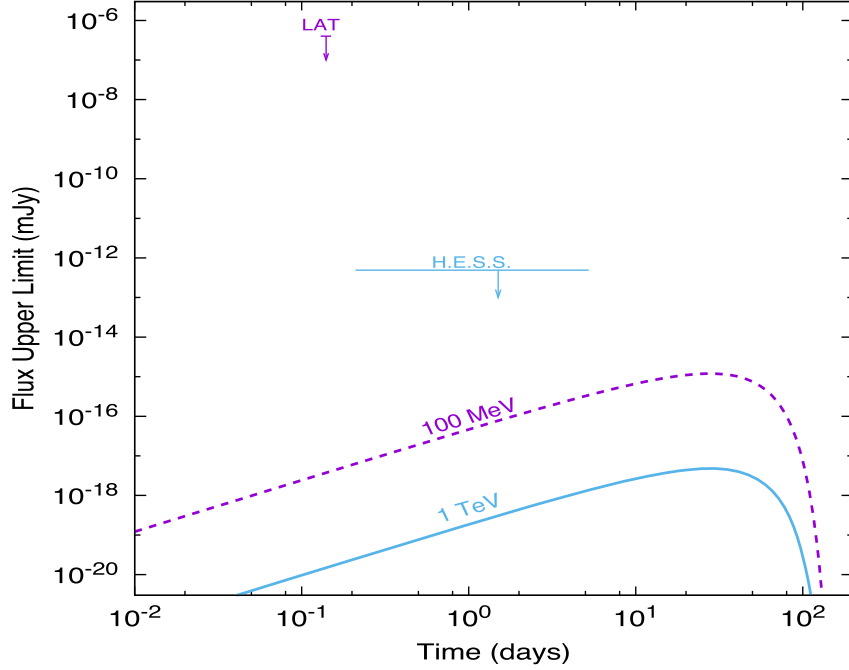


**Figure 15.** Upper limits placed by the Fermi-LAT and the H.E.S.S. experiment (Abdalla et al. 2017) with the SSC light curves obtained in our model at 100 MeV (purple) and 1 TeV (blue) generated in a uniform ISM-like medium. The effect of the EBL absorption described in Franceschini & Rodighiero (2017) is considered. We use the best-fit values found with our MCMC code after modeling the X-ray, optical, and radio data points of GRB 170817A (see Table 5 in Fraija et al. 2019a).

$A_\star = 1$–$10^4$, $\epsilon_B = 10^{-4} - 10^{-1}$, $\Delta\theta = 15° - 30°$ and $\alpha_s = 1.1$–$2.1$ for the values of $\epsilon_e = 0.1$, $p = 2.2$ and $D = 100$ Mpc.

Burns et al. (2018) analyzed the prompt phase of GRB 150101B. These authors argued that the prompt emission was formed by a two-component structure; a short hard spike followed by a longer soft tail. Authors concluded that the cocoon shock

breakout models disfavor the description of the two-component structure in this light curve. They derived the conditions for radius of acceleration to take place below the photospheric radius, assuming a wind-like medium in the vicinity of the NS merger. These authors found that the values of the density parameter and mass density were $A \gtrsim 4.5 \times 10^{35}$ g cm$^{-1}$ and

$\rho \gtrsim 10^{-2} \, \mathrm{g \, cm^{-3}}$, respectively. In the model proposed in this paper, we showed that the flux emitted from synchrotron forward-shock emission in a wind-like medium is in the range of the Fermi GBM for values of $A \sim 10^{39} \, \mathrm{g \, cm^{-1}}$ and $\rho \sim 1 \, \mathrm{g \, cm^{-3}}$, which agree with those derived in Burns et al. (2018) and Bauswein et al. (2013). If this is the case, a transition phase from a wind-like medium to a homogeneous medium is expected, as indicated in Fraija et al. (2017b).

In particular, we have analyzed GRB 080503, GRB 140903A, GRB 150101B, GRB 160821B, and GRB 170817A. For GRB 080503, GRB 140903A, GRB 150101B, and GRB 160821B we have shown that the origin of the delayed and long-lasting afterglow emission could be interpreted by a scenario similar to the one used to describe GRB 170817A; the radio, optical and X-ray light curves with the upper limits through the synchrotron forward-shock model (e.g., see Lazzati et al. 2018; Troja et al. 2018a, 2017b). The non-thermal radio, optical, and X-ray fluxes with upper limits are consistent with the synchrotron forward-shock model in a homogeneous circumburst medium, indicating that the multi-wavelength observations were generated by the same power laws and the peak times are consistent with the fact that the beaming cone of the radiation reaches our line of sight. For GRB 160821B, we show additionally that the proposed scenario agrees with the VHE $\gamma$-ray upper limits derived by the TeV $\gamma$-ray observatories. The SSC fluxes are 4–8 orders of magnitude less than the high-energy upper limits. For GRB 170817A, the gamma-ray spike and the delayed non-thermal emission were described in Fraija et al. (2019a). Here, we show that the proposed scenario agrees with the VHE $\gamma$-ray upper limits derived by the TeV $\gamma$-ray observatories. The SSC fluxes are 8–10 orders of magnitude less than the high-energy upper limits. It is worth emphasizing that in GRB 080503, GRB 140903A, GRB 160821B, and GRB 170817A, the synchrotron forward-shock radiation emitted from a homogeneous medium was favored over the radiation emitted from a stratified stellar-wind medium. For GRB 150101B, the emission of synchrotron forward-shock radiation emitted from both a wind or a homogeneous medium is consistent with the X-ray data and optical upper limits. In the case of the stratified wind-like medium, our results are consistent with those reported by the GBM collaboration after the description of the short and hard gamma-ray peak. Based on the parameter values found using our model, we point out that:

(i) The values of the homogeneous medium required to describe the non-thermal long-lasting afterglow emission suggest that the progenitor of these bursts exploded in a very low density environment. These values are in agreement with the larger offsets of sGRBs compared with lGRBs.

(ii) The values of the spectral indexes of the electron populations are consistent with the typical values reported when relativistic electrons accelerated in the forward shocks are cooled down by synchrotron radiation (see, e.g., Kumar & Zhang 2015; Fraija et al. 2017a; Becerra et al. 2019a, 2019b). It reaffirms that the long-lasting afterglow emission was originated in the GRB afterglow.

(iii) Assuming a value in the range of $4°–6°$ for the jet opening angle for these bursts, the viewing angles become $1° \lesssim \theta_{\mathrm{obs}} \lesssim 10°$. Given the observed fluxes of the hard and short spikes and the long-lasting afterglow emissions, the spike components are fainter than the long-lasting afterglow components. The fact that the total energy of the delayed non-thermal emission can exceed that of the hard spikes by a large factor is a problem for the NS merger scenario which is limited to some seconds by the viscous timescale (see, e.g., Lee et al. 2004). However, it could be reconciled with the merger scenario, as proposed in our model where the hard spikes focused in a collimated jet are viewed nearly off-axis whereas the long-lasting afterglow emissions are more widely beamed.

(iv) The derived values of the kinetic energies $\sim 10^{51-52}$ erg suggest that pair annihilation of neutrinos and anti-neutrinos is a possible mechanism to provide the energy budget $L_{\nu\bar{\nu}} \lesssim 10^{51} \mathrm{erg \, s^{-1}}$. This result agrees with numerical simulation of merging NS–NS or NS–BH systems.

(v) The VHE upper limits set by Fermi-LAT, MAGIC, and H.E.S.S. are below the SSC energy break derived in the KN regime. This result indicates that the SSC break energy is not drastically attenuated, which encourages us to keep observing these events in VHEs.

The multiwavelength light curves indicate that GRB 080503, GRB 140903A, GRB 150101B, GRB 160821B, and GRB 170817A originated from the same kind of progenitors, despite their diversity. We might argue that the short bursts detected by the BAT and GBM instruments without their corresponding emissions in other electromagnetic bands were too faint during the first second to be detected and followed up.

## ORCID iDs

N. Fraija ⬤ https://orcid.org/0000-0002-0173-6453
P. Veres ⬤ https://orcid.org/0000-0002-2149-9846

## References

Abbott, B. P., Abbott, R., Abbott, T. D., et al. 2017a, PhRvL, 119, 161101
Abbott, B. P., Abbott, R., Abbott, T. D., et al. 2017b, ApJL, 848, L12
Abdalla, H., Abramowski, A., Aharonian, F., et al. 2017, ApJL, 850, L22
Abdo, A. A., Ackermann, M., Ajello, M., et al. 2009, ApJL, 706, L138
Ackermann, M., Ajello, M., Asano, K., et al. 2013, ApJS, 209, 11
Ackermann, M., Ajello, M., Asano, K., et al. 2014, Sci, 343, 42
Alexander, K. D., Berger, E., Fong, W., et al. 2017, ApJL, 848, L21
Barniol Duran, R., & Kumar, P. 2011, MNRAS, 412, 522
Barniol Duran, R., Nakar, E., Piran, T., & Sari, R. 2015, MNRAS, 448, 417
Bauswein, A., Goriely, S., & Janka, H.-T. 2013, ApJ, 773, 78
Becerra, R. L., Dichiara, S., Watson, A. M., et al. 2019a, ApJ, 881, 12
Becerra, R. L., Watson, A. M., Fraija, N., et al. 2019b, ApJ, 872, 118
Becerra, R. L., Watson, A. M., Lee, W. H., et al. 2017, ApJ, 837, 116
Berger, E. 2014, ARA&A, 52, 43
Birkl, R., Aloy, M. A., Janka, H.-T., & Müller, E. 2007, A&A, 463, 51
Blandford, R. D., & McKee, C. F. 1976, PhFl, 19, 1130
Burns, E., Veres, P., Connaughton, V., et al. 2018, ApJL, 863, L34
Chevalier, R. A., & Li, Z.-Y. 2000, ApJ, 536, 195
Coulter, D. A., Foley, R. J., Kilpatrick, C. D., et al. 2017, Sci, 358, 1556
Duffell, P. C., & Laskar, T. 2018, ApJ, 865, 94
Evans, P. A., Willingale, R., Osborne, J. P., et al. 2010, A&A, 519, A102
Fong, W., Margutti, R., Chornock, R., et al. 2016, ApJ, 833, 151
Fraija, N. 2014, MNRAS, 437, 2187
Fraija, N. 2015, ApJ, 804, 105
Fraija, N., Barniol Duran, R., Diachara, S., & Beniamini, P. 2019e, ApJ, 883, 162

Fraija, N., De Colle, F., Veres, P., et al. 2019a, ApJ, 871, 123
Fraija, N., Dichiara, S., Pedreira, A. C. C. d. E. S., et al. 2019b, ApJL, 879, L26
Fraija, N., Lee, W., & Veres, P. 2016a, ApJ, 818, 190
Fraija, N., Lee, W. H., Araya, M., et al. 2017a, ApJ, 848, 94
Fraija, N., Lee, W. H., Veres, P., & Barniol Duran, R. 2016b, ApJ, 831, 22
Fraija, N., Lopez-Camara, D., Pedreira, A., et al. 2019d, ApJ, 884, 71
Fraija, N., Pedreira, A. C. C. d. E. S., & Veres, P. 2019c, ApJ, 871, 200
Fraija, N., & Veres, P. 2018, ApJ, 859, 70
Fraija, N., Veres, P., Beniamini, P., et al. 2020, arXiv:2003.11252
Fraija, N., Veres, P., Zhang, B. B., et al. 2017b, ApJ, 848, 15
Franceschini, A., & Rodighiero, G. 2017, A&A, 603, A34
Gao, H., Ding, X., Wu, X.-F., Dai, Z.-G., & Zhang, B. 2015, ApJ, 807, 163
Giacomazzo, B., & Perna, R. 2013, ApJL, 771, L26
Giacomazzo, B., Perna, R., Rezzolla, L., Troja, E., & Lazzati, D. 2013, ApJL, 762, L18
Gill, R., Granot, J., De Colle, F., & Urrutia, G. 2019, arXiv:1902.10303
Goldstein, A., Veres, P., Burns, E., et al. 2017, ApJL, 848, L14
Granot, J., Gill, R., Guetta, D., & De Colle, F. 2017, arXiv:1710.06421
Granot, J., Panaitescu, A., Kumar, P., & Woosley, S. E. 2002, ApJL, 570, L61
Haggard, D., Nynka, M., Ruan, J. J., Evans, P., & Kalogera, V. 2018, ATel, 11242, 1
Hascoët, R., Daigne, F., & Mochkovitch, R. 2012, A&A, 541, A88
Hotokezaka, K., Kiuchi, K., Shibata, M., Nakar, E., & Piran, T. 2018, ApJ, 867, 95
Hotokezaka, K., Kyutoku, K., Tanaka, M., et al. 2013, ApJL, 778, L16
Hotokezaka, K., & Piran, T. 2015, MNRAS, 450, 1430
Ioka, K., & Nakamura, T. 2017, arXiv:1710.05905
Jin, Z.-P., Li, X., Wang, H., et al. 2018, ApJ, 857, 128
Kasliwal, M. M., Nakar, E., Singer, L. P., et al. 2017, Sci, 358, 1559
Kathirgamaraju, A., Tchekhovskoy, A., Giannios, D., & Barniol Duran, R. 2019, MNRAS, 484, L98
Kumar, P., & Zhang, B. 2015, PhR, 561, 1
Kyutoku, K., Ioka, K., & Shibata, M. 2014, MNRAS, 437, L6
Lamb, G. P., & Kobayashi, S. 2017, MNRAS, 472, 4953
Lamb, G. P., Lyman, J. D., Levan, A. J., et al. 2019a, ApJL, 870, L15
Lamb, G. P., Mandel, I., & Resmi, L. 2018, MNRAS, 481, 2581
Lamb, G. P., Tanvir, N. R., Levan, A. J., et al. 2019b, ApJ, 883, 48
Lazzati, D., Deich, A., Morsony, B. J., & Workman, J. C. 2017, MNRAS, 471, 1652
Lazzati, D., Perna, R., Morsony, B. J., et al. 2018, PhRvL, 120, 241103
Lee, W. H., Ramirez-Ruiz, E., & Page, D. 2004, ApJL, 608, L5
Li, L.-X., & Paczyński, B. 1998, ApJL, 507, L59
Liu, B., Chen, W., Liang, Y.-F., et al. 2014, ApJL, 787, L6
Longo, F., Bissaldi, E., Vianello, G., et al. 2016, GCN, 19413, 1
Lü, H.-J., Zhang, H.-M., Zhong, S.-Q., et al. 2017, ApJ, 835, 181
Margutti, R., Alexander, K. D., Xie, X., et al. 2018, arXiv:1801.03531
Margutti, R., Berger, E., Fong, W., et al. 2017a, ApJL, 848, L20
Margutti, R., Fong, W., Eftekhari, T., et al. 2017b, ATel, 11037, 1
Mirzoyan, R. E. A., Noda, K., Moretti, E., et al. 2019, GCN, 23701, 1
Mooley, K. P., Nakar, E., Hotokezaka, K., et al. 2018, Natur, 554, 207
Nagakura, H., Hotokezaka, K., Sekiguchi, Y., Shibata, M., & Ioka, K. 2014, ApJL, 784, L28
Nakar, E., Piran, T., & Granot, J. 2002, ApJ, 579, 699
Palatiello, Noda, K., Inoue, S., et al. 2017, in 7th Int. Fermi Symp. (Trieste: SISSA), 84
Panaitescu, A., & Kumar, P. 2000, ApJ, 543, 66
Perley, D. A., Metzger, B. D., Granot, J., et al. 2009, ApJ, 696, 1871
Piran, T., & Nakar, E. 2010, ApJL, 718, L63
Piron, F. 2016, CRPhy, 17, 617
Planck Collaboration, Aghanim, N., Akrami, Y., et al. 2018, arXiv:1807.06209
Sari, R. 1997, ApJL, 489, L37
Sari, R., & Esin, A. A. 2001, ApJ, 548, 787
Sari, R., & Mészáros, P. 2000, ApJL, 535, L33
Sari, R., Piran, T., & Halpern, J. P. 1999, ApJL, 519, L17
Sari, R., Piran, T., & Narayan, R. 1998, ApJL, 497, L17
Savchenko, V., Ferrigno, C., Kuulkers, E., et al. 2017, ApJL, 848, L15
Setiawan, S., Ruffert, M., & Janka, H.-T. 2004, MNRAS, 352, 753
Stanbro, M., & Meegan, C. 2016, GCN, 19843, 1
Takahashi, K., Murase, K., Ichiki, K., Inoue, S., & Nagataki, S. 2008, ApJL, 687, L5
Tan, J. C., Matzner, C. D., & McKee, C. F. 2001, ApJ, 551, 946
Troja, E., Castro-Tirado, A. J., Becerra González, J., et al. 2019, MNRAS, 489, 2104
Troja, E., Lipunov, V. M., Mundell, C. G., et al. 2017a, Natur, 547, 425
Troja, E., Piro, L., Ryan, G., et al. 2018a, MNRAS, 478, L18
Troja, E., Piro, L., van Eerten, H., et al. 2017b, Natur, 551, 71
Troja, E., Ryan, G., Piro, L., et al. 2018b, NatCo, 9, 4089
Troja, E., Sakamoto, T., Cenko, S. B., et al. 2016, ApJ, 827, 102
Zhang, S., Jin, Z.-P., Wang, Y.-Z., & Wei, D.-M. 2017, ApJ, 835, 73

# Polarization From A Radially Stratified Off-Axis GRB Outflow

A. C. Caligula Do E. S. Pedreira, [1] N. Fraija,[1] A. Galvan-Gamez,[1] B. Betancourt Kamenetskaia,[2,3]
S. Dichiara,[4] M.G. Dainotti,[5,6,7,8] R. L. Becerra,[9] and P. Veres[10]

[1]*Instituto de Astronomía, Universidad Nacional Autónoma de México, Circuito Exterior, C.U., A. Postal 70-264, 04510, CDMX, Mexico*
[2]*TUM Physics Department, Technical University of Munich, James-Franck-Str, 85748 Garching, Germany*
[3]*Max-Planck-Institut für Physik (Werner-Heisenberg-Institut), Föhringer Ring 6, 80805 Munich, Germany*
[4]*Department of Astronomy and Astrophysics, The Pennsylvania State University, 525 Davey Lab, University Park, PA 16802, USA*
[5]*Division of Science, National Astronomical Observatory of Japan, 2-21-1 Osawa, Mitaka, Tokyo 181-8588, Japan*
[6]*The Graduate University for Advanced Studies (SOKENDAI), 2-21-1 Osawa, Mitaka, Tokyo 181-8588, Japan*
[7]*Space Science Institute, 4750 Walnut Street, Boulder, CO 80301, USA*
[8]*SLAC National Accelerator Laboratory, 2575 Sand Hill Road, Menlo Park, CA 94025, USA*
[9]*Instituto de Ciencias Nucleares, Universidad Nacional Autónoma de México, Apartado Postal 70-264, 04510 México, CDMX, Mexico*
[10]*Center for Space Plasma and Aeronomic Research (CSPAR), University of Alabama in Huntsville, Huntsville, AL 35899, USA*

## ABSTRACT

While the dominant radiation mechanism gamma-ray bursts (GRBs) remains a question of debate, synchrotron emission is one of the foremost candidates to describe the multi-wavelength afterglow observations. As such, it is expected that GRBs should present some degree of polarization across their evolution – presenting a feasible means of probing these bursts' energetic and angular properties. Although obtaining polarization data is difficult due to the inherent complexities regarding GRB observations, advances are being made, and theoretical modeling of synchrotron polarization is now more relevant than ever. In this manuscript, we present the polarization for a fiduciary model where the synchrotron forward-shock emission evolving in the radiative-adiabatic regime is described by a radially stratified off-axis outflow. This is parameterized with a power-law velocity distribution and decelerated in a constant-density and wind-like external environment. We apply this theoretical polarization model for selected bursts presenting evidence of off-axis afterglow emission, including the nearest orphan GRB candidates observed by the *Neil Gehrels Swift Observatory* and a few Gravitational Wave (GWs) events that could generate electromagnetic emission. In the case of GRB 170817A, we require the available polarimetric upper limits in radio wavelengths to constrain its magnetic field geometry.

**Key words:** Physical data and processes: polarization – (stars:) gamma-ray burst: general – (stars:) gamma-ray burst: individual:... – Physical data and processes:acceleration of particles – Physical data and processes:magnetic fields

## 1 INTRODUCTION

Gamma-ray Bursts (GRBs) are the most luminescent phenomena in the universe. They result from the deaths of massive stars (Woosley 1993; Paczyński 1998; Woosley & Bloom 2006; Cano et al. 2017) or the merger of two compact objects, such as neutron stars (NSs; Duncan & Thompson 1992; Usov 1992; Thompson 1994; Metzger et al. 2011) or a NS with a black hole (BH, Narayan et al. 1992). GRBs are evaluated based on the phenomenology seen during their early and late phases and are often characterized by the fireball model (Sari et al. 1998) to distinguish their various sources. The principal and earliest emission, known as the "prompt emission", is detected from hard X-rays to $\gamma$-rays. This phase can be explained by the interactions of internal shells of material launched forcefully from the central engine at various speeds (Rees & Meszaros 1994; Paczynski & Xu 1994), photospheric emission from the fireball (Thompson et al. 2007; Lazzati et al. 2013; Mizuta et al. 2011) or discharges from a Poynting-flux dominated ejecta (Giannios 2008; Beniamini & Granot 2016; Kumar & Crumley 2015; Zhang & Yan 2011). Later emission, known as "afterglow", (e.g., Costa et al. 1997; Sari et al. 1998; Granot & Sari 2002; van Paradijs et al. 1997; Piro et al. 1998; Gehrels et al. 2009; Wang et al. 2015) is a long-lasting multi-wavelength emission detectable in gamma-rays, X-rays, optical, and radio. It is modeled using synchrotron radiation produced when the external environment decelerates the relativistic outflow, and a significant portion of its energy is transferred. Long GRBs (lGRBs) and short GRBs (sGRBs) are categorized based on their duration:[1] $T_{90} \leq 2\,\mathrm{s}$ or $T_{90} \geq 2\,\mathrm{s}$,[2] respectively (Mazets et al. 1981; Kouveliotou et al. 1993).

---

[1] For a debate of controversial situations, see Kann et al. (2011).
[2] $T_{90}$ is the time over which a GRB releases from 5% to 95% of the total measured counts.

Synchrotron radiation is the fundamental emission mechanism in GRB afterglows in a forward-shock (FS) scenario (Kumar & Zhang 2015; Mészáros & Rees 1997). Nevertheless, synchrotron is contingent on the existence of magnetic fields. The origin and arrangement of these magnetic fields behind the shock remain debatable. They can originate from the compression of an existing magnetic field within the interstellar medium (ISM; Laing 1980; Teboul & Shaviv 2021) and shock-generated two-stream instabilities (Weibel 1959; Medvedev & Loeb 1999). The magnetic field generated by these plasma instabilities is random in orientation but mostly confined to the plane of the shock (Gill & Granot 2020). Modeling the source and arrangement of those fields and other physical properties of GRBs presents a challenging task. This has necessitated the development of other methods for investigating these complicated systems. Among these techniques is linear polarization.

Linear polarization has been measured, up to a few percent, from the afterglow of several GRBs. Some examples include GRB 191221B ($\Pi = 1.2\%$; Buckley et al. 2021) at the late afterglow, GRB 190114C ($\Pi = 0.8 \pm 0.13\%$; Laskar et al. 2019) on the radio band, and the upper limits determinations of GRB 991216 (yielding $\Pi < 7\%$; Granot & Taylor 2005) and GRB 170817A (yielding $\Pi < 12\%$, on the 2.8 GHz radio band Corsi et al. 2018). Since the degree of polarization relies on the configuration of the magnetic field, analyzing the degree of polarization permits us to investigate these configurations and, therefore, their origins. Previous works, including Granot & Königl (2003); Gill et al. (2020); Rutledge & Fox (2004); Lyutikov et al. (2003); Nakar et al. (2003); Teboul & Shaviv (2021); Stringer & Lazzati (2020), have already investigated the practicality of utilizing polarization models to acquire source-related information. Due to the unfortunate short number of orbital polarimeters and the normal difficulty of seeing these extreme events, collecting polarization data has been one of the most significant impediments. Despite this, progress has been made in the field as a result of initiatives like the POLAR project (Orsi & Polar Collaboration 2011), and it is anticipated that we will have abundant data to test various models in the coming years.

This study expands the analytical synchrotron afterglow scenario of the off-axis homogeneous jet in a stratified environment, which was required to characterize the multi-wavelength data of GRB 170817A (Fraija et al. 2019a) and a sample of GRBs exhibiting off-axis emission.[3] The phenomenological model is extended from adiabatic to radiative regime, including the self-absorption synchrotron phase and the dimensionless factor, which provides information on the equal arrival time surface (EATS). We show the temporal development of polarization from the synchrotron afterglow stratification model and compute the expected polarization for GRB 080503 (Perley et al. 2009; Gao et al. 2015), GRB 140903A (Troja et al. 2016; Zhang et al. 2017), GRB 150101B (Troja et al. 2018), GRB 160821B (Troja et al. 2019) and GRB 170817A (Kasliwal et al. 2017; Lamb & Kobayashi 2017; Mooley et al. 2018b; Hotokezaka et al. 2018; Fraija et al. 2019d). For GRB 170817A in particular, we employ the available polarimetric upper limits from Corsi et al. (2018). Furthermore, taking into account the multi-wavelength upper limits of the closest Swift-detected bursts and the Gravitational Wave (GW) events that potentially produce electromagnetic emission,[4] we create a polarization curve in order to constrain some of the parameters of our off-axis jet model. Keeping this in mind, the following is the structure of the paper: In Section 2, we briefly describe the off-axis jet synchrotron model derived in Fraija et al. (2019a) with the extension. In Section 3, we introduce the polarization model used in this paper. In Section 4, we compute the assumed polarization and give the outcomes for a sample of off-axis afterglow-emitting bursts. In Section 5 and Section 6, we give analogous analyses for the closest Swift-detected bursts and the GW events that could have emitted an electromagnetic signature, respectively. Finally, in Section 7, we present the conclusion and provide closing thoughts.

## 2 SYNCHROTRON FORWARD-SHOCK MODEL FROM A RADIALLY STRATIFIED OFF-AXIS JET

The multi-wavelength afterglow observations of GRB 170817A are consistent with the synchrotron FS scenario in the fully adiabatic regime from a radially stratified off-axis outflow decelerated in a homogeneous medium (Fraija et al. 2019b). Fraija et al. (2019a) extended the synchrotron FS approach to a stratified environment based on the immediate vicinity of a binary NS merger proposed to explain the gamma-ray flux in GRB 150101B. Additionally, Fraija et al. (2019a) successfully explained the multi-wavelength afterglow observations in GRB 080503, GRB 140903A and GRB 160821B using the synchrotron off-axis model.

In order to present a polarization model and perform a fully time-evolving analysis, we extend the synchrotron scenario described in Fraija et al. (2019b,a) from adiabatic to radiative regime including the self-absorption phase and the dimensionless factor $\xi$ which provides information on the EATS (Panaitescu & Mészáros 1998; Chevalier & Li 2000).

### 2.1 Synchrotron scenario

Relativistic electrons are accelerated in the FS and cooled down mainly via synchrotron emission in the presence of a comoving magnetic field $B' = \sqrt{8\pi\varepsilon_B e}$, where $e$ is the energy density and $\varepsilon_B$ the fraction of magnetic energy given in the FS. Hereafter, we use the prime and unprimed quantities to refer them in the comoving and observer frames, respectively. The acceleration process leads to that electrons with Lorentz factors ($\gamma_e$) come by a distribution of the form $N(\gamma_e)\, d\gamma_e \propto \gamma_e^{-p}\, d\gamma_e$ with $p$ the electron power index. We consider a radially off-axis

---

[3] We use the values of the cosmological constants $H_0 = 69.6\,\mathrm{km\,s^{-1}\,Mpc^{-1}}$, $\Omega_M = 0.286$ and $\Omega_\Lambda = 0.714$ (Planck Collaboration et al. 2016), which correspond to a spatially flat universe $\Lambda$CDM model.

[4] These events were associated to at least one NS by Advanced Laser Interferometer Gravitational-Wave Observatory (LIGO) and Advanced VIRGO detectors (Abbott et al. 2021; The LIGO Scientific Collaboration et al. 2021).

jet with an equivalent kinetic energy given by:

$$E = \tilde{E}\,\Gamma^{-\alpha_s}\,\frac{1}{(1 + \Delta\theta^2\Gamma^2)^3}\,, \tag{1}$$

where $\tilde{E}$ is the characteristic energy, $\Delta\theta = \theta_{\rm obs} - \theta_{\rm j}$ corresponds to the viewing angle ($\theta_{\rm obs}$) and the half-opening angle of the jet ($\theta_{\rm j}$) and $\Gamma$ is the bulk Lorentz factor. We consider that the circumburst medium can be constant ($n$) or stratified (with a profile given by the stellar-wind $\propto A_{\rm W}r^{-2}$ with $A_{\rm W}$ the density parameter).

### 2.1.1 Constant-density medium

We assume an evolution of the FS with an isotropic equivalent-kinetic energy $E = \frac{4\pi}{3}m_pc^2nr^3\Gamma_0^\epsilon\Gamma^{2-\epsilon}$ (Blandford-McKee solution; Blandford & McKee 1976), where $\epsilon = 0$ corresponds to the adiabatic regime and $\epsilon = 1$ to the fully radiative one, and a radial distance $r = c\xi\Gamma^2t/(1+z)$ with $c$ the speed of light, $m_p$ is the proton mass and $z$ the redshift. Therefore, the evolution of the bulk Lorentz factor is given by:

$$\Gamma = 9.8\left(\frac{1+z}{1.022}\right)^{\frac{3}{\delta+8-\epsilon}}\xi^{-\frac{6}{\delta+8-\epsilon}}n_{-4}^{-\frac{1}{\delta+8-\epsilon}}\Delta\theta_{15°}^{-\frac{6}{\delta+8-\epsilon}}\Gamma_0^{-\frac{\epsilon}{\delta+8-\epsilon}}\tilde{E}_{52}^{\frac{1}{\delta+8-\epsilon}}t_5^{-\frac{3}{\delta+8-\epsilon}}\,, \tag{2}$$

with $\delta = \alpha_s + 6$. Using the bulk Lorentz factor (eq. 2) and the synchrotron afterglow theory introduced in Sari et al. (1998) for the fully adiabatic regime, we derive, in this formalism, the relevant quantities of synchrotron emission originated from the FS. The minimum and cooling electron Lorentz factors can be written as:

$$
\begin{aligned}
\gamma_m &= 32.6\left(\frac{1+z}{1.022}\right)^{\frac{3}{\delta+8-\epsilon}}\xi^{-\frac{6}{\delta+8-\epsilon}}g(p)\,\varepsilon_{e,-2}\,n_{-4}^{-\frac{1}{\delta+8-\epsilon}}\Delta\theta_{15°}^{-\frac{6}{\delta+8-\epsilon}}\Gamma_0^{-\frac{\epsilon}{\delta+8-\epsilon}}\tilde{E}_{52}^{\frac{1}{\delta+8-\epsilon}}t_5^{-\frac{3}{\delta+8-\epsilon}}\,, \\
\gamma_c &= 4.0\times10^8\left(\frac{1+z}{1.022}\right)^{\frac{\delta-1-\epsilon}{\delta+8-\epsilon}}\xi^{\frac{2(1-\delta+\epsilon)}{\delta+8-\epsilon}}(1+Y)^{-1}\varepsilon_{B,-4}^{-1}n_{-4}^{-\frac{\delta+5-\epsilon}{\delta+8-\epsilon}}\Delta\theta_{15°}^{\frac{18}{\delta+8-\epsilon}}\Gamma_0^{\frac{3\epsilon}{\delta+8-\epsilon}}\tilde{E}_{52}^{-\frac{3}{\delta+8-\epsilon}}t_5^{\frac{1-\delta+\epsilon}{\delta+8-\epsilon}}\,,
\end{aligned}
\tag{3}
$$

respectively. Here, $Y$ is the Compton parameter, $g(p) = (p-2)/(p-1)$ whereas $\epsilon_e$ is the fraction of energy given to accelerate the electron population. Using the electron Lorentz factors (eq. 3), the characteristic and cooling spectral breaks for synchrotron radiation are

$$
\begin{aligned}
\nu_{\rm m} &\simeq 2.0\times10^{-3}\,{\rm GHz}\left(\frac{1+z}{1.022}\right)^{\frac{4-\delta+\epsilon}{\delta+8-\epsilon}}\xi^{-\frac{24}{\delta+8-\epsilon}}\varepsilon_{e,-2}^2\varepsilon_{B,-4}^{\frac{1}{2}}n_{-4}^{\frac{\delta-\epsilon}{2(\delta+8-\epsilon)}}\Delta\theta_{15°}^{-\frac{24}{\delta+8-\epsilon}}\Gamma_0^{-\frac{4\epsilon}{\delta+8-\epsilon}}E_{52}^{\frac{4}{\delta+8-\epsilon}}t_5^{-\frac{12}{\delta+8-\epsilon}}\,, \\
\nu_{\rm c} &\simeq 7.6\times10^4\,{\rm keV}\left(\frac{1+z}{1.022}\right)^{\frac{\delta-4-\epsilon}{\delta+8-\epsilon}}\xi^{-\frac{4(2+\delta-\epsilon)}{\delta+8-\epsilon}}(1+Y)^{-2}\varepsilon_{B,-4}^{-\frac{3}{2}}n_{-4}^{-\frac{16+3\delta-3\epsilon}{2(\delta+8-\epsilon)}}\Delta\theta_{15°}^{\frac{24}{\delta+8-\epsilon}}\Gamma_0^{\frac{4\epsilon}{\delta+8-\epsilon}}E_{52}^{-\frac{4}{\delta+8-\epsilon}}t_5^{-\frac{2(2+\delta-\epsilon)}{\delta+8-\epsilon}}\,,
\end{aligned}
\tag{4}
$$

respectively. Considering the maximum emissivity, the total number of radiating electrons and the luminosity distance $D_z$, the maximum flux emitted by synchrotron radiation is given by

$$F_{\rm max} \simeq 0.2\,{\rm mJy}\left(\frac{1+z}{1.022}\right)^{\frac{16-\delta+\epsilon}{\delta+8-\epsilon}}\xi^{\frac{6(\delta-\epsilon)}{\delta+8-\epsilon}}\varepsilon_{B,-4}^{\frac{1}{2}}n_{-4}^{\frac{8+3\delta-3\epsilon}{2(\delta+8-\epsilon)}}\Delta\theta_{15°}^{-\frac{48}{\delta+8-\epsilon}}D_{z,26.3}^{-2}\Gamma_0^{-\frac{8\epsilon}{\delta+8-\epsilon}}E_{52}^{\frac{8}{\delta+8-\epsilon}}t_5^{\frac{3(\delta-\epsilon)}{\delta+8-\epsilon}}\,. \tag{5}$$

The synchrotron spectral breaks in the self-absorption regime are derived from $\nu_{\rm a,1} = \nu_c\tau_m^{\frac{3}{5}}$, $\nu_{\rm a,2} = \nu_m\tau_m^{\frac{2}{p+4}}$ and $\nu_{\rm a,3} = \nu_m\tau_c^{\frac{3}{5}}$ with the optical depths given by $\tau_m \simeq \frac{5}{3}\frac{q_enr}{B'\gamma_m^5}$ and $\tau_c \simeq \frac{5}{3}\frac{q_enr}{B'\gamma_c^5}$.

The light curves in the fast cooling regime are:

$$F_\nu^{\rm syn} \propto \begin{cases} t\,\nu^{\frac{1}{3}}, & {\rm for}\ \ \nu < \nu_{\rm a,3}, \\ t^{\frac{4+11(\delta-\epsilon)}{3(\delta+8-\epsilon)}}\nu^{-\frac{1}{2}}, & {\rm for}\ \ \nu_{\rm a,3} < \nu < \nu_{\rm c}^{\rm syn}, \\ t^{\frac{2(\delta-1-\epsilon)}{\delta+8-\epsilon}}\nu^{-\frac{p-1}{2}}, & {\rm for}\ \ \nu_{\rm c}^{\rm syn} < \nu < \nu_{\rm m}^{\rm syn}, \\ t^{\frac{2(2-3p+\delta-\epsilon)}{\delta+8-\epsilon}}\nu^{-\frac{p}{2}}, & {\rm for}\ \ \nu_{\rm m}^{\rm syn} < \nu, \end{cases} \tag{6}$$

and in the slow cooling regime are:

$$F_\nu^{\rm syn} \propto \begin{cases} t^{\frac{2(2+\delta-\epsilon)}{\delta+8-\epsilon}}\nu^2, & {\rm for}\ \ \nu < \nu_{\rm a,1}, \\ t^{\frac{4+3(\delta-\epsilon)}{\delta+8-\epsilon}}\nu^{\frac{1}{3}}, & {\rm for}\ \ \nu_{\rm a,1} < \nu < \nu_{\rm m}^{\rm syn}, \\ t^{\frac{3(2-2p+\delta-\epsilon)}{\delta+8-\epsilon}}\nu^{-\frac{p-1}{2}}, & {\rm for}\ \ \nu_{\rm m}^{\rm syn} < \nu < \nu_{\rm c}^{\rm syn}, \\ t^{\frac{2(2-3p+\delta-\epsilon)}{\delta+8-\epsilon}}\nu^{-\frac{p}{2}}, & {\rm for}\ \ \nu_{\rm c}^{\rm syn} < \nu. \end{cases} \tag{7}$$

$$F_\nu^{\rm syn} \propto \begin{cases} t^{\frac{2(2+\delta-\epsilon)}{\delta+8-\epsilon}}\nu^2, & {\rm for}\ \ \nu < \nu_{\rm m}^{\rm syn}, \\ t^{\frac{2(5+\delta-\epsilon)}{\delta+8-\epsilon}}\nu^{\frac{5}{2}}, & {\rm for}\ \ \nu_{\rm m}^{\rm syn} < \nu < \nu_{\rm a,2}, \\ t^{\frac{3(2-2p+\delta-\epsilon)}{\delta+8-\epsilon}}\nu^{-\frac{p-1}{2}}, & {\rm for}\ \ \nu_{\rm a,2} < \nu < \nu_{\rm c}^{\rm syn}, \\ t^{\frac{2(2-3p+\delta-\epsilon)}{\delta+8-\epsilon}}\nu^{-\frac{p}{2}}, & {\rm for}\ \ \nu_{\rm c}^{\rm syn} < \nu. \end{cases} \tag{8}$$

### 2.1.2  Stellar-wind medium

In the case of a stratified stellar-wind like medium, the number density is given by $n(r) = \frac{\rho(r)}{m_p} = \frac{A}{m_p} r^{-2}$ where $A = \frac{\dot{M}}{4\pi v} = 5\times10^{11} A_W$ g cm$^{-1}$, with $\dot{M}$ the mass-loss rate and $v$ the velocity of the outflow (e.g., see Fraija et al. 2016). Taking into account the Blandford-McKee solution for a stratified stellar-wind like medium, the bulk Lorentz factor derived through the adiabatic evolution (Blandford & McKee 1976; Sari 1997) is given by

$$\Gamma = 16.2 \left(\frac{1+z}{1.022}\right)^{\frac{1}{\delta+4-\epsilon}} \xi^{-\frac{2}{\delta+4-\epsilon}} A_{W,-1}^{-\frac{1}{\delta+4-\epsilon}} \Delta\theta_{15°}^{-\frac{6}{\delta+4-\epsilon}} \Gamma_0^{-\frac{\epsilon}{\delta+4-\epsilon}} \tilde{E}_{52}^{\frac{1}{\delta+4-\epsilon}} t_5^{-\frac{1}{\delta+4-\epsilon}} , \tag{9}$$

with the characteristic energy given by $\tilde{E} = \frac{16\pi}{3} (1+z)^{-1} \xi^2 A_W \Delta\theta^6 \Gamma_0^\epsilon \Gamma^{\delta+4-\epsilon} t$. Using the bulk Lorentz factor (eq. 9) and the synchrotron afterglow theory for a wind-like medium (Chevalier & Li 2000; Panaitescu & Kumar 2000), we derive the relevant quantities of synchrotron emission for our model in the fully adiabatic regime. The minimum and cooling electron Lorentz factors are given by:

$$\begin{aligned}
\gamma_m &= 41.5 \left(\frac{1+z}{1.022}\right)^{\frac{1}{\delta+4-\epsilon}} \xi^{-\frac{2}{\delta+4-\epsilon}} g(p)\, \varepsilon_{e,-2} \Delta\theta_{15°}^{\frac{-6}{\delta+4-\epsilon}} A_{W,-1}^{-\frac{1}{\delta+4-\epsilon}} \Gamma_0^{-\frac{\epsilon}{\delta+4-\epsilon}} \tilde{E}_{52}^{\frac{1}{\delta+4-\epsilon}} t_5^{-\frac{1}{\delta+4-\epsilon}} , \\
\gamma_c &= 52.1 \left(\frac{1+z}{1.022}\right)^{-\frac{\delta+3-\epsilon}{\delta+4-\epsilon}} (1+Y)^{-1} \xi^{\frac{2(\delta+3-\epsilon)}{\delta+4-\epsilon}} \varepsilon_{B,-4}^{-1} A_{W,-1}^{-\frac{\delta+5-\epsilon}{\delta+4-\epsilon}} \Delta\theta_{15°}^{-\frac{6}{\delta+4-\epsilon}} \Gamma_0^{-\frac{\epsilon}{\delta+4-\epsilon}} \tilde{E}_{52}^{\frac{1}{\delta+4-\epsilon}} t_5^{\frac{\delta+3-\epsilon}{\delta+4-\epsilon}} .
\end{aligned} \tag{10}$$

The characteristic and cooling spectral breaks for synchrotron emission are:

$$\begin{aligned}
\nu_m &\simeq 1.0\times10^{14}\text{Hz} \left(\frac{1+z}{1.022}\right)^{\frac{2}{\delta+4-\epsilon}} \xi^{-\frac{2(\delta+6-\epsilon)}{\delta+4-\epsilon}} \varepsilon_{e,-2}^2 \varepsilon_{B,-4}^{\frac{1}{2}} A_{W,-1}^{\frac{\delta-\epsilon}{2(\delta+4-\epsilon)}} \Delta\theta_{15°}^{-\frac{12}{\delta+4-\epsilon}} \Gamma_0^{-\frac{2\epsilon}{\delta+4-\epsilon}} E_{52}^{\frac{2}{\delta+4-\epsilon}} t_5^{-\frac{\delta+6-\epsilon}{\delta+4-\epsilon}} , \\
\nu_c &\simeq 1.1\times10^{14}\text{Hz} \left(\frac{1+z}{1.022}\right)^{-\frac{2(\delta+3-\epsilon)}{\delta+4-\epsilon}} \xi^{\frac{2(\delta+2-\epsilon)}{\delta+4-\epsilon}} (1+Y)^{-2} \varepsilon_{B,-4}^{-\frac{3}{2}} A_{W,-1}^{-\frac{3\delta+16-3\epsilon}{2(\delta+4-\epsilon)}} \Delta\theta_{15°}^{-\frac{12}{\delta+4-\epsilon}} \Gamma_0^{-\frac{2\epsilon}{\delta+4-\epsilon}} E_{52}^{\frac{2}{\delta+4-\epsilon}} t_5^{\frac{\delta+2-\epsilon}{\delta+4-\epsilon}} ,
\end{aligned} \tag{11}$$

respectively. Given the maximum emissivity in a stratified stellar-wind like medium, the maximum flux radiated by synchrotron emission is given by:

$$F_{\max} \simeq 1.9\times10^3 \text{ mJy} \left(\frac{1+z}{1.022}\right)^{\frac{2(\delta+5-\epsilon)}{\delta+4-\epsilon}} \xi^{-\frac{4}{\delta+4-\epsilon}} \varepsilon_{B,-4}^{\frac{1}{2}} A_{W,-1}^{\frac{3\delta+8-3\epsilon}{2(\delta+4-\epsilon)}} D_{z,26.3}^2 \Delta\theta_{15°}^{-\frac{12}{\delta+4-\epsilon}} \Gamma_0^{-\frac{2\epsilon}{\delta+4-\epsilon}} E_{52}^{\frac{2}{\delta+4-\epsilon}} t_5^{-\frac{2}{\delta+4-\epsilon}} . \tag{12}$$

The synchrotron spectral breaks in the self-absorption regime are derived from $\nu_{a,1} = \nu_c \tau_m^{\frac{3}{5}}$, $\nu_{a,2} = \nu_m \tau_m^{\frac{2}{p+4}}$ and $\nu_{a,3} = \nu_m \tau_c^{\frac{3}{5}}$ with the optical depths given by $\tau_m \propto \frac{q_e A_W r^{-1}}{B' \gamma_m^5}$ and $\tau_c \propto \frac{q_e A_W r^{-1}}{B' \gamma_c^5}$.

The light curves in the fast cooling regime are:

$$F_\nu^{\text{syn}} \propto \begin{cases} t^{\frac{8+3(\delta-\epsilon)}{\delta+4-\epsilon}} \nu^{\frac{1}{3}} , & \text{for } \nu < \nu_{a,3}, \\ t^{\frac{\epsilon-\delta-8}{3(\delta+4-\epsilon)}} \nu^{-\frac{1}{2}} , & \text{for } \nu_{a,3} < \nu < \nu_c^{\text{syn}}, \\ t^{\frac{\delta-2-\epsilon}{2(\delta+4-\epsilon)}} \nu^{-\frac{p-1}{2}} , & \text{for } \nu_c^{\text{syn}} < \nu < \nu_m^{\text{syn}}, \\ t^{\frac{2(2-3p)+(\epsilon-\delta)(p-2)}{2(\delta+4-\epsilon)}} \nu^{-\frac{p}{2}} , & \text{for } \nu_m^{\text{syn}} < \nu , \end{cases} \tag{13}$$

whereas in the slow cooling regime are:

$$F_\nu^{\text{syn}} \propto \begin{cases} t^{\frac{2(2+\delta-\epsilon)}{\delta+4-\epsilon}} \nu^2 , & \text{for } \nu < \nu_{a,1}, \\ t^{\frac{\delta-\epsilon}{3(\delta+4-\epsilon)}} \nu^{\frac{1}{3}} , & \text{for } \nu_{a,1} < \nu < \nu_m^{\text{syn}}, \\ t^{\frac{2+\delta-\epsilon-p(6+\delta-\epsilon)}{2(\delta+4-\epsilon)}} \nu^{-\frac{p-1}{2}} , & \text{for } \nu_m^{\text{syn}} < \nu < \nu_c^{\text{syn}}, \\ t^{\frac{2(2-3p)+(\epsilon-\delta)(p-2)}{2(\delta+4-\epsilon)}} \nu^{-\frac{p}{2}} , & \text{for } \nu_c^{\text{syn}} < \nu . \end{cases} \tag{14}$$

$$F_\nu^{\text{syn}} \propto \begin{cases} t^{\frac{2(2+\delta-\epsilon)}{\delta+4-\epsilon}} \nu^2 , & \text{for } \nu < \nu_m^{\text{syn}}, \\ t^{\frac{14+5(\delta-\epsilon)}{2(\delta+4-\epsilon)}} \nu^{\frac{5}{2}} , & \text{for } \nu_m^{\text{syn}} < \nu < \nu_{a,2}, \\ t^{\frac{2+\delta-\epsilon-p(6+\delta-\epsilon)}{2(\delta+4-\epsilon)}} \nu^{-\frac{p-1}{2}} , & \text{for } \nu_{a,2} < \nu < \nu_c^{\text{syn}}, \\ t^{\frac{2(2-3p)+(\epsilon-\delta)(p-2)}{2(\delta+4-\epsilon)}} \nu^{-\frac{p}{2}} , & \text{for } \nu_c^{\text{syn}} < \nu . \end{cases} \tag{15}$$

## 3  POLARIZATION MODEL

Since 1999, the phenomena of polarization, the confinement of wave vibrations to a certain geometrical direction, has been detected in GRBs (Covino et al. 1999). Further studies indicate that the polarization degree ($\Pi$) can have high variability, but the polarization angle (P.A.; $\theta_p$)

remains roughly the same, for an observer outside the jet (Teboul & Shaviv 2021). Polarization is commonly attributed to synchrotron radiation behind shock waves. This makes it dependent on the magnetic field configuration and the geometry of the shock, as they will define the the the P.D. on each point and its integration over the whole image (Gill et al. 2020). The Stokes parameters (I, Q, U, and V) control the approach to polarization calculation, and normally only linear polarization is considered. From this point on, we refer to the observer and comoving frames as unprimed and primed, respectively. The stokes parameters are expressed as

$$V = 0, \qquad\qquad \theta_P = \frac{1}{2}\arctan\frac{U}{Q},$$
$$\frac{U}{I} = \Pi'\sin 2\theta_P, \qquad\qquad \frac{Q}{I} = \Pi'\cos 2\theta_P. \tag{16}$$

And the measured stokes parameters are the sum over the flux (Granot 2003), so

$$\frac{U}{I} = \frac{\int dF_\nu \Pi'\sin 2\theta_P}{\int dF_\nu}, \qquad\qquad \frac{Q}{I} = \frac{\int dF_\nu \Pi'\cos 2\theta_P}{\int dF_\nu}, \tag{17}$$

$$\Pi = \frac{\sqrt{Q^2+U^2}}{I}. \tag{18}$$

The relationship $dF_\nu \propto \delta_D^3 L'_{\nu'} d\Omega$ – where $L'_{\nu'}$ is the spectral luminosity and $d\Omega$ is the element of solid angle of the fluid element in relation to the source – allows the introduction of the factors regarding the geometry of the magnetic field and outflow by using (Rybicki & Lightman 1979)

$$L'_{\nu'} \propto (\nu')^{-\alpha}(\sin\chi')^\epsilon r^m \propto (\nu')^{-\alpha}(1-\hat{n}'\cdot\hat{B}')^{\epsilon/2} r^m. \tag{19}$$

The parameter $\chi$ is the angle between the local magnetic field and the particle's direction of motion, and due to the highly beamed nature of synchrotron emission, this angle is also the pitch angle. The geometrical considerations of polarization can then be taken by averaging this factor over the local probability distribution of the magnetic field (see Eq. 15 of Gill et al. 2020),

$$\Lambda = \left\langle (1-\hat{n}'\cdot\hat{B}')^{\epsilon/2} \right\rangle. \tag{20}$$

It is possible to do a Lorentz transformation on the unit vectors, like $\hat{n}$, or a certain configuration of $\hat{B}$ to express $\Lambda$ in terms of different magnetic field configurations (Gill et al. 2020; Lyutikov et al. 2003; Granot 2003):

$$\Lambda_{\mathrm{ord}} \approx \left[\left(\frac{1-\tilde{\xi}}{1+\tilde{\xi}}\right)\cos^2\varphi_B + \sin^2\varphi_B\right]^{\epsilon/2}, \tag{21}$$

$$\Lambda_\perp \approx \left\langle \Lambda_{ord}(\tilde{\xi},\varphi_B) \right\rangle_{\varphi_B}, \tag{22}$$

$$\Lambda_\parallel \approx \left[\frac{\sqrt{4\tilde{\xi}}}{1+\tilde{\xi}}\right]^\epsilon, \tag{23}$$

where $\varphi_B$ as the azimuthal angle of the magnetic field measured from a reference point. $\tilde{\xi} \equiv (\Gamma\tilde{\theta})^2$, taking in consideration the approximations of $\tilde{\mu} = \cos\tilde{\theta} \approx 1 - \tilde{\theta}^2/2$ and $\beta \approx 1 - 1/2\Gamma^2$, which leads to $\delta_D \approx \frac{2\Gamma}{1+\tilde{\xi}}$ where $\tilde{\theta}$ the polar angle measured from the Line of Sight (LOS).

One of the still-unsolved mysteries of GRBs is the configuration of the magnetic field present at different regions of emission. As such, various possible configurations must be explored in a topic where magnetic field geometry is of paramount relevance, like polarization. The considerations regarding the magnetic field geometry are varied based on the GRB epoch of relevance. For a scenario where the afterglow is described by a FS, two of the most suitable configurations are: a random perpendicular configuration – where the anisotropy factor $b \equiv \frac{2\langle B_\parallel^2 \rangle}{\langle B_\perp^2 \rangle} = 0$ – confined to the shock plane; and an ordered configuration parallel to the velocity vector, where $b \to \infty$. More complex configurations with multi-component, where the anisotropy is $b > 0$, magnetic fields have been done (Gill & Granot 2020; Teboul & Shaviv 2021; Stringer & Lazzati 2020; Corsi et al. 2018), as it is warranted and needed, however, for the purposes of this paper we limit ourselves to the two following cases.

**Random magnetic field ($B_\perp$, $b = 0$)** In this scenario, the symmetry of the random magnetic field configuration, perpendicular to the shock plane, causes the polarization over the image to disappear when if the beaming cone is wholly contained within the jet aperture or if it is seen along the axis ($\theta_{\mathrm{obs}} = 0$). To break the symmetry, the jet must be viewed close to its edge ($q \equiv \frac{\theta_{\mathrm{obs}}}{\theta_j} \gtrsim 1 + \xi_j^{-1/2}$), where missing emission (from $\theta > \theta_j$) results only in partial cancellation (Waxman 2003). The equation necessary to calculate this polarization is explicitly laid out as Eq. 5 in (Granot 2003).

**Ordered magnetic field ($B_\parallel$, $b \to \infty$)** For the ordered magnetic field, a configuration parallel to the velocity vector, the same symmetry observations hold true and the calculation follows (Granot 2003; Gill et al. 2020), with $\Lambda(\tilde{\xi}) = \Lambda_\parallel$ from Section 3.

By substituting the following integration limits

$$\cos\psi(\tilde{\xi}) = \frac{(1-q)^2\xi_j - \tilde{\xi}}{2q\sqrt{\xi_j\tilde{\xi}}}, \qquad \xi_j = (\Gamma\theta_j)^2, \qquad \xi_\pm = (1\pm q)^2\xi_j, \tag{24}$$

with an appropriate prescription of the bulk Lorentz factor $\Gamma(t)$, the evolution of the opening angle of the jet $\theta_j(t)$, and the parameters required to describe these expressions as described in Section 2 and Fraija et al. (2019a), we can obtain the temporal evolution of polarization.

### 3.1 Polarization evolution for a Forward-Shock

Figures 1 and 2 show the temporal evolution of polarization degree for our chosen magnetic field configurations in two distinct scenarios regarding the density of the circumburst medium – here considered a constant density and a wind-like medium. Each column of these figures represents a chosen combination of the $\epsilon$ and $\xi$ parameters. Table 1 shows the values required to generate Figures 1 and 2. We highlight that the generic values were determined based on the typical range reported for each parameter in the GRB synchrotron literature (for reviews, see Kumar & Zhang 2015; Berger 2014). The values of observation angle are varied over a range between 8 and 15 deg.[5] This range of values is shown in these figures with different colored lines, each one standing for a value of $q_0 = \frac{\theta_{obs}}{\theta_{j,0}}$, the ratio between the observation angle and initial opening angle of the jet.

The synchrotron model chosen is a homogeneous off-axis jet, in which the equivalent kinetic energy is parameterized with a power-law velocity distribution (see Section 2.1), that suffers sideways expansion (SE) with the comoving speed of sound given as Eq. 10 in Huang et al. (2000). The homogeneous jet case has been studied by a few works now, such as Granot et al. (2002); Rossi et al. (2004), however, these works only have explored random magnetic field on a fully adiabatic regime in a constant medium. Nonetheless, comparing results with the leftmost column of Figure 1, we see the typical double peak behavior for a homogeneous SE jet, reported by Rossi et al. (2004) for $q_0 < 5$, is presented for us as well. Some discrepancies are shown, with our polarization being initially higher at early times (increasingly so as $q_0 \to 1$) and overall in the magnitude of the peaks. The highest likelihood culprit for these differences is the choice of synchrotron model and parameter values. The center column of Figure 1 presents the case for a partially radiative scenario, and it behaves quite similarly to the adiabatic case, with only a change in magnitude of the peaks being observable. The deceleration of the relativistic outflow by the circumburst medium is faster when it lies in the radiative regime rather than adiabatic one, and the temporal evolution of polarization is modified (Böttcher & Dermer 2000; Wu et al. 2005). For our model, this has resulted in an enhancement of the increase in polarization as $q_0$ grows, but smaller second peaks. The rightmost side of Figure 1 displays the case for an adiabatic regime with $\xi = 0.56$ (Chevalier & Li 2000). The variation on $\xi$ causes the emission to arrive earlier or later, and this produces a difference in the magnitudes of the peaks, as observed in Figure 1 (Waxman 1997; Chevalier & Li 2000; Panaitescu & Mészáros 1998). The polarization behaviour flips in comparison with $\xi = 1$, with the peak increasing as $q_0 \to 1$; comparatively, the second peak remains mostly the same. The parallel case presents similar behavior for all three considered cases. A small change is observed at the sharpness of decline of polarization at jet-break (where the synchrotron model bulk Lorentz factor changes regime to follow the on-axis calculations presented by Fraija et al. (2019a)) and post-break, with a stronger discontinuity happening with a decreasing value of $\xi$.

Figure 2 shows the polarization evolution for the wind-like medium. Lazzati et al. (2004) expected that the polarization evolved slower for a wind-like medium, as the relationship between afterglow timescale and density was $t \propto (E/n)^{\frac{1}{(3-k)}}$ (Kumar & Zhang 2015; Fraija et al. 2022, and with $k = 2$ for a wind-like medium), and this is observed here too. For a convenience of observation, the limits of the timescale have been expanded. Other significant differences between the constant-density medium and this scenario are the higher initial polarization peak and lower magnitude of the second peak, in all likelihood due to the lower value of bulk Lorentz factor at later times. Between the chosen values of $\xi$ and $\epsilon$, we see that a lower value of $\xi$ increases the magnitude of the first peak while decreasing the magnitude of the second one. This is similar to the constant-density medium case, with the addendum that the second peak is reduced further when compare to $\xi = 1$. For the partially radiative case, the first polarization peak is similar to the adiabatic case with higher magnitude, but the second polarization peak is further reduced.

## 4 POLARIZATION FROM GRB OFF-AXIS AFTERGLOWS

In this section, we describe the polarization for a group of GRBs that show similar characteristics on their afterglow: GRB 080503, GRB 140903A, GRB 150101B, GRB 160821B, and GRB 170817A. In Fraija et al. (2019a), the authors have explored the similarities between those bursts. We use the parameter values obtained by Fraija et al. (2019a) via Markov Chain Monte Carlo (MCMC) simulations to calculate polarization. For this section, we will adopt the notation $f(q_0 = x_{\pm z}^{\pm y}) = a_{\pm c}^{\pm b}$ when the chosen values of $q_0$ result in significant differentiation on polarization or peak time.

---

[5] Over the course of this manuscript we will be using deg as the abbreviation of degree.

**4.0.0.1 GRB 080503** The first column in Figure 4 shows the expected polarization evolution calculated for GRB 080503 for our two configurations. The parameters for calculating this polarization are presented in the first row of Table 2. The granular increment of $q_0$ shows little effect in the polarization curves in either configuration, with the only major difference being the magnitude of the minimum located between peaks. The initial polarization for the time-frame we have chosen is $|\Pi/\Pi_{max}| \approx 5\%$ and $\Pi/\Pi_{max} \approx 92\%$ for $B_\perp$ and $B_\parallel$, respectively. For $B_\perp$, the polarization evolves towards a peak of $|\Pi/\Pi_{max}| \approx 46\%$, with a second peak of $|\Pi/\Pi_{max}| \approx 33\%$ at $\sim 0.3$ and $\sim 0.8$ days, respectively. For the parallel configuration, the initial polarization decreases softly during the off-axis period by roughly $10\%$. After the jet break, the polarization drops sharply, and zero polarization is reached at $\sim 17$ days.

**4.0.0.2 GRB 140903A** The second column in Figure 4 shows the expected polarization evolution estimated for GRB 140903A. The parameters for calculating this polarization are presented in the second row of Table 2. For this burst, a slightly higher degree of influence of $q_0$ is observed. The initial polarization values are $|\Pi/\Pi_{max}|(q_0 = 2.19^{+0.11}_{-0.11}) \approx 7.1^{-0.6}_{+0.7}\%$ and $\Pi/\Pi_{max}(q_0 = 2.19^{+0.11}_{-0.11}) \approx 91^{+0.7}_{-1.0}\%$ for $B_\perp$ and $B_\parallel$, respectively. For the perpendicular field, the peak of $|\Pi/\Pi_{max}| \approx 42^{+0.4}_{-0.2}\%$ is seen at $t_{peak}(q_0 = 2.19^{+0.11}_{-0.11}) \approx 4.4^{+0.6}_{-1.0} \times 10^{-2}$ days with a second peak of $|\Pi/\Pi_{max}| \approx 33^{+2}_{-1}\%$ at $t_{peak} \approx 1.9^{+0.2}_{-0.5} \times 10^{-1}$ days, respectively. For the parallel configuration, the polarization at the break is $\Pi/\Pi_{max} \approx 79^{+1.0}_{-0.8}\%$, and zero is achieved roughly at the same time of $\sim 6$ days.

**4.0.0.3 GRB 150101B** The third column in Figure 4 shows the expected polarization calculated for GRB 150101B. The parameters for calculating this polarization are presented in the third row of Table 2. The higher value of $q_0$ makes so the minute variation of the chosen values has little influence on the polarization. The initial values of polarization are $|\Pi/\Pi_{max}| \approx 1.5\%$ and $\Pi/\Pi_{max} \approx 97\%$, for $B_\perp$ and $B_\parallel$, respectively. For $B_\perp$, the first polarization peak is $|\Pi/\Pi_{max}|(q_0 = 4.21^{+0.05}_{-0.05}) \approx 40^{+0.5}_{-2.0}\%$, and the second $|\Pi/\Pi_{max}| \approx 42\%$ at $\sim 2$ and $\sim 7$ days, respectively. For the parallel configuration, the polarization decreases by $\sim 13\%$ until the break is achieved and decreases to zero rapidly, reaching it at $\sim 40$ days.

**4.0.0.4 GRB 160821B** The fourth column in Figure 4 shows the expected evolution of polarization calculated for GRB 160821B. The parameters for calculating this polarization are presented in the fourth row of Table 2. The initial polarization values are $|\Pi/\Pi_{max}|(q_0 = 1.69^{+0.03}_{-0.03}) \approx 17^{-0.6}_{+0.8}\%$ and $\Pi/\Pi_{max}(q_0 = 1.69^{+0.03}_{-0.03}) \approx 85.5^{+0.5}_{-0.5}\%$ for $B_\perp$ and $B_\parallel$, respectively. For the perpendicular case, the peak of $|\Pi/\Pi_{max}| \approx 50\%$ is seen at $t_{peak}(q_0 = 1.69^{+0.03}_{-0.03}) \approx 2.0^{+0.2}_{-0.3} \times 10^{-2}$ days with a second peak of $|\Pi/\Pi_{max}| \approx 26\%$ at $t_{peak} \approx 7.5^{+1.1}_{-0.9} \times 10^{-2}$ days. For the parallel configuration, the polarization at the break is $\Pi/\Pi_{max} \approx 73^{+1.0}_{-0.8}\%$, and zero is achieved roughly at the same time of $\sim 6$ days.

**4.0.0.5 GRB 170817A** Figure 3 shows the expected polarization, calculated with our model, for the different configurations of magnetic fields. GRB 170817A has been modelled by a variety of different synchrotron scenarios, while the more traditional top-hat off-axis jet has been disfavored, other models such as radially stratified ejecta (Mooley et al. 2018a; Hotokezaka et al. 2018; Fraija et al. 2019b), and structured jets (Kasliwal et al. 2017; Lamb & Kobayashi 2017; Lazzati et al. 2018) can properly describe the multiwavelength afterglow observations. One thing to note is that for the period starting two weeks after the burst, the flux can be described by a relativistic collimated jet (see references above and Fraija et al. 2019d). As such, the angular structure of the jet is less relevant regarding whether (or not) a homogeneous jet can successfully describe the late afterglow. We use the phenomenological model presented in this paper for a constant-density medium with $\xi = 1$ and $\epsilon = 0$ to obtain the polarization. These conditions reduce our model to the one used in Fraija et al. (2019b), where the authors have fitted the synchrotron light curves. We have used the values reported in Table 3 in Fraija et al. (2019b) to generate the polarization curves. Based on these conditions, the polarization presents a similar behavior as the left side of Figure 1.

For the perpendicular configuration of magnetic field, we observe an initial $\sim 1.8\%$ polarization for all values of $q_0$. Then, the polarization begins its evolution towards a maximum of $|\Pi/\Pi_{max}|(q_0 = 4.05^{+0.15}_{-0.15}) \approx 55^{-1}_{+1}\%$ at $t \approx 27$ days, with a second peak of $|\Pi/\Pi_{max}| \approx 57.5^{+0.5}_{-0.5}\%$ at $t \approx 100$ days. The parallel configuration has an initially high degree of polarization across the board and low influence of $q_0$, with $\Pi/\Pi_{max} \approx 97\%$, and $\Pi/\Pi_{max} \approx 84\%$ at the break. The blue inverted triangles Figure 3 show the upper limits, of $|\Pi| \approx 12\%$ at $t \approx 243$ days (derived by Corsi et al. 2018), normalized by our arbitrarily chosen value of $\Pi_{max} = 70\%$. Upper limits are broken by the polarization curves, with $|\Pi/\Pi_{max}|(B_\perp) \approx 25\%$ and $\Pi/\Pi_{max}(B_\parallel) \approx 33\%$. This indicates that the chosen configurations cannot successfully describe the polarization observed for GRB 170817A. Several attempts at constraining the magnetic field configuration of GRB 170817A have been performed (e.g., see Gill & Granot 2018; Stringer & Lazzati 2020; Gill & Granot 2020; Teboul & Shaviv 2021), using the available polarimetric upper limits and multiple types of outflows. These works agree that a configuration with $b = 0$ ($b \to \infty$) is ruled out. An exception is the case of a wide-angled quasi-spherical outflow with energy injection, calculated by Gill & Granot (2018), which does not break the upper limits. However, this particular model is disfavoured to describe the afterglow flux of the burst. Teboul & Shaviv (2021) and Gill & Granot (2020) have constrained the anisotropy of the magnetic fields to a dominant perpendicular component with a sub-dominant parallel component ($0.85 \lesssim b \lesssim 1.16$ and $0.66 \lesssim b \lesssim 1.49$, for each paper, respectively). More observations on a shorter post-burst period would be needed to constrain the magnetic field configuration further, and proper modeling of the afterglow light curve is necessary for breaking the degeneracy between models. Unfortunately, there were no polarization observations at any other frequency and time (Corsi et al. 2018).

## 5 THE CLOSEST SGRBS DETECTED BY SWIFT SATELLITE

Dichiara et al. (2020) presented a systematic search for nearby sGRBs with similar features to GRB 170817A in the Swift database, covering 14 years of operations. A subset of four potential candidates: GRB 050906, GRB 070810B, GRB 080121, and GRB 100216A, were found between 100 and 200 Mpc. These candidates were used to constrain the range of properties for X-ray counterparts of a merger of two NSs, and derived optical upper limits on the onset of a "blue" KN, implying a low amount of lanthanide-poor ejecta (see Section 3.2 from Dichiara et al. (2020) and references therein).

### 5.1 Light curves and Polarization

Figure 7 presents three rows, where the first one corresponds to a set of Swift-identified bursts between 100 and 200 Mpc. Each panel in the row shows the optical upper limits with the synchrotron light curves expected from an off-axis jet decelerating in a constant-density medium for two different viewing angles; $\theta_{obs}$ = 4 (solid lines) and 15 deg (dashed lines). The synchrotron light curves are presented at the R-band (red) and the u-band (green). The parameter values are reported in Table 3 with $\Gamma = 100$, $\varepsilon_e = 0.3$, $p = 2.5$, $\zeta_e = 1.0$ and $\varepsilon_B = 10^{-4}$. For the chosen afterglow values, higher viewing angles (more than 15 deg) are favored by our model.

Figure 6 shows the expected polarization curves that could be present on account of the parameters used to obtain Figure 7. We have the perpendicular and parallel configurations presented from left to right. Two values of $q_0$ were used for these calculations, and two curves were calculated based on the different angles constrained by fitting the upper flux limits. We can notice that the set of parameters for an observation angle of $\theta_{obs}$ = 4 deg violates the optical upper limits. As such, we will call this set of parameters "disallowed", and the set for which the flux is below the upper limits, with $\theta_{obs}$ = 15 deg as "allowed".

Looking at the perpendicular configuration, the disallowed set presents an initially high polarization ($|\Pi/\Pi_{max}| = 22\%$) compared to the allowed set ($|\Pi/\Pi_{max}| = 2\%$). The peak polarization also happens earlier for the disallowed set and reaches zero earlier. Considering both evolutions, rough limits can be set for these orphan afterglows of similar characteristics. The intersection between curves would set so that the polarization must be $|\Pi/\Pi_{max}| < 31\%$ for $t \approx 1.5 \times 10^{-2}$. However, since the disallowed set decreases past this point (while the allowed set increases), the requirement is that $|\Pi/\Pi_{max}| > 31\%$ for $t > 1.5 \times 10^{-2}$ s.

For the parallel configuration, we consider the behavior that the $\Pi/\Pi_{max}$ is higher than $q_0$ increases, with a slower descent until the jet break time, where the polarization plummets. The disallowed set faster decrease would indicate that the polarization at break times must remain high, if we consider the best fit option for the set of Swift-identified bursts is a sufficiently off-axis emission. As such, a polarization $\Pi/\Pi_{max} > 80\%$ would be required, at the time of the break, by our model.

## 6 PROMISING GW EVENTS IN THE THIRD OBSERVING RUN (O3) THAT COULD GENERATE ELECTROMAGNETIC EMISSION

### 6.1 Multi-band observations

During the O3 observing run (from 2019 April 01 to 2020 March 27), the Advanced LIGO and Advanced Virgo GW detectors reported 56 GW events. The run was homogeneously split into two periods called "O3a" (from 2019 April 01 to September 30) and "O3b" (from 2019 November 01 to 2020 March 27). The candidate GW events in the O3a and O3b runs are reported in Gravitational Wave Transient (GWTC-2) Catalog 2 and (GWTC-3) Catalog 3, respectively. The potential candidates reported that are consistent with a source with $m_2 < 3M_\odot$ – where $m_2$ is the mass of the secondary component of the binary merger – and that could generate electromagnetic emission are GW190425, GW190426_152155, GW190814 in GWTC-2 (Abbott et al. 2021) and GW191219_163120, GW200105_162426, GW200115_042309, GW200210_092254 in GWTC-3 (The LIGO Scientific Collaboration et al. 2021).

### 6.2 Light Curves and Polarization

Figure 7 second and third rows presents the five promising GW events in the third observing run (O3) which are more likely to generate an electromagnetic counterpart, that is, in whose binary system there is at least one neutron star. Each panel shows the multi-band upper limits and the synchrotron light curves from the off-axis jet decelerating in a constant-density medium with different viewing angles $\theta_{obs}$ = 6 (solid) and 17 deg (dashed). The synchrotron light curves are presented at 1 keV (green), UVOT (orange), R-band (yellow) and 3 GHz (brown). Optical data were retrieved for the follow-up campaign carried out by the DDOTI collaboration (Becerra et al. 2021). For the chosen values, the values of viewing angle less than 7 deg are ruled out in our model for the S190425z (GW190425), S190426C (GW190426_152155) and S190814bv (GW190814) events which are consistent with the ones reported in Dobie et al. (2019); Ackley et al. (2020); Gomez et al. (2019) using different off-axis models. More observations on duration ranging seconds from the burst trigger to months and years after the merging period are needed to infer tighter constraints.

Figure 7 shows the expected polarization curves that could be present because of the parameters used to satisfy the upper limits of the GW

events. Similar to the Swift-identified bursts, we will be referring to the two sets of parameters as "disallowed" (for $\theta_{obs} = 6 \deg$) and "allowed" (for $\theta_{obs} = 17 \deg$).

Similar considerations can be taken as with the Swift-identified bursts; with the intersection happening at $t \approx 3.8 \times 10^{-2}$ s and $|\Pi/\Pi_{max}| \approx 47\%$, we can set the rough upper limit of $< 47\%$ for $t < 3.8 \times 10^{-2}$ s, and the requirement of $|\Pi/\Pi_{max}| > 47\%$ for later times. Furthermore, the narrow $\theta_j$ and large $\theta_{obs}$ constrain the allowed set at $q_0 > 5$. Rossi et al. (2004) have shown that for a homogeneous sideways expanding jet model, the value of $q_0 > 5$ threshold leads to a merging of the dual peaks present for $q_0 < 5$, which is consistent with Figure 7 and an extra condition imposed on the polarization for this burst. Following the same procedure applied for the Swift-identified bursts, a rough limit for the parallel field would be $\Pi/\Pi_{max} > 83\%$ at the jet break time.

# 7 CONCLUSIONS

We have introduced a polarization phenomenological model as an extension of the analytical synchrotron afterglow off-axis scenario presented in Fraija et al. (2019c,a). This synchrotron model can describe the multi-wavelength afterglow observations for both a constant-density and wind-like medium. We have shown the expected temporal evolution of polarization with a dependency on the physical parameters associated with afterglow GRB emission for two configurations of a magnetic field. Regarding our fiducial model, the calculated polarization took into consideration a broad set of parameters constrained within the typical values observed for off-axis GRBs. We were able to see the differences in possible polarization caused by the two different ambient media and the chosen synchrotron model. We showed that our fiducial model generally agrees with previously found results for a homogeneous sideways expanding jet for the conditions of constant-density medium and adiabatic case with $\xi = 1$ (Granot et al. 2002; Rossi et al. 2004). We have expanded the scenarios for a partially radiative regime and a case where $\xi < 1$. We expect that variation of these parameters present modifications on the temporal evolution of polarization; A partially radiative regime hastens the deceleration of the relativist outflow by the circumburst medium (Böttcher & Dermer 2000; Wu et al. 2005), and this has exacerbated the baseline ($\xi = 1$, $\epsilon = 0$) profile of polarization – with peak $\Pi/\Pi_{max}$ increasing further as $q_0$ grows, but second bump decreasing slightly. On the other hand, changing $\xi$ alters the arrival time of the emission (Waxman 1997; Chevalier & Li 2000; Panaitescu & Mészáros 1998) and our chosen value of $\xi = 0.56$ (Chevalier & Li 2000) has caused the polarization behavior regarding $q_0$ to flip, with the magnitude of the peaks now decreasing as $q_0$ increases. Furthermore, we have calculated the same polarization for a wind-like medium to verify the possible differences. For the change in circumburst medium we have found that the polarization evolves slower in time and changes in the magnitude of polarization compared to the constant-density medium, in agreement with Lazzati et al. (2004).

We have obtained the expected polarization curves for a sample of bursts showing similar off-axis afterglow emissions – GRB 080503, GRB 140903A, GRB 150101B, GRB 160821B, and GRB 170817A. In particular, we have used the available polarimetric upper limits of GRB 170817A; $\Pi < 12\%$ at 2.8 GHz and $t \approx 244$ days (Corsi et al. 2018) to rule out our chosen magnetic field configurations of anisotropy factors $b = 0$ and $b \to \infty$. Although the remaining bursts have neither detected polarization nor constrained upper limits, from our calculations, we can observe a few patterns that reinforce the similarity between these bursts. For the perpendicular field configuration, GRB 080503 and GRB 140903A showed similar magnitudes of polarization, but somewhat dephased in time. Regarding GRB 150101B, the second peak also has a similar polarization degree to the first one of the previously mentioned bursts; however, the peaks happen much later. GRB 160821B is the most distinct out of these bursts, as the polarization happens considerably faster, with a higher first peak (but not too dissimilar to the previous bursts) and a much lower second peak. This is likely due to the angular properties of the burst, as $q_0$ is closer to unity. GRB 170817A is immersed in a lower external density, with a somewhat more energetic jet seen at wider angles, which in combination causes the peaks to be higher than the other bursts by roughly 10% and happens at later times. The peaks of polarization also roughly coincide with the afterglow flux peak in time (see Fraija et al. 2019c,a, for the flux fitting), which is a result that agrees with the literature (Ghisellini & Lazzati 1999; Granot & Königl 2003; Rossi et al. 2004; Teboul & Shaviv 2021). Overall, we could observe the similarities between the bursts' polarization. However, the particularities of each are sufficient to cause observable differences between them.

With the model presented in Section 2 and Fraija et al. (2019a), we have constrained the possible values of the physical parameters of our system. We take into consideration the upper limits of the four closest sGRBs detected by Swift - GRB 050906, GRB 070810B, GRB 080121 and GRB 100216A - and a set of five GW events that could produce an electromagnetic counterpart - S190425z, S190436c, S190814bv, S200105ae, and S200115j - under the condition they must be narrowly collimated jets and seen sufficiently off-axis. We have obtained two sets of parameters, one allowed by the upper limits and one disallowed, and the projected polarization for these values. We used these two sets to obtain what could be considered as a rough constrain on polarization degree, dependent on the geometry of the magnetic field chosen.

More observations, from seconds after the trigger to months and years, are needed to infer tighter constraints on polarization and adequate fitting of the light curves is necessary to obtain adequate parameter values and break degeneracy between synchrotron models.

**DATA AVAILABILITY**

The data used for this study was obtained from the respective credited references: upper limits of linear polarization for GRB 170817A (obtained by Corsi et al. 2018); upper limits of GRB 050906, GRB 070810B, GRB 080121, and GRB 100216A (taken from Dichiara et al. 2020); and upper limits for GW190425, GW190426_152155, GW190814 in GWTC-2 (Abbott et al. 2021) and GW191219_163120, GW200105_162426, GW200115_042309, GW200210_092254 in GWTC-3 (The LIGO Scientific Collaboration et al. 2021). Optical upper limits were obtained by Becerra et al. (2021). Other than cited sources, there is no new data generated or analysed in support of this research.

**REFERENCES**

Abbott R., Abbott T. D., Abraham S., Acernese F., Ackley K., LIGO Scientific Collaboration Virgo Collaboration 2021, Physical Review X, 11, 021053
Ackley K., Amati L., Barbieri C., Bauer F. E., Benetti S., Bernardini M. G., et al. 2020, arXiv e-prints, p. arXiv:2002.01950
Becerra R. L., et al., 2021, MNRAS, 507, 1401
Beniamini P., Granot J., 2016, MNRAS, 459, 3635
Berger E., 2014, ARA&A, 52, 43
Blandford R. D., McKee C. F., 1976, Physics of Fluids, 19, 1130
Böttcher M., Dermer C. D., 2000, ApJ, 532, 281
Buckley D. A. H., et al., 2021, MNRAS, 506, 4621
Cano Z., Wang S.-Q., Dai Z.-G., Wu X.-F., 2017, Advances in Astronomy, 2017, 8929054
Chevalier R. A., Li Z.-Y., 2000, ApJ, 536, 195
Corsi A., et al., 2018, ApJ, 861, L10
Costa E., et al., 1997, Nature, 387, 783
Covino S., et al., 1999, A&A, 348, L1
Dichiara S., Troja E., O'Connor B., Marshall F. E., Beniamini P., Cannizzo J. K., Lien A. Y., Sakamoto T., 2020, MNRAS, 492, 5011
Dobie D., Stewart A., Murphy T., Lenc E., Wang Z., Kaplan D. L., et al. 2019, ApJ, 887, L13
Duncan R. C., Thompson C., 1992, ApJ, 392, L9
Fraija N., Lee W., Veres P., 2016, ApJ, 818, 190
Fraija N., De Colle F., Veres P., Dichiara S., Barniol Duran R., Pedreira A. C. C. d. E. S., Galvan-Gamez A., Betancourt Kamenetskaia B., 2019a, arXiv e-prints, p. arXiv:1906.00502
Fraija N., De Colle F., Veres P., Dichiara S., Barniol Duran R., Galvan-Gamez A., Pedreira A. C. C. d. E. S., 2019b, ApJ, 871, 123
Fraija N., Pedreira A. C. C. d. E. S., Veres P., 2019c, ApJ, 871, 200
Fraija N., Lopez-Camara D., Pedreira A. C. C. d. E. S., Betancourt Kamenetskaia B., Veres P., Dichiara S., 2019d, ApJ, 884, 71
Fraija N., Galvan-Gamez A., Betancourt Kamenetskaia B., Dainotti M. G., Dichiara S., Veres P., Becerra R. L., Pedreira A. C. C. d. E. S., 2022, arXiv e-prints, p. arXiv:2205.02459
Gao H., Ding X., Wu X.-F., Dai Z.-G., Zhang B., 2015, ApJ, 807, 163
Gehrels N., Ramirez-Ruiz E., Fox D. B., 2009, ARA&A, 47, 567
Ghisellini G., Lazzati D., 1999, MNRAS, 309, L7
Giannios D., 2008, A&A, 480, 305
Gill R., Granot J., 2018, MNRAS, 478, 4128
Gill R., Granot J., 2020, MNRAS, 491, 5815
Gill R., Granot J., Kumar P., 2020, MNRAS, 491, 3343
Gomez S., Hosseinzadeh G., Cowperthwaite P. S., Villar V. A., Berger E., Gardner T., et al. 2019, ApJ, 884, L55
Granot J., 2003, ApJ, 596, L17
Granot J., Königl A., 2003, ApJ, 594, L83
Granot J., Sari R., 2002, ApJ, 568, 820
Granot J., Taylor G. B., 2005, ApJ, 625, 263
Granot J., Panaitescu A., Kumar P., Woosley S. E., 2002, ApJ, 570, L61
Hotokezaka K., Kiuchi K., Shibata M., Nakar E., Piran T., 2018, ApJ, 867, 95
Huang Y. F., Gou L. J., Dai Z. G., Lu T., 2000, ApJ, 543, 90
Kann D. A., et al., 2011, ApJ, 734, 96
Kasliwal M. M., et al., 2017, Science, 358, 1559
Kouveliotou C., Meegan C. A., Fishman G. J., Bhat N. P., Briggs M. S., Koshut T. M., Paciesas W. S., Pendleton G. N., 1993, The Astrophysical Journal, 413, L101
Kumar P., Crumley P., 2015, MNRAS, 453, 1820
Kumar P., Zhang B., 2015, Phys. Rep., 561, 1
Laing R. A., 1980, MNRAS, 193, 439
Lamb G. P., Kobayashi S., 2017, MNRAS, 472, 4953
Laskar T., et al., 2019, ApJ, 878, L26
Lazzati D., et al., 2004, A&A, 422, 121
Lazzati D., Morsony B. J., Margutti R., Begelman M. C., 2013, ApJ, 765, 103
Lazzati D., Perna R., Morsony B. J., Lopez-Camara D., Cantiello M., Ciolfi R., Giacomazzo B., Workman J. C., 2018, Phys. Rev. Lett., 120, 241103
Lyutikov M., Pariev V. I., Blandford R. D., 2003, ApJ, 597, 998
Mazets E., et al., 1981, Astrophysics and Space Science, 80, 3
Medvedev M. V., Loeb A., 1999, ApJ, 526, 697
Mészáros P., Rees M. J., 1997, ApJ, 476, 232
Metzger B. D., Giannios D., Thompson T. A., Bucciantini N., Quataert E., 2011, MNRAS, 413, 2031

Mizuta A., Nagataki S., Aoi J., 2011, ApJ, 732, 26
Mooley K. P., et al., 2018a, Nature, 554, 207
Mooley K. P., et al., 2018b, Nature, 561, 355
Nakar E., Piran T., Waxman E., 2003, J. Cosmology Astropart. Phys., 2003, 005
Narayan R., Paczynski B., Piran T., 1992, ApJ, 395, L83
Orsi S., Polar Collaboration 2011, Astrophysics and Space Sciences Transactions, 7, 43
Paczyński B., 1998, ApJ, 494, L45
Paczynski B., Xu G., 1994, ApJ, 427, 708
Panaitescu A., Kumar P., 2000, ApJ, 543, 66
Panaitescu A., Mészáros P., 1998, ApJ, 493, L31
Perley D. A., et al., 2009, ApJ, 696, 1871
Piro L., et al., 1998, A&A, 331, L41
Planck Collaboration Ade P. A. R., Aghanim N., Arnaud M., Ashdown M., Aumont J., et al. 2016, A&A, 594, A13
Rees M. J., Meszaros P., 1994, ApJ, 430, L93
Rossi E. M., Lazzati D., Salmonson J. D., Ghisellini G., 2004, MNRAS, 354, 86
Rutledge R. E., Fox D. B., 2004, MNRAS, 350, 1288
Rybicki G. B., Lightman A. P., 1979, Radiative processes in astrophysics
Sari R., 1997, ApJ, 489, L37
Sari R., Piran T., Narayan R., 1998, ApJ, 497, L17
Stringer E., Lazzati D., 2020, ApJ, 892, 131
Teboul O., Shaviv N. J., 2021, MNRAS, 507, 5340
The LIGO Scientific Collaboration et al., 2021, arXiv e-prints, p. arXiv:2111.03606
Thompson C., 1994, MNRAS, 270, 480
Thompson C., Mészáros P., Rees M. J., 2007, ApJ, 666, 1012
Troja E., et al., 2016, ApJ, 827, 102
Troja E., et al., 2018, Nature Communications, 9, 4089
Troja E., et al., 2019, MNRAS, 489, 2104
Usov V. V., 1992, Nature, 357, 472
Wang X.-G., et al., 2015, ApJS, 219, 9
Waxman E., 1997, ApJ, 491, L19
Waxman E., 2003, Nature, 423, 388
Weibel E. S., 1959, Phys. Rev. Lett., 2, 83
Woosley S. E., 1993, ApJ, 405, 273
Woosley S. E., Bloom J. S., 2006, ARA&A, 44, 507
Wu X. F., Dai Z. G., Huang Y. F., Lu T., 2005, ApJ, 619, 968
Zhang B., Yan H., 2011, ApJ, 726, 90
Zhang S., Jin Z.-P., Wang Y.-Z., Wei D.-M., 2017, ApJ, 835, 73
van Paradijs J., et al., 1997, Nature, 386, 686

**Table 1.** Parameters used to calculate the polarization curves for the fiducial model

| $\tilde{E}$ ($10^{50}$ erg) | n (cm$^{-3}$) | $A_\mathrm{w}$[6] | $\theta_\mathrm{j}$ (deg) | $\theta_\mathrm{obs}$ (deg) | $\Gamma_0$ |
|:---:|:---:|:---:|:---:|:---:|:---:|
| 1 | $10^{-2}$ | $10^{-4}$ | 5.0 | [8, 15] | 100 |

The range [8, 15] for $\theta_\mathrm{obs}$ represents the three chosen values of $\theta_\mathrm{obs}$ = [8.0, 11.5, 15.0]

**Table 2.** Posterior distribution for the parameters used to calculate the polarization for our sample of atypical GRBs

| Parameters | $\tilde{E}$ ($10^{50}$ erg) | n ($10^{-2}$ cm$^{-3}$) | $\theta_\mathrm{j}$ (deg) | $\theta_\mathrm{obs}$ (deg) | $p$ |
|:---|:---:|:---:|:---:|:---:|:---:|
| GRB 080503 | $1.19^{+0.10}_{-0.10}$ | $1.0^{+0.10}_{-0.10}$ | 5.0 | $12.45^{+0.35}_{-0.35}$ | |
| GRB 140903A | $1.50^{+0.49}_{-0.48} \times 10$ | $1.307^{+0.49}_{-0.48} \times 10^2$ | 5.0 | $13.4^{+0.5}_{-0.5}$ | |
| GRB 150101B | $1.10^{+0.29}_{-0.30} \times 10$ | $1.0^{+0.29}_{-0.29}$ | 5.0 | $21.95^{+0.45}_{-0.45}$ | |
| GRB 160821B | $1.99^{+0.10}_{-0.10}$ | $0.98^{+0.10}_{-0.09} \times 10$ | 5.0 | $8.0^{+0.3}_{-0.3}$ | |

**Table 3.** Values used in the calculation of polarization for the closest sGRBs detected by the Swift satellite and GW events detected by Ligo-Virgo reported on run O3 catalog.

| Event | $\tilde{E}$ (erg) | n (cm$^{-3}$) | $\varepsilon_e$ | $\varepsilon_B$ | $\theta_{obs}$ (deg) |
|---|---|---|---|---|---|
| GRB 050906 | $10^{50.7}$ | $10^{-1}$ | $10^{-1}$ | $10^{-4}$ | 4 |
|  | $10^{50}$ | $10^{-1}$ | $10^{-1}$ | $10^{-4}$ | 15 |
| GRB 070810B | $10^{51.7}$ | $10^{-1}$ | $10^{-1}$ | $10^{-4}$ | 4 |
|  | $10^{50}$ | $10^{-1}$ | $10^{-1}$ | $10^{-4}$ | 15 |
| GRB 080121 | $10^{51.7}$ | $10^{-1}$ | $10^{-1}$ | $10^{-4}$ | 4 |
|  | $10^{50.7}$ | $10^{-1}$ | $10^{-1}$ | $10^{-4}$ | 15 |
| GRB 100216A | $10^{51}$ | $10^{-1}$ | $10^{-1}$ | $10^{-4}$ | 4 |
|  | $10^{50}$ | $10^{-1}$ | $10^{-1}$ | $10^{-4}$ | 15 |
| S190423z | $10^{51}$ | $1$ | $10^{-1}$ | $10^{-3}$ | 6 |
|  | $10^{49}$ | $1$ | $10^{-1}$ | $10^{-3}$ | 17 |
| S190426c | $10^{51}$ | $1$ | $10^{-1}$ | $10^{-3}$ | 6 |
|  | $10^{49}$ | $10^{-1}$ | $10^{-1}$ | $10^{-3}$ | 17 |
| S190814bv | $10^{51}$ | $1$ | $10^{-1}$ | $10^{-2}$ | 6 |
|  | $10^{48}$ | $1$ | $10^{-1}$ | $10^{-3}$ | 17 |
| S200105ae | $10^{51}$ | $1$ | $10^{-1}$ | $10^{-3}$ | 6 |
|  | $10^{49}$ | $1$ | $10^{-1}$ | $10^{-3}$ | 17 |
| S200115j | $10^{51}$ | $1$ | $10^{-1}$ | $10^{-2}$ | 6 |
|  | $10^{49}$ | $1$ | $10^{-1}$ | $10^{-2}$ | 17 |
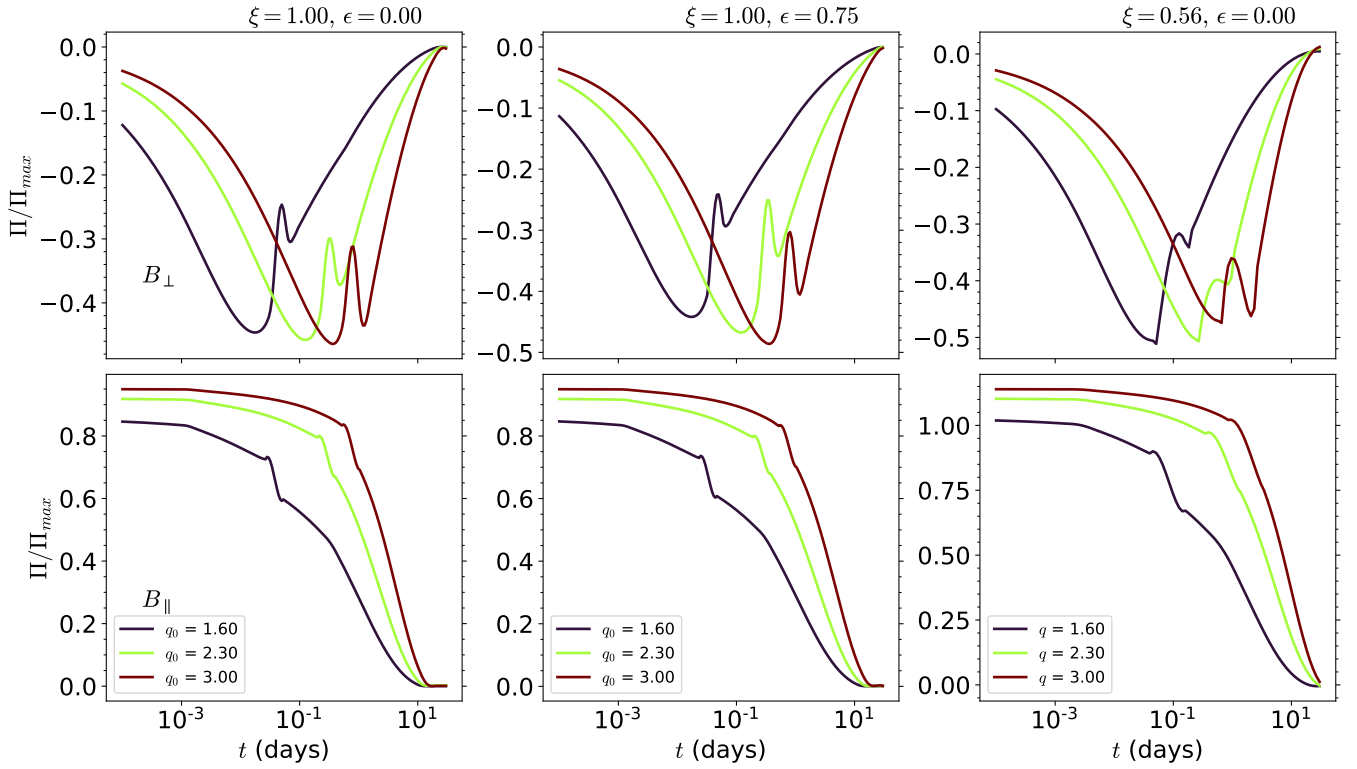
**Figure 1.** Polarization curves for our fiducial model, considering a constant-medium. The top row shows the perpendicular magnetic field configuration, the bottom row shows the parallel one. Each column represent a different pairing $\xi$ and $\epsilon$.
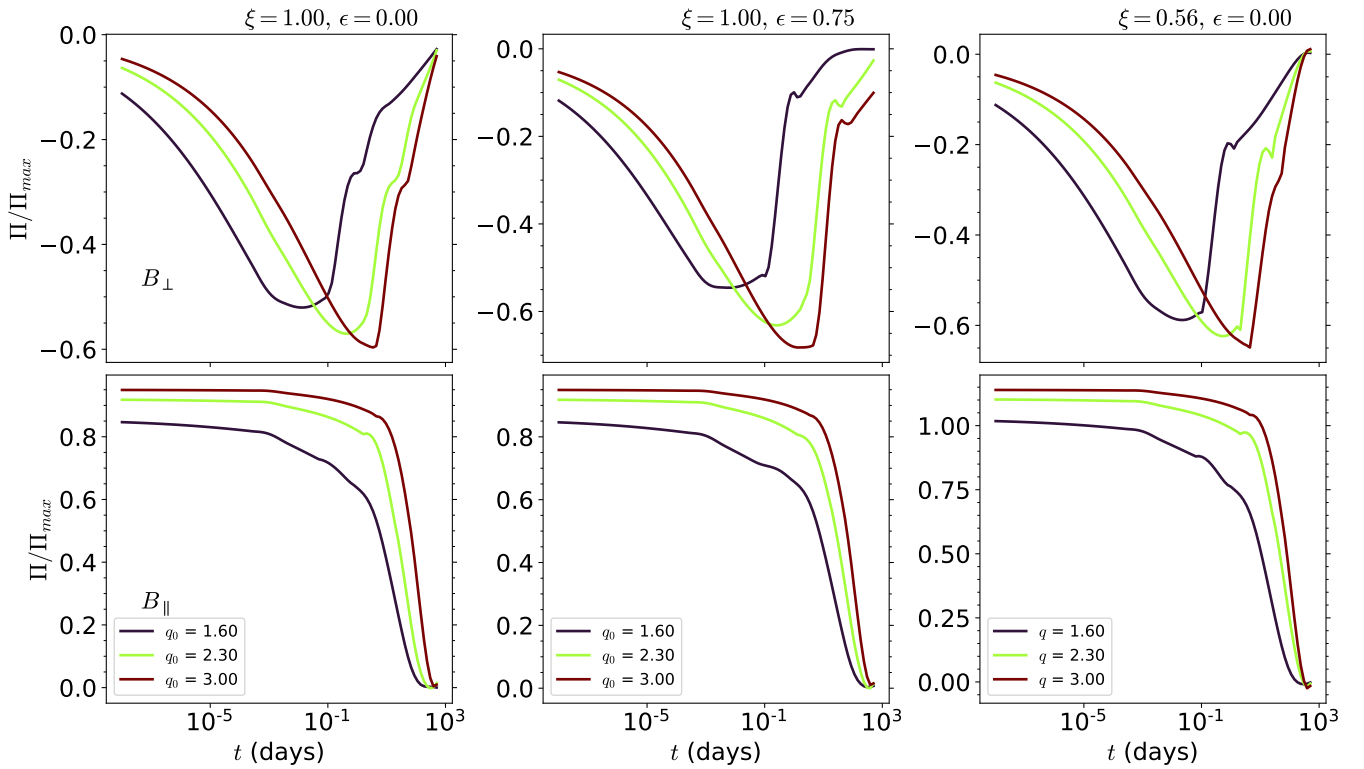


**Figure 2.** Same as Figure 1, but for a wind-like medium.
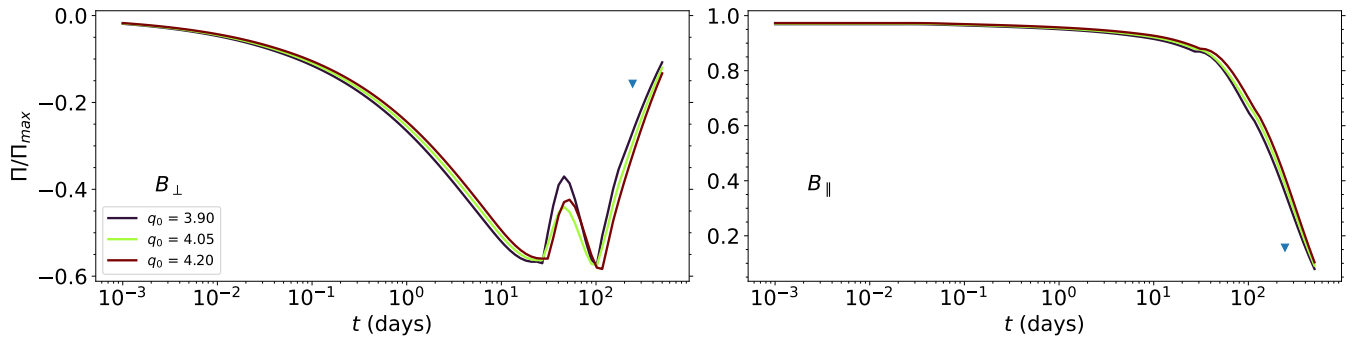
**Figure 3.** Expected Temporal evolution of the polarization for GRB 170817A for two configurations of magnetic fields - Perpendicular ($B_\perp$) and Parallel ($B_\parallel$). These polarization curves were calculated using the best fit values presented in Table 5 of Fraija et al. (2019b): $\tilde{E} \approx 0.7 \times 10^{51}$ erg, $n \approx 1.0 \times 10^{-4}$ cm$^{-3}$, and $\theta_j = 5.0$ deg. For $\theta_{\rm obs}$, we have used the range of 20.5 ± 0.5 deg with three values linearly spaced between the limits. The inverted triangles represent the polarization upper limits $|\Pi| = 12\%$ (derived by Corsi et al. 2018), re-scaled by our chosen $\Pi_{\rm max} = 70\%$.
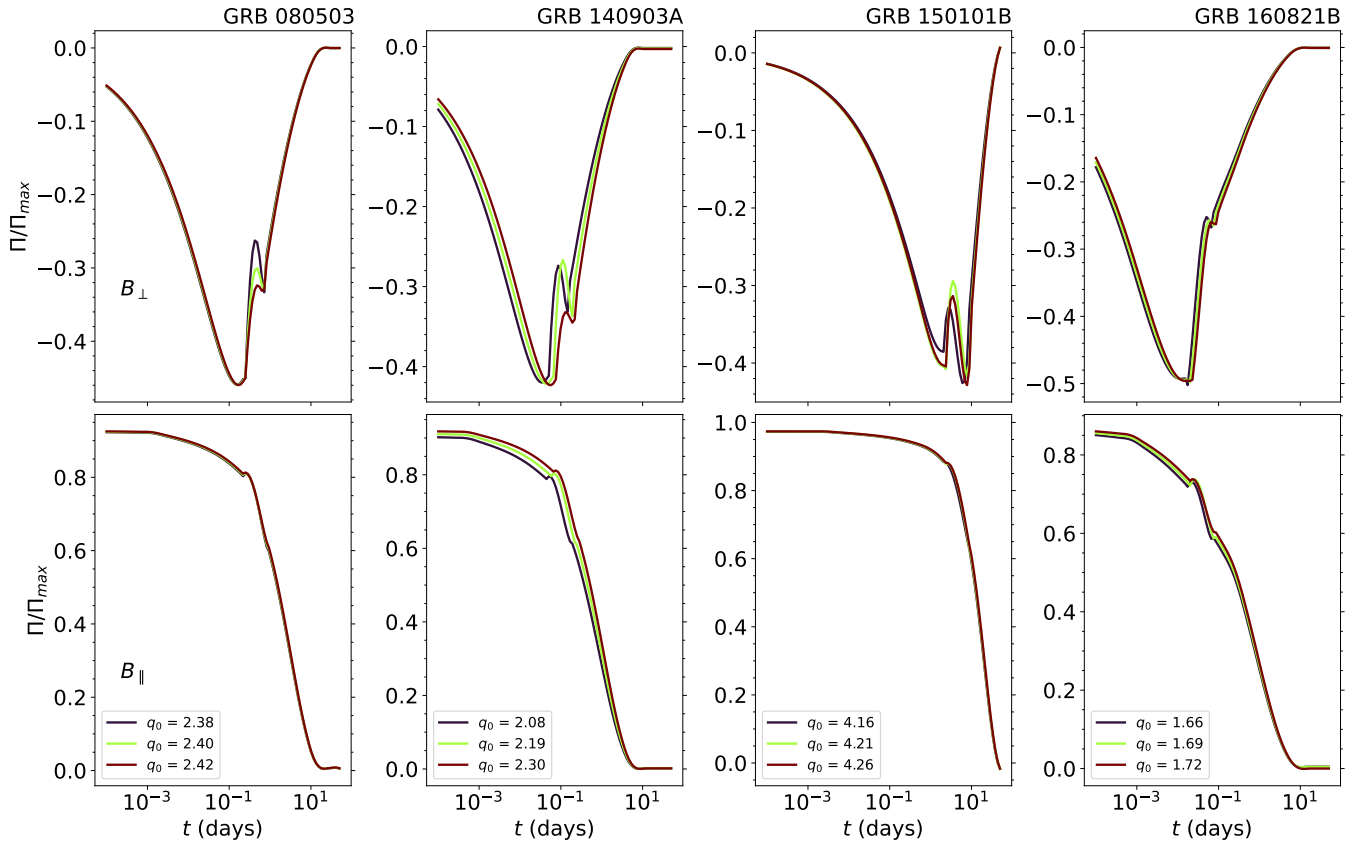
**Figure 4.** Expected temporal evolution of the polarization for the bursts GRB 080503, GRB 140903, GRB 150101B, GRB 160821B - respectively, from left to right – for the parameters presented in Table 2. The uncertainty of the observation angle, $\theta_{\text{obs}}$, was used to return a range of values for the fraction $q$, represented by the colormap legend on the figure. All polarizations are calculated for the case $k = 0$.
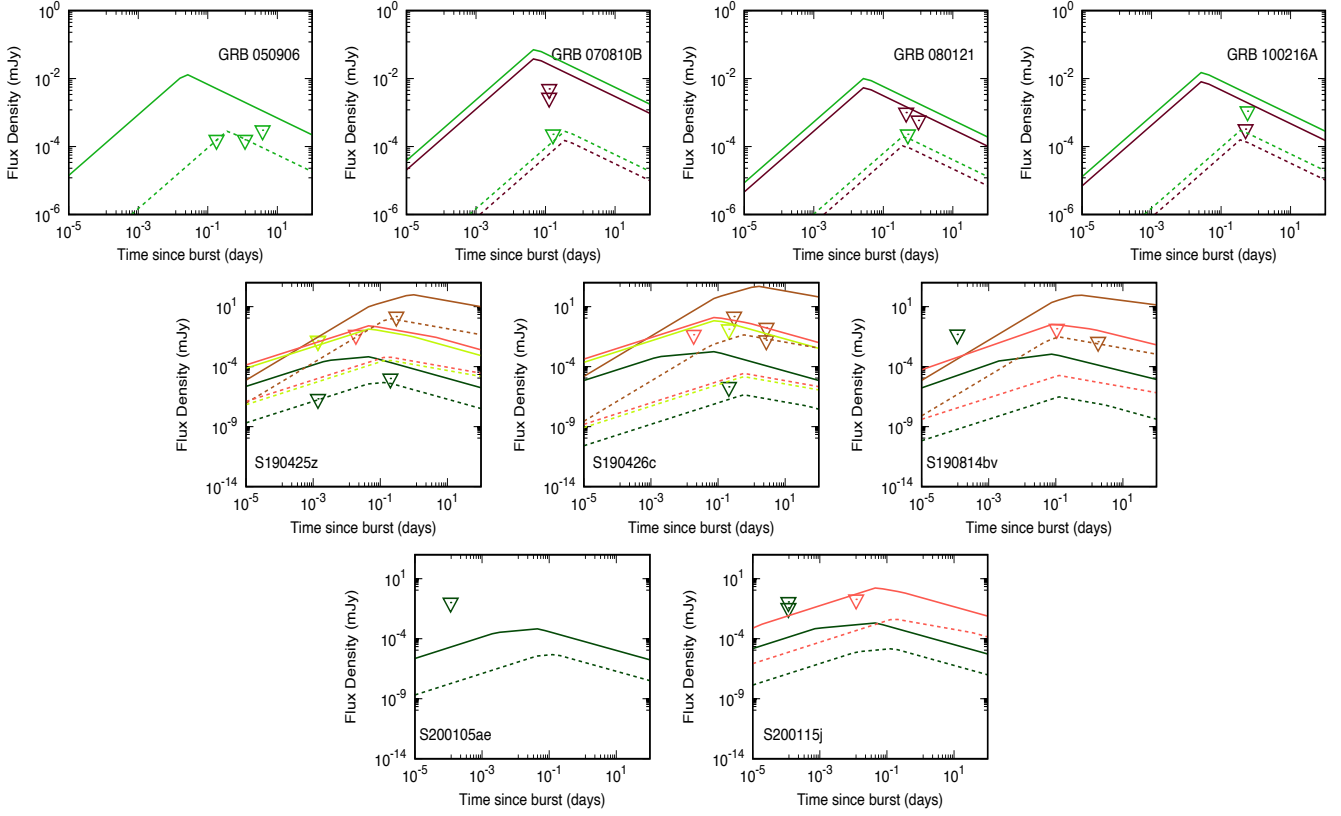
**Figure 5.** Upper limits for GRB 050906, GRB 070810B, GRB 080121, and GRB 100216A (top row, taken from Dichiara et al. 2020) and the set of GW events that could produce an electromagnetic counterpart (middle and bottom rows, taken from The LIGO Scientific Collaboration et al. 2021). The dashed and solid lines correspond to synchrotron light curves evolving in a constant-density medium, where the solid lines represent the value of $\theta_{\rm obs} = 4\,{\rm deg}\,(6\,{\rm deg})$ and the dashed ones use $\theta_{\rm obs} = 15\,{\rm deg}\,(17\,{\rm deg})$. The parameter values used are presented in Table 3.
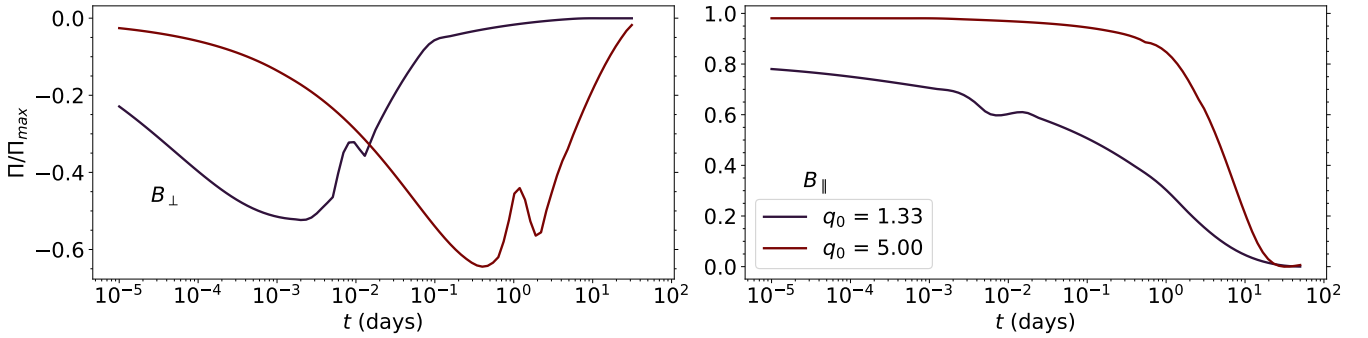


**Figure 6.** Expected temporal polarization evolution for the Swift-detected short GRBs located between 100 and 200 Mpc. The parameters used to calculate these polarization curves are presented in Table 3.
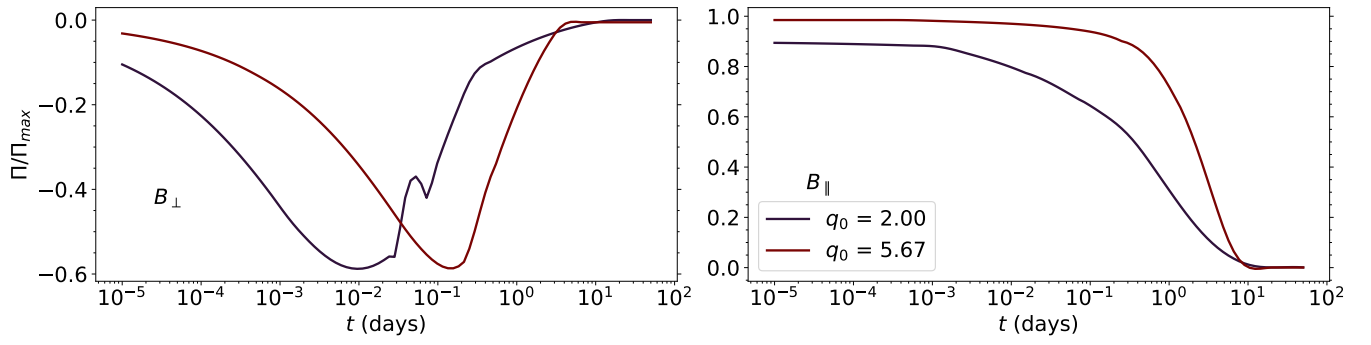
**Figure 7.** Expected temporal polarization evolution for the set of promising GW events observed in the third run (03) capable of generating electromagnetic emissions. This polarization is calculated requiring the relevant parameters presented in Table 3

This paper has been typeset from a TEX/LATEX file prepared by the author.

## 3.3 Modeling of VHE Gamma-Ray Bursts - Polarization and Light Curves

- **Pedreira, A. C. C. d. E. S.**, Fraija, N., Dichiara, S., Veres, P., Dainotti, M. G., Galvan-Gamez, A., Becerra, R. L., Betancourt Kamenetskaia, B., 2022, Exploring the Early Afterglow Polarization of GRB 190829A, ApJ (Submitted), doi: `10.48550/ARXIV.2210.12904`

- Fraija, N., Dichiara, S., **Pedreira, A. C. C. d. E. S.**, Galvan-Gamez, A., Becerra, R. L., Barniol Duran, R., Zhang, B. B., 2019a, ApJ, 879, L26, doi: `10.3847/2041-8213/ab2ae4`

- Fraija, N., Dichiara, S., **Pedreira, A. C. C. d. E. S.**, Galvan-Gamez, A., Becerra, R. L., Montalvo, A., Montero, J., Betancourt Kamenetskaia, B., Zhang, B. B., 2019, ApJ, 885, 29, doi: `10.3847/1538-4357/ab3e4b`

On this section, we present the work related to a couple of special, very-high energy, GRBs. Currently, there are five recorded bursts with photons observed at $> 10$ GeV energies: GRB 180720B, GRB 190114C, GRB 190829A, GRB 201216C and GRB 221009A. We present our work in relation to three of these bursts, GRB 180720B, GRB 190114C and GRB 190829A. Furthermore, two new papers are currently under preparation, however not further along enough to be shown as preprint in this document.

In Fraija et al. (2019b) we present a modeling of GRB 190114C light curves. We show that it presents similar features to other LAT-detected bursts, and that the likely emission mechanism for the VHE photons was SSC, in a reverse-shock framework, while the long lasting afterglow observations were consistent with a synchrotron forward shock model, evolving from a stratified wind-like medium to a homogeneous one. We also claim that an outflow endowed with magnetic fields could describe the polarization properties exhibited in the light curve of this burst.

In Fraija et al. (2019e) we present a modeling of GRB 180720B light curves. We argue that similarly to GRB 190114C, this burst presents similar features to other LAT-detected bursts, and that the likely emission mechanism for the VHE photons and X-ray flare was SSC, in a reverse-shock framework, while the long lasting afterglow observations were consistent with a synchrotron forward shock model in a homogeneous medium. Our best-fit parameters, obtained with MCMC simulations, indicate the presence of magnetic fields in the outflow, with the radio emission being in the synchrotron self-absorption regime.

In Pedreira et al. (2022a) we present the polarization of GRB 190829A, assuming that the observed polarization was generated by synchrotron emission. In this paper, we explore a wide range of parameter sets from previously published works. We find that an off-axis scenario is a poor descriptor of observed data when considering simplifying assumptions. In turn, an on-axis emission is fully capable of describing the imposed polarization upper limits. These results are in agreement with the light curve modeling

found in the literature, which expect this burst to have been observed on-axis. However, the off-axis scenario cannot be fully ruled out, since assuming different field anisotropies allow to solve the discrepancy between flux and polarization fitting. This work is currently under peer-review process. Unfortunately, an accepted version cannot be presented in time for the submission of this document.

# Analysis and Modeling of the Multi-wavelength Observations of the Luminous GRB 190114C

N. Fraija[1] , S. Dichiara[2,3], A. C. Caligula do E. S. Pedreira[1], A. Galvan-Gamez[1], R. L. Becerra[1] , R. Barniol Duran[4], and
B. B. Zhang[5,6]

[1] Instituto de Astronomía, Universidad Nacional Autónoma de México, Apdo. Postal 70-264, Cd. Universitaria, Ciudad de México 04510, México
nifraija@astro.unam.mx
[2] Department of Astronomy, University of Maryland, College Park, MD 20742-4111, USA
[3] Astrophysics Science Division, NASA Goddard Space Flight Center, 8800 Greenbelt Road, Greenbelt, MD 20771, USA
[4] Department of Physics and Astronomy, California State University, Sacramento, 6000 J Street, Sacramento, CA 95819-6041, USA
[5] School of Astronomy and Space Science, Nanjing University, Nanjing 210093, People's Republic of China
[6] Key Laboratory of Modern Astronomy and Astrophysics (Nanjing University), Ministry of Education, People's Republic of China
Received 2019 April 27; revised 2019 June 12; accepted 2019 June 18; published 2019 July 11

## Abstract

Very-high-energy (VHE; $\geqslant 10\,\mathrm{GeV}$) photons are expected from the nearest and brightest gamma-ray bursts (GRBs). VHE photons, at energies higher than 300 GeV, were recently reported by the MAGIC Collaboration for this burst. Immediately, GRB 190114C was followed up by a massive observational campaign covering a large fraction of the electromagnetic spectrum. In this Letter, we obtain the Large Area Telescope (LAT) light curve of GRB 190114C and show that it exhibits similar features to other bright LAT-detected bursts; the first high-energy photon ($\geqslant 100\,\mathrm{MeV}$) is delayed with the onset of the prompt phase and the flux light curve exhibits a long-lasting emission (much longer than the prompt phase) and a short-lasting bright peak (located at the beginning of long-lasting emission). Analyzing the multi-wavelength observations, we show that the short-lasting LAT and Gamma-Ray Burst Monitor bright peaks are consistent with the synchrotron self-Compton reverse-shock model, and that the long-lasting observations are consistent with the standard synchrotron forward-shock model that evolves from a stratified stellar-wind–like medium to a uniform interstellar-medium–like medium. Given the best-fit values, a bright optical flash produced by synchrotron reverse-shock emission is expected. From our analysis we infer that the high-energy photons are produced in the deceleration phase of the outflow, and some additional processes to synchrotron in the forward shocks should be considered to properly describe the LAT photons with energies beyond the synchrotron limit. Moreover, we claim that an outflow endowed with magnetic fields could describe the polarization and properties exhibited in the light curve of GRB 190114C.

*Key words:* acceleration of particles – gamma-ray burst: individual (GRB 190114C) – ISM: general – magnetic fields – radiation mechanisms: non-thermal

## 1. Introduction

Gamma-ray bursts (GRBs), the most luminous gamma-ray transient events in the universe, are non-repeating flashes that are usually associated with the core collapse of massive stars when the duration of the prompt emission is longer than $\gtrsim 2\,\mathrm{s}$, or to the merger of compact object binaries when the duration is less than $\lesssim 2\,\mathrm{s}$ (e.g., see Zhang & Mészáros 2004; Kumar & Zhang 2015, for reviews). Irrespective of the progenitor associated to the prompt emission, a long-lasting afterglow emission is generated via the deceleration of the outflow in the cirbumburst medium. The transition between the prompt and afterglow phase is recognized by early signatures observed in multi-wavelength light curves and broadband spectral energy distributions (SEDs). These signatures are associated with abrupt changes in the spectral features (Giblin et al. 1999), the sudden decrease in the density flux interpreted as high-latitude emission (Kumar & Panaitescu 2000; Fraija et al. 2019a), rapid variations in the evolution of the polarimetric observations (Granot 2003; Fraija et al. 2017a; Troja et al. 2017), and an outstanding multi-frequency peak generated by the reverse shock (Kobayashi & Zhang 2007; Fraija et al. 2016a; Fraija & Veres 2018; Becerra et al. 2019a).

The detection of very-high-energy (VHE; $\gtrsim 10\,\mathrm{GeV}$) photons and their arrival times provides a crucial piece of information to quantify the baryonic composition of the outflow, the particle acceleration efficiency, the emitting region, and the radiation processes, among others (e.g., see Zhang & Mészáros 2004; Kumar & Zhang 2015, for reviews). The Large Area Telescope (LAT) on board the *Fermi* satellite has detected more than 100 GRBs that exhibited photons greater than $\geqslant 100\,\mathrm{MeV}$, and only one dozen bursts with VHE ($\geqslant 10\,\mathrm{GeV}$) photons. The most powerful bursts have shown that the energetic photons arrive late with respect to the onset of the prompt emission, and the LAT light curves display two distinct components: one that lasts much longer than the prompt emission (called long-lasting emission), and another short-lasting bright peak located at the beginning of the long-lasting emission. Using multi-wavelength observations at lower energies for these powerful events, several authors modeled the long-lasting emission with the standard synchrotron forward-shock model (Kumar & Barniol Duran 2009, 2010; Zou et al. 2009; Ghisellini et al. 2010; Nava et al. 2014; Becerra et al. 2017), and the short-lasting bright peak with the synchrotron self-Compton reverse-shock model (Fraija 2015a; Fraija et al. 2016a, 2017a), indicating that the LAT fluxes were generated during the external shocks. However, this is not the case for VHE photons, which cannot be interpreted in the framework of the synchrotron forward-shock model. The maximum photon energy generated by this radiative process is $\sim 10\,\mathrm{GeV}\left(\frac{\Gamma}{100}\right)(1+z)^{-1}$, where $\Gamma$ is the bulk Lorentz factor

and $z$ the redshift (Abdo et al. 2009a; Piran & Nakar 2010; Barniol Duran & Kumar 2011). Given that the bulk Lorentz factor evolves during the afterglow as $\propto t^{-\frac{3}{8}}$ and $\propto t^{-\frac{1}{4}}$ for a uniform interstellar-medium (ISM)-like medium and a stratified stellar-wind–like medium, respectively, VHE photons from synchrotron radiation are not expected at the end of this phase. Therefore, we want to emphasize that the LAT photons below the maximum synchrotron energy can be explained well by synchrotron forward shock; beyond the synchrotron limit, some additional mechanisms must be invoked to explain the VHE LAT photons.

The BAT (Burst Area Telescope) instrument on board the *Swift* satellite triggered on GRB 190114C on 2019 January 14 at 20:57:06.012 UTC (trigger 883832; Gropp et al. 2019). GRB 190114C was also detected by the two instruments on board the *Fermi* satellite; Gamma-Ray Burst Monitor (GBM; Kocevski et al. 2019) and LAT (Kocevski et al. 2019). Immediately after the detection, counterparts were observed by the X-ray Telescope (XRT; Gropp et al. 2019; Osborne et al. 2019) and Ultraviolet/Optical Telescope (UVOT; Gropp et al. 2019; Siegel et al. 2019) on board the *Swift* satellite, the SPI-ACS instrument on board the *International Gamma-ray Astrophysics Laboratory* (*INTEGRAL*; Minaev & Pozanenko 2019), the Mini-CALorimeter instrument on board the Astrorivelatore Gamma ad Immagini ultra LEggero (AGILE) satellite (Ursi et al. 2019), the Hard X-ray Modulation Telescope instrument on board the Insight satellite (Xiao et al. 2019), the Konus-Wind (Frederiks et al. 2019), the the Atacama Large Millimeter/submillimeter Array (ALMA), the Very Large Array (VLA; Laskar et al. 2019), and by a massive campaign of optical instruments and telescopes (Alexander et al. 2019; Bolmer & Shady 2019; D'Avanzo et al. 2019; Im et al. 2019a, 2019b; Izzo et al. 2019; Kim & Im 2019a, 2019b; Kumar et al. 2019; Lipunov et al. 2019; Mazaeva et al. 2019; Mirzoyan et al. 2019; Selsing et al. 2019; Tyurina et al. 2019). For the first time an excess of gamma-ray events with a significance of $20\sigma$ was detected during the first 20 minutes and photons with energies above 300 GeV were reported by the MAGIC Collaboration from GRB 190114C (Mirzoyan et al. 2019).

In this Letter, we analyze the LAT light curve obtained at the position for GRB 190114C and show that it exhibits similar features of other LAT-detected bursts. Analyzing the multi-wavelength observations, we show that the short-lasting LAT and GBM bright peaks are consistent with synchrotron self-Compton reverse-shock model and the long-lived LAT, GBM, X-ray, optical, and radio emissions with the synchrotron forward-shock model that evolves from a stratified stellar-wind–like medium to a uniform ISM-like medium. This Letter is arranged as follows. In Section 2 we present multi-wavelength observations and/or data reduction. In Section 3 we describe the multi-wavelength observations through the synchrotron forward-shock model and the SSC reverse-shock model in a stratified stellar-wind–like and a uniform ISM-like medium. In Section 4, the discussion and results of the analysis executed using the multi-wavelength data are presented. Finally, in Section 5 we give a brief summary. The convention $Q_x = Q/10^x$ in cgs units and the universal constants $c = \hbar = 1$ in natural units will be adopted throughout this Letter.

## 2. GRB 190114C: Multi-wavelength Observations and/or Data Reduction

### 2.1. Fermi-*LAT Observations and Data Reduction*

The *Fermi*-LAT instrument detected VHE emission from GRB 190114C. LAT data exhibited a representative increase in the event rate. The preliminary photon index above 100 MeV was $\Gamma_{LAT} = \beta_{LAT} + 1 = 1.98 \pm 0.06$, with an estimated energy flux of $(2.06 \pm 0.14) \times 10^{-6}$ erg cm$^{-2}$ s$^{-1}$. Later, Wang et al. (2019) analyzed the LAT spectrum in two time intervals, $\sim$6–7 s and 11–14 s, reporting power-law (PL) indexes of $\Gamma_{LAT} = \beta_{LAT} + 1 = 2.06 \pm 0.30$ and $2.10 \pm 0.31$, respectively.

*Fermi*-LAT event data files are retrieved from the online data repository[7] starting few seconds before the GBM trigger time, 20:57:02.63 UT (Hamburg et al. 2019). These data are analyzed using Fermi Science tools[8] version v11r06p03 and reprocessed with Pass 8 extended, spacecraft data, and the instrument response functions "P8R3_TRANSIENT020_V2." Transient events are selected using *gtselect* (evtclass = 16) in the energy range between 100 MeV and 300 GeV, within 15° of the reported GRB position and with a maximum zenith angle of 100°. After taking into account of a model for the source and diffuse components (galactic and extragalactic) using *gtdiffrsp*, we generate the spectra and related response files using *gtbin* and *gtrspgen*, respectively. Data are binned in seven time bins: [1–5, 5–10, 10–15, 15–35, 35–65, 65–90, 90–150] s from the trigger. This binning pattern results from a trade-off aimed to preserve the time profile of the signal and the minimum statistical significance needed to analyze the spectrum. We derive the spectrum for each bin and fit it with a simple power law (SPL) using the software XSPECv12.10.1 (Arnaud 1996). The resulting fluxes are computed after the fit with 90% confidence errors in each time bin. The light curves with the flux above 100 MeV are shown in the upper panel of Figure 1.

Figure 1 shows the *Fermi*-LAT energy flux (blue) and photon flux (red) light curves obtained between 0.1 and 300 GeV (upper panel) and the energies of all the photons ($\geqslant$100 MeV) with probabilities >90% of being associated with this burst (lower panel). In the upper panel we can observe that the energy flux and the photon flux light curves exhibit a bright peak at $\sim$6–7 s followed by a monotonic decreasing emission extended for $\sim$70 s.

In order to model the *Fermi*-LAT data, the function (Vestrand et al. 2006)

$$F(t) = A\left(\frac{t - t_0}{t_0}\right)^{-\alpha_{\gamma,pk}} e^{-\frac{\tau}{t - t_0}}, \qquad (1)$$

and an SPL ($\propto t^{-\alpha_{LAT}}$) are used to describe the short-lasting bright peak and the long-lasting emission, respectively. Here, $t_0$ is the starting time, $A$ is the amplitude, $\tau$ is the timescale of the flux rise, and $\alpha_{\gamma,pk}$ is the temporal decay index of the peak. The energy flux light curve, together with the best-fit curve, are shown in this upper panel. The best-fit values found are $t_0 = 2.61 \pm 0.15$ s, $\tau = 8.11 \pm 1.22$ s, $\alpha_{\gamma,pk} = 2.65 \pm 0.19$ and $\alpha_{LAT} = 1.10 \pm 0.15$ ($\chi^2 = 0.86$).

The lower panel in Figure 1 displays several features. (i) The first high-energy photon of 571.4 MeV that was observed at

---

7 http://fermi.gsfc.nasa.gov/ssc/data
8 https://fermi.gsfc.nasa.gov/ssc/data/analysis/software/
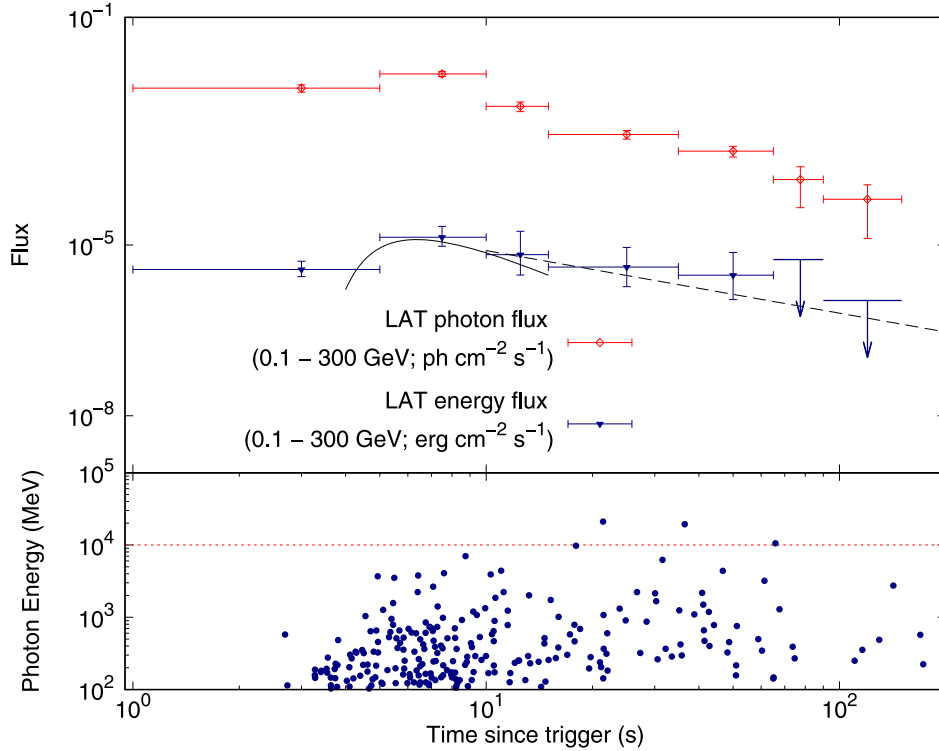
**Figure 1.** Upper panel: *Fermi*-LAT energy flux (blue) and photon flux (red) light curves obtained between 0.1 and 300 GeV. The solid black line represents the best-fit curve found using our model. Lower panel: all the photons with energies >100 MeV and probabilities >90% of being associated with GRB 190114C. *Fermi*-LAT data were reduced using the public database at the *Fermi* website.

2.7 s after the GBM trigger. (ii) This burst exhibited 238 photons with energies larger than 100 MeV, 41 with energies larger than 1 GeV, and five with energies larger than 10 GeV. (iii) The highest-energy photon exhibited in the LAT observations was 21.42 GeV detected at 21 s after the GBM trigger.[9]

### 2.2. GBM Observations

The *Fermi* GBM instrument triggered and localized GRB 190114C at 2019 January 14 20:57:02.63 UTC. During the first 15 s after the trigger, the GBM light curve showed a very bright, multi-peaked pulse followed by a weaker pulse occurring between 15 and 25 s. In addition, a fainter emission with a duration of 200 s after the trigger was detected. The GBM team reported a duration of the main emission of $T_{90} = 116$ s (50–300 keV). This burst presented an equivalent isotropic energy of $3 \times 10^{53}$ erg in the energy range of 1 keV–10 MeV (Hamburg et al. 2019).

Recently, Ravasio et al. (2019) analyzed the GBM data, finding two different spectral components: a smoothly broken PL (SBPL) and a PL. Authors showed that the EPL component in the energy range of 10 keV–40 MeV reached the maximum flux (at the peak) of $(1.7 \pm 0.2) \times 10^{-5}$ erg cm$^{-2}$ s in the time interval of ∼6–7 s. After the peak, this component decreased with a temporal index of 2.8 up to 15 s and finally, with 1. They reported a spectral PL index for the GBM spectrum of $\Gamma_{\rm GBM} = \beta_{\rm GBM} + 1 = 1.81 \pm 0.08$

Given the similarity between the LAT (see Figure 1) and GBM (see Figure 1 in Ravasio et al. 2019) light curves, we take the *Fermi* GBM data reported in Ravasio et al. (2019) and

model the EPL component. Again, the function described by Equation (1) and a SPL ($\propto t^{-\alpha_{\rm GBM}}$) are used to describe the short-lasting peak and the long-lasting emission, respectively. In this case, the best-fit values found are $t_0 = 3.09 \pm 0.23$ s, $\tau = 7.29 \pm 0.46$ s, $\alpha_{\gamma,\rm pk} = 2.96 \pm 0.19$ and $\alpha_{\rm GBM} = 1.05 \pm 0.13$ ($\chi^2 = 1.33$). The values obtained with our model are very similar to those ones reported by Ravasio et al. (2019).

The upper left-hand panel in Figure 2 shows the GBM light curve of the EPL component at 10 MeV. The continuous and dashed red lines correspond to the best-fit curves. Data were taken from Ravasio et al. (2019).

### 2.3. X-Ray Observations and Data Reduction

The *Swift* BAT instrument triggered on GRB 190114C at 2019 January 14 20:57:06.012 UTC (Gropp et al. 2019). During the first 25 s, the BAT light curve exhibited a very bright multi-peaked structure. The main brightest emission consist of two complex pulses, ending at about 50 s after the trigger time. Afterward, the X-ray flux appeared to decay exponentially out to beyond 720 s after the trigger, when the burst went out of the BAT field of view. GRB 190114C returned to the BAT field of view at ∼3800 s after the trigger, although no significant flux was detected at that time (Krimm et al. 2019).

The *Swift* XRT instrument began observing GRB 190114C at 64 s after the trigger time. This instrument found a bright, uncatalogued X-ray source from 03:38:01.20 to 26:56:47.6 (J2000) with a 90% uncertainty radius of 1.4 arcsec (Gropp et al. 2019; Osborne et al. 2019).

The upper right-hand panel in Figure 2 shows the *Swift* X-ray light curve obtained with *Swift* BAT (black) and XRT

---

[9] It is worth noting that photons at energy higher than ∼300 GeV were reported by MAGIC Collaboration.
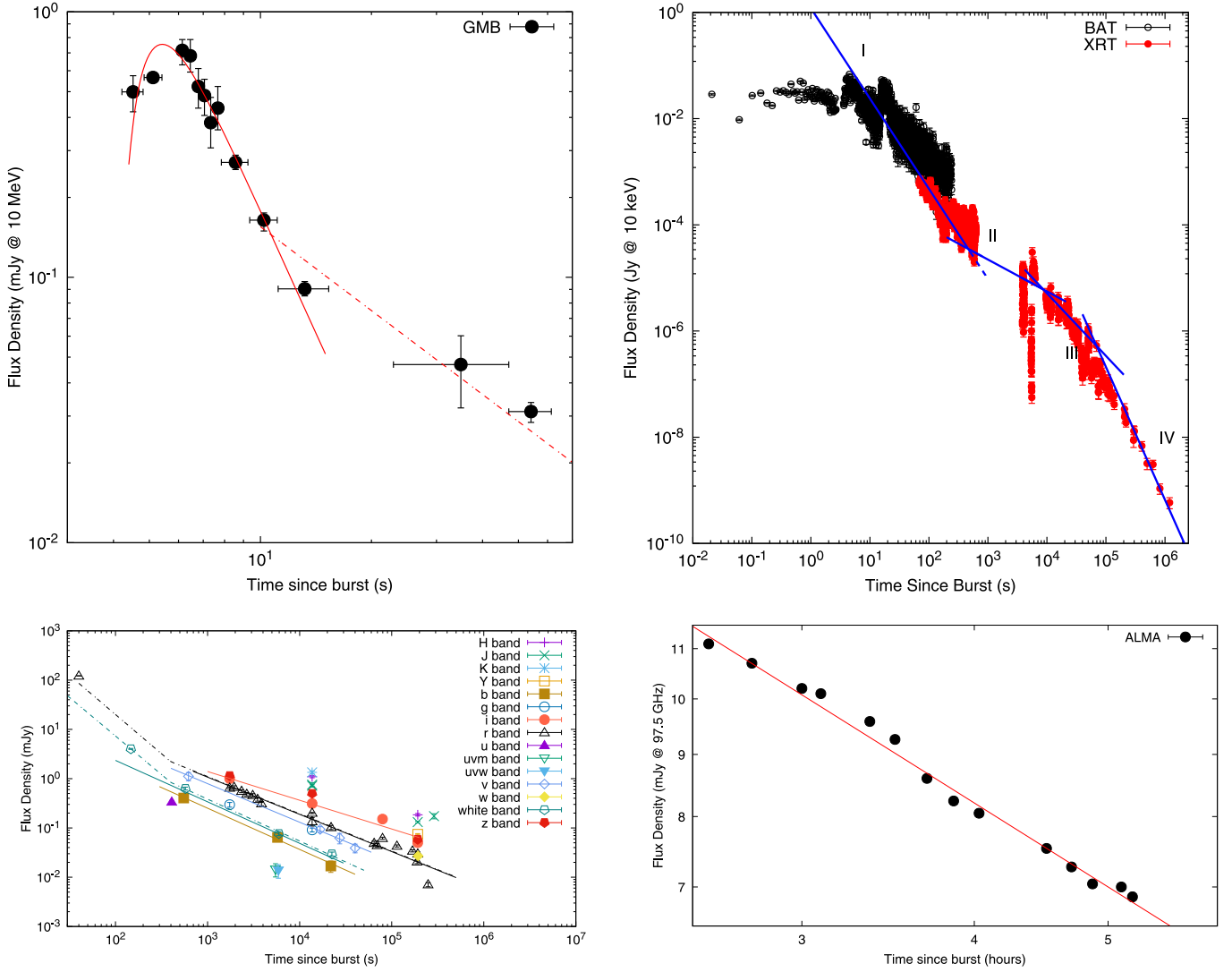
**Figure 2.** The upper left-hand panel shows the GBM light curve at 10 MeV. The solid red line corresponds to the best-fit curve using Equation (1), and the dashed red line corresponds to an SPL. Data were taken from Ravasio et al. (2019). The upper right-hand panel shows the X-ray light curve obtained with *Swift* BAT (black) and XRT (red) instruments at 10 keV. Blue lines correspond to the best-fit curves using SPL functions. The *Swift* data were obtained using the publicly available database on the official *Swift* website. The lower left-hand panel shows the optical light curves of GRB 190114C in different filters with the best-fit functions. The continuous line corresponds to the best-fit curve using an SPL function, and the dotted–dashed line using a broken PL (BPL) function. Optical data were collected from Izzo et al. (2019), Mirzoyan et al. (2019), Bolmer & Shady (2019), Im et al. (2019a), Alexander et al. (2019), D'Avanzo et al. (2019), Kim & Im (2019a), Kumar et al. (2019), Kim & Im (2019b), Im et al. (2019b), and Mazaeva et al. (2019). The lower right-hand panel shows the radio light curve obtained with ALMA at 97.5 GHz. The red line corresponds to the best-fit curve using an SPL function. Radio data were taken from Laskar et al. (2019).

(red) instruments at 10 keV. Blue lines correspond to the best-fit curves using SPL functions. *Swift* data were obtained using the public available database at the official *Swift* website. Four PL segments are identified in the X-ray light curve. (I) An initial PL segment with a temporal index of $1.59 \pm 0.12$. This value clearly is not related with the typical decay slope, which is explained in terms of the high-latitude emission of the prompt GRB (the emission has abruptly ceased; Kumar & Panaitescu 2000). (II) A PL segment with a temporal index of $0.57 \pm 0.09$. This value is consistent with shallow "plateau" decay segment (Zhang et al. 2006; Stratta et al. 2018). (III) A PL segment with a temporal index of $1.09 \pm 0.11$ (Zhang et al. 2006). This value is consistent with the normal decay segment. (IV) A late steeper decay with a temporal PL index of $2.54 \pm 0.14$. This value is consistent with the jet break

**Table 1**
*Swift* X-Ray Light Curve of GRB 190114C with the Best-fit Values of the Temporal PL Index with their Respective $\chi^2$/NDF

| X-Rays (PL Function) | Period | Index ($\alpha_X$) | $\chi^2$/ndf |
|---|---|---|---|
| I | $\leqslant 400$ s | $1.59 \pm 0.12$ | 0.6 |
| II | $400-10^4$ s | $0.57 \pm 0.09$ | 0.81 |
| III | $10^4-10^5$ s | $1.09 \pm 0.11$ | 0.83 |
| IV | $\geqslant 10^5$ s | $2.54 \pm 0.14$ | 0.91 |

(Vaughan et al. 2006). The best-fit values of the X-ray data are reported in Table 1.

**Table 2**
Optical Light Curves of GRB 190114C in Different Filters with the Best-fit
Values of the Temporal PL Index with their Respective $\chi^2$/NDF

| Optical Band | Index $\alpha_O$ | Break Time $t_{br}(s)$ | Index $\alpha_O$ | $\chi^2$/ndf |
|---|---|---|---|---|
| $b$ | ... | ... | $0.8374 \pm 0.0064$ | 0.61 |
| $i$ | ... | ... | $0.5835 \pm 0.0089$ | 1.32 |
| $r$ | ... | ... | $0.7554 \pm 0.0073$ | 1.41 |
| | $1.593 \pm 0.012$ | 8.1 | $0.7554 \pm 0.0034$ | 1.22 |
| $v$ | ... | ... | $0.7828 \pm 0.0551$ | 0.41 |
| White | ... | ... | $0.912 \pm 0.0719$ | 1.45 |
| | $1.567 \pm 0.097$ | 26.3 | $0.911 \pm 0.081$ | 1.72 |

## 2.4. Optical Observations and Data Reduction

The *Swift* UVOT began observing a candidate afterglow of GRB 190114C at 73 s after the trigger trigger (Gropp et al. 2019). The observations using the near-ultraviolet (NUV) filters of the first few orbits indicated that the afterglow faded rapidly (Siegel et al. 2019).

Using the MASTER-IAC telescope, Tyurina et al. (2019) pointed to GRB 190114C 25 s after notice time and 47 s after trigger time. On their first set they found one optical transient within the *Swift* error-box (R.A. = 54.5042, decl. = −26.9383) that was brighter than 16.54 mag. Furthermore, MASTER-SAAO with MASTER-IAC telescopes reported a polarization photometry in four position angles (Lipunov et al. 2019). de Ugarte Postigo et al. (2019) detected a source in the Pan-STARRS archival in the field of GRB 190114C, suggesting that this source as the possible host galaxy of GRB 190114C. This was confirmed by NOT (Selsing et al. 2019), which derived a redshift of $z = 0.42$. Additional photometry was reported in Izzo et al. (2019), Mirzoyan et al. (2019), Bolmer & Shady (2019), Im et al. (2019a, 2019b), Alexander et al. (2019), D'Avanzo et al. (2019), Kim & Im (2019a, 2019b), Kumar et al. (2019), and Mazaeva et al. (2019).

The lower left-hand panel of Figure 2 shows the optical light curves of GRB 190114C in different filters with the best-fit functions. The continuous line corresponds to the best-fit curve using an SPL function and the dotted–dashed line using a BPL function. SPL functions are used for the $i$, $r$, $v$, white, and $b$ bands (solid lines) and BPL functions for the $r$ and white bands (dotted–dashed lines). Optical data were collected from several instruments and taken from the GCN circulars showed above. The optical fluxes and their corresponding uncertainties used in this work were calculated using the standard conversion for AB magnitudes shown in Fukugita et al. (1996). The optical data were corrected by the galactic extinction using the relation derived in Becerra et al. (2019b). The values of $\beta_O = 0.83$ for optical filters and a reddening of $E_{B-V} = 0.01$ (Bolmer & Shady 2019) were used.

The best-fit values of the temporal PL indexes with their respective $\chi^2$/ndf are reported in Table 2. This table shows that optical fluxes present two distinct decays separated by a break at ~400 s. Before this break, the temporal PL indexes are stepper ($\alpha_O = 1.593 \pm 0.012$ for the $r$-band and $1.567 \pm 0.097$) and after they lie in the range of $0.6 \lesssim \alpha_O \lesssim 0.9$. Due to the large amount of optical data collected in the $r$-band, the multi-wavelength analysis is done considering the optical $r$-band data points. The $r$-band optical observation collected the ninth day after the burst trigger was

removed due to the contamination by the host galaxy and supernova associated with this burst (Burenin et al. 2019; Melandri et al. 2019).

## 2.5. Radio Observations

ALMA (at 97.5 GHz) and the Karl G. Jansky VLA (at 5–38 GHz) began observing the afterglow of GRB 190114C at 2.2 and 4.7 hr after the burst trigger, respectively (Laskar et al. 2019). The ALMA and VLA observations were extended up to 5.2 and 6.3 hr after the burst trigger, respectively. Authors described the SED of the radio data at 0.2 days; VLA at radio cm-band and ALMA at mm-band. Using a BPL model they found a spectral index of $\beta_R = 0.3 \pm 0.2$ below the break of $24 \pm 4$ GHz. In addition, (Laskar et al. 2019) found that the GROND $K$-band and ALMA observations were consistent with a SPL at 0.16 days. The lower right-hand panel in Figure 2 shows the radio light curves of the ALMA observations with the best-fit curve using a SPL function. The best-fit value of the temporal index of $0.71 \pm 0.01$ is reported in Table 3. Radio data were taken from Laskar et al. (2019).

## 2.6. VHE Observations

MAGIC telescopes detected VHE gamma-ray emission from GRB 190114C. Their data showed a clear excess of gamma-ray events with the significance $20\sigma$ in the first 20 minutes (starting at $T + 50$ s) for photon energies around 300 GeV. Other TeV gamma-ray observatories such as the High Altitude Water Cherenkov (HAWC) and H.E.S.S. reported neither VHE detection nor upper limits in the directions of GRB 190114C.

## 3. Description of the Multi-wavelength Observations

### 3.1. Multi-wavelength Analysis of Observations

Figure 3 shows the LAT, GBM, X-ray, optical, and radio light curves (upper panel) and the broadband SED of the X-ray and optical (UVOT) observations during the period of 5539–57216 s (lower panel) of GRB 190114C with the best-fit curves. The shaded period in the upper panel corresponds to the spectrum on the lower panel. The best-fit values of the temporal PL indexes obtained through the chi-square $\chi^2$ minimization function are reported in Table 3. In order to obtain the best-fit values of the spectral PL indexes, we analyze the broadband SED of GRB 190114C, taking into account the available X-ray and optical data, and the values reported for the LAT, GBM, and radio bands.

During the first 70 s, the observations are almost covered by the LAT and GBM instruments with only one optical ($r$-band) data point. The LAT collaboration reported a spectral PL index above 100 MeV of $\beta_{LAT} = 1.98 \pm 0.06$ (Kocevski et al. 2019). Analyzing the LAT spectrum, Wang et al. (2019) reported PL indexes of $\beta_{LAT} = 1.06 \pm 0.30$ and $1.10 \pm 0.31$ for two time intervals ~6–7 s and 11–14 s, respectively. Analyzing the PL component of the GBM data, Ravasio et al. (2019) reported a spectral index of $\beta_{GBM} = 0.81 \pm 0.08$. From 70 to 400 s, X-rays dominate the observations with one optical data point in the white band.

During the time interval from 5539 to 57216 s, the optical (UVOT) and X-ray (XRT) available data are quasi-simultaneous, as shown in the lower panel in Figure 3. From X-ray to optical data, the SED is modeled with a SPL with PL index $\beta_X = 0.83 \pm 0.04$. The blue dashed line is the best-fit curve

**Table 3**
The Best-fit Values of the Spectral and Temporal Indexes Using the LAT, X-Ray and Optical Observational Data

| | Observation ($\leqslant 400$ s) | Theory (Stratified Medium) | Observation | | Theory (Uniform Medium) | | Observation ($\geqslant 10^5$ s) | Theory (Uniform Medium) |
|---|---|---|---|---|---|---|---|---|
| | | | ($400-10^4$ s) | ($10^4-10^5$ s) | | | | |
| **LAT flux** | | | | | | | | |
| $\alpha_{\rm LAT}$ | $1.10 \pm 0.15$ | $1.15 \pm 0.22$ | ... | | ... | | ... | ... |
| $\beta_{\rm LAT}$ | $1.10 \pm 0.31$[a] | $1.10 \pm 0.15$ | ... | | ... | | − | − |
| **GBM flux** | | | | | | | | |
| $\alpha_{\rm GBM}$ | $1.05 \pm 0.13$ | $1.15 \pm 0.22$ | ... | | ... | | ... | ... |
| $\beta_{\rm GBM}$ | $0.81 \pm 0.08$[b] | $1.10 \pm 0.15$ | ... | | ... | | ... | ... |
| **X-ray flux** | I | | II | III | II | III | IV | |
| $\alpha_{\rm X}$ | $1.59 \pm 0.12$ | $1.40 \pm 0.22$ | $0.57 \pm 0.09$ | $1.09 \pm 0.11$ | $(0.1-0.6)$ | $1.15 \pm 0.22$ | $2.54 \pm 0.14$ | $2.2 \pm 0.3$ |
| $\beta_{\rm X}$ | ... | ... | | $0.83 \pm 0.04$ | | $0.60 \pm 0.15$ | ... | ... |
| **Optical flux** | | | | | | | | |
| $\alpha_{\rm O}$ | $1.593 \pm 0.012$ | $1.40 \pm 0.22$ | | $0.755 \pm 0.003$ | | $0.90 \pm 0.22$ | ... | ... |
| $\beta_{\rm O}$ | ... | ... | | $0.83 \pm 0.04$ | | $0.60 \pm 0.15$ | ... | ... |
| **Radio flux** | | | | | | | | |
| $\alpha_{\rm R}$ | ... | ... | | $0.71 \pm 0.01$ | | $0.90 \pm 0.22$ | ... | ... |
| $\beta_{\rm R}$ | ... | ... | | $-(0.3 \pm 0.2)$[c] | | $-0.33$[d] | ... | ... |

**Notes.** In addition, the theoretical predictions of the spectral and temporal indexes are calculated for $p = 2.2 \pm 0.3$. Values in round parentheses are the chi-square minimization ($\chi^2$/N.D.F.).
[a] This value was reported in Wang et al. (2019).
[b] This value was reported in Ravasio et al. (2019).
[c] This value was reported in Laskar et al. (2019) below 24 GHz. Above this value, the radio mm-band and optical data can be described with an SPL.
[d] The value between radio mm-band and optical data is $0.60 \pm 0.15$.

obtained from XSPEC. During this period, Laskar et al. (2019) described the SED of the radio data at 0.2 days: VLA at radio cm-band and ALMA at mm-band. Using a BPL model they found a value of spectral index $\beta_{\rm R} = 0.3 \pm 0.2$ below a break of $24 \pm 4$ GHz. In addition, the authors found that the GROND $K$-band and ALMA observations were consistent with an SPL at 0.16 days. For the period of time longer than 57216 s, it is not possible to analyze the multi-wavelength observations because there is no quasi-simultaneous available data. The best-fit values of the temporal and spectral PL indexes of the LAT, GBM, X-ray, optical, and radio fluxes are reported in Table 3.

### 3.2. Synchrotron Forward-shock Model and Analysis of the Long-lasting Multi-wavelength Observations

#### 3.2.1. Light Curves in a Stratified Stellar-wind–like Medium

Taking into consideration a Wolf–Rayet (WR) star as progenitor with typical values of a mass-loss rate of $\dot{M} \simeq 10^{-6} M_\odot$ yr$^{-1}$ and a constant wind velocity of $v_W \simeq 10^8$ cm s$^{-1}$, the density of the stratified stellar-wind–like medium is given by $\rho(r) = A\, r^{-2}$, where $A = \frac{\dot{M}}{4\pi v_{W}} = A_\star\, (5 \times 10^{11})\mathrm{g\ cm}^{-1}$ with $A_\star$ a parameter of stellar wind density (Dai & Lu 1998; Chevalier & Li 2000; Panaitescu & Kumar 2000; Vink et al. 2000; Chevalier et al. 2004; Vink & de Koter 2005). Using the typical timescales together with the maximum power emitted by relativistic electrons, the characteristic (for $p \geqslant 2$) and cooling energy breaks and the maximum flux evolve as $\epsilon_{\rm m,f}^{\rm syn} \propto t^{-\frac{3}{2}}$, $\epsilon_{\rm c,f}^{\rm syn} \propto t^{\frac{1}{2}}$ and $F_{\rm max,f}^{\rm syn} \propto t^{-\frac{1}{2}}$, respectively. The subscript f refers throughout this manuscript to the forward shock. The synchrotron

breaks and the maximum flux are functions of $\varepsilon_{\rm e,f}$, $\varepsilon_{\rm B,f}$, $E$, and $A$. The terms $\varepsilon_{\rm e,f}$ and $\varepsilon_{\rm B,f}$ refer to the microphysical parameters given to accelerate electrons and to amplify the magnetic field, respectively, $E$ is the equivalent kinetic energy given by the isotropic energy $E_{\gamma,\rm iso}$ and the efficiency $\eta$ to convert the kinetic to gamma-ray energy, and $\xi$ is a constant parameter which lies in the range of $0.4 < \xi < 0.78$ (Panaitescu & Mészáros 1998; Chevalier & Li 2000). Given the synchrotron spectra for the fast- and slow-cooling regimes, together with the synchrotron spectral breaks and the maximum flux, the synchrotron light curves in the fast (slow)- cooling regime are

$$
F_{\nu,\rm f}^{\rm syn}
$$
$$
\propto
\begin{cases}
t^{-\frac{2}{3}}(t^0)\,\epsilon_\gamma^{\frac{1}{3}}, & \epsilon_\gamma < \epsilon_{\rm c,f}^{\rm syn}(\epsilon_{\rm m,f}^{\rm syn}), \\
t^{-\frac{1}{4}}\epsilon_\gamma^{-\frac{1}{2}}(t^{-\frac{3p-1}{4}}\epsilon_\gamma^{-\frac{p-1}{2}}), & \epsilon_{\rm c,f}^{\rm syn}(\epsilon_{\rm m,f}^{\rm syn}) < \epsilon_\gamma < \epsilon_{\rm m,f}^{\rm syn}(\epsilon_{\rm c,f}^{\rm syn}) \\
t^{-\frac{3p-2}{4}}(t^{-\frac{3p-2}{4}})\,\epsilon_\gamma^{-\frac{p}{2}}, & \epsilon_{\rm m,f}^{\rm syn}(\epsilon_{\rm c,f}^{\rm syn}) < \epsilon_\gamma < \epsilon_{\rm max,f}^{\rm syn},
\end{cases}
$$
$$
\tag{2}
$$

where $\epsilon_\gamma$ is the energy at which the flux is detected. Given the evolution of the bulk Lorentz factor in the stellar-wind–like medium $\Gamma \propto t^{-\frac{1}{4}}$, the maximum synchrotron energy in this case evolves as $\epsilon_{\rm max,f}^{\rm syn} \propto t^{-\frac{1}{4}}$.

#### 3.2.2. Light Curves in a Uniform ISM–like Medium

The dynamics of the forward shocks for a relativistic outflow interacting with a homogeneous medium (n) is usually analyzed through the deceleration timescale and the equivalent kinetic energy evolved in the shock (e.g., see Sari & Piran 1995;
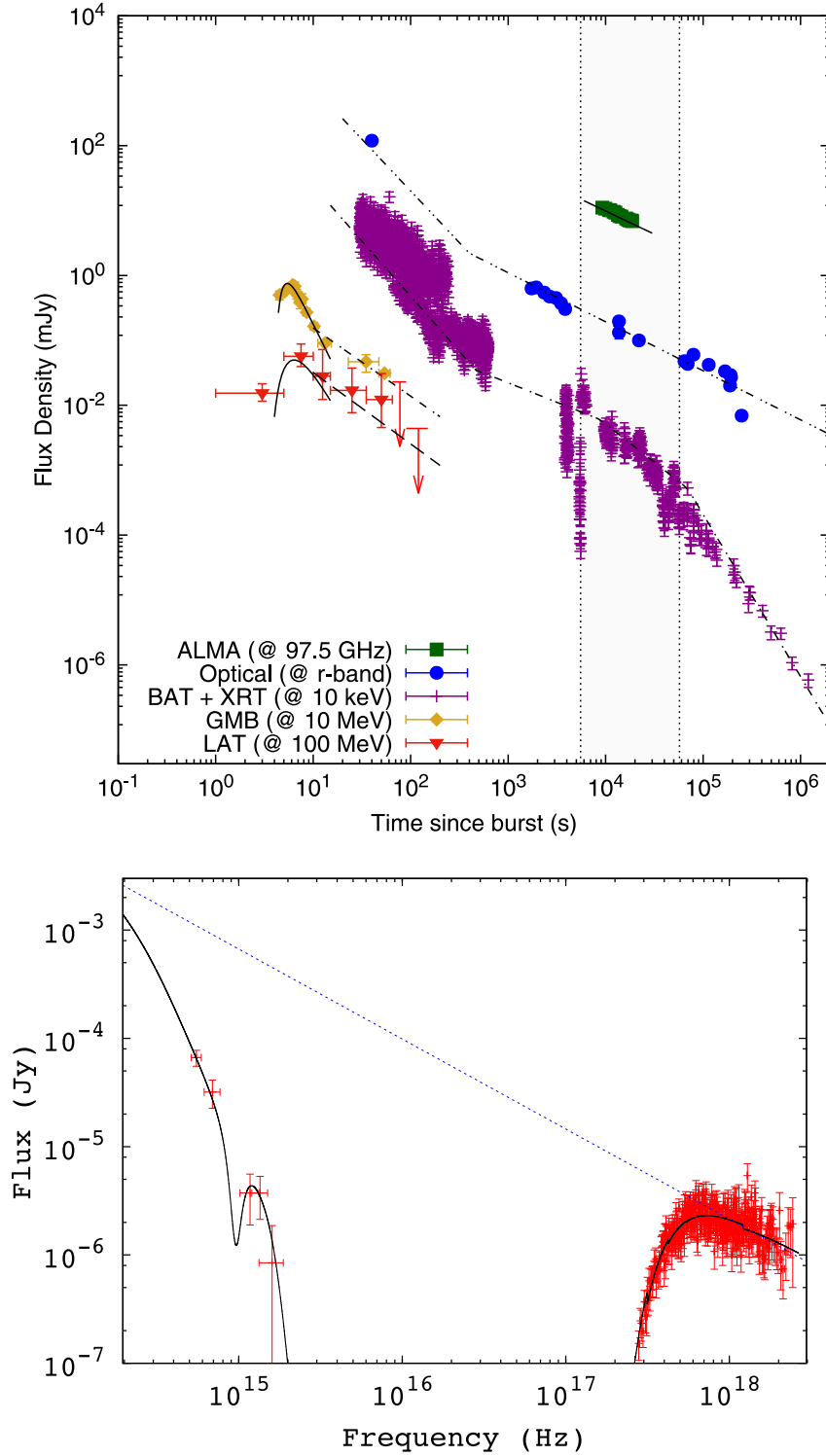
**Figure 3.** Top panel: light curves and fits of the multi-wavelength observation of GRB 190114C with the synchrotron forward-shock and SSC reverse-shock models. Bottom panel: the broadband SED of the X-ray and optical (UVOT) observations during the period of 5539–57216 s. The solid black line is the best-fit curve from XSPEC. The shaded period in the upper panel corresponds to the spectrum on the lower panel.

Sari et al. 1998; Sari & Piran 1999; Kumar & Piran 2000). Taking into account the typical timescales together with the maximum power emitted by the electron population, the synchrotron spectral breaks and the maximum flux evolve as $\epsilon_{\rm m,f}^{\rm syn} \propto t^{-\frac{3}{2}}$, $\epsilon_{\rm c,f}^{\rm syn} \propto t^{-\frac{1}{2}}$ and $F_{\rm max,f}^{\rm syn} \propto t^{0}$, respectively (Sari et al. 1998). Given the synchrotron spectra for the fast- and slow-

cooling regimes, together with the synchrotron spectral breaks and the maximum flux, the synchrotron light curves in the fast

7

(slow)-cooling regime are

$$
F_{\nu,f}^{\rm syn} \propto
\begin{cases}
t^{\frac{1}{6}}\,(t^{\frac{1}{2}})\,\epsilon_\gamma^{\frac{1}{3}}, & \epsilon_\gamma < \epsilon_{\rm c,f}^{\rm syn}(\epsilon_{\rm m,f}^{\rm syn}), \\
t^{-\frac{1}{4}}\epsilon_\gamma^{-\frac{1}{2}}(t^{-\frac{3p-3}{4}}\epsilon_\gamma^{-\frac{p-1}{2}})\,\epsilon_{\rm c,f}^{\rm syn}(\epsilon_{\rm m,f}^{\rm syn}) < \epsilon_\gamma < \epsilon_{\rm m,f}^{\rm syn}(\epsilon_{\rm c,f}^{\rm syn}) \\
t^{-\frac{3p-2}{4}}(t^{-\frac{3p-2}{4}})\epsilon_\gamma^{-\frac{p}{2}}, & \epsilon_{\rm m,f}^{\rm syn}(\epsilon_{\rm c,f}^{\rm syn}) < \epsilon_\gamma < \epsilon_{\rm max,f}^{\rm syn},
\end{cases}
\tag{3}
$$

where $\epsilon_\gamma$ is the energy at which the flux is detected. Given the evolution of the bulk Lorentz factor $\Gamma \propto t^{-\frac{3}{8}}$ in the forward shock, the maximum synchrotron energy evolves as $\epsilon_{\rm max,f}^{\rm syn} \propto t^{-\frac{3}{8}}$.

### 3.2.3. Analysis of Long-lasting Multi-wavelength Observations

Given the spectral and temporal indexes of the LAT, GBM, X-ray, optical, and radio bands, it can be observed from Table 3 that the evolution of synchrotron emission can be separated into four distinct periods.

During the first period ($t \lesssim 400$ s), the temporal decays of the optical and X-ray observations are equal and are steeper ($\Delta\alpha \sim 0.4$) than those of the LAT and GBM light curves. During this period, the spectral indexes of the LAT and GBM observations are each consistent within the uncertainties. It is worth noting that the temporal PL index of the X-ray light curve cannot be associated with the end of prompt emission that is larger than 2.5. We conclude that both the LAT and GBM observations evolve in the third PL segment, and the optical and X-ray fluxes evolve in the second PL segment of the slow-cooling regime in the stratified stellar-wind–like medium for $p = 2.2 \pm 0.3$.

During the second and third periods ($400 \lesssim t \lesssim 10^5$), the X-ray flux presents a chromatic break at $\sim 10^4$ s. During this transition, the temporal PL index varied from $0.57 \pm 0.09$ to $1.09 \pm 0.11$, while the spectral index remained unchanged. The temporal PL index after the break is consistent with the afterglow model evolving in a uniform IMS-like medium, while the temporal index before the break is associated with the "plateau" phase. It is worth mentioning that during this shallow-to-normal transition found in a large fraction of GRBs, the spectral index does not vary. During this period, the spectral analysis presented in this work reveals that the optical and X-ray observations are consistent with an SPL. Moreover, the temporal PL indexes of radio (ALMA) and optical observations are consistent each other, and the spectral analysis reported by Laskar et al. (2019) indicated that these observations are consistent with an SPL. Similarly, their analysis reported that the radio observations between VLA and ALMA are consistent with a BPL that has a break at 24 GHz. Therefore, we conclude that X-ray, optical, and radio (ALMA) fluxes evolve in the second PL segment between the cutoff and characteristic energy breaks, and the radio (VLA) evolves in first PL segment of the slow-cooling regime in the uniform ISM-like medium for $p = 2.2 \pm 0.3$.

During the four periods ($t \gtrsim 10^5$), the temporal index in the X-ray flux is consistent with the jet break.

The temporal and spectral theoretical indices obtained by the evolution of the standard synchrotron model in the stratified stellar-wind–like medium and in the uniform ISM-like medium are reported in Table 3. Theoretical and observational spectral and temporal indices are in agreement. The best explanation for this behavior is that the synchrotron radiation undergoes a phase transition from a stratified stellar-wind–like to a uniform ISM-like medium around $\sim 400$ s.

### 3.3. The SSC Reverse-shock Model and Analysis of the Short-lasting Bright LAT Peak

#### 3.3.1. SSC Model in the Stratified Stellar-wind–like Medium

The quantities of synchrotron reverse-shock model such as the spectral breaks, fluxes, and light curves that describe the optical flashes are introduced in Chevalier & Li (2000). In the thick-shell case ($\Gamma < \Gamma_c$) where the deceleration time is assumed to be smaller than the duration of the prompt phase; the outflow is decelerated by the reverse shock are derived in Zhang & Kobayashi (2005). The term $\Gamma_c$ is the critical Lorentz factor. The relationship among the characteristic energy breaks and maximum fluxes in the forward and reverse shocks were derived in Zhang & Kobayashi (2005).

The quantities of the SSC reverse-shock model as the spectral breaks, the fluxes, and the light curves have been widely explored (e.g., see, Wang et al. 2001a, 2001b; Veres & Mészáros 2012; Fraija et al. 2016a). In the thick-shell case, the SSC light curve at the shock crossing time ($t_{\rm d}$) was presented in Fraija et al. (2016a). At $t < t_{\rm d}$, the SSC emission increases as $\propto t^{1/2}$ reaches at the shock crossing time the maximum value of $F_{\nu,r} \sim F_{\nu,{\rm max},r}\left(\frac{\epsilon_{\rm LAT}}{\epsilon_{\rm c,r}^{\rm ssc}}\right)^{-\frac{1}{2}}$, where the energy range observed by the LAT instrument ($\epsilon_{\rm LAT}$) is constrained by the characteristic break ($\epsilon_{\rm LAT} < \epsilon_{\rm m,r}^{\rm ssc}$). After $t > t_{\rm d}$, the LAT flux initially evolves as $\propto t^{-\frac{p+1}{2}}$, later as $\propto t^{-\frac{5}{2}}$, and finally as $\propto t^{-\frac{p+4}{2}}$ induced by the angular time delay effect (Kumar & Panaitescu 2000; Kobayashi & Zhang 2003). The shock-crossing time can be estimated as $t_d \sim (\Gamma/\Gamma_c)^{-4}T_{90}$ (Kobayashi & Zhang 2007).

#### 3.3.2. Analysis of the LAT/GBM-peak Observations

In order to model the *Fermi*-LAT/GBM data, the function given by Equation (1) was used (Fraija et al. 2017b). The best-fit values of $t_0 = 2.61 \pm 0.51$ s and $3.09 \pm 0.23$ s indicate the onset of the reverse shock as suggested by Vestrand et al. (2006). The values of the temporal decay indices of $\alpha_{\gamma,\rm pk} = 2.65 \pm 0.19$ and $2.96 \pm 0.19$ are consistent with the decay slope of the synchrotron/SSC reverse-shock emission from high latitudes (due to the curvature effect; Zhang et al. 2003; Fraija et al. 2017a, 2019a). The values of the bulk Lorentz factor and the parameter of the stellar wind density can be constrained through the deceleration time $t_{\rm dec} \propto (1 + z)\xi^{-2}\, E\, A^{-1}\, \Gamma^{-4}$ with the LAT/GBM-peak flux at $\sim 6$–7 s and the critical Lorentz factor in the thick-shell regime $\Gamma > \Gamma_c$ (Zhang et al. 2003). In the thick-shell regime, the shock-crossing time is $t_d \sim (\Gamma/\Gamma_c)^{-4}T_{90} \simeq 6$–7 s (Kobayashi & Zhang 2007), which is much shorter than the duration of the main burst. The peak of the LAT and GBM fluxes will be modeled with $F_{\nu,r} \sim F_{\nu,{\rm max},r}\left(\frac{\epsilon_\gamma}{\epsilon_{\rm c,r}^{\rm ssc}}\right)^{-\frac{1}{2}}$ (Zhang et al. 2003; Fraija et al. 2016b) and the value of the spectral index of electrons $p = 2.2 \pm 0.3$ found with multi-wavelength observations and synchrotron forward-shock model will be used. We want to emphasize that the synchrotron emission from the reverse shock is usually invoked to describe early optical afterglows (Kobayashi 2000; Kobayashi & Zhang 2003; Fraija et al. 2016a), so the SSC emission used in this work is required to describe the LAT/GBM-peak observations.

**Table 4**
Median Values of Parameters Found with Symmetrical Quantiles (15%, 50%, 85%); Our Model was used to Constrain the Values of Parameters

| Parameters | Median | | | | |
|---|---|---|---|---|---|
| | LAT (100 MeV) | GBM (10 MeV) | X-ray (10 keV) | Optical (1 eV) | Radio (97.5 GHz) |
| $A_\star(10^{-2})$ | $5.999^{+0.297}_{-0.295}$ | $6.149^{+0.298}_{-0.296}$ | $6.101^{+0.099}_{-0.101}$ | $5.950^{+0.098}_{-0.099}$ | $6.000^{+0.100}_{-0.100}$ |
| $n(\mathrm{cm}^{-3})$ | $\cdots$ | $\cdots$ | $1.060^{+0.099}_{-0.101}$ | $1.100^{+0.098}_{-0.096}$ | $1.084^{+0.099}_{-0.097}$ |
| $\epsilon_{B,f}(10^{-5.3})$ | $1.001^{+0.302}_{-0.298}$ | $1.200^{+0.301}_{-0.296}$ | $1.148^{+0.304}_{-0.293}$ | $0.951^{+0.298}_{-0.301}$ | $0.993^{+0.228}_{-0.190}$ |
| $\epsilon_{e,f}(10^{-2})$ | $1.000^{+0.304}_{-0.303}$ | $1.150^{+0.294}_{-0.302}$ | $1.140^{+0.604}_{-0.585}$ | $1.139^{+0.298}_{-0.297}$ | $1.095^{+0.156}_{-0.137}$ |
| $\epsilon_{B,r}(10^{-1})$ | $1.000^{+0.304}_{-0.303}$ | $0.999^{+0.298}_{-0.297}$ | $\cdots$ | $\cdots$ | $\cdots$ |
| $\epsilon_{e,r}(10^{-1})$ | $0.999^{+0.100}_{-0.099}$ | $1.150^{+0.104}_{-0.100}$ | $\cdots$ | $\cdots$ | $\cdots$ |
| $p$ | $2.300^{+0.100}_{-0.099}$ | $2.202^{+0.098}_{-0.098}$ | $2.250^{+0.098}_{-0.101}$ | $2.280^{+0.099}_{-0.101}$ | $2.296^{+0.010}_{-0.010}$ |

### 3.4. Transition from a Stratified Stellar-wind–like to Uniform ISM-like Medium

As indicated in Section 3.2.1, the progenitor of GRB 190114C can be associated with the core collapse of a WR star, indicating that the circumburst medium close to the progenitor is principally composed by the stratified stellar wind of the WR. At a distance away from the parent a uniform medium is expected. Therefore, a transition phase between the stratified to uniform medium is expected at a distance larger than $\gtrsim 10^{-2}$ pc (Castor et al. 1975; Weaver et al. 1977; Fryer et al. 2006). Weaver et al. studied this phase, considering a four-region structure that includes (i) the unshocked stratified stellar-wind–like medium with density $\rho(r)$, (ii) a quasi-isobaric zone consisting of the stellar wind mixed with a small fraction of interstellar gas, (iii) a dense-thin shell formed by most of ISM, and (iv) the unshocked ambient ISM (see Figure 1 in Pe'er & Wijers 2006).

Taking into consideration an adiabatic expansion, two strong shocks are formed; these are the outer and inner shocks. The outer termination (forward) shock radius can be estimated as

$$R_{\mathrm{FS},W} = 1.2 \times 10^{19}\ \mathrm{cm}\ \dot{M}_{-6}^{\frac{1}{5}}\ v_{W,8}^{\frac{2}{5}}\ n^{-\frac{1}{5}}\ t_{\star,5}^{-\frac{3}{5}}, \qquad (4)$$

where $t_\star$ is the lifetime of the WR.

The inner (reverse) shock radius for which the transition from stratified to uniform medium occurs ($R_{\mathrm{tr}}$; Pe'er & Wijers 2006) is obtained by equaling the pressures in regions (ii) and (iii) (e.g., see, Pe'er & Wijers 2006; Garcia-Segura & Franco 1996)

$$P_{(\mathrm{ii})} = P_{(\mathrm{iii})} = 1.4 \times 10^{-11}\ \mathrm{dynes\ cm}^{-2}\ \dot{M}_{-6}^{\frac{2}{5}}\ v_{W,8}^{\frac{4}{5}}\ n^{-\frac{3}{5}}\ t_{\star,5}^{\frac{4}{5}}. \quad (5)$$

The distance from the progenitor to the wind-to-homogeneous transition is given by

$$R_{\mathrm{tr}} \equiv R_{\mathrm{RS},W} = 5.1 \times 10^{18}\ \mathrm{cm}\ \dot{M}_{-6}^{\frac{3}{10}}\ v_{W,8}^{\frac{1}{10}}\ n^{-\frac{3}{10}}\ t_{\star,5}^{\frac{2}{5}}. \quad (6)$$

The density of the stellar wind medium at $r = R_{\mathrm{tr}}$ can be written as

$$\rho(R_{\mathrm{tr}}) = 1.8 \times 10^{-27}\ \mathrm{g\ cm}^{-3}\ R_{\mathrm{tr}}^{-2}\ \dot{M}_{-6}\ v_{W,8}^{-1}, \quad (7)$$

which corresponds to a particle number density of $\sim 10^{-3}\ \mathrm{cm}^{-3}$.

### 4. Results and Discussion

We show that temporal and spectral analysis of the long-lived multi-wavelength observations of GRB 190114C is consistent with the closure relations of the synchrotron

forward-shock model and the short-lasting LAT and GBM peaks with SSC reverse-shock model. The LAT and GBM observations favor the emission originated from the forward and reverse shocks in a stratified stellar-wind–like medium, and the X-ray and optical observations are consistent with the emission from forward shocks in both a stratified stellar-wind–like and a uniform ISM-like medium. The radio observations are consistent with the synchrotron emission radiated in a uniform ISM-like medium. The transition from the stratified to uniform medium is found to be around ~400 s after the GBM trigger. Now, we obtain the electron spectral index, the microphysical parameters, and the circumburst densities for which our model is satisfied. The photon energies of each PL segment at $\epsilon_\gamma = 97.5$ GHz, 1 eV, 10 keV, 10 MeV, and 100 MeV are considered to describe the radio, optical, X-ray, GBM, and LAT fluxes, respectively. We use the synchrotron light curves in the slow-cooling regime evolving in a stratified stellar-wind–like medium (Equation (2)) before $\lesssim 400$ s and in a uniform ISM-like medium (Equation (3)) after $\gtrsim 400$ s. The values reported of the observed quantities such as the redshift $z = 0.42$, the equivalent isotropic energy $3 \times 10^{53}$ erg, and the duration of the prompt emission $T_{90} = 116$ s are required. In order to compute the luminosity distance, the values of cosmological parameters derived in Planck Collaboration et al. (2018) are used (Hubble constant $H_0 = 67.4 \pm 0.5$ km s$^{-1}$ Mpc$^{-1}$ and the matter density parameter $\Omega_m = 0.315 \pm 0.007$). The equivalent kinetic energy is obtained using the isotropic energy and the efficiency to convert the kinetic to photons of $\eta = 0.15$ (Beniamini et al. 2015). The value of the parameter $\xi = 0.6$ was chosen when taking into account the range of values reported in the literature (Panaitescu & Mészáros 1998; Chevalier & Li 2000).

To find the best-fit values of the parameters that reproduce the multi-wavelength observations of GRB 190114C, we use the Bayesian statistical technique based on the Markov-chain Monte Carlo (MCMC) method (see Fraija et al. 2019b, 2019c, 2019d). The MCMC code computes the synchrotron forward-shock and the SSC reverse-shock models using, in general, a set of seven parameters, $\{A_\star, n, \epsilon_{B,f}, \epsilon_{e,f}, \epsilon_{B,r}, \epsilon_{e,r}$ and $p\}$. In particular, we use in each electromagnetic band only five parameters. For instance, the parameter $\{n\}$ is not used for the LAT and GBM observations, the parameters $\{\epsilon_{B,r}$ and $\epsilon_{e,r}\}$ are not used for radio, optical, and X-ray observations and the microphysical parameters $\{\epsilon_{e,f}$ and $\epsilon_{B,f}\}$ are used to fit the radio observations. A total of 16,000 samples with 4000 tuning steps were run. The best-fit value of each parameter for LAT, GBM, X-ray, optical, and radio observations is reported in Table 4. The obtained values are typical for those reported by other luminous GRBs
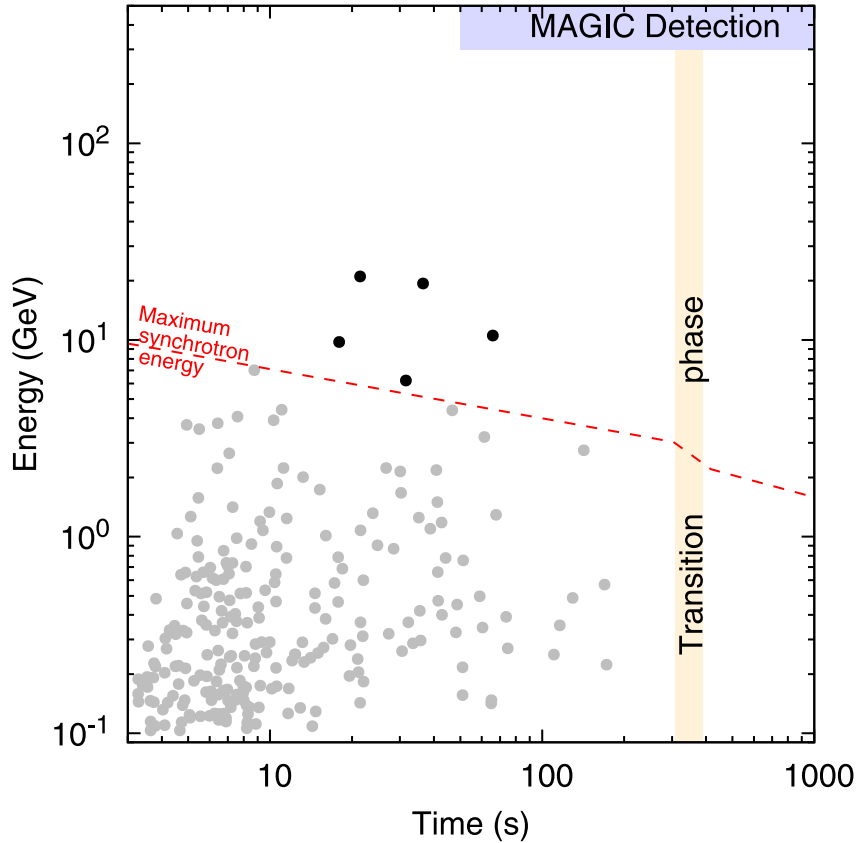
**Figure 4.** All the photons with energies >100 MeV and probabilities >90% of being associated with GRB 190114C. The red dashed line is the maximum photon energies released by synchrotron forward-shock model in a stratified stellar-wind–like medium and a uniform ISM-like medium. The yellow region represents the transition phase from a stratified to uniform medium and, the purple region the interval and the energy range of VHE photons reported by the MAGIC Collaboration. Photons with energy above the maximum synchrotron energy are in black, and those below are in gray.

(Ackermann et al. 2010, 2013, 2014; Fraija 2015a; Fraija et al. 2016a, 2016b, 2017a). Given the values of the observed quantities and the best-fit values reported in Table 4, the results are discussed as follows.

Taking into account the evolution of the maximum photon energy radiated by synchrotron emission from forward shock in both a stratified stellar-wind–like and a uniform ISM-like medium, and the best-fit values of both densities, we plot in Figure 4 all photons with energies larger than >100 MeV detected by *Fermi*-LAT and associated to GRB 190114C. In addition, this figure shows in a yellow region the transition from the stratified to uniform medium, and the interval and the energy range of VHE photons (purple region) reported by the MAGIC Collaboration (Mirzoyan et al. 2019). Photons with energies above the maximum photon energy radiated by synchrotron emission (synchrotron limit) are in black, and those below are in gray. This figure shows that the standard synchrotron forward-shock model can hardy explain all photons, therefore this model has to be varied or some additional processes to synchrotron in the forward shocks, such as SSC emission, photo-hadronic interactions (Fraija 2014, 2015b) and proton synchrotron radiation, have to be evoked to interpret these VHE photons. We want to emphasize that the LAT photons below the maximum synchrotron energy (the red dashed line) can be interpreted in the synchrotron forward-shock framework and beyond the synchrotron limit some additional mechanisms must be present to explain the VHE LAT photons. It is worth noting that a

combination of synchrotron and SSC emission originating in the forward shock works well to explain the LAT photons (e.g., see Beniamini et al. 2015).

The best-fit values of the microphysical parameters found in forward- and reverse-shock regions are different. The microphysical parameter associated to the magnetic field in the reverse shock lies in the range of the expected values for the reverse shock to be formed and leads to an estimate of the magnetization parameter that is defined as the ratio of Poynting flux to matter energy flux $\sigma = \frac{L_{pf}}{L_{kn}} \simeq \frac{B_r^2}{4\pi\rho(r)\Gamma^2} \simeq 8\epsilon_{B,r} \simeq 0.8$ (Drenkhahn 2002; Zhang & Kobayashi 2005). This value indicates that the outflow is magnetized. In a different situation (e.g., $\sigma \gg 1$), particle acceleration would be inefficient, and the LAT and GBM emissions from the reverse shock would have been suppressed (Fan et al. 2004). Considering the microphysical parameter associated with the magnetic field in the reverse-shock region, we found that the strength of magnetic field in this region is stronger that the magnetic field in the forward-shock region ($\simeq$20 times). This suggests that the jet composition of GRB 190114C could be Poynting dominated. Zhang & Kobayashi (2005) described the emission generated in the reverse shock from an outflow with an arbitrary value of the magnetization parameter. They found that the Poynting energy is transferred to the medium only until the reverse shock has disappeared. Given the timescale of the reverse shock associated to the short-lasting LAT and GBM peaks (<100 s), the shallow decay segment observed in the X-ray light curve of

GRB 190114C might be interpreted as the late transferring of the Poynting energy to the uniform medium. This result agrees with the linear polarization reported in radio (Laskar et al. 2019) during the "plateau" phase. These results agree with some authors who claim that Poynting flux-dominated models with a moderate degree of magnetization can explain the LAT observations in several powerful GRBs (Zhang & Yan 2011; Uhm & Zhang 2014), and in particular the properties exhibited in the light curve of GRB 190114C.

Using the synchrotron reverse-shock model (Kobayashi 2000; Kobayashi & Zhang 2003) and the best-fit values found, the self-absorption, characteristic, and cutoff energy breaks of $4.5 \times 10^{-8}$ eV, 0.5 eV, and $8.1 \times 10^{-3}$ eV, respectively, indicate that the synchrotron radiation evolves in the fast-cooling regime. Therefore, an optical bright flash with a maximum flux (at the peak) of $F_{\nu,r} \sim F_{\max,r} \left( \frac{\epsilon_\gamma}{\epsilon_{c,r}} \right)^{-\frac{1}{2}} \sim 10^4$ mJy in temporal coincidence with the LAT bright peaks that are similar to that reported for GRB 130427A is expected (see, Kobayashi & Zhang 2003; Fraija et al. 2016b). The maximum flux and the spectral break of the cutoff energy are calculated with the best-fit parameters reported in Table 4 for $\epsilon_\gamma = 1$ eV. Given that the self-absorption energy break is smaller than the cutoff and characteristic ones, the synchrotron emission is in the weak self-absorption regime, and hence a thermal component from the reverse shock cannot be expected (Kobayashi & Zhang 2003). Taking into consideration the fact that the outflow composition is Poynting dominated and the synchrotron emission from the reverse shock is stronger than the radiation originated from the forward shock, polarization is expected in different wavelength bands.

Using the best-fit values we calculate the theoretical fluxes at the maximum fluxes reported by the LAT and GBM instruments. We find that the synchrotron emission from the forward-shock region is ~3 times smaller than the SSC one from the reverse-shock. Once the LAT flux decreases, the synchrotron emission from forward shock begins dominating. Therefore, the SSC emission from the reverse shock can only explain the short-lasting LAT peak and the high-energy photons associated temporally with it, and not the high-energy photons detected at different time intervals ($\gtrsim 10$ s).

The spectral and temporal analysis of the forward and reverse shocks at the beginning of the afterglow phase together the best-fit value of the circumburst density lead to an estimate of the initial bulk Lorentz factor, the critical Lorentz factor and the shock crossing time $\Gamma \simeq 600$, $\Gamma_c \simeq 270$ and $t_d \simeq 4$ s, respectively. The value of the initial bulk Lorentz factor lies in the range of values reported for the luminous LAT-detected GBRs (Veres & Mészáros 2012). This value is consistent with the evolution of reverse shock in the thick-shell case and the duration of the short-lasting LAT and GBM peaks.

The best-fit values found after modeling the LAT, GBM, X-ray, optical, and radio observations with reverse and forward shocks indicate that the high-energy photons originated in external shocks as was previously suggested for others GRBs (Kumar & Barniol Duran 2009, 2010; Zou et al. 2009; Ghisellini et al. 2010; He et al. 2011; Nava et al. 2014; Fraija et al. 2016b, 2017b). It is worth highlighting that the values found of $t_0$ are in the range of the first high-energy photons detected by Fermi-LAT.

Given the best-fit values of the wind-like and homogeneous medium, the deceleration radius and the bulk Lorentz factor at the transition from the stratified to uniform medium is

$R_{\text{tr}} \simeq 2.3 \times 10^{17}$ cm and $\Gamma_{\text{tr}} \simeq 220$, respectively, which agree with the breaks in the X-ray and optical light curves. In comparison with other bursts that exhibited this transition (GRB 050319, 081109A, and 160626B; Kamble et al. 2007; Jin et al. 2009; Fraija et al. 2017b), the value obtained for GRB 190114C corresponds to the nearest value to the progenitor.

With the best-fit values, we find that the characteristic and cutoff energy breaks the synchrotron emission in the uniform medium at $6 \times 10^3$ ($6 \times 10^4$) s as indicated with dotted lines in the upper panel are 93.2 (5.1) GHz and 166.5 (27.6) keV, respectively. It indicates that during this time interval, X-ray, optical, and radio fluxes evolve in the second PL segment, as shown in Figure 3. The dotted lines mark the period for which the energy breaks were calculated. At 0.2 days, the characteristic and cutoff energy breaks are 22.1 GHZ and 77.6 keV, respectively. This result is consistent with the radio observations reported by Laskar et al. (2019): (i) the optical and radio (ALMA) observations evolved in the similar PL segment and, (ii) the break energy of $24 \pm 4$ GHz found in the radio spectrum between VLA and ALMA data. In this case this energy break is explained with the characteristic energy calculated in our model.

The Fermi-LAT photon flux light curve of GRB 190114C presented similar features to other bright LAT-detected bursts, as shown in Figure 5. For instance, the equivalent isotropic energy of these bursts was measured to be larger than $>10^{53}$ erg;[10] they exhibited long-lasting emission that was much longer than the prompt phase, and had a short-lasting bright peak located at the beginning of the long-lasting emission (Kumar & Barniol Duran 2009, 2010; Piran & Nakar 2010; Ackermann et al. 2013; Fraija 2015a; Fraija et al. 2016a, 2016b, 2017a, 2017b). All of them presented high-energy photons ($\geqslant 100$ MeV), which arrived delayed alongside the onset of the prompt phase. In addition to exhibiting the previous features, GRB 160625B showed the wind-to-uniform transition. These bursts have been interpreted in the framework of external shocks. The best-fit parameters found for GRB 190114C lie in the range of the values reported in these bursts $0.01 \leqslant \epsilon_{e,f} \leqslant 0.1$, $10^{-5} \leqslant \epsilon_{B,f} \leqslant 10^{-3}$, and $2.15 \leqslant p \leqslant 2.4$. Figure 5 shows that GRB 190114C (red filled stars) is one of the brightest during the first ~100 s and, given that it is the second-closest one, VHE photons are expected from this burst.

## 5. Conclusions

We have obtained the Fermi-LAT light curve around the reported position of GRB 190114C and showed that it exhibits similar features to the LAT-detected bursts. The first photon detected by the LAT instrument had an energy of 571.4 MeV, arriving at ~2.7 s late with respect to first low-energy photon reported by GBM. The time arrival of this energetic photon is consistent with the starting times of the LAT ($t_0 = 2.61 \pm 0.51$ s) and GBM ($t_0 = 3.09 \pm 0.23$ s) emissions. The highest-energy photons of 10, 21, 6, 19, and 11 GeV detected by the LAT instrument at 18, 21, 32, 36, and 65 s, respectively, after the GBM trigger can be hardly interpreted in the standard synchrotron forward-shock model and some additional mechanisms must be present to interpret the VHE

---

[10] GRB 080916C (Abdo et al. 2009b), GRB 090510 (Ackermann et al. 2010), GRB 090902B (Abdo et al. 2009a), GRB 090926A (Ackermann et al. 2011) GRB 110721A (Ackermann et al. 2013; Fraija et al. 2017a), GRB 110731A (Ackermann et al. 2013), GRB 130427A (Ackermann et al. 2014), and GRB 160625B (Fraija et al. 2017b).
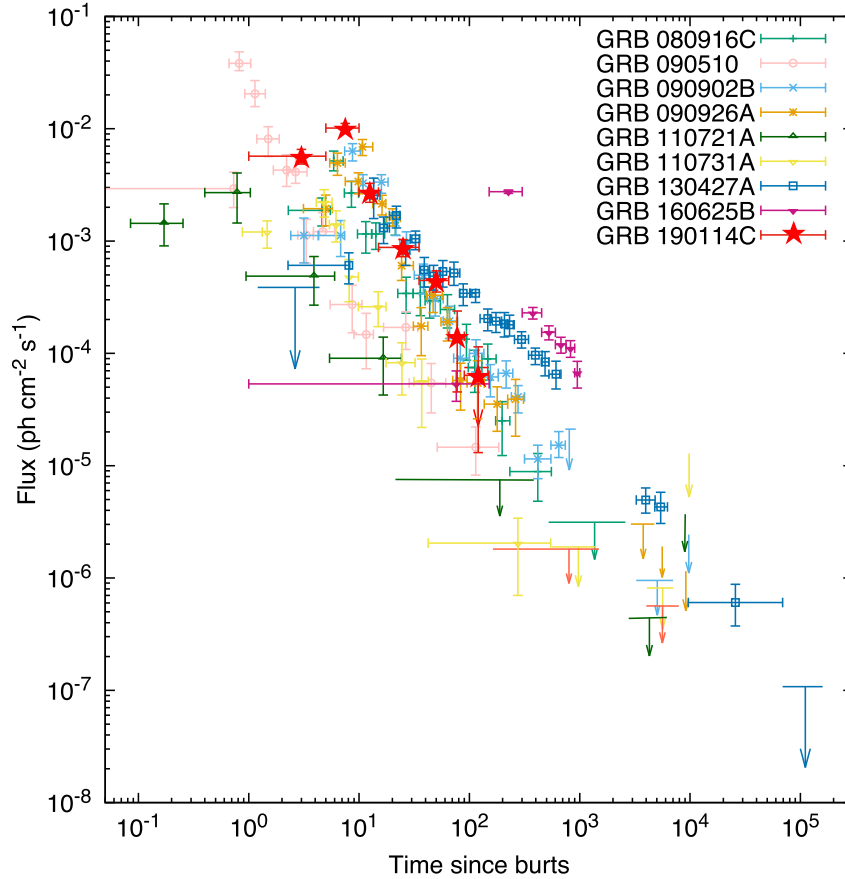
**Figure 5.** Comparison of the *Fermi*-LAT photon flux light curve from GRB 190114C (red filled stars) with those LAT-detected burst with short-lasting bright peaks and long-lasting emissions. The LAT-detected burst data are taken from Ackermann et al. (2013, 2013, 2014) and Fraija et al. (2017a).

LAT photons. We want to emphasize that the MAGIC-detected photons cannot either be interpreted in the standard synchrotron forward-shock model. The other LAT photons can be explained well by synchrotron emission from the forward shock. The LAT and GBM light curves exhibited a short-lasting bright peak and a long-lasting extended emission. The temporal and spectral indices of the long-lasting extended component are consistent with synchrotron forward-shock model and the short-lasting bright peaks with SSC reverse-shock model. Given the best-fit values, a bright optical flash produced by synchrotron reverse-shock is expected.

The X-ray and optical light curves are consistent with a BPL function with a break at ∼400 s. Using the closure relations and the synchrotron forward-shock model among the LAT, GBM, X-ray, optical, and radio observations, we claim that this break corresponded to a transition phase between a stratified stellar-wind–like and uniform ISM-like medium.

With the values of best-fit values of the stratified and uniform medium, we infer that high-energy observed photons are produced in the deceleration phase of the outflow and a different mechanism of the standard synchrotron model such as SSC emission, photo-hadronic interactions, and proton synchrotron radiation from forward shocks has to be invoked to interpret these VHE photons. Given the values of the microphysical parameters, we claim that the outflow is endowed with magnetic fields.

The best-fit values of the microphysical parameters and the derived value of $\sigma$-parameter indicates that an outflow with

arbitrary magnetization could explain the features exhibited in the light curves of GRB 190114C (the short-lasting peaks, the "plateau" phase, etc.). Taking into consideration the fact that the ejecta must be magnetized and the synchrotron emission from the reverse shock is stronger than the radiation originated in the forward shock, then polarization in distinct wavelengths is expected.

## ORCID iDs

N. Fraija ⓘ https://orcid.org/0000-0002-0173-6453
R. L. Becerra ⓘ https://orcid.org/0000-0002-0216-3415

## References

Abdo, A. A., Ackermann, M., Ajello, M., et al. 2009a, ApJL, 706, L138
Abdo, A. A., Ackermann, M., Arimoto, M., et al. 2009b, Sci, 323, 1688
Ackermann, M., Ajello, M., Asano, K., et al. 2011, ApJ, 729, 114

Ackermann, M., Ajello, M., Asano, K., et al. 2013, ApJS, 209, 11
Ackermann, M., Ajello, M., Asano, K., et al. 2014, Sci, 343, 42
Ackermann, M., Asano, K., Atwood, W. B., et al. 2010, ApJ, 716, 1178
Ackermann, M., Ajello, M., Asano, K., et al. 2013, ApJ, 763, 71
Alexander, K. D., Laskar, T., Berger, E., et al. 2019, GCN, 23726, 1
Arnaud, K. A. 1996, in ASP Conf. Ser. 101, Astronomical Data Analysis Software and Systems V, ed. G. H. Jacoby & J. Barnes (San Francisco, CA: ASP), 17
Barniol Duran, R., & Kumar, P. 2011, MNRAS, 412, 522
Becerra, R. L., Dichiara, S., Watson, A. M., et al. 2019a, arXiv:1904.05987
Becerra, R. L., Watson, A. M., Fraija, N., et al. 2019b, arXiv:1901.06051
Becerra, R. L., Watson, A. M., Lee, W. H., et al. 2017, ApJ, 837, 116
Beniamini, P., Nava, L., Duran, R. B., & Piran, T. 2015, MNRAS, 454, 1073
Bolmer, J., & Shady, P. 2019, GCN, 23702, 1
Burenin, R., Bikmaev, I., Irtuganov, E., et al. 2019, GCN, 23766, 1
Castor, J., McCray, R., & Weaver, R. 1975, ApJL, 200, L107
Chevalier, R. A., & Li, Z.-Y. 2000, ApJ, 536, 195
Chevalier, R. A., Li, Z.-Y., & Fransson, C. 2004, ApJ, 606, 369
Dai, Z. G., & Lu, T. 1998, MNRAS, 298, 87
D'Avanzo, P., Covino, S., Fugazza, D., et al. 2019, GCN, 23729, 1
Drenkhahn, G. 2002, A&A, 387, 714
Fan, Y. Z., Wei, D. M., & Wang, C. F. 2004, A&A, 424, 477
Fraija, N. 2015a, ApJ, 804, 105
Fraija, N. 2015b, MNRAS, 450, 2784
Fraija, N. 2014, MNRAS, 437, 2187
Fraija, N., De Colle, F., Veres, P., et al. 2019a, ApJ, 871, 123
Fraija, N., De Colle, F., Veres, P., et al. 2019c, ApJ, submitted (arXiv:1906.00502)
Fraija, N., Lopez-Camara, D., Pedreira, A. C., et al. 2019d, ApJ, submitted (arXiv:1904.07732)
Fraija, N., Lee, W., & Veres, P. 2016a, ApJ, 818, 190
Fraija, N., Lee, W. H., Araya, M., et al. 2017a, ApJ, 848, 94
Fraija, N., Lee, W. H., Veres, P., et al. 2016b, ApJ, 831, 22
Fraija, N., Pedreira, A. C. C. d. E. S., & Veres, P. 2019b, ApJ, 871, 200
Fraija, N., & Veres, P. 2018, ApJ, 859, 70
Fraija, N., Veres, P., Zhang, B. B., et al. 2017b, ApJ, 848, 15
Frederiks, D., Golenetskii, S., Aptekar, R., et al. 2019, GCN, 23737, 1
Fryer, C. L., Rockefeller, G., & Young, P. A. 2006, ApJ, 647, 1269
Fukugita, M., Ichikawa, T., Gunn, J. E., et al. 1996, AJ, 111, 1748
Garcia-Segura, G., & Franco, J. 1996, ApJ, 469, 171
Ghisellini, G., Ghirlanda, G., Nava, L., & Celotti, A. 2010, MNRAS, 403, 926
Giblin, T. W., van Paradijs, J., Kouveliotou, C., et al. 1999, ApJL, 524, L47
Granot, J. 2003, ApJL, 596, L17
Gropp, J. D., Kennea, J. A., Klinger, N. J., et al. 2019, GCN, 23688, 1
Hamburg, R., Veres, P., Meegan, C., et al. 2019, GCN, 23707, 1
He, H.-N., Wu, X.-F., Toma, K., Wang, X.-Y., & Mészáros, P. 2011, ApJ, 733, 22
Im, M., Paek, G. S., Kim, S., et al. 2019a, GCN, 23717, 1
Im, M., Paek, G. S. H., Choi, C., et al. 2019b, GCN, 23740, 1
Izzo, L., Noschese, A., D'Avino, L., et al. 2019, GCN, 23699, 1
Jin, Z. P., Xu, D., Covino, S., et al. 2009, MNRAS, 400, 1829
Kamble, A., Resmi, L., & Misra, K. 2007, ApJL, 664, L5
Kim, J., & Im, M. 2019a, GCN, 23732, 1
Kim, J., Im, M., Lee, C.-U., et al. 2019b, GCN, 23734, 1
Kobayashi, S. 2000, ApJ, 545, 807
Kobayashi, S., & Zhang, B. 2003, ApJ, 597, 455
Kobayashi, S., & Zhang, B. 2007, ApJ, 655, 973
Kocevski, D., Omodei, N., Axelsson, M., et al. 2019, GCN, 23709, 1
Krimm, H. A., Barthelmy, S. D., Cummings, J. R., et al. 2019, GCN, 23724, 1
Kumar, H., Srivastav, S., Waratkar, G., et al. 2019, GCN, 23733, 1
Kumar, P., & Barniol Duran, R. 2009, MNRAS, 400, L75
Kumar, P., & Barniol Duran, R. 2010, MNRAS, 409, 226
Kumar, P., & Panaitescu, A. 2000, ApJL, 541, L51
Kumar, P., & Piran, T. 2000, ApJ, 532, 286
Kumar, P., & Zhang, B. 2015, PhR, 561, 1
Laskar, T., Alexander, K. D., Gill, R., et al. 2019, ApJL, 878, L26
Lipunov, V., Tyurina, N., Kuznetsov, A., et al. 2019, GCN, 23693, 1
Mazaeva, E., Pozanenko, A., Volnova, A., et al. 2019, GCN, 23741, 1
Melandri, A., Izzo, L., D'Avanzo, P., et al. 2019, GCN, 23983, 1
Minaev, P., & Pozanenko, A. 2019, GCN, 23714, 1
Mirzoyan, R., et al. 2019, GCN, 23701, 1
Nava, L., Vianello, G., Omodei, N., et al. 2014, MNRAS, 443, 3578
Osborne, J. P., Beardmore, A. P., Evans, P. A., et al. 2019, GCN, 23704, 1
Panaitescu, A., & Kumar, P. 2000, ApJ, 543, 66
Panaitescu, A., & Mészáros, P. 1998, ApJL, 493, L31
Pe'er, A., & Wijers, R. A. M. J. 2006, ApJ, 643, 1036
Piran, T., & Nakar, E. 2010, ApJL, 718, L63
Planck Collaboration, Aghanim, N., Akrami, Y., et al. 2018, arXiv:1807.06209
Ravasio, M. E., Oganesyan, G., Salafia, O. S., et al. 2019, A&A, 626, A12
Sari, R., & Piran, T. 1995, ApJL, 455, L143
Sari, R., & Piran, T. 1999, A&AS, 138, 537
Sari, R., Piran, T., & Narayan, R. 1998, ApJL, 497, L17
Selsing, J., Fynbo, J. P. U., Heintz, K. E., et al. 2019, GCN, 23695, 1
Siegel, M. H., & Gropp, J. D. 2019, GCN, 23725, 1
Stratta, G., Dainotti, M. G., Dall'Osso, S., Hernandez, X., & Cesare, G. De 2018, ApJ, 869, 155
Troja, E., Lipunov, V. M., Mundell, C. G., et al. 2017, Natur, 547, 425
Tyurina, N., Lipunov, V., Kuznetsov, A., et al. 2019, GCN, 23690, 1
de Ugarte Postigo, A., Kann, D. A., Thoene, C. C., & Izzo, L. 2019, GCN, 23692, 1
Uhm, Z. L., & Zhang, B. 2014, NatPh, 10, 351
Ursi, A., Tavani, M., Marisaldi, M., et al. 2019, GCN, 23712, 1
Vaughan, S., Goad, M. R., Beardmore, A. P., et al. 2006, ApJ, 638, 920
Veres, P., & Mészáros, P. 2012, ApJ, 755, 12
Vestrand, W. T., Wren, J. A., Wozniak, P. R., et al. 2006, Natur, 442, 172
Vink, J. S., & de Koter, A. 2005, A&A, 442, 587
Vink, J. S., de Koter, A., & Lamers, H. J. G. L. M. 2000, A&A, 362, 295
Wang, X. Y., Dai, Z. G., & Lu, T. 2001a, ApJL, 546, L33
Wang, X. Y., Dai, Z. G., & Lu, T. 2001b, ApJ, 556, 1010
Wang, Y., Li, L., Moradi, R., & Ruffini, R. 2019, arXiv:1901.07505
Weaver, R., McCray, R., Castor, J., Shapiro, P., & Moore, R. 1977, ApJ, 218, 377
Xiao, S., Li, C. K., Li, X. B., et al. 2019, GCN, 23716, 1
Zhang, B., Fan, Y. Z., Dyks, J., et al. 2006, ApJ, 642, 354
Zhang, B., & Kobayashi, S. 2005, ApJ, 628, 315
Zhang, B., Kobayashi, S., & Mészáros, P. 2003, ApJ, 595, 950
Zhang, B., & Mészáros, P. 2004, IJMPA, 19, 2385
Zhang, B., & Yan, H. 2011, ApJ, 726, 90
Zou, Y.-C., Fan, Y.-Z., & Piran, T. 2009, MNRAS, 396, 1163

# Modeling the Observations of GRB 180720B: from Radio to Sub-TeV Gamma-Rays

N. Fraija[1] , S. Dichiara[2,3], A. C. Caligula do E. S. Pedreira[1], A. Galvan-Gamez[1], R. L. Becerra[1] , A. Montalvo[1], J. Montero[1],
B. Betancourt Kamenetskaia[1], and B. B. Zhang[4,5]

[1] Instituto de Astronomía, Universidad Nacional Autónoma de México, Apdo. Postal 70-264, Cd. Universitaria, Ciudad de México 04510, Mexico
nifraija@astro.unam.mx
[2] Department of Astronomy, University of Maryland, College Park, MD 20742-4111, USA
[3] Astrophysics Science Division, NASA Goddard Space Flight Center, 8800 Greenbelt Road, Greenbelt, MD 20771, USA
[4] School of Astronomy and Space Science, Nanjing University, Nanjing 210093, People's Republic of China
[5] Key Laboratory of Modern Astronomy and Astrophysics (Nanjing University), Ministry of Education, People's Republic of China

## Abstract

Early and late multiwavelength observations play an important role in determining the nature of the progenitor, circumburst medium, physical processes, and emitting regions associated with the spectral and temporal features of bursts. GRB 180720B is a long and powerful burst detected by a large number of observatories at multiple wavelengths that range from radio bands to sub-TeV gamma-rays. The simultaneous multiwavelength observations were presented over multiple periods of time beginning just after the trigger time and extending to more than 30 days. The temporal and spectral analysis of *Fermi* Large Area Telescope (LAT) observations suggests that it presents similar characteristics to other bursts detected by this instrument. Coupled with X-ray and optical observations, the standard external shock model in a homogeneous medium is favored by this analysis. The X-ray flare is consistent with the synchrotron self-Compton (SSC) model from the reverse-shock region evolving in a thin shell and previous LAT, X-ray, and optical data with the standard synchrotron forward-shock model. The best-fit parameters derived with Markov chain Monte Carlo simulations indicate that the outflow is endowed with magnetic fields and that the radio observations are in the self-absorption regime. The SSC forward-shock model with our parameters can explain the LAT photons beyond the synchrotron limit as well as the emission recently reported by the HESS Collaboration.

*Key words:* acceleration of particles – gamma-ray burst: individual (GRB 180720B) – ISM: general – magnetic fields – radiation mechanisms: non-thermal

## 1. Introduction

The most energetic gamma-ray sources in the observable universe are gamma-ray bursts (GRBs). These events display short and bright irregular flashes of gamma-rays originated inside the relativistic outflows launched by a central engine. This engine may result from a merger of either two neutron stars (NSs) or an NS and a black hole (BH), in which case the events are known as short GRBs (sGRBs). On the other hand, if the engine comes from cataclysmic events at the end of the life cycles of massive stars, these events are referred to as long GRBs (lGRBs). The duration of sGRBs lasts $\lesssim$ few seconds and lGRBs last $\gtrsim$ few seconds (see, i.e., Zhang & Mészáros 2004; Kumar & Zhang 2015, for reviews). The most accepted mechanism for producing the bright flashes known as prompt emission is the standard fireball model (Rees & Meszaros 1992; Mészáros & Rees 1997). According to this model, long-lasting afterglow emission in wavelengths ranging from radio bands to gamma-rays is also expected. The prompt emission is expected when inhomogeneities in the jet lead to internal collisionless shocks (when matter ejected with low velocity is hit by matter with high velocity; Rees & Meszaros 1994) and the afterglow when the relativistic outflow sweeps up enough external "circumburst" medium (Mészáros & Rees 1997). The transition between the prompt and early afterglow emission is determined by the steep decay usually interpreted as the high-latitude emission (Kumar & Panaitescu 2000; Nousek et al. 2006) and by an X-ray flare or optical flash explained in terms of the reverse shock (Kobayashi 2000; Kobayashi & Zhang 2007; Kobayashi et al. 2007; Fraija & Veres 2018; Becerra et al. 2019a).

Multiwavelength observations play an important role in determining the physical processes and emitting places associated with the spectral and temporal features of bursts (Ackermann et al. 2013a; Fraija 2015; Fraija et al. 2017c). The early-time afterglow observations are useful to determine the nature of the central engine and constrain the density of the circumburst medium (Fraija et al. 2016a, 2016b; Becerra et al. 2017, 2019b; Fraija et al. 2019a). In these cases, GRBs become potentially more interesting and informative, allowing afterglow models to be tested more rigorously.

Since the discovery of the first GRB in 1967 by the *Vela* satellites (Klebesadel et al. 1973), the detection of high-energy (HE) photons ($\gtrsim 100\,\mathrm{MeV}$) has been possible in only a small fraction of them ($\sim 150$ bursts[6]). At higher energies, in the GeV energy range, few detections have been reported and interpreted in the leptonic and hadronic scenarios operating at several possible emitting regions. The HE and very-high-energy (VHE; $\gtrsim 10\,\mathrm{GeV}$) photons have been detected during the prompt and long-lived emission (Ajello et al. 2019). Different analyses of multiwavelength observations covering from radio to GeV energies have indicated that the HE and VHE emission is produced during the internal and external shocks (e.g., see Kumar & Zhang 2015). During the afterglow phase the synchrotron emission from electrons accelerated in the external shocks dominates from radio wavelengths to gamma-rays, and the synchrotron self-Compton (SSC) emission and photohadronic processes (Mészáros & Rees 2000; Alvarez-Muñiz et al. 2004; Fraija 2014) are expected to dominate in the GeV–TeV energy range (Zhang & Mészáros 2001; Fraija et al. 2019c). The

---

[6] https://fermi.gsfc.nasa.gov/ssc/observations/types/grbs/lat_grbs/

maximum photon energy radiated by the synchrotron process during the deceleration phase is $\sim 10\,\mathrm{GeV}\left(\frac{\Gamma}{100}\right)(1+z)^{-1}$, where $\Gamma$ is the bulk Lorentz factor and $z$ is the redshift (Abdo et al. 2009a; Piran & Nakar 2010; Barniol Duran & Kumar 2011). Consequently, we emphasize that the VHE photons below the maximum photon energy radiated in the synchrotron forward-shock model can be interpreted in this scenario, but beyond the synchrotron limit other scenarios must be invoked to explain them.

GRB 180720B was detected and followed up by the three instruments on board the *Swift* satellite (Barthelmy et al. 2018; Palmer et al. 2018)—the Burst Area Telescope (BAT), the X-ray Telescope (XRT), and the Ultraviolet/Optical Telescope —by both instruments on board the *Fermi* satellite (Bissaldi & Racusin 2018; Roberts & Meegan 2018)—the Gamma-ray Burst Monitor (GBM) and the Large Area Telescope (LAT)— by the MAXI Gas Slit Camera (Negoro et al. 2018), by Konus-Wind (Frederiks et al. 2018), by the *Nuclear Spectroscopic Telescope Array* (Bellm & Cenko 2018), by the CALorimetric Electron Telescope Gamma-ray Monitor (Cherry et al. 2018), by the Giant Metrewave Radio Telescope (GMRT; Chandra et al. 2018), by the Arcminute Microkelvin Imager Large Array (AMI-LA; Sfaradi et al. 2018) and by several optical ground telescopes (Covino & Fugazza 2018; Horiuchi et al. 2018; Izzo et al. 2018; Jelinek et al. 2018; Lipunov et al. 2018; Schmalz et al. 2018; Watson et al. 2018; Zheng & Filippenko 2018).

In this paper, we derive and analyze the LAT light curve and spectrum for GRB 180720B and show that it exhibits similar features to other powerful bursts. We show that the photon-flux light curve recently reported in the second GRB catalog (Ajello et al. 2019) is consistent with the one obtained in this work. In addition, we determine the GBM light curve and show that it is consistent with the prompt emission. Analyzing the multi-wavelength observations covering from radio bands to GeV gamma-rays, we show that LAT, X-ray, optical, and radio observations are consistent with the synchrotron forward-shock model in a homogeneous medium. We also show that the LAT photons beyond the synchrotron limit, as well as the emission recently reported by the HESS Collaboration are consistent with the SSC forward-shock model. The X-ray flare is consistent with SSC emission from the reverse-shock region in a homogeneous medium. The paper is arranged as follows. In Section 2 we present multiwavelength observations and/or data reduction. In Section 3 we describe the multiwavelength observations through the synchrotron forward-shock model and the SSC reverse-shock model. In Section 4, we exhibit the discussion and results of the analysis done using the multi-wavelength data. Finally, in Section 5 we give a brief summary and emphasize our conclusions. The convention $Q_{\mathrm{x}} = Q/10^{\mathrm{x}}$ in cgs units will be adopted throughout this paper. The sub-indexes "f" an "r" are related to the derived quantities in the forward and reverse shocks, respectively.

## 2. Observations and Data Analysis

### 2.1. Fermi-*LAT Data*

The data files used for this analysis were obtained from the data website.[7] They contain information 600 s before up to 1000 s from the trigger time ($T_0$) (2018-07-20 14:21:39.65 UTC; Bissaldi & Racusin 2018). *Fermi*-LAT data were analyzed in

the 0.1–100 GeV energy range and the time interval of $T_0 + 10\,\mathrm{s}$ up to $T_0 + 630\,\mathrm{s}$ with the *Fermi* Science tools[8] ScienceTools v10r00p05. For this analysis we adopt the P8R2_TRANSIENT020_V6 response, following the unbinned likelihood analysis presented by the *Fermi*-LAT team.[9] Using the gtselect tool, we select, with an eventclass 16, a region of interest (ROI) around the position of this burst within a radius of 10°. We apply a cut on the zenith angle above 100°. Then we select the appropriate time intervals (GTIs) using the gtmktime tool on the data selected before considering the ROI cut. In order to define the model needed to describe the source and the diffuse components, we use modeleditor. We define a point source at the position of this burst, assuming a power-law spectrum, and we define a galactic diffuse component using GALPROP gll_iem_v06 as well as the extragalactic background iso_P8R3_SOURCE_V2.[10] We use gtdiffrsp to take into account all of these components. Following the likelihood procedure, we produce a lifetime cube with the tool gtltcube, using a step $\delta\theta = 0.025$, a bin size of 0.5 and a maximum zenith angle of 100°. The exposure map was created using gtexpmap, considering a region of 30° around the GRB position and defining 100 spatial bins in longitude/latitude and 50 energy bins. Finally, we perform the likelihood analysis with gtlike, obtaining a photon flux of $(5.2 \pm 0.4) \times 10^{-5}$ photons cm$^{-2}$ s$^{-1}$ and a test statistic of 883.267.

We find photons with a probability greater than 90% of being associated with GRB 180720B using the gtsrcprob. In this case, we use gtbin in order to obtain the light curve, considering eight logarithmically uniform temporal bins. The photon flux is generated using the counts and the exposure in each bin. The exposure is obtained with gtexposure. To derive the energy flux we compute the spectra integrated over each interval assuming logarithmic binning for the energy between 100 MeV and 100 GeV. Then we obtain the Detector Response Matrix with the gtrspgen tool assuming a point=like source, a maximum cutoff angle of 60°, and a bin size of 0.05 into 30 logarithmically uniform bins between 100 and 100 GeV. Finally, we derive the background spectra using gtbkg and subtract it to the source using XSPEC (v12.10.1; Arnaud 1996) in order to obtain the energy flux with a 90% confidence error.

The left panel of Figure 1 displays the *Fermi*-LAT energy flux (blue) and photon-flux (red) light curves (upper panel) and all the photons with energies >100 MeV associated with GRB 180720B (lower panel). The filled circles in the bottom panel correspond to the individual photons and their energies with a >0.9 probability of being associated with GRB 180720B and the open circles indicate the LAT gamma Transient class photons. The dotted and dashed lines on the photon-flux light curve correspond to the best-fit curves using a power-law (PL) function and a broken power-law (BPL) function. The best-fit values are $\alpha = 1.81 \pm 0.16$ for the PL function and $\alpha_1 = 1.49 \pm 0.12$ $^*\alpha_2 = 3.09 \pm 0.64$ for the BPL function. These values are consistent with the ones from the photon-flux light curve reported in Table 5 of Ajello et al. (2019). The right panel of Figure 1 shows the *Fermi*-LAT spectrum.

We modeled the energy flux light curve and spectrum using the closure relation $F_{\nu,\mathrm{f}}^{\mathrm{syn}} \propto t^{-\alpha_{\mathrm{LAT}}} \epsilon_\gamma^{-\beta_{\mathrm{LAT}}}$. The best-fit values of the
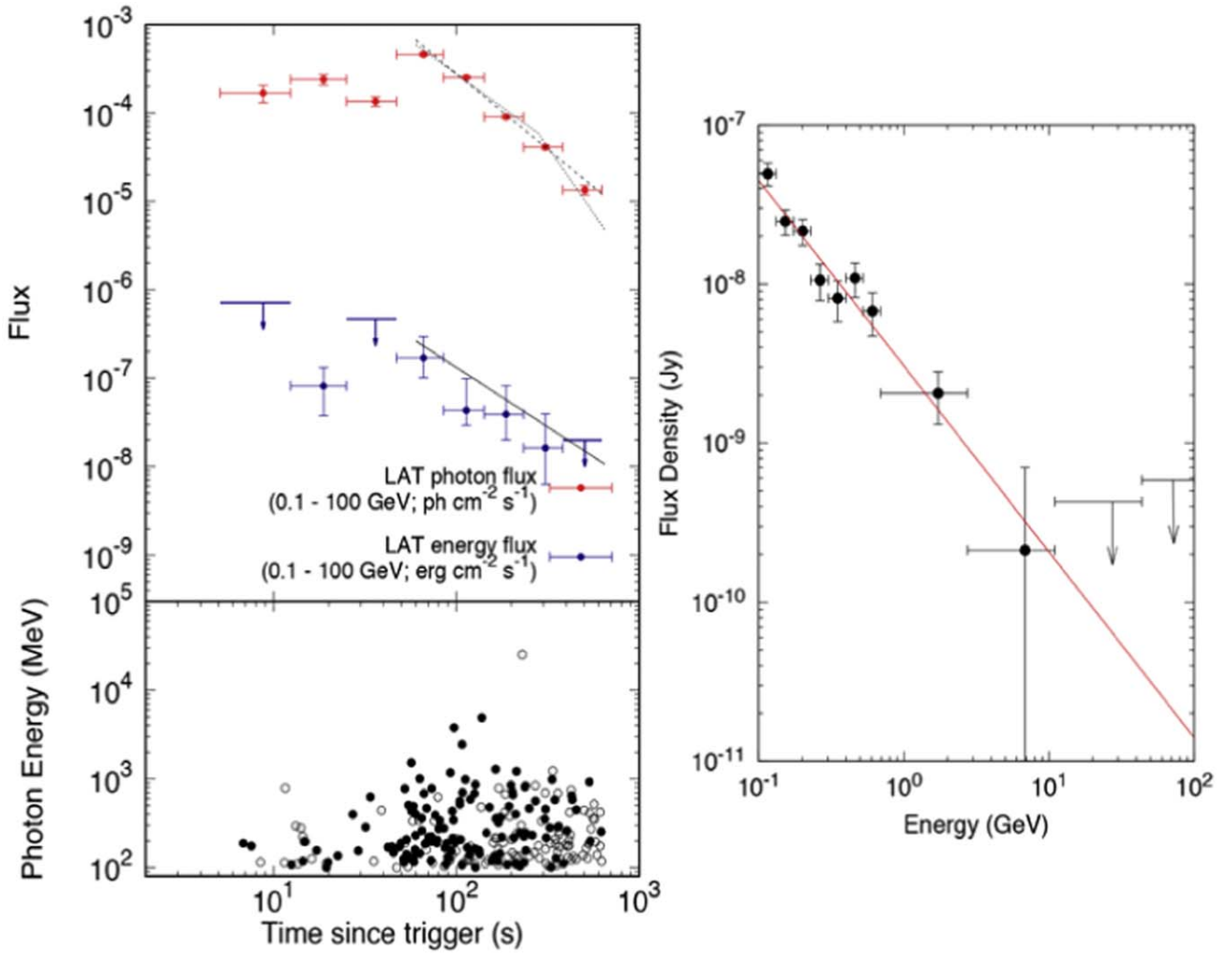
---

**Figure 1.** The left panel shows the *Fermi*-LAT energy flux (blue) and photon-flux (red) light curves obtained between 0.1 and 300 GeV (upper panel) and all the photons with energies >100 MeV in the direction of GRB 180720B (lower panel). The filled circles correspond to the individual photons with a >0.9 probability of being associated with this burst and the open circles indicate the LAT gamma Transient class photons. The right panel shows the *Fermi*-LAT spectrum obtained between 0.15 and 900.45 s.

temporal and spectral PL indexes were $\alpha_{\rm LAT} = 1.45 \pm 0.53$ ($\chi^2 = 1.11$) and $\beta_{\rm LAT} = 1.17 \pm 0.15$ ($\chi^2 = 1.09$), respectively. These PL indexes are compatible with the third PL segment of the synchrotron forward-shock model ($\propto t^{-\frac{3p-2}{4}} \epsilon_\gamma^{-\frac{p}{2}}$) for $p \approx 2.6 \pm 0.2$. It is worth emphasizing that this PL segment is equal for the wind and homogeneous afterglow model.

Some relevant characteristics can be observed in the lower panel of Figure 1: (i) the first HE photon (101 MeV) was detected 19.4 s after the trigger time, (ii) this burst exhibited 130 photons with energy greater than 100 MeV and 8 photons with energies greater than 1 GeV, (iii) the highest-energy photon[11] exhibited in the LAT observations (4.9 GeV) was detected 142.43 s after the trigger time, and (iv) the photon density increased dramatically for a time longer than $\gtrsim 50$ s.

### 2.2. Fermi-*GBM* Data

The *Fermi*-GBM data were obtained using the public database at the GBM website.[12] The event data files were

obtained using the *Fermi*-GBM Burst Catalog[13] and the GBM trigger time for GRB 180720B at 14:21:39.65 UT (Roberts & Meegan 2018). Flux values were derived using the spectral analysis package Rmfit version 432.[14] In order to analyze the signal we used the time-tagged event files of the two triggered NaI detectors $n_7$ and $n_{11}$ and the BGO detector $b_1$. Two different models were used to fit the spectrum in the energy range of 10–1000 keV over different time intervals. The Band and the Comptonized models were used to fit the spectrum during the time interval [0.000, 60.416 s]. Each time bin was chosen by adopting the minimum resolution required to preserve the shape of the time resolution.

The upper left panel in Figure 2 displays the GBM light curve in the 10–1000 keV energy range. This light curve shows a bright, fast-rise exponential-decay (FRED)-like peak with a maximum flux of $2.74 \times 10^{-5}$ erg cm$^{-2}$ s$^{-1}$ at 15 s, followed by two significant peaks with fluxes of $1.64 \times 10^{-5}$ and $5.5 \times 10^{-6}$ erg cm$^{-2}$ s$^{-1}$ at 26 s and 50 s, respectively. The

[11] This photon was associated with this burst with a probability of 1.
[12] http://fermi.gsfc.nasa.gov/ssc/data
[13] https://heasarc.gsfc.nasa.gov/W3Browse/fermi/fermigbrst.html
[14] https://fermi.gsfc.nasa.gov/ssc/data/analysis/rmfit/
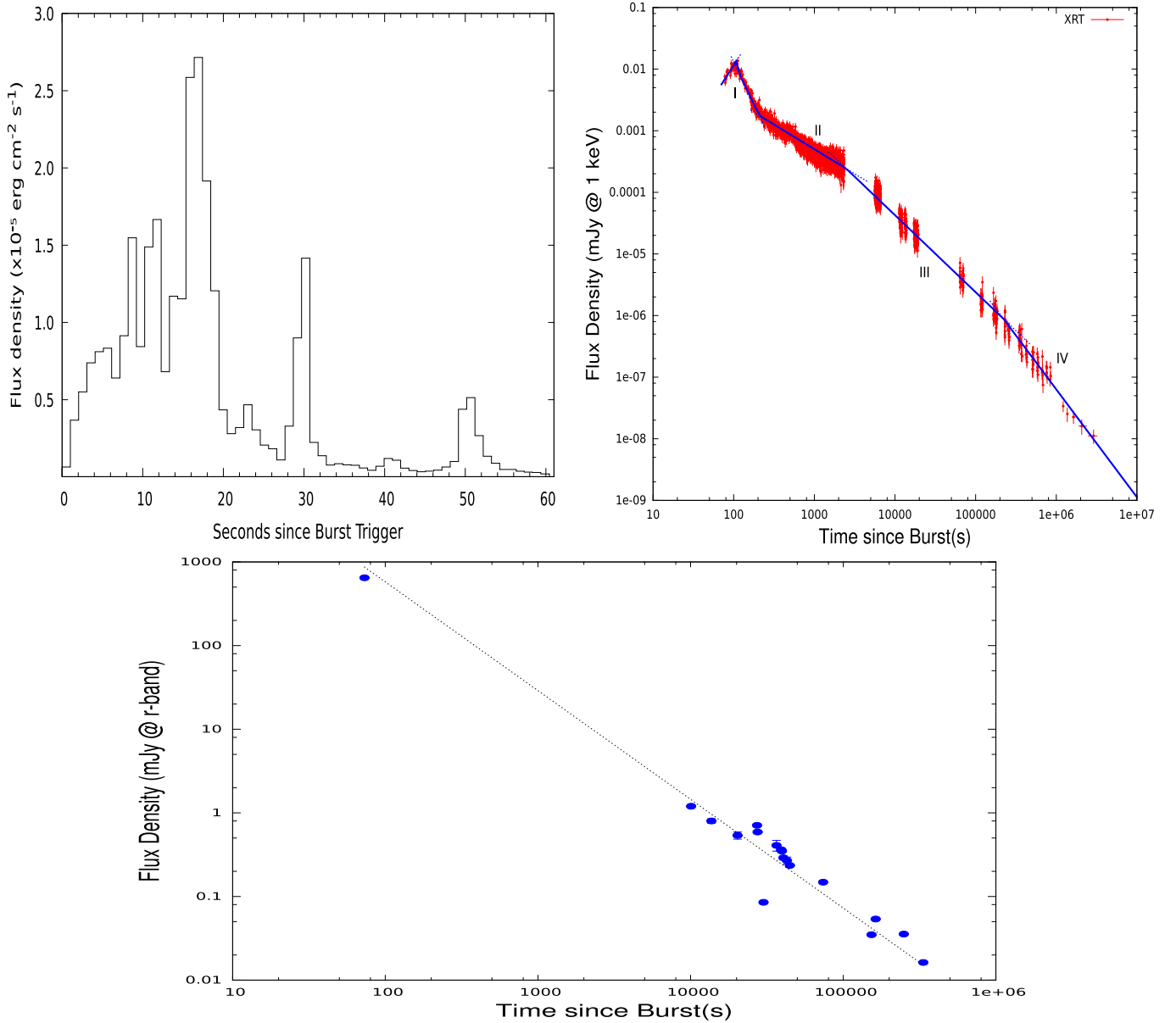
**Figure 2.** The upper left panel shows the GBM light curve obtained in the 10–1000 keV energy range. GBM data were reduced using the public database at the *Fermi* website. The upper right panel shows the X-ray light curve obtained with the *Swift* XRT instrument at 1 keV. The blue lines correspond to the best-fit curves using PL functions. The *Swift* data were obtained using the publicly available database at the official *Swift* website. The lower panel shows the optical *R*-band light curve with the best-fit PL function.

fluence over the prompt emission was $(2.985 \pm 0.001) \times 10^{-4} \, \mathrm{erg \, cm^{-2}}$, which corresponds to an equivalent isotropic energy of $3 \times 10^{53} \, \mathrm{erg}$ for a measured redshift of $z = 0.654$ (Vreeswijk et al. 2018). This light curve exhibits a high-variability $\delta t / t \ll 1$,[15] which favors the prompt phase scenario. Theoretically, this timescale is interpreted as the time difference of two photons emitted at two different radii (Sari & Piran 1997).

### 2.3. X-Ray Data

The *Swift* BAT triggered on GRB 180720B on 2018 July 20 at 14:21:44 UT. This instrument located this burst at the coordinates: R.A. $= 00^{\mathrm{h}}02^{\mathrm{m}}07^{\mathrm{s}}$ and decl. $= -02^{\mathrm{d}}56'00''$ (J2000), with an uncertainty of $3'$. The XRT instrument started observing this burst 86.5 s after the trigger, and monitored the afterglow for the following 33.5 days, giving a total net exposure of 13 ks in Windowed Timing (WT) mode and $2.8 \times 10^3 \, \mathrm{ks}$ in Photon Counting (PC) mode. The *Swift* data used in this analysis are publicly available in the website database.[16] In the WT mode, the reported value of the photon spectral index was $\Gamma_{\mathrm{X}} = \beta_{\mathrm{X}} + 1 = 1.761 \pm 0.01$ for a galactic (intrinsic) absorption of $N_{\mathrm{H}} = 3.92(17.7 \pm 0.7) \times 10^{20} \, \mathrm{cm^{-2}}$. In the PC mode, the reported value of the photon spectral index was $\Gamma_{\mathrm{X}} = \beta_{\mathrm{X}} + 1 = 1.83 \pm 0.06$ for $N_{\mathrm{H}} = 3.92(24.0 \pm 0.4) \times 10^{20} \, \mathrm{cm^{-2}}$.

The upper right panel in Figure 2 shows the *Swift* X-ray light curve obtained with the XRT (WC and PC modes) instrument

---

[15] $\delta t$ is the width of the peak and $t$ is the timescale of the flux.

[16] http://www.swift.ac.uk/xrtproducts/

**Table 1**
The Best-fit values of the Temporal PL Indexes Derived from the XRT Light Curve of GRB 180720B

| X-rays | Interval (s) | Index ($\alpha_X$) | $\chi^2$/ndf |
|---|---|---|---|
| I | $\leqslant 1.3 \times 10^2$ | $-2.05 \pm 0.27$ | 1.12 |
|  | $> 1.3 \times 10^2$ | $2.74 \pm 0.06$ | 1.27 |
| II | $(0.2–2.5) \times 10^3$ | $0.79 \pm 0.08$ | 1.31 |
| III | $(0.25–26.1) \times 10^4$ | $1.26 \pm 0.06$ | 1.29 |
| IV | $\geqslant 2.6 \times 10^5$ | $1.75 \pm 0.09$ | 1.21 |

at 1 keV. The flux density of the XRT data was extrapolated from 10 to 1 keV using the conversion factor introduced in Evans et al. (2010). The blue curves correspond to the best-fit PL functions obtained using the chi-square minimization algorithm installed in ROOT (Brun & Rademakers 1997). In accordance with the observational X-ray data, three PL segments ($t^{-\alpha_X}$) with an X-ray flare were identified in this light curve. We evaluated the X-ray light curve at four time intervals, designated as epochs I, II, III, and IV: $70 \lesssim t \lesssim 200$ s (I), $200 \lesssim t \lesssim 2.5 \times 10^3$ s (II), $2500 \lesssim t \lesssim 2.6 \times 10^5$ s (III) and $t \geqslant 2.6 \times 10^5$ (IV). The time intervals were chosen in accordance with the variations of each slope. The temporal PL indexes are $\alpha_{X,rise} = -2.05 \pm 0.27 (\chi^2/\text{ndf} = 1.12)$ and $\alpha_{X,decay} = 2.74 \pm 0.08$ (1.27) during epoch "I" and $\alpha_X = 0.79 \pm 0.06(1.31)$, $1.26 \pm 0.06(1.29)$ and $1.75 \pm 0.09(1.21)$ for epochs "II," "III," and "IV," respectively. The best-fit values of each epoch are reported in Table 1.

### 2.4. Optical Data

GRB 180720B began to be detected in the optical and near-infrared bands on 2018 July 20 at 14:22:57 UT, 73 s after the trigger time (Sasada et al. 2018). Using the HOWPol and HONIR instruments attached to the 1.5 m Kanata telescope, these authors reported a bright optical $R$-band counterpart of $m_R = 9.4$ mag. Vreeswijk et al. (2018) observed the optical counterpart of this burst using the VLT/X-shooter spectrograph. They detected a bright continuum with some absorption lines (Fe II, Mg II, Mg I, and Ca II) associated with a redshift of $z = 0.654$. Additional photometry in different optical bands is reported in Martone et al. (2018), Reva et al. (2018), Itoh et al. (2018), Crouzet & Malesani (2018), Horiuchi et al. (2018), Watson et al. (2018), Schmalz et al. (2018), and Lipunov et al. (2018).

The lower panel in Figure 2 shows the optical light curve of GRB 180720B in the $R$-band. The solid line represents the best-fit PL function. Optical data taken from the GCN circulars reported in this subsection were detected by different telescopes. The optical observations with their uncertainties were obtained using the standard conversion for AB magnitudes shown in Fukugita et al. (1996). The optical data were corrected by the galactic extinction using the relation derived in Becerra et al. (2019b). The values of $\beta_O = 0.80 \pm 0.04$ for optical filters and a reddening of $E_{B-V} = 0.037$ mag (Bolmer & Shady 2019) were used. The best-fit value of the temporal decay is $1.22 \pm 0.02$ ($\chi^2/\text{ndf} = 1.05$; see Table 2).

### 2.5. Radio Data

Sfaradi et al. (2018) observed the position of this burst with AMI-LA at 15.5 GHz for 3.9 hr. The observations began 2 days

after the BAT trigger, providing an integrated flux of $\sim1$ mJy. Chandra et al. (2018) detected GRB 180720B with GMRT at the 1.4 GHz band, reporting a flux of $\sim390 \pm 59$ $\mu$Jy.

### 2.6. HESS Observations

During the Cerenkov Telescope Array (CTA) Science Symposium 2019, the HESS collaboration reported the discovery of late-time VHE emission from GRB 180720B. The VHE emission with $\sim5\sigma$ was in the energy range from 100 to 400 GeV. The observations began $\sim10$ hr after the burst trigger.[17]

## 3. Broadband Afterglow Modeling

Figure 3 shows the broadband SEDs, including the X-ray and optical observations at 1000 s (left) and 10000 s (right) with the best-fit PL with spectral indexes $0.68 \pm 0.06$ ($\chi^2/\text{ndf} = 0.96$) and $0.70 \pm 0.05$ (0.97), respectively. The dashed gray lines correspond to the best-fit curves from XSPEC.

The left panel in Figure 4 shows the LAT, X-ray, optical, and radio data with the best-fit PL functions given in Section 2. The LAT data are displayed at 100 MeV, X-ray data are at 1 keV, optical data are at the $R$-band, and radio data are at 15.5 and 1.4 GHz. The best-fit parameters of the temporal PL indexes obtained through the $\chi^2$ minimization function are reported in Table 2. It is worth emphasizing that radio data are not included in our analysis because there is only one data point for each energy band.

In order to analyze the LAT, X-ray, and optical light curves we used the time intervals (epoch "I," "II," "III," and "IV") proposed for the X-ray light curve. Taking into account that to analyze epoch II, it is necessary to have the results of epochs III and IV, this epoch will be the last one to be analyzed.

### 3.1. Epoch I: $75 s \lesssim t \lesssim 200 s$

During this epoch, the LAT and the optical light curves are modeled with PL functions and the X-ray flare is modeled with two PLs. Considering that during this epoch the X-ray flare, the LAT and the optical light curves have different origins, we first analyze the LAT and the optical light curves and then we examine the X-ray flare.

#### 3.1.1. Analysis of LAT and Optical Light Curves

The best-fit values of the temporal and spectral PL indexes for the LAT observations are $\alpha_{LAT} = 1.45 \pm 0.53$ and $\beta_{LAT} = 1.17 \pm 0.15$, respectively, and the temporal index for the optical observations is $\alpha_O = 1.22 \pm 0.02$. Taking into account that the LAT observations can be described by the third PL segment of the synchrotron forward-shock model, and also that its temporal index is larger than the index of the optical observations ($\Delta\alpha \approx 0.3$), the optical observation can be described by the second PL segment ($\propto t^{-\frac{(3p-3)}{4}}\epsilon_\gamma^{-\frac{p-1}{2}}$) of the synchrotron forward-shock model in the homogeneous medium. In this case, the electron spectral index that explains both the LAT and optical observations would be $p \approx 2.6 \pm 0.2$ and $p \approx 2.62 \pm 0.02$, respectively, when the synchrotron emission radiates in the homogeneous medium. In the case of the afterglow wind model, the temporal index of the optical observations is usually larger than that one of the LAT observations.
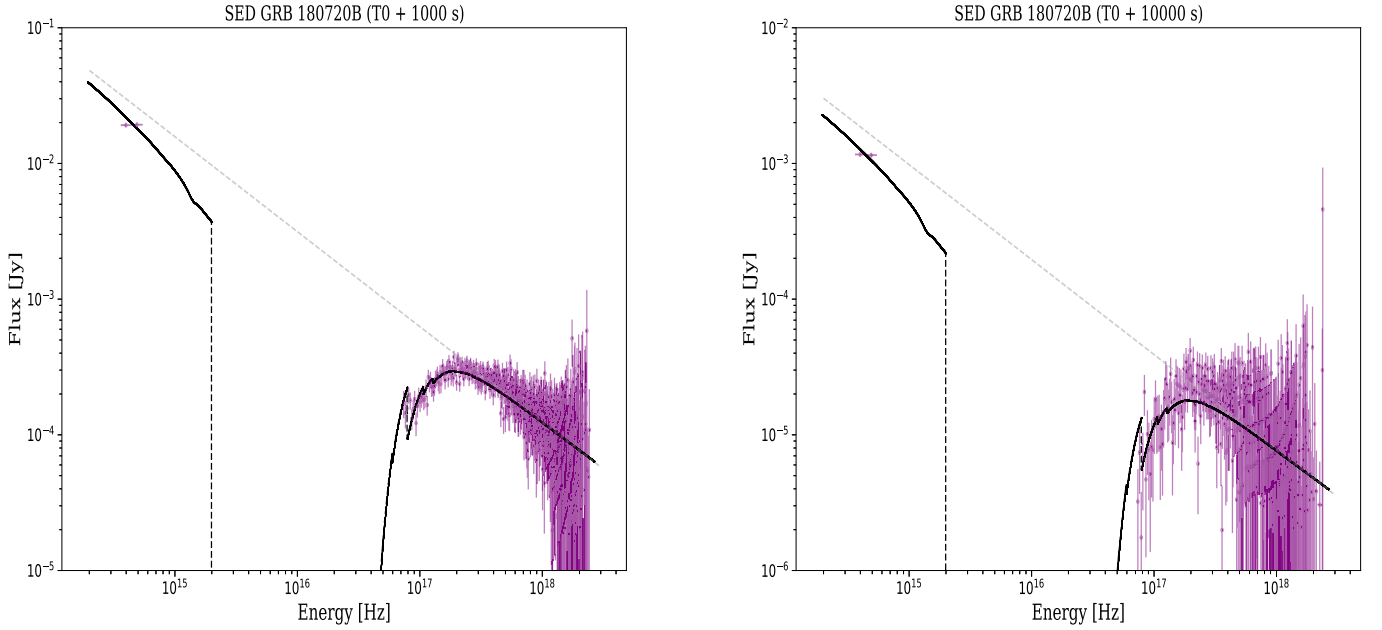
---

[17] https://indico.cta-observatory.org/event/1946/timetable/

**Figure 3.** Broadband SEDs of the X-ray and optical observations shown 1000 s (left) and 10000 s (right) after the trigger time. The dashed gray lines are the best-fit curve from XSPEC.

**Table 2**
The Best-fit Parameters of the Spectral and Temporal Indexes Using the LAT, X-Ray, and Optical Observations

|  | Observation I | Theory | Observation II | Theory | Observation III | Theory | Observation IV | Theory |
|---|---|---|---|---|---|---|---|---|
| *LAT flux* | | | | | | | | |
| $\alpha_{LAT}$ | $1.45 \pm 0.53$ | $1.45 \pm 0.15$ | $1.45 \pm 0.53$ | $1.45 \pm 0.15$ | ... | ... | ... | ... |
| $\beta_{LAT}$ | $1.17 \pm 0.15$ | $1.30 \pm 0.10$ | $1.15 \pm 0.15$ | $1.30 \pm 0.10$ | ... | ... | ... | ... |
| *X-ray flux* | | | | | | | | |
| $\alpha_X$ ($\lesssim 1.3 \times 10^2$ s) | $-(2.05 \pm 0.27)$ | $-(2.00 \pm 0.25)$ | ... | ... | ... | ... | ... | ... |
| $\alpha_X$ ($> 1.3 \times 10^2$ s) | $2.74 \pm 0.08$ | $3.03 \pm 0.25$ | $0.79 \pm 0.08$ | $\sim(0.5 - 0.8)$ | $1.26 \pm 0.06$ | $1.20 \pm 0.15$ | $1.70 \pm 0.19$ | $1.45 \pm 0.15$ |
| $\beta_X$ | ... | ... | $0.68 \pm 0.06$ | $0.80 \pm 0.10$ | $0.70 \pm 0.05$ | $0.80 \pm 0.1-$ | ... | ... |
| *Optical flux* | | | | | | | | |
| $\alpha_O$ | $1.22 \pm 0.012$ | $1.20 \pm 0.15$ | $1.22 \pm 0.012$ | $1.20 \pm 0.15$ | $1.22 \pm 0.012$ | $1.20 \pm 0.15$ | ... | ... |
| $\beta_O$ | ... | ... | $0.68 \pm 0.06$ | $0.80 \pm 0.10$ | $0.70 \pm 0.05$ | $0.80 \pm 0.10$ | ... | ... |

**Note.** In addition, the theoretical predictions of the spectral and temporal indexes are calculated for $p = 2.6 \pm 0.2$.

### 3.1.2. Analysis of the X-Ray Flare

We used two PLs to fit the X-ray flare empirically (e.g., see, Becerra et al. 2019b). Therefore, the X-ray flare is defined by the rise and decay of the temporal indexes by $-(2.05 \pm 0.27)$ and $2.74 \pm 0.06$, respectively, and a variability timescale of $\delta t/t \sim 1$. These values are discussed in terms of the reverse-shock emission and late central-engine activity.

*Reverse-shock emission.* A reverse shock is believed to occur in the interaction between the expanding relativistic outflow and the external circumburst medium. During this shock, relativistic electrons heated and cooled down mainly by synchrotron and Compton scattering emission generate a single flare emission (see, e.g., Kobayashi et al. 2007; Fraija et al. 2012, 2017b). The evolution of reverse-shock emission is considered in the thick and thin shell regimes, depending on the crossing time and the duration of the prompt phase (e.g., see,

Kobayashi & Zhang 2003). In the thick shell, the flare overlaps with the prompt emission and in the thin shell it is separated from the prompt phase. Because the X-ray flare in GRB 180720B took place later than the burst emission, the reverse-shock emission must evolve in the thin shell.

Kobayashi et al. (2007) discussed the generation of an X-ray flare by Compton scattering emission in the early afterglow phase when the reverse shock originated in the homogeneous medium and evolved in the thin shell. These authors found that the X-ray emission created in the reverse-shock region displays a time-variability scale of $\delta t/t \sim 1$ and varies as $F_{\nu,r}^{ssc} \propto t^{\frac{5(p-1)}{4}}$ before the peak and $\propto t^{-\frac{3p+1}{3}}$ after the peak. Taking into account the best-fit values of the rise and decay indexes, the electron spectral indexes are $2.64 \pm 0.22$ and $2.42 \pm 0.06$, respectively.

Considering the reverse shock evolving in a thin shell and in a homogenous medium, the Lorentz factor is bounded by the critical
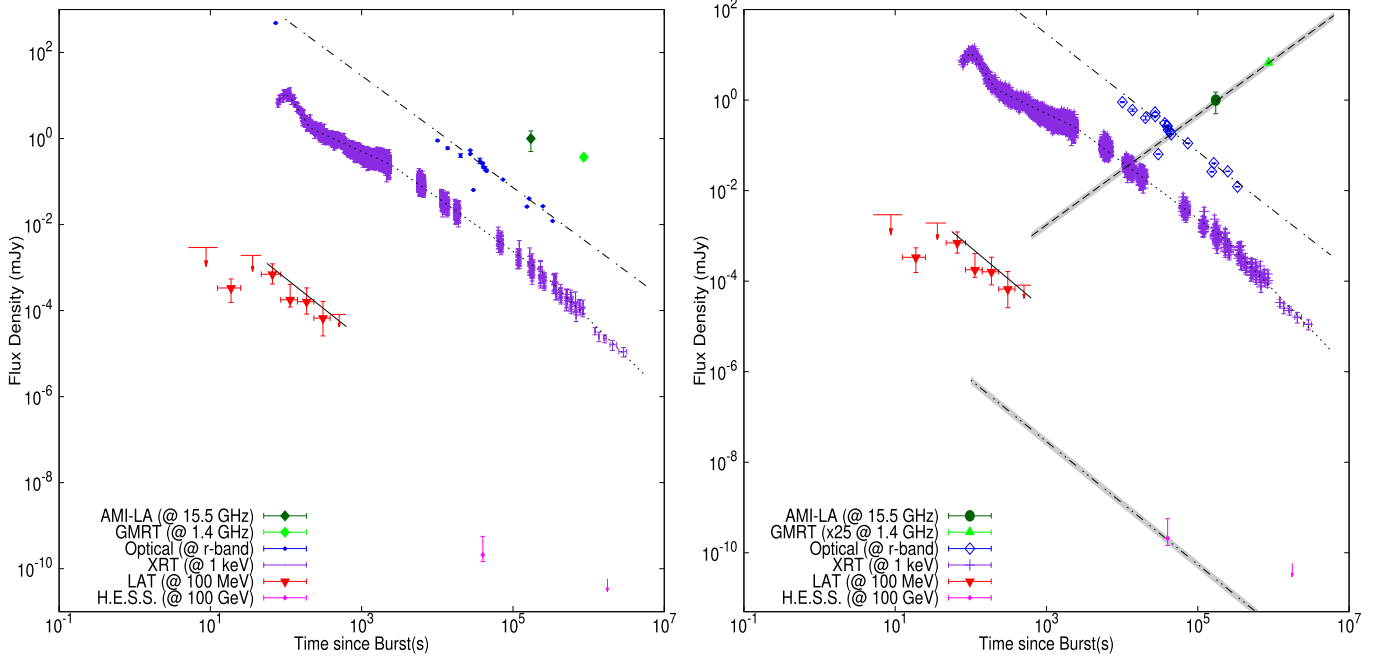
**Figure 4.** The left panel shows multiwavelength light curves and fits of the LAT, X-ray, and optical observations of GRB 180720B. The right panel is the same as the left-hand panel, but the radio wavelengths and the VHE gamma-rays are at 100 GeV.

Lorentz factor $\Gamma < \Gamma_c$ (Zhang et al. 2003) and the deceleration time $t_{dec} \approx 130\,\text{s}$. The critical Lorentz factor and deceleration timescale are defined by $\Gamma_c = \left(\frac{3}{32\pi m_p}\right)^{\frac{1}{8}} (1+z)^{\frac{3}{8}} E^{\frac{1}{8}} n^{-\frac{1}{8}} T_{90}^{\frac{3}{8}}$ and $t_{dec} \approx \left(\frac{3}{32\pi m_p}\right)^{\frac{1}{3}} (1+z) E^{\frac{1}{3}} n^{-\frac{1}{3}} \Gamma^{\frac{8}{3}}$, respectively, where $E$ is the equivalent kinetic energy obtained using the isotropic energy and the efficiency of converting the kinetic energy into photons, $m_p$ is the proton mass, and $T_{90}$ is the duration of the burst. The maximum flux can be calculated by $F_{\nu,r}^{ssc} = F_{\max,r}^{ssc} \left(\frac{\epsilon_\gamma}{\epsilon_{c,r}^{ssc}}\right)^{-\frac{1}{2}}$ with $F_{\max,r}^{ssc}$ and $\epsilon_{c,r}^{ssc}$ as the maximum flux and the cutoff energy break of the SSC emission, respectively (Zhang et al. 2003; Fraija et al. 2016b).

*Late central-engine activity.* In the framework of late central-engine activity, the ultra-relativistic jet has several mini-shells and the X-ray flare is the result of multiple internal shell collisions. The light curve is built as the superposition of the prompt emission from the late activity and the standard afterglow. In this context, the fast rise is naturally explained in terms of the short time-variability of the central engine $\delta t/t \ll 1$. For a random magnetic field caused by internal shell collisions, the flux decays as $F_{\nu,is} \propto t^{-2p}$ in the slow-cooling regime (see e.g., Zhang et al. 2006). In this case, the electron spectral index corresponds to an atypical value of $p = 1.37 \pm 0.03$.

Given the temporal analysis, we conclude that the X-ray flare is most consistently explained by the reverse-shock emission rather than by the late activity of the central engine.

### 3.2. Epoch III: $2.5 \times 10^3\,s \lesssim t \lesssim 2.6 \times 10^5\,s$

During this epoch, the spectral analysis indicates that the optical and X-ray observations are described with a PL with an index $\beta_{X,III} = 0.70 \pm 0.05$. The temporal analysis shows that the indexes of optical ($\alpha_O = 1.22 \pm 0.02$) and X-ray ($\alpha_{X,III} = 1.26 \pm 0.06$) observations are consistent. Therefore, the optical and X-ray fluxes evolve in the second PL segment

of synchrotron emission in the homogeneous medium for predicted values of $p \approx 2.62 \pm 0.02$ and $p \approx 2.68 \pm 0.08$, respectively. In the context of the X-ray light curve, this phase is known as the normal decay (e.g., see Zhang et al. 2006).

### 3.3. Epoch IV: $t \gtrsim 2.6 \times 10^5\,s$

The X-ray light curve during this time interval decays with $\alpha_{X,IV} = 1.70 \pm 0.19$, which is consistent with the LAT light curve reported in epoch II. Taking into account epoch III, the temporal PL index varied as $\Delta\alpha \approx 0.45$ (from $\alpha_{X,II} = 1.26 \pm 0.06$ to $1.70 \pm 0.19$), which is consistent with the evolution from the second to the third PL segments of synchrotron emission in the homogeneous medium for $p \approx 2.60 \pm 0.2$. Therefore, the break observed in the X-ray light curve during the transition from epochs III to IV can be explained as the transition of the synchrotron energy break below the X-ray observations at 1 keV.

### 3.4. Epoch II: $200\,s \lesssim t \lesssim 2500\,s$

In order to describe the LAT, X-ray, and optical light curves correctly during this time interval, epochs I and III are taken into account. Temporal and spectral analysis of the X-ray light curve shows that during epoch II the PL indexes are $\alpha_{X,II} = 0.79 \pm 0.08$ and $\beta_{X,II} = 0.68 \pm 0.06$, respectively. The spectral indexes associated with the X-ray observations during epochs II and III are very similar ($\beta_{X,II} \approx \beta_{X,III}$), and the spectral and temporal PL indexes of LAT and optical observations during epochs I and II are unchanged. Taking into account that $\beta_{X,II} \approx \beta_{X,III}$, that there are no breaks in the LAT and optical light curves, and that the value of the temporal decay index is followed by the normal decay phase in the X-ray light curve, epoch II is consistent with the shallow "plateau" phase (e.g., see Vedrenne & Atteia 2009). It is worth highlighting that during this transition there was no variation of the spectral index. A priori, we could think that X-ray
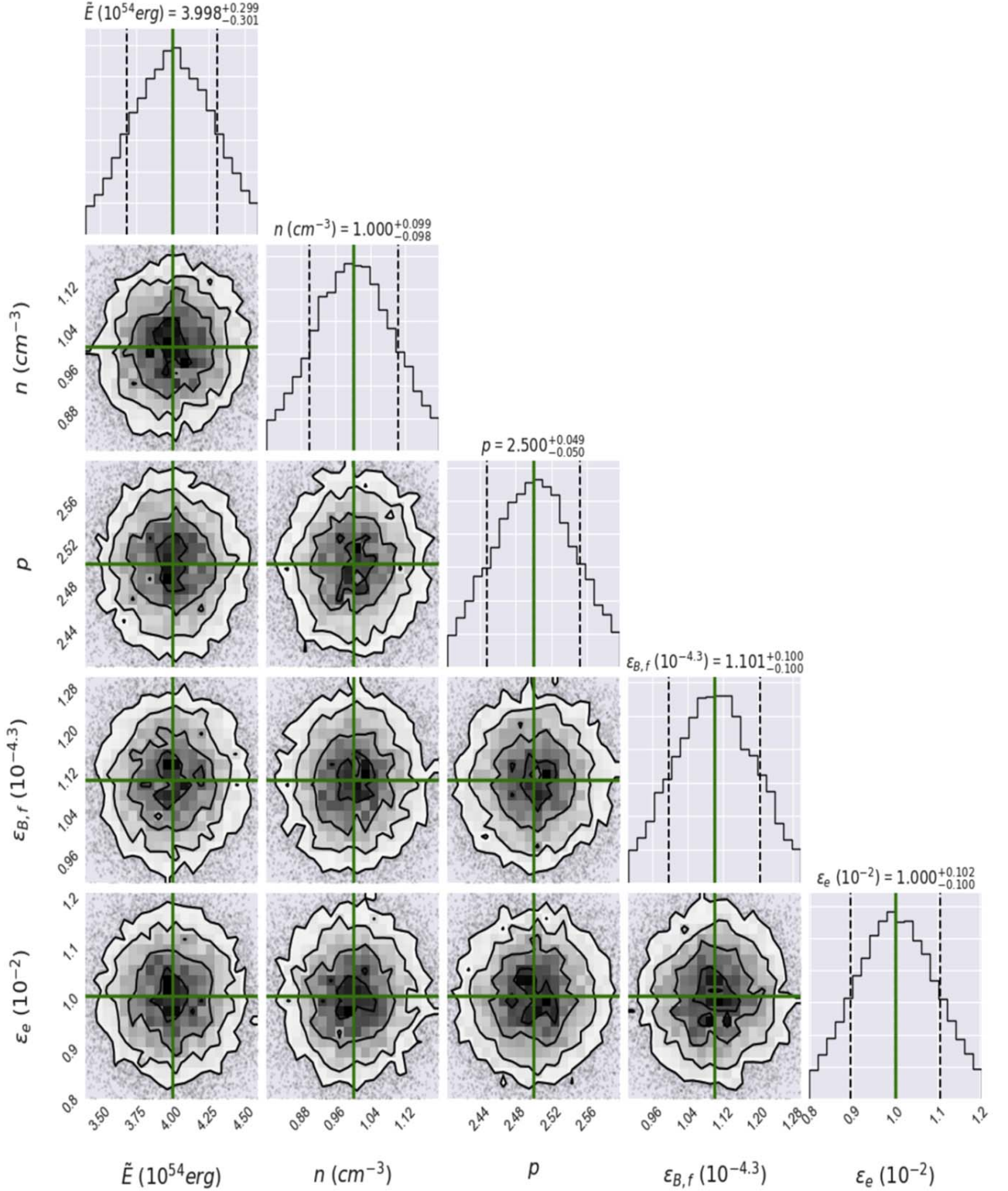
**Figure 5.** Best-fit results for the LAT light curve at 100 MeV using our model and the MCMC calculations for GRB 180720B. The "corner plots" exhibit the results obtained from the MCMC simulation. Labels above the 1D KDE plot illustrate the 15%, 50%, and 85% quantiles for all parameters. The best-fit values are shown in green and reported in column 2 of Table 3.

observations during this epoch could be associated with the second PL segment ($\propto t^{-\frac{(3p-3)}{4}}\epsilon_\gamma^{-\frac{p-1}{2}}$) of synchrotron emission. In this case the spectral index of the electron population, taking into account the temporal and spectral analysis, would be

$p = 2.05 \pm 0.11$ and $p = 0.53 \pm 0.11$, respectively, which is different from the LAT and optical observations derived in the previous subsection. Hence, this hypothesis is rejected and we postulate the "plateau" phase.
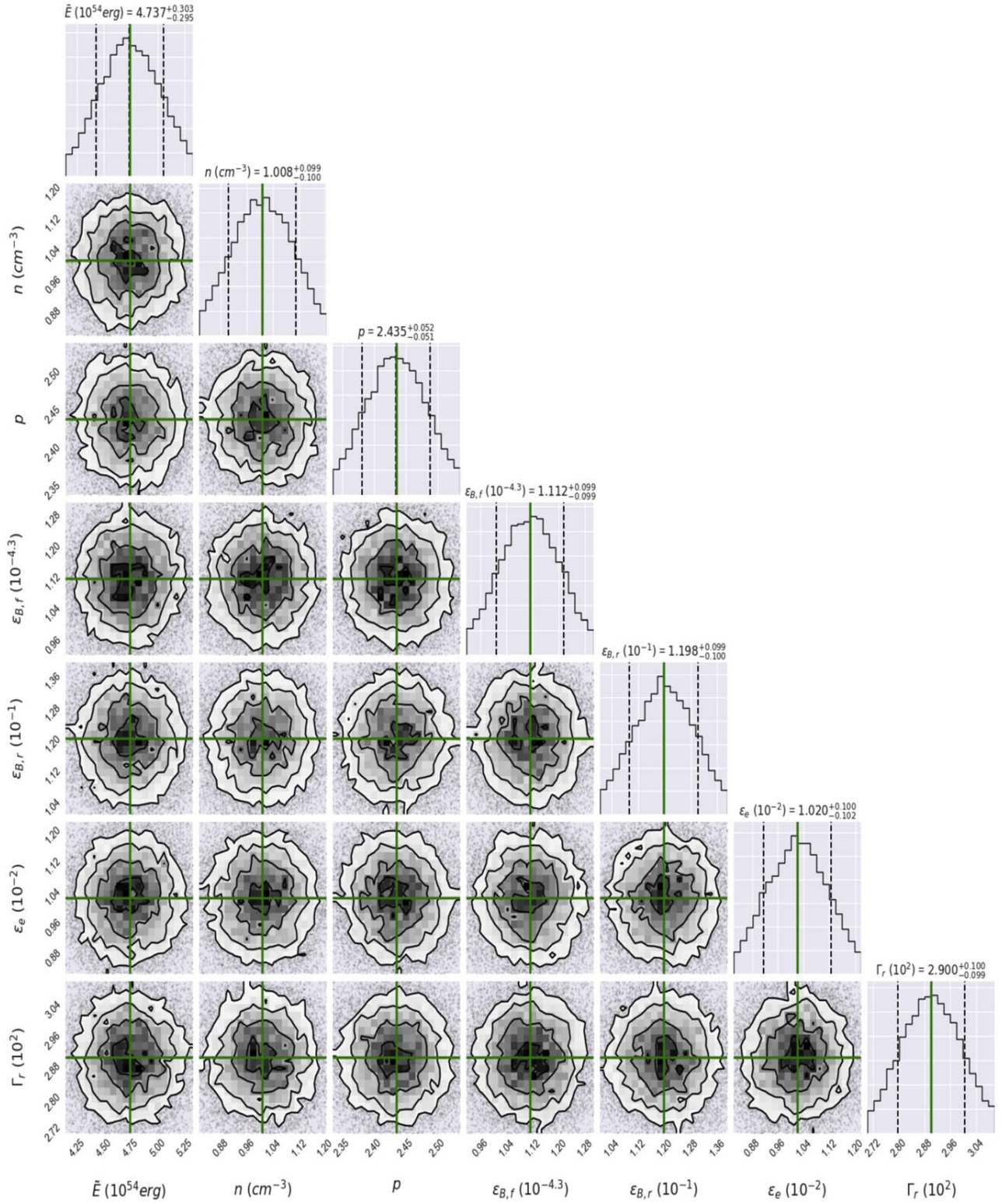
**Figure 6.** Same as Figure 5 but for the X-ray light curve at 10 keV. The best-fit values are shown in green and reported in column 3 of Table 3.

The temporal and spectral theoretical indexes obtained by the evolution of the standard synchrotron model in the homogeneous medium are reported in Table 2. Theoretical and observational spectral and temporal indexes are consistent for $p \approx 2.6 \pm 0.2$.

## 4. Discussion and Description of Radio Wavelengths and VHE Gamma-Rays

We have shown that the temporal and spectral analysis of the multiwavelength (LAT, X-rays, and optical bands) afterglow observed in GRB 180720B is consistent with the closure
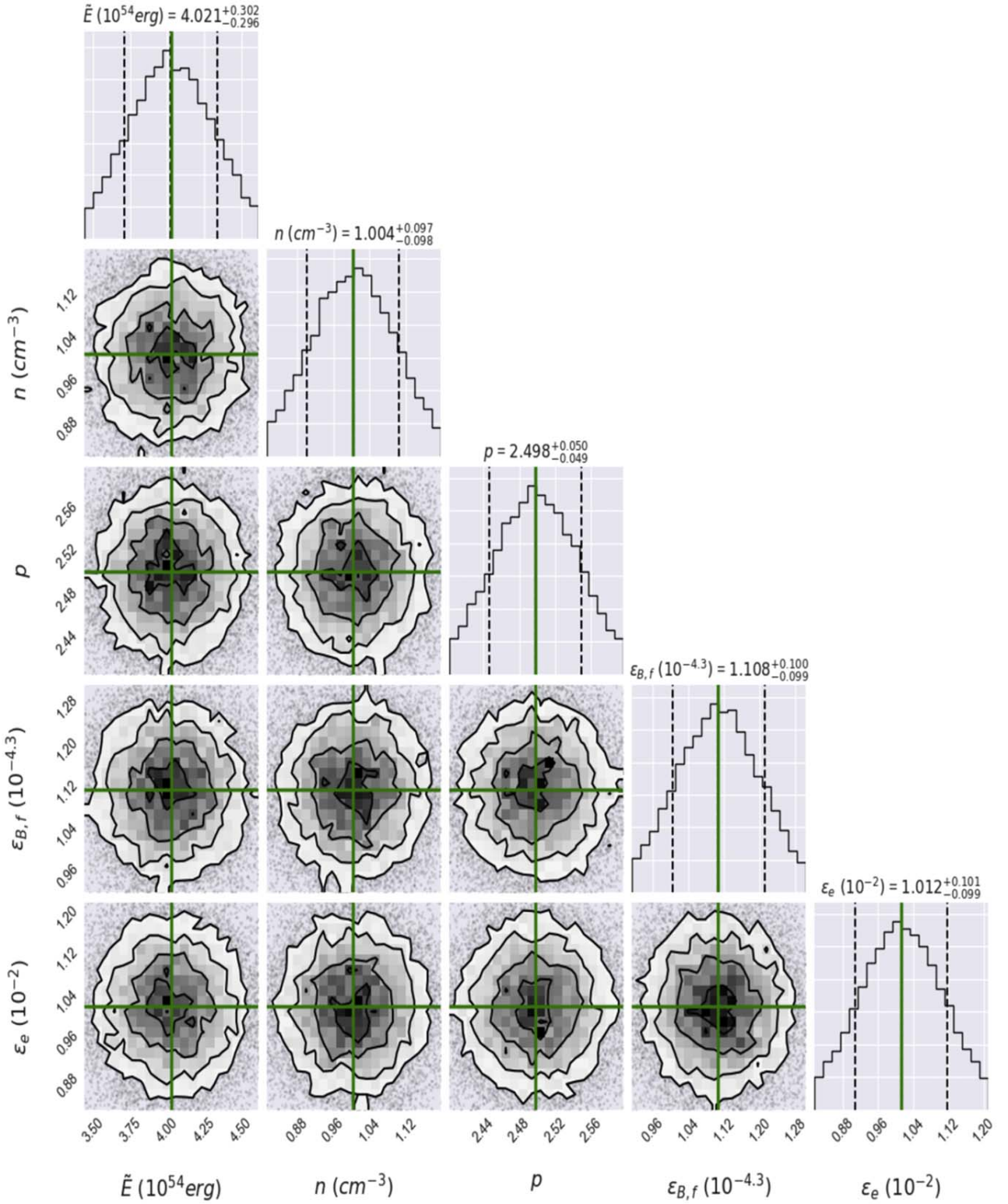
**Figure 7.** Same as Figure 5 but for the optical light curve at 1 eV. The best-fit values are shown in green and reported in column 4 of Table 3.

relations of the synchrotron forward-shock model evolving in a homogeneous medium. Additionally, we have shown that the X-ray flare is consistent with the SSC reverse-shock model evolving in the thin shell in a homogeneous medium. In order to describe the LAT, X-ray, and optical observations with our model, we have constrained the electron spectral index, the

microphysical parameters and the circumburst density using the Bayesian statistical technique based on the Markov chain Monte Carlo (MCMC) method (see Fraija et al. 2019b, 2019d). These parameters were found by normalizing the PL segments at $\epsilon_\gamma = 100\,\mathrm{MeV}$, 1 keV, and 1 eV for LAT, X-ray, and optical observations, respectively. We have used the synchrotron and

SSC light curves in the slow-cooling regime when the outflow is decelerated in a homogeneous medium and the reverse shock evolves in a thin shell. The values reported for GRB 180720B, such as the redshift $z = 0.65$ (Vreeswijk et al. 2018), the equivalent isotropic energy $3 \times 10^{53}$ erg, and the duration of the prompt emission $T_{90} = 50$ s (Roberts & Meegan 2018), were used. In order to compute the luminosity distance, the values of the cosmological parameters derived by Planck Collaboration et al. (2018) were used (Hubble constant $H_0 = (67.4 \pm 0.5)$ km s$^{-1}$ Mpc$^{-1}$ and the matter density parameter $\Omega_{\rm m} = 0.315 \pm 0.007$). The equivalent kinetic energy was obtained using the isotropic energy and the efficiency to convert the kinetic energy into photons (Beniamini et al. 2015).

The best-fit value of each parameter found with our MCMC code is shown with a green line in Figures 5–7 for LAT, X-ray, and optical observations, respectively. A total of 16,000 samples with 4000 tuning steps were run. The best-fit values for GRB 180720B are reported in Table 3. The obtained values are similar to those reported by other powerful GRBs (Ackermann et al. 2010, 2013a, 2014; Fraija 2015; Fraija et al. 2016a, 2016b, 2017a, 2019a). Given the values of the observed quantities and the best-fit values reported in Table 3, the results are discussed as follows.

### 4.1. Describing the Radio Emission

During the afterglow, the self-absorption energy break lies in the radio bands and falls into two groups depending on the regime (fast- or slow-cooling) of the electron energy distribution. For $\min\{\epsilon_{\rm a,f}^{\rm syn}, \epsilon_{\rm m,f}^{\rm syn}\} < \epsilon_{\rm c,f}^{\rm syn}$, the observed synchrotron radiation flux can be in the weak ($\epsilon_{\rm a,f}^{\rm syn} \leqslant \epsilon_\gamma \leqslant \epsilon_{\rm m,f}^{\rm syn}$) or strong ($\epsilon_{\rm m,f}^{\rm syn} \leqslant \epsilon_\gamma \leqslant \epsilon_{\rm a,f}^{\rm syn}$) absorption regime (e.g., see, Gao et al. 2013).

*Weak-absorption regime.* In this case the synchrotron spectrum in the radio bands can be written as

$$F_{\nu,f}^{\rm syn} = F_{\nu,\max}^{\rm syn} \begin{cases} \left(\frac{\epsilon_{\rm a,f}^{\rm syn}}{\epsilon_{\rm m,f}^{\rm syn}}\right)^{\frac{1}{3}} \left(\frac{\epsilon_\gamma}{\epsilon_{\rm a}^{\rm syn}}\right)^2, & \epsilon_\gamma < \epsilon_{\rm a,f}^{\rm syn}, \\ \left(\frac{\epsilon_\gamma}{\epsilon_{\rm m,f}^{\rm syn}}\right)^{\frac{1}{3}} & \epsilon_{\rm a,f}^{\rm syn} < \epsilon_\gamma < \epsilon_{\rm m,f}^{\rm syn}, \end{cases} \quad (1)$$

where the self-absorption energy break is

$$\epsilon_{\rm a,f}^{\rm syn} \propto (1+z)^{-\frac{8}{5}} \epsilon_{\rm e}^{-1} \, \epsilon_{\rm B,f}^{\frac{1}{5}} \Gamma^{\frac{8}{5}} \, n^{\frac{4}{5}} \, t^{\frac{3}{5}}. \quad (2)$$

From Equations (1) and (2), the radio light curve becomes $F_{\nu,f}^{\rm syn} \propto t^{\frac{1}{2}} \epsilon_\gamma^2$ for $\epsilon_\gamma < \epsilon_{\rm a,f}^{\rm syn}$ and $t^{\frac{1}{2}} \epsilon_\gamma^{\frac{1}{3}}$ for $\epsilon_{\rm a,f}^{\rm syn} < \epsilon_\gamma < \epsilon_{\rm m,f}^{\rm syn}$.[18]

*Strong-absorption regime.* In this case, the synchrotron spectrum in the radio bands is

$$F_{\nu,f}^{\rm syn} = F_{\nu,\max}^{\rm syn} \begin{cases} \left(\frac{\epsilon_{\rm m,f}^{\rm syn}}{\epsilon_{\rm a,f}^{\rm syn}}\right)^{\frac{p+4}{2}} \left(\frac{\epsilon_\gamma}{\epsilon_{\rm m,f}^{\rm syn}}\right)^2, & \epsilon_\gamma < \epsilon_{\rm m,f}^{\rm syn}, \\ \left(\frac{\epsilon_{\rm a,f}^{\rm syn}}{\epsilon_{\rm m,f}^{\rm syn}}\right)^{-\frac{p-1}{2}} \left(\frac{\epsilon_\gamma}{\epsilon_{\rm a,f}^{\rm syn}}\right)^{\frac{5}{2}} & \epsilon_{\rm m,f}^{\rm syn} < \epsilon_\gamma < \epsilon_{\rm a,f}^{\rm syn}, \end{cases} \quad (3)$$

where the self-absorption energy break in this case is

$$\epsilon_{\rm a,f}^{\rm syn} \propto (1+z)^{-\frac{p+6}{p+4}} \epsilon_{\rm e}^{-\frac{2(p-1)}{p+4}} \, \epsilon_{\rm B,f}^{\frac{p+2}{2(p+4)}} \Gamma^{\frac{4(p+2)}{p+4}} \, n^{\frac{p+6}{2(p+4)}} \, t^{\frac{2}{p+4}}. \quad (4)$$

From Equations (3) and 4, the radio light curve becomes $F_{\nu,f}^{\rm syn} \propto t^{\frac{1}{2}} \epsilon_\gamma^2$ for $\epsilon_\gamma < \epsilon_{\rm m,f}^{\rm syn}$ and $t^{\frac{5}{4}} \epsilon_\gamma^{\frac{5}{2}}$ for $\epsilon_{\rm m,f}^{\rm syn} < \epsilon_\gamma < \epsilon_{\rm a,f}^{\rm syn}$.

Taking into account the best-fit values reported in Table 3, the synchrotron energy breaks are $\epsilon_{\rm m,f}^{\rm syn} = 25.43$ GHz, $\epsilon_{\rm a,f}^{\rm syn} = 13.6$ GHz (weak absorption) and $\epsilon_{\rm a,f}^{\rm syn} = 2.4 \times 10^3$ GHz (strong absorption) at 1 day, and $\epsilon_{\rm m,f}^{\rm syn} = 0.8$ GHz, $\epsilon_{\rm a,f}^{\rm syn} = 13.6$ GHz (weak absorption) and $\epsilon_{\rm a,f}^{\rm syn} = 4.5 \times 10^2$ GHz (strong absorption) at 10 days. Clearly, the synchrotron spectrum lies in the regime $\epsilon_{\rm m,f}^{\rm syn} \leqslant \epsilon_\gamma \leqslant \epsilon_{\rm a,f}^{\rm syn}$ and radio observations are in the second PL segment.

Using the best-fit parameters obtained with our MCMC code, we describe the radio data points as shown in the right panel of Figure 4. In order to describe the radio data at 15.5 and 1.4 GHz with a PL, we multiply the radio data point at 1.4 GHz by 25 and we also normalize the synchrotron flux at the same radio band.

### 4.2. Describing the LAT Photons

Using the best-fit value of the homogeneous density found with our MCMC code. in Figure 8 we plot the evolution of the maximum photon energy radiated by synchrotron emission from the forward-shock region (red dashed line) and all individual photons with probabilities >90% of being associated with GRB 180720B and energies above $\gtrsim 100$ MeV. Photons with energies above the synchrotron limit are in gray and ones with energy below this limit are in black. The sensitivities of CTA and HESS-CT5 observatories at 75 and 80 GeV are shown as yellow and blue dashed lines, respectively (Piron 2016). The emission reported by the HESS Collaboration during the CTA symposium[19] is shown in green. Figure 8 shows that all photons cannot be interpreted in the standard synchrotron forward-shock model. Although this burst is a good candidate for accelerating particles up to very high energies and then producing TeV neutrinos, no neutrinos were spatially or temporally associated with this event. This negative result could be explained in terms of the low amount of baryon load in the outflow. In this case the production of VHE photons favors leptonic over hadronic models. Therefore, we propose that LAT photons above the synchrotron limit would be interpreted in the SSC framework. Note that LAT photons below the synchrotron limit (the red dashed line) could be explained in the standard synchrotron forward-shock model and beyond this limit the SSC model describes the LAT photons. For instance, a superposition of synchrotron and SSC emission originated in the forward-shock region could be invoked to interpret the LAT photons (e.g., see Beniamini et al. 2015).

The *Fermi*-LAT photon-flux light curve of GRB 180720B presents characteristics similar to other LAT-detected GRBs, such as GRB 080916C (Abdo et al. 2009b), GRB 090510 (Ackermann et al. 2010), GRB 090902B (Abdo et al. 2009a), GRB 090926A (Ackermann et al. 2011) GRB 110721A (Ackermann et al. 2013a), GRB 110731A (Ackermann et al. 2013a), GRB 130427A (Ackermann et al. 2014), GRB 160625B (Fraija et al. 2017c), and GRB 190114C (Fraija et al. 2019a), as shown in Figure 9. All of these GRBs exhibited VHE photons and emission lasting more than the prompt phase. This figure shows that during the prompt phase, the high-energy emission from GRB 180720B is weaker and during the afterglow it is stronger.
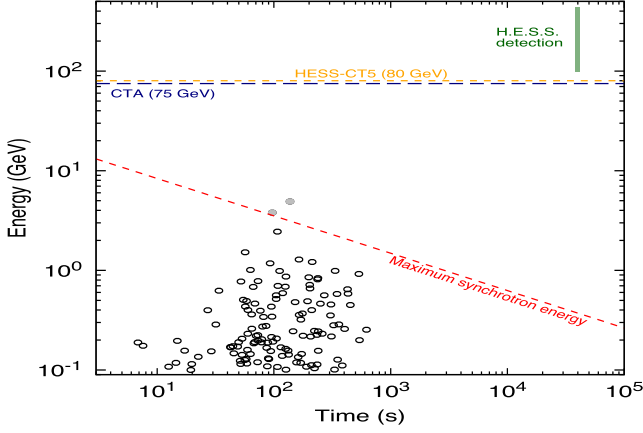
---

[18] We have used $\epsilon_{\rm m,f}^{\rm syn} \propto t^{-\frac{3}{2}}$ and $F_{\nu,\max} \propto t^0$ with the bulk Lorentz factor $\Gamma \propto t^{-\frac{3}{8}}$ (Sari et al. 1998).

[19] https://indico.cta-observatory.org/event/1946/timetable/

**Figure 8.** All the photons with energies >100 MeV and probabilities >90% of being associated with GRB 180720B. The red dashed line represents the maximum photon energies released by the synchrotron forward-shock model. Photons with energies above the synchrotron limit are in gray and those below it are in black. The sensitivities of CTA and HESS-CT5 observatories at 75 and 80 GeV are shown as yellow and blue dashed lines, respectively (Piron 2016).
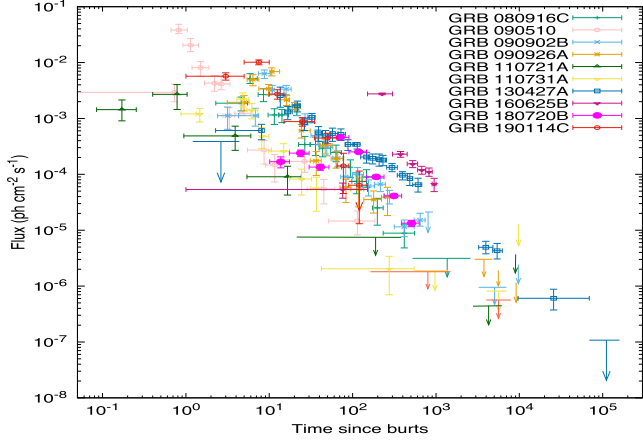


**Figure 9.** Comparison of the *Fermi*-LAT photon-flux light curve from GRB 180720B (blue circles) with other LAT-detected bursts. LAT data of energetic GRBs are taken from Ackermann et al. (2013a, 2013b, 2014) and Fraija et al. (2019a).

### 4.3. Production of VHE Gamma-Rays to Be Detected by GeV–TeV Observatories

The dynamics of the synchrotron forward-shock emission in a homogeneous medium have been widely explored (e.g., see, Sari et al. 1998). Synchrotron photons radiated in the forward shocks can be upscattered by the same electron population. The inverse Compton scattering model has been described in Panaitescu & Mészáros (2000) and Kumar & Piran (2000). Given the energy breaks, the maximum flux, the spectra, and the light curves of the synchrotron radiation, the SSC light curves for the fast-cooling and slow-cooling regimes become

$$F_{\nu,f}^{ssc} \propto \begin{cases} t^{\frac{1}{3}}\, \epsilon_\gamma^{\frac{1}{3}}, & \epsilon_\gamma < \epsilon_{c,f}^{ssc}, \\ t^{\frac{1}{8}}\, \epsilon_\gamma^{-\frac{1}{2}}, & \epsilon_{c,f}^{ssc} < \epsilon_\gamma < \epsilon_{m,f}^{ssc}, \\ t^{-\frac{9p-10}{8}}\, \epsilon_\gamma^{-\frac{p}{2}}, & \epsilon_{m,f}^{ssc} < \epsilon_\gamma, \end{cases} \quad (5)$$

and

$$F_{\nu,f}^{ssc} \propto \begin{cases} t\, \epsilon_\gamma^{\frac{1}{3}}, & \epsilon_\gamma < \epsilon_{m,f}^{ssc}, \\ t^{-\frac{9p-11}{8}}\, \epsilon_\gamma^{-\frac{p-1}{2}}, & \epsilon_{m,f}^{ssc} < \epsilon_\gamma < \epsilon_{c,f}^{ssc}, \\ t^{-\frac{9p-10}{8}}\, \epsilon_\gamma^{-\frac{p}{2}}, & \epsilon_{c,f}^{ssc} < \epsilon_\gamma, \end{cases} \quad (6)$$

respectively, where the SSC energy breaks are

$$\epsilon_{m,f}^{ssc} \propto (1 + z)^{\frac{5}{4}}\, \epsilon_e^4\, \epsilon_{B,f}^{\frac{1}{2}}\, n^{-\frac{1}{4}}\, E^{\frac{3}{4}}\, t^{-\frac{9}{4}}$$

$$\epsilon_{c,f}^{ssc} \propto (1 + z)^{-\frac{3}{4}}(1 + Y)^{-4}\, \epsilon_{B,f}^{-\frac{7}{2}}\, n^{-\frac{9}{4}}\, E^{-\frac{5}{4}}\, t^{-\frac{1}{4}}, \quad (7)$$

with $Y$ being the Compton parameter. In the Klein–Nishina regime the break energy is given by

$$E_c^{KN} \propto (1 + z)^{-1}\, (1 + Y)^{-1}\, \epsilon_{B,f}^{-1}\, n^{-\frac{2}{3}}\, \Gamma^{\frac{2}{3}}\, E^{-\frac{1}{3}}\, t^{-\frac{1}{4}}. \quad (8)$$

In this case the maximum flux emitted in this process is $F_{\nu,max}^{ssc} \propto (1 + z)^{\frac{3}{4}}\, \epsilon_{B,f}^{\frac{1}{2}}\, n^{\frac{5}{4}}\, d^{-2}\, E^{\frac{5}{4}}\, t^{\frac{1}{4}}$, where $d$ is the luminosity distance.

Given the best-fit parameters reported in Table 3, the SSC light curve at 100 GeV is plotted in Figure 4 (right). The break energy in the KN regime is 851.7 and 478.9 GeV at 1 and 10 hr, respectively, which is above the flux at 100 GeV. The characteristic and cutoff break energies are $4.4 \times 10^3$ and 24.7 eV, and 50.1 and 43.2 GeV at 1 and 10 hr, respectively, which indicates that at 100 GeV, the SSC emission is evolving in the third PL segment of the slow-cooling regime. The right panel in Figure 4 shows the SSC flux computed at 100 GeV with the parameters derived in our model using the multiwavelength observations of GRB 180720B. Our model explains the VHE emission announced by the HESS team during the high-energy emission at the CTA symposium.[20] Note that the SSC flux equations are degenerate in the parameter values such that for a distinct set of parameter values similar results could be obtained, as shown in Wang et al. (2019).

### 4.4. The Magnetic Microphysical Parameters

The best-fit parameters of the magnetic fields found in the forward- and reverse-shock regions are different. The parameter associated with the magnetic field in the reverse shock lies in the range of the expected values for the reverse shock to be formed and leads to an estimate of the magnetization parameter of $\sigma \simeq 0.4$. In the opposite situation (e.g., $\sigma \gg 1$), particle acceleration would hardly be efficient and the X-ray flare from the reverse shock would have been suppressed (Fan et al. 2004). Considering the microphysical parameter associated with the reverse-shock region, we found that the strength of the magnetic field in this region is stronger than the magnetic field in the forward-shock region ($\simeq 45$ times). This suggests that the jet composition of GRB 180720B could be Poynting-dominated. Zhang & Kobayashi (2005) described the emission generated in the reverse shock from an outflow with an arbitrary value of the magnetization parameter. They found that the Poynting energy is transferred to the medium only until the reverse shock has disappeared. Given the timescale of the reverse shock associated with the X-ray flare, the shallow decay segment observed in the X-ray light curve of GRB

---

[20] https://indico.cta-observatory.org/event/1946/timetable/

**Table 3**
Median Values of Parameters Found with Symmetrical Quantiles (15%, 50%, 85%)

| Parameters | Median | | |
| --- | --- | --- | --- |
| | LAT (100 MeV) | X-ray (1 keV) | Optical (1 eV) |
| $E(10^{54}$ erg) | $3.998^{+0.299}_{-0.301}$ | $4.737^{+0.303}_{-0.100}$ | $4.021^{+0.302}_{-0.296}$ |
| $n(\text{cm}^{-3})$ | $1.000^{+0.099}_{-0.098}$ | $1.008^{+0.099}_{-0.100}$ | $1.004^{+0.097}_{-0.098}$ |
| $\epsilon_{\text{B,f}}(10^{-4.3})$ | $1.101^{+0.100}_{-0.100}$ | $1.112^{+0.099}_{-0.099}$ | $1.108^{+0.100}_{-0.099}$ |
| $\epsilon_{\text{e}}(10^{-2})$ | $1.000^{+0.102}_{-0.100}$ | $1.020^{+0.100}_{-0.102}$ | $1.012^{+0.101}_{-0.099}$ |
| $\epsilon_{\text{B,r}}(10^{-1})$ | ⋯ | $1.200^{+0.099}_{-0.098}$ | ⋯ |
| $p$ | $2.500^{+0.049}_{-0.050}$ | $2.435^{+0.052}_{-0.051}$ | $2.498^{+0.050}_{-0.049}$ |
| $\Gamma_r (10^2)$ | ⋯ | $2.900^{+0.100}_{-0.099}$ | ⋯ |

**Note.** The external shock model was used to constrain the values of the parameters.

180720B could be interpreted as the late transfer of the Poynting energy to the homogeneous medium. These results agree with some authors who claim that Poynting flux-dominated models with a moderate degree of magnetization can explain the LAT observations in powerful GRBs (Zhang & Yan 2011; Uhm & Zhang 2014), and in particular the properties exhibited in the light curve of GRB 180720B.

Using the synchrotron reverse-shock model (Kobayashi 2000; Kobayashi & Zhang 2003) and the best-fit values (see Table 3), the self-absorption, the characteristic and cutoff energy breaks of $3.4 \times 10^{-7}$ eV, 0.4 eV and $7.3 \times 10^{-4}$ eV, respectively, indicate that the synchrotron radiation evolves in the fast-cooling regime. Given that the self-absorption energy break is smaller than the cutoff and characteristic breaks, the synchrotron emission originated from the reverse-shock region lies in the weak self-absorption regime, hence a thermal component in this region cannot be expected (Kobayashi & Zhang 2003).

The spectral and temporal analysis of the forward and reverse shocks at the beginning of the afterglow phase, together with the best-fit value of the circumburst density, lead to an estimate of the initial bulk Lorentz factor, the critical Lorentz factor, and the shock crossing time $\Gamma \simeq 200$, $\Gamma_c \simeq 330$ and $t_d \simeq 100$ s, respectively. These values are consistent with the evolution of the reverse shock in the thin shell case and the duration of the X-ray flare.

## 5. Conclusions

GRB 180720B is a long burst detected and followed up by a large number of observatories at multiple wavelengths that range from radio bands to GeV gamma-rays. The simultaneous GeV, gamma-ray, X-ray, optical, and radio bands are presented over multiple observational periods beginning just after the BAT trigger time and extending to more than 33 days.

The GBM light curve and spectrum were analyzed using the Band and Comptonized functions in the energy range of 10–1000 keV during the time interval [0.000, 60,416 s]. The light curve formed from a bright FRED-like peak and followed by two significant peaks is consistent with the prompt phase. The *Fermi*-LAT light curve and spectrum were derived around the reported position of GRB 180720B. We have shown that the photon-flux light curve recently reported in the second GRB catalog (Ajello et al. 2019) is consistent with the one obtained in this work. The highest-energy photons with energies of 3.8 and 4.9 GeV detected by the LAT instrument

at 97 and 138 s after the GBM trigger, respectively, can hardly be interpreted in the standard synchrotron forward-shock model. Photons below the synchrotron limit can be explained well by synchrotron emission from the forward shock. The temporal and spectral indexes of the *Fermi*-LAT observations are compatible and consistent with the synchrotron forward-shock afterglow.

The temporal and spectral analysis of the X-ray observations suggested four different behaviors, whereas the optical *R*-band observations suggested just one. We find that the X-ray flare is most consistently interpreted with the SSC model from the reverse-shock region evolving in a thin shell. This model can explain the timescales, the maximum observed flux, and the rise and fall of temporal PL indexes. The temporal decay index in the range between 0.2 and 0.8, as found in a large fraction of bursts with no variation of the spectral index during the transition, is consistent with the shallow plateau phase (e.g., see Vedrenne & Atteia 2009). The temporal PL index after the break is consistent with the normal decay in a uniform IMS-like medium. The chromatic break at $2 \times 10^5$ s observed in the X-ray but not in the optical light curve is consistent with the fact that the cooling energy break of the synchrotron model becomes less than the X-ray observations at 1 keV.

Temporal and spectral PL indexes observed in the LAT, X-ray, and optical bands during different intervals favor the model of an afterglow in a homogeneous medium. The best-fit parameters derived with our MCMC code indicate that the outflow is endowed with magnetic fields, the radio data are in the self-absorption regime, and the LAT photons above the synchrotron limit are consistent with SSC forward-shock model. The SSC forward-shock model with our parameters can explain the LAT photons beyond the synchrotron limit, as well as the emission reported by the HESS Collaboration. The X-ray flare and the "plateau" phase with their corresponding timescales could be explained by the late transfer of the magnetic energy into the uniform medium, emphasizing that the outflow is magnetized.

### ORCID iDs

N. Fraija ⓘ https://orcid.org/0000-0002-0173-6453
R. L. Becerra ⓘ https://orcid.org/0000-0002-0216-3415

### References

Abdo, A. A., Ackermann, M., Ajello, M., et al. 2009a, ApJL, 706, L138
Abdo, A. A., Ackermann, M., Arimoto, M., et al. 2009b, Sci, 323, 1688
Ackermann, M., Ajello, M., Asano, K., et al. 2011, ApJ, 729, 114
Ackermann, M., Ajello, M., Asano, K., et al. 2013a, ApJ, 763, 71
Ackermann, M., Ajello, M., Asano, K., et al. 2013b, ApJS, 209, 11
Ackermann, M., Ajello, M., Asano, K., et al. 2014, Sci, 343, 42
Ackermann, M., Asano, K., Atwood, W. B., et al. 2010, ApJ, 716, 1178
Ajello, M., Arimoto, M., Axelsson, M., et al. 2019, ApJ, 878, 52
Alvarez-Muñiz, J., Halzen, F., & Hooper, D. 2004, ApJL, 604, L85

Arnaud, K. A. 1996, in ASP Conf. Ser, 101, Astronomical Data Analysis Software and Systems V, ed. G. H. Jacoby & J. Barnes (San Francisco, CA: ASP), 17
Barniol Duran, R., & Kumar, P. 2011, MNRAS, 412, 522
Barthelmy, S. D., Cummings, J. R., Krimm, H. A., et al. 2018, GCN, 22998, 1
Becerra, R. L., Dichiara, S., Watson, A. M., et al. 2019a, arXiv:1904.05987
Becerra, R. L., Watson, A. M., Fraija, N., et al. 2019b, ApJ, 872, 118
Becerra, R. L., Watson, A. M., Lee, W. H., et al. 2017, ApJ, 837, 116
Bellm, E. C., & Cenko, S. B. 2018, GCN, 23041, 1
Beniamini, P., Nava, L., Duran, R. B., & Piran, T. 2015, MNRAS, 454, 1073
Bissaldi, E., & Racusin, J. L. 2018, GCN, 22980, 1
Bolmer, J., & Shady, P. 2019, GCN, 23702, 1
Brun, R., & Rademakers, F. 1997, NIMPA, 389, 81
Chandra, P., Nayana, A. J., Bhattacharya, D., Cenko, S. B., & Corsi, A. 2018, GCN, 23073
Cherry, M. L., Yoshida, A., Sakamoto, T., et al. 2018, GCN, 23042, 1
Covino, S., & Fugazza, D. 2018, GCN, 23021, 1
Crouzet, N., & Malesani, D. B. 2018, GCN, 22988, 1
Evans, P. A., Willingale, R., Osborne, J. P., et al. 2010, A&A, 519, A102
Fan, Y. Z., Wei, D. M., & Wang, C. F. 2004, A&A, 424, 477
Fraija, N. 2014, MNRAS, 437, 2187
Fraija, N. 2015, ApJ, 804, 105
Fraija, N., Barniol Duran, R., Diachiara, S., & Beniamini, P. 2019c, ApJ, 883, 162
Fraija, N., Dichiara, S., Pedreira, A. C. C. d. E. S., et al. 2019a, ApJ, 879, 26
Fraija, N., González, M. M., & Lee, W. H. 2012, ApJ, 751, 33
Fraija, N., Lee, W., & Veres, P. 2016a, ApJ, 818, 190
Fraija, N., Lee, W. H., Araya, M., et al. 2017a, ApJ, 848, 94
Fraija, N., Lee, W. H., Veres, P., & Barniol Duran, R. 2016b, ApJ, 831, 22
Fraija, N., Lopez-Camara, D., Pedreira, A. C., et al. 2019d, arXiv:1904.07732
Fraija, N., Pedreira, A. C. C. d. E. S., & Veres, P. 2019b, ApJ, 871, 200
Fraija, N., & Veres, P. 2018, ApJ, 859, 70
Fraija, N., Veres, P., Colle, F. De., et al. 2017b, arXiv:1710.08514
Fraija, N., Veres, P., Zhang, B. B., et al. 2017c, ApJ, 848, 15
Frederiks, D., Golenetskii, S., Aptekar, R., et al. 2018, GCN, 23011, 1
Fukugita, M., Ichikawa, T., Gunn, J. E., et al. 1996, AJ, 111, 1748
Gao, H., Lei, W.-H., Zou, Y.-C., Wu, X.-F., & Zhang, B. 2013, NewAR, 57, 141
Horiuchi, T., Hanayama, H., Honma, M., et al. 2018, GCN, 23004, 1
Itoh, R., Murata, K. L., Tachibana, Y., et al. 2018, GCN, 22983, 1
Izzo, L., Kann, D. A., de Ugarte Postigo, A., et al. 2018, GCN, 23040, 1
Jelinek, M., Strobl, J., Hudec, R., & Polasek, C. 2018, GCN, 23024, 1
Klebesadel, R. W., Strong, I. B., & Olson, R. A. 1973, ApJL, 182, L85

Kobayashi, S. 2000, ApJ, 545, 807
Kobayashi, S., & Zhang, B. 2003, ApJ, 597, 455
Kobayashi, S., & Zhang, B. 2007, ApJ, 655, 973
Kobayashi, S., Zhang, B., Mészáros, P., & Burrows, D. 2007, ApJ, 655, 391
Kumar, P., & Panaitescu, A. 2000, ApJL, 541, L51
Kumar, P., & Piran, T. 2000, ApJ, 532, 286
Kumar, P., & Zhang, B. 2015, PhR, 561, 1
Lipunov, V., Gorbovskoy, E., Tiurina, N., et al. 2018, GCN, 23023, 1
Martone, R., Guidorzi, C., Kobayashi, S., et al. 2018, GCN, 22976, 1
Mészáros, P., & Rees, M. J. 1997, ApJ, 476, 232
Mészáros, P., & Rees, M. J. 2000, ApJL, 541, L5
Negoro, H., Tanimoto, A., Nakajima, M., et al. 2018, GCN, 22993, 1
Nousek, J. A., Kouveliotou, C., Grupe, D., et al. 2006, ApJ, 642, 389
Palmer, D., Siegel, M. H., Burrows, D. N., et al. 2018, GCN, 22973, 1
Panaitescu, A., & Mészáros, P. 2000, ApJL, 544, L17
Piran, T., & Nakar, E. 2010, ApJL, 718, L63
Piron, F. 2016, CRPhy, 17, 617
Planck Collaboration, Aghanim, N., Akrami, Y., et al. 2018, arXiv:1807.06209
Rees, M. J., & Meszaros, P. 1992, MNRAS, 258, 41P
Rees, M. J., & Meszaros, P. 1994, ApJL, 430, L93
Reva, I., Pozanenko, A., Volnova, A., et al. 2018, GCN, 22979, 1
Roberts, O. J., & Meegan, C. 2018, GCN, 22981, 1
Sari, R., & Piran, T. 1997, ApJ, 485, 270
Sari, R., Piran, T., & Narayan, R. 1998, ApJL, 497, L17
Sasada, M., Nakaoka, T., Kawabata, M., et al. 2018, GCN, 22977, 1
Schmalz, S., Graziani, F., Pozanenko, A., et al. 2018, GCN, 23020, 1
Sfaradi, I., Bright, J., Horesh, A., et al. 2018, GCN, 23037, 1
Uhm, Z. L., & Zhang, B. 2014, NatPh, 10, 351
Vedrenne, G., & Atteia, J.-L. 2009, Gamma-Ray Bursts: The Brightest Explosions in the Universe (Springer: Berlin)
Vreeswijk, P. M., Kann, D. A., Heintz, K. E., et al. 2018, GCN, 22996, 1
Wang, X.-Y., Liu, R.-Y., Zhang, H.-M., Xi, S.-Q., & Zhang, B. 2019, arXiv:1905.11312
Watson, A. M., Butler, N., Becerra, R. L., et al. 2018, GCN, 23017, 1
Zhang, B., Fan, Y. Z., Dyks, J., et al. 2006, ApJ, 642, 354
Zhang, B., & Kobayashi, S. 2005, ApJ, 628, 315
Zhang, B., Kobayashi, S., & Mészáros, P. 2003, ApJ, 595, 950
Zhang, B., & Mészáros, P. 2001, ApJ, 559, 110
Zhang, B., & Mészáros, P. 2004, IJMPA, 19, 2385
Zhang, B., & Yan, H. 2011, ApJ, 726, 90
Zheng, W., & Filippenko, A. V. 2018, GCN, 23033, 1

# Exploring the Early Afterglow Polarization of GRB 190829A

A. C. CALIGULA DO E. S. PEDREIRA,[1] N. FRAIJA,[1] S. DICHIARA,[2] P. VERES,[3] M.G. DAINOTTI,[4,5,6,7] A. GALVAN-GAMEZ,[1] R. L. BECERRA,[8] AND B. BETANCOURT KAMENETSKAIA[9,10]

[1]*Instituto de Astronomía, Universidad Nacional Autónoma de México, Circuito Exterior, C.U., A. Postal 70-264, 04510, CDMX, Mexico*
[2]*Department of Astronomy and Astrophysics, The Pennsylvania State University, 525 Davey Lab, University Park, PA 16802, USA*
[3]*Center for Space Plasma and Aeronomic Research (CSPAR), University of Alabama in Huntsville, Huntsville, AL 35899, USA*
[4]*Division of Science, National Astronomical Observatory of Japan, 2-21-1 Osawa, Mitaka, Tokyo 181-8588, Japan*
[5]*The Graduate University for Advanced Studies (SOKENDAI), 2-21-1 Osawa, Mitaka, Tokyo 181-8588, Japan*
[6]*Space Science Institute, 4750 Walnut Street, Boulder, CO 80301, USA*
[7]*SLAC National Accelerator Laboratory, 2575 Sand Hill Road, Menlo Park, CA 94025, USA*
[8]*Instituto de Ciencias Nucleares, Universidad Nacional Autónoma de México, Apartado Postal 70-264, 04510 México, CDMX, Mexico*
[9]*TUM Physics Department, Technical University of Munich, James-Franck-Str, 85748 Garching, Germany*
[10]*Max-Planck-Institut für Physik (Werner-Heisenberg-Institut), Föhringer Ring 6, 80805 Munich, Germany*

## ABSTRACT

The GRB 190829A has been widely studied due to its nature and the high energy emission presented. Due to the detection of a very-high-energy component by the High Energy Stereoscopic System and the event's atypically middling luminosity, it has been categorized in a select, limited group of bursts bordering classic GRBs and nearby sub-energetic events. Given the range of models utilized to adequately characterize the afterglow of this burst, it has proven challenging to identify the most probable explanation. Nevertheless, the detection of polarization data provided by the MASTER collaboration has added a new aspect to GRB 190829A that permits us to attempt to explore this degeneracy. In this paper, we present a polarization model coupled with a synchrotron forward-shock model – a component in all models used to describe GRB 190829A's afterglow – in order to fit the polarization's temporal evolution with the existing upper limits ($\Pi < 6\%$). We find that the polarization generated from an on-axis emission is favored for strongly anisotropic magnetic field ratios, while an off-axis scenario cannot be fully ruled out when a more isotropic framework is taken into account.

*Keywords:* polarization – gamma-ray burst: individual: GRB 190829A – acceleration of particles – magnetic fields

## 1. INTRODUCTION

GRBs (gamma-ray bursts) are among the brightest phenomena in the universe. They are originated when massive stars die (Woosley 1993; Paczyński 1998; Woosley & Bloom 2006; Cano et al. 2017) or two compact objects, such as neutron stars (NSs; Duncan & Thompson 1992; Usov 1992; Thompson 1994; Eichler et al. 1989; Metzger et al. 2011) and a NS - black hole (BH, Narayan et al. 1992), merge. Long GRBs (lGRBs) and short GRBs (sGRBs), usually associated with the dying of massive stars and a merging of compact objects, are commonly classified based on their duration:[1] $T_{90} \leq 2$ s or $T_{90} \geq 2$ s,[2] respectively (Mazets et al.

1981; Kouveliotou et al. 1993). GRBs are studied according to their phenomenology detected during the early and late temporal phases. From hard X-rays to $\geq 100$ MeV *gamma*-rays, the early and main episode known as the "prompt emission" is detected and explained by interactions with internal shells of material launched by a central engine at varying velocities and therefore, at different Lorentz factors (Rees & Meszaros 1994; Paczynski & Xu 1994), the photospheric emission (Thompson et al. 2007; Mizuta et al. 2011; Lazzati et al. 2013) or discharges from a Poynting-flux dominated outflow (Giannios 2008; Zhang & Yan 2011; Kumar & Crumley 2015; Beniamini & Granot 2016). The long-lasting multi-wavelength emission observed in $\gamma$-rays, X-rays, optical, and radio is known as "afterglow" (e.g., Costa et al. 1997; van Paradijs et al. 1997; Piro et al. 1998; Sari et al. 1998; Granot & Sari 2002; Gehrels et al. 2009; Wang et al. 2015). It is often modelled with synchrotron radiation occurring when

---

[1] For a debate of controversial situations, see Kann et al. (2011); Becerra et al. (2019).

[2] $T_{90}$ is the time over which a GRB releases from 5% to 95% of the total measured counts.

the relativistic outflow is decelerated by an external medium, and a significant portion of its energy is transferred to it (e.g., see Sari et al. 1998).

The synchrotron radiation produced at the afterglow is typically explored in a forward-shock (FS) scenario, and this mechanism is contingent on the existence of magnetic fields in the emission zone. The origin of magnetic fields in GRBs is still a topic of discussion. Magnetic fields can be advected from the burst's source (Lyutikov & Blandford 2003; Sironi & Spitkovsky 2011), be generated from compression of an existing interstellar medium (ISM) magnetic field (Laing 1980; Teboul & Shaviv 2021), from shock-generated plasma instabilities (Weibel 1959; Medvedev & Loeb 1999), and even by magnetic reconnection in Poyinting-flux dominated outflows (Zhang & Yan 2011). Probing these fields, and their originating sources, alongside other properties of GRBs, is a challenging task that requires multiple directions of theoretical considerations and observational data. One way is exploring the polarization characteristics of an observed emission. As the polarization relies on the configuration of the magnetic field, it analysis allow us to look into their configurations and, therefore, their origins.

Several authors have implemented polarization models in order to acquire source-related information (e.g., see Granot & Königl 2003; Lyutikov et al. 2003; Nakar et al. 2003; Rossi et al. 2004; Gill et al. 2020; Stringer & Lazzati 2020; Teboul & Shaviv 2021; Shrestha et al. 2022). Unfortunately, despite the number of GRB observations, collecting polarization data remains being a challenge. Nevertheless, afterglow polarization measurements have been obtained for several GRBs at this point: at the early afterglow phase, the observations of GRB 090102 ($\Pi = 10.2 \pm 1.3\%$, Steele et al. (2009)), GRB 120308A ($\Pi = 28 \pm 4\%$, Mundell et al. (2013)) and the upper limits of GRB 190829A ($\Pi < 6\%$, Dichiara et al. (2022)) were obtained; examples at the late afterglow include GRB 191221B ($\Pi = 1.2\%$, Buckley et al. 2021), GRB 190114C ($\Pi = 0.8 \pm 0.13\%$; Laskar et al. 2019) on the radio band, and the upper limits of GRB 991216 (with $\Pi < 7\%$; Granot & Taylor 2005) and GRB 170817A (with $\Pi < 12\%$, on the 2.8 GHz radio band Corsi et al. 2018). Furthermore, several global collaborations like the POLAR project (Orsi & Polar Collaboration 2011), the Multicolour OPTimised Optical Polarimeter (MOPTOP; Shrestha et al. 2020), and the MASTER project (Lipunov et al. 2019), which are underway, or in preparation phases, could provide future observations and the much-needed polarization data of different GRB epochs.

In this work, we calculate the temporal evolution of the expected polarization for GRB 190829A in a synchrotron FS scenario, proven to allow for analysis of GRB 190829A's afterglow in terms of the physical parameters of the system. We use the available polarimetric upper limits from Dichiara et al. (2022) to test the parameters and models required to

explain the multi-wavelength afterglow observations of GRB 190829A. The paper is structured as follows; In Section 2, we briefly introduce the polarization model used in this paper in the synchrotron FS framework during the off-axis phase. In Section 3, we apply as particular case our polarization model to GRB 190829A using the best-fit parameters obtained in different scenarios. In Section 4, we discuss the results. Finally, in Section 5, we offer a brief summary and our concluding remarks.

## 2. LINEAR POLARIZATION FROM OFF-AXIS SYNCHROTRON AFTERGLOW

### 2.1. *Linear Polarization model*

Polarization is commonly attributed to synchrotron radiation behind shock waves. This makes it dependent on the arrangement of the magnetic field and the geometry of the shock, as they determine the degree of polarization ($\Pi$) in each position as well the integrated value throughout the entire image (Gill et al. 2020). The Stokes parameters ($I$, $Q$, $U$, and $V$) set the method for calculating polarization, and only linear polarization is generally taken into account (see Nava et al. 2016, for an analysis of circular polarization in GRBs). Hereinafter, quantities in the observer and comoving frames will be referred to as unprimed and primed, respectively. The linear polarization Stokes parameters are written as:

$$V = 0, \qquad \theta_p = \frac{1}{2}\arctan\frac{U}{Q},$$
$$\frac{U}{I} = \Pi'\sin 2\theta_p, \qquad \frac{Q}{I} = \Pi'\cos 2\theta_p. \qquad (1)$$

The sum over the flux returns the measured Stokes parameters (Granot 2003), so:

$$\frac{U}{I} = \frac{\int dF_\nu \Pi' \sin 2\theta_p}{\int dF_\nu}, \qquad \frac{Q}{I} = \frac{\int dF_\nu \Pi' \cos 2\theta_p}{\int dF_\nu}, \qquad (2)$$

$$\Pi = \frac{\sqrt{Q^2 + U^2}}{I}. \qquad (3)$$

Considering $dF_\nu \propto \delta_D^3 L'_{\nu'} d\Omega$ – where $L'_{\nu'}$ is the spectral luminosity, $\delta_D$ is the Doppler factor and $d\Omega$ is the element of solid angle of the fluid element in relation to the source – the factors regarding the geometry of the magnetic field and outflow can be introduced by (Rybicki & Lightman 1979) are:

$$L'_{\nu'} \propto (\nu')^{-\alpha}(\sin \chi')^\epsilon r^m \propto (\nu')^{-\alpha}(1 - \hat{n}' \cdot \hat{B}')^{\epsilon/2} r^m. \quad (4)$$

The term $\epsilon = 1 + \alpha$, with $\alpha$ the spectral index, which can be obtained with the electron power-law index $p$; i.e., $\alpha = (p-1)/2$ (Granot 2003). Throughout the text, we also assume the index $m = 0$, i.e., a radially constant emissivity.

The angle between the local magnetic field and the direction of motion of the particle, $\chi$, is also the pitch angle due to

the highly beamed effect of the synchrotron emission. The geometrical considerations of polarization can then be taken by averaging this factor over the local probability distribution of the magnetic field (Gill et al. 2020),

$$\Lambda = \left\langle (1 - \hat{n}' \cdot \hat{B}')^{\epsilon/2} \right\rangle. \qquad (5)$$

Using the Lorentz transformation of the unit vector $\hat{n}$ or a prescription of $\hat{B}$, it is possible to obtain $\Lambda$ in terms of different magnetic field configurations and minimize the number of parameters required to obtain the polarization degree (Lyutikov et al. 2003; Granot 2003; Granot & Taylor 2005; Gill et al. 2020):

$$\Lambda_\perp \approx \left\langle \left[ \left( \frac{1 - \tilde{\xi}}{1 + \tilde{\xi}} \right) \cos^2 \varphi_B + \sin^2 \varphi_B \right]^{\epsilon/2} \right\rangle_{\varphi_B}, \qquad (6)$$

$$\Lambda_\parallel \approx \left[ \frac{\sqrt{4\tilde{\xi}}}{1 + \tilde{\xi}} \right]^\epsilon, \qquad (7)$$

$$\Lambda_{tor} \approx \left[ \left( \frac{1 - \tilde{\xi}}{1 + \tilde{\xi}} \right) + \frac{4\tilde{\xi}}{(1 + \tilde{\xi})^2} \frac{(a + \cos \tilde{\varphi})^2}{1 + a^2 + 2a \cos \tilde{\varphi}} \right]^{\epsilon/2}, \qquad (8)$$

where $\varphi_B$ is the azimuthal angle of the magnetic field measured from a reference point; $\tilde{\xi} \equiv (\Gamma\tilde{\theta})^2$, taking in consideration the approximations of $\tilde{\mu} = \cos\tilde{\theta} \approx 1 - \tilde{\theta}^2/2$ and $\beta \approx 1 - 1/2\Gamma^2$, which leads to $\delta_D \approx \frac{2\Gamma}{1+\tilde{\xi}}$; and $a \equiv \tilde{\theta}/\theta_{obs}$, where $\tilde{\theta}$ is the polar angle measured from the Line of Sight (LOS), $\Gamma$ is the bulk Lorentz factor, and $\beta$, is the velocity of the material in terms of the speed of light.

The uncertainty regarding the present magnetic field configuration in the region of emission requires the exploration of multiple configurations, as well as consider the relevance of magnetic field geometry regarding the polarization degree evolution. For the early afterglow, three of the most suitable configurations are: a random perpendicular configuration – where the anisotropy factor $b \equiv \frac{2\langle B_\parallel^2 \rangle}{\langle B_\perp^2 \rangle} = 0$ – confined to the shock plane; an ordered configuration parallel to the velocity vector, where $b \to \infty$; and an ordered toroidal magnetic field configuration arising from an axisymmetric field configuration with a poloidal ($B_p \propto r^{-2}$) and toroidal component ($B_\phi \propto r^{-1}$). More complex configurations with multi-component, where the anisotropy is more generalized, magnetic fields have been explored (Corsi et al. 2018; Stringer & Lazzati 2020; Gill & Granot 2020; Teboul & Shaviv 2021), as it is warranted and needed, however, for the purposes of this paper we limit ourselves to the three following cases.

*Random magnetic field – Perpendicular ($B_\perp$, $b = 0$).* —In this scenario, the symmetry of the random magnetic field configuration, perpendicular to the shock plane, causes the disappearance of the polarization over the image if the beaming cone is wholly contained within the jet aperture or if it is seen along the axis ($\theta_{obs} = 0$). To break the symmetry, the jet must be viewed close to its edge ($q \equiv \frac{\theta_{obs}}{\theta_j} \gtrsim 1 + \xi_j^{-1/2}$), where missing emission (from $\theta > \theta_j$) results only in partial cancellation (Waxman 2003). The equation necessary to calculate this polarization is explicitly laid out as Eq. 5 in Granot (2003).

*Ordered magnetic field – Parallel ($B_\parallel$, $b \to \infty$).* —For the ordered magnetic field, a configuration parallel to the velocity vector, the same symmetry observations hold true and the calculation follows Granot (2003); Gill et al. (2020), with $\Lambda(\tilde{\xi}) = \Lambda_\parallel$ from Eq. 7.

*Ordered magnetic field – Toroidal ($B_{tor}$).* —For the ordered magnetic field in a toroidal configuration, the same symmetry concerns are maintained. The calculation follows Granot & Taylor (2005); Gill et al. (2020), with $\Lambda(\tilde{\xi}) = \Lambda_{tor}$ from Eq. 8.

By substituting the following integration limits:

$$\cos\psi(\tilde{\xi}) = \frac{(1-q)^2 \xi_j - \tilde{\xi}}{2q\sqrt{\xi_j\tilde{\xi}}}, \qquad (9)$$

$$\xi_j = (\Gamma\theta_j)^2, \qquad \xi_\pm = (1 \pm q)^2 \xi_j, \qquad (10)$$

with an appropriate prescription of the bulk Lorentz factor $\Gamma(t)$, the evolution of the opening angle of the jet $\theta_j(t)$, and the parameters required to describe these expressions, we can obtain the temporal evolution of polarization.

### 2.2. *Synchrotron off-axis afterglow scenario: An homogeneous case*

We assume an adiabatic evolution of the forward shock in a homogeneous medium $n$ with an isotropic equivalent-kinetic energy $E = \frac{\Omega}{3} r^3 m_p c^2 n \Gamma^2$ (Blandford-McKee solution; Blandford & McKee 1976) and a radial distance $r = c\beta t / [(1 + z)(1 - \beta\mu)]$. Then, the evolution of the bulk Lorentz factor is given by:

$$\Gamma = \left( \frac{3}{4\pi m_p c^5} \right)^{\frac{1}{2}} (1 + z)^{\frac{3}{2}} (1 - \beta \cos \Delta\theta)^{\frac{3}{2}} n^{-\frac{1}{2}} E^{\frac{1}{2}} t^{-\frac{3}{2}} (11)$$

with $\beta = \sqrt{\Gamma^2 - 1}/\Gamma$, $\Delta\theta = \theta_{obs} - \theta_j$, $\Omega$ is the solid angle, $m_p$ is the proton mass and $c$ is the speed of light. In forward-shock models, accelerated electrons are described by taking into account their Lorentz factors ($\gamma_e$) and the electron power index $p$. This leads to a distribution of the form $N(\gamma_e) d\gamma_e \propto \gamma_e^{-p} d\gamma_e$ for $\gamma_m \leq \gamma_e$, where $\gamma_m = m_p/m_e g(p) \varepsilon_e (\Gamma - 1) \zeta_e^{-1}$ is the minimum electron Lorentz factor with $m_e$ the electron mass, $\varepsilon_e$ the fraction of energy given to accelerate electrons, $\zeta_e$ the fraction of electrons that were accelerated by the shock front (Fan & Piran 2006) and $g(p) = \frac{p-2}{p-1}$. The comoving

magnetic field strength in the blast wave can be expressed as $B'^2/(8\pi) = \varepsilon_B e$, where knowledge of the energy density $e = [(\hat{\gamma}\Gamma+1)/(\hat{\gamma}-1)](\Gamma-1)nm_p c^2$, adiabatic index $\hat{\gamma}$ (Huang et al. 1999), fraction of energy provided to the magnetic field ($\varepsilon_B$) is necessary with $n$ the constant-density medium of the circumburst environment. The cooling electron Lorentz factor is written as $\gamma_c = (6\pi m_e c/\sigma_T)(1+Y)^{-1}\Gamma^{-1}B'^{-2}t^{-1}$, where $\sigma_T$ is the Thomson cross-section and $Y$ is the Compton parameter (Sari & Esin 2001; Wang et al. 2010). The synchrotron spectral breaks can now be expressed in terms of previously defined quantities as $\nu'_i = q_e/(2\pi m_e c)\gamma_i^2 B'$, where the subindex i = m and c will stand for the characteristic or cooling break, respectively. The constant $q_e$ represents the elementary charge. The synchrotron radiation power per electron in the comoving frame is given by $P'_{\nu'_m} \simeq \sqrt{3}q_e^3/(m_e c^2)B'$ (e.g., see Sari et al. 1998; Fraija 2015). Considering the total number of emitting electrons $N_e = \frac{\Omega n r^3}{3}$ and also taking into account the transformation laws for the solid angle ($\Omega = \Omega'/\delta_D^2$), the radiation power ($P_{\nu_m} = \delta_D/(1+z)P'_{\nu'_m}$) and the spectral breaks ($\nu_i = \delta_D/(1+z)\nu'_i$), the maximum flux given by synchrotron radiation is:

$$F_{\nu,\max} = \frac{(1+z)^2\delta_D^3}{4\pi d_z^2}N_e P'_{\nu'_m}, \tag{12}$$

where $d_z = (1+z)\frac{c}{H_0}\int_0^z \frac{d\tilde{z}}{\sqrt{\Omega_M(1+\tilde{z})^3+\Omega_\Lambda}}$ (Weinberg 1972) is the luminosity distance. For the cosmological constants, we assume a spatially flat universe $\Lambda$CDM model with $H_0 = 69.6\,\mathrm{km\,s^{-1}\,Mpc^{-1}}$, $\Omega_M = 0.286$ and $\Omega_\Lambda = 0.714$ (Planck Collaboration et al. 2016).

## 3. APPLICATION: GRB 190829A

### 3.1. *The Prompt Episode*

GRB 190829A was triggered and located by the *Fermi*/Gamma-ray Monitor (GBM) and *Swift*/Burst Alert Telescope (BAT) instruments at $T$ = 2019 August 29 19:55:53.13 UTC and 19:56:44.60 UTC, respectively (The Fermi GBM team 2019; Dichiara et al. 2019). *Swift*/BAT localized GRB 190829A with coordinates RA, DEC(J2000)=44.540, -8.968 with a 90% error radius of 3 arcmin. The *Fermi*/GBM light curve exhibited an initial pulse followed by a brighter peak released total isotropic-equivalent energies of $E_{\gamma,\mathrm{iso}} = (9.151\pm0.504)\times10^{49}$ erg and $(2.967 \pm 0.032) \times 10^{50}$ erg, respectively (Fraija et al. 2021). The *Fermi*/GBM and *Swift*/BAT observations are presented and interpreted in several scenarios (e.g., see Fraija et al. 2021; Chand et al. 2020; Zhang et al. 2021a; Sato et al. 2021; Salafia et al. 2022).

### 3.2. *The Afterglow Phase*

Long term follow-up observations of this burst were performed by X-ray Telescope (XRT) and UltraViolet Optical Telescope (UVOT) on board the Neil Gehrels Swift Observatory, and MASTER Telescopes (Dichiara et al. 2021). The *Swift*/XRT instrument started detecting this burst at 19:58:21.9 UTC, 97.3 s after the BAT trigger. The observations with *Swift*/UVOT at 106 s after the BAT trigger. This instrument detected in V, B, white, U, UVW1, UVW2 and UVM2 filters exhibiting a bright flare peaking at $\sim 2 \times 10^3$ s. The MASTER network observed GRB 190829A at $T+1239$ s after the burst trigger time. GRB 190829A was observed with the Clear (C) and the polarization filters (P). The optical fluxes from the P filter corresponds to superposition of B and R standard Johnson filters (0.2 B + 0.8 R) (Dichiara et al. 2022).

The multi-wavelength afterglow observations of GRB 190829A were modelled by several collaborations (Rhodes et al. 2020; Sato et al. 2021, 2022; Fraija et al. 2021; Salafia et al. 2022; Dichiara et al. 2022; Zhang et al. 2021a,b). These observations have shown to be consistent with a FS plus reverse shock (RS) scenario with Synchrotron Self-Compton (SSC) emission (Rhodes et al. 2020; Salafia et al. 2022; Dichiara et al. 2022). On the other hand, Sato et al. (2021, 2022) applied a dual component model – with a narrow off-axis jet describing the VHE component and early afterglow; while a wide-angle, slower, jet seen closer to its edge describes the late time afterglow observations, to model the complex afterglow of GRB 190829A. Fraija et al. (2021) presented a synchrotron forward shock model originating from a spin-down millisecond magnetar source as a strong candidate for this burst. Zhang et al. (2021a) defined a set of archetypical rules and applied them to a synchrotron FS + SSC model to describe GRB 190829A's observations; while Zhang et al. (2021b) shown the afterglow to be compatible with a synchrotron FS + inverse Compton (iC) case, assuming both SSC and external inverse Compton (eiC) components.

This kind of degeneracy between models is expected in GRB afterglows (Rossi et al. 2004; Kumar & Barniol Duran 2009, 2010; Fraija et al. 2017), therefore, the approach of a scenario requires a profound analysis of each possibility. GRB 190829A had observed $|Q|$ values, and consequently, upper limits imposed upon its early afterglow (Dichiara et al. 2022) and fitting this data can be useful in an attempt to break the models' degeneracy. In the following subsections we present our semi-analytical model, an off-axis top-hat jet with synchrotron FS dynamics, similar to the ones presented by the authors, mentioned before, to describe the FS, which we use to calculate the polarization evolution of this burst, using the parameters obtained by the aforementioned works.

## 4. RESULTS AND DISCUSSION

Figures 1 and 3 to 7 show the polarization degree for three magnetic field configurations, with each figure representing the parameters used by Sato et al. (2021), Sato et al. (2022), Salafia et al. (2022), Dichiara et al. (2022), Fraija et al. (2021) and Zhang et al. (2021a,b), respectively. The magnetic field configurations are arranged from left to right: $B_\perp$, $B_\parallel$, and $B_{\text{tor}}$; and from top to bottom: a non-expanding jet configuration (i.e., homogeneous jet where $\theta_j$ does not evolve) viewed off-axis, an expanding jet configuration[3] (i.e., homogeneous jet where $\theta_j = \theta_j(t)$, according to Huang et al. (2000) hydrodynamical equations) also viewed off-axis, and the same expanding jet viewed from within the jet's beaming cone ($\theta_{\text{obs}} < \theta_j$). For all cases, we present the polarization for a range of initial values of $q_0 = \frac{\theta_{\text{obs}}}{\theta_{j,0}}$, with solid lines as markers for the observation angle reported/assumed by the mentioned authors.

Sato et al. (2021, 2022) used a narrow jet FS synchrotron model to describe the early afterglow of GRB 190829A. They reported this model to be satisfactory in explaining the multiwavelength observations in the range from $8 \times 10^2$ to $2 \times 10^4$ s. We use the most recent best-fit parameters reported in this work (see the first row of table 1), with the additional parameters of $\varepsilon_e = 3.5 \times 10^{-2}$, $\varepsilon_B = 6 \times 10^{-5}$, and $\zeta_e = 0.2$ and a maximum flux at time $t_{\text{peak}} = 2 \times 10^3$ s. We present in Figure 1 the polarization evolution considering these parameters. The solid line represents the values presented by Sato et al. (2022). Regardless of the choice of jet (expanding or not), the polarization values returned from these parameters break the upper limits of $\Pi(t \approx [1700 - 6000]\text{s}) \lesssim 6\%$ imposed by Dichiara et al. (2022). For an expanding jet, the set of parameters presented by the authors return the following polarization values $\Pi(B_\perp, t \approx 2000\,\text{s}) \approx 30\%$, $\Pi(B_\perp, t \approx 4000\,\text{s}) \approx 22.2\%$ and $\Pi(B_\perp, t \approx 6000\,\text{s}) \approx 0\%$. For a toroidal field, the polarization observed is $\Pi(B_{\text{tor}}, t \approx 2000\text{s}) \approx 63\%$, $\Pi(B_{\text{tor}}, t \approx 4000\,\text{s}) \approx 2\%$ and $\Pi(B_{\text{tor}}, t \approx 6000\,\text{s}) \approx 0\%$. At first glance, this should enough to exclude the possibility of a viewing angle this high ($\theta_{\text{obs}} = 2\theta_j$). However, it is worth noting that polarization is highly dependent on the magnetic field anisotropy, and we only explore the extremely anisotropic cases ($b = 0$; $b \to \infty$). A more isotropic field, where $b$ is closer to unity, would severely reduce the polarization degree (e.g., see Gill & Granot 2018; Corsi et al. 2018; Gill & Granot 2020; Teboul & Shaviv 2021, for the case of GRB 170817A) without any interference on the flux light curves (which does not take into consideration the magnetic field's geometry). Exploring this parameter set with a more isotropic configuration could amend the discrepancy between polarization and flux fitting.

---

[3] The choice to include both approaches to the homogeneous jet comes from the nearly identical flux light curves, but different polarizations (e.g. see Rossi et al. 2004)

Figure 2 shows the polarization calculated for a less extreme anisotropy scenario. To obtain this polarization, we use Eq. 4 of Granot & Königl (2003) to sum the contributions of ordered and random components and take the absolute value:

$$\Pi = \frac{\eta \Pi_{\text{ord}}}{(1+\eta)} \left[ 1 + \left( \frac{\Pi_{\text{rnd}}}{\eta \Pi_{\text{ord}}} \right)^2 - \frac{2\Pi_{\text{rnd}}}{\eta \Pi_{\text{ord}}} \cos 2\delta \right]^{\frac{1}{2}}. \quad (13)$$

This equation introduces two new parameters, $\eta$ and $\delta$, where $\eta = \frac{\langle B_{\text{ord}}^2 \rangle}{\langle B_{\text{rnd}}^2 \rangle}$ and $\delta$ is the angle between the ordered magnetic field and the jet axis (see Fig. 1 of the aforementioned paper). Information regarding these parameters cannot be obtained from Sato et al. (2021, 2022). We explore a possible case where $\eta = 0.25$ and $\delta = \pi/2$. The change to a less extreme anisotropic scenario reduces the polarization significantly and, as is seen in Figure 2, allows to describe the polarization data observed by Dichiara et al. (2022). This implies the requirement of a sub-dominant ordered component a quarter as strong as the random one, perpendicular to the jet axis, to validate this parameter set.

Salafia et al. (2022) described the afterglow of GRB 190829A with a dual component; a RS and FS emission. They proposed that the RS emission describes the early multiwavelength afterglow, while the FS emission dominates after $t > 1$day. The parameters reported by the authors for the FS emission are found in the second row of table 1, and additionally, $\varepsilon_e = 3.0^{+2.9}_{-1.7} \times 10^{-2}$, $\varepsilon_B = 2.5^{+3.5}_{-1.3} \times 10^{-5}$, and $\zeta_e = 0.04$. The authors also constrained $\Delta\theta < 2$ deg based on a compactness argument and assumed an on-axis (i.e., the observation angle within the beaming cone of the jet) observation angle. For purposes of the calculation we take $\theta_{\text{obs}} = \theta_j$ as the authors' choice, as indicated by Fig. 5 of their work, but also presented the values for $\theta_{\text{obs}} = 0.25\theta_j$ and $\theta_{\text{obs}} = 0.62\theta_j$. Figure 3 shows that the authors' chosen values indicate a good fit for the polarization upper limits of $\Pi \lesssim 6\%$, with all values of on-axis $q_0$ returning polarization within the upper limits for the random magnetic field configuration $B_\perp$. We find a polarization degree of $\Pi(B_\perp, t \approx 2000\,\text{s}) \approx 1.0\%$, $\Pi(B_\perp, t \approx 4000\,\text{s}) \approx 1.2\%$, and $\Pi(B_\perp, t \approx 6000\,\text{s}) \approx -1.4\%$, with $q_0 \lesssim 0.62$ required to allow for a polarization originating from a $B_\parallel$ field and $B_{\text{tor}}$ ruled out for $q_0 \gtrsim 0.25$. While we limited ourselves to the forward shock synchrotron calculations in this dual component model, the polarization for iC has been explored before (Gill & Granot 2020; Lazzati et al. 2004; Toma et al. 2009). These authors have found that polarization for iC is remarkably similar to the corresponding curves for synchrotron emission, with the caveat of a higher possible maximum polarization ($\Pi_{\text{max,syn}} \simeq 75\%$, $\Pi_{\text{max,iC}} \to 100\%$); however, the maximum polarization is directly linked to the spectral index $\alpha$ through $\Pi_{max} = (\alpha+1)/(\alpha+1.66)$. As such, with a known $\alpha$ (or $p$) and maximum polarization, the the-

oretical limit of maximum polarization is of little relevance. The polarization curves would be similar to the ones shown here, with the parameters used to calculate the RS emission.

Dichiara et al. (2022) have also described the afterglow of GRB 190829A with dual component RS plus FS emission. The authors proposed that the rebrightening in the X-ray and optical observations is consistent with the RS component of the emission. The parameters reported by the authors are presented in the third row of table 1. Additionally, the authors expected $\varepsilon_e \approx 10^{-1}$ and $\varepsilon_B \approx 10^{-4}$. No fundamental assumptions were made on the observation angle for the emission. However, the authors used the polarization model presented by Rossi et al. (2004) to rule out a homogeneous jet viewed off-axis with a 90% confidence. We then present the curves for $q_0 \leq 1$ as the authors' considered values and assume a value of $\Gamma_0 = 100$, between a minimal value for a typical off-axis jet and the typical values of $\Gamma_0$ for on-axis jets.[4] The polarization results are presented in Figure 4. For all configurations, $q_0 \geq 1$ is ruled out, while a value of $q_0 = 0.62$ returns the following polarizations $\Pi(B_\perp, t \approx 2000s) \approx 1.8\%$, $\Pi(B_\perp, t \approx 4000s) \approx -2.5\%$, and $\Pi(B_\perp, t \approx 6000s) \approx -4.0\%$. For a parallel field configuration, we note that the upper limits rule out $q_0 = 1.0, 0.62$, but a value of $q_0 < 0.62$ can still fit the polarization upper limits. This is in line with the conclusions reached by the authors, who expect that the low radiative efficiency ($< 1\%$) could be explained by a jet viewed from $\theta_{\rm obs} < \theta_{\rm j}$. The considerations regarding iC done for Salafia et al. (2022) are the same for this model.

Fraija et al. (2021) proposed a synchrotron forward shock model originating from a spin-down millisecond magnetar source to describe the X-ray and optical observations of GRB 190829A, but expect an iC component as necessary to describe the high-energy and VHE photons observed. The parameters reported by the authors are found in the fourth row of table 1, with the additional parameters of $\varepsilon_e = 0.8^{+0.1}_{-0.1} \times 10^{-1}$ and $\varepsilon_B = 1.1^{+0.1}_{-0.1} \times 10^{-4}$. The authors also assume an on-axis emission to fit the light curves, and we present the polarization assuming $q_0 \leq 1$ as the canonical choice. Figure 5 shows that, like the parameter set of Salafia et al. (2022), all choices of $q_0 \leq 1$ are well poised to fit the set upper limits. The highest value of on-axis $q_0 = 1$, an observation angle set at the edge of the jet, returns polarization values of $\Pi(B_\perp, t \approx 2000\,{\rm s}) \approx 4.3\%$, $\Pi(B_\perp, t \approx 4000\,{\rm s}) \approx 2.1\%$, and $\Pi(B_\perp, t \approx 6000\,{\rm s}) \approx -1.9\%$. For a parallel field configuration, we note that the $q_0 = 1$ is ruled out, but a value of $q_0 \lesssim 0.62$ can still fit the polarization upper limits. As such, a choice of $\theta_{\rm obs} = \theta_{\rm j}$ would make $B_\perp$ the sole possible config-

uration (assuming an extremely anisotropic configuration), while $\theta_{\rm obs} < \theta_{\rm j}$ would only rule out the globally ordered, toroidal field configuration.

Zhang et al. (2021a) proposed a paradigm to explain GRB 190829A. With the condition of a quasi-isotropic ejecta, the authors fit the X-ray, radio, and optical afterglow light curves with a forward shock model, where the afterglow emission is attributed to synchrotron and iC radiation. The parameters reported by the authors are found in the fifth row of table 1, with the additional parameters of $\log_{10} \varepsilon_e = -0.49^{+0.46}_{-0.22}$ and $\log_{10} \varepsilon_B = -3.22^{+1.21}_{-0.80}$. The authors assume an on-axis observation of the burst. As such, we take $q_0 \lesssim 1$ as their canonical choice. We see from Figure 6 that for $q_0 = 1$ we find $\Pi(B_\perp, t \approx 2000\,{\rm s}) \approx -4.1\%$, $\Pi(B_\perp, t \approx 4000\,{\rm s}) \approx -1.0\%$, and $\Pi(B_\perp, t \approx 6000\,{\rm s}) \approx 0.0\%$. The values of $q_0 = 1.0, 0.62$ rule out the globally ordered configurations, which require an $\theta_{\rm obs} \lesssim 0.25\theta_{\rm j}$ to fit the upper limits with these parameters.

Zhang et al. (2021b) proposed a combination of the external FS and a late prompt emission to describe the afterglow of GRB 190829A. The authors expected an eiC+SSC mechanism to describe the very-high-energy component by the High Energy Stereoscopic System (H.E.S.S.) observations and the typical FS model accounts for the lower-frequency emissions. The parameters reported by the authors are found in the sixth row of table 1, with the additional parameters of $\varepsilon_e = 0.39$, $\varepsilon_e = 8.7 \times 10^{-5}$, and $\zeta_e = 0.34$. The authors assumed an on-axis observation of the burst. As such we take $q_0 \lesssim 1$ as their canonical choice. Figure 7 presents the polarization curves. We see that with this on-axis condition in mind, both a random ($B_\perp$) and ordered ($B_\parallel$) return a polarization within the upper limits of $< 6\%$. Taking $q_0 = 1$, we find $\Pi(B_\perp, t \approx 2000\,{\rm s}) \approx 0.0\%$, $\Pi(B_\perp, t \approx 4000\,{\rm s}) \approx 0.5\%$, and $\Pi(B_\perp, t \approx 6000\,{\rm s}) \approx 3.4\%$ and $\Pi(B_\parallel, t \approx 2000\,{\rm s}) \approx 0.0\%$, $\Pi(B_\parallel, t \approx 4000\,{\rm s}) \approx -1.4\%$, and $\Pi(B_\parallel, t \approx 6000\,{\rm s}) \approx -5.0\%$. A globally ordered toroidal configuration is ruled out.

## 5. SUMMARY AND CONCLUSIONS

In this work, we have applied a semi-analytical FS synchrotron model, analogous with a homogeneous jet, to a polarization model and obtained a set of time-dependent polarization curves. This polarization depends on the parameters associated with the evolution of the bulk Lorentz factor and half-opening angle of synchrotron theory. Additionally, the polarization model depends on the geometry of the magnetic field, and we have explored the extremely anisotropic scenarios ($b = 0$, $b \rightarrow \infty$) of a random and two ordered field configurations. We have used different parameter sets of previously published works capable of adequately describing the afterglow of GRB 190829A (e.g. see Sato et al. 2021, 2022; Salafia et al. 2022; Dichiara et al. 2022; Fraija et al. 2021; Zhang et al. 2021a,b) to fit the upper limits on polarization set by Dichiara et al. (2022).

---

[4] This value is also within the constrained values of Salafia et al. (2022), based on their compactness argument.

The curves obtained favor the scenario where the observation angle is within the jet's beaming cone ($\theta_{obs} \lesssim \theta_j$) while disfavoring an off-axis scenario. This result is in agreement with Salafia et al. (2022); Dichiara et al. (2022); Fraija et al. (2021); Zhang et al. (2021a,b) that predicted GRB 190829A to have been seen on-axis. However, the observations provided by Dichiara et al. (2022) cannot entirely exclude the off-axis scenario. This conclusion comes from the polarization's dependency on magnetic field anisotropy. The presence of a subdominant field (i.e., $b \neq 0$, $b \nrightarrow \infty$) would decrease the observed polarization by a factor $> 2$ (model dependent; see Gill & Granot 2018; Corsi et al. 2018; Gill & Granot 2020; Teboul & Shaviv 2021), which is significant enough to reconcile the discrepancy between flux and polarization fitting.

While current evidence indicates that GRB 190829A was seen on-axis, more polarization data and deeper scrutiny of the afterglow fitting would be required to solve the degeneracy present between models properly.

## REFERENCES

Becerra R. L., et al., 2019, ApJ, 881, 12

Beniamini P., Granot J., 2016, MNRAS, 459, 3635

Blandford R. D., McKee C. F., 1976, Physics of Fluids, 19, 1130

Buckley D. A. H., et al., 2021, MNRAS, 506, 4621

Cano Z., Wang S.-Q., Dai Z.-G., Wu X.-F., 2017, Advances in Astronomy, 2017, 8929054

Chand V., et al., 2020, ApJ, 898, 42

Corsi A., et al., 2018, ApJL, 861, L10

Costa E., et al., 1997, Nature, 387, 783

Dichiara S., Bernardini M. G., et al. 2019, GRB Coordinates Network, Circular Service, No. 25552, #1 (2019), 25552

Dichiara S., et al., 2021, ApJL, 911, L28

Dichiara S., et al., 2022, MNRAS, 512, 2337

Duncan R. C., Thompson C., 1992, ApJL, 392, L9

Eichler D., Livio M., Piran T., Schramm D. N., 1989, Nature, 340, 126

Fan Y., Piran T., 2006, MNRAS, 369, 197

Fraija N., 2015, ApJ, 804, 105

Fraija N., et al., 2017, ApJ, 848, 15

Fraija N., Veres P., Beniamini P., Galvan-Gamez A., Metzger B. D., Barniol Duran R., Becerra R. L., 2021, ApJ, 918, 12

Fraija N., Galvan-Gamez A., Betancourt Kamenetskaia B., Dainotti M. G., Dichiara S., Veres P., Becerra R. L., Pedreira A. C. C. d. E. S., 2022, arXiv e-prints, p. arXiv:2205.02459

Gehrels N., Ramirez-Ruiz E., Fox D. B., 2009, ARA&A, 47, 567

Giannios D., 2008, A&A, 480, 305

Gill R., Granot J., 2018, MNRAS, 478, 4128

Gill R., Granot J., 2020, MNRAS, 491, 5815

Gill R., Granot J., Kumar P., 2020, MNRAS, 491, 3343

Granot J., 2003, ApJL, 596, L17

Granot J., Königl A., 2003, ApJL, 594, L83

Granot J., Sari R., 2002, ApJ, 568, 820

Granot J., Taylor G. B., 2005, ApJ, 625, 263

Huang Y. F., Dai Z. G., Lu T., 1999, MNRAS, 309, 513

Huang Y. F., Gou L. J., Dai Z. G., Lu T., 2000, ApJ, 543, 90

Kann D. A., et al., 2011, ApJ, 734, 96

Kouveliotou C., Meegan C. A., Fishman G. J., Bhat N. P., Briggs M. S., Koshut T. M., Paciesas W. S., Pendleton G. N., 1993, The Astrophysical Journal, 413, L101

Kumar P., Barniol Duran R., 2009, MNRAS, 400, L75

Kumar P., Barniol Duran R., 2010, MNRAS, 409, 226

Kumar P., Crumley P., 2015, MNRAS, 453, 1820

Laing R. A., 1980, MNRAS, 193, 439

Laskar T., et al., 2019, ApJL, 878, L26

Lazzati D., Rossi E., Ghisellini G., Rees M. J., 2004, MNRAS, 347, L1

Lazzati D., Morsony B. J., Margutti R., Begelman M. C., 2013, ApJ, 765, 103

Lipunov V. M., et al., 2019, Astronomy Reports, 63, 293

Lyutikov M., Blandford R., 2003, arXiv e-prints, pp astro–ph/0312347

Lyutikov M., Pariev V. I., Blandford R. D., 2003, ApJ, 597, 998

Mazets E., et al., 1981, Astrophysics and Space Science, 80, 3

Medvedev M. V., Loeb A., 1999, ApJ, 526, 697

Metzger B. D., Giannios D., Thompson T. A., Bucciantini N., Quataert E., 2011, MNRAS, 413, 2031

Mizuta A., Nagataki S., Aoi J., 2011, ApJ, 732, 26

Mundell C. G., et al., 2013, Nature, 504, 119

Nakar E., Piran T., Waxman E., 2003, JCAP, 2003, 005

Narayan R., Paczynski B., Piran T., 1992, ApJL, 395, L83

Nava L., Nakar E., Piran T., 2016, MNRAS, 455, 1594

Orsi S., Polar Collaboration 2011, Astrophysics and Space Sciences Transactions, 7, 43

Paczyński B., 1998, ApJL, 494, L45

Paczynski B., Xu G., 1994, ApJ, 427, 708

Panaitescu A., Mészáros P., 1998, ApJ, 501, 772

Piro L., et al., 1998, A&A, 331, L41

Planck Collaboration Ade P. A. R., Aghanim N., Arnaud M., Ashdown M., Aumont J., et al. 2016, A&A, 594, A13

Rees M. J., Meszaros P., 1994, ApJL, 430, L93

Rhodes L., et al., 2020, MNRAS, 496, 3326

Rossi E. M., Lazzati D., Salmonson J. D., Ghisellini G., 2004, MNRAS, 354, 86

Rybicki G. B., Lightman A. P., 1979, Radiative processes in astrophysics

Salafia O. S., et al., 2022, ApJL, 931, L19

Sari R., Esin A. A., 2001, ApJ, 548, 787

Sari R., Piran T., Narayan R., 1998, ApJL, 497, L17

Sato Y., Obayashi K., Yamazaki R., Murase K., Ohira Y., 2021, MNRAS, 504, 5647

Sato Y., Obayashi K., Theodre Zhang B., Tanaka S. J., Murase K., Ohira Y., Yamazaki R., 2022, arXiv e-prints, p. arXiv:2208.13987

Shrestha M., Steele I. A., Piascik A. S., Jermak H., Smith R. J., Copperwheat C. M., 2020, MNRAS, 494, 4676

Shrestha M., et al., 2022, MNRAS,

Sironi L., Spitkovsky A., 2011, ApJ, 726, 75

Steele I. A., Mundell C. G., Smith R. J., Kobayashi S., Guidorzi C., 2009, Nature, 462, 767

Stringer E., Lazzati D., 2020, ApJ, 892, 131

Teboul O., Shaviv N. J., 2021, MNRAS, 507, 5340

The Fermi GBM team 2019, GRB Coordinates Network, Circular Service, No. 23714, #1 (2019), 25551

Thompson C., 1994, MNRAS, 270, 480

Thompson C., Mészáros P., Rees M. J., 2007, ApJ, 666, 1012

Toma K., et al., 2009, ApJ, 698, 1042

Usov V. V., 1992, Nature, 357, 472

Wang X.-Y., He H.-N., Li Z., Wu X.-F., Dai Z.-G., 2010, ApJ, 712, 1232

Wang X.-G., et al., 2015, ApJS, 219, 9

Waxman E., 2003, Nature, 423, 388

Weibel E. S., 1959, Phys. Rev. Lett., 2, 83

Weinberg S., 1972, Gravitation and Cosmology

Woosley S. E., 1993, ApJ, 405, 273

Woosley S. E., Bloom J. S., 2006, ARA&A, 44, 507

Zhang B., Yan H., 2011, ApJ, 726, 90

Zhang L.-L., Ren J., Huang X.-L., Liang Y.-F., Lin D.-B., Liang E.-W., 2021a, ApJ, 917, 95

Zhang B. T., Murase K., Veres P., Mészáros P., 2021b, ApJ, 920, 55

van Paradijs J., et al., 1997, Nature, 386, 686

**Table 1.** Table of parameters reported for GRB 190819A

| References | $E\ (10^{53}\ \mathrm{erg})$ | $n\ (\mathrm{cm}^{-3})$ | $\Gamma_0$ | $\theta_\mathrm{j}\ (\mathrm{deg})$ | $\theta_\mathrm{obs}\ (\mathrm{deg})$ | $p$ |
|---|---|---|---|---|---|---|
| Sato et al. (2022) | 4 | $10^{-2}$ | 350 | 0.86 | 1.7 | 2.44 |
| Salafia et al. (2022) | $2.5^{+1.9}_{-1.3}$ | $2.1^{+3.7}_{-1.0} \times 10^{-1}$ | $57^{+4}_{-5}$ | $15.4^{+1.3}_{-0.9}$ | – | 2.01 |
| Dichiara et al. (2022) | $2 \times 10^{-1}$ | $10^{-2} - 10^{-1}$ | $--$ | 16 | $--$ | 2.5 |
| Fraija et al. (2021) | $2.4^{+0.2}_{-0.2} \times 10^{-2}$ | $1^{+0.1}_{-0.1} \times 10^{-1}$ | 34 | 8 | $--$ | $2.3^{+0.2}_{-0.2}$ |
| Zhang et al. (2021a) | $1.02^{+1.73}_{-0.55} \times 10^{-2}$ | $2.18^{+5.76}_{-1.74} \times 10^{-1}$ | $35.5^{+16.9}_{-19.0}$ | 3.2 | $--$ | $2.12^{+0.08}_{-0.17}$ |
| Zhang et al. (2021b) | $9.8 \times 10^{-2}$ | $9 \times 10^{-2}$ | 25 | 11.46 | $--$ | 2.1 |

The mean values of the distributions were used for calculation of the polarization curves. Additionally to the $\theta_\mathrm{obs}$ used by the authors, we include the polarization curves for $q = [0.25, 0.62, 1.50, 2.00, 2.50]$



**Figure 1.** Temporal evolution for the polarization of GRB 190829A, obtained with the parameters used by Sato et al. (2021) (for the narrow jet component) for three configurations of magnetic field - Perpendicular ($B_\perp$) and Parallel ($B_\parallel$) and Toroidal ($B_\mathrm{tor}$). Dashed lines represent different values of $q_0$, used for illustration, while solid lines represent the value of $q_0$ obtained from the authors' $\theta_\mathrm{obs}$ and $\theta_\mathrm{j}$. Top and middle rows show a non-expanding jet and an expanding jet viewed off-axis, respectively, while bottom row shows an expanding jet viewed within the jet's beaming cone. Upper limits taken from Dichiara et al. (2022).

**Figure 2.** Temporal evolution for the polarization modulus, of GRB 190829A, obtained with the parameters used by Sato et al. (2021) (for the narrow jet component) for a value of $\eta = 0.25$ – a dominant random component plus a subdominant ordered component. Dashed lines represent different values of $q_0$, used for illustration, while solid lines represent the value of $q_0$ obtained from the authors' $\theta_{obs}$ and $\theta_j$. Data points taken from Dichiara et al. (2022).
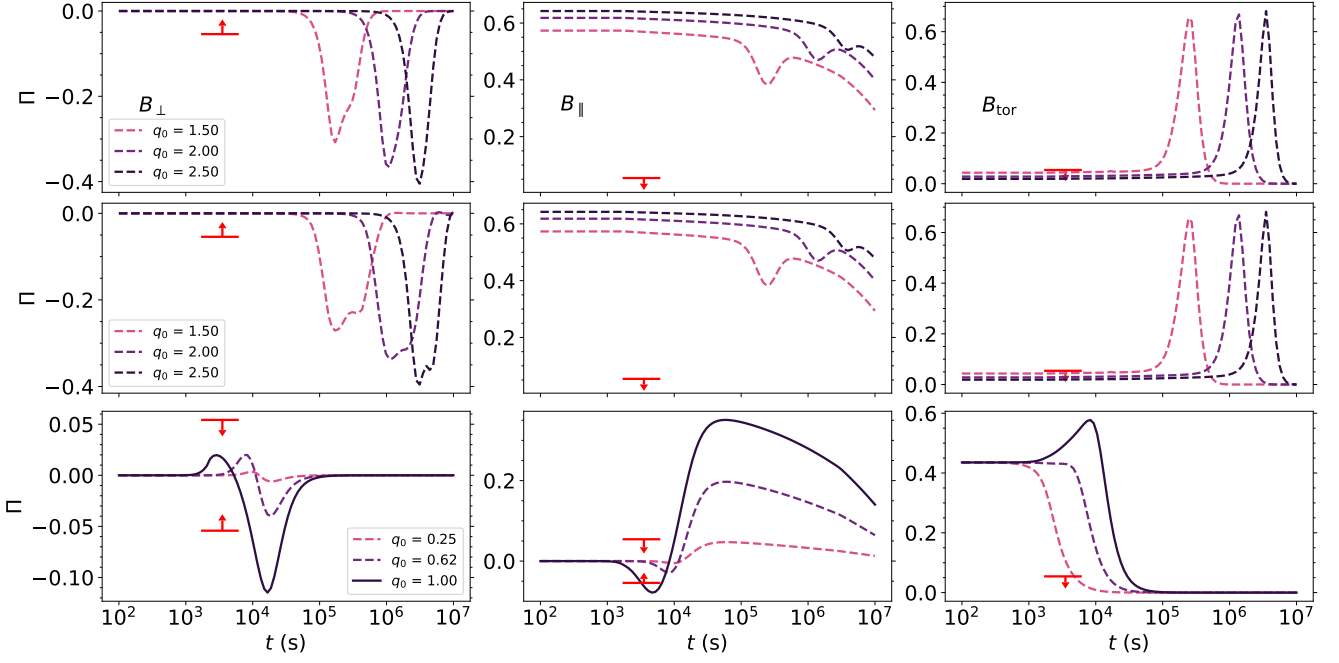
**Figure 3.** Temporal evolution for the polarization of GRB 190829A, obtained with the parameters used by Salafia et al. (2022) (for the forward shock component) for three configurations of magnetic field - Perpendicular ($B_\perp$) and Parallel ($B_\parallel$) and Toroidal ($B_{tor}$). Dashed lines represent different values of $q_0$, used for illustration, while solid lines represent the value of $q_0$ obtained from the authors' $\theta_{obs}$ and $\theta_j$. Top and middle rows show a non-expanding jet and an expanding jet viewed off-axis, respectively, while bottom row shows an expanding jet viewed within the jet's beaming cone. Upper limits taken from Dichiara et al. (2022).
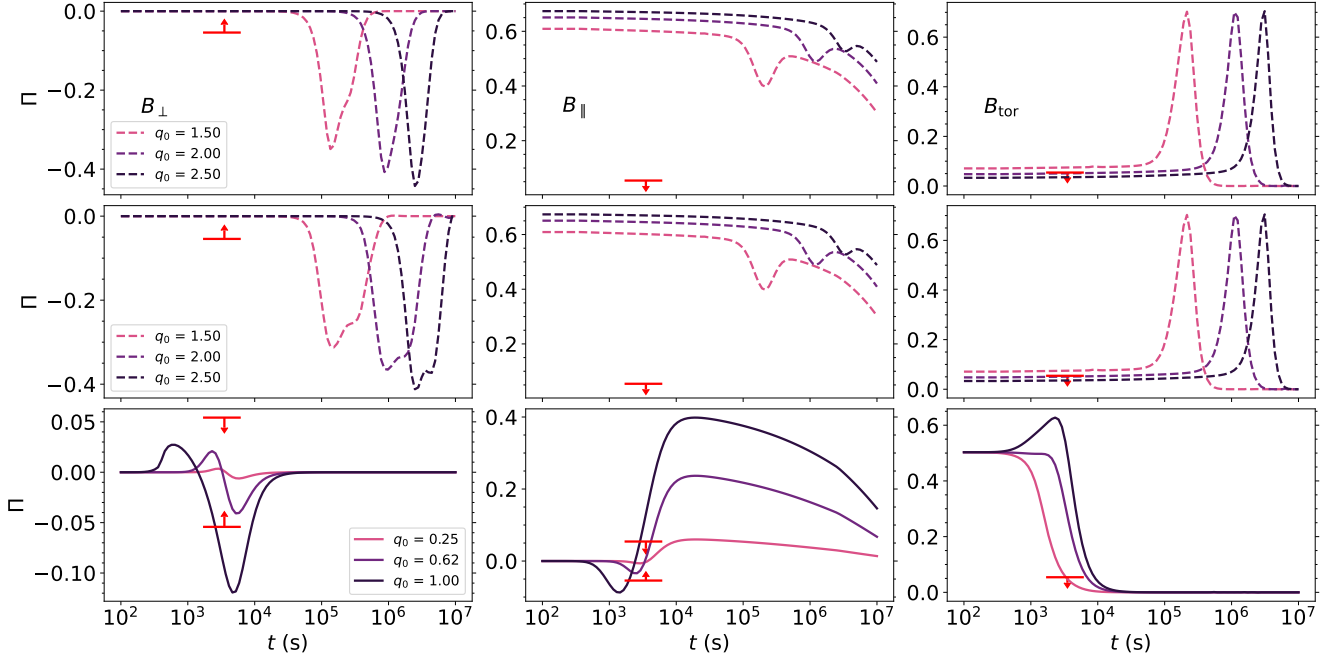
**Figure 4.** Temporal evolution for the polarization of GRB 190829A, obtained with the parameters used by Dichiara et al. (2022) (for the forward shock component) for three configurations of magnetic field - Perpendicular ($B_\perp$) and Parallel ($B_\parallel$) and Toroidal ($B_{tor}$). The values of $\Gamma_0 = 100$ and $n = 5 \times 10^{-2}$ were assumed. Dashed lines represent different values of $q_0$, used for illustration, while solid lines represent the value of $q_0$ obtained from the authors' $\theta_{obs}$ and $\theta_j$. Top and middle rows show a non-expanding jet and an expanding jet viewed off-axis, respectively, while bottom row shows an expanding jet viewed within the jet's beaming cone. Upper limits taken from Dichiara et al. (2022).
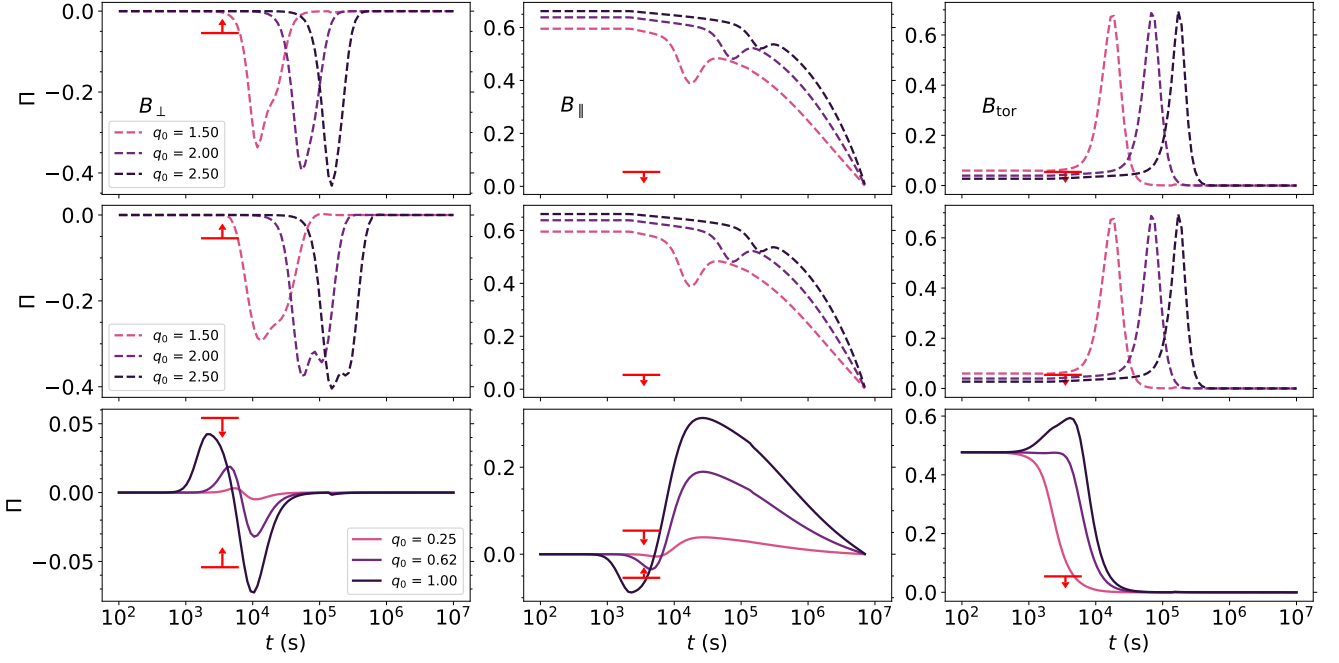
**Figure 5.** Temporal evolution for the polarization of GRB 190829A, obtained with the parameters used by Fraija et al. (2021) (for the forward shock component) for three configurations of magnetic field - Perpendicular ($B_\perp$) and Parallel ($B_\parallel$) and Toroidal ($B_{tor}$). Dashed lines represent different values of $q_0$, used for illustration, while solid lines represent the value of $q_0$ obtained from the authors' $\theta_{obs}$ and $\theta_j$. Top and middle rows show a non-expanding jet and an expanding jet viewed off-axis, respectively, while bottom row shows an expanding jet viewed within the jet's beaming cone. Upper limits taken from Dichiara et al. (2022).

CALIGULA ET AL.
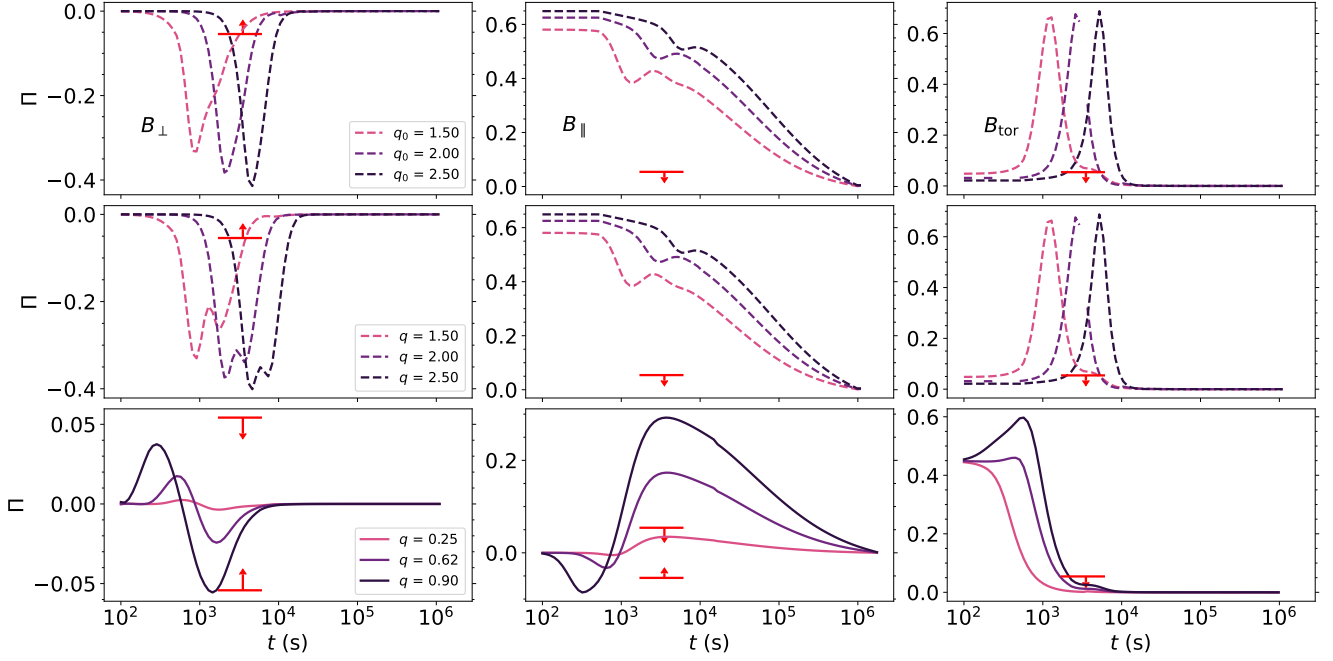


**Figure 6.** Temporal evolution for the polarization of GRB 190829A, obtained with the parameters used by Zhang et al. (2021a) (for the forward shock component) for three configurations of magnetic field - Perpendicular ($B_\perp$) and Parallel ($B_\parallel$) and Toroidal ($B_{tor}$). Dashed lines represent different values of $q_0$, used for illustration, while solid lines represent the value of $q_0$ obtained from the authors' $\theta_{obs}$ and $\theta_j$. Top and middle rows show a non-expanding jet and an expanding jet viewed off-axis, respectively, while bottom row shows an expanding jet viewed within the jet's beaming cone. Upper limits taken from Dichiara et al. (2022).
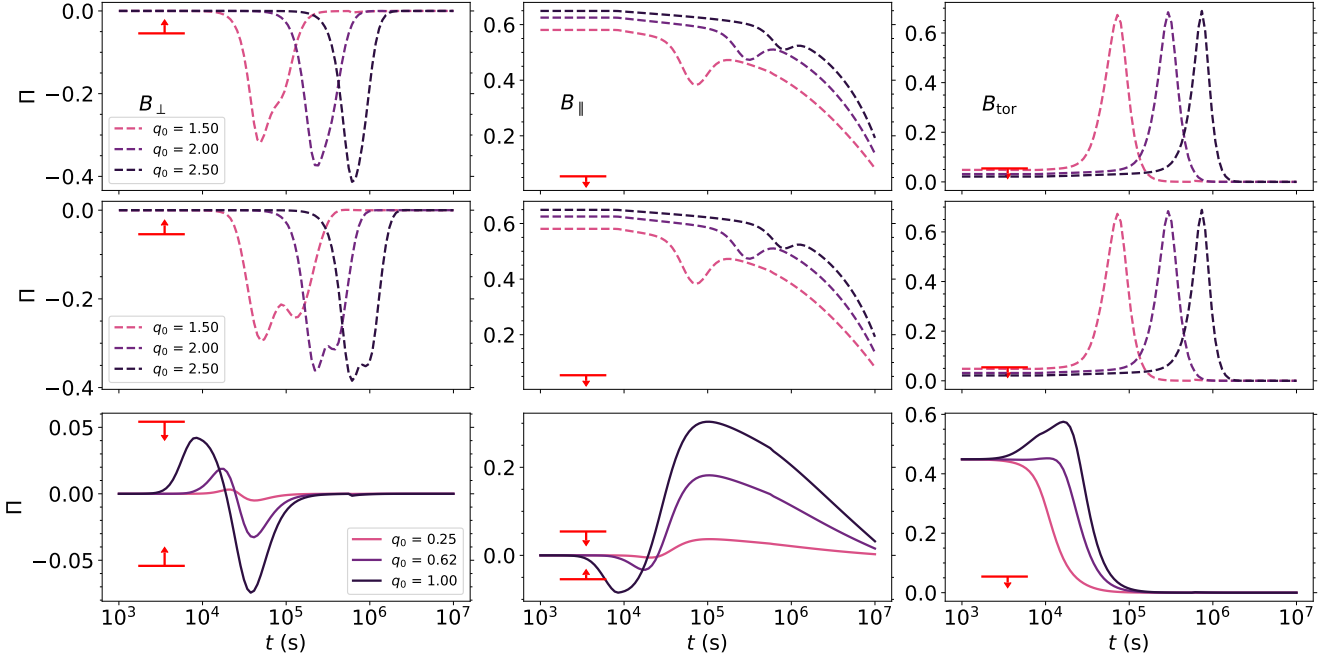
**Figure 7.** Temporal evolution for the polarization of GRB 190829A, obtained with the parameters used by Zhang et al. (2021b) (for the forward shock component) for three configurations of magnetic field - Perpendicular ($B_\perp$) and Parallel ($B_\parallel$) and Toroidal ($B_{tor}$). Dashed lines represent different values of $q_0$, used for illustration, while solid lines represent the value of $q_0$ obtained from the authors' $\theta_{obs}$ and $\theta_j$. Top and middle rows show a non-expanding jet and an expanding jet viewed off-axis, respectively, while bottom row shows an expanding jet viewed within the jet's beaming cone. Upper limits taken from Dichiara et al. (2022).

APPENDIX

## A. SYNCHROTRON FS OFF-AXIS MODEL

During the deceleration phase before afterglow emission enters in the observer's field of view, the bulk Lorentz factor is given by Eq. 11. The minimum and cooling electron Lorentz factors are given by

$$
\gamma_m = 2.8 \times 10^5 \left(\frac{1+z}{1.078}\right)^{\frac{3}{2}} \zeta_e^{-1} n_0^{-\frac{1}{2}} \varepsilon_{e,-1} \theta_{j,5}^{-1} \Delta\theta_8^3 E_{51}^{\frac{1}{2}} t_3^{-\frac{3}{2}}
$$

$$
\gamma_c = 2.3 \times 10^3 \left(\frac{1+z}{1.078}\right)^{-\frac{1}{2}} n_0^{-\frac{1}{2}} (1+Y)^{-1} \varepsilon_{B,-3}^{-1} \theta_{j,5} \Delta\theta_8^{-1} E_{51}^{-\frac{1}{2}} t_3^{\frac{1}{2}} ,
$$
(A1)

respectively, which correspond to a comoving magnetic field given by $B' \propto \left(\frac{1+z}{1.078}\right)^{\frac{3}{2}} \varepsilon_{B,-3}^{\frac{1}{2}} \theta_{j,5}^{-1} \Delta\theta_8^3 E_{51}^{\frac{1}{2}} t_3^{-\frac{3}{2}}$. The synchrotron spectral breaks can be written as

$$
\nu_m = 434.3 \text{ Hz} \left(\frac{1+z}{1.078}\right)^2 \zeta_e^{-2} n_0^{-\frac{1}{2}} \varepsilon_{e,-1}^2 \varepsilon_{B,-3}^{\frac{1}{2}} \theta_{j,5}^{-2} \Delta\theta_8^4 E_{51} t_3^{-3}
$$

$$
\nu_c = 7.3 \times 10^{-3} \text{ Hz} \left(\frac{1+z}{1.078}\right)^{-2} n_0^{-\frac{1}{2}} (1+Y)^{-2} \varepsilon_{B,-3}^{-\frac{3}{2}} \theta_{j,5}^2 \Delta\theta_8^{-4} E_{51}^{-1} t_3
$$
(A2)

respectively. The synchrotron spectral breaks in the self-absorption regime are derived from $\nu'_{a,1} = \nu'_c \tau_{0,m}^{\frac{3}{5}}$, $\nu'_{a,2} = \nu'_m \tau_{0,m}^{\frac{2}{p+4}}$ and $\nu'_{a,3} = \nu'_m \tau_{0,c}^{\frac{3}{5}}$ with the optical depth given by $\tau_{0,i} \simeq \frac{5}{3}\frac{q_e n(r) r}{B' \gamma_i^5}$, with $r$ the shock radius (Panaitescu & Mészáros 1998). Therefore, the spectral breaks in the self-absorption regime are given by

$$
\nu_{a,1} \simeq 9.7 \times 10^{-15} \text{ Hz} \left(\frac{1+z}{1.078}\right)^{-4} \zeta_e^{\frac{8}{5}} n_0^{\frac{8}{5}} \varepsilon_{e,-1}^{-1} \varepsilon_{B,-3}^{\frac{1}{5}} \theta_{j,5}^{\frac{8}{5}} \Delta\theta_8^{-8} E_{51}^{-\frac{4}{5}} t_3^3
$$

$$
\nu_{a,2} \simeq 4.7 \times 10^{-5} \text{ Hz} \left(\frac{1+z}{1.078}\right)^{-\frac{2(6-p)}{p+4}} \zeta_e^{\frac{2(2-p)}{p+4}} n_0^{\frac{10-p}{2(p+4)}} \varepsilon_{B,-3}^{\frac{p+2}{2(p+4)}} \varepsilon_{e,-1}^{\frac{2(p-1)}{p+4}} \theta_{j,5}^{\frac{2(2-p)}{p+4}} \Delta\theta_8^{\frac{4(p-6)}{p+4}} E_{51}^{\frac{p-2}{p+4}} t_3^{\frac{8-3p}{p+4}}
$$

$$
\nu_{a,3} \simeq 3.3 \times 10^{-7} \text{ Hz} \left(\frac{1+z}{1.078}\right)^{-2} \zeta_e^{\frac{3}{5}} (1+Y) n_0^{\frac{8}{5}} \varepsilon_{B,-3}^{\frac{6}{5}} \theta_{j,5}^{-\frac{2}{5}} \Delta\theta_8^{-4} E_{51}^{\frac{1}{5}} t_3 .
$$
(A3)

The deceleration time scale $t_{\text{dec}}$ can be defined using Eq. 11 and the maximum flux is

$$
F_{\max} = 4.5 \times 10^{-11} \text{ mJy} \left(\frac{1+z}{1.078}\right)^{-4} \zeta_e n_0^{\frac{5}{2}} \varepsilon_{B,-3}^{\frac{1}{2}} d_{z,27}^{-2} \theta_{j,5}^2 \Delta\theta_8^{-18} E_{51}^{-1} t_3^6 .
$$
(A4)

The dynamics of the model post the off-axis phase, generalized for a stratified ambient, are explored in further detail in Fraija et al. (2022).

# Conclusions

In this work we aimed to explore the polarization in sGRBs environments, often associated with kilonovae scenarios, and in specific, the individual GRB 170817A. To obtain that, we worked in developing a set of models that could fully explore the light curves of both sGRBs and lGRBs under Synchrotron and SSC emission mechanisms and link them to a polarization model. The works presented in this thesis were successful in their intent and were published, or are currently in peer-review process, in international journals of high impact factor. Summarily:

**Afterglow Polarization From Off-Axis GRB Jets (Pedreira et al., 2022c).** We presented the temporal evolution of polarization for the fiducial model of Fraija et al. (2022). We modeled the theoretical polarization for a set of bursts with similar afterglow characteristics, but no observed polarization data, and successfully modeled the polarization upper limits of GRB 170817A. We showed that the most commonly assumed scenarios for magnetic field anisotropy do not respect the imposed upper limits, when taking in consideration the off-axis synchrotron forward shock model as the underlying physics of the afterglow. Our obtained results were in accordance with the literature, further corroborating the underlying models.

**Polarization From A Radially Stratified Off-Axis GRB Outflow (Pedreira et al., 2022b).** We presented the temporal evolution of polarization for the fiducial model of Fraija et al. (2020), further expanded to include the possibility of partially radiative scenarios. In addition, we model the theoretical polarization for the set of bursts modeled in the aforementioned paper (no observed polarization data) and successfully modeled the polarization upper limits of GRB 170817A, obtaining results in agreement with the literature. We use these curves to further strengthen the observed similarities between these atypical bursts.

**Exploring the Early Afterglow Polarization of GRB 190829A (Pedreira et al., 2022a).** We presented the polarization of GRB 190829A, assuming that the observed polarization was generated by forward-shock synchrotron emission. We explore

a wide range of parameter sets from previously published works, where the underlying model used to describe the peculiarities of this burst varied wildly. We found that an off-axis scenario is a poor descriptor of observed data when considering simplifying assumptions. In turn, an on-axis emission is fully capable of describing the imposed polarization upper limits. These results are in agreement with the light curve modeling found in the literature, which expect this burst to have been observed on-axis. However, the off-axis scenario cannot be fully ruled out, since assuming different field anisotropies allow to solve the discrepancy between flux and polarization fitting.

**Analysis and Modeling of the Multi-wavelength Observations of the Luminous GRB 190114C (Fraija et al., 2019b).** We showed that this burst presents similar features to other LAT-detected bursts, and that the likely emission mechanism for the VHE photons was SSC, in a reverse-shock framework. The long lasting afterglow observations were consistent with a synchrotron forward shock model, evolving from a stratified wind-like medium to a homogeneous one. We infer that high-energy photons are produced in the deceleration phase, and that additional processes to synchrotron are required to describe the LAT photons with energies beyond synchrotron limit. We also claim that an outflow endowed with magnetic fields could describe the polarization properties exhibited in the light curve of this burst.

**Signatures from a Quasi-Spherical Outflow and an Off-axis Top-hat Jet Launched in a Merger of Compact Objects: An Analytical Approach (Fraija et al., 2019c).** We presented a scenario where the outflow is modeled by an off-axis homogeneous jet and a quasi-spherical component. We reported the fiducial calculations for homogeneous and wind-like media, with both Synchrotron and SSC emission mechanisms. Furthermore, we showed that the synchrotron emission of the quasi-spherical component dominates the light curve in early times ($< 20$ days), but is weaker than the off-axis emission afterwards. In addition, we presented the particular case of GRB 170817A, which we successfully model the data by applying a MCMC algorithm to the model, and show that the synchrotron emission generated by the quasi-spherical and off-axis top-hat outflows increases as $F_\nu \propto t^\alpha$, with $\alpha \leq 0.8$ and $\alpha > 3$, respectively.

**Modeling the Observations of GRB 180720B: from Radio to Sub-TeV Gamma-Rays (Fraija et al., 2019e).** We presented that similarly to GRB 190114C, this burst has similar features to other LAT-detected bursts, and that the likely emission mechanism for the VHE photons and X-ray flare was SSC, in a reverse-shock framework. The long lasting afterglow observations, on the other hand, were consistent with a synchrotron forward shock model in a homogeneous medium. Our best-fit parameters, obtained with MCMC simulations, indicate the presence of magnetic fields in the outflow, and the radio emission being in the synchrotron self-absorption regime.

**Description of Atypical Bursts Seen Slightly Off-Axis (Fraija et al., 2020).** We presented a radially stratified outflow, parameterized with a power-law velocity

distribution, to model GRB afterglows with Synchrotron and SSC emissions mechanism in a forward shock scenario. The calculations for both a homogeneous and wind-like media were demonstrated. As particular case, we show in this work that the delayed, long-lasting afterglow emission in GRB 080503, GRB 140903A, GRB 150101B, and GRB 160821B can be interpreted in a scenario likened to GRB 170817A, indicating the possibility of similar origins. Additionally, we show that this proposed scenario agrees with the Major Atmospheric Gamma-Ray Imaging Cherenkov telescope, Fermi-Large Area Telescope, and High Energy Stereoscopic System gamma-ray upper limits of GR 160921B and GRB 170817A.

**Modeling Gamma-Ray Burst Afterglow Observations With An Off-Axis Jet Emission (Fraija et al., 2022).** We presented the full extent of the synchrotron afterglow model for an off-axis homogeneous jet, generalized for any degree of ambient media stratification. This model demonstrates the outflow behavior during the coasting, deceleration and post-jet-break phases. We present the light curves of several bursts with similar afterglow characteristics: GRB 080503, GRB 140903A, GRB 150101B, GRB 160821B, and SN 2020bvc. To obtain the parameters required to calculate the light curves, we once again apply a MCMC algorithm and show that our model is consistent with observed data.

These works showed the importance of exploring multiple avenues as form of corroborating models used in GRB analysis. Afterglow modeling continues to be the main source of information regarding the physics of GRBs, but we have shown that polarization is an important and valid avenue to obtain information regarding the geometry of magnetic fields present within shock regions and to discriminate between synchrotron models. However, our works also highlight the need of more complete observations over the burst's duration, especially regarding polarization data.

While we hope our works can provide some small help towards the understanding of underlying physics GRB, we believe that more avenues should be explored in tandem to photometry and polarimetry. The exploration of numerical modeling can bring to light much more complex scenarios and help probe the processes in central engines, and the exploration of gravitational events remain an exciting prospect in this era of multi-messenger astrophysics.

We have explored many works during the PhD period. However, we lacked the time to explore a few other polarization topics, such as: a variety of structured jets; magnetic fields closer to isotropy; and the exploration of recently observed or relevant events, such as the GRB 221009A (with the highest energy photons observed to date, $\sim 18$ TeV) or a polarization modeling follow up of GRB 190114C and other bursts with VHE photons and polarization data. Works regarding these topics are currently being written, prepared to submission, or in planning phases.

# Bibliography

Abbott, B. P., Abbott, R., Abbott, T. D., & et al. 2017a, The Astrophysical Journal Letters, 848, L12. http://stacks.iop.org/2041-8205/848/i=2/a=L12

Abbott, B. P., Abbott, R., Abbott, T. D., et al. 2017b, Phys. Rev. Lett., 119, 161101, doi: 10.1103/PhysRevLett.119.161101

Abdalla, H., Adam, R., Aharonian, F., et al. 2019, Nature, 575, 464, doi: 10.1038/s41586-019-1743-9

Band, D., Matteson, J., Ford, L., et al. 1993, ApJ, 413, 281, doi: 10.1086/172995

Bayes, T., & Price, n. 1763, Philosophical Transactions of the Royal Society of London, 53, 370, doi: 10.1098/rstl.1763.0053

Becerra, R. L. 2019, PhD thesis, Universidad Autónoma Nacional de México

Beloborodov, A. M. 2000, ApJ, 539, L25, doi: 10.1086/312830

Berger, E. 2014, A, 52, 43, doi: 10.1146/annurev-astro-081913-035926

Betancourt, M. 2017, arXiv preprint arXiv:1701.02434

Blandford, R. D., & McKee, C. F. 1976, Physics of Fluids, 19, 1130, doi: 10.1063/1.861619

Cano, Z., Wang, S.-Q., Dai, Z.-G., & Wu, X.-F. 2017, Advances in Astronomy, 2017, 8929054, doi: 10.1155/2017/8929054

Covino, S., Ghisellini, G., Lazzati, D., & Malesani, D. 2003, Polarization of Gamma–Ray Burst Optical and Near-Infrared Afterglows. https://arxiv.org/abs/astro-ph/0301608

Dichiara, S., Troja, E., Lipunov, V., et al. 2022, MNRAS, 512, 2337, doi: 10.1093/mnras/stac454

Duncan, R. C., & Thompson, C. 1992, ApJ, 392, L9, doi: 10.1086/186413

Eichler, D., Livio, M., Piran, T., & Schramm, D. N. 1989, Nature, 340, 126, doi: 10.1038/340126a0

Fraija, N., De Colle, F., Veres, P., et al. 2020, ApJ, 896, 25, doi: 10.3847/1538-4357/ab88b7

Fraija, N., Dichiara, S., Pedreira, A. C. C. d. E. S., et al. 2019a, ApJ, 879, L26, doi: 10.3847/2041-8213/ab2ae4

—. 2019b, ApJ, 879, L26, doi: 10.3847/2041-8213/ab2ae4

Fraija, N., Galvan-Gamez, A., Betancourt Kamenetskaia, B., et al. 2022, arXiv e-prints, arXiv:2205.02459. https://arxiv.org/abs/2205.02459

Fraija, N., Lopez-Camara, D., Pedreira, A. C. C. d. E. S., et al. 2019c, ApJ, 884, 71, doi: 10.3847/1538-4357/ab40a9

Fraija, N., Pedreira, A. C. C. d. E. S., & Veres, P. 2019d, ApJ, 871, 200, doi: 10.3847/1538-4357/aaf80e

Fraija, N., Dichiara, S., Pedreira, A. C. C. d. E. S., et al. 2019e, ApJ, 885, 29, doi: 10.3847/1538-4357/ab3e4b

Fraija, Nissim, De Colle, F., Veres, P., et al. 2019, ApJ, 871, 123, doi: 10.3847/1538-4357/aaf564

Freedman, D. A. 2009, Statistical Models: Theory and Practice, 2nd edn. (Cambridge: Cambridge University Press), doi: 10.1017/CBO9780511815867

F.R.S., K. P. 1900, The London, Edinburgh, and Dublin Philosophical Magazine and Journal of Science, 50, 157, doi: 10.1080/14786440009463897

Galama, T. J., Vreeswijk, P. M., van Paradijs, J., et al. 1998, Nature, 395, 670, doi: 10.1038/27150

Gehrels, N., Piro, L., & Leonard, P. J. 2002, Scientific American, 287, 84

Gehrels, N., Ramirez-Ruiz, E., & Fox, D. B. 2009, A, 47, 567, doi: 10.1146/annurev.astro.46.060407.145147

Gelman, A., Carlin, J. B., Stern, H. S., & Rubin, D. B. 2004, Bayesian Data Analysis, 2nd edn. (Chapman and Hall/CRC)

Gill, R., Granot, J., & Kumar, P. 2020, MNRAS, 491, 3343, doi: 10.1093/mnras/stz2976

Goldstein, A., Veres, P., Burns, E., et al. 2017, ApJ, 848, L14, doi: 10.3847/2041-8213/aa8f41

Goodman, J., Dar, A., & Nussinov, S. 1987, ApJ, 314, L7, doi: 10.1086/184840

Granot, J. 2003, ApJ, 596, L17, doi: 10.1086/379110

—. 2005, ApJ, 631, 1022, doi: 10.1086/432676

Granot, J., Piran, T., & Sari, R. 1999, ApJ, 513, 679, doi: 10.1086/306884

Granot, J., & Taylor, G. B. 2005, ApJ, 625, 263, doi: 10.1086/429536

Guetta, D., Spada, M., & Waxman, E. 2001, ApJ, 557, 399, doi: 10.1086/321543

Hairer, E., Lubich, C., & Wanner, G. 2003, Acta Numerica, 12, 399–450, doi: 10.1017/S0962492902000144

Hastings, W. K. 1970, Biometrika, 57, 97, doi: 10.1093/biomet/57.1.97

Hoffman, M. D., Gelman, A., et al. 2014, J. Mach. Learn. Res., 15, 1593

Hotokezaka, K., & Piran, T. 2015, MNRAS, 450, 1430, doi: 10.1093/mnras/stv620

Jakobsson, P., Levan, A., Fynbo, J. P. U., et al. 2006, A&A, 447, 897, doi: 10.1051/0004-6361:20054287

Kann, D. A., Klose, S., Zhang, B., et al. 2011, ApJ, 734, 96, doi: 10.1088/0004-637X/734/2/96

Kasen, D., Badnell, N. R., & Barnes, J. 2013, ApJ, 774, 25, doi: 10.1088/0004-637X/774/1/25

Kawai, N. 2018, Nobuyuki Kawai - Exploring the origins of the Universe and elements with gamma-ray bursts, https://www.titech.ac.jp/english/public-relations/research/stories/faces30-kawai

Klebesadel, R. W., Strong, I. B., & Olson, R. A. 1973, ApJ, 182, L85, doi: 10.1086/181225

Kluyver, T., Ragan-Kelley, B., Pérez, F., et al. 2016, in Positioning and Power in Academic Publishing: Players, Agents and Agendas, ed. F. Loizides & B. Schmidt, IOS Press, 87 – 90

Kobayashi, S., Piran, T., & Sari, R. 1999, ApJ, 513, 669, doi: 10.1086/306868

Kolmogoroff, A. 1931, Mathematische Annalen, 104, 415. http://eudml.org/doc/159476

Kouveliotou, C., Meegan, C. A., Fishman, G. J., et al. 1993, The Astrophysical Journal, 413, L101

Kumar, P., & Zhang, B. 2015, Physics Reports, 561, 1, doi: https://doi.org/10.1016/j.physrep.2014.09.008

Lee, W. H., & Ramirez-Ruiz, E. 2007, New Journal of Physics, 9, 17, doi: 10.1088/1367-2630/9/1/017

Lee, W. H., Ramirez-Ruiz, E., & Page, D. 2004, ApJ, 608, L5, doi: 10.1086/422217

—. 2005, ApJ, 632, 421, doi: 10.1086/432373

Li, L.-X., & Paczyński, B. 1998, ApJ, 507, L59, doi: 10.1086/311680

Lyutikov, M., Pariev, V. I., & Blandford, R. D. 2003, ApJ, 597, 998, doi: 10.1086/378497

MacFadyen, A. I., & Woosley, S. E. 1999, ApJ, 524, 262, doi: 10.1086/307790

Mazets, E., Golenetskii, S., Il'Inskii, V., et al. 1981, Astrophysics and Space Science, 80, 3

McBreen, B., Foley, S., & Hanlon, L. 2010, Gamma-Ray Bursts Overview, arXiv, doi: 10.48550/ARXIV.1003.4440

Mészáros, P., & Rees, M. J. 1997, ApJ, 476, 232, doi: 10.1086/303625

Metzger, B. D. 2017, Living Reviews in Relativity, 20, 3, doi: 10.1007/s41114-017-0006-z

Metzger, B. D., Giannios, D., Thompson, T. A., Bucciantini, N., & Quataert, E. 2011, MNRAS, 413, 2031, doi: 10.1111/j.1365-2966.2011.18280.x

Metzger, B. D., Martínez-Pinedo, G., Darbha, S., et al. 2010, MNRAS, 406, 2650, doi: 10.1111/j.1365-2966.2010.16864.x

Mooley, K. P., Deller, A. T., Gottlieb, O., et al. 2018, Nature, 561, 355, doi: 10.1038/s41586-018-0486-3

Murdin, P. 2000, Encyclopedia of Astronomy and Astrophysics

Nakar, E. 2007, Phys. Rep., 442, 166, doi: 10.1016/j.physrep.2007.02.005

Nakar, E., & Piran, T. 2011, Nature, 478, 82, doi: 10.1038/nature10365

Narayan, R., Paczynski, B., & Piran, T. 1992, ApJ, 395, L83, doi: 10.1086/186493

Nava, L., Nakar, E., & Piran, T. 2016, MNRAS, 455, 1594, doi: 10.1093/mnras/stv2434

Paczyński, B. 1998, ApJ, 494, L45, doi: 10.1086/311148

Paczynski, B., & Rhoads, J. E. 1993, ApJ, 418, L5, doi: 10.1086/187102

Paczynski, B., & Xu, G. 1994, ApJ, 427, 708, doi: 10.1086/174178

Panaitescu, A., & Kumar, P. 2001, ApJ, 560, L49, doi: 10.1086/324061

Pedreira, A. C. C. d. E. S., Fraija, N., Dichiara, S., et al. 2022a, Exploring the Early Afterglow Polarization of GRB 190829A, ApJ(Submitted), doi: 10.48550/ARXIV.2210.12904

Pedreira, A. C. C. d. E. S., Fraija, N., Galvan-Gamez, A., et al. 2022b, Polarization From A Radially Stratified Off-Axis GRB Outflow, MNRAS(Submitted), doi: 10.48550/ARXIV.2211.12477

—. 2022c, Afterglow Polarization from Off-Axis GRB Jets, in press, ApJ, doi: 10.48550/ARXIV.2210.12904

Piran, T. 1999, Phys. Rep., 314, 575, doi: 10.1016/S0370-1573(98)00127-6

Piran, T., Nakar, E., & Rosswog, S. 2013, MNRAS, 430, 2121, doi: 10.1093/mnras/stt037

Rees, M. J., & Meszaros, P. 1992, MNRAS, 258, 41, doi: 10.1093/mnras/258.1.41P

—. 1994, ApJ, 430, L93, doi: 10.1086/187446

Robbins, H., & Monro, S. 1951, The Annals of Mathematical Statistics, 22, 400 , doi: 10.1214/aoms/1177729586

Rosswog, S. 2005, ApJ, 634, 1202, doi: 10.1086/497062

Rybicki, G. B., & Lightman, A. P. 1979, Radiative processes in astrophysics

Salvatier, J., Wiecki, T. V., & Fonnesbeck, C. 2016, PeerJ Computer Science, 2, e55

Sari, R., Piran, T., & Narayan, R. 1998, ApJ, 497, L17, doi: 10.1086/311269

Savchenko, V., Ferrigno, C., Kuulkers, E., et al. 2017, ApJ, 848, L15, doi: 10.3847/2041-8213/aa8f94

Thompson, C. 1994, MNRAS, 270, 480, doi: 10.1093/mnras/270.3.480

Troja, E., Ryan, G., Piro, L., et al. 2018, Nature Communications, 9, 4089, doi: 10.1038/s41467-018-06558-7

Usov, V. V. 1992, Nature, 357, 472, doi: 10.1038/357472a0

Van Rossum, G., & Drake, F. L. 2009, Python 3 Reference Manual (Scotts Valley, CA: CreateSpace)

Wakefield, J. 2013, Bayesian and Frequentist Regression Methods, Springer Series in Statistics (Springer New York). https://books.google.com.mx/books?id=OUJEAAAAQBAJ

Waxman, E. 2003, Nature, 423, 388, doi: 10.1038/423388a

Wiecki, T. 2013, The Inference Button: Bayesian GLMs made easy with PyMC3. https://twiecki.io/blog/2013/08/12/bayesian-glms-1/

Woosley, S. E. 1993a, ApJ, 405, 273, doi: 10.1086/172359

—. 1993b, ApJ, 405, 273, doi: 10.1086/172359

Woosley, S. E., & Bloom, J. S. 2006, A, 44, 507, doi: 10.1146/annurev.astro.43.072103.150558

Woosley, S. E., Eastman, R. G., & Schmidt, B. P. 1999, ApJ, 516, 788, doi: 10.1086/307131

Zhang, B. 2014, International Journal of Modern Physics D, 23, 1430002, doi: 10.1142/S021827181430002X

Zhang, B.-B., Uhm, Z. L., Connaughton, V., Briggs, M. S., & Zhang, B. 2016, ApJ, 816, 72, doi: 10.3847/0004-637X/816/2/72

Zhang, B.-B., Zhang, B., Murase, K., Connaughton, V., & Briggs, M. S. 2014, The Astrophysical Journal, 787, 66

# List of Figures

# List of Tables